frontiers | Research Topics

Patient-derived tumor models for drug development

Edited by
Hatim E. Sabaawy, Massimo Broggini and Shiv K. Gupta

Published in
Frontiers in Oncology

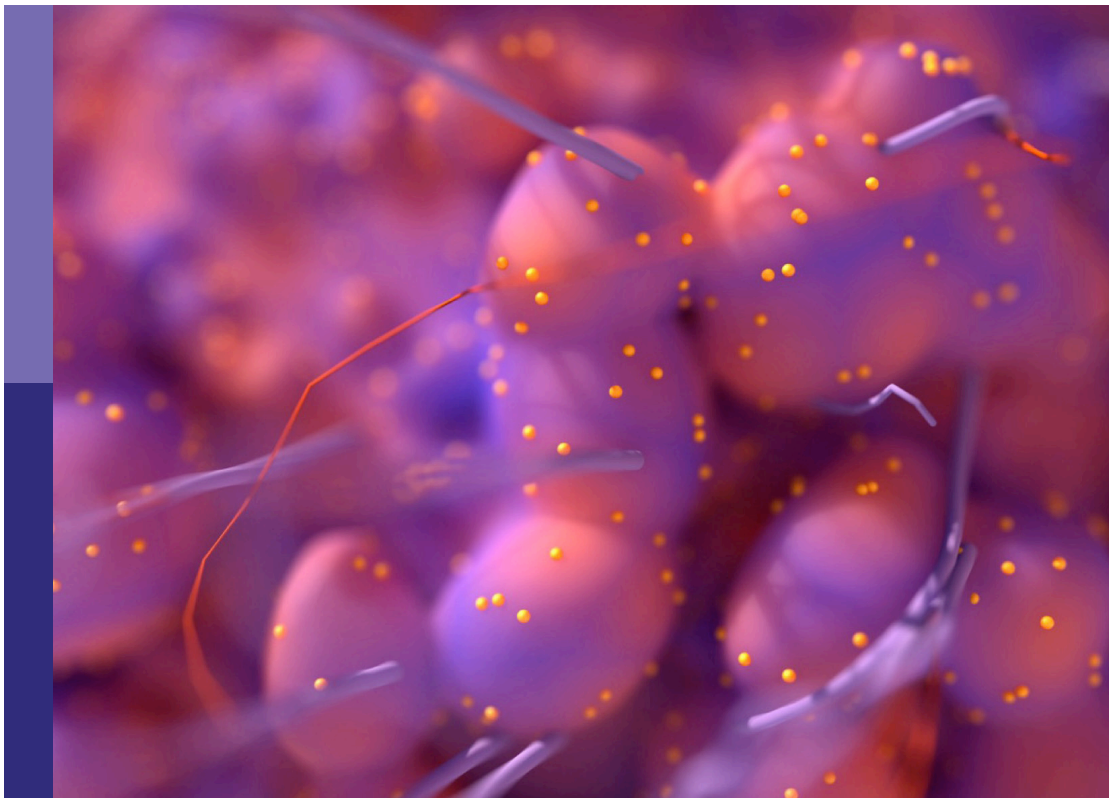

ISSN 1664-8714
ISBN 978-2-8325-3054-2
DOI 10.3389/978-2-8325-3054-2

About Frontiers

Frontiers is more than just an open access publisher of scholarly articles: it is a pioneering approach to the world of academia, radically improving the way scholarly research is managed. The grand vision of Frontiers is a world where all people have an equal opportunity to seek, share and generate knowledge. Frontiers provides immediate and permanent online open access to all its publications, but this alone is not enough to realize our grand goals.

Frontiers journal series

The Frontiers journal series is a multi-tier and interdisciplinary set of open-access, online journals, promising a paradigm shift from the current review, selection and dissemination processes in academic publishing. All Frontiers journals are driven by researchers for researchers; therefore, they constitute a service to the scholarly community. At the same time, the *Frontiers journal series* operates on a revolutionary invention, the tiered publishing system, initially addressing specific communities of scholars, and gradually climbing up to broader public understanding, thus serving the interests of the lay society, too.

Dedication to quality

Each Frontiers article is a landmark of the highest quality, thanks to genuinely collaborative interactions between authors and review editors, who include some of the world's best academicians. Research must be certified by peers before entering a stream of knowledge that may eventually reach the public - and shape society; therefore, Frontiers only applies the most rigorous and unbiased reviews. Frontiers revolutionizes research publishing by freely delivering the most outstanding research, evaluated with no bias from both the academic and social point of view. By applying the most advanced information technologies, Frontiers is catapulting scholarly publishing into a new generation.

What are Frontiers Research Topics?

Frontiers Research Topics are very popular trademarks of the *Frontiers journals series*: they are collections of at least ten articles, all centered on a particular subject. With their unique mix of varied contributions from Original Research to Review Articles, Frontiers Research Topics unify the most influential researchers, the latest key findings and historical advances in a hot research area.

Find out more on how to host your own Frontiers Research Topic or contribute to one as an author by contacting the Frontiers editorial office: frontiersin.org/about/contact

Patient-derived tumor models for drug development

Topic editors

Hatim E. Sabaawy — University of Colorado, United States

Massimo Broggini — Mario Negri Institute for Pharmacological Research (IRCCS), Italy

Shiv K. Gupta — Mayo Clinic, United States

Citation

Sabaawy, H. E., Broggini, M., Gupta, S. K., eds. (2023). *Patient-derived tumor models for drug development*. Lausanne: Frontiers Media SA.

doi: 10.3389/978-2-8325-3054-2

Table of contents

frontiers | Frontiers in Oncology

TYPE Editorial
PUBLISHED 07 July 2023
DOI 10.3389/fonc.2023.1243534

OPEN ACCESS

EDITED AND REVIEWED BY
John J. Turchi,
Indiana University Bloomington,
United States

*CORRESPONDENCE
Hatim E. Sabaawy
Hatim.Sabaawy@cuanschutz.edu

RECEIVED 20 June 2023
ACCEPTED 23 June 2023
PUBLISHED 07 July 2023

CITATION
Sabaawy HE, Broggini M and Gupta SK (2023) Editorial: Patient-derived tumor models for drug development.
Front. Oncol. 13:1243534.
doi: 10.3389/fonc.2023.1243534

Editorial: Patient-derived tumor models for drug development

Hatim E. Sabaawy[1]*, Massimo Broggini[2] and Shiv K. Gupta[3]

[1]Department of Medicine, Division of Medical Oncology, University of Colorado Anschutz Medical Campus, Aurora, CO, United States, [2]Laboratory of Molecular Pharmacology, Department of Oncology, Istituto di Ricerche farmacologiche Mario Negri (IRCCS), Milan, Italy, [3]Department of Radiation Oncology, Mayo Clinic, Rochester, MN, United States

KEYWORDS

patient-derived models of cancer, organoid, patient-derived xenograft (PDX), syngeneic graft, pre-clinical drug screen for cancer, immune checkpoint inhibitors, precision oncology, precision medicine

Editorial on the Research Topic
Patient-derived tumor models for drug development

The need for pre-clinical models to better predict the individual clinical outcome has driven the development of improved patient-derived models. Among variety of cancer models, patient derived xenografts (PDXs) and patient-derived organoids (PDOs) have shown promise to advance the field towards realizing the goals of precision cancer medicine (1–4). However, despite tremendous progress in preclinical models and technological advancement in drug screening, tumor models are not yet perfect. Ongoing studies continue to improve these models especially to address the need to - 1) reflect the intra- and inter-tumoral heterogeneity, which include but not limited to key molecular determinants of prognosis and therapeutic response (5); 2) unmask the effects of the tumor microenvironment (TME) which supports tumor progression and recurrence (6), and 3) allow testing of broader panels of novel drugs and targeted combinations, along with limiting exposure to unforeseen toxicity. These recent advances in tumor models have increasingly been incorporating components of the human immune system and have shown great potential for guiding personalized cancer therapies.

Through the collection of several insightful reviews, perspectives, and original research articles, this Research Topic aims to highlight recent progress and facilitate scintillating discussion to advance the preclinical research aligned with the goals of precision cancer medicine. We summarize here some of the key aspects covered in the various contributions, offering the readers a comprehensive understanding of this impactful area of research.

Cancer cell line models, for decades, have been extensively used in studies to gain valuable insights into tumor progression and drug responses. However, due to clonal selection and repeated passages under serum-containing medium for years, cell lines tend to have genetic drift from the original tumors (7). Nevertheless, cancer cell lines remain a primary resource to study molecular mechanisms and drug responses. Therefore, establishing cancer cell lines, especially for the rare tumor entities with limited tissue availability, is highly important. Andus et al., report the establishment and characterization of three patient derived cell lines (PDCs) for non-small cell lung cancer (NSCLC) subtypes:

adeno-, squamous cell, and pleomorphic carcinoma. PDCs of pleomorphic cell type carcinoma, for which the biological and drug response information are scarce, represent new preclinical models. Similarly, Driesch et al., report the establishment of a PDC as well as the first in-depth characterization of Medullary pancreatic carcinoma, a rare subtype of pancreatic ductal adenocarcinoma. These PDC models, with the detailed characterization of their molecular and morphological features and drug-sensitivity profile, represent valuable pre-clinical tools for advancement of precision cancer therapy.

Models of prostate cancer (PCa) are also scarce, with nearly a dozen established cell lines and fewer organoid models (8), yet personalized approaches for PCa therapy have been promising (9). Developing additional models to represent heterogeneity of PCa, that include adenocarcinoma and neuroendocrine phenotypes, are necessary. Beraud et al., report the development and characterization of five PDX models and their utility in evaluating therapeutic modalities such as androgen deprivation, PARP inhibitors and chemotherapy. These prostate cancer PDXs included hormone naïve, castrate resistant and neuroendocrine subtypes, and revealed a favorable response to PARP inhibitors in a *BRCA2* mutant neuroendocrine model. Similarly, Yu et al. report the generation of a large panel of 171 PDX models, including 85 colorectal cancer (CRC), 21 esophageal, and 65 gastric cancer PDX models. The authors correlated the clinicopathological and molecular features of tumors with PDX take rates and demonstrated that tumor biomarkers and proliferation index could be validated in PDXs. Interestingly, cetuximab had a significantly lower overall tumor response rate in patients with RAS mutation. Screening of drug sensitivity in PDX models led the authors to identify two patients with K-Ras mutant tumors that responded to cetuximab, demonstrating the use of PDX models in patient case reports of CRC therapy. Two different incisive reviews by Liu et al. and Aaltonen et al., describe recent advances and knowledge gaps in lung cancer and neuroblastoma research, respectively, where patient derived models have been extensively used in co-clinical avatar studies for precision medicine.

Beyond the evaluation of drug distribution and therapeutic responses in live animals, PDX models can serve in multiple ways. For example, readily available PDX samples can be leveraged to identify novel targets and biomarkers through exploratory studies, which otherwise may not be feasible due to paucity of patient tissue. Ferrarini et al., performed a proof-of-concept study using lung adenocarcinoma PDXs and demonstrated plurimetabolic state in 9 of 14 PDXs analyzed. Expanding on the utility of PDXs in Neurooncology, Alcaniz et al., established and characterized 23 IDH-wt glioblastoma (GBM) PDXs, initially as heterotopic GBM PDXs, then propagated as brain orthotopic models, to assess drug resistance, and the impact of TME and blood brain barrier (BBB), which are key limitations to therapeutic response in orthotopic GBM models (10). Deng et al., demonstrated the efficacy of small molecule inhibitor of Sonic hedgehog (Shh) signaling in limiting cholesterol metabolism which supports medulloblastoma growth. Despite the extensive utility of PDXs propagated in immune compromised animals and ex vivo in tissue culture, PDX models have limited applicability specially to study TME or tumor immune response. Furthermore, tumor take rates are variable, consequently only a fraction of any given tumor type can be timely established as PDXs for co-clinical avatar studies. Slower growth rate and clonal selection in the mouse background can also cause unpredictability, these challenges have been overlooked with their growing list of advantages in oncology.

Patient-derived tumor organoids (PDOs) are cultures of cells resected tumors from an individual patient. PDOs can serve as models to understand patient-specific drug responses and to investigate cancer cell growth, and molecular analysis. The overall importance of PDOs has been nicely highlighted by a review article (Verduin et al.) and a perspective article (Wang et al.). The review collected data obtained from 60 published data spanning different tumor types. The authors concluded that PDOs have indeed the potential to predict response to treatment and have high translatability to the clinics. They highlighted the possibility to use PDOs in high-throughput studies to define targets, examine treatment response and further personalize these treatments. The authors especially highlight the discordance between *in vitro* vs. *in vivo* drug efficacy, that could be due to dose limiting toxicity in normal tissues. Therefore, evaluating drug sensitivity using normal tissue organoids in parallel with that in cancer organoids is a valuable addition to the organoid based co-clinical avatars in precision cancer medicine. Wang et al. specifically touched on the potential of PDOs as models in cancer immunotherapy. The use of complex organoids with enhanced heterogeneity of cell populations is an approach we must encourage to have the potential of studying the interaction between cancer cells and stroma, especially immune cells, at the basic and translational levels. Since PDOs lack vasculature, nervous system and drug metabolic pathways, this platform cannot be used for testing all drugs. Considering these limitations, Tan et al., adapted a strategy to use PDOs with available PDXs, established for the advanced gallbladder cancer, for initial rapid drug screening and *in vivo* drug efficacy validation, respectively, and allude to making these two models complementary. This approach can guide the individualized treatment strategies for cancer patients, when PDXs could be established in timely fashion.

Cancer immunotherapy has revolutionized the field of oncology by prolonging survival and quality of life for cancer patients. However, a comprehensive *in vivo* evaluation of immunotherapies is not possible in PDX models raised in immune compromised animals. Humanized mouse models, i.e., severely immune deficient strain engrafted with a human immune system, represent the most relevant platform to test and validate cancer immunotherapy approaches. Here, two original manuscripts describe the results from *in vivo* evaluation of immune checkpoint inhibitors (ICIs) using humanized mouse models. First, Tan et al, report that gallbladder tumor PDXs in humanized mice, generated with human peripheral blood mononuclear cells and treated with

nivolumab, show immune cell death in tumors and that PD-L1 expression is not a direct indicator of the tumor suppressive activity of ICI, a finding that reflects the consensus on the unreliability of PD-L1 expression as a biomarker and the need for better biomarkers for response to ICI-based immunotherapy. Second, Marie et al., report the improvement of the traditional CRC PDX models by developing novel humanized CRC PDX models utilizing autologous (from same CRC patient) or allogeneic (from healthy donor) PBMCs. Marie et al., elegantly demonstrated that while immune (HLA)-mismatched allogeneic models developed graft-vs-tumor effects limiting their utility, autologous humanized mice were proven useful, when used within a window-of-treatment, in detecting T-cell responses, myeloid cell infiltration and predicting responses to ICIs and potential combination therapies. The authors also demonstrate that modulation of immuno-suppressive cells, such as regulatory T cells within the TME can augment the efficacy of ICI agents in CRC. The use of newly available mouse strains with expression of human cytokines or those lacking mouse major histocompatibility proteins could potentially improve the support of engrafted immune cells and the therapeutic window in humanized animals.

Overall, the collection of articles in this Research Topic provides important additions to the arena of clinically relevant patient derived models to be utilized for drug testing and offers a roadmap to build on to achieve the goals of precision cancer medicine.

Author contributions

All authors listed have made a substantial, direct, and intellectual contribution to the work and approved it for publication.

Funding

HS is supported by the National Cancer Institute (7R01CA226746 to HS), University of Colorado Cancer Center, supported, in part, with funding from NCI-CCSG (P30CA04693424), and in part, with funding from the National Pancreatic Cancer Foundation. SKG is supported by the Eagles 5th District Cancer Telethon- Cancer Research Fund, R03CA201612 and U19CA264362 - Center of Innovation for Brain Tumor Therapeutics, Pilot Program.

Acknowledgments

We thank all the patients for consenting to donating their tissues for the generation of patient derived models. We also thank all the authors who contributed to this Research Topic.

Conflict of interest

The authors declare that the research was conducted in the absence of any commercial or financial relationships that could be construed as a potential conflict of interest.

Publisher's note

References

1. Hidalgo M, Amant F, Biankin AV, Budinska E, Byrne AT, Caldas C, et al. Patient-derived xenograft models: an emerging platform for translational cancer research. *Cancer Discov* (2014) 4(9):998–1013. doi: 10.1158/2159-8290.CD-14-0001

2. Gao H, Korn JM, Ferretti S, Monahan JE, Wang Y, Singh M, et al. High-throughput screening using patient-derived tumor xenografts to predict clinical trial drug response. *Nat Med* (2015) 21(11):1318–25. doi: 10.1038/nm.3954

3. Vlachogiannis G, Hedayat S, Vatsiou A, Jamin Y, Fernandez-Mateos J, Khan K, et al. Patient-derived organoids model treatment response of metastatic gastrointestinal cancers. *Science* (2018) 359(6378):920–6. doi: 10.1126/science.aao2774

4. Li M, Izpisua Belmonte JC. Organoids - preclinical models of human disease. *N Engl J Med* (2019) 380(6):569–79. doi: 10.1056/NEJMra1806175

5. Iezzi A, Caiola E, Colombo M, Marabese M, Broggini M. Molecular determinants of response to PI3K/akt/mTOR and KRAS pathways inhibitors in NSCLC cell lines. *Am J Cancer Res* (2020) 10(12):4488–97.

6. Junttila MR, de Sauvage FJ. Influence of tumour micro-environment heterogeneity on therapeutic response. *Nature* (2013) 501(7467):346–54. doi: 10.1038/nature12626

7. Gillet JP, Calcagno AM, Varma S, Marino M, Green LJ, Vora MI, et al. Redefining the relevance of established cancer cell lines to the study of mechanisms of clinical anti-cancer drug resistance. *Proc Natl Acad Sci U.S.A.* (2011) 108(46):18708–13. doi: 10.1073/pnas.1111840108

8. Pamarthy S, Sabaawy HE. Patient derived organoids in prostate cancer: improving therapeutic efficacy in precision medicine. *Mol Cancer* (2021) 20(1):125. doi: 10.1186/s12943-021-01426-3

9. Bartucci M, Ferrari AC, Kim IY, Ploss A, Yarmush M, Sabaawy HE. Personalized medicine approaches in prostate cancer employing patient derived 3D organoids and humanized mice. *Front Cell Dev Biol* (2016) 4:64. doi: 10.3389/fcell.2016.00064

10. Gupta SK, Smith EJ, Mladek AC, Tian S, Decker PA, Kizilbash SH, et al. PARP inhibitors for sensitization of alkylation chemotherapy in glioblastoma: impact of blood-brain barrier and molecular heterogeneity. *Front Oncol* (2018) 8:670. doi: 10.3389/fonc.2018.00670

frontiers in Oncology

REVIEW
published: 18 March 2021
doi: 10.3389/fonc.2021.641980

Patient-Derived Cancer Organoids as Predictors of Treatment Response

Maikel Verduin[1]*, *Ann Hoeben*[2], *Dirk De Ruysscher*[1] and *Marc Vooijs*[1]

[1] Department of Radiation Oncology (MAASTRO), GROW School for Oncology and Developmental Biology, Maastricht University Medical Center+, Maastricht, Netherlands, [2] Department of Medical Oncology, GROW School for Oncology and Developmental Biology, Maastricht University Medical Center+, Maastricht, Netherlands

Patient-derived cancer organoids have taken a prominent role in pre-clinical and translational research and have been generated for most common solid tumors. Cancer organoids have been shown to retain key genetic and phenotypic characteristics of their tissue of origin, tumor subtype and maintain intratumoral heterogeneity and therefore have the potential to be used as predictors for individualized treatment response. In this review, we highlight studies that have used cancer organoids to compare the efficacy of standard-of-care and targeted combination treatments with clinical patient response. Furthermore, we review studies using cancer organoids to identify new anti-cancer treatments using drug screening. Finally, we discuss the current limitations and improvements needed to understand the full potential of cancer organoids as avatars for clinical management of cancer therapy.

Keywords: organoids, precision medicine, treatment response, treatment prediction, cancer, patient-derived

OPEN ACCESS

Edited by:
Massimo Broggini,
Istituto di Ricerche Farmacologiche Mario Negri (IRCCS), Italy

Reviewed by:
Sabrina Fritah,
Luxembourg Institute of Health, Luxembourg
Atish Mohanty,
City of Hope National Medical Center, United States

***Correspondence:**
Maikel Verduin
maikel.verduin@mumc.nl;
marc.vooijs@maastrichtuniversity.nl

Specialty section:
This article was submitted to Cancer Molecular Targets and Therapeutics, a section of the journal Frontiers in Oncology

Received: *15 December 2020*
Accepted: *01 March 2021*
Published: *18 March 2021*

Citation:
Verduin M, Hoeben A, De Ruysscher D and Vooijs M (2021) Patient-Derived Cancer Organoids as Predictors of Treatment Response. Front. Oncol. 11:641980. doi: 10.3389/fonc.2021.641980

INTRODUCTION

Cancer remains one of the leading causes of death in the 21st century. Despite enormous progress in the identification of mechanisms of tumor progression and treatment resistance and the development of new tumor targeted treatments many patients do not get cured. The main challenge remains to achieve accurate patient selection. Tumor biopsies used for clinical diagnostics do not capture the extensive intratumoral heterogeneity that masks emergent tumor clones with intrinsic or acquired resistance. This can result in patients receiving suboptimal treatment, or overtreatment leading to long-lasting harmful side-effects. The development of specific biomarkers and predictive model systems are therefore essential to personalized treatment leading to more durable responses with fewer side effects.

In the last decade, translational cancer research has witnessed a revolution with the development of methods that enable the reproducible derivation, maintenance and biobanking of primary human normal and cancer tissues. These primary cell cultures, called organoids, are three dimensional stem-cell derived cultures that support the propagation of phenotypic, genetic and transcriptomic characteristics from the original tissue and retain the self-renewal properties of stem cells and their ability to undergo multilineage differentiation indefinitely. This revolution took off after the development of 'mini-guts' from Lgr5+ intestinal stem cells which replicate the dynamic proliferation and differentiation of the intestinal crypt epithelium in culture (1) and thereafter from colorectal cancer biopsies to derive colorectal cancer (CRC) organoids (2). Importantly cancer organoids have been shown to retain intratumoral heterogeneity and tumor clonal hierarchy; a

major limiting factor in treatment effectiveness and recurrence (3). Excellent comprehensive reviews on the derivation and characterization of organoid systems can be found here and will not be further elaborated on in this review (4). To date cancer organoids have been developed from many cancer types and have been shown to maintain a stable genetic and phenotypic representation of the original tumor in culture compared to classic 2D monolayer cell cultures. Like patient-derived xenograft (PDX), cancer organoids also have maintained intratumor heterogeneity but are less expensive and labor-intensive and reduce laboratory animal usage. On the other hand, PDX models include the tumor micro-environment and *in vivo* drug metabolism which are currently not accounted for in cancer organoids (5).

Whether cancer organoids can also function as avatars for prospective target identification and treatment selection at the patient level is not yet known. If so, cancer organoids could have a profound impact on individualized cancer treatment. In this review, we describe studies that have addressed whether cancer organoids are predictors for clinical response.

MATERIALS AND METHODS

A literature search was conducted using publicly available databases (PubMed, MEDLINE, and Web of Science) up to October 2020. For the purpose of this review, cancer organoids were defined as stem-cell derived three-dimensional cell culture models derived from primary patient-derived solid tumors using a basement membrane extract (BME). Articles describing patient-derived-xenograft (PDX)-derived cancer organoids, iPSC based models or three-dimensional cell culture systems lacking a BME (i.e. slice cultures or tumor-on-a-chip approaches) were excluded. Search keywords included [ORGANOID] or [TUMOROID] and, [CANCER] and [TREATMENT]. Only articles in which cancer organoids were subjected to treatment and correlated to patient outcome or potential biomarkers were included. Establishment, characterization and comparison of cancer organoids towards the parental tumor have already been previously described and fall outside the scope of this review (6, 7).

RESULTS

A total of 60 studies were included in this review. For almost all papers the cancer organoids used were (previously) compared on a genetic and phenotypic level to the parental tumor in order to validate the model. Study characteristics are summarized in **Table 1**.

Gastro-intestinal (GI) Cancer

In 2015 the first colorectal cancer (CRC) organoid biobank was established and used for drug screening. Based on these drug screens, gene-drug interactions could be studied to identify potential biomarkers and study the molecular basis for drug response to both new therapeutic agents as well as current standard-of-care chemotherapeutics (2).

Esophageal adenocarcinoma organoids were subjected to standard-of-care chemotherapy (5-FU, epirubicin and cisplatin). All but one of the patients used for organoid derivation showed poor clinical response to chemotherapy which was recapitulated in the corresponding cancer organoids, though organoids from the patient that showed clinical response were not available for drug testing (13). This overlap between organoid and tumor response for four patients towards chemotherapeutics (cisplatin, paclitaxel, 5-FU, epirubicin and irinotecan) was also observed in another study (28).

A similar approach was taken using gastric cancer organoids. In one study, gastric cancer organoids derived from one patient at pre-treatment were sensitive to standard-of-care chemotherapy (5-fluorouracil (5-FU), cisplatin, oxaliplatin and irinotecan) which reflected the complete pathologic response in the patient after chemoradiation, albeit the contribution of radiotherapy to the clinical response was not investigated (12). In another study conflicting results for combined treatment with 5-FU, oxaliplatin and epirubicin were obtained. From the seven gastric cancer patients included in the study, correlation of treatment sensitivity (5-FU, oxaliplatin and epirubicin combination treatment) with clinical response could only be made for two patients. Only for one of these patients the organoid response matched the clinical response (21).

Ascites-derived gastric cancer organoids showed a heterogeneous response towards standard-of-care chemotherapeutics (oxaliplatin, 5-FU, cisplatin, docetaxel, irinotecan, epirubicin and paclitaxel) between patients, similar to the mixed clinical responses seen in patients with peritoneal metastases, though no direct clinical comparison could be made (16).

CRC organoids were used to identify patients that benefit from the PARP inhibitor olaparib and cross sensitivity to oxaliplatin, which causes PARP-dependent DNA damage repair. In two patients that responded to oxaliplatin the organoids were sensitive to both olaparib and oxaliplatin. In another patient that responded, the organoids showed resistance to both treatments. Notably the organoids from this patient were highly responsive towards panitumumab which was also part of the clinical treatment and might have been a main factor in the clinical response and explain the discrepancy between organoid and clinical response (29).

The TUMOROID study used organoids derived from metastatic CRC and correlated the organoid treatment response towards the corresponding clinical response. Organoids were able to predict the response to irinotecan-based therapies in more than 80% of patients without misclassifying patients who responded to the treatment. This predictive value was not identified for 5-FU and oxaliplatin combined treatment. A possible explanation for this could be that the tumor micro-environment (stromal and immune cells), not present in organoids, might influence the efficacy of one treatment more than the other (23). In another study, organoids

TABLE 1 | Summary of study characteristics and main results.

Study	Cancer type	Organoid establishment success rate (%)	# of organoid lines used for treatment experiments	Multiple organoid lines per patient	Matched healthy tissue organoids	Standard-of-care testing	Clinical comparison	Drug screen	Outcomes regarding prediction of clinical treatment response
Gastro-intestinal cancer									
van de Wetering M. et al. (2)	Colorectal cancer	90%	19						Drug screen on organoids. No clinical comparison.
Koppens M. et al. (8)	Colon cancer	not reported	2						Efficacy of EZH2 inhibition in organoids. No clinical comparison.
Verissimo CS. et al. (9)	RAS mutant colorectal cancer	n.a.	2						Organoid response towards EGFR-RAS-ERK targeting in relation to KRAS mutation status. No clinical comparison.
Buzzelli JN. et al. (10)	Colorectal cancer liver metastases	76.5%	3						Efficacy of standard-of-care chemotherapy in organoids. No clinical comparison.
Vlachogiannis G. et al. (11)	Metastatic gastrointestinal tumors	not reported	21						Sensitivity 100%, specificity 93%, PPV 88%, NPV 100% for organoids in forecasting clinical response to targeted agents or chemotherapeutics.
Gao M. et al. (12)	Gastric cancer	not reported	2 (from 1 patient)						Testing of standard-of-care chemotherapeutics. Descriptive clinical comparison (N=1) showed lowest IC50 value for 5-FU (out of 4 chemotherapeutics tested) and clinical complete response after 5-FU/RTx treatment. No testing for contribution of RTx to clinical effect.
Li X. et al. (13)	Esophageal adenocarcinoma	31%	9						Drug screen on organoids. Descriptive comparison showing lack of chemotherapy sensitivity in most organoid cultures which resembled the poor clinical response observed.
Yan HHN. et al. (14)	Gastric cancer	50% (cancer), 100% (healthy)	9 (from 7 patients)						Drug screen on organoids. Descriptive comparison showing lack of organoid response to 5-FU in a patient that showed progressive disease upon 5-FU. Two other patients showed a clinical response to 5-FU/cisplatin which was resembled in the organoids.
Votanopoulos KI. et al. (15)	Appendiceal cancer	75%	9						Chemosensitivity testing of organoids. No clinical comparison.
Li J. et al. (16)	Gastric cancer (ascites-derived)	92%	7						Drug screening of organoids. No clinical comparison.
Schumacher D. et al. (17)	Colorectal cancer	not reported	38						Efficacy of EGFR-targeted therapy and its downstream targets (MEK and mTOR) in relation to KRAS mutation status in organoids. No clinical comparison.
Seidlitz T. et al. (18)	Gastric cancer	not reported	4						Drug testing of organoids (targeting HER2, c-KIT or

(Continued)

TABLE 1 | Continued

Study	Cancer type	Organoid establishment success rate (%)	# of organoid lines used for treatment experiments	Multiple organoid lines per patient	Matched healthy tissue organoids	Standard-of-care testing	Clinical comparison	Drug screen	Outcomes regarding prediction of clinical treatment response
									CDK4/6). No clinical comparison.
Ubink I. et al. (19)	Colorectal peritoneal metastases	Not reported	5						Sensitivity to HIPEC chemotherapy and efficacy of addition of ATR inhibitor. No clinical comparison.
Pasch CA. et al. (20)	Multiple types of cancer (treatment only on (m)CRC)	76%	5						Descriptive clinical comparison (N=1). Clinical response to FOLFOX in a patient of which the organoid showed an intermediate response towards 5-FU/oxaliplatin treatment.
Steele NG. et al. (21)	Gastric cancer	not reported	6						Drug screening of organoids. Descriptive clinical comparison (N=2) showing a similar response in the organoid for one patient but not in the other.
Ganesh K. et al. (22)	Rectal cancer	77%	21						Drug screening of organoids. Clinical comparison for chemotherapy (N=7) showing a correlation of AUC for both 5-FU and FOLFOX with progression-free survival of the corresponding patient (r=0.86, p=0.024). Descriptive comparison of radiosensitivity (N=7) showing organoid responds corresponds with clinical radiotherapy response.
Ooft SN. et al. (23)	Metastatic colorectal cancer	63%	Varies per treatment						Prediction of response to irinotecan monotherapy (N=10): accuracy of classifier 80%. Prediction of response to 5-FU/irinotecan combination therapy (N=12): 83.3% correctly classified. Prediction of response to 5-FU-oxaliplatin (N=16): no correlation with clinical response.
Costales-Carrera A. et al. (24)	Colon cancer	not reported	3						Efficacy of plocabulin in organoids. No clinical comparison.
Yao Y. et al. (25)	Locally advanced rectal cancer	85.7%	80						High correlation between organoid response and clinical outcomes for prediction of neoadjuvant chemoradiation efficacy: AUC 88.20% (76.46-98.67%), accuracy 84.43% (72.40-93.75%), sensitivity 78.01% (55.56-95%), specificity 91.97% (77.78-100%).
Narasimhan V. et al. (26)	Colorectal peritoneal metastases	68%	15						Drug screening of organoids. Descriptive clinical comparison (N=3) in which drug treatment was selected based on organoid sensitivity which was successful for 1 patient.

(Continued)

TABLE 1 | Continued

Study	Cancer type	Organoid establishment success rate (%)	# of organoid lines used for treatment experiments	Multiple organoid lines per patient	Matched healthy tissue organoids	Standard-of-care testing	Clinical comparison	Drug screen	Outcomes regarding prediction of clinical treatment response
Zerp SF. et al. (27)	Colorectal cancer	not reported	3						Efficacy of APG-880 as a radiosensitizer in organoids. No clinical comparison.
Derouet MF. et al. (28)	Esophageal adenocarcinoma	57.2%	16						Descriptive clinical comparison (N=4) showing an overlap between the organoid and tumor response.
Arena S. et al. (29)	Colorectal cancer	not reported	5						Drug testing on organoids. Descriptive clinical comparison (N=3) which corresponded with organoid sensitivity.
Abdominal (non-GI tract) cancer									
Huang L. et al. (30)	Pancreatic cancer	not reported	5						Drug screen of organoids. No clinical comparison.
Broutier L. et al. (31)	Liver cancer	44%	6						Drug sensitivity testing of organoids. No clinical comparison.
Nuciforo S. et al. (32)	Hepatocellular carcinoma	26%	12						Efficacy of sorafenib on organoids. No clinical comparison.
Tiriac ML. 2018 (33)	Pancreatic cancer	75%	66						Descriptive comparison of organoid response towards clinical response. For one patient retrospective clinical data paralleled the chemosensitivity profile of the organoid.
Li L. et al. (34)	Liver cancer	not reported	27 (from 5 patients)						Drug screen of organoids. No clinical comparison.
Hennig A. et al. (35)	Pancreatic cancer	71%	10						Efficacy of standard-of-care chemotherapy stratified for KRT81 status. No clinical comparison.
Bian B. et al. (36)	Pancreatic cancer	not reported	24						Efficacy of BET-inhibitor treatment on organoids. No clinical comparison.
Driehuis E. et al. (37)	Pancreatic cancer	62%	24						Drug screen on organoids. Descriptive comparison towards clinical response (N=4) showing an overall correlation between organoid and clinical response.
Ponz-Sarvise M. et al. (38)	Pancreatic cancer	not reported	2						Drug sensitivity testing of organoids. No clinical comparison.
Castven D. et al. (39)	Liver cancer	11%	5						Testing efficacy of targeted agents based on mutational variants in organoids. No clinical comparison.
Sharick JT. et al. (40)	Pancreatic and Breast cancer	64% (for pancreatic cancer), 54% (for breast cancer)	7 (pancreas), 11 (breast)						Using metabolic heterogeneity to predict treatment response in pancreatic cancer organoids (N=7). Three patients were classified as predicted non-responders and all showed tumor recurrence within one year whereas four patients that were classified as predicted responders all remained free of

(Continued)

TABLE 1 | Continued

Study	Cancer type	Organoid establishment success rate (%)	# of organoid lines used for treatment experiments	Multiple organoid lines per patient	Matched healthy tissue organoids	Standard-of-care testing	Clinical comparison	Drug screen	Outcomes regarding prediction of clinical treatment response
									tumor recurrence for more than one year.
Seppälä TT. et al. (41)	Pancreatic cancer	77%	13						Pharmacotyping of organoids. No clinical comparison.
Saltsman J. et al. (42)	Hepatoblastoma	not reported	1						Drug testing on normal liver and tumor organoid from one patient. No clinical comparison.
Liu J. et al. (24)	Liver cancer	not reported	4						Effect of co-culture system with cancer-associated fibroblasts on drug sensitivity in organoids. No clinical comparison.
Urogenital and gynecological cancer									
Gao D. et al., 2014 (43)	Metastatic prostate cancer or CTCs	15-20%	6						Sensitivity to androgen receptor and PI3K inhibitors in organoids. No clinical comparison.
Girda E. et al. (44)	Endometrial cancer	100%	14 (varies per drug)						Drug testing on organoids. No clinical comparison.
Lee SH. et al. (45)	Bladder cancer	70%	11						Drug screen of organoids and comparison to in vivo (mice) response. No clinical comparison.
Puca L. et al. (46)	Prostate cancer	16%	6						Drug screening on organoids. No clinical comparison.
Kopper O. et al. (47)	Ovarian cancer	65%	21						Descriptive clinical comparison: organoids derived from clinical resistant recurrent disease were more resistant compared to the clinically sensitive primary disease counterpart (N=1). Drug screen of organoids and comparison to in vivo (mice) response.
Boretto M. et al. (48)	Endometrial cancer	20%	5						Drug response to standard-of-care chemotherapeutics. No clinical comparison.
Mullenders J. et al. (49)	Bladder cancer	57.9%	3						Drug response to standard-of-care chemotherapeutics. No clinical comparison.
Calandrini C. et al. (50)	Childhood kidney cancer	100% for healthy tissue, 75% for Wilms tumor, 100% for MRTK, 75% for RCC. Unsuccessful for rare kidney tumor types	4						Drug screen of cancer and healthy tissue organoids. No clinical comparison.
de Witte C.J. et al. (51)	Ovarian cancer	not reported	36						Drug screening on organoids. Organoid drug response to carboplatin+paclitaxel treatment showed significant correlation with clinical response (N=7, P<0.01). PDOs generated at interval debulking recapitulated the clinical response to first-line carboplatin and paclitaxel combination treatment for

(Continued)

TABLE 1 | Continued

Study	Cancer type	Organoid establishment success rate (%)	# of organoid lines used for treatment experiments	Multiple organoid lines per patient	Matched healthy tissue organoids	Standard-of-care testing	Clinical comparison	Drug screen	Outcomes regarding prediction of clinical treatment response
									histopathological (p = 5.821e 05), biochemical (p = 0.0004), and radiological (p = 0.0092) outcomes.
Central nervous system cancer									
Hubert CG. et al. (52)	Glioblastoma	not reported	1						Identification of radioresistant cells in organoids. No clinical comparison.
Saengwimol D. et al. (53)	Retinoblastoma	83%	1						Effects of standard-of-care chemotherapeutics. No clinical comparison.
Scognamiglio G. et al. (54)	Chordoma	not reported	3						Efficacy study of nivolumab. No clinical comparison.
Loong HF. et al. (55)	Glioblastoma	n.a.	1						Prospective identification of everolimus as treatment option using organoids showing subsequent partial clinical response.
Chadwick M. et al. (56)	Glioblastoma	not reported	4						Drug screen on organoids. No clinical comparison.
Breast cancer									
Sachs N. et al. (57)	Breast cancer	>80%	28						Drug screening of organoids and comparison to in vivo response in mice. No clinical comparison.
Li X. et al. (58)	Breast cancer	n.a.	1						Case-report for drug screening on organoids. No clinical comparison.
Pulmonary cancer									
Sachs N. 2019 (59)	NSCLC	28%	4						Response to multiple chemotherapeutics and TKI's. No clinical comparison.
Kim M. et al. (60)	Lung cancer	87%	5						Response to docetaxel, olaparib, erlotinib and crizotinib. No clinical comparison.
Chen J. et al. (61)	NSCLC	not reported	7						Response to chemotherapeutics and targeted agents in organoids. No clinical comparison.
Li Z. et al. (62)	NSCLC	80%	12						Drug screen on organoids. No clinical comparison.
Head-and-neck cancer									
Tanaka N. et al. (63)	Head-and-neck cancer	37.2%	4						Response to cisplatin and docetaxel. No clinical comparison.
Driehuis E. et al. (64)	HNSCC	65%	13						Descriptive comparison of response to radiotherapy (N=7). Organoid response for 6 patients was similar to the observed clinical response. Healthy organoids were not subjected to treatment.
Driehuis E. et al. (65)	HNSCC	n.a.	8						Efficacy of EGFR-targeted photodynamic therapy. No clinical comparison.

from one metastatic CRC patient showed an intermediate response towards 5-FU and oxaliplatin combination treatment which mimicked the clinical response observed after re-treatment with FOLFOX (20).

Treatment sensitivity analysis on peritoneal CRC metastasis organoids could not separate patients with clinical partial response from those with progressive disease after FOLFOX. However, most of the patients in this study received pre-operative chemotherapy which may have led to selection of chemo-resistant subclones. Two patients did not receive oxaliplatin-based therapies and showed the highest sensitivity towards the treatment *in vitro*. Furthermore, two treatment-refractory patients were treated with a drug that was selected based on the drug sensitivity observed in their corresponding organoids. One patient received vandetanib (pan-tyrosine-kinase inhibitor) which strongly reduced organoid viability, however no clinical response was observed. For another patient, gemcitabine showed an initial partial clinical response but after two additional months of treatment, disease progression was again observed (26). Peritoneal CRC-metastases organoids were also treated for efficacy towards mitomycin C and oxaliplatin (commonly used in HIPEC; intra-peritoneal chemotherapy treatment) and showed a general resistance, corresponding with the high recurrence rates observed in clinic (19).

Organoids from metastatic GI cancers also predicted sensitivity towards cetuximab (anti-EGFR monoclonal antibody), and reflected clinical resistance in a patient who, based on molecular markers (EGFR amplification and KRAS wild-type), was expected to respond to the treatment (11).

Rectal cancer organoids were exposed to standard-of-care chemotherapy (5-FU alone or FOLFOX (5-FU with leucovortin and oxaliplatin)) or radiotherapy (single dose, 0-8Gy). A high correlation (r=0.86) for 5-FU or FOLFOX was observed when compared to the progression-free survival (PFS) of the corresponding seven patients. For radiotherapy, organoids that showed resistance to radiotherapy were derived from previously irradiated tumors or from tumors that showed no to minimal clinical response. On the other hand, more radiosensitive organoids were derived from patients who had a minimal 50% reduction in tumor circumference endoscopically or a near-complete or a clinical complete response following radiotherapy (22). Additionally organoids (N=80) treated with neoadjuvant chemoradiation (5-FU and irinotecan) also reported promising predictive value for clinical response to neoadjuvant chemoradiation (sensitivity 78.01%, specificity 91.97%) (25).

As a proof-of-concept, the influence of KRAS mutation-mediated resistance to EGFR-targeted therapy using cetuximab was tested in rectal cancer organoids. In accordance with clinical trial data, KRAS-mutated organoids showed more resistance towards cetuximab compared to the KRAS wild-type organoids (22). These findings were also confirmed in an independent rectal cancer organoid biobank (66) and for combined EGFR and MEK inhibition in CRC organoids (9).

Multiple studies have used organoids to screen for efficacious targeted agents based on genomic targetable variants present in the organoids. This approach was taken using gastric cancer organoid biobanks, CRC cancer organoids and in esophageal cancer organoids in which drug screening approaches identified patient subsets with potential vulnerability to new targeted agents (8, 13, 14, 17, 18, 24, 67).

Finally, organoids were used to improve current treatments. CRC organoids showed an enhanced response to radiotherapy when organoids were simultaneously exposed to radiosensitizer APG-880 (27). Peritoneal CRC-metastases organoids were used to optimize HIPEC treatment. Because mitomycin C (used in HIPEC) mainly induces interstrand crosslinks which activates ATR, the addition of ATR inhibitors to mitomycin C improved treatment efficacy on cancer organoids, identifying a potential new clinical strategy (19).

Hepatobiliary Tract and Pancreatic Cancer

Pancreatic cancer is one of the most lethal malignancies as it is often diagnosed in an advanced stage, has a high recurrence rate and only a minor survival benefit can be achieved with systemic therapy. This resistance to gemcitabine was also observed in pancreatic cancer organoids, though no clinical correlation could be made (30).

An organoid-derived pharmaco-transcriptomic signature was developed to predict drug sensitivity to gemcitabine monotherapy but it did not predict response in patients receiving a combination treatment with other chemotherapeutics (33). Similar correlation between clinical response and gemcitabine sensitivity in pancreatic cancer organoids were found by others as well (37). Another study also showed the feasibility of pharmacotyping pancreatic cancer organoids in a timely manner to guide postoperative chemotherapeutic selection (41).

Pancreatic cancer organoid cultures derived from multiple different metastatic sites from the same patient showed a differential sensitivity towards 5-FU, but not towards the other chemotherapeutics tested. This suggests the existence of cancer subclones that differ between metastatic sites which are maintained in their respective cancer organoids (33).

Optical metabolic imaging (OMI) was used to assess treatment response in pancreatic cancer organoids and classify patients. OMI is a high-resolution fluorescence microscopy technique that quantifies the metabolic state of individual cells. This technique measures drug response in heterogeneous 3D populations faster than more traditional methods, as changes in cell metabolism precede changes in cell viability (40). Using OMI on cancer organoids, three patients were classified as predicted non-responders and all showed tumor recurrence within one year whereas four patients that were classified as predicted responders all remained free of tumor recurrence for more than one year (40).

Novel approaches for pancreatic cancer organoids include the co-culture with cancer-associated fibroblasts (CAFs) and using matched pancreatic ductal organoids. CAFs were shown to increase treatment resistance which shows the importance of tumor micro-environmental aspects on treatment efficacy (68). Using matched pancreatic ductal organoids and pancreatic cancer organoids the lack of therapeutic response of dual

MEK-AKT inhibition observed in a clinical phase II trial (69) was investigated. These findings recapitulated in human and murine organoids a tumor cell specific negative feedback loop causing upregulation of ERBB2, which was not observed in normal pancreatic ductal organoids. This provides a rationale for combining dual MEK-AKT inhibition with ERBB2 blockade with a high therapeutic ratio (38).

Liver cancer organoids can be derived from liver cancer subtypes (hepatocellular carcinoma (HCC) cholangiocarcinoma (CC) or mixed type (HCC/CC)). Overall differential sensitivity was found between organoids from different patients to chemotherapies (gemcitabine) and targeted therapies (taselisib, AZD8931, SCH772984 and dasatanib or sorafenib) (31, 32), though no clinical correlations could be made.

Liver cancer organoids (n=7) were also subjected to targeted therapies (KRAS, MET and KIT targeting). Sensitivity to these treatments however did not fully correlate with the presence of these driver mutations (39). In a more comprehensive study, liver cancer organoids from different tumor regions from the same patient were developed (n=5, 27 organoid lines) and tested for their sensitivity to conventional therapies and drug screening. Most interestingly, pan-effective drugs were identified that could uniformly kill many organoid lines whereas other drugs were only moderately sensitive in a few organoids from the same patient. This study highlights the intratumoral heterogeneity and differential sensitivity towards treatment within one patient and that a single patient organoid may not be sufficient to predict treatment outcome (34).

Cancer organoids were also derived from pediatric hepatoblastoma. For one patient drug testing was performed on the matched normal liver and tumor organoids. This screen identified one drug (JQ1) to have an increased efficacy on tumor organoids compared to normal organoids whereas standard-of-care cisplatin had not differential effect (42). Matched normal liver tissue organoids were also developed by others, providing opportunities to test normal tissue toxicity (32).

Urogenital and Gynecological Cancer

Bladder cancer organoids were tested for sensitivity to chemotherapeutics (epirubicin, mitomycin C, gemcitabine, vincristine, doxorubicin or cisplatin), though no correlations could be made with patient response (49). Another study took a drug screening approach using bladder cancer organoids and observed strong, but variable responses. For example, in some organoids from patients with FGFR3 activating mutations, MEK/ERK inhibition was effective but not in all. Correlations were seen between more aggressive clinical phenotypes (metastasis and recurrence) and treatment resistance to a wide range of drugs in organoids (45).

A biobank (>50 organoid lines) of pediatric kidney cancer organoids was used to test treatment sensitivity towards standard-of-care chemotherapy (neoadjuvant actinomycin D (ACT-D) and vincristine; adjuvant doxorubicin and/or etoposide) on a specific subset of pediatric kidney cancers (Wilms tumor). Organoids derived from patients that received neoadjuvant chemotherapy were less sensitive to vincristine than those from patients not receiving prior chemotherapy. This suggests that resistance already develops *in vivo* and is maintained in cancer organoids. Furthermore, high-throughput drug screens in Wilms tumor organoids identified MEK and HDAC inhibitors as novel candidate interventions. Importantly, matched normal kidney organoids used in this study as well were equally sensitivity to romidepsin (HDAC inhibitor) and MEK inhibition compared to the tumor organoids. For pabinostat (pan-HDAC inhibitor) a significant increased sensitivity was observed in the tumor organoids compared to the normal kidney organoids making this the most interesting for clinical use. Using this approach, this study sets an example of using matched healthy and tumor organoids to identify treatments with the best therapeutic ratio, considering both tumor efficacy and normal tissue toxicity (50).

Prostate cancer organoids were developed from neuro-endocrine prostate cancer (NEPC) and used for screening of cytotoxic drugs and identified alisertib (aurora A-kinase inhibitor). Organoids from two patients enrolled in a phase 2 clinical trial of alisertib mimicked the clinical response of the patients (one responder, one non-responder), supporting the potential clinical relevance of NEPC organoids as a predictive platform (46, 70).

Castrate-resistant prostate cancer (CRPC)-derived organoid lines (n=7) could successfully be established from biopsies and circulating tumor cells from all subtypes. A very limited drug study showed a response towards androgen suppression therapy (enzalutamide) in an organoid with androgen receptor amplification. This organoid line also showed a response to everolimus (mTOR inhibitor) and buparlisib (PI3K inhibitor) correlating with mutations in PTEN and PIK3R1 (43).

Endometrial cancer organoids (EC-O) representing early hyperplastic endometrium (n=13) and different stages and grades were derived (n=16) and exposed to standard-of-care treatment (paclitaxel, 5-FU, carboplatin, doxorubicin) and everolimus. These studies showed differential response between organoids from different patients (48). Similar patient-specific responses were observed in another study with low- and high-grade EC-O (n=15) (44). Additionally, organoids from a patient with uterine carcinosarcoma and a patient with endometrial adenocarcinoma were used for drug screening. In both patients PI3K-inhibitors (buparlisib) were most effective, consistent with PIK3CA mutation present and strongly interacted with HDAC inhibitors as the most potent combinations treatment for both cancer organoids (67). For all three studies, no clinical comparison could be made.

Ovarian cancer organoids (OC-O) were successfully developed from multiple stages and subtypes (56 organoid lines). Standard-of-care drugs (platinum/taxanes) as well as targeted agents (PIK3K/AKT/mTOR inhibitors or PARP inhibitors) were used to test treatment sensitivity of OC-O. Unsupervised hierarchical clustering based upon platinum/taxane sensitivity could distinguish chemosensitive high-grade serous (HGS) organoids and chemoresistant non-HGS organoids which corresponded to the clinical findings. For one patient, HGS organoids clustered with the resistant group, corresponding

to its clinically chemo-resistant phenotype and status as recurrent disease. The pre-treated counterpart of this patient did cluster with the chemo-sensitive group, correlating with clinical behavior (47). Another study also developed OC-O from different subtypes and found significant correlations between organoid response towards carboplatin and paclitaxel combination treatment and clinical response (N=7, $p<0.01$). During follow-up, organoid drug response did not correlate with 6-month progression-free survival. However, organoids derived from the patient with the shortest overall survival was least responsive. Interestingly, for a subset of patients, organoids were derived from multiple biopsies from the same tumor. This identified a differential response in monotreatment between different cancer lesions of seven patients in 31% of the cases, with at least one-mismatch for every drug tested. This emphasizes that intratumor heterogeneity may not be captured by a single biopsy indicating the importance of using multiple biopsies from different locations to predict sensitivity (51).

Central Nervous System Cancer

As a proof-of-concept, organoids from one GBM patient, progressive after standard-of-care treatment, was used to identify potential drug candidates based on genomic alterations. This identified everolimus to be a potential therapeutic agent which correlated with a partial clinical response in this case-study (55). Cancer organoids derived from GBM patients were also used to test drug sensitivity to both standard-of-care chemotherapy (temozolomide) and molecular targeted agents towards mTOR, PI3K or DNA damage response. Differential response towards monotherapy as well as combined treatments with temozolomide and targeted agents was observed between organoids from different patients (56).

Chordoma organoids, a rare spinal cancer, were established that retained PD1 positive CD8 T-cells and were used to predict response towards nivolumab (PD-L1 blockade). A dose-dependent effect was observed in both PD-L1 positive and PD-L1 negative patients which corresponds with previous findings that low expression of PD-L1 can still lead to responses towards PD-L1 blockade (i.e. the approval of PD-L1 inhibitor pembrolizumab in NSCLC starting at 1% PD-L1 positivity). This study shows that this treatment response can potentially be predicted in cancer organoids, regardless of PD-L1 status though no correlation towards individual patient response could be made (54).

Multiple organoid lines of retinoblastoma were developed and tested for response to standard-of-care chemotherapy (melphalan, topotecan and methotrexate) which showed a similar response towards tumor cells in advanced disease in clinical practice, but here no direct comparison to the patient response was made (53).

Breast Cancer

Breast cancer is one of the most prevalent types of cancer, comprising over 20 different subtypes. To include all these subtypes, a large (>100 organoid lines) breast cancer organoid biobank was established. For 12 patients with metastatic breast cancer a comparison with patient outcome was made. In this subset, the *in vitro* response to tamoxifen (estrogen receptor antagonist) matched that of the patients, showing their potential as treatment predictors. This biobank was used for high-throughput drug screening in which most, but not all, organoids responded to treatment as predicted from their mutations. Some organoid lines were insensitive to HER2 targeting despite HER2 overexpression which emphasizes the value of functional *in vitro* drug tests using cancer organoids (57).

In another proof-of-concept study breast cancer organoids were derived from one patient and drug screening identified fulvestrant (estrogen receptor antagonist) as the most optimal treatment for this patient whereas based on genetic analysis (PTEN mutant), everolimus was expected to be the most effective treatment. Possibly this discrepancy can be explained by subclonal PTEN alterations resulting in differential efficacy of everolimus. Since this patient was not treated with either of these agents no correlation to the clinical response could be made, however it does show the additive value of drug screen on cancer organoids to genetic analysis of the tumor (58).

Pulmonary Cancer

Lung cancer is the leading cause of cancer mortality and can be subdivided in non-small cell lung cancer (NSCLC) and small cell lung cancer (SCLC). The first lung cancer organoid biobank was established using 80 lung cancer (SCLC and NSCLC) patients. Drug sensitivity testing was performed for both cytotoxic drugs (docetaxel) and targeted agents (olaparib and erlotinib). Sensitivity to PARP inhibitor olaparib correlated with BRCA2 mutation status as expected. EGFR-targeting by erlotinib did correlate with EGFR mutation status in most, but not all, lung cancer organoids. In one patient that harbored an EGFR mutation but was resistant to erlotinib, a MET amplification was present explaining resistance (60). In another study, NSCLC organoids were derived from lung adenocarcinoma using a TP53 activator (nutlin) to eliminate normal lung stem cells and organoids were used as a potential drug screening model from which findings could be correlated to molecular markers. Lung cancer organoids with an ALK1 mutation were shown to be resistant to crizotinib whereas ERBB2 mutated cancer organoids were sensitive to erlotinib and gefitinib (59). Both studies did not compare the organoid response with that observed in the patient. Two more studies used NSCLC organoids for drug screening and correlation to molecular alterations found in the tumor. Both studies identified differential response towards treatment between organoids from different patients (61, 62) but also some treatments (such as vincristine) which showed comparable activity across all organoid lines (62).

Head-and-Neck Cancer

Head-and-neck squamous cell carcinoma (HNSCC) organoids were developed and tested for treatment response towards standard-of-care chemotherapy in the metastasized setting (cisplatin and docetaxel). This study observed the highest IC50 value for docetaxel in the organoids derived from a pre-treated relapsed patient. Furthermore, *in vitro* resistance towards either

one of the treatments could be confirmed in *in vivo* mouse models (63). HNSCC organoids were subjected to drug screening for targeted agents and standard-of-care treatments (cisplatin, carboplatin, cetuximab or radiotherapy) and differential responses were observed between organoids from different patients. Additionally, for a subset of patients, radiosensitivity of the organoids could be compared to clinical response. For six out of seven patients the organoid response towards radiation was similar to the clinical outcome of the patient (64). Another study used HNSCC organoids to test a novel treatment approach, EGFR-targeted photodynamic therapy. A patient-specific response was observed which correlated with EGFR levels exhibited in the tumor and corresponding organoids (65).

DISCUSSION

In the past decade, cancer organoids have been established for large set of solid tumors and extensively characterized on a genetic, transcriptomic and phenotypic level. Overall, the conclusion is that cancer organoids are genetically and phenotypically stable replicates of the tissue and tumor subtype characteristics. Multiple studies have also used cancer organoids for drug screening approaches. However, only few studies have been able to make a quantitative clinical comparison to derive predictive values (11, 23, 25, 51). Most studies to date still provide a descriptive comparison between the organoid and clinical response which highlights the potential value of cancer organoids for this utility. Nonetheless, larger cancer organoid studies that make a quantitative comparison to the clinical response are warranted to make accurate statements about the sensitivity and specificity of cancer organoids as clinical predictors of response and outcome. Cancer organoids have the potential to improve patient selection as multiple studies have shown that in some cases cancer organoids responded differently than predicted by driver mutations in the tumor (51, 57). This could for example be due to small tumor subclones or mutations downstream or parallel to the targeted pathway (60). Recently, a protocol has been published as a standardized method to successfully establish organoids from different cancer types and perform drug screening thereof (71). Such guidelines are crucial to develop a robust and reproducible co-clinical platform for cancer organoids.

Limitations in Cancer Organoids Studies

Several limitations currently exist that need to be addressed before cancer organoids can be implemented as a co-clinical track to aid clinical decision making. First, the derivation of organoids is not equally effective for all solid cancers. For example, NSCLC has shown a low establishment rate due to frequent overgrowth of lung cancer organoids by normal airway cells (72). This overgrowth of somatic stem cells has been observed in the derivation of liver, prostate and endometrial cancer organoids as well (31, 43, 48). Approaches using omission of growth factors or addition of drugs based on molecular alterations of the tumor cells have been used to achieve pure cancer cell populations. However, these approaches are not universally applicable and vary greatly between cancer types but also between samples within the same cancer type (59, 73). Such approaches however should be avoided as they will reduce heterogeneity by eliminating subsets of tumor clones and may stimulate the outgrowth of others which will result in a reduced tumor representation and ability to predict treatment response. Future studies, including single-cell sequencing of organoids should be conducted to investigate how such counter selections affect tumor representation. Second, the derivation time of most cancer organoids is currently still weeks to months. If cancer organoids were to be used as co-clinical avatars this derivation time needs to be shortened to be of actual clinical value to the patient. Third, at the moment most patients die from metastatic disease. Heterogeneity between the primary tumor and developed metastases is an important cause of treatment failure in the metastasized setting. The opportunity to derive cancer organoids form different tumor sites provides the opportunity to select treatment options to which all distinct tumor locations share sensitivity. Multiple studies have successfully used this approach and showed differential as well as similar treatment responses for several anti-cancer agents between organoids derived from multiple tumor sites (33, 34, 51, 52). In clinical practice, taking multiple biopsies from one tumor or taking biopsies from multiple metastases might however not always be feasible which could potentially limit this application into the clinic.

Finally, the usage of exogenous growth factors and animal-derived basement membrane extracts (BME) in organoid cultures might influence reproducibility between organoid studies. There is currently no consensus on which medium components should be used, also not within one tumor type, which could explain differences found between studies with regards to treatment sensitivity. Moreover, the BMEs that are mostly used (i.e. Matrigel) feature variable compositions and the protein composition does not always reflect the stromal composition of the tissue the cancer cells were derived from. Utilizing a well-defined 3D matrix, adjusted to specific tumor types, might help to further improve cancer organoid studies (74).

Incorporation of the Tumor Micro-environment in Cancer Organoids

Cells from the tumor micro-environment, such as stromal cells, immune cells and endothelial cells are lacking from cancer organoids. This may limit the utility of patient cancer organoids as predictors of treatment response as the tumor micro-environment is a key determinant of therapeutic outcome and a potential therapeutic target (75, 76). Importantly, hypoxia, a common characteristic of the tumor micro-environment of solid tumors which greatly contributes to malignant behavior and chemo- and radioresistance does develop in organoids once they reach a certain size (52). The importance of the tumor micro-environment has also been shown by incorporating cancer-associated fibroblasts in pancreatic cancer organoids which led to increased resistance towards treatment (68).

Several attempts have already been made towards incorporating aspects of the tumor micro-environment into the cancer organoid system (77). These include co-culture of tumor cells and immune cells or the preservation of original tumor micro-environmental components in the culture system (15). An example of this is the development of a co-culture system of peripheral blood mononuclear cells (PBMCs) and NSCLC or CRC cells. In this system, autologous tumor-reactive T-cells could be induced which were also shown to specifically kill tumor organoids whereas matched healthy airway organoids were unaffected (78). An air-liquid-interface (ALI) system was used to propagate cancer organoids directly from human or mouse tumor biopsies with preservation of the immune stroma and original tumor T-cell receptor spectrum and used to model immune checkpoint blockade therapy (79). In another example, glioblastoma biopsies were cut into small pieces without using a BME. This approach showed retention of immune and endothelial cells during culture and could be used to test for CAR-T cell treatment. However, whether these immune cells remain functional after prolonged culture is still uncertain (80).

Whereas endothelial cells can be preserved in acute slice culture systems and by starting a culture directly from a tumor biopsy without disturbing the tissue architecture, re-creating functional blood vessels requires a very different approach. Towards this goal, human vascularized brain organoids by co-culturing brain organoids and *in vitro* differentiated iPSCs towards endothelial cells were generated (81). Furthermore, tumor-on-a-chip models have been developed that include a microfluidic model to mimic vasculature and a running blood stream to further mimic the *in vivo* drug delivery situation (82).

Drug Response Standardization in Cancer Organoid Studies

In order to fully understand the potential of cancer organoids as patient avatars important aspects need to be addressed. Most studies to date have used arbitrary drug dosages or titration curves. While this is a fairly common approach in pre-clinical research, it is recommended to use human equivalent dosages (i.e. measured drug concentrations in cancer tissue *in vivo*) in treatment experiments using cancer organoids. These differences in drug dose could lead to survival of cell populations *in vitro* that do not die *in vivo* or vice versa. Furthermore, since all studies use different drugs schedules and dosages, discrepancies of the predictive value of organoids between different studies can occur. Changes in drug concentration due to differences in diffusion of metabolites, *in vivo* drug metabolism and limited drug penetrance as a result of physiological barriers such as the blood-brain-barrier (BBB) can change the efficacy of a treatment option due to inadequate drug concentration in the cancer organoid. Microfluidics and an artificial BBB using organ on a chip technology may advance the field in this respect (82, 83). Furthermore, anti-cancer drugs are administered in specific treatment schedules in clinical practice. Especially concurrent treatment with multiple systemic agents and/or radiotherapy is still lacking in most cancer organoid studies whereas this is a common treatment strategy in daily clinical practice. Another important consideration that requires critical analysis are the treatment endpoint assays used in cancer organoid studies. It is well established that short term proliferation and viability/cell death (apoptosis, BrdU, ATP assays) are not predictive for long term survival and tumor control probability in response to

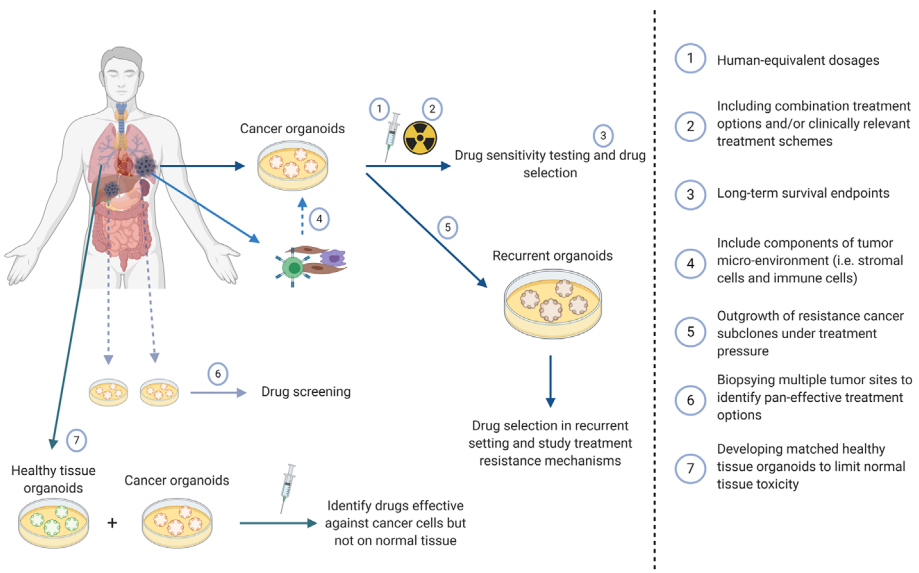

FIGURE 1 | Potential applications of cancer organoids to improve treatment prediction and clinical applicability.

radiotherapy and chemotherapy. Organoids are composed of heterogeneous cell population in which cancer stem cells have different responses to treatment and constitute only a minor fraction of the organoid population. Therefore, ninety percent cell death may not involve the most resistant clones within the organoid or the tumor in the patient. As tumor stem cells are intrinsically more resistant to treatment (84, 85) than bulk -non tumor stem cells–treatment schedules should also include long term survival assays (e.g. organoid replating studies, clonogenic assays) combined with tumor stem cell biomarkers to be more predictive for the tumor cure dose *in vivo*.

Development of Recurrent Cancer Organoids

An interesting application of cancer organoids to be further explored is the development of organoids from recurrent cancer. Some studies describe organoids from biopsies from recurrent tumors, both with and without matched primary tumors (45, 47). Another interesting approach could be the *in vitro* development of a recurrent organoid from primary tumor organoids (10). Under selection of treatment pressure, resistant subpopulations within the tumor could potentially outgrow the treatment-sensitive cell populations or cause the acquisition of new mutations that cause resistance or may identify new therapeutic targets. Future studies should address if *in vitro* induced resistance mechanisms mimic the behavior of recurrent disease in patients.

Corresponding Cancer and Healthy Tissue Organoids

Another important advantage of organoids is the possibility to simultaneously culture cancer and healthy tissue organoids from the same patient. Several studies have already implemented this technique in which it supported selection of the most promising treatment option (38, 50, 78, 86). Normal tissue toxicity is one of the main dose-limiting factors in cancer therapy, and being able to predict this can be of great benefit towards both optimal cancer treatment as well as maximizing quality of life. Thus, organoids are not only useful to individualize treatment in order to eradicate cancer cells but also to exclude potentially toxic treatments. The use of normal tissue organoids in parallel is only just emerging but would be a key feature to the armamentarium of organoids as clinical avatars for personalized precision medicine.

CONCLUSION

In conclusion, cancer organoids exhibit the potential to act as predictors for clinical treatment response. However, quantitative data to make accurate statements about their predictive value is mainly lacking from current studies which is warranted to work towards their clinical implementation.

Biobanks of cancer organoids can be used to identify targetable mutations and patient subgroups to stratify patients for specific anti-cancer treatment options, beyond single predictive molecular markers. This approach is currently utilized by actively involving cancer organoids in ongoing clinical trials to improve patient selection (NCT03416244; NCT03307538).

Finally, cancer organoids can act as living surrogates (patient avatars) to use for high-throughput drug screening approaches to aid directly in the treatment of the specific patient that the organoid has been derived from and for the discovery of novel drug and targets. This possibility opens up major possibilities in the selection of personalized treatment options and the prevention of normal tissue toxicity.

AUTHOR CONTRIBUTIONS

MVe: conceptualization, data curation, investigation, writing (original draft, review, and editing), and final approval. AH: analysis and interpretation of data, writing (review), and final approval. DD: analysis and interpretation of data, writing (review), and final approval. MVo: conceptualization, data curation, investigation, supervision, writing (original draft, review, and editing), and final approval. All authors contributed to the article and approved the submitted version.

FUNDING

KWF Kankerbestrijding (Dutch Cancer Society) Unique High Risk (16698/2018-1).

ACKNOWLEDGMENTS

Figure 1 was created using Biorender.com.

REFERENCES

1. Sato T, Vries RG, Snippert HJ, van de Wetering M, Barker N, Stange DE, et al. Single Lgr5 stem cells build crypt-villus structures in vitro without a mesenchymal niche. *Nature* (2009) 459(7244):262–5. doi: 10.1038/nature07935
2. van de Wetering M, Francies HE, Francis JM, Bounova G, Iorio F, Pronk A, et al. Prospective derivation of a living organoid biobank of colorectal cancer patients. *Cell* (2015) 161(4):933–45. doi: 10.1016/j.cell.2015.03.053
3. Roerink SF, Sasaki N, Lee-Six H, Young MD, Alexandrov LB, Behjati S, et al. Intra-tumour diversification in colorectal cancer at the single-cell level. *Nature* (2018) 556(7702):457–62. doi: 10.1038/s41586-018-0024-3
4. Clevers H. Modeling Development and Disease with Organoids. *Cell* (2016) 165(7):1586–97. doi: 10.1016/j.cell.2016.05.082
5. Weeber F, Ooft SN, Dijkstra KK, Voest EE. Tumor Organoids as a Pre-clinical Cancer Model for Drug Discovery. *Cell Chem Biol* (2017) 24(9):1092–100. doi: 10.1016/j.chembiol.2017.06.012
6. Bleijs M, van de Wetering M, Clevers H, Drost J. Xenograft and organoid model systems in cancer research. *EMBO J* (2019) 38(15):e101654. doi: 10.15252/embj.2019101654
7. Drost J, Clevers H. Organoids in cancer research. *Nat Rev Cancer* (2018) 18 (7):407–18. doi: 10.1038/s41568-018-0007-6
8. Koppens MA, Bounova G, Cornelissen-Steijger P, de Vries N, Sansom OJ, Wessels LF, et al. Large variety in a panel of human colon cancer organoids in

response to EZH2 inhibition. *Oncotarget* (2016) 7(43):69816–28. doi: 10.18632/oncotarget.12002
9. Verissimo CS, Overmeer RM, Ponsioen B, Drost J, Mertens S, Verlaan-Klink I, et al. Targeting mutant RAS in patient-derived colorectal cancer organoids by combinatorial drug screening. *Elife* (2016) 5. doi: 10.7554/eLife.18489
10. Buzzelli JN, Ouaret D, Brown G, Allen PD, Muschel RJ. Colorectal cancer liver metastases organoids retain characteristics of original tumor and acquire chemotherapy resistance. *Stem Cell Res* (2018) 27:109–20. doi: 10.1016/j.scr.2018.01.016
11. Vlachogiannis G, Hedayat S, Vatsiou A, Jamin Y, Fernandez-Mateos J, Khan K, et al. Patient-derived organoids model treatment response of metastatic gastrointestinal cancers. *Science* (2018) 359(6378):920–6. doi: 10.1126/science.aao2774
12. Gao M, Lin M, Rao M, Thompson H, Hirai K, Choi M, et al. Development of Patient-Derived Gastric Cancer Organoids from Endoscopic Biopsies and Surgical Tissues. *Ann Surg Oncol* (2018) 25(9):2767–75. doi: 10.1245/s10434-018-6662-8
13. Li X, Francies HE, Secrier M, Perner J, Miremadi A, Galeano-Dalmau N, et al. Organoid cultures recapitulate esophageal adenocarcinoma heterogeneity providing a model for clonality studies and precision therapeutics. *Nat Commun* (2018) 9(1):2983. doi: 10.1038/s41467-018-05190-9
14. Yan HHN, Siu HC, Law S, Ho SL, Yue SSK, Tsui WY, et al. A Comprehensive Human Gastric Cancer Organoid Biobank Captures Tumor Subtype Heterogeneity and Enables Therapeutic Screening. *Cell Stem Cell* (2018) 23(6):882–97.e11. doi: 10.1016/j.stem.2018.09.016
15. Votanopoulos KI, Mazzocchi A, Sivakumar H, Forsythe S, Aleman J, Levine EA, et al. Appendiceal Cancer Patient-Specific Tumor Organoid Model for Predicting Chemotherapy Efficacy Prior to Initiation of Treatment: A Feasibility Study. *Ann Surg Oncol* (2019) 26(1):139–47. doi: 10.1245/s10434-018-7008-2
16. Li J, Xu H, Zhang L, Song L, Feng D, Peng X, et al. Malignant ascites-derived organoid (MADO) cultures for gastric cancer in vitro modelling and drug screening. *J Cancer Res Clin Oncol* (2019) 145(11):2637–47. doi: 10.1007/s00432-019-03004-z
17. Schumacher D, Andrieux G, Boehnke K, Keil M, Silvestri A, Silvestrov M, et al. Heterogeneous pathway activation and drug response modelled in colorectal-tumor-derived 3D cultures. *PloS Genet* (2019) 15(3):e1008076. doi: 10.1371/journal.pgen.1008076
18. Seidlitz T, Merker SR, Rothe A, Zakrzewski F, von Neubeck C, Grutzmann K, et al. Human gastric cancer modelling using organoids. *Gut* (2019) 68(2):207–17. doi: 10.1136/gutjnl-2017-314549
19. Ubink I, Bolhaqueiro ACF, Elias SG, Raats DAE, Constantinides A, Peters NA, et al. Organoids from colorectal peritoneal metastases as a platform for improving hyperthermic intraperitoneal chemotherapy. *Br J Surg* (2019) 106(10):1404–14. doi: 10.1002/bjs.11206
20. Pasch CA, Favreau PF, Yueh AE, Babiarz CP, Gillette AA, Sharick JT, et al. Patient-Derived Cancer Organoid Cultures to Predict Sensitivity to Chemotherapy and Radiation. *Clin Cancer Res* (2019) 25(17):5376–87. doi: 10.1158/1078-0432.CCR-18-3590
21. Steele NG, Chakrabarti J, Wang J, Biesiada J, Holokai L, Chang J, et al. An Organoid-Based Preclinical Model of Human Gastric Cancer. *Cell Mol Gastroenterol Hepatol* (2019) 7(1):161–84. doi: 10.1016/j.jcmgh.2018.09.008
22. Ganesh K, Wu C, O'Rourke KP, Szeglin BC, Zheng Y, Sauve CG, et al. A rectal cancer organoid platform to study individual responses to chemoradiation. *Nat Med* (2019) 25(10):1607–14. doi: 10.1038/s41591-019-0584-2
23. Ooft SN, Weeber F, Dijkstra KK, McLean CM, Kaing S, van Werkhoven E, et al. Patient-derived organoids can predict response to chemotherapy in metastatic colorectal cancer patients. *Sci Transl Med* (2019) 11(513). doi: 10.1126/scitranslmed.aay2574
24. Costales-Carrera A, Fernandez-Barral A, Bustamante-Madrid P, Guerra L, Cantero R, Barbachano A, et al. Plocabulin Displays Strong Cytotoxic Activity in a Personalized Colon Cancer Patient-Derived 3D Organoid Assay. *Mar Drugs* (2019) 17(11). doi: 10.3390/md17110648
25. Yao Y, Xu X, Yang L, Zhu J, Wan J, Shen L, et al. Patient-Derived Organoids Predict Chemoradiation Responses of Locally Advanced Rectal Cancer. *Cell Stem Cell* (2020) 26(1):17–26.e6. doi: 10.1016/j.stem.2019.10.010
26. Narasimhan V, Wright JA, Churchill M, Wang T, Rosati R, Lannagan TR, et al. Medium-throughput drug screening of patient-derived organoids from colorectal peritoneal metastases to direct personalized therapy. *Clin Cancer Res* (2020) 26:3662–71. doi: 10.1158/1078-0432.CCR-20-0073
27. Zerp SF, Bibi Z, Verbrugge I, Voest EE, Verheij M. Enhancing radiation response by a second-generation TRAIL receptor agonist using a new in vitro organoid model system. *Clin Transl Radiat Oncol* (2020) 24:1–9. doi: 10.1016/j.ctro.2020.05.012
28. Derouet MF, Allen J, Wilson GW, Ng C, Radulovich N, Kalimuthu S, et al. Towards personalized induction therapy for esophageal adenocarcinoma: organoids derived from endoscopic biopsy recapitulate the pre-treatment tumor. *Sci Rep* (2020) 10(1):14514. doi: 10.1038/s41598-020-71589-4
29. Arena S, Corti G, Durinikova E, Montone M, Reilly NM, Russo M, et al. A Subset of Colorectal Cancers with Cross-Sensitivity to Olaparib and Oxaliplatin. *Clin Cancer Res* (2020) 26(6):1372–84. doi: 10.1158/1078-0432.CCR-19-2409
30. Huang L, Holtzinger A, Jagan I, BeGora M, Lohse I, Ngai N, et al. Ductal pancreatic cancer modeling and drug screening using human pluripotent stem cell- and patient-derived tumor organoids. *Nat Med* (2015) 21(11):1364–71. doi: 10.1038/nm.3973
31. Broutier L, Mastrogiovanni G, Verstegen MM, Francies HE, Gavarro LM, Bradshaw CR, et al. Human primary liver cancer-derived organoid cultures for disease modeling and drug screening. *Nat Med* (2017) 23(12):1424–35. doi: 10.1038/nm.4438
32. Nuciforo S, Fofana I, Matter MS, Blumer T, Calabrese D, Boldanova T, et al. Organoid Models of Human Liver Cancers Derived from Tumor Needle Biopsies. *Cell Rep* (2018) 24(5):1363–76. doi: 10.1016/j.celrep.2018.07.001
33. Tiriac H, Belleau P, Engle DD, Plenker D, Deschenes A, Somerville TDD, et al. Organoid Profiling Identifies Common Responders to Chemotherapy in Pancreatic Cancer. *Cancer Discovery* (2018) 8(9):1112–29. doi: 10.1158/1538-7445.PANCA19-C57
34. Li L, Knutsdottir H, Hui K, Weiss MJ, He J, Philosophe B, et al. Human primary liver cancer organoids reveal intratumor and interpatient drug response heterogeneity. *JCI Insight* (2019) 4(2). doi: 10.1172/jci.insight.121490
35. Hennig A, Wolf L, Jahnke B, Polster H, Seidlitz T, Werner K, et al. CFTR Expression Analysis for Subtyping of Human Pancreatic Cancer Organoids. *Stem Cell Derived Organ Hum Dis Develop* (2019) 2019:1024614. doi: 10.1155/2019/1024614
36. Bian B, Juiz NA, Gayet O, Bigonnet M, Brandone N, Roques J, et al. *Front Oncol* (2019) 9:475. doi: 10.3389/fonc.2019.00475
37. Driehuis E, van Hoeck A, Moore K, Kolders S, Francies HE, Gulersonmez MC, et al. Pancreatic cancer organoids recapitulate disease and allow personalized drug screening. *Proc Natl Acad Sci U S A* (2019) 116:26580–90. doi: 10.1073/pnas.1911273116
38. Ponz-Sarvise M, Corbo V, Tiriac H, Engle DD, Frese KK, Oni TE, et al. Identification of Resistance Pathways Specific to Malignancy Using Organoid Models of Pancreatic Cancer. *Clin Cancer Res* (2019) 25(22):6742–55. doi: 10.1158/1078-0432.CCR-19-1398
39. Castven D, Becker D, Czauderna C, Wilhelm D, Andersen JB, Strand S, et al. Application of patient-derived liver cancer cells for phenotypic characterization and therapeutic target identification. *Int J Cancer* (2019) 144(11):2782–94. doi: 10.1002/ijc.32026
40. Sharick JT, Walsh CM, Sprackling CM, Pasch CA, Pham DL, Esbona K, et al. Metabolic Heterogeneity in Patient Tumor-Derived Organoids by Primary Site and Drug Treatment. *Front Oncol* (2020) 10:553. doi: 10.3389/fonc.2020.00553
41. Seppala TT, Zimmerman JW, Sereni E, Plenker D, Suri R, Rozich N, et al. Patient-derived Organoid Pharmacotyping is a Clinically Tractable Strategy for Precision Medicine in Pancreatic Cancer. *Ann Surg* (2020) 272:427–35. doi: 10.1097/SLA.0000000000004200
42. Saltsman JA, Hammond WJ, Narayan NJC, Requena D, Gehart H, Lalazar G, et al. A Human Organoid Model of Aggressive Hepatoblastoma for Disease Modeling and Drug Testing. *Cancers (Basel)* (2020) 12(9). doi: 10.3390/cancers12092668
43. Gao D, Vela I, Sboner A, Iaquinta PJ, Karthaus WR, Gopalan A, et al. Organoid cultures derived from patients with advanced prostate cancer. *Cell* (2014) 159(1):176–87. doi: 10.1016/j.cell.2014.08.016
44. Girda E, Huang EC, Leiserowitz GS, Smith LH. The Use of Endometrial Cancer Patient-Derived Organoid Culture for Drug Sensitivity Testing Is Feasible. *Int J Gynecol Cancer* (2017) 27(8):1701–7. doi: 10.1097/IGC.0000000000001061

45. Lee SH, Hu W, Matulay JT, Silva MV, Owczarek TB, Kim K, et al. Tumor Evolution and Drug Response in Patient-Derived Organoid Models of Bladder Cancer. *Cell* (2018) 173(2):515–28.e17. doi: 10.1016/j.cell.2018.03.017
46. Puca L, Bareja R, Prandi D, Shaw R, Benelli M, Karthaus WR, et al. Patient derived organoids to model rare prostate cancer phenotypes. *Nat Commun* (2018) 9(1):2404. doi: 10.1038/s41467-018-04495-z
47. Kopper O, de Witte CJ, Lohmussaar K, Valle-Inclan JE, Hami N, Kester L, et al. An organoid platform for ovarian cancer captures intra- and interpatient heterogeneity. *Nat Med* (2019) 25(5):838–49. doi: 10.1038/s41591-019-0422-6
48. Boretto M, Maenhoudt N, Luo X, Hennes A, Boeckx B, Bui B, et al. Patient-derived organoids from endometrial disease capture clinical heterogeneity and are amenable to drug screening. *Nat Cell Biol* (2019) 21(8):1041–51. doi: 10.1038/s41556-019-0360-z
49. Mullenders J, de Jongh E, Brousali A, Roosen M, Blom JPA, Begthel H, et al. Mouse and human urothelial cancer organoids: A tool for bladder cancer research. *Proc Natl Acad Sci USA* (2019) 116(10):4567–74. doi: 10.1073/pnas.1803595116
50. Calandrini C, Schutgens F, Oka R, Margaritis T, Candelli T, Mathijsen L, et al. An organoid biobank for childhood kidney cancers that captures disease and tissue heterogeneity. *Nat Commun* (2020) 11(1):1310. doi: 10.1038/s41467-020-15155-6
51. de Witte CJ, Espejo Valle-Inclan J, Hami N, Lohmussaar K, Kopper O, Vreuls CPH, et al. Patient-Derived Ovarian Cancer Organoids Mimic Clinical Response and Exhibit Heterogeneous Inter- and Intrapatient Drug Responses. *Cell Rep* (2020) 31(11):107762. doi: 10.1016/j.celrep.2020.107762
52. Hubert CG, Rivera M, Spangler LC, Wu Q, Mack SC, Prager BC, et al. A Three-Dimensional Organoid Culture System Derived from Human Glioblastomas Recapitulates the Hypoxic Gradients and Cancer Stem Cell Heterogeneity of Tumors Found In Vivo. *Cancer Res* (2016) 76(8):2465–77. doi: 10.1158/0008-5472.CAN-15-2402
53. Saengwimol D, Rojanaporn D, Chaitankar V, Chittavanich P, Aroonroch R, Boontawon T, et al. A three-dimensional organoid model recapitulates tumorigenic aspects and drug responses of advanced human retinoblastoma. *Sci Rep* (2018) 8(1):15664. doi: 10.1038/s41598-018-34037-y
54. Scognamiglio G, De Chiara A, Parafioriti A, Armiraglio E, Fazioli F, Gallo M, et al. Patient-derived organoids as a potential model to predict response to PD-1/PD-L1 checkpoint inhibitors. *Br J Cancer* (2019) 121(11):979–82. doi: 10.1038/s41416-019-0616-1
55. Loong HH, Wong AM, Chan DT, Cheung MS, Chow C, Ding X, et al. Patient-derived tumor organoid predicts drugs response in glioblastoma: A step forward in personalized cancer therapy? *J Clin Neurosci* (2020) 78:400–2. doi: 10.1016/j.jocn.2020.04.107
56. Chadwick M, Yang C, Liu L, Gamboa CM, Jara K, Lee H, et al. Rapid Processing and Drug Evaluation in Glioblastoma Patient-Derived Organoid Models with 4D Bioprinted Arrays. *iScience* (2020) 23(8):101365. doi: 10.1016/j.isci.2020.101365
57. Sachs N, de Ligt J, Kopper O, Gogola E, Bounova G, Weeber F, et al. A Living Biobank of Breast Cancer Organoids Captures Disease Heterogeneity. *Cell* (2018) 172(1-2):373–86.e10. doi: 10.1016/j.cell.2017.11.010
58. Li X, Pan B, Song X, Li N, Zhao D, Li M, et al. Breast cancer organoids from a patient with giant papillary carcinoma as a high-fidelity model. *Cancer Cell Int* (2020) 20:86. doi: 10.1186/s12935-020-01171-5
59. Sachs N, Papaspyropoulos A, Zomer-van Ommen DD, Heo I, Bottinger L, Klay D, et al. Long-term expanding human airway organoids for disease modeling. *EMBO J* (2019) 38(4). doi: 10.15252/embj.2018100300
60. Kim M, Mun H, Sung CO, Cho EJ, Jeon HJ, Chun SM, et al. Patient-derived lung cancer organoids as in vitro cancer models for therapeutic screening. *Nat Commun* (2019) 10(1):3991. doi: 10.1038/s41467-019-11867-6
61. Chen JH, Chu XP, Zhang JT, Nie Q, Tang WF, Su J, et al. Genomic characteristics and drug screening among organoids derived from non-small cell lung cancer patients. *Thorac Cancer* (2020) 11(8):2279–90. doi: 10.1111/1759-7714.13542
62. Li Z, Qian Y, Li W, Liu L, Yu L, Liu X, et al. Human Lung Adenocarcinoma-Derived Organoid Models for Drug Screening. *iScience* (2020) 23(8):101411. doi: 10.1016/j.isci.2020.101411
63. Tanaka N, Osman AA, Takahashi Y, Lindemann A, Patel AA, Zhao M, et al. Head and neck cancer organoids established by modification of the CTOS method can be used to predict in vivo drug sensitivity. *Oral Oncol* (2018) 87:49–57. doi: 10.1016/j.oraloncology.2018.10.018
64. Driehuis E, Kolders S, Spelier S, Lohmussaar K, Willems SM, Devriese LA, et al. Oral Mucosal Organoids as a Potential Platform for Personalized Cancer Therapy. *Cancer Discovery* (2019) 9(7):852–71. doi: 10.1158/2159-8290.CD-18-1522
65. Driehuis E, Spelier S, Beltran Hernandez I, de Bree R, MW S, Clevers H, et al. Patient-Derived Head and Neck Cancer Organoids Recapitulate EGFR Expression Levels of Respective Tissues and Are Responsive to EGFR- Targeted Photodynamic Therapy. *J Clin Med* (2019) 8(11). doi: 10.3390/jcm8111880
66. Janakiraman H, Zhu Y, Becker SA, Wang C, Cross A, Curl E, et al. Modeling rectal cancer to advance neoadjuvant precision therapy. *Int J Cancer* (2020) 147(5):1405–18. doi: 10.1002/ijc.32876
67. Pauli C, Hopkins BD, Prandi D, Shaw R, Fedrizzi T, Sboner A, et al. Personalized In Vitro and In Vivo Cancer Models to Guide Precision Medicine. *Cancer Discovery* (2017) 7(5):462–77. doi: 10.1158/2159-8290.CD-16-1154
68. Liu J, Li P, Wang L, Li M, Ge Z, Noordam L, et al. Cancer-Associated Fibroblasts Provide a Stromal Niche for Liver Cancer Organoids That Confers Trophic Effects and Therapy Resistance. *Cell Mol Gastroenterol Hepatol* (2020) 11:407–31. doi: 10.1016/j.jcmgh.2020.09.003
69. Chung V, McDonough S, Philip PA, Cardin D, Wang-Gillam A, Hui L, et al. Effect of Selumetinib and MK-2206 vs Oxaliplatin and Fluorouracil in Patients With Metastatic Pancreatic Cancer After Prior Therapy: SWOG S1115 Study Randomized Clinical Trial. *JAMA Oncol* (2017) 3(4):516–22. doi: 10.1001/jamaoncol.2016.5383
70. Beltran H, Oromendia C, Danila DC, Montgomery B, Hoimes C, Szmulewitz RZ, et al. A Phase II Trial of the Aurora Kinase A Inhibitor Alisertib for Patients with Castration-resistant and Neuroendocrine Prostate Cancer: Efficacy and Biomarkers. *Clin Cancer Res* (2019) 25(1):43–51. doi: 10.1158/1078-0432.CCR-18-1912
71. Driehuis E, Kretzschmar K, Clevers H. Establishment of patient-derived cancer organoids for drug-screening applications. *Nat Protoc* (2020) 15:3380–409. doi: 10.1038/s41596-021-00494-5
72. Dijkstra KK, Monkhorst K, Schipper LJ, Hartemink KJ, Smit EF, Kaing S, et al. Challenges in Establishing Pure Lung Cancer Organoids Limit Their Utility for Personalized Medicine. *Cell Rep* (2020) 31(5):107588. doi: 10.1016/j.celrep.2020.107588
73. Wallaschek N, Niklas C, Pompaiah M, Wiegering A, Germer CT, Kircher S, et al. Establishing Pure Cancer Organoid Cultures: Identification, Selection and Verification of Cancer Phenotypes and Genotypes. *J Mol Biol* (2019) 431(15):2884–93. doi: 10.1016/j.jmb.2019.05.031
74. Gjorevski N, Sachs N, Manfrin A, Giger S, Bragina ME, Ordonez-Moran P, et al. Designer matrices for intestinal stem cell and organoid culture. *Nature* (2016) 539(7630):560–4. doi: 10.1038/nature20168
75. Junttila MR, de Sauvage FJ. Influence of tumour micro-environment heterogeneity on therapeutic response. *Nature* (2013) 501(7467):346–54. doi: 10.1038/nature12626
76. Joyce JA. Therapeutic targeting of the tumor microenvironment. *Cancer Cell* (2005) 7(6):513–20. doi: 10.1016/j.ccr.2005.05.024
77. Bar-Ephraim YE, Kretzschmar K, Clevers H. Organoids in immunological research. *Nat Rev Immunol* (2020) 20(5):279–93. doi: 10.1038/s41577-019-0248-y
78. Dijkstra KK, Cattaneo CM, Weeber F, Chalabi M, van de Haar J, Fanchi LF, et al. Generation of Tumor-Reactive T Cells by Co-culture of Peripheral Blood Lymphocytes and Tumor Organoids. *Cell* (2018) 174(6):1586–98.e12. doi: 10.1016/j.cell.2018.07.009
79. Neal JT, Li X, Zhu J, Giangarra V, Grzeskowiak CL, Ju J, et al. Organoid Modeling of the Tumor Immune Microenvironment. *Cell* (2018) 175(7):1972–88 e16. doi: 10.1016/j.cell.2018.11.021
80. Jacob F, Salinas RD, Zhang DY, Nguyen PTT, Schnoll JG, Wong SZH, et al. A Patient-Derived Glioblastoma Organoid Model and Biobank Recapitulates Inter- and Intra-tumoral Heterogeneity. *Cell* (2020) 180(1):188–204 e22. doi: 10.1016/j.cell.2019.11.036
81. Pham MT, Pollock KM, Rose MD, Cary WA, Stewart HR, Zhou P, et al. Generation of human vascularized brain organoids. *Neuroreport* (2018) 29(7):588–93. doi: 10.1097/WNR.0000000000001014
82. Ayuso JM, Virumbrales-Munoz M, McMinn PH, Rehman S, Gomez I, Karim MR, et al. Tumor-on-a-chip: a microfluidic model to study cell response to

environmental gradients. *Lab Chip* (2019) 19(20):3461–71. doi: 10.1039/C9LC00270G
83. Ahn SI, Sei YJ, Park HJ, Kim J, Ryu Y, Choi JJ, et al. Microengineered human blood-brain barrier platform for understanding nanoparticle transport mechanisms. *Nat Commun* (2020) 11(1):175. doi: 10.1038/s41467-019-13896-7
84. Cojoc M, Mabert K, Muders MH, Dubrovska A. A role for cancer stem cells in therapy resistance: cellular and molecular mechanisms. *Semin Cancer Biol* (2015) 31:16–27. doi: 10.1016/j.semcancer.2014.06.004
85. Baumann M, Krause M, Hill R. Exploring the role of cancer stem cells in radioresistance. *Nat Rev Cancer* (2008) 8(7):545–54. doi: 10.1038/nrc2419
86. Hou S, Tiriac H, Sridharan BP, Scampavia L, Madoux F, Seldin J, et al. Advanced Development of Primary Pancreatic Organoid Tumor Models for High-Throughput Phenotypic Drug Screening. *SLAS Discovery* (2018) 23 (6):574–84. doi: 10.1177/2472555218766842

Conflict of Interest: The authors declare that the research was conducted in the absence of any commercial or financial relationships that could be construed as a potential conflict of interest.

frontiers | Frontiers in Oncology

PERSPECTIVE
published: 05 April 2022
doi: 10.3389/fonc.2022.872531

Patient-Derived Tumor Organoids: New Progress and Opportunities to Facilitate Precision Cancer Immunotherapy

Ji Wang[1†], Chao Chen[2,3,4†], Lu Wang[1], Mingjun Xie[5,6], Xinyang Ge[7], Sufan Wu[1], Yong He[4,5,6,8], Xiaozhou Mou[1], Chenyang Ye[3,4,9*] and Yi Sun[1*]*

[1] Center for Plastic & Reconstructive Surgery, Department of Plastic & Reconstructive Surgery, Zhejiang Provincial People's Hospital (Affiliated People's Hospital, Hangzhou Medical College), Hangzhou, China, [2] Department of Colorectal Surgery and Oncology, Key Laboratory of Cancer Prevention and Intervention, Ministry of Education, The Second Affiliated Hospital, Zhejiang University School of Medicine, Hangzhou, China, [3] Cancer Institute (Key Laboratory of Cancer Prevention and Intervention, China National Ministry of Education), The Second Affiliated Hospital, School of Medicine, Zhejiang University, Hangzhou, China, [4] Cancer Center, Zhejiang University, Hangzhou, China, [5] State Key Laboratory of Fluid Power and Mechatronic Systems, School of Mechanical Engineering, Zhejiang University, Hangzhou, China, [6] Key Laboratory of Materials Processing and Mold, Zhengzhou University, Zhengzhou, China, [7] College of Letters and Science, University of California, Los Angeles, Los Angeles, CA, United States, [8] Key Laboratory of 3D Printing Process and Equipment of Zhejiang Province, College of Mechanical Engineering, Zhejiang University, Hangzhou, China, [9] Department of Medical Oncology, The Second Affiliated Hospital of Zhejiang University School of Medicine, Hangzhou, China

OPEN ACCESS

Edited by:
Manash K. Paul,
California State University,
Los Angeles, United States

Reviewed by:
Dr Jyotirmoi Aich,
Padmashree Dr. D.Y. Patil University,
India

***Correspondence:**
Yi Sun
13157166766@163.com
Chenyang Ye
yechenyang@zju.edu.cn
Ji Wang
jiwang1004@zju.edu.cn

[†]These authors have contributed equally to this work

Specialty section:
This article was submitted to Cancer Molecular Targets and Therapeutics, a section of the journal Frontiers in Oncology

Received: 09 February 2022
Accepted: 14 March 2022
Published: 05 April 2022

Citation:
Wang J, Chen C, Wang L, Xie M, Ge X, Wu S, He Y, Mou X, Ye C and Sun Y (2022) Patient-Derived Tumor Organoids: New Progress and Opportunities to Facilitate Precision Cancer Immunotherapy. Front. Oncol. 12:872531. doi: 10.3389/fonc.2022.872531

Cancer immunotherapy has revolutionized the field of cancer treatment in recent years. However, not all patients receiving cancer immunotherapy exhibit durable responses, and reliable, high-throughput testing platforms are urgently needed to guide personalized cancer immunotherapy. The ability of patient-derived tumor organoids to recapitulate pivotal features of original cancer tissues makes them useful as a preclinical model for cancer research and precision medicine. Nevertheless, many challenges exist in the translation of tumor organoid research to clinical decision making. Herein we discuss the applications of patient-derived tumor organoid models and the advances and potential of using complex immune-organoid systems as testing platforms to facilitate precision cancer immunotherapy. In addition, we highlight intriguing applications of tumor organoids with novel multi-omics in preclinical cancer research, highlighting genetic editing, proteomics, and liquid biopsy.

Keywords: tumor organoid, tumor microenvironment (TME), precision medicine, multi-omics, exosome (vesicle), CRISPR, proteomics

INTRODUCTION

Despite developments in early detection and treatment in the past decade, cancer remains the second leading cause of death worldwide (1). Recently, the emergence of cancer immunotherapy has revolutionized conventional cancer therapeutics and rejuvenated the field of cancer immunology (2–5). Nevertheless, only a select group of cancer patients have achieved marked clinical responses to cancer immunotherapy (6–9). The pressing need to improve cancer immunotherapies has brought great attention to the tumor immune microenvironment (TIME), whose study requires

robust and faithful preclinical research models recapitulating patient-specific tumor-immune interactions.

The TIME, including immune cells and cancer-associated fibroblasts (CAFs), greatly fosters carcinogenesis and tumor progression and influences the therapeutic responses of malignant cells (10–12). However, it was previously difficult to model this TIME in experiments (13). Cancer cell lines and patient-derived xenograft models (PDXs) suffer from several limitations. The former fail to adequately reflect the heterogeneity of tumor epithelial cells (13), and the latter are based on the murine immune system, which cannot replicate the tumor-immune interactions in humans (14). Patient-derived tumor organoids (PDTOs) have emerged as a useful model that can maintain tumor epithelial cells in a near-native state (15). PDTOs are able to maintain the heterogeneity of original cancers and can recapitulate the human TIME (16–18), thus providing an intriguing opportunity to facilitate precision cancer immunotherapy.

In this paper, we will discuss the state of the art of organoids in cancer immunological research. The limitations and prospects of this complex tumor organoid culture system are presented. We propose the potential applications of complex tumor organoids as testing platforms for various cancer immunotherapeutic approaches including antibody-based immunotherapy, oncolytic virus therapy and adoptive cell transfer therapy. We also highlight the intriguing combination of PDTOs with cutting-edge multi-omics and their applications in investigating cancer immunobiology and developing immunotherapy drugs.

PATIENT-DERIVED TUMOR ORGANOIDS

Organoids are 3D self-organized structures derived from adult tissue stem cells, embryonic stem cells, or induced pluripotent stem cells that mimic key structural and functional features of their *in vivo* counterpart organs (18–20). In 2009, Hans Clevers's group developed the first organoids from mouse intestinal stem cells (21), which established the starting point for other culture protocols for mouse and human tissue-derived organoids. The development of tumor organoid culture has allowed the application of PDTOs to test and predict drug responses in the context of precision cancer treatment. Currently, tumor organoid biobanks have been established from various types of cancer, including breast (17), lung (22, 23), colorectum (24–28), stomach (29–31), liver (32, 33), pancreas (34), ovary (35, 36), prostate (37), and brain (38). Although these epithelial-only PDTOs are generally available, their lack of immune and other nonimmune components of the TIME impedes immunotherapy assessment, such as checkpoint inhibition blockade and adaptive T-cell therapy. Therefore, significant effort is needed to optimize the tumor organoid culture system, forging a path toward organoid-guided personalized cancer immunotherapy.

RECENT ADVANCES IN COMPLEX TUMOR ORGANOID CULTURE

An increasing number of studies have focused on the essential factors of organoid development and novel organoid culture methods to recapitulate the TIME, facilitating the basic research and clinical translation of immuno-oncology. In this section, we describe the recent advances in complex tumor organoid culture systems (**Table 1**).

Adding Immune Cells to Organoid Culture

Currently, there are two conceptually different approaches to organoid–immune cell coculture models: the reconstitution approach expands tumor organoids and immune cells separately and then generates a coculture system with both components, whereas the holistic approach uses tumor organoids cultured

TABLE 1 | Overview of currently established tumor organoid-immune cell co-culture systems.

Co-culture approach	Tissue of origin	Sample type	Species	Immune cell type	Duration (days)	Functionality	Refs
Holistic approach	MC38 CRC cell line/ Melanoma	Cell implantation orthotopically/Surgical specimens	MDOTS/ PDOTS	T cells, B cells, granulocytic, monocytic lineages, dendritic cells,	9 days	Preserve immune cell reaction to immune checkpoint inhibitors	(39)
	MC38 CRC cell line	Subcutaneous mouse tumors	MDOTS	T cells	5 days	Preserve immune cell reaction to CDK4 and CDK6 inhibitors plus immune checkpoint inhibitors	(40)
	Colon, pancreas, and lung (14 distinct tissue sites)	Subcutaneous mouse tumors/Surgical specimens	MDOTS/ PDOTS	Macrophages, T cells, NK cells, and B cells	30 days	Preserve the TCR repertoire of the original fresh tumor	(41)
	CRC or lung cancer	Surgical specimens	PDOTS	$CD45^+$ tumour-resident leukocytes	>10 days	*In vitro* survival of $CD45^+$ cells	(42)
	Breast	Surgical specimens	PDOTS	Peripheral blood and tumour-derived γδ T cells	2-3 w	Preserve γδ T cell activation and tumour cell line cytolysis	(43)
Reconstitution approach	Gastric cancer	Triple-transgenic mouse model	MDOTS	CD8+ splenocytes and bone marrow-derived DCs	2 days	Organoid cytolysis	(44)
	Pancreatic cancer	Surgical specimens	PDOTS	peripheral blood lymphocytes & CAFs	6 days	Tumor-dependent lymphocyte infiltration and activation of myofibroblast-like CAFs	(45)

MDOTS, murine-derived organotypic tumor spheroids; PDOTS, patient-derived organotypic tumor spheroids; CAFs, cancer-associated fibroblasts.

directly from tumors while retaining endogenous immune cells (16, 46) (**Table 1**).

Reconstitution approaches initially expand organoids and immune cells separately and then establish cocultures for the investigation of organoid-immune cell interactions. The reconstitution of tumor organoids with various immune cell populations has been explored (**Table 1**). One study reported a triple coculture of mouse gastric tumor organoids with dendritic cells (DCs) and cytotoxic T lymphocytes (CTLs) (44). The stimulated CTLs resulted in significant death of gastric tumor organoids in the presence of an anti-PD-L1 neutralizing antibody (44). Additionally, PDTO-T cell cocultures hold the potential to predict the functionality of tumor-infiltrating lymphocytes (TILs) after immune checkpoint blockade. In a proof-of-principle study, the authors cocultured human colorectal cancer organoids with TILs using a reconstitution approach (47). The authors exposed the coculture to anti–PD-1 antibody and identified partial restoration of antitumor immunity in TILs with increased PD1 expression (47), revealing that these coculture assays have potential as a platform to evaluate the efficacy of cancer immunotherapy.

In contrast to reconstitution approaches, which add exogenous immune cells into epithelial-only tumor organoids, holistic approaches expand and activate endogenous immune cells within tumor organoids as a cohesive unit. A study in 2016 reported that intraepithelial lymphocytes were retained within organoids derived from human epithelial breast tissue (43). The authors then treated organoids for up to 4 weeks with aminobisphosphonate drugs that have been proven to selectively activate $V\delta2^+$ T cells, a subset of IFNγ-producing T cells. In a subsequent experiment, stimulated Vδ2+ T cells from breast organoids produced the antitumor cytokine IFNγ and efficiently killed breast carcinoma cells (43). In early 2018, two groups described 3D microfluidic-based culture to recapitulate anti-PD1/PDL1 cancer immunotherapy using mouse-derived and patient-derived organotypic tumor spheroids (MDOTS and PDOTS, respectively) (39, 40). Tumor spheroids together with endogenous lymphocyte and myeloid populations could be preserved for short-term (5-9 days) culture, allowing the investigation of endogenous immune–tumor interactions (39, 40). Later in the same year, one study described a sophisticated air-liquid interface (ALI) organoid culture method that enabled the coculture of the original tumor epithelium with its diverse endogenous immune cells (41). The authors showed that a diversity of endogenous immune cell types, including tumor-associated macrophages, T cells [T helper (Th), cytotoxic (Tc), regulatory (Treg), and exhausted (Tex)], natural killer (NK) cells, and B cells, were successfully cultured for up to 30 days in ALI organoid cultures (41). Strikingly, the ALI PDTOs could preserve the T cell receptor (TCR) heterogeneity found in the original tumor and model immune checkpoint blockade, which led to the proliferation and activation of tumor antigen-specific T cells and subsequent tumor cytotoxicity (41).

Adding Cancer-Associated Fibroblasts

CAFs account for a large proportion of the tumor stroma and play considerable roles in the TIME (48–50). Therefore, it is important to include CAFs in the culture system of tumor organoids. Indeed, PDTOs and CAFs have recently been employed in 3D coculture systems to investigate the reciprocal interaction between tumor cells and CAFs (51–53). CAFs have been utilized to supplement PDTO cultures using a reconstitution approach (52–54). One study explored CAF heterogeneity by coculturing pancreatic cancer organoids and CAFs and identified two spatially separated subtypes of CAFs with distinct protein expression profiles: high α-smooth muscle actin (αSMA)-expressing myofibroblast-like CAFs proximal to tumor cells and high IL-6-expressing inflammatory CAFs distally located from neoplastic cells (53). The dynamic tumor-stroma interaction was investigated in a 3D coculture system of lung squamous carcinoma (LUSC) organoids with CAFs and extracellular matrix (ECM) (55). Intriguingly, the authors showed that CAFs could override cell intrinsic oncogenic changes in determining the disease phenotype in the LUSC setting (55). The ability to retain the heterogeneity and phenotype of the original tumor tissue makes the 3D coculture system of PDTOs and CAFs a promising model for tumor immune microenvironment research.

Adding Vasculature

Another major issue in the current organoid system is the lack of vascular circulation. Without a blood supply, organoids can grow only to a limited size, beyond which the center of the organoid would develop necrosis (56, 57). To overcome this challenge, developments in organoid vascularization and perfusion are required to maintain the complexity and scale of organoids.

Organoid vascularization could be generated by the transplantation of organoids into vasculature-rich animal tissue, including chicken chorion allantois membrane models, with the host vasculature integrating into the organoids (58, 59). The methods of adding vasculature *in vitro* include the layer-by-layer deposition of endothelial cells and the selective removal of material to form tubular voids that are connected to perfusion networks (60). Moreover, vasculature is also induced in organoid-endothelial cell cocultures in microfluidic devices (60). In one recent study, 3D tumor spheroids were integrated with human umbilical vein endothelial cells (HUVECs) and normal human lung fibroblasts (nhLFs) in a fibrin gel, which developed a perfusable vasculature *in vitro* (61).

Adding Extracellular Matrix

The *in vivo* ECM is a dynamic polymer network that not only provides structural support but also delivers biochemical signaling cues (62, 63). In relation to cancer research, the ECM plays critical roles in tumor growth, invasion, metastasis, and metabolism (64, 65). Therefore, it is crucial to integrate an appropriate ECM into tumor organoid culture models. Over the last decade, the most commonly used matrix for the culture of tumor organoids has been basement membrane extracts (BMEs) (66). The BMEs have been commercially available under the trade name Corning Matrigel, a solubilized basement membrane matrix secreted by Engelbreth-Holm-Swarm (EHS) mouse sarcoma cells. BMEs that include ECM proteins (laminin, collagen IV, and entactin) are simple to

prepare and use in organoid culture. Although BMEs have provided a tumor-relevant environment for human tumor organoid culture, several limitations hinder our understanding of organoid-ECM interactions, including extensive batch-to-batch variability, xenogenic contamination, ill-defined ECM components, and poor control of mechanical properties (67). Collagen is the most abundant structural ECM component in human tumor tissues. Collagen type I matrices are also widely used as scaffolds for tumor organoid studies because they share biochemical and biophysical features of the TIME, such as cell adhesion sites and stiffness (68). Tumor organoids with a collagen type I matrix could be utilized for the investigation of invasive cell phenotypes (69, 70). Nevertheless, as collagen is often animal derived, collagen type I matrices suffer from similar limitations to BMEs. Thus, it is imperative to develop new ECM materials to replace the current animal-derived matrices. Engineered matrices are promising alternatives for scaffolds in tumor organoid models, offering well-defined, tunable ECMs with high batch-to-batch reproducibility (71). Nevertheless, engineered matrices also have some limitations, including low culture efficiency and a lack of sufficient spatiotemporal control to model the dynamics of the TIME. Overall, further efforts are still required to develop the optimal ECM for tumor organoid culture, facilitating a more complete understanding of cancer-ECM interactions *in vitro*.

COMPLEX ORGANOIDS AND IMMUNOTHERAPEUTICS

An ideal preclinical platform to test cancer immunotherapies requires a cancer–immune cell coculture which reflects the cellular distribution of the original tumor and recapitulates the response to immunotherapeutic. Recent advances in complex tumor organoids have shown this organoid system could be used as efficient and pivotal platforms to assess the efficacy of cancer immunotherapy and the identification of novel combination treatment strategies.

Antibody-Based Immunotherapy

Antibody-based immunotherapy is a major form of cancer immunotherapeutics that can specifically limit cancer cell survival and activate the immune system to eradicate cancer cells (72). Currently, tumor organoids have mainly been employed as preclinical models to investigate the efficacy of antibody-based checkpoint blockade immunotherapy. Using either reconstitution or holistic approach, the efficacy of PD-1/PD-L1 immunotherapy could be recapitulated in complex organoid culture system in the presence of functional immune cell populations (41, 45). Intriguingly, the immune–tumor organoids system could also be used to identify novel strategies for antibody-based combination cancer treatments. Small molecule inhibitors such as TBK1/IKKe inhibitor or CDK4/6 inhibitor were reported to synergize with PD-1 blockade and lead to enhanced tumor killing (39, 40). Bispecific immunomodulatory antibodies could simultaneously bind two different antigens located on cytotoxic cell and target tumor cell respectively, resulting in tumor cytotoxicity. Cibisatamab is a bispecific antibody designed to target CD3 on T cells and CEA in colorectal cancer cells. In one recent study, the complex cancer organoids were used to identify potential novel strategy for enhanced therapeutic effect of cibisatamab (73).

Oncolytic Virus Therapy

Oncolytic viruses that preferentially infect and replicate in cancer cells, provide an intriguing immunotherapeutic option for cancer patients (74). Oncolytic viruses can not only result in direct destruction of cancer cells, but also trigger host anti-tumor immune system responses (75). Several groups used tumor organoids to evaluate the efficacy of oncolytic virus therapy in preclinical settings. These studies demonstrated that oncolytic adenovirus could show selective replication in PDTOs while not in organoids derived from normal tissue, and tumor organoids are ideal preclinical models to predict responses to oncolytic adenovirus therapy (76–78). However, these studies failed to investigate oncolytic virus therapy in complex immune–organoids. One recent study first described the efficacy of a novel oncolytic adenovirus treatment in PDTOs with various immune cell populations. In order to activate multiple immune effector populations including neutrophils and natural killer cells, the authors engineered a Fc-fusion peptide against PD-L1 consisting of a cross-hybrid Fc region containing constant regions of an IgG1 and an IgA1. This Fc-fusion peptide was cloned into an oncolytic adenovirus, and enhanced oncolytic efficacy was observed in complex immune–organoids platform (79).

Adoptive Cell Transfer Therapy

Adoptive cell transfer therapy represents an important alternative to immune checkpoint inhibitors and uses genetically engineered T cells with chimeric antigen receptors (CARs) or high-affinity T cell receptors (TCRs) recognizing tumor-associated antigens (80). In this scenario, antitumor lymphocytes are expanded ex vivo and then given back to the patients. While CAR-T cells targeting CD19 show prominent effects in hematological malignancies including B cell lymphoma and acute lymphoblastic leukemia, efficacy in solid tumor remains elusive. Complex organoids have shown great potential to serve as efficient platforms for evaluation of CAR cell efficacy. PDTOs have now been used to test specific tumor killing of CAR-NK92 targeting EGFRvIII or FRIZZLED in colorectal cancer setting (81). Additionally, PDTOs could be utilized as culture platforms to enrich tumor reactive T cells and induce more effective anticancer immune responses (82).

COMBINATION OF PDTOS WITH MULTIOMICS

Recent advances in organoids have not only facilitated biobank-based disease modeling, cancer therapeutic strategies, and personalized medicine (15) but also revolutionized the field of cancer studies by improving the understanding of mechanisms

and disease modeling at the molecular level (18, 83). Nevertheless, based on current knowledge and applications, further improvements on the road to tumor organoid-based clinical decision making are still required. In this section, we will discuss the latest applications and promising prospects of tumor organoids in various omics disciplines that could help move precision medicine forward (**Figure 1**).

Genetic Engineering

Genetic engineering, especially the CRISPR–Cas9 system, has substantially improved genetic modification and screening in both *in vitro* and *in vivo* human cancer models, such as cell lines and mouse models, revealing previously unknown cancer drivers (84–90). Nevertheless, it is difficult for these preclinical models to accurately recapitulate *in vivo* tumor biology. To this end, there has been a growing interest in performing CRISPR–Cas9 genome editing in tumor organoids. In 2013, Hans Clevers's group was the first to implement CRISPR–Cas9 technology in an organoid model (91). They successfully corrected the CFTR gene in intestinal organoids, demonstrating that the CRISPR/Cas9 system is feasible and efficient for genome editing in patient-derived organoids (91). In one study, Han and coworkers performed genome-wide CRISPR screens in both 2D and 3D lung cancer models and found that screening in 3D models captured the characteristics of oncogenes and tumor suppressor genes more accurately than the use of 2D models (92). Interestingly, the authors reported that the knockout of the cancer driver gene CREBBP exerts a positive growth impact on a 3D model but a negative growth effect in a 2D cancer cell line (92). CRISPR–Cas9 could also be used to investigate the clonal evolution of carcinogenesis. Successful multihit oncogenic transformation of normal-tissue-derived organoids to carcinoma has been achieved by introducing simultaneous or sequential oncogenic mutations into tissues such as breast, stomach, pancreas and colon (31, 93–96). Although several limitations need to be addressed including heterogeneous growth rates of organoids and single-guide RNA coverage (97), cancer organoids could serve as a promising platform for CRISPR–Cas9-mediated genome editing and large-scale screens to improve the efficacy of cancer immunotherapy.

Proteomics and Immunopeptidomics

Mass spectrometry (MS)-based proteomics shows great promise to yield important insights for cancer therapy, yet poor resolution, the need for large amounts of samples, and the absence of high-throughput capacity are limiting factors. Recent advances in sample processing, separations and MS instrumentation highlight the possibility of personalized proteomics (98). The potentially unlimited supply of well-characterized patient material makes organoids a unique platform for personalized proteomic analysis. In 2017, Cristobal and coworkers first performed deep proteome profiling of human colon organoids and identified common features shared by the original cancer samples, as well as individual diversity that could aid in personalized cancer treatment (99). Over the past years, the recognition of neoantigens has been an important driver of the clinical activity of T cell-based cancer immunotherapy, and various strategies to identify accurate neoantigens have been pursued (100). In a 2019 study, the authors greatly improved neoantigen identification by using deep learning and large datasets of human leukocyte antigen (HLA) peptide mass spectrometry based on human tumor tissues to create an optimal model of antigen presentation for neoantigen prediction (101). It is likely that tumor organoids could serve as an ideal system to further advance the identification of neoantigens. In 2020, Demmers and coworkers were the first to perform tumor organoid proteomics for the investigation of intrapatient clonal diversity in HLA peptide presentation (102). Single-cell-derived tumor organoids showed high diversity in HLA peptide

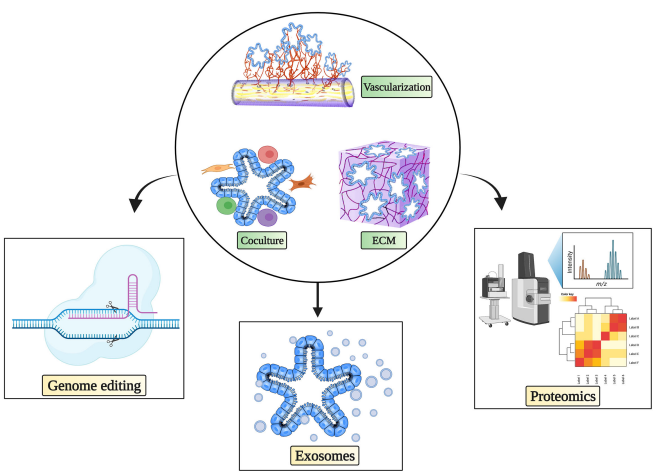

FIGURE 1 | Complex culture system and possibilities for tumor organoids in cancer immunotherapy research. Complex immune organoid culture systems including fibroblasts, various immune cells, and vasculature in addition to tumor organoids could be leveraged to serve as platforms for testing cancer immunotherapy. Various state-of-the-art technologies can be used in combination with complex tumor organoid culture systems to propel precision medicine. The figure was generated on Biorender.com.

presentation even within the same cancer patient (102). In summary, organoid-based proteomic analyses are currently feasible and could expand the technical toolbox for precision cancer therapy in the near future.

Exosomes

Exosomes are small (30-150 nm) extracellular vesicles surrounded by a lipid bilayer membrane and secreted by most eukaryotic cells (103, 104). The components of exosomes, including proteins, nucleic acids (DNA, mRNA, microRNA, lncRNA, etc.), lipids, and metabolites, play important roles in regulating tumor growth, metastasis, metabolism and immune escape (56, 105, 106). Exosomes have been detected in multiple bodily fluids, including blood, urine, cerebrospinal fluid, bile, and saliva, revealing great potential to serve as novel biomarkers for cancer diagnosis (107, 108).

Tumor-derived exosomes are crucial in transferring intercellular signals to modulate the TIME (109, 110). Recently, exosomal PD-L1 has been reported to play vital roles in systemically suppression of the anti-tumor immune response, which illustrates potential mechanism of resistance to PD-L1 blockade (111, 112). Of note, exosomal PD-L1 before and during anti-PD-1 treatment could indicate dynamic states of anti-tumor immunity (111). Therefore, tumor organoid-derived exosomes hold great promise to provide valuable insights regarding immunosurveillance and ultimately cancer immunotherapy. To date, only a few groups have explored the merits of PDTO-derived exosomes in preclinical cancer research. In one study, the authors cocultured esophageal adenocarcinoma-derived exosomes with normal human gastric epithelial organoids (gastroids) and found that exosomal miR-25 and miR-210 could induce an oncogenic phenotype in gastroids (113). Another recent study indicated that PDTO-derived exosomal miRNAs had potential as diagnostic biomarkers for precancerous lesions of colorectal cancer (114). PDTOs could be the source of standardized and scalable production platforms for tumor-derived exosomes, facilitating cancer diagnosis and immunotherapy. However, the availability of organoid-derived exosomes in sufficient quantities, potential contaminants from complex PDTO cultures, and heterogeneous growth rates of PDTOs could be challenging issues, and further research is needed. More studies focusing on the application of organoid-derived exosomes for cancer immunotherapy are underway, and the results are eagerly awaited.

CONCLUSION AND FUTURE OUTLOOK

The current efficacy of cancer immunotherapy is not satisfactory, and there is a high unmet need for a faithful preclinical model that allows better translation from bench to bedside. Tumor-derived organoids have shown promise for modeling the effects of cancer immunotherapy. While the clinical application of organoid technology is attractive, several significant challenges remain to be overcome. One major bottleneck is that tumor organoids are often derived from biopsies representing only a small part of the entire tumor. In this way, the complexity of the original malignant lesion will always be underrated, and intratumoral heterogeneity could hinder clinical translation. Additionally, the long-term preservation of various immune cells and CAFs needs further optimization.

There are many clinical trials currently ongoing to appraise the merits of PDTOs in precision cancer treatment. Complex tumor organoid culture systems hold promise to unravel the dynamic interactions between the cancer and the immune system and to support drug screening for personalized immunotherapy in the contexts of basic research and clinical trials. As a research tool, tumor organoids currently offer the most accurate *in vitro* system to recapitulate the original human cancer tissues. The applications of genome-wide CRISPR screens, proteomics and exosomes in tumor organoids show great potential for both basic and translational cancer research in the foreseeable future.

DATA AVAILABILITY STATEMENT

The original contributions presented in the study are included in the article/supplementary material. Further inquiries can be directed to the corresponding authors.

AUTHOR CONTRIBUTIONS

JW, CC, and CY conceived this paper. JW, CC, and LW collected the literature. LW and MX drew the schematic diagram. CC and XG prepared the tables. JW, CC, and CY wrote the manuscript. SW, YH, and XM corrected and provide advices for the manuscript and figure. JW, CY, and YS conducted the study supervision and revised the manuscript. All authors read and approved the final manuscript.

FUNDING

This work was supported by research grant from the National Natural Science Foundation of China (82103102 to CY). This research was also supported by Zhejiang Provincial Natural Science Foundation of China under Grant No. LQ22H160020 to JW and Grant No. LGF21H150004 to SW.

REFERENCES

1. Siegel RL, Miller KD, Fuchs HE, Jemal A. Cancer Statistics, 2022. *CA Cancer J Clin* (2022) 72(1):7–33. doi: 10.3322/caac.21708

2. Topalian SL, Hodi FS, Brahmer JR, Gettinger SN, Smith DC, McDermott DF, et al. Safety, Activity, and Immune Correlates of Anti-PD-1 Antibody in Cancer. *N Engl J Med* (2012) 366(26):2443–54. doi: 10.1056/NEJMoa1200690

3. Pardoll DM. The Blockade of Immune Checkpoints in Cancer Immunotherapy. *Nat Rev Cancer* (2012) 12(4):252–64. doi: 10.1038/nrc3239
4. Brahmer JR, Tykodi SS, Chow LQ, Hwu WJ, Topalian SL, Hwu P, et al. Safety and Activity of Anti-PD-L1 Antibody in Patients With Advanced Cancer. *N Engl J Med* (2012) 366(26):2455–65. doi: 10.1056/NEJMoa1200694
5. Sharma P, Allison JP. The Future of Immune Checkpoint Therapy. *Science* (2015) 348(6230):56–61. doi: 10.1126/science.aaa8172
6. Chen L, Diao L, Yang Y, Yi X, Rodriguez BL, Li Y, et al. CD38-Mediated Immunosuppression as a Mechanism of Tumor Cell Escape From PD-1/PD-L1 Blockade. *Cancer Discov* (2018) 8(9):1156–75. doi: 10.1158/2159-8290.CD-17-1033
7. Eckstein M, Gupta S. New Insights in Predictive Determinants of the Tumor Immune Microenvironment for Immune Checkpoint Inhibition: A Never Ending Story? *Ann Transl Med* (2019) 7(Suppl 3):S135. doi: 10.21037/atm.2019.06.12
8. Jiang Y, Zhao X, Fu J, Wang H. Progress and Challenges in Precise Treatment of Tumors With PD-1/PD-L1 Blockade. *Front Immunol* (2020) 11:339. doi: 10.3389/fimmu.2020.00339
9. Haslam A, Prasad V. Estimation of the Percentage of US Patients With Cancer Who Are Eligible for and Respond to Checkpoint Inhibitor Immunotherapy Drugs. *JAMA Netw Open* (2019) 2(5):e192535. doi: 10.1001/jamanetworkopen.2019.2535
10. Binnewies M, Roberts EW, Kersten K, Chan V, Fearon DF, Merad M, et al. Understanding the Tumor Immune Microenvironment (TIME) for Effective Therapy. *Nat Med* (2018) 24(5):541–50. doi: 10.1038/s41591-018-0014-x
11. Hanahan D, Weinberg RA. Hallmarks of Cancer: The Next Generation. *Cell* (2011) 144(5):646–74. doi: 10.1016/j.cell.2011.02.013
12. Chen DS, Mellman I. Oncology Meets Immunology: The Cancer-Immunity Cycle. *Immunity* (2013) 39(1):1–10. doi: 10.1016/j.immuni.2013.07.012
13. Junttila MR, de Sauvage FJ. Influence of Tumour Micro-Environment Heterogeneity on Therapeutic Response. *Nature* (2013) 501(7467):346–54. doi: 10.1038/nature12626
14. Roerink SF, Sasaki N, Lee-Six H, Young MD, Alexandrov LB, Behjati S, et al. Intra-Tumour Diversification in Colorectal Cancer at the Single-Cell Level. *Nature* (2018) 556(7702):457–62. doi: 10.1038/s41586-018-0024-3
15. Tuveson D, Clevers H. Cancer Modeling Meets Human Organoid Technology. *Science* (2019) 364(6444):952–5. doi: 10.1126/science.aaw6985
16. Bar-Ephraim YE, Kretzschmar K, Clevers H. Organoids in Immunological Research. *Nat Rev Immunol* (2020) 20(5):279–93. doi: 10.1038/s41577-019-0248-y
17. Sachs N, de Ligt J, Kopper O, Gogola E, Bounova G, Weeber F, et al. A Living Biobank of Breast Cancer Organoids Captures Disease Heterogeneity. *Cell* (2018) 172(1-2):373–86.e10. doi: 10.1016/j.cell.2017.11.010
18. Drost J, Clevers H. Organoids in Cancer Research. *Nat Rev Cancer* (2018) 18(7):407–18. doi: 10.1038/s41568-018-0007-6
19. Clevers H. Modeling Development and Disease With Organoids. *Cell* (2016) 165(7):1586–97. doi: 10.1016/j.cell.2016.05.082
20. Sato T, Clevers H. Growing Self-Organizing Mini-Guts From a Single Intestinal Stem Cell: Mechanism and Applications. *Science* (2013) 340(6137):1190–4. doi: 10.1126/science.1234852
21. Sato T, Vries RG, Snippert HJ, van de Wetering M, Barker N, Stange DE, et al. Single Lgr5 Stem Cells Build Crypt-Villus Structures *In Vitro* Without a Mesenchymal Niche. *Nature* (2009) 459(7244):262–5. doi: 10.1038/nature07935
22. Kim M, Mun H, Sung CO, Cho EJ, Jeon HJ, Chun SM, et al. Patient-Derived Lung Cancer Organoids as *In Vitro* Cancer Models for Therapeutic Screening. *Nat Commun* (2019) 10(1):3991. doi: 10.1038/s41467-019-11867-6
23. Shi R, Radulovich N, Ng C, Liu N, Notsuda H, Cabanero M, et al. Organoid Cultures as Preclinical Models of Non-Small Cell Lung Cancer. *Clin Cancer Res* (2020) 26(5):1162–74. doi: 10.1158/1078-0432.CCR-19-1376
24. van de Wetering M, Francies HE, Francis JM, Bounova G, Iorio F, Pronk A, et al. Prospective Derivation of a Living Organoid Biobank of Colorectal Cancer Patients. *Cell* (2015) 161(4):933–45. doi: 10.1016/j.cell.2015.03.053
25. Fujii M, Shimokawa M, Date S, Takano A, Matano M, Nanki K, et al. A Colorectal Tumor Organoid Library Demonstrates Progressive Loss of Niche Factor Requirements During Tumorigenesis. *Cell Stem Cell* (2016) 18(6):827–38. doi: 10.1016/j.stem.2016.04.003
26. Vlachogiannis G, Hedayat S, Vatsiou A, Jamin Y, Fernández-Mateos J, Khan K, et al. Patient-Derived Organoids Model Treatment Response of Metastatic Gastrointestinal Cancers. *Science* (2018) 359(6378):920–6. doi: 10.1126/science.aao2774
27. Weeber F, van de Wetering M, Hoogstraat M, Dijkstra KK, Krijgsman O, Kuilman T, et al. Preserved Genetic Diversity in Organoids Cultured From Biopsies of Human Colorectal Cancer Metastases. *Proc Natl Acad Sci USA* (2015) 112(43):13308–11. doi: 10.1073/pnas.1516689112
28. Yao Y, Xu X, Yang L, Zhu J, Wan J, Shen L, et al. Patient-Derived Organoids Predict Chemoradiation Responses of Locally Advanced Rectal Cancer. *Cell Stem Cell* (2020) 26(1):17–26.e6. doi: 10.1016/j.stem.2019.10.010
29. Seidlitz T, Merker SR, Rothe A, Zakrzewski F, von Neubeck C, Grützmann K, et al. Human Gastric Cancer Modelling Using Organoids. *Gut* (2019) 68(2):207–17. doi: 10.1136/gutjnl-2017-314549
30. Yan HHN, Siu HC, Law S, Ho SL, Yue SSK, Tsui WY, et al. A Comprehensive Human Gastric Cancer Organoid Biobank Captures Tumor Subtype Heterogeneity and Enables Therapeutic Screening. *Cell Stem Cell* (2018) 23(6):882–97.e11. doi: 10.1016/j.stem.2018.09.016
31. Nanki K, Toshimitsu K, Takano A, Fujii M, Shimokawa M, Ohta Y, et al. Divergent Routes Toward Wnt and R-Spondin Niche Independency During Human Gastric Carcinogenesis. *Cell* (2018) 174(4):856–69.e17. doi: 10.1016/j.cell.2018.07.027
32. Broutier L, Mastrogiovanni G, Verstegen MM, Francies HE, Gavarró LM, Bradshaw CR, et al. Human Primary Liver Cancer-Derived Organoid Cultures for Disease Modeling and Drug Screening. *Nat Med* (2017) 23(12):1424–35. doi: 10.1038/nm.4438
33. Nuciforo S, Fofana I, Matter MS, Blumer T, Calabrese D, Boldanova T, et al. Organoid Models of Human Liver Cancers Derived From Tumor Needle Biopsies. *Cell Rep* (2018) 24(5):1363–76. doi: 10.1016/j.celrep.2018.07.001
34. Huang L, Holtzinger A, Jagan I, BeGora M, Lohse I, Ngai N, et al. Ductal Pancreatic Cancer Modeling and Drug Screening Using Human Pluripotent Stem Cell- and Patient-Derived Tumor Organoids. *Nat Med* (2015) 21(11):1364–71. doi: 10.1038/nm.3973
35. Kopper O, de Witte CJ, Lõhmussaar K, Valle-Inclan JE, Hami N, Kester L, et al. An Organoid Platform for Ovarian Cancer Captures Intra- and Interpatient Heterogeneity. *Nat Med* (2019) 25(5):838–49. doi: 10.1038/s41591-019-0422-6
36. Hill SJ, Decker B, Roberts EA, Horowitz NS, Muto MG, Worley MJJr., et al. Prediction of DNA Repair Inhibitor Response in Short-Term Patient-Derived Ovarian Cancer Organoids. *Cancer Discov* (2018) 8(11):1404–21. doi: 10.1158/2159-8290.CD-18-0474
37. Beshiri ML, Tice CM, Tran C, Nguyen HM, Sowalsky AG, Agarwal S, et al. A PDX/Organoid Biobank of Advanced Prostate Cancers Captures Genomic and Phenotypic Heterogeneity for Disease Modeling and Therapeutic Screening. *Clin Cancer Res* (2018) 24(17):4332–45. doi: 10.1158/1078-0432.CCR-18-0409
38. Jacob F, Salinas RD, Zhang DY, Nguyen PTT, Schnoll JG, Wong SZH, et al. A Patient-Derived Glioblastoma Organoid Model and Biobank Recapitulates Inter- and Intra-Tumoral Heterogeneity. *Cell* (2020) 180(1):188–204.e22. doi: 10.1016/j.cell.2019.11.036
39. Jenkins RW, Aref AR, Lizotte PH, Ivanova E, Stinson S, Zhou CW, et al. Ex Vivo Profiling of PD-1 Blockade Using Organotypic Tumor Spheroids. *Cancer Discov* (2018) 8(2):196–215. doi: 10.1158/2159-8290.CD-17-0833
40. Deng J, Wang ES, Jenkins RW, Li S, Dries R, Yates K, et al. CDK4/6 Inhibition Augments Antitumor Immunity by Enhancing T-Cell Activation. *Cancer Discov* (2018) 8(2):216–33. doi: 10.1158/2159-8290.CD-17-0915
41. Neal JT, Li X, Zhu J, Giangarra V, Grzeskowiak CL, Ju J, et al. Organoid Modeling of the Tumor Immune Microenvironment. *Cell* (2018) 175(7):1972–88.e16. doi: 10.1016/j.cell.2018.11.021
42. Finnberg NK, Gokare P, Lev A, Grivennikov SI, MacFarlane A, Campbell KS, et al. Application of 3D Tumoroid Systems to Define Immune and Cytotoxic Therapeutic Responses Based on Tumoroid and Tissue Slice Culture Molecular Signatures. *Oncotarget* (2017) 8(40):66747–57. doi: 10.18632/oncotarget.19965
43. Zumwalde NA, Haag JD, Sharma D, Mirrielees JA, Wilke LG, Gould MN, et al. Analysis of Immune Cells From Human Mammary Ductal Epithelial

Organoids Reveals Vδ2+ T Cells That Efficiently Target Breast Carcinoma Cells in the Presence of Bisphosphonate. *Cancer Prev Res (Phila)* (2016) 9 (4):305–16. doi: 10.1158/1940-6207.CAPR-15-0370-T
44. Chakrabarti J, Holokai L, Syu L, Steele NG, Chang J, Wang J, et al. Hedgehog Signaling Induces PD-L1 Expression and Tumor Cell Proliferation in Gastric Cancer. *Oncotarget* (2018) 9(100):37439–57. doi: 10.18632/oncotarget.26473
45. Tsai S, McOlash L, Palen K, Johnson B, Duris C, Yang Q, et al. Development of Primary Human Pancreatic Cancer Organoids, Matched Stromal and Immune Cells and 3D Tumor Microenvironment Models. *BMC Cancer* (2018) 18(1):335. doi: 10.1186/s12885-018-4238-4
46. Yuki K, Cheng N, Nakano M, Kuo CJ. Organoid Models of Tumor Immunology. *Trends Immunol* (2020) 41(8):652–64. doi: 10.1016/j.it.2020.06.010
47. Kong JCH, Guerra GR, Millen RM, Roth S, Xu H, Neeson PJ, et al. Tumor-Infiltrating Lymphocyte Function Predicts Response to Neoadjuvant Chemoradiotherapy in Locally Advanced Rectal Cancer. *JCO Precis Oncol* (2018) 2):1–15. doi: 10.1200/PO.18.00075
48. Kalluri R. The Biology and Function of Fibroblasts in Cancer. *Nat Rev Cancer* (2016) 16(9):582–98. doi: 10.1038/nrc.2016.73
49. Erez N, Truitt M, Olson P, Arron ST, Hanahan D. Cancer-Associated Fibroblasts Are Activated in Incipient Neoplasia to Orchestrate Tumor-Promoting Inflammation in an NF-kappaB-Dependent Manner. *Cancer Cell* (2010) 17(2):135–47. doi: 10.1016/j.ccr.2009.12.041
50. Liu T, Han C, Wang S, Fang P, Ma Z, Xu L, et al. Cancer-Associated Fibroblasts: An Emerging Target of Anti-Cancer Immunotherapy. *J Hematol Oncol* (2019) 12(1):86. doi: 10.1186/s13045-019-0770-1
51. Bleijs M, van de Wetering M, Clevers H, Drost J. Xenograft and Organoid Model Systems in Cancer Research. *EMBO J* (2019) 38(15):e101654. doi: 10.15252/embj.2019101654
52. Seino T, Kawasaki S, Shimokawa M, Tamagawa H, Toshimitsu K, Fujii M, et al. Human Pancreatic Tumor Organoids Reveal Loss of Stem Cell Niche Factor Dependence During Disease Progression. *Cell Stem Cell* (2018) 22 (3):454–67.e6. doi: 10.1016/j.stem.2017.12.009
53. Öhlund D, Handly-Santana A, Biffi G, Elyada E, Almeida AS, Ponz-Sarvise M, et al. Distinct Populations of Inflammatory Fibroblasts and Myofibroblasts in Pancreatic Cancer. *J Exp Med* (2017) 214(3):579–96. doi: 10.1084/jem.20162024
54. Biffi G, Oni TE, Spielman B, Hao Y, Elyada E, Park Y, et al. IL1-Induced JAK/STAT Signaling Is Antagonized by Tgfβ to Shape CAF Heterogeneity in Pancreatic Ductal Adenocarcinoma. *Cancer Discov* (2019) 9(2):282–301. doi: 10.1158/2159-8290.CD-18-0710
55. Chen S, Giannakou A, Wyman S, Gruzas J, Golas J, Zhong W, et al. Cancer-Associated Fibroblasts Suppress SOX2-Induced Dysplasia in a Lung Squamous Cancer Coculture. *Proc Natl Acad Sci USA* (2018) 115(50): E11671–e80. doi: 10.1073/pnas.1803718115
56. Hirschhaeuser F, Menne H, Dittfeld C, West J, Mueller-Klieser W, Kunz-Schughart LA. Multicellular Tumor Spheroids: An Underestimated Tool Is Catching Up Again. *J Biotechnol* (2010) 148(1):3–15. doi: 10.1016/j.jbiotec.2010.01.012
57. Langan LM, Dodd NJ, Owen SF, Purcell WM, Jackson SK, Jha AN. Direct Measurements of Oxygen Gradients in Spheroid Culture System Using Electron Parametric Resonance Oximetry. *PloS One* (2016) 11(2):e0149492. doi: 10.1371/journal.pone.0149492
58. Mansour AA, Gonçalves JT, Bloyd CW, Li H, Fernandes S, Quang D, et al. An *In Vivo* Model of Functional and Vascularized Human Brain Organoids. *Nat Biotechnol* (2018) 36(5):432–41. doi: 10.1038/nbt.4127
59. Wörsdörfer P, Dalda N, Kern A, Krüger S, Wagner N, Kwok CK, et al. Generation of Complex Human Organoid Models Including Vascular Networks by Incorporation of Mesodermal Progenitor Cells. *Sci Rep* (2019) 9(1):15663. doi: 10.1038/s41598-019-52204-7
60. Grebenyuk S, Ranga A. Engineering Organoid Vascularization. *Front Bioeng Biotechnol* (2019) 7:39. doi: 10.3389/fbioe.2019.00039
61. Haase K, Offeddu GS, Gillrie MR, Kamm RD. Endothelial Regulation of Drug Transport in a 3D Vascularized Tumor Model. *Adv Funct Mater* (2020) 30(48):2002444. doi: 10.1002/adfm.202002444
62. Lu P, Weaver VM, Werb Z. The Extracellular Matrix: A Dynamic Niche in Cancer Progression. *J Cell Biol* (2012) 196(4):395–406. doi: 10.1083/jcb.201102147
63. Pickup MW, Mouw JK, Weaver VM. The Extracellular Matrix Modulates the Hallmarks of Cancer. *EMBO Rep* (2014) 15(12):1243–53. doi: 10.15252/embr.201439246
64. Winkler J, Abisoye-Ogunniyan A, Metcalf KJ, Werb Z. Concepts of Extracellular Matrix Remodelling in Tumour Progression and Metastasis. *Nat Commun* (2020) 11(1):5120. doi: 10.1038/s41467-020-18794-x
65. Kai F, Drain AP, Weaver VM. The Extracellular Matrix Modulates the Metastatic Journey. *Dev Cell* (2019) 49(3):332–46. doi: 10.1016/j.devcel.2019.03.026
66. LeSavage BL, Suhar RA, Broguiere N, Lutolf MP, Heilshorn SC. Next-Generation Cancer Organoids. *Nat Mater* (2022) 21:143–59. doi: 10.1038/s41563-021-01057-5
67. Aisenbrey EA, Murphy WL. Synthetic Alternatives to Matrigel. *Nat Rev Mater* (2020) 5(7):539–51. doi: 10.1038/s41578-020-0199-8
68. Szot CS, Buchanan CF, Freeman JW, Rylander MN. 3d In Vitro Bioengineered Tumors Based on Collagen I Hydrogels. *Biomaterials* (2011) 32(31):7905–12. doi: 10.1016/j.biomaterials.2011.07.001
69. Cheung KJ, Gabrielson E, Werb Z, Ewald AJ. Collective Invasion in Breast Cancer Requires a Conserved Basal Epithelial Program. *Cell* (2013) 155 (7):1639–51. doi: 10.1016/j.cell.2013.11.029
70. Nguyen-Ngoc KV, Cheung KJ, Brenot A, Shamir ER, Gray RS, Hines WC, et al. ECM Microenvironment Regulates Collective Migration and Local Dissemination in Normal and Malignant Mammary Epithelium. *Proc Natl Acad Sci USA* (2012) 109(39):E2595–604. doi: 10.1073/pnas.1212834109
71. Lee HJ, Mun S, Pham DM, Kim P. Extracellular Matrix-Based Hydrogels to Tailoring Tumor Organoids. *ACS Biomater Sci Eng* (2021) 7(9):4128–35. doi: 10.1021/acsbiomaterials.0c01801
72. Weiner LM, Murray JC, Shuptrine CW. Antibody-Based Immunotherapy of Cancer. *Cell* (2012) 148(6):1081–4. doi: 10.1016/j.cell.2012.02.034
73. Gonzalez-Exposito R, Semiannikova M, Griffiths B, Khan K, Barber LJ, Woolston A, et al. CEA Expression Heterogeneity and Plasticity Confer Resistance to the CEA-Targeting Bispecific Immunotherapy Antibody Cibisatamab (CEA-TCB) in Patient-Derived Colorectal Cancer Organoids. *J Immunother Cancer* (2019) 7(1):101. doi: 10.1186/s40425-019-0575-3
74. Harrington K, Freeman DJ, Kelly B, Harper J, Soria JC. Optimizing Oncolytic Virotherapy in Cancer Treatment. *Nat Rev Drug Discov* (2019) 18(9):689–706. doi: 10.1038/s41573-019-0029-0
75. Heidbuechel JPW, Engeland CE. Oncolytic Viruses Encoding Bispecific T Cell Engagers: A Blueprint for Emerging Immunovirotherapies. *J Hematol Oncol* (2021) 14(1):63. doi: 10.1186/s13045-021-01075-5
76. Raimondi G, Mato-Berciano A, Pascual-Sabater S, Rovira-Rigau M, Cuatrecasas M, Fondevila C, et al. Patient-Derived Pancreatic Tumour Organoids Identify Therapeutic Responses to Oncolytic Adenoviruses. *EBioMedicine* (2020) 56:102786. doi: 10.1016/j.ebiom.2020.102786
77. Zhu Z, Mesci P, Bernatchez JA, Gimple RC, Wang X, Schafer ST, et al. Zika Virus Targets Glioblastoma Stem Cells Through a SOX2-Integrin α(V)β(5) Axis. *Cell Stem Cell* (2020) 26(2):187–204.e10. doi: 10.1016/j.stem.2019.11.016
78. Ferreira RO, Granha I, Ferreira RS, Bueno HS, Okamoto OK, Kaid C, et al. Effect of Serial Systemic and Intratumoral Injections of Oncolytic ZIKV(BR) in Mice Bearing Embryonal CNS Tumors. *Viruses* (2021) 13(10):2103. doi: 10.3390/v13102103
79. Hamdan F, Ylösmäki E, Chiaro J, Giannoula Y, Long M, Fusciello M, et al. Novel Oncolytic Adenovirus Expressing Enhanced Cross-Hybrid IgGA Fc PD-L1 Inhibitor Activates Multiple Immune Effector Populations Leading to Enhanced Tumor Killing *In Vitro*, In Vivo and With Patient-Derived Tumor Organoids. *J Immunother Cancer* (2021) 9(8):e003000. doi: 10.1136/jitc-2021-003000
80. Waldman AD, Fritz JM, Lenardo MJ. A Guide to Cancer Immunotherapy: From T Cell Basic Science to Clinical Practice. *Nat Rev Immunol* (2020) 20 (11):651–68. doi: 10.1038/s41577-020-0306-5
81. Schnalzger TE, de Groot MH, Zhang C, Mosa MH, Michels BE, Röder J, et al. 3D Model for CAR-Mediated Cytotoxicity Using Patient-Derived Colorectal Cancer Organoids. *EMBO J* (2019) 38(12):e100928. doi: 10.15252/embj.2018100928
82. Dijkstra KK, Cattaneo CM, Weeber F, Chalabi M, van de Haar J, Fanchi LF, et al. Generation of Tumor-Reactive T Cells by Co-Culture of Peripheral

Blood Lymphocytes and Tumor Organoids. *Cell* (2018) 174(6):1586–98.e12. doi: 10.1016/j.cell.2018.07.009
83. Bellin M, Marchetto MC, Gage FH, Mummery CL. Induced Pluripotent Stem Cells: The New Patient? *Nat Rev Mol Cell Biol* (2012) 13(11):713–26. doi: 10.1038/nrm3448
84. Cong L, Ran FA, Cox D, Lin S, Barretto R, Habib N, et al. Multiplex Genome Engineering Using CRISPR/Cas Systems. *Science* (2013) 339(6121):819–23. doi: 10.1126/science.1231143
85. Shalem O, Sanjana NE, Hartenian E, Shi X, Scott DA, Mikkelson T, et al. Genome-Scale CRISPR-Cas9 Knockout Screening in Human Cells. *Science* (2014) 343(6166):84–7. doi: 10.1126/science.1247005
86. O'Connell MR, Oakes BL, Sternberg SH, East-Seletsky A, Kaplan M, Doudna JA. Programmable RNA Recognition and Cleavage by CRISPR/Cas9. *Nature* (2014) 516(7530):263–6. doi: 10.1038/nature13769
87. Chen S, Sanjana NE, Zheng K, Shalem O, Lee K, Shi X, et al. Genome-Wide CRISPR Screen in a Mouse Model of Tumor Growth and Metastasis. *Cell* (2015) 160(6):1246–60. doi: 10.1016/j.cell.2015.02.038
88. Wang T, Yu H, Hughes NW, Liu B, Kendirli A, Klein K, et al. Gene Essentiality Profiling Reveals Gene Networks and Synthetic Lethal Interactions With Oncogenic Ras. *Cell* (2017) 168(5):890–903.e15. doi: 10.1016/j.cell.2017.01.013
89. Gilbert LA, Horlbeck MA, Adamson B, Villalta JE, Chen Y, Whitehead EH, et al. Genome-Scale CRISPR-Mediated Control of Gene Repression and Activation. *Cell* (2014) 159(3):647–61. doi: 10.1016/j.cell.2014.09.029
90. Behan FM, Iorio F, Picco G, Gonçalves E, Beaver CM, Migliardi G, et al. Prioritization of Cancer Therapeutic Targets Using CRISPR-Cas9 Screens. *Nature* (2019) 568(7753):511–6. doi: 10.1038/s41586-019-1103-9
91. Schwank G, Koo BK, Sasselli V, Dekkers JF, Heo I, Demircan T, et al. Functional Repair of CFTR by CRISPR/Cas9 in Intestinal Stem Cell Organoids of Cystic Fibrosis Patients. *Cell Stem Cell* (2013) 13(6):653–8. doi: 10.1016/j.stem.2013.11.002
92. Han K, Pierce SE, Li A, Spees K, Anderson GR, Seoane JA, et al. CRISPR Screens in Cancer Spheroids Identify 3D Growth-Specific Vulnerabilities. *Nature* (2020) 580(7801):136–41. doi: 10.1038/s41586-020-2099-x
93. Dekkers JF, Whittle JR, Vaillant F, Chen HR, Dawson C, Liu K, et al. Modeling Breast Cancer Using CRISPR-Cas9-Mediated Engineering of Human Breast Organoids. *J Natl Cancer Inst* (2020) 112(5):540–4. doi: 10.1093/jnci/djz196
94. Li X, Nadauld L, Ootani A, Corney DC, Pai RK, Gevaert O, et al. Oncogenic Transformation of Diverse Gastrointestinal Tissues in Primary Organoid Culture. *Nat Med* (2014) 20(7):769–77. doi: 10.1038/nm.3585
95. Matano M, Date S, Shimokawa M, Takano A, Fujii M, Ohta Y, et al. Modeling Colorectal Cancer Using CRISPR-Cas9-Mediated Engineering of Human Intestinal Organoids. *Nat Med* (2015) 21(3):256–62. doi: 10.1038/nm.3802
96. Drost J, van Jaarsveld RH, Ponsioen B, Zimberlin C, van Boxtel R, Buijs A, et al. Sequential Cancer Mutations in Cultured Human Intestinal Stem Cells. *Nature* (2015) 521(7550):43–7. doi: 10.1038/nature14415
97. Teriyapirom I, Batista-Rocha AS, Koo BK. Genetic Engineering in Organoids. *J Mol Med (Berl)* (2021) 99(4):555–68. doi: 10.1007/s00109-020-02029-z
98. Kelly RT. Single-Cell Proteomics: Progress and Prospects. *Mol Cell Proteomics* (2020) 19(11):1739–48. doi: 10.1074/mcp.R120.002234
99. Cristobal A, van den Toorn HWP, van de Wetering M, Clevers H, Heck AJR, Mohammed S. Personalized Proteome Profiles of Healthy and Tumor Human Colon Organoids Reveal Both Individual Diversity and Basic Features of Colorectal Cancer. *Cell Rep* (2017) 18(1):263–74. doi: 10.1016/j.celrep.2016.12.016
100. Schumacher TN, Scheper W, Kvistborg P. Cancer Neoantigens. *Annu Rev Immunol* (2019) 37:173–200. doi: 10.1146/annurev-immunol-042617-053402
101. Bulik-Sullivan B, Busby J, Palmer CD, Davis MJ, Murphy T, Clark A, et al. Deep Learning Using Tumor HLA Peptide Mass Spectrometry Datasets Improves Neoantigen Identification. *Nat Biotechnol* (2019) 37:55–63. doi: 10.1038/nbt.4313
102. Demmers LC, Kretzschmar K, Van Hoeck A, Bar-Epraïm YE, van den Toorn HWP, Koomen M, et al. Single-Cell Derived Tumor Organoids Display Diversity in HLA Class I Peptide Presentation. *Nat Commun* (2020) 11 (1):5338. doi: 10.1038/s41467-020-19142-9
103. Hoshino A, Costa-Silva B, Shen TL, Rodrigues G, Hashimoto A, Tesic Mark M, et al. Tumour Exosome Integrins Determine Organotropic Metastasis. *Nature* (2015) 527(7578):329–35. doi: 10.1038/nature15756
104. Théry C, Zitvogel L, Amigorena S. Exosomes: Composition, Biogenesis and Function. *Nat Rev Immunol* (2002) 2(8):569–79. doi: 10.1038/nri855
105. Isaac R, Reis FCG, Ying W, Olefsky JM. Exosomes as Mediators of Intercellular Crosstalk in Metabolism. *Cell Metab* (2021) 33(9):1744–62. doi: 10.1016/j.cmet.2021.08.006
106. Daassi D, Mahoney KM, Freeman GJ. The Importance of Exosomal PDL1 in Tumour Immune Evasion. *Nat Rev Immunol* (2020) 20(4):209–15. doi: 10.1038/s41577-019-0264-y
107. Thakur BK, Zhang H, Becker A, Matei I, Huang Y, Costa-Silva B, et al. Double-Stranded DNA in Exosomes: A Novel Biomarker in Cancer Detection. *Cell Res* (2014) 24(6):766–9. doi: 10.1038/cr.2014.44
108. Jin G, Liu Y, Zhang J, Bian Z, Yao S, Fei B, et al. A Panel of Serum Exosomal microRNAs as Predictive Markers for Chemoresistance in Advanced Colorectal Cancer. *Cancer Chemother Pharmacol* (2019) 84(2):315–25. doi: 10.1007/s00280-019-03867-6
109. Wolfers J, Lozier A, Raposo G, Regnault A, Théry C, Masurier C, et al. Tumor-Derived Exosomes are a Source of Shared Tumor Rejection Antigens for CTL Cross-Priming. *Nat Med* (2001) 7(3):297–303. doi: 10.1038/85438
110. Mincheva-Nilsson L, Baranov V. Cancer Exosomes and NKG2D Receptor-Ligand Interactions: Impairing NKG2D-Mediated Cytotoxicity and Anti-Tumour Immune Surveillance. *Semin Cancer Biol* (2014) 28:24–30. doi: 10.1016/j.semcancer.2014.02.010
111. Chen G, Huang AC, Zhang W, Zhang G, Wu M, Xu W, et al. Exosomal PD-L1 Contributes to Immunosuppression and Is Associated With Anti-PD-1 Response. *Nature* (2018) 560(7718):382–6. doi: 10.1038/s41586-018-0392-8
112. Poggio M, Hu T, Pai CC, Chu B, Belair CD, Chang A, et al. Suppression of Exosomal PD-L1 Induces Systemic Anti-Tumor Immunity and Memory. *Cell* (2019) 177(2):414–27.e13. doi: 10.1016/j.cell.2019.02.016
113. Ke X, Yan R, Sun Z, Cheng Y, Meltzer A, Lu N, et al. Esophageal Adenocarcinoma-Derived Extracellular Vesicle MicroRNAs Induce a Neoplastic Phenotype in Gastric Organoids. *Neoplasia* (2017) 19(11):941–9. doi: 10.1016/j.neo.2017.06.007
114. Handa T, Kuroha M, Nagai H, Shimoyama Y, Naito T, Moroi R, et al. Liquid Biopsy for Colorectal Adenoma: Is the Exosomal miRNA Derived From Organoid a Potential Diagnostic Biomarker? *Clin Transl Gastroenterol* (2021) 12(5):e00356. doi: 10.14309/ctg.0000000000000356

Conflict of Interest: The authors declare that the research was conducted in the absence of any commercial or financial relationships that could be construed as a potential conflict of interest.

Publisher's Note: All claims expressed in this article are solely those of the authors and do not necessarily represent those of their affiliated organizations, or those of the publisher, the editors and the reviewers. Any product that may be evaluated in this article, or claim that may be made by its manufacturer, is not guaranteed or endorsed by the publisher.

frontiers | Frontiers in Oncology

TYPE Original Research
PUBLISHED 21 September 2022
DOI 10.3389/fonc.2022.994333

OPEN ACCESS

EDITED BY
Hatim E. Sabaawy,
The State University of New Jersey,
United States

REVIEWED BY
Braden C. McFarland,
University of Alabama at Birmingham,
United States
Michael Linnebacher,
University Medical Center Rostock,
Germany

*CORRESPONDENCE
Scott Kopetz
skopetz@mdanderson.org

†These authors have contributed equally to this work

SPECIALTY SECTION
This article was submitted to Cancer Molecular Targets and Therapeutics, a section of the journal Frontiers in Oncology

RECEIVED 14 July 2022
ACCEPTED 02 September 2022
PUBLISHED 21 September 2022

CITATION
Kanikarla Marie P, Sorokin AV, Bitner LA, Aden R, Lam M, Manyam G, Woods MN, Anderson A, Capasso A, Fowlkes N, Overman MJ, Menter DG and Kopetz S (2022) Autologous humanized mouse models to study combination and single-agent immunotherapy for colorectal cancer patient-derived xenografts. *Front. Oncol.* 12:994333. doi: 10.3389/fonc.2022.994333

Autologous humanized mouse models to study combination and single-agent immunotherapy for colorectal cancer patient-derived xenografts

Preeti Kanikarla Marie[1†], Alexey V. Sorokin[1†], Lea A. Bitner[1], Rebecca Aden[1], Michael Lam[1], Ganiraju Manyam[2], Melanie N. Woods[1], Amanda Anderson[1], Anna Capasso[3], Natalie Fowlkes[4], Michael J. Overman[1], David G. Menter[1] and Scott Kopetz[1*]

[1]Department of Gastrointestinal Medical Oncology, The University of Texas MD Anderson Cancer Center, Houston, TX, United States, [2]Department of Bioinformatics & Computational Biology, The University of Texas MD Anderson Cancer Center, Houston, TX, United States, [3]Department of Oncology, The University of Texas Health Austin, Austin, TX, United States, [4]Department of Veterinary Medicine & Surgery, The University of Texas MD Anderson Cancer Center, Houston, TX, United States

Designing studies of immunotherapy is limited due to a lack of pre-clinical models that reliably predict effective immunotherapy responses. To address this gap, we developed humanized mouse models of colorectal cancer (CRC) incorporating patient-derived xenografts (PDX) with human peripheral blood mononuclear cells (PBMC). Humanized mice with CRC PDXs were generated *via* engraftment of autologous (isolated from the same patients as the PDXs) or allogeneic (isolated from healthy donors) PBMCs. Human T cells were detected in mouse blood, tissues, and infiltrated the implanted PDXs. The inclusion of anti-PD-1 therapy revealed that tumor responses in autologous but not allogeneic models were more comparable to that of patients. An overall non-specific graft-vs-tumor effect occurred in allogeneic models and negatively correlated with that seen in patients. In contrast, autologous humanized mice more accurately correlated with treatment outcomes by engaging pre-existing tumor specific T-cell populations. As autologous T cells appear to be the major drivers of tumor response thus, autologous humanized mice may serve as models at predicting treatment outcomes in pre-clinical settings for therapies reliant on pre-existing tumor specific T-cell populations.

KEYWORDS

humanized mice, immunotherapy, colorectal cancer, pre-clinical studies, T cells

Introduction

Cancer immunotherapy enhances the immune response in targeting cancer cells. The cytotoxic $CD8^+$ T cells are among some of the predominant subsets of effectors in cancer immunotherapy that eradicate cancer cells (1). Effector cells depend on the evolution of an intra-tumoral niche (2) or tertiary lymphoid structures (3). T-cell exhaustion may also come into play that affects the tumor immune response (4). Despite the complexities of intratumoral immune responses, peripheral T cell expansion seems to help predict tumor infiltration and clinical response (5). In colorectal cancer (CRC) patients, tumors lacking activated $CD8^+$ T cells predicted disease recurrence within 5 years. In contrast, a long disease-free survival was predicted for patients who had intratumoral T cells (6), thereby highlighting the importance of tumor-infiltrating immune cells in controlling the growth and recurrence of tumors. The key benefits of immunotherapy in CRC are typically limited to those with high mutational burden such as microsatellite instability-high (MSI-H) tumors (7–10). This high mutational burden is most commonly associated with an immunogenic neoantigen load that attracts tumor-infiltrating lymphocytes, consequently making them more likely to benefit from immune checkpoint inhibitors (7, 8, 11). These notions are supported by our studies that combined nivolumab and ipilimumab, which improved efficacy compared to anti-PD-1 monotherapy in MSI-H metastatic CRC, which is restricted to 5% of metatstatic CRC tumors (12). Although MSI-H early stage CRC tumor incidence is high (~15%), prognostically, these patients have a more favorable outcome compared to early stage MSS CRC resulting in a reduced percentage of MSI-H metastatic CRC (13, 14). The majority of metastatic CRC tumors are microsatellite stable (MSS) with a low neoantigen burden that is accompanied by reduced clinical benefit from immunotherapy. Pre-clinical models for evaluating MSS tumors may therefore represent an unmet need that can benefit from the development of patient centric approaches for testing broader panels of novel drugs and targeted combinations along with limiting exposure to unforeseen toxicity.

Predicting responses to combination treatments with immunotherapy requires relevant *in vivo* models that can faithfully predict tumor responses. However, pre-clinical *in vivo* models for testing the immunotherapy responses are lacking. As others and we have shown, patient-derived xenograft models (PDX) commonly use immunocompromised mice to establish a tumor growth-supportive microenvironment that more reliably reproduces clinical outcomes (15–17). These approaches depend on the immune status of the mouse strain utilized for any given study and principally interrogate the human tumor intrinsic properties of a given drug response without reflecting the human immune components. As one immunocompetent alternative, syngeneic mouse models and genetically engineered mouse models offer a robust and well-characterized system, which reflects species-specific characteristics that require careful interpretation based on macromolecular homologies and systemic immune differences. This has prompted the PDX field to develop a variety of humanized mouse models, whereby an immune deficient mouse strain is engrafted with functional human cells and tissue. These approaches reflect model specific functionality of the human immune components (18–20), but can be poorly predictive of tumor responses. Increasingly, humanized mice are used in immuno-modulation studies to interrogate interactions of the immune system with tumor cells and mechanisms of tumor escape (21–24). However, when these models utilize immune cells that do not match the tumor origin or rely on very limited HLA matching they may not manifest a clearly interpretable immune response. Mismatch of the immune system and tumor can lead to a potent allogeneic response, in which efficacy signals attributed to tumor response instead may be due to a nonspecific graft-versus-tumor response between implanted tumors and donor's immune cells used to repopulate the immunocompromised mouse. Consequently, a genuine need exists for better models involving autologous tissues that obviate the need for HLA matching or any confounding non-personalized patient factors. To address this lack of relevant *in vivo* models this study developed a humanized mice model wherein immunodeficient mice were implanted with autologous immune cells and tumor tissue obtained from the same patient to replicate the interaction between the tumor and matched immune system *in vivo*.

Materials and methods

Tumor and PBMC collection

Surgically resected tumor tissue samples or biopsy samples were collected from CRC patients under a research laboratory protocol LAB10-0982 approved by The University of Texas MD Anderson Cancer Center Institutional Review Board, after patients provided written informed signed consent. In our laboratory, the samples were linked with patients but the patients remained anonymous. Confidentiality was ensured and preserved for all patient-related data. Tumor samples of metastatic CRC sites, primarily the liver, were obtained from the patients, prepared as described previously (25), and implanted subcutaneously in NSG. Tumors were harvested when they reached a volume of 1500 mm^3. Suitable patients (MSI-H and MSS) from whom PDXs were established were identified and gave informed consent for blood draws. Blood samples were collected *via* venipuncture in tubes containing EDTA. Human PBMCs were isolated from whole blood using Lymphoprep density gradient medium (STEMCELL Technologies, # 07801)

and viably frozen in fetal bovine serum with 10% dimethyl sulfoxide. Donor PBMCs were isolated from Buffy coats purchased from Gulf Coast Regional Blood Center's research blood products.

Animals

All mouse handling procedures were approved by the Institutional Animal Care and Use Committee. The vertebrate animals used in this study were female 4- to 6-week old NSG mice (NOD.*Cg-Prkdc*^{scid}*Il2rg*^{tm1Wjl}/SzJ, #005557) purchased from The Jackson laboratory. The mice were housed in a specific-pathogen barrier animal facility at the MD Anderson Department of Veterinary Medicine and Surgery. The veterinary care provided included feeding the animals acidified water, a Uniprim diet (Envigo, #TD.06596), and adequate crude protein, minerals, and vitamins.

Nivolumab (Opdivo, Bristol-Myers Squibb Company) was administered intraperitoneally every 5 days at 20 mg per kg body weight for 25 days. Regorafenib (#HY-10331, MedChemExpress LLC) was administered orally every day at 10 mg per kg body weight for 25 days.

Humanized PBMC model

Human PBMCs (~4 to 5 x 10^6) were injected into unconditioned NSG mice to generate the humanized PBMC model. Human PBMCs were suspended in sterile phosphate-buffered saline at a density of 4×10^6 cells per 0.1 ml and injected intraperitoneally using 1-cc tuberculin syringes with 25-g × 5/8-inch needles (26). Similar engraftment rates were observed with intraperitoneal and intravenous PBMC injections. NSG mice received patient PBMCs that were matched with the PDXs implanted into them or donor PBMCs that were not matched. No HLA typing was done on donor blood samples. Flow cytometric analysis was performed to evaluate human cell engraftment in mice at about 2 weeks after the injections. Mice with human $CD45^+$ cell percentages ≥1% were enrolled into the experimental arms. The mice were monitored daily for any health concerns after human cell engraftment. Time to GVHD symptoms and mortality were determined using time-to-event analyses. Depending on the tumor growth rates, MSI-H or MSS tumors were implanted subcutaneously into mice within the time frame of human cell engraftment as described above. Tumor fragments (~10-30 mm^3) were cut using a scalpel, coated with 50-100 µL of Matrigel, and implanted subcutaneously in the flank regions of the mice under anesthesia. On average, three to six mice with bilaterally implanted tumors were enrolled in each experimental arm. Tumor growth was recorded every 3 to 4 days and tumor volume was calculated using the formula V = ½ (Length × Width^2).

Flow cytometry

Initial human cell engraftment in the study mice was done by collecting ~100 µL peripheral blood from all mice to be tested along with a blood sample from a non-engrafted mouse to be used as a negative control. Blood cells were stained with fluorochrome-conjugated antibodies. Mouse CD45-PerCP antibody was used for gating out murine leukocytes. This was followed by red blood cell lysis using BD FACS lysing solution and sample fixation for flow cytometric analysis to determine the percent engraftment in each mouse. For end point analysis of different immune cell populations, mouse blood was collected *via* cardiac puncture and processed similary. Tumors were extracted from mice, minced and enzymatically digested to generate a single cell suspension and processed for flow cytometric analysis. Single –cell suspensions from spleen, bone marrow were also prepared using standard procedures. Antibodies used for flow cytometric analysis were purchased from BD Biosciences (Supplemental Table 1A). All samples were run on a Gallios flow cytometer (Beckman Coulter) and data analysis was carried using FlowJo software.

Immunohistochemistry and immunofluorescence multiplex staining

PDX tumor samples were collected and fixed in 10% neutral buffered formalin and processed routinely for histopathology. Tissues were embedded in paraffin and sectioned at 4 µm. Multiplex staining was performed using Opal 4-Color IHC Automation kit plus opal 620 (Akoya Biosciences) on a Leica Bond RXm autostainer. See antibody tables below. After staining, slides were rinsed in DI water and Vector TrueVIEW Auto fluorescence Quenching Kit was used per manufacturer's instructions. Slides were hand-coverslipped and imaged at 20x using a Leica Versa 8 fluorescent digital scanning microscope system. Digital slides were accessed through Leica eslide manager and opened in Imagescope software. Leica digital image analysis software was utilized for quantification. A cellular immunofluorescence algorithm was tuned for each panel. Quantitative data was exported into excel spreadsheets. Antibodies used for tissue staining are included in Supplemental Table 1B.

Multiplex cytokine analysis

Multiplex Cytokine analysis of mouse plasma was performed using Bio-Plex™ 200 Instrument (Bio-Rad Laboratories). Mouse blood was drawn into BD collection tubes containing citrate as an anticoagulant, and then inverted several times to mix. Blood samples were then centrifuged at 1000xg for 15 min at 4^0C. Plasma was transferred into clean 1.5 mL tubes and centrifuged

again at 10,000xg for 10 min at 4^0C. Next, plasma samples were diluted in Bio-Plex diluent (Bio-Rad Laboratories). Human cytokines in mouse plasma samples were detected using a Bio-Plex Pro™ Human Cytokine 27-plex Assay (#M500KCAF0Y; Bio-Rad Laboratories). Plasma samples obtained from mice that did not receive any human PBMCs or PDX implantations were also analyzed to ensure that the human antibodies did not cross-react with mouse cytokines. Human plasma samples were used as positive controls. All samples were prepared and run according to the manufacturer's recommended instructions. Analysis was carried out using Bio-Plex Manager™ Software (Bio-Rad Laboratories).

TCR repertoire

The sequencing data for the human PBMC samples and mouse PBMC, tumor and spleen samples were analyzed using a Human reference sequence. RNA sequencing data were analyzed using a SMARTer Human TCR α/β Profiling Kit (Takara Bio). FASTQC was used to assess the quality of the data. Xenome was used to classify the sequencing data as human or mouse data. Human sequence data was only used for further analysis. MiXCR was used to align sequencing data and assemble clonotypes for the TCR repertoire. The clones corresponding to TRA and TRB chains were quantified separately. Downstream analysis of the clonotypes was performed using VDJ-tools. Analysis was done in the R computing language (version 3.6.0). Data is included in Supplemental Table 2

Statistics

Analysis of data was performed using Prism software (version 8.0; GraphPad Software). Data in different groups were analyzed using an unpaired Student's t-tests, ANOVA, or unpaired nonparametric tests (Mann-Whitney Two Sample Test) between different groups. *P* values less than 0.05 were considered significant. All tumor volume change and body weight data were summarized using means ± SD. Probability of survival was calculated using the Kaplan-Meier method.

CRC PDX details. Details of PDX models used in this study are included in Supplemental Table 3

Results

Characteristics of the humanized mouse model

Patient derived xenografts were generated from CRC patient tumor biopsies or surgical samples as the first required step in establishing our patient-specific humanized model. In considering another unique aspect of this particular model, we also collected blood from the same patients to match the source of immune cells required for establishing patient-specific autologous humanized mice. Human PBMCs injections were performed by multiple cell numbers and delivery routes, all of which achieved successful engraftment. The approach ultimately selected for routine use was four million PBMCs that were recovered from cryopreservation and injected by intraperitoneal delivery (data not shown). The percentage of human PBMCs as a function of human $CD45^+$ ($hCD45^+$) cells in mouse blood at 3-5 weeks reached ~ 50% compared to the uninjected controls (Figure 1A and Supplemental Figure 1A), these $hCD45^+$ engraftment frequencies varied in a time- and donor–dependent fashion. Within the $hCD45^+$ cell population, we observed that $CD3^+$T cells were the predominating subpopulation in the mouse circulation along with a limited number of $CD19^+$B, $CD56^+$NK and $CD11b^+/CD14^+$ myeloid cells remaining after the first week of PBMC injections (Figure 1B and Supplemental Figure 1B). The highest number of human $CD45^+$ immune cells were found in the mouse spleen followed by the mouse bone marrow and then the implanted PDXs (Figure 1C). The distribution of human immune cells in circulation over a seven-week period as defined by FACS analysis of $CD45^+$ cells peaked at 5 weeks and leveled off at 7 weeks (Supplemental Figure 1A). The human $CD3^+$T cell subpopulation represented nearly 100 percent of all cells found in the mouse circulation represented as a percentage of the total $CD45^+$ population with B, NK and myeloid cells ranging from near zero to 8 percent of $CD45^+$ cells (Supplemental Figure 1B). Human $CD3^+$ immunofluorescent staining immune cells were widely dispersed throughout in the patient xenograft of the PBMC injected but not the uninjected control mice (Supplemental Figure 1C). We also observed human B cells, and macrophages in the implanted PDXs, although in limited numbers. To determine if these engrafted human immune cells had any anti-tumor activity in the implanted PDXs, we analyzed the tumor growth curves for PBMC-injected versus non-PBMC injected mice and observed that these cells did not impact tumor growth by themselves (Supplemental Figure 1D). Mouse plasma levels of human interferon gamma revealed a direct correlation with the injection of human PBMC as a function of human $CD45^+$ cells present (Figure 1D). Other human cytokines levels in mouse plasma also substantially correlated with $hCD45^+$ cell engraftment, indicating that they are active and functional within a murine xenographic hematologic environment (Supplemental Figures 1E–H).

Difference in response between autologous and allogeneic models

To address the possibility that differences in immune response exist between autologous and allogeneic sample

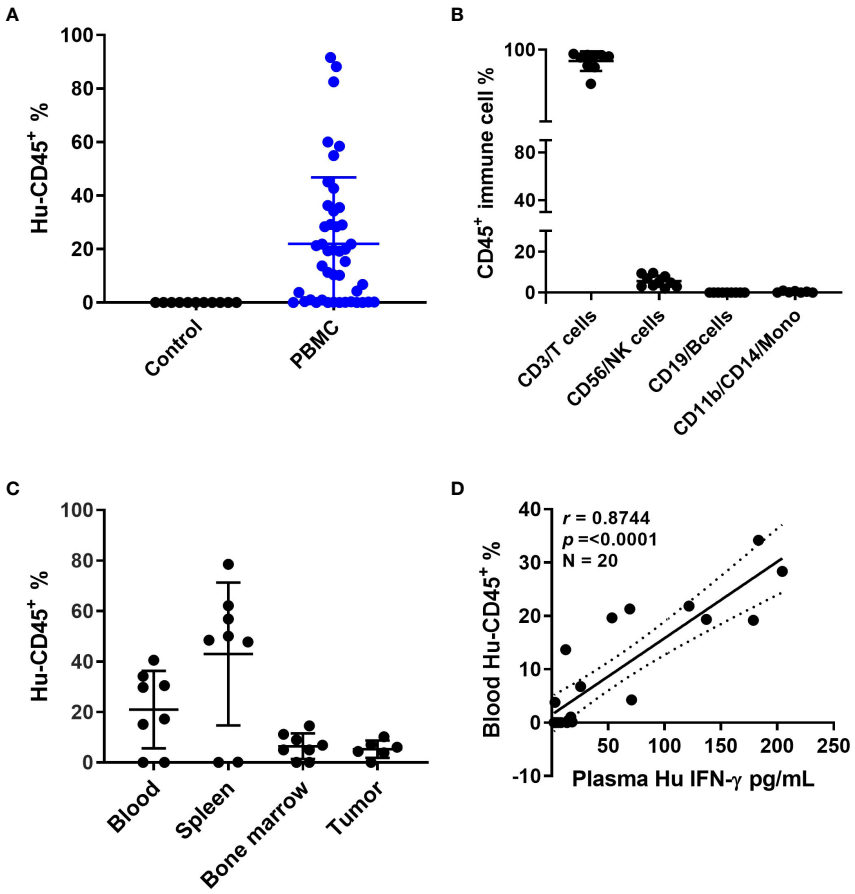

FIGURE 1
Humanized mouse development and characterization **(A)** Human CD45$^+$ cell% engraftment in mice 5 weeks after injection of human PBMCs. **(B)** Different immune cell percentages in mouse blood 5 weeks after PBMC injection. **(C)** Human CD45$^+$ cell percentage in different mouse tissues. **(D)** Correlation between human CD45 cell percentage in mouse blood and human interferon (IFN)-γ levels in mouse plasma.

pairings we generated two different series of genetic stability models. To that end, we compared the tumor volume changes under allogeneic (un matched donor immune cells) and autologous (matched patient immune cells) conditions in five PDX models with anti-PD-1 therapy. Three were MSI-H and two were MSS models that were done in parallel using patient PBMCs or donor PBMCs. To better understand any potential therapeutic connections of our mouse models to the immunotherapy responses of our patients, PDXs were subcategorized further into anti-PD-1 responders or non-responders (Figure 2). Following this stratification, two of the MSI-H tumors segregated into the responding group (B8120 & B8114) as might be expected, whereas one of the MSI-H (B8176) segregated with the non-responding MSS tumors (C1208 & C1185). When all five sub-stratified PDXs remained void of any human PBMCs, no significant difference was observed in growth rate or volume between anti-PD-1 treated and untreated tumors (Figures 2A–E). This finding also ruled out the impact of any human immune infiltrates that may be present within the passaged PDXs. Figures 2F–J show the five PDXs under allogeneic conditions subjected to anti-PD-1 therapy. Figures 2K–O show the five PDXs under autologous conditions also subjected to anti-PD-1 therapy. Any effects on tumor growth from allogeneic PBMCs was far less predictable and was less profound in anti-PD-1 treated mice. Unexpectedly, however, MSI-H-PD-1 responsive tumors (Figures 2F, G) were less responsive to anti-PD-1 in allogeneic conditions. Furthermore, in some cases the responses seen in allogeneic models (Figure 2J) contradict with that seen in a patient. These results are consistent with the hypothesis that allogeneic sources produce nonspecific immune responses.

In contrast, when patient PDXs were matched with autologous PBMCs followed by anti-PD-1 therapy, the MSI-H tumors B8120 and B8114 showed the greatest overall response consistent with the corresponding patients response (Figures 2K, L). Similarly, the response to anti-PD-1 therapy in

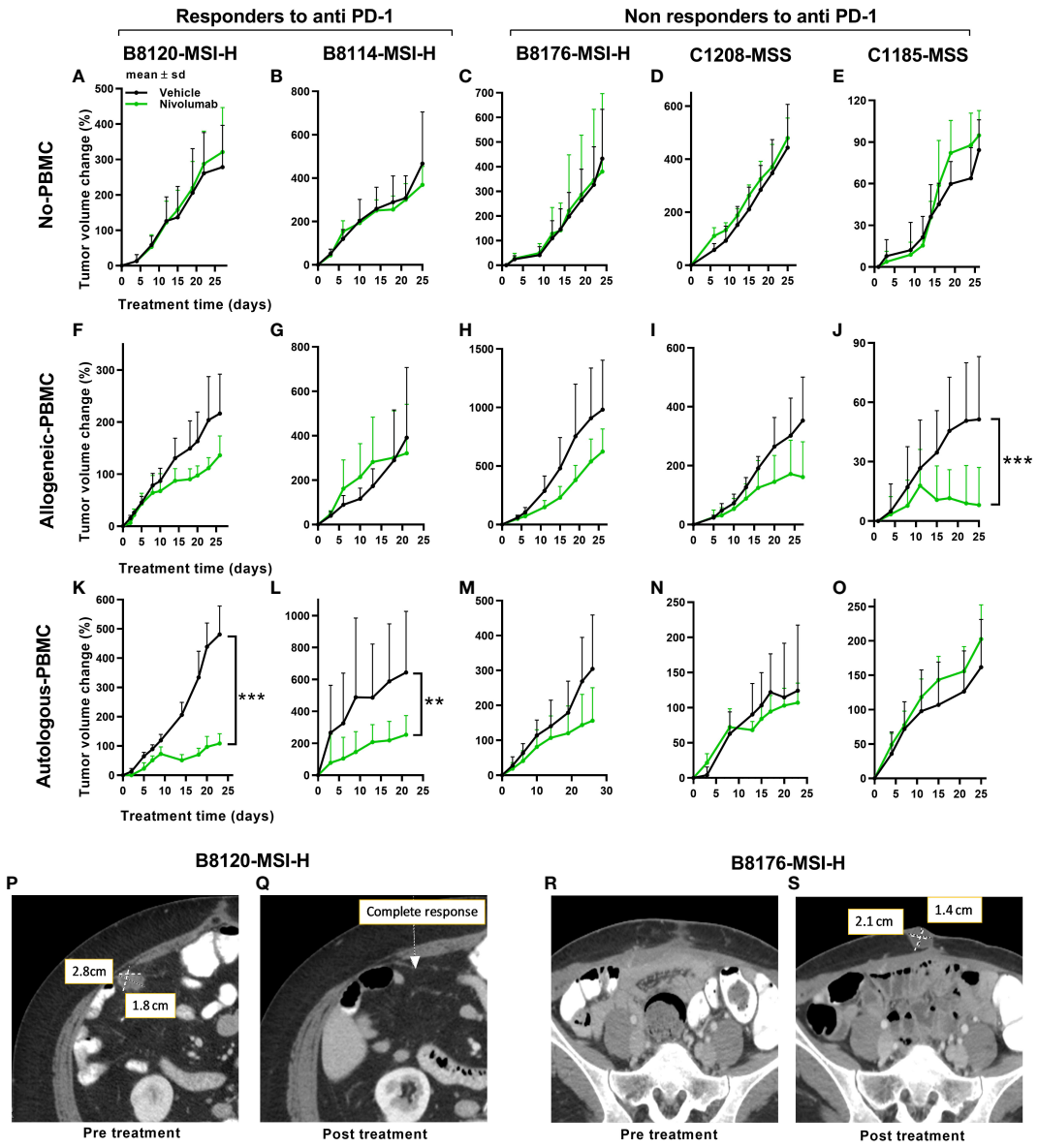

FIGURE 2
Tumor responses to anti-PD-1 therapy under non-humanized, allogeneic, and autologous conditions. Tumor volume change [$\Delta V_{\%}=100*(V_t-V_0)/V_0$] plots are shown here. **(A–E)** Results of anti-PD-1 therapy for five PDXs under non-humanized conditions (n=6-9 tumors/arm). **(F–J)** Results of anti-PD-1 therapy for five PDXs under allogeneic conditions (n=6-9 tumors/arm). **(K–O)** Results of anti-PD-1 therapy for five PDXs under autologous condition (n=6-9 tumors/arm). The green lines and dots represent treatment with nivolumab at 20mpk Q5D. **(P, Q)** Scans of the patient corresponding to the B8120 model before **(P)** and after **(Q)** immune checkpoint therapy. **(R, S)** Scans of the patient corresponding to the B8176 model before **(P)** and after **(Q)** immune checkpoint therapy. *P* values ≤ 0.001 were represented as ***. and P values ≤ 0.01 were represented as **.

autologous models generated from non-responding patients was more consistent with the response seen in patients (Figures 2M–O). The anti-PD-1 treated PDX taken from a non-responding MSI-H patient, B8176, corresponded more accurately to what occurred in the CRC patient donor who progressed on anti-PD-1 therapy. Also and more consistent with therapeutic response to anti-PD-1 therapy commonly seen in MSS patient donors who progress on anti-PD-1 therapy, the autologous condition showed no response when similar treatments were performed in our humanized mouse models (Figures 2N, O). Our results suggest that allogeneic conditions do not represent the outcome of treatment as effectively as autologous models. Body weight changes were minimal in all mice, including non-humanized (Supplemental Figure 2A), allogeneic (Supplemental Figure 2B), and autologous condition (Supplemental Figure 2C) suggesting that this approach was well tolerated. Human immune cell

engraftment percentages were also high based on hCD45$^+$% presence in the peripheral blood before and after treatment are shown in Supplemental Figures 2D, E for allogeneic and autologous models respectively. Tumor immune infiltrates after anti-PD-1 therapy are shown in Supplemental Figures 2F, G for allogeneic and autologous models respectively.

Proof-of-concept study using humanized mouse models of CRC

In further support of autologous PBMC and PDX humanized mice being more representative of patient responses, anti-PD-1 treatment of two MSI-H tumors in mice more accurately reflected the before and after patient response by MRI in MSI-H responders (Figures 2K–L) compared to MSI-H non-responders (Figures 2M–O). Our results show a responding MSI-H PDX model B8120 (Figure 2K) and a non-responding MSI-H PDX model B8176 (Figure 2M) to anti-PD-1 therapy in an autologous setting. Radiographic scans of the patient corresponding to the B8120 model before (Figure 2P) and after (Figure 2Q) immune checkpoint therapy showing complete response, along with the scans of the patient corresponding to the B8176 model before (Figure 2R) and after (Figure 2S) immune checkpoint therapy showing a progressive disease are included here to highlight the results from our autologous mouse models and how they compare to that of the patients.

T-cell receptor repertoire in the humanized mouse model of CRC

To examine how the T-cell receptor (TCR) repertoire is altered when human T cells are injected into a murine xenographic system under autologous conditions, we performed total cross-species TCR α/β profiling to compare the clonotypes of human PBMCs in mouse tissues before injection and when dissociated from mouse tissues for two separate human tumor xenografts (B8120 and B8176) after injection. Figure 3A shows the overlap of clonotypes observed between human and mouse PBMCs. The number of TCR α chain (TRA) and TCR β chain (TRB) clones in human and mouse blood samples for models B8120 and B8176 revealed similar distributions (Figures 3B, C). When comparing clonotypes between mouse blood, tumor, and spleen samples only a small clonal population occurred between all three mouse tissues (Figure 3D). Further post-injection analysis revealed similar fluctuations between B8120 and B8176 with the highest preponderance of engraftment occurring in the spleen for both TRA and TRB clonotypes (Figures 3E, F). We observed that although the overall TCR diversity of the implanted PBMCs and

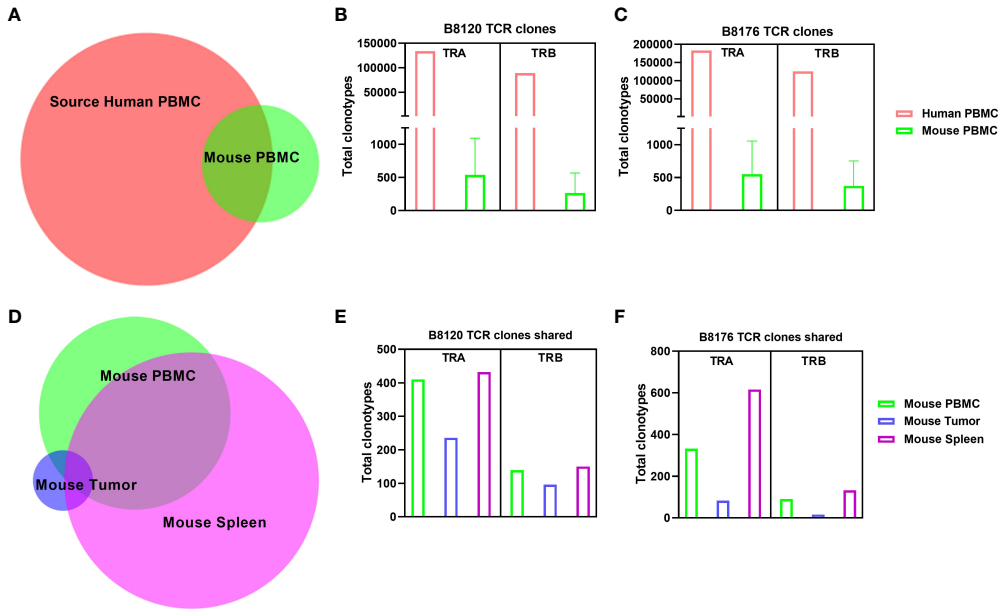

FIGURE 3
Comparison of human TCR sequences in human and humanized mouse samples **(A)** The overlap of clonotypes between human PBMCs and mouse PBMCs. **(B, C)** The number of TRA and TRB clones in human and mouse blood samples in the models B8120 **(B)** and B8176 **(C)**. **(D)** The extent of overlap of clones in different mouse tissues. **(E, F)** Bar charts of the B8120 **(E)** and B8176 **(F)** clonotypes that are common in human PBMCs injected into mice and mouse tissues after injection.

persisting PBMCs in mouse samples decreased, homogeneity (overlap) of the TCR repertoire between human PBMCs and mouse tissue samples was maintained. The rearrangement patterns for the TCR chains within the TRA clones are represented in circos plots in Supplemental Figures 3A–D and those within the TRB clones are represented in circos plots in Supplemental Figures 3E–H for model B8120. Similarly, circos plots of these rearrangement patterns in model B8176 are shown in Supplemental Figures 3I–L (TRA) and 3M-3P (TRB). We observed that clones that were infrequent or undetermined in human PBMC samples appeared to be outgrown in mouse tissue samples. Decreased TCR diversity in mouse samples along (shown by fewer circumferential designations) with low overlap with human PBMC clonotypes in these samples suggested that a fraction of the T cells present at low frequencies in human blood expanded in mouse tissues. This might be the case in the complementarity-determining region TRBV5-1(orange spoke)/TRBJ1-2 (dark blue spoke) clonotype for example that is present in in all B8120 and B8176 samples. In contrast, complementarity-determining regions TRAV30/TRAJ53 were prominently present in mouse PBMC, mouse spleen and B8176 PDX tumors that were generated from MSI-H/anti-PD-1 unresponsive donor samples. The disparity of complementarity-determining regions was greater in B8120 generated from MSI-H/anti-PD-1 responsive donor samples, with no distinct complementarity-determining regions clearly observed potentially reflecting a higher neoantigen load.

Combination treatment strategies for MSS CRC PDXs

Because we saw synonymous responses to anti PD-1 therapy in CRC patients and their PDXs in humanized mice in the autologous setting, we next explored the viability and activity of combination treatment strategies in MSS CRC PDX models. The combination of regorafenib and nivolumab has demonstrated clinical activity, albeit modest, in MSS CRC patients (REGONIVO trial) (27, 28), whereas treatment with either agent alone has not resulted in tumor regression. Similar activity reported in abstract form has been seen with other combinations of VEGFR tyrosine kinase inhibitors and PD-1/PDL1 inhibition (29, 30). Pre-treatment and post-treatment biopsies for patients in the REGONIVO study demonstrated modulation of the percentage of T-cell infiltrates. To determine whether our models can recapitulate these clinical findings, we tested regorafenib in combination with nivolumab in the MSS CRC PDX model C1221 under autologous conditions and observed that the combination was more efficacious in reducing tumor volume than was either agent alone (Figure 4A). The human immune cell percentages in mouse blood before and after treatment are shown in Figure 4B. The percentages of $CD8^+$ and $CD4^+$ T cells in the blood of mice did not appear to vary with different treatments (Figures 4C, D). Assessment of tumor $CD8^+$ and $CD4^+$ T-cell percentages using flow cytometry revealed a trend toward a higher $CD8^+$ T-cell percentage (Figure 4E), a significantly lower $CD4^+$ T-cell percentages (P=0.0004, Figure 4F) and a higher $CD8^+$:$CD4^+$ T-cell ratio (P = 0.004, Figure 4G) in the combination arm than in the nivolumab-alone arm. $CD8^+$ and $CD4^+$ T-cell numbers per gram of tumor weight are shown in Supplemental Figures 4A, B. We observed increased total cleaved caspase 3 positivity in the regorafenib-alone (significantly, p=0.017) and combination (P=0.174, Figure 4H) groups than in the nivolumab-alone group. We also analyzed tumor $CD3^+$, $CD4^+$, and $CD8^+$ T-cell and $FOXP3^+$ cell percentages *via* immunofluorescence staining (Figures 4I–L). Furthermore, our analysis shows how the total cell percentage was distributed within the intratumoral (Supplemental Figures 4C–F) stromal (Supplemental Figures 4I–L) and tumor compartments. We observed a slight down modulation in the distribution of $CD4^+$ T-cells (Supplemental Figure 4K), and nuclear $FOXP3^+$ cells (Supplemental Figure 4L) within the stromal compartment of the tumors in the combination treatment arm. We also saw a reduction in the distribution of the number of $CD4^+$ T-cells with combined treatment with regorafenib and nivolumab in this model, which was consistent with the findings in reported studies (27).

We further explored other immune cell markers with multiplexing immunofluorescence to identify other immune cell infiltrates in the PDXs. Notably; we identified CD20+ B cells and some myeloid cells in the mouse tumors even though the percentages of these cells in the blood of the mice were at most minimal. In the case of B cells, we observed a trend toward a higher percentage (Supplemental Figure 4M) and a significantly lower percentage of macrophages (P=0.013, Supplemental Figure 4N) in the stromal compartment in the combination group than in the nivolumab-alone group. Supplemental Figure 4O shows that combining anti-PD-1 therapy with a reduced regorafenib dose (50% lower than the clinically tested dose) resulted in a markedly lower tumor volume than did single-agent treatments in the MSS CRC PDX model C1211.

Graft-versus-host disease onset and window of treatment in PBMC humanized mice

Though this humanized PBMC mouse model provides co-clinical experimental advantages when compared with humanized $CD34^+$ model, with quick engraftment times and requiring few milliliters of patient blood, it does present with the limitation of graft-versus-host disease (GVHD) onset as a function of enrichment in engrafted human T cells. As in other transplant models, onset of GVHD in the model we used in the present study has been attributed to the expansion of human T cells that are reactive to murine tissues and actively target mouse cells (31–33). We used a scoring system to assess the extent of GVHD in our model. The scoring criteria for

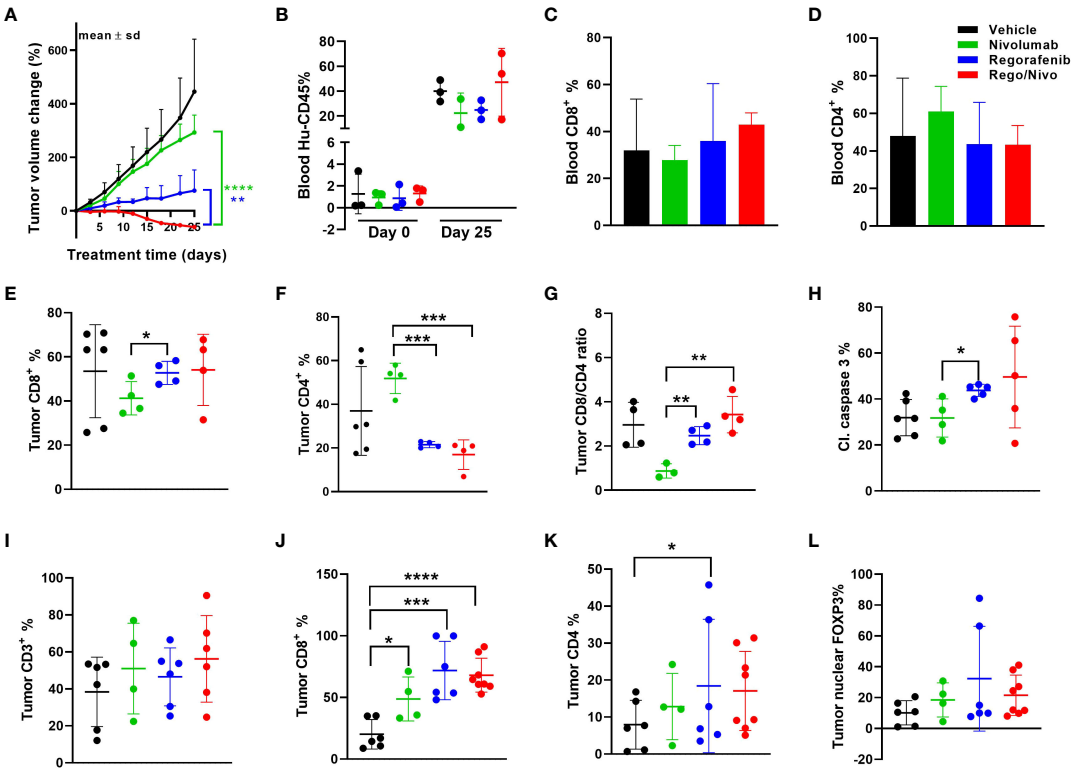

FIGURE 4
Results of anti-PD-1 and regorafenib combination therapy for MSS CRC model **(A)** Tumor volume change [$\Delta V_{\%}$=100*(V_t-V_0)/V_0] plots for the C1221 model engrafted with autologous PBMCs and given treatment with nivolumab and regorafenib (n=4-8 tumors/arm). **(B)** Human hCD45$^+$ cell percentages in mouse blood before and after the experiment. **(C, D)** Percentages of CD8$^+$ **(C)** and CD4$^+$ **(D)** T cells (percent of CD45$^+$ cells) in mouse blood at the experimental end point. **(E, F)** Tumor CD8$^+$ **(E)** and CD4$^+$ **(F)** T-cell percentages determined using flow cytometry (percent of CD45$^+$ cells). **(G)** Tumor CD8$^+$:CD4$^+$ T-cell ratios. **(H)** Cleaved caspase 3$^+$ cell percentages in tumors assessed using immunohistochemistry. **(I)** Results of Immunohistochemical analysis of CD3$^+$ T cells in tumors. **(J, K)** CD8$^+$ **(J)** and CD4$^+$ **(K)** T-cell percentages in tumors. **(L)** Nuclear FOXP3$^+$ cell percentages in tumors assessed using immunofluorescent staining. The green lines and dots represent nivolumab-based treatment (every 5 days, 20 mpk), the blue lines and dots represent regorafenib-based treatment (everyday, 10 mpk), and the red lines and dots represent combination treatment. All *P* values ≤ 0.05 were represented as *, *P* values ≤ 0.01 were represented as **, *P* values ≤ 0.001 were represented as ***, and *P* values ≤ 0.0001 were represented as ****.

GVHD that we used were based on weight loss, hunched posture, poor fur texture, diminished skin integrity, and diarrhea based on previous studies (34). Figure 5A shows survival curves for mice based on their GVHD scores. Acceptable body weight loss and other symptoms suggested that the window of treatment could be within 45-50 days after PBMC injection, with mice with higher GVHD scores having higher mortality rates. We observed considerable differences in the survival curves for mice that received 1-5 million PBMCs and those that received 10 million PBMCs (Figure 5B), suggesting that injecting low cell numbers can delay the impact of GVHD in these mice. GVHD progression in mice skin and liver with human CD3+ cell infiltration are shown in Figures 5C, D. We also observed that as the percent human cell engraftment in these mice increased their survival times decreased (Figure 5E), possibly due to a predominance of T cells in these mice leading to the onset of GVHD and manifestations of cytokine storm (35). Because GVHD can have a significant impact on mouse health, we sought to determine if GVHD by itself causes changes in tumor volume in these mice. Figure 5F shows that the human CD45$^+$ cell percentages in mouse blood were not correlated with their tumor volume change percentages. This suggests that onset of GVHD alone does not cause a reduction in tumor volumes in anti-PD-1 antibody treated mice, attributing any changes seen in tumor volume to the anti-tumor activity of T cells.

Discussion

The use of humanized mouse models for immuno-oncology research is emerging as a way to help interrogate and manipulate human immune function in a complex immune compromised organism. This area of research has benefitted from the

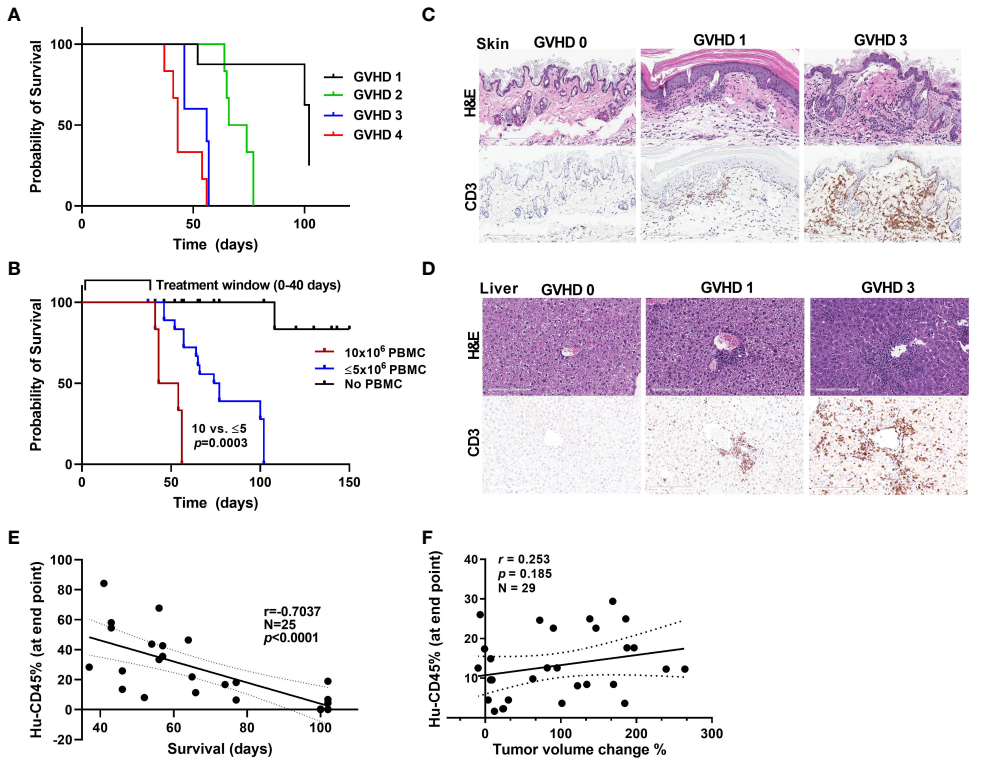

FIGURE 5
GVHD onset and the window of treatment **(A)** Survival curves for mice based on their GVHD scores. **(B)** Survival curves for mice that received different numbers of PBMCs. **(C, D)** Stains showing the level of infiltration of human $CD3^+$ cells into mouse skin **(C)** and liver **(D)** samples at different stages of GVHD. **(E)** The correlation between the hCD45 cell percentage in mouse blood at 5 weeks after injection of PBMCs and survival time in mice. **(F)** The correlation between the hCD45 cell percentage in mouse blood at the experimental end point (at 5 weeks after injection of PBMCs) and percent tumor volume change in anti-PD-1 antibody-treated mice.

development of a variety of immunocompromised mouse strains genetically engineered to support specific immune function or immune cell type behavior (36, 37). Studies reported in the literature have used mouse models generated from human $CD34^+$ cells and PBMC sources to evaluate tumor-immune responses with different immunotherapeutic agents (38–41). Humanized mouse models on a BALB/c-$Rag2^{null}Il2r\gamma^{null}SIRP\alpha^{NOD}$ 9B (BRSG) background demonstrated human immunity and PD-1-expressing T cells, thereby, providing the basis for pre-clinical immunotherapy studies (23). NSG-beta2m$^{(-/-)}$ that lack *Prkdc* gene, the X-linked *Il2rg* gene and the *B2m* gene have also been used to support PBMC growth to test Bintrafusp alfa (M7824) a bifunctional fusion protein composed of the extracellular domain of the TGF-betaRII to function (42). We have tested multiple immunocompromised strains in support of our patient PBMC growth to settle upon the use of unconditioned NSG (NOD.*Cg-Prkdc^{scid}Il2rg^{tm1Wjl}*/SzJ) mice as balanced against closely monitored GVHD (34), which provided a very workable window of treatment of 45-50 days. The advantage of using PBMCs to generate a humanized mouse model over other sources is that this model enables rapid engraftment and enriches for human $CD3^+$ T-cell engraftment, which is ideal for T cell-mediated tumor regression studies (43, 44). However, most of the currently available humanized mouse models of cancer have some degree of allogeneic response due to partial or complete mismatch of the implanted human tumors and injected immune cells. This led to our development of an autologous humanized mouse model of CRC using patient PBMCs to address this gap.

In our humanized PBMC mouse model, engrafted T-cells were functional, with the ability to produce cytokines. In addition, the T-cell clonotypes originally seen in human PBMC sources were retained in this mouse model, and our TCR profiling showed that some T-cell clones are shared by mouse blood and PDXs whereas others are expanded only in PDXs, suggesting that these clonotypes could be specific against tumors. Clonotype-driven responses are critical to understanding the underlying biology of immune responses (45). This seems to be particularly true of cancer immunobiology whereby TCR profiling can help determine the differences between immune tissues, circulating or tumor

infiltrating lymphocytes and responses to checkpoint inhibitor responses. In one study TCR β chain complementarity-determining regions in non–small cell lung cancer (NSCLC) treated with checkpoint inhibitors can help determine the degree of overlap of the TCR repertoire between tumor-infiltrating lymphocytes and circulating PD-1+CD8+T cells to determine the shared TCR clones. The resulting TIR index correlated with response and survival outcomes of anti–PD-(L) 1 treatment (46). Other complementarity-determining regions TRBV2/TRBJ1-2 and TRBV2/TRBJ1-1 have been reported before as potential prognostic markers in the case of papillary thyroid cancers (47). These studies focused on TCR-B signatures, which may be more reflective of the infiltrating T-cell clonotypes, much like our results showing complementarity-determining region TRBV5-1/TRBJ1-2 clonotype that is present in all B8120 and B8176 samples. Therefore, this T cell immune recognition could be a potential mechanism by which tumor growth reduction occurs in such autologous models. Moreover, the diversity of TCRs decreased in the mouse samples with expansion of clones that were present at lower frequencies in the human PBMC samples. These results are similar to reductions in TCR diversity 14 days after transplantation in comparison to TCR diversity at the initial infusion of allogeneic PBMCs that was dependent on the HLA status of the mouse background strain, either an NSG or an NSG-HLA-A2/HHD (48). Allogeneic PBMCs in these studies were paired with luciferase-expressing THP-1 cells to evaluate graft-versus-leukemia soluble tumor effects and revealed a greater anti-tumor effect on the NSG-HLA-A2/HHD vs the NSG mouse strain (48). In our case the unconditioned NSG mouse background did not seem to influence our autologous pairings, which maintained the PD-1 response profile exhibited by the patient tumors.

Most current approaches to humanization of mice and models used for immuno-oncology are limited by access to patients and matching immune cells. As a result, the models rely on very limited human leukocyte antigen matching for $CD34^+$ cell implantation at considerable expense and with limited reproducibility. Moreover, the major drawback of using some of these models may arise from the allogeneic responses resulting from the unmatched human immune cells and human tumors, which are by their very nature more difficult to predict than autologous responses. When we performed a head-to-head comparison between matched patient PDX and autologous PBMCs versus unmatched allogeneic tissues in humanized mice the allogeneic responses were less predictable. When we sub stratified our findings based on donor responses to checkpoint inhibitors, autologous models with anti-PD-1 therapy more closely reflected the patient responses. These comparable responses in our autologous PDXs and their corresponding patient tumors suggests concordance and reliability of the model in predicting cancer responses to immunotherapy. We have previously observed concordance between responses in pre-clinical PDX and clinical trial observations in both immune and non-immune approaches (23, 25). In the present study, we observed that this concordance was lacking in our allogeneic models. Our proof-of-concept results regarding anti-PD-1 therapy in the MSI-H and MSS PDXs demonstrate that tumor responses to this therapy differ in the allogeneic and autologous settings. The responses seen in most PDX models under allogeneic conditions do not reflect those seen in the corresponding patients. Using PBMCs isolated from CRC patients, we showed in the present study that our autologous models could capture responses based on the patients' immune potential, T-cell recognition status and clinical responses that can potentially serve as a personalized co-clinical approach or tumor subclass analytical tool.

As the majority of CRCs are MSS and fail to show any clinical benefit with immunotherapy, they are ideal for generation of models for use in pre-clinical trials of new agents administered alone and in combinations. Modulation of immuno-suppressive cells is being explored to overcome the limited efficacy of immunotherapy for MSS CRC. Regorafenib is a multi-kinase inhibitor that targets various receptor tyrosine kinases, and research has shown that it can reduce the number of immunosuppressive regulatory T cells and tumor-associated macrophages (27, 28). This led us to explore combination anti-PD-1 therapy with regorafenib in our humanized models with MSS CRC PDXs. Similar to early results reported with this combination in patients and similar results recently presented for other VEGFR tyrosine kinase inhibitors and anti-PD-1 combinations, we observed considerably greater tumor volume reduction with the combination of regorafenib and nivolumab than with either agents alone in our models C1221 and C1211 (29, 30, 49). In addition, flow cytometry and immunofluorescent analysis of tumor samples demonstrated a significant reduction in the percentage of $CD4^+$ T cells along with Arginase-1^+ cells/macrophages in the tumors in the combination treatment arm than in the nivolumab-alone arm. This is consistent with paired biopsy findings from the clinical trial, further highlighting the applicability and benefits of such autologous humanized mouse models in understanding how immune cells are modulated by a given therapy. Future studies focusing on combining VEGF and anti-PD-1 combinations using these mouse models can provide insights on tumor immune microenvironment changes.

One of the limitations of the present study is the use of patient PBMCs to populate the mouse immune system, where most of the cells are already differentiated and mature. Others have noted that while differences may be observed in some myeloid and B-cell lineages using NSG-beta2m$^{(-/-)}$ mice at the time of injection, appropriate freeze/thawing of adoptively transferred cells prior to injection does not appear to change survival or phenotypes of T-cells post engraftment (42). Similarly, our method using unconditioned NSG to support lymphoprep prepared PBMCs from whole blood and cryopreserved in contrast to using patient-isolated $CD34^+$ cells, predominantly enriches in T cells and is less supportive

of other immune cell types in the circulation. However, our results showed that other immune cell types could also engraft and infiltrate tumors. Furthermore, we observed that these infiltrated immune cell types and their numbers can be modulated with anti-PD-1 combination therapy. The infiltration of myeloid cells and their modulation in these humanized mouse tumors with therapy is a novel observation. Mouse models generated using $CD34^+$ cells have proven to be beneficial in studies requiring T-cell priming and in vaccine studies, and they have the advantage of including most if not all immune cell lineages (39, 50). However, autologous modeling requires isolation of $CD34^+$ cells from cancer patients through invasive procedures such as bone marrow biopsies and leukapheresis, which are not routinely feasible. Given the complexity of the procedures and safety concerns that arise in isolating hematopoietic stem cells from cancer patients, we believe that the present humanized PBMC model is the most practical option for studies of immuno-oncology. The ability to generate humanized mice with minimal peripheral blood volumes also makes it feasible. The use of newly available mouse strains with expression of human cytokines or those lacking mouse major histocompatibility proteins could potentially improve support of engrafted immune cells but our therapeutic window was adequate when balanced against autologous PDX growth. However, we are aware of the bias of the results generated from established PDXs over those models that were not established.

Another limitation of the PBMC-humanized mouse model is the development of GVHD within 5-8 weeks (51). The onset of GVHD has been attributed to expansion of the population of human $CD8^+$ T cells that actively target mouse cells *via* recognition of the major histocompatibility complex I proteins on mouse cells (31–33). Our results from using different PDX models suggest that we can delay the onset of GVHD by reducing the number of PBMCs injected to generate this model. We found that immune cells from different donors have varying engraftment rates even when the same numbers of cells were injected, with some donor cells engrafting at a higher rate than others and exacerbating GVHD. To determine if a large increase in the number of human immune cells in mouse blood can cause tumor volume regression, skewing our observed results, we looked at the correlation between the $hCD45^+$ cell percentage in mouse blood at the experimental end points and the changes in the tumor volumes of mice given anti-PD-1 therapy. We did not observe an obvious correlation between them, suggesting that high numbers of human cells did not cause a reduction in tumor volume. This observation that T cells are not active toward the tumor with anti-PD-1 treatment despite heavy T-cell infiltration (~60%) suggests that the T-cell responses toward the tumor are very specific.

Overall, these autologous humanized mouse models provide the opportunity to perform immediate short-term studies that can reduce the time of pre-clinical efforts with more reliable patient specific tumor responses that have the potential to better inform therapeutic options when compared with allogeneic models. These results are essential to developing and building up-on these models for future drug combination and efficacy studies. Furthermore, these PDXs were generated from late-stage metastatic CRC patients who have already undergone first- and second-line therapy. The efficacy readouts for novel therapies will indeed reflect the potential of these therapies in CRC patients whose disease does not respond to standard-of-care treatment. These models also provide considerable diversity as they originate from tumors with different mutational statuses that we expect to see reflected in a diverse patient population.

Data availability statement

The original contributions presented in the study are included in the article/Supplementary Material. Further inquiries can be directed to the corresponding author.

Ethics statement

The studies involving human participants were reviewed and approved by The University of Texas MD Anderson Cancer Center Institutional Review Board (under a research laboratory protocol LAB10-0982 for obtaining tumor and blood samples from patients). Patients provided consent for tumor and blood specimens to be used for research purposes along with the generation of PDXs. Written informed consent was also obtained from the individual(s) for the publication of any potentially identifiable images or data included in this article. The animal study was reviewed and approved by The University of Texas MD Anderson Institutional Animal Care and Use Committee (protocol #1077-RN02). All in vivo experiments utilizing PDXs were performed in accordance with institutional policies.

Author contributions

PK: Conceptualization, validation, visualization, methodology, data recording, sample collection and processing, formal analysis, writing original draft and editing. AS: Conceptualization, validation, visualization, methodology, formal analysis, writing original draft and editing. LB: Investigation, data recording, animal care and maintenance, sample collection and processing. RA: Investigation, animal care and maintenance, sample collection and processing. ML: Conceptualization, writing original draft and editing. GM: Software, formal analysis, and methodology. MW: animal care and maintenance, and sample collection. AA: Immunostaining and data analysis. AC: Conceptualization, writing and editing. NF: Immunostaining data, software, data analysis, methodology, writing and editing. DM: Project administration, supervision, visualization,

funding acquisition, writing and editing. MO: Conceptualization, resources, and supervision. SK: Conceptualization, resources, formal analysis, supervision, funding acquisition, investigation, visualization, methodology, writing original draft, project administration, and editing. All authors contributed to the article and approved the submitted version.

Funding

The Cancer Prevention Research Training Program, Janice Davis Gordon Memorial Postdoctoral Fellowship in Colorectal Cancer Prevention at MD Anderson, supports PM. SK and DM are supported by the GI-SPORE-5P50CA221707, 5U54CA224065, MD Anderson's Institutional Research Grant, MD Anderson's Colorectal Cancer Moon Shots ProgramTM and The E.L. and Thelma Gaylord Foundation. AC is supported by CPRIT Scholar in Cancer Research grant RR160093 and DoD Career Development Award W81XWH-20-1-0366. This study used the Flow cytometry and Cellular Imaging Core Facility, Advanced Technology Genomics Core, and Biospecimen Extraction Facility core, which are supported in part by the National Institutes of Health through MD Anderson's Cancer Support Grant CA016672.

Acknowledgments

The authors would also like to acknowledge MD Anderson Cancer Center's Research Medical Library for editing of this manuscript. Sample processing for IHC and IF multiplex immune staining was performed in MD Anderson's DVMS veterinary pathology lab.

Conflict of interest

SK reports stock or ownership interests in Navire and Lutris; consulting or advisory roles to EMD Serono, Merck, Holy Stone Healthcare, Novartis, Lilly, Boehringer Ingelheim, AstraZeneca/MedImmune, Bayer Health, Pierre Fabre, Redx Pharma, Ispen, Daiichi Sankyo, Natera, HalioDx, Lutris, Jacobio, Pfizer, Repare Therapeutics, Inivata, Jazz Pharmaceuticals, Roche, Navire, and Amgen; and research funding (to the institution) from Roche, EMD Serono, MedImmune, Novartis, Amgen, Lilly, and Daiichi Sankyo; and research funding (to self) from Merck, Navire, Holy Stone Healthcare, Boehringer Ingelheim, AstraZeneca/MedImmune, Bayer Health, Pierre Fabre, Redx Pharma, Ispen, Natera, HalioDx, Lutris, Jacobio, Pfizer, Repare Therapeutics, Inivata, and Jazz Pharmaceuticals. MJO: Consulting or Advisory Role: 3D Medicines, Bristol Myers Squibb, Roche/Genentech, Gritstone Oncology, MedImmune, Merck, Novartis, Promega, Spectrum Pharmaceuticals, Array BioPharma, Janssen, PfizerResearch Funding: Bristol Myers Squibb, Merck, Roche, MedImmune. Consulting: Merck, Astra-Zeneca, Takeda, Pfizer, Array, Gritstone, and Promega.

The remaining authors declare that the research was conducted in the absence of any commercial or financial relationships that could be construed as a potential conflict of interest.

Publisher's note

Supplementary material

The Supplementary Material for this article can be found online at: https://www.frontiersin.org/articles/10.3389/fonc.2022.994333/full#supplementary-material

References

1. Jackson SR, Yuan J, Teague RM. Targeting CD8+ T-cell tolerance for cancer immunotherapy. *Immunotherapy* (2014) 6(7):833–52. doi: 10.2217/imt.14.51

2. Jansen CS, Prokhnevska N, Master VA, Sanda MG, Carlisle JW, Bilen MA, et al. An intra-tumoral niche maintains and differentiates stem-like CD8 T cells. *Nature* (2019) 576(7787):465–70. doi: 10.1038/s41586-019-1836-5

3. Sautes-Fridman C, Petitprez F, Calderaro J, Fridman WH. Tertiary lymphoid structures in the era of cancer immunotherapy. *Nat Rev Cancer* (2019) 19(6):307–25. doi: 10.1038/s41568-019-0144-6

4. Kallies A, Zehn D, Utzschneider DT. Precursor exhausted T cells: key to successful immunotherapy? *Nat Rev Immunol* (2020) 20(2):128–36. doi: 10.1038/s41577-019-0223-7

5. Wu TD, Madireddi S, de Almeida PE, Banchereau R, Chen YJ, Chitre AS, et al. Peripheral T cell expansion predicts tumour infiltration and clinical response. *Nature* (2020) 579(7798):274–8. doi: 10.1038/s41586-020-2056-8

6. Mlecnik B, Tosolini M, Kirilovsky A, Berger A, Bindea G, Meatchi T, et al. Histopathologic-based prognostic factors of colorectal cancers are associated with the state of the local immune reaction. *J Clin Oncol* (2011) 29(6):610–8. doi: 10.1200/JCO.2010.30.5425

7. Galon J, Costes A, Sanchez-Cabo F, Kirilovsky A, Mlecnik B, Lagorce-Pages C, et al. Type, density, and location of immune cells within human colorectal tumors predict clinical outcome. *Sci (New York NY)* (2006) 313(5795):1960–4. doi: 10.1126/science.1129139

8. Timmermann B, Kerick M, Roehr C, Fischer A, Isau M, Boerno ST, et al. Somatic mutation profiles of MSI and MSS colorectal cancer identified by whole exome next

generation sequencing and bioinformatics analysis. *PloS One* (2010) 5(12):e15661. doi: 10.1371/journal.pone.0015661

9. Mehrvarz Sarshekeh A, Overman MJ, Kopetz S. Nivolumab in the treatment of microsatellite instability high metastatic colorectal cancer. *Future Oncol (London England)* (2018) 14(18):1869–74. doi: 10.2217/fon-2017-0696

10. Overman MJ, McDermott R, Leach JL, Lonardi S, Lenz HJ, Morse MA, et al. Nivolumab in patients with metastatic DNA mismatch repair-deficient or microsatellite instability-high colorectal cancer (CheckMate 142): an open-label, multicentre, phase 2 study. *Lancet Oncol* (2017) 18(9):1182–91. doi: 10.1016/S1470-2045(17)30422-9

11. Kanikarla Marie P, Haymaker C, Parra ER, Kim YU, Lazcano R, Gite S, et al. Pilot clinical trial of perioperative durvalumab and tremelimumab in the treatment of resectable colorectal cancer liver metastases. *Clin Cancer Res* (2021) 27 (11):3039–49. doi: 10.1158/1078-0432.CCR-21-0163

12. Overman MJ, Lonardi S, Wong KYM, Lenz HJ, Gelsomino F, Aglietta M, et al. Durable clinical benefit with nivolumab plus ipilimumab in DNA mismatch repair-Deficient/Microsatellite instability-high metastatic colorectal cancer. *J Clin Oncol* (2018) 36(8):773–9. doi: 10.1200/JCO.2017.76.9901

13. Buchler T. Microsatellite instability and metastatic colorectal cancer – a clinical perspective. *Front Oncol* (2022) 12. doi: 10.3389/fonc.2022.888181

14. Ribic CM, Sargent DJ, Moore MJ, Thibodeau SN, French AJ, Goldberg RM, et al. Tumor microsatellite-instability status as a predictor of benefit from fluorouracil-based adjuvant chemotherapy for colon cancer. *New Engl J Med* (2003) 349(3):247–57. doi: 10.1056/NEJMoa022289

15. Hong DS, Morris VK, El Osta B, Sorokin AV, Janku F, Fu S, et al. Phase IB study of vemurafenib in combination with irinotecan and cetuximab in patients with metastatic colorectal cancer with BRAFV600E mutation. *Cancer discov* (2016) 6(12):1352–65. doi: 10.1158/2159-8290.CD-16-0050

16. Kopetz S, Lemos R, Powis G. The promise of patient-derived xenografts: The best laid plans of mice and men. *Clin Cancer Res* (2012) 18(19):5160–2. doi: 10.1158/1078-0432.CCR-12-2408

17. Corcoran RB, Atreya CE, Falchook GS, Kwak EL, Ryan DP, Bendell JC, et al. Combined BRAF and MEK inhibition with dabrafenib and trametinib in BRAF V600-mutant colorectal cancer. *J Clin Oncol* (2015) 33(34):4023–31. doi: 10.1200/JCO.2015.63.2471

18. Sari G, Meester EJ, van der Zee LC, Wouters K, van Lennep JR, Peppelenbosch M, et al. A mouse model of humanized liver shows a human-like lipid profile, but does not form atherosclerotic plaque after western type diet. *Biochem Biophys Res Commun* (2020) 524(2):510–5.. doi: 10.1016/j.bbrc.2020.01.067

19. Kohler C, Smole U, Kratzer B, Trapin D, Schmetterer KG, Pickl WF. Allergen alters IL-2/alphaIL-2-based treg expansion but not tolerance induction in an allergen-specific mouse model. *Allergy* (2020) 75(7):1618–29. doi: 10.1111/all.14203

20. Coronel-Ruiz C, Gutierrez-Barbosa H, Medina-Moreno S, Velandia-Romero ML, Chua JV, Castellanos JE, et al. Humanized mice in dengue research: A comparison with other mouse models. *Vaccines* (2020) 8(1):39. doi: 10.3390/vaccines8010039

21. Shultz LD, Goodwin N, Ishikawa F, Hosur V, Lyons BL, Greiner DL. Human cancer growth and therapy in immunodeficient mouse models. *Cold Spring Harbor Protoc* (2014) 2014(7):694–708. doi: 10.1101/pdb.top073585

22. Shultz LD, Ishikawa F, Greiner DL. Humanized mice in translational biomedical research. *Nat Rev Immunol* (2007) 7(2):118–30. doi: 10.1038/nri2017

23. Capasso A, Lang J, Pitts TM, Jordan KR, Lieu CH, Davis SL, et al. Characterization of immune responses to anti-PD-1 mono and combination immunotherapy in hematopoietic humanized mice implanted with tumor xenografts. *J immunother cancer* (2019) 7(1):37. doi: 10.1186/s40425-019-0518-z

24. Johanna I, Hernandez-Lopez P, Heijhuurs S, Bongiovanni L, de Bruin A, Beringer D, et al. TEG011 persistence averts extramedullary tumor growth without exerting off-target toxicity against healthy tissues in a humanized HLA-A*24:02 transgenic mice. *J Leukocyte Biol* (2020) 107(6):1069–79. doi: 10.1002/JLB.5MA0120-228R

25. Katsiampoura A, Raghav K, Jiang Z-Q, Menter DG, Varkaris A, Morelli MP, et al. Modeling of patient-derived xenografts in colorectal cancer. *Mol Cancer Ther* (2017) 16(7):1435–42. doi: 10.1158/1535-7163.MCT-16-0721

26. Pearson T, Greiner DL, Shultz LD. Creation of "humanized" mice to study human immunity. *Curr Protoc Immunol* (2008) 15:15.21. doi: 10.1002/0471142735.im1521s81

27. Fukuoka S, Hara H, Takahashi N, Kojima T, Kawazoe A, Asayama M, et al. Regorafenib plus nivolumab in patients with advanced gastric (GC) or colorectal cancer (CRC): An open-label, dose-finding, and dose-expansion phase 1b trial (REGONIVO, EPOC1603). *J Clin Oncol* (2019) 37(15_suppl):2522. doi: 10.1200/JCO.2019.37.15_suppl.2522

28. Fukuoka S, Hara H, Takahashi N, Kojima T, Kawazoe A, Asayama M, et al. Regorafenib plus nivolumab in patients with advanced gastric or colorectal cancer: An open-label, dose-escalation, and dose-expansion phase ib trial (REGONIVO, EPOC1603). *J Clin Oncol Off J Am Soc Clin Oncol* (2020) 38(18):2053–61. doi: 10.1200/JCO.19.03296

29. Guo Y, Zhang W, Ying J, Zhang Y, Pan Y, Qiu W, et al. Preliminary results of a phase 1b study of fruquintinib plus sintilimab in advanced colorectal cancer. *J Clin Oncol* (2021) 39(15_suppl):2514. doi: 10.1200/JCO.2021.39.15_suppl.2514

30. Gomez-Roca CA, Yanez E, Im S-A, Alvarez EC, Senellart H, Doherty M, et al. LEAP-005: A phase 2 multicohort study of lenvatinib plus pembrolizumab in patients with previously treated selected solid tumors–results from the colorectal cancer cohort. *J Clin Oncol* (2021) 39(15_suppl):3564. doi: 10.1200/JCO.2021.39.3_suppl.94

31. Golovina TN, Mikheeva T, Suhoski MM, Aqui NA, Tai VC, Shan X, et al. CD28 costimulation is essential for human T regulatory expansion and function. *J Immunol (Baltimore Md 1950)* (2008) 181(4):2855–68. doi: 10.4049/jimmunol.181.4.2855

32. Mosier DE. Adoptive transfer of human lymphoid cells to severely immunodeficient mice: models for normal human immune function, autoimmunity, lymphomagenesis, and AIDS. *Adv Immunol* (1991) 50:303–25. doi: 10.1016/s0065-2776(08)60828-7

33. Pino S, Brehm MA, Covassin-Barberis L, King M, Gott B, Chase TH, et al. Development of novel major histocompatibility complex class I and class II-deficient NOD-SCID IL2R gamma chain knockout mice for modeling human xenogeneic graft-versus-host disease. *Methods Mol Biol* (2010) 602:105–17. doi: 10.1007/978-1-60761-058-8_7

34. Naserian S, Leclerc M, Thiolat A, Pilon C, Le Bret C, Belkacemi Y, et al. Simple, reproducible, and efficient clinical grading system for murine models of acute graft-versus-Host disease. *Front Immunol* (2018) 9(10). doi: 10.3389/fimmu.2018.00010.

35. Ye C, Yang H, Cheng M, Shultz LD, Greiner DL, Brehm MA, et al. A rapid, sensitive, and reproducible *in vivo* PBMC humanized murine model for determining therapeutic-related cytokine release syndrome. *FASEB J* (2020) 34 (9):12963–75. doi: 10.1096/fj.202001203R

36. Morillon YM2nd, Sabzevari A, Schlom J, Greiner JW. The development of next-generation PBMC humanized mice for preclinical investigation of cancer immunotherapeutic agents. *Anticancer Res* (2020) 40(10):5329–41. doi: 10.21873/anticanres.14540

37. Saito Y, Shultz LD, Ishikawa F. Understanding normal and malignant human hematopoiesis using next-generation humanized mice. *Trends Immunol* (2020) 41(8):706–20. doi: 10.1016/j.it.2020.06.004

38. Verma B, Ritchie M, Mancini M. Development and applications of patient-derived xenograft models in humanized mice for oncology and immune-oncology drug discovery. *Curr Protoc Pharmacol* (2017) 78:14.41.1–14.41.12. doi: 10.1002/cpph.26

39. Verma B, Wesa A. Establishment of humanized mice from peripheral blood mononuclear cells or cord blood CD34+ hematopoietic stem cells for immune-oncology studies evaluating new therapeutic agents. *Curr Protoc Pharmacol* (2020) 89(1):e77. doi: 10.1002/cpph.77

40. Zafar S, Basnet S, Launonen IM, Quixabeira DCA, Santos J, Hemminki O, et al. Oncolytic adenovirus type 3 coding for CD40L facilitates dendritic cell therapy of prostate cancer in humanized mice and patient samples. *Hum Gene Ther* (2020) 32(3–4):192–202. doi: 10.1016/j.annonc.2020.10.567

41. Maser I-P, Hoves S, Bayer C, Heidkamp G, Nimmerjahn F, Eckmann J, et al. The tumor milieu promotes functional human tumor-resident plasmacytoid dendritic cells in humanized mouse models. *Front Immunol* (2020) 11(2082). doi: 10.3389/fimmu.2020.02082

42. Morillon YMI, Smalley Rumfield C, Pellom ST, Sabzevari A, Roller NT, Horn LA, et al. The use of a humanized NSG-beta2m(-/-) model for investigation of immune and anti-tumor effects mediated by the bifunctional immunotherapeutic bintrafusp Alfa. *Front Oncol* (2020) 10:549. doi: 10.3389/fonc.2020.00549

43. Sanmamed MF, Rodriguez I, Schalper KA, Oñate C, Azpilikueta A, Rodriguez-Ruiz ME, et al. Nivolumab and urelumab enhance antitumor activity of human T lymphocytes engrafted in Rag2–/–IL2Rγnull immunodeficient mice. *Cancer Res* (2015) 75(17):3466–78. doi: 10.1158/0008-5472.CAN-14-3510

44. Lin S, Huang G, Cheng L, Li Z, Xiao Y, Deng Q, et al. Establishment of peripheral blood mononuclear cell-derived humanized lung cancer mouse models for studying efficacy of PD-L1/PD-1 targeted immunotherapy. *mAbs* (2018) 10 (8):1301–11. doi: 10.1080/19420862.2018.1518948

45. Tu AA, Gierahn TM, Monian B, Morgan DM, Mehta NK, Ruiter B, et al. TCR sequencing paired with massively parallel 3' RNA-seq reveals clonotypic T cell signatures. *Nat Immunol* (2019) 20(12):1692–9. doi: 10.1038/s41590-019-0544-5

46. Han J, Yu R, Duan J, Li J, Zhao W, Feng G, et al. Weighting tumor-specific TCR repertoires as a classifier to stratify the immunotherapy delivery in non-small cell lung cancers. *Sci Adv* (2021) 7(21):eabd6971. doi: 10.1126/sciadv.abd6971

47. Sun G, Qiu L, Cheng Z, Pan W, Qiu J, Zou C, et al. Association of the characteristics of b- and T-cell repertoires with papillary thyroid carcinoma. *Oncol Lett* (2018) 16(2):1584–92. doi: 10.3892/ol.2018.8800

48. Ehx G, Somja J, Warnatz H-J, Ritacco C, Hannon M, Delens L, et al. Xenogeneic graft-Versus-Host disease in humanized NSG and NSG-HLA-A2/HHD mice. *Front Immunol* (2018) 9:1943–. doi: 10.3389/fimmu.2018.01943

49. Wang Y, Wei B, Gao J, Cai X, Xu L, Zhong H, et al. Combination of fruquintinib and anti-PD-1 for the treatment of colorectal cancer. *J Immunol (Baltimore Md 1950)* (2020) 205(10):2905–15. doi: 10.4049/jimmunol.2000463

50. Marín-Jiménez JA, Capasso A, Lewis MS, Bagby SM, Hartman SJ, Shulman J, et al. Testing cancer immunotherapy in a human immune system mouse model: Correlating treatment responses to human chimerism, therapeutic variables and immune cell phenotypes. *Front Immunol* (2021) 12:607282. doi: 10.3389/fimmu.2021.607282

51. King M, Pearson T, Shultz LD, Leif J, Bottino R, Trucco M, et al. A new hu-PBL model for the study of human islet alloreactivity based on NOD-scid mice bearing a targeted mutation in the IL-2 receptor gamma chain gene. *Clin Immunol (Orlando Fla)* (2008) 126(3):303–14. doi: 10.1016/j.clim.2007.11.001

frontiers | Frontiers in Oncology

TYPE Original Research
PUBLISHED 18 November 2022
DOI 10.3389/fonc.2022.985154

OPEN ACCESS

EDITED BY
Hatim E. Sabaawy,
University of Colorado, United States

REVIEWED BY
Stephen B. Keysar,
University of Colorado Anschutz Medical Campus, United States
Sharon R. Pine,
University of Colorado Anschutz Medical Campus, United States
Qunyi Li,
Fudan University, China

*CORRESPONDENCE
Lisong Teng
lsteng@zju.edu.cn
Haohao Wang
coldhot33@163.com
Haibin Zhang
854770282@qq.com

†These authors have contributed equally to this work

SPECIALTY SECTION
This article was submitted to Cancer Molecular Targets and Therapeutics, a section of the journal Frontiers in Oncology

RECEIVED 03 July 2022
ACCEPTED 28 October 2022
PUBLISHED 18 November 2022

CITATION
Yu X, Chen Y, Lu J, He K, Chen Y, Ding Y, Jin K, Wang H, Zhang H, Wang H and Teng L (2022) Patient-derived xenograft models for gastrointestinal tumors: A single-center retrospective study. *Front. Oncol.* 12:985154. doi: 10.3389/fonc.2022.985154

Patient-derived xenograft models for gastrointestinal tumors: A single-center retrospective study

Xiongfei Yu[1†], Yiran Chen[1†], Jun Lu[1], Kuifeng He[1], Yanyan Chen[1], Yongfeng Ding[2], Ketao Jin[3], Haiyong Wang[1], Haibin Zhang[1*], Haohao Wang[1*] and Lisong Teng[1*]

[1]Department of Surgical Oncology, The First Affiliated Hospital, College of Medicine, Zhejiang University, Hangzhou, Zhejiang, China, [2]Department of Medical Oncology, The First Affiliated Hospital, College of Medicine, Zhejiang University, Hangzhou, Zhejiang, China, [3]Department of Colorectal Surgery, Affiliated Jinhua Hospital, Zhejiang University School of Medicine, Jinhua, China

Background: Patient-derived xenograft (PDX) models have shown a great efficiency in preclinical and translational applications. Gastrointestinal (GI) tumors have a strong heterogeneity, and the engraftment rate of PDX models remarkably vary. However, the clinicopathological and molecular characteristics affecting the engraftment rate still remain elusive.

Methods: A total of 312 fresh tumor tissue samples from patients with GI cancer were implanted into immunodeficient mice. The median follow-up time of patients was 37 months. Patients' characteristics were compared in terms of PDX growth and overall survival. PDX models of 3-6 generations were used for drug evaluation.

Results: In total, 171 (54.8%, 171/312) PDX models were established, including 85 PDX models of colorectal cancer, 21 PDX models of esophageal cancer, and 65 PDX models of gastric cancer. Other than tumor site, histology, differentiation degree, and serum alpha-fetoprotein (AFP) level, no significant differences were found between transplantation of xenografts and patients' characteristics. For patients who had undergone neoadjuvant therapy, the incidence of tumor formation was higher in those with progressive disease (PD) or stable disease (SD). In gastric cancer, the results showed a higher transplantation rate in deficient mismatch repair (dMMR) tumors, and Ki-67 could be an important factor affecting the engraftment rate. The gene mutation status of RAS and BRAF, two important molecular markers in colorectal cancer, showed a high degree of consistency between patients' tumors and PDXs. However, no significant effects of these two mutations on PDX engraftment rate were observed. More importantly, in this study although KRAS mutations were detected in two clinical cases, evident tumor inhibition was still observed after cetuximab treatment in both PDX models and patients.

Conclusion: A large-scale PDX model including 171 cases was successfully established for GI tumors in our center. The relationship between clinicopathological and

molecular features and engraftment rates were clarified. Furthermore, this resource provides us with profound insights into tumor heterogeneity, making these models valuable for PDX-guided treatment decisions, and offering the PDX model as a great tool for personalized treatment and translation research.

KEYWORDS

patient-derived xenograft model, gastrointestinal cancer, mutational status of RAS and BRAF, drug sensitivity, clinical transformation

Introduction

Animal tumor model is an effective tool for preclinical efficacy and toxicity evaluation of antitumor drugs, and it can also be used to screen molecular markers related to drug efficacy prediction. Patient-derived tumor xenograft (PDX) model is an animal tumor model that is established by the engraftment of human tumors into immunodeficient mice, maintaining the characteristics of tumors. It has been proved as an effective tool for tumor biology research and for the efficacy evaluation of antitumor drugs in various tumors (1, 2). To date, several PDX models were presented for gastric cancer covering common pathological types, alpha-fetoprotein (AFP) secretion type and human epidermal growth factor receptor 2 (HER-2)-positive gastric cancer, which provided a promising tool for translation research of gastric cancer (3–5). The clinicopathological and molecular characteristics of PDX models of gastric cancer have been confirmed to be highly consistent with those of human models (6), indicating their important role in the evaluation of drug efficacy.

There were an estimated 3.5 million people who were newly diagnosed with gastrointestinal (GI) cancer, which led to the death of 2.2 million people globally in 2020 (7). Different types of GI cancer share similar endodermal developmental origins, display a spectrum of common molecular features and expose to common attacks (8). An enormous progress has been made in the last half-century in the development of non-surgical treatments. However, it is still essential to find out new biomarkers for more precisely targeting tumors. Until 2010, our team has attempted to develop PDX models for GI tumors (6, 9). Over the recent decade, based on the international modeling consensus and our team's experience, a standardized procedure was developed for surgical sampling, specimen transfer, transplantation and tumor inoculation, cryopreservation, and resuscitation. To date, we have established nearly two hundred PDX models using tissue samples, and a number of them have been utilized for the preclinical evaluation of anticancer agents (3, 10–16).

In the present study, we analyzed clinical parameters that were associated with the engraftment rate of PDXs from patients with GI cancer to identify factors that could improve engraftment rate. We also established and assessed several PDX models to show their significance in clinical practice.

Materials and methods

Patients and samples

312 fresh gastrointestinal tract tumor samples from patients diagnosed with gastrointestinal tract cancer in Department of Surgical Oncology, The First Affiliated Hospital, College of Medicine, Zhejiang University were collected from January 2015 to February 2019 for the establishment of PDXs, including surgically resected specimens, endoscopic biopsy samples and needle biopsy samples. The clinical data were collected from patient records. The tumors were staged according to the eighth edition of AJCC/UICC TNM staging system. Follow-up data were obtained by phone, letter, and the out-patient clinical database (last follow-up was September 2021, median follow-up time was 37 months) and follow-up information were available in 284 patients. The overall survival (OS) time was calculated from the date of diagnosis to the last day of follow-up or the date of death. Patients derived paraffin-embedded tissue samples were used in accordance with ethical guidelines in the First Affiliated Hospital, School of Medicine, Zhejiang University (No.2018-378 and IIT20221079A). All study participants had provided informed written consent before any experiments.

PDX establishment

Four-to-six-week-old female BALB/c nude mice, purchased from Shanghai Slac Laboratory Animal Corporation (Shanghai, China), were housed with regular 12-hour light/12-hour dark cycles for at least three days before use. Ambient temperature was 20 ~ 22°C, kept at constant humidity of 40 ~ 60%. PDX models were established as in Figure 1A. Fresh tumor samples

from patients were transported to the laboratory in complete medium (RPMI 1640 medium supplemented with 20% FBS and 0.05% penicillin/streptomycin solution) in an ice bath immediately after resection. Then tumors were transferred to a sterile Petri dish containing complete medium. Thin slices of tumor were diced into 2×2×2 mm3 pieces and washed thrice with complete medium. Under anesthesia with isofluorane, tumors were implanted into BALB/c nude mice by a small incision and subcutaneous pocket made in one side of the lower back in which one tumor piece is deposited in the pocket. While the pocket was still open, one drop of 100× penicillin/streptomycin solution was placed into the opening. We monitored xenograft growth at least twice weekly by vernier caliper measuring the length (L) and width (W) of the tumor and then removed them for serial transplantation after the volume reached about 1000 mm^3 (Figure 1B). The tumor volume (V) was calculated according to the following formula: $V= L\times W^2/2$. Tumors were passaged no more than six times. Numerous samples from early passages were stored in the tissue bank and cryopreserved in liquid nitrogen, and used for further experiments (Figure 1C). Animal care and experiments were performed under the approval and supervision of the Animal Experimental Ethical Inspection of the First Affiliated Hospital, College of Medicine, Zhejiang University (No.2018-378).

Drug sensitivity analysis

We used xenografts from the third to seventh generation for the experiments once the tumor volume reached about 150–200mm3. *In vivo* experiments were performed to evaluate the chemosensitivity, as well as the antitumor activity of several targeted drugs, including: trastuzumab, cetuximab, apatinib and bevacizumab. Experiments were ended once the tumor volume surpassed 1500mm3 or mouse weight loss reached 20%. The percentage of tumor growth inhibition (TGI) was calculated according to the following formula: TGI = (1 − T/C) × 100%, where T/C represents the relative tumor volume of treatment group and control group. After the mice had been killed, we conducted immunoblot to assess the expression of various markers.

Mutational analysis for RAS and BRAF

All the samples from patients and PDXs were fixed with formalin and embedded in paraffin. To detect RAS/BRAF mutations, the AmoyDx KRAS/NRAS/BRAF Mutations Detection Kit (AmoyDx, Xiamen, China) approved by the China Food and Drug Administration (CFDA) was used.

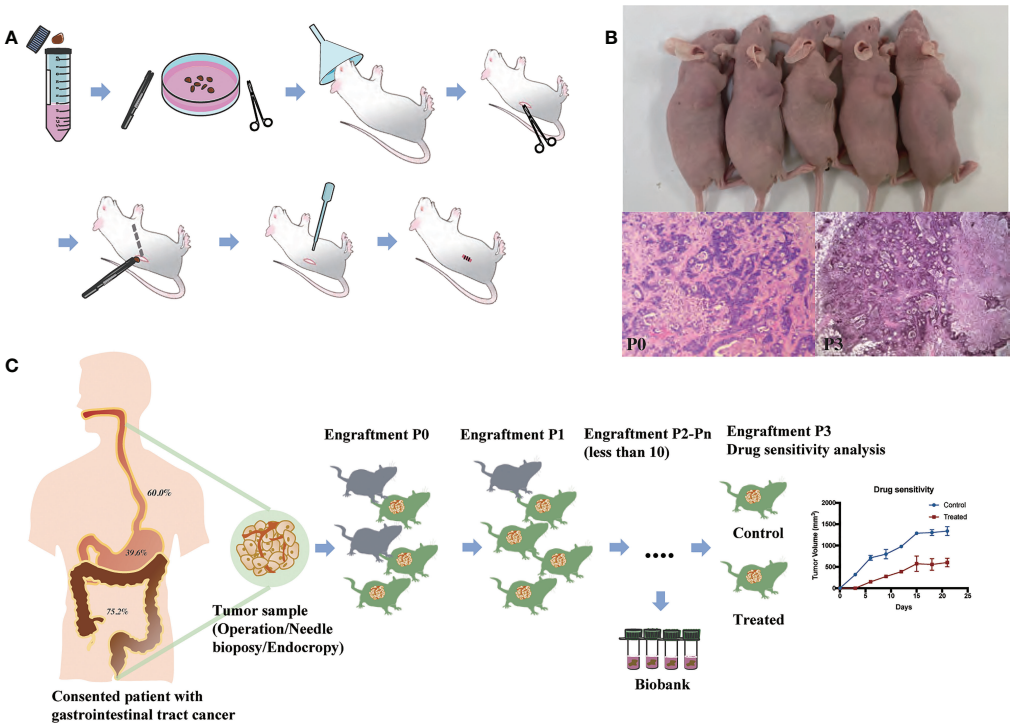

FIGURE 1
Establishment and application of patient-derived xenografts (PDXs). **(A)** Schema for the establishment of PDX models. **(B)** Representative PDX models and histology of paired patient-PDX tumors. **(C)** Engraftment rate of gastrointestinal cancers and applications of PDX models.

Based on Amplification Transformation System (ARMS) technology, the study was conducted in an accredited laboratory.

Statistical analysis

The differences between two categorical variables were examined by Pearson's Chi square test and Fisher's exact tests where appropriate. Two continuous variables were compared using unpaired t-test. Non-parametric variables were compared using the Mann–Whitney test. The assumptions required to interpret the statistics have been verified using F test and QQ-plots. $P < 0.05$ was considered statistically significant. Statistical analysis was performed using SPSS 23.0 software.

Results

Patients' characteristics for PDX establishment

We collected 312 fresh tumor samples from patients who were diagnosed with GI cancer (including esophageal cancer (n=35), gastric cancer (n=164), and colorectal cancer (n=113)) between 2015 and 2019, and implanted them into immunodeficient mice (BALB/c nude mice) to generate PDX models. Among 312 patients, there were 205 (65.7%) male patients, and their median age at diagnosis was 61.82 (range, 17-91) years old. Besides, 281 (90.1%) patients had primary tumors, and the remaining nine (9.9%) patients had recurrent tumors; 53 (18.9%) metastatic tumors were collected as well. Most of these specimens were obtained by surgery (289/312, 92.6%), and samples from some patients who could not undergo surgery due to the advanced tumor stage were obtained by endoscopy (9/312, 2.9%) or needle biopsy (14/312, 4.5%). There were 12 (3.8%) cases of well differentiation, 106 (34.0%) cases of moderate differentiation, and 193 (61.9%) cases of poor differentiation. Other detailed information of patients and tumor samples are summarized in Table S1.

The characteristics of patients and tumors for successful growth of PDX models

PDX models were successfully generated from 171 tumor implants and were passaged for 2-6 generations. The histopathological morphology of tumor in experimental mice was consistent with the original pathological diagnosis (Figure 1B). The time from the implantation of fresh specimens to the first passage (maximum tumor volume, 1000 mm^3) was 1-4 months, with an average time of 2.6 months. The overall engraftment rate was 54.8%.

We then analyzed clinical characteristics that affected the engraftment rates of specimens. Univariate analysis showed that several factors were significantly associated with the engraftment rate ($P < 0.05$, Table 1 and Figure 2). Colorectal cancer showed a higher engraftment rate (75.2%) compared with esophageal cancer (60.0%) or gastric cancer (39.6%). Squamous cell carcinoma had a higher engraftment rate (63.6%), while signet ring cell carcinoma (SRCC) had a lower engraftment rate (25.9%) compared with adenocarcinoma (56.9%) or other histological types (50.0%). Moderately differentiated tumors had a higher engraftment rate (73.6%) compared with well-differentiated (33.3%) or poorly differentiated (46.1%) tumors. In contrast, neoadjuvant therapy was found to have no significant effect on tumor engraftment rates. However, as for patients who had received neoadjuvant therapy, the engraftment rate of progressive disease (PD) or stable disease (SD) specimens was significantly higher than that of partial response (PR) specimens (65.4% *vs.* 29.4%, $P = 0.021$, Figure 2A).

We further analyzed the differences between transplantation rate and clinical characteristics in esophageal cancer, gastric cancer, and colorectal cancer separately. In esophageal cancer, smaller tumors and ulcerative type tumors had a higher engraftment rate (Figure 2B and Table S2). In addition, samples from recurrent tumors tended to have a higher engraftment rate (60.0% *vs.* 37.6%) in gastric cancer (Figure 2C and Table S3). Specimens from male patients (80.9% *vs.* 66.7%), ulcerative type tumors (80.6% *vs.* 65.9%), poorly and moderately differentiated tumors (75.0% and 78.1% *vs.* 25.0%) seemed to have a higher engraftment rate (Figure 2D and Table S4) in colorectal cancer.

Molecular parameters for successful establishment of PDX models

Subsequently, we analyzed the relationship between the engraftment rate and some tumor biomarkers, including serum tumor markers (AFP, carcinoembryonic antigen (CEA), cancer antigen 199 (CA199), and cancer antigen 125 (CA125)), immunohistochemical markers (Ki-67, HER-2, and MMR status), as well as the mutational status of RAS and BRAF genes, and molecular therapeutic targets of colon cancer. The results showed that serum tumor biomarkers were not associated with the successful establishment of PDX models except for AFP ($P = 0.021$, Table 1). For Ki-67, we found that a high Ki-67-positive rate (>60%+) was associated with a higher engraftment rate than a low Ki-67-positive rate (45.7% *vs.* 24.0%, $P = 0.081$, Table 1). Transplantation rates of samples from deficient mismatch repair (dMMR) tumors were higher than those from

10.3389/fonc.2022.985154

TABLE 1 Clinicopathological factors related to PDX establishment.

Factors	PDX succeed (n=171)	PDX fail (n=141)	$\chi 2$	P value
Age				
Mean (year)	62.25	61.3	–	0.528[a]
Gender				
Male	116(56.6%)	89(43.4%)	0.763	0.403[b]
Female	55(51.4%)	52(48.6%)		
Primary tumor site				
Esophagus	21(60.0%)	14(40.0%)	34.637	<0.001[b]
Stomach	65(39.6%)	99(60.4%)		
Colorectum	85(75.2%)	28(24.8%)		
Sample collection method				
Operation	160(55.4%)	129(44.6%)	0.650	0.755[c]
Endoscopy	4(44.4%)	5(55.6%)		
Needle biopsy	7(50.0%)	7(50.0%)		
Sample source (Primary or metastasis)				
Primary tumor	138(54.5%)	115(45.5%)	0.037	0.885[b]
Metastasis tumor	33(55.9%)	26(44.1%)		
Sample source (Primary or recurrence)				
Primary tumor	152(54.1%)	129(45.9%)	0.584	0.456[b]
Recurrence tumor	19(61.3%)	12(38.7%)		
Treatment before biopsy				
No	149(55.4%)	120(44.6%)	0.268	0.361[b]
Yes	22(51.2%)	21(48.8%)		
Distant metastasis status				
No	103(52.8%)	92(47.2%)	0.858	0.671[b]
Single	46(59.0%)	32(41.0%)		
Multiple	21(55.3%)	17(44.7%)		
NA	1	0		
Tumor size (longest diameter)				
Mean (mm)	5.29	5.43	–	0.663[a]
Histology				
Adenocarcinoma	140(56.9%)	106(43.1%)	10.627	0.011[c]
Squamous cell carcinoma	21(63.6%)	12(36.4%)		
Signet ring cell carcinoma	7(25.9%)	20(74.1%)		
Others	3(50.0%)	3(50.0%)		
Differentiation				
Poor	89(46.1%)	104(53.9%)	23.225	<0.001[c]
Moderate	78(73.6%)	28(26.4%)		
Well	4(33.3%)	8(66.7%)		
NA	0	1		
T stage				
0	1(25.0%)	3(75.0%)	7.027	0.123[c]
1	4(30.8%)	9(69.2%)		
2	19(51.4%)	18(48.6%)		
3	107(59.8%)	72(40.2%)		
4	39(50.0%)	39(50.0%)		
NA	1	0		
N stage				
0	60(58.8%)	42(41.2%)	4.65	0.200[b]

(Continued)

TABLE 1 Continued

Factors	PDX succeed (n=171)	PDX fail (n=141)	$\chi 2$	P value
1	41(58.6%)	29(41.4%)		
2	36(56.3%)	28(43.8%)		
3	33(44.0%)	42(56.0%)		
NA	1	0		
M stage				
0	126(52.7%)	113(47.3%)	1.798	0.226[b]
1	45(61.6%)	28(38.4%)		
TNM stage				
I	11(40.7%)	16(59.3%)	4.078	0.256[b]
II	50(57.5%)	37(42.5%)		
III	64(52.0%)	59(48.0%)		
IV	46(61.3%)	29(38.7%)		
Ki-67				
>60%+	21(45.7%)	25(54.3%)	3.222	0.081[b]
≤60%+	6(24.0%)	19(76.0%)		
NA	144	97		
Serum AFP level				
≤20ng/ml	165(56.3%)	128(43.7%)	7.208	0.012[c]
>20ng/ml	1(11.1%)	8(88.9%)		
NA	5	5		
Serum CEA level				
≤5ng/ml	111(55.0%)	91(45.0%)	0.000	>0.999[b]
>5ng/ml	55(55.0%)	45(45.5%)		
NA	5	5		
Serum CA199 level				
≤37U/ml	132(55.0%)	34(54.8%)	0.001	>0.999[b]
>37U/ml	108(45.0%)	28(45.2%)		
NA	5	5		
Serum CA125 level				
≤35U/ml	134(53.6%)	31(60.8%)	0.883	0.360[b]
>35U/ml	116(46.4%)	20(39.2%)		
NA	5	5		

NA, not available.
[a]Unpaired two-tailed t test, [b]Pearson's Chi square test, [c]Fisher's exact test.

proficient mismatch repair (pMMR) tumors both in gastric cancer (83.3% *vs*. 23.1%, P =0.041, Figure 2 and Table S3) and colorectal cancer (100% *vs*. 73.2%, P =0.166, Figure 2 and Table S4). As for the important therapeutic target HER-2 in gastric cancer, the correlation between HER-2 status and PDX engraftment was not identified (Table S3). Besides, 46 PDX tissues of colorectal cancer were detected with the mutation status of RAS/BRAF genes, including 24 patients with RAS mutation and five patients with BRAF mutation. The correlation between mutation status and PDX engraftment rate was not found. There was also no significant association between RAS mutation and survival outcomes. The detailed mutation data of the 46 colorectal cancer-associated PDX models are presented in Table S5.

Application of individualized therapy in the PDX models

One of the most important elements to evaluate the PDX models is the therapeutic response. In present study, we present two representative colon cancer patients with KRAS mutations who received individualized therapy using the PDX models. The detailed data of these two patients are shown in Table S6.

Case 1 (No. CoZ0116) was first diagnosed with colon cancer in October 2015. After seven cycles of neoadjuvant therapy (mFOLFOX6 + bevacizumab), surgical treatment was performed. Postoperative pathology indicated PR, and chemotherapy with mFOLFOX6 regimen was continued postoperatively. However, in September 2016, the patient was

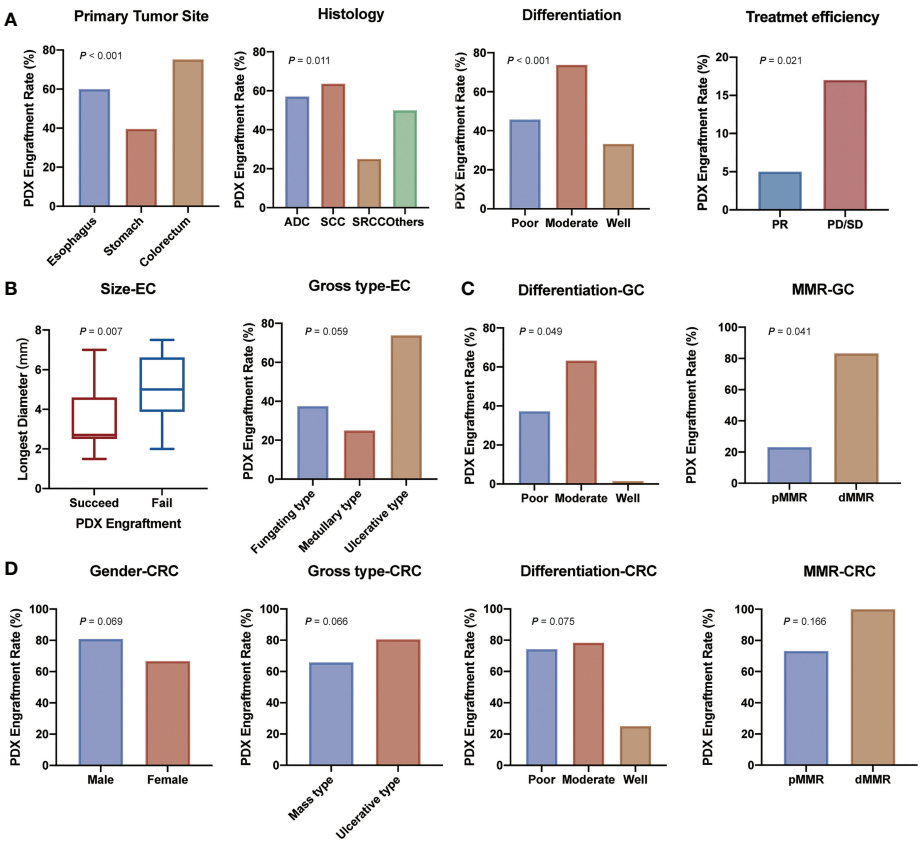

FIGURE 2
Demographic and clinical parameters associated with engraftment of gastrointestinal tract cancer patient-derived xenografts. **(A)** Clinicopathological factors related to PDX establishment. **(B)** Clinicopathological factors related to esophagus cancer PDX establishment. **(C)** Clinicopathological factors related to gastric cancer PDX establishment. **(D)** Clinicopathological factors related to colorectal cancer PDX establishment. (ADC, adenocarcinoma; SCC, squamous cell carcinoma; SRCC, signet ring cell carcinoma; PR, partial response; PD/SD, progressive disease or stable disease; EC, esophagus cancer; GC, gastric cancer; CRC, colorectal cancer).

diagnosed with a single liver metastasis and received the second surgery. After surgery, establishment of the PDX model was performed on liver metastatic specimens obtained by surgery. Drug sensitivity results showed that cetuximab, irinotecan, and 5-fluorouracil (5-FU) were sensitive (Figure 3A). According to the guideline of colorectal cancer, the patient was treated with FOLFIRI regime for 11 cycles due to the mutation of RAS gene. Regrettably, the patient presented with lung metastasis in September 2017. According to the PDX sensitivity results and the patient's willingness to refuse intravenous chemotherapy, we selected cetuximab + capecitabine as an advanced line of treatment. Importantly, the patient's lung metastases were controlled and a progression-free survival (PFS) of 6 months was achieved (Figures 3B, C).

Another patient (Case 2, CoY0011) was a 57-year-old man who first diagnosed with colon cancer in September 2015 and received surgical treatment. PDX model was successfully established after surgical treatment and tissue samples were obtained. Drug sensitivity test was initially conducted and showed that all groups, except for the apatinib group, inhibited tumor growth compared with control group that did not receive drug treatment (Figure 3D). According to the patient's tumor stage and guidelines, the patient received FOLFIRI chemotherapy. No local recurrence or distant metastasis were found during the following 1 year's periodic re-examinations. In September 2016, the patient was admitted to our hospital because of decreased appetite with fatigue and bone pain. Imageological examination and levels of serum tumor biomarkers both suggested the possibility of liver and bone metastases. In order to find out a better treatment plan, we resuscitated the PDX model and conducted drug sensitivity test again (Figure 3E). SOX (oxaliplatin + S-1) + bevacizumab was selected according to the results of two drug sensitivity tests. After four cycles of SOX + bevacizumab treatment, the levels of serum tumor biomarkers slightly decreased. In November 2016, the patient developed peritoneal metastasis, which revealed that our patient did not respond well to these therapeutic regimens. The antitumor effect of cetuximab was confirmed in both drug

sensitivity tests, even though the patient had RAS mutation (Figures 3D, E). The patient was subsequently treated with cetuximab in combination with chemotherapy and achieved a PFS of 4 months (Figure 3G). Figure 3F shows the radiographic changes during cetuximab treatment.

Discussion

The incidence of GI cancer is still increasing gradually, which is an important cause of cancer-related death (7). To date, several drugs have been presented for GI cancer with a

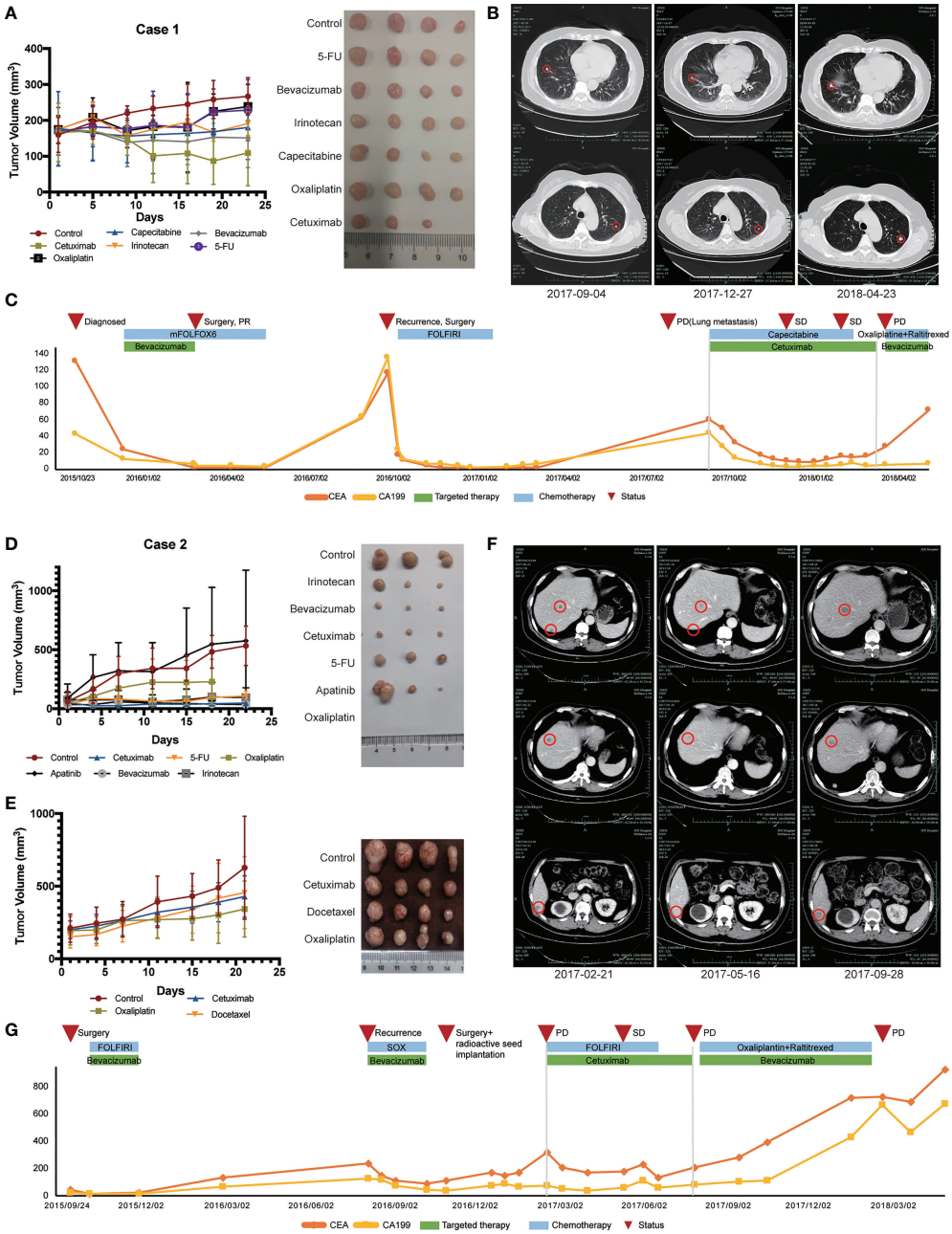

FIGURE 3
Therapeutic response of PDX models and corresponding patients. **(A)** *In vivo* drug sensitivity of Case 1 with KRAS mutation using PDX models. **(B)** Imaging changes of lung metastasis during treatment in Case 1. **(C)** Changes of serum tumor markers during treatment in Case 1. **(D)** The first *in vivo* drug sensitivity of Case 2 with KRAS mutation using PDX models. **(E)** *In vivo* drug sensitivity of Case 2 with KRAS mutation using PDX models after recurrence. **(F)** Imaging changes of liver metastasis during Ftreatment in Case 2. **(G)** Changes of serum tumor markers during treatment in Case 2.

certain efficacy. However, due to the strong individual heterogeneity, personalized precision treatment is still a favorable alternative for physicians and patients. The *in vitro* tumor model has been used as a standard tool for preclinical antitumor drug research, while the high failure rate of drugs has questioned the prediction ability of this traditional tumor model. Compared with the *in vitro* tumor model, the PDX model can better maintain the histopathological, genetic, and phenotypic characteristics of the tumor tissue, leading to enhance the prediction of the drug response (9, 17, 18). In recent years, a large number of PDX models have been established in various tumors, including gastric cancer (11, 16, 19), colorectal cancer (20), lung cancer (21), cervical cancer (22), etc. The PDX models have gradually become an effective tool for tumor biology research and anti-tumor drugs' efficacy evaluation. However, the PDX models have not been widely used in clinical practice, mainly due to the instability of establishing PDX models.

Several factors including technicians' skills contribute to the engraftment of PDX models. In our study, sample inoculation was initially carried out by five laboratory staff with at least 1 year of experience, minimizing the difference in engraftment rate. The successful establishment of PDX models can be influenced by experimental, clinicopathological, and molecular parameters. To date, few studies have reported the factors influencing engraftment rate of PDX models for GI cancer separately. Zhu et al. found no significant difference between transplantation rate and clinicopathological characteristics except for chemotherapy for gastric cancer (19). However, Zou et al. reported that transplantation rates of biopsied samples from stage III or IV (17.7%, 22/124) were significantly higher than those from early stage (0, 0/19, $P < 0.05$) in esophageal cancer (23). In colorectal cancer, a significantly higher successful PDX establishment rate was found in liver metastatic specimens than that in primary specimens (N=26; 76.7% *vs.* 57.7%). No clinicopathological features led to significant differences in the PDX establishment rate for metastatic colorectal cancer (20). However, no study has regarded GI tumors as a whole to study factors influencing PDX engraftment rate.

In our study, we identified a number of these factors associated with PDX engraftment. Colorectal cancer showed a higher engraftment rate (75.2%) compared with esophageal cancer (60.0%) or gastric cancer (39.6%). The results revealed that there were significant differences in the tumor engraftment rate of diverse digestive tract tumors. Among them, engraftment rate of stomach was the least, which could be related to the high heterogeneity of gastric cancer. Squamous cell carcinoma had a higher engraftment rate (63.6%), while SRCC, which is more common in gastric cancer, had a lower engraftment rate (25.9%). It is noteworthy that it is easier to establish a PDX model for moderately differentiated tumors than for poorly differentiated and well-differentiated tumors. It could be related to the fact that mesenchymal cells are less essential in moderately differentiated tumors than poorly differentiated tumors, while the tumor load in well-differentiated tumors might be extremely low to engraftment in PDX models. For instance, a previous study reported that poorly differentiated adenocarcinoma required the use of transforming growth factor-β (TGF-β) during stromal response, whereas human TGF-β may not interact with mouse stromal cells (24). In addition, we found that for patients who had received neoadjuvant therapy, the tumor engraftment rate of PD or SD specimens was significantly higher than that of PR specimens (65.4% *vs.* 29.4%, $P = 0.021$, Figure 2). This may explain the influence of the degree of malignancy of tumor on the tumor formation rate of PDX. In addition, PDX can be established for drug sensitivity test to screen effective drugs for patients who have failed in conventional neoadjuvant therapy. Another important finding is that although SRCC is considered a histological type with a highly malignant biological behavior (25–27), it has a significantly lower engraftment rate than other histological types in our study. The unique biological feature of SRCC is associated with the production and accumulation of abundant mucins in the cytoplasm and plasma membrane. Murakami H et al. found that their newly established SRCC cell lines grew retarded *in vivo* in nude mice and found inflammatory responses around subcutaneous tumors, possibly in response to extracellular mucin secretion. It suggested that this may not only be related to the low growth rate of the tumor cells, but also the inflammatory or immune responses of macrophages and natural killer cells to the host (28). We also considered that the low PDX engraftment rate of SRCC might be correlated with it.

The predictive value of data obtained from PDX-based studies in biomarker analysis is highly valuable for the PDX modeling in cancer research. Previous researches demonstrated that PDX models are biologically and genetically similar to primary tumors (29, 30). Our study mainly concentrated on some molecular characteristics related to prognosis and treatment, such as Ki67, HER-2, RAS, BRAF, and MMR status. Ki67 is widely recognized as a proliferation index, which is expressed in the cell nucleus during mitosis. Our data showed that a strongly positive Ki-67 could be correlated with a high engraftment rate. One possibility for the higher engraftment rate is that when tumor tissue samples are implanted into immunodeficient mice, cells with strongly positive Ki-67 own high proliferation capacity. Similar results were also reported in PDX models of other types of cancer (31–34). Besides, our results showed that a higher engraftment rate was observed in dMMR tumors, while no significant association was observed between other important gene mutations (e.g., KRAS and BRAF mutations) and engraftment rate.

Another approach to determine the value of PDX models in cancer research is analyzing the predictive value of the data obtained from PDX-based studies with consideration of drug efficacy and patient outcome. KRAS and BRAF are two downstream molecules of epidermal growth factor receptor (EGFR) and play important roles in EGFR signaling cascade. Activating mutations in KRAS exon 2 can induce infinite proliferation of tumor cells, thereby freeing the pathway from the control of EGFR (35, 36). The

mutation status of RAS and BRAF genes is considered to be of great significance in guiding the treatment and predicting the prognosis of colorectal cancer patients (37–41). The development of cetuximab, a mouse/human chimeric monoclonal antibody against EGFR, bring new expectations to patients. The guidelines and studies generally recommended cetuximab therapy only to patients with RAS and BRAF wild-type colorectal cancer (42). In previous clinical studies, cetuximab had a significantly lower overall tumor response rate in patients with RAS mutation than in patients with RAS wild-type colorectal cancer. However, few patients with PR or CR were reported, which could be related to the heterogeneity of the tumor (43–46). In our study, several PDX models of KRAS mutant patients showed efficacy against cetuximab therapy. In the current study, we presented two typical patients with KRAS mutations who developed recurrence and distant metastasis after treatments. The drug sensitivity screening of PDX model showed that cetuximab had a certain efficacy, so that cetuximab was applied to the patients. The levels of tumor indicators (CA199 and CEA) significantly decreased in the two patients, and both patients achieved the best efficacy of PR with PFS reaching 6 and 4 months respectively. This suggests that cetuximab may have a promising effect on some patients with RAS or BRAF mutation, and some patients may lose the opportunity of undergoing effective targeted therapies because of the genetic test results. This further indicated that the establishment of a PDX model is of great importance for medication of patients, especially for the posterior line treatment of patients with recurrence and metastasis.

Conclusions

In the present study, we successfully established a large-scale PDX model for GI tumors in our center. The relationship between clinicopathological and molecular features and engraftment rates were clarified. Furthermore, this resource provides us with profound insights into tumor heterogeneity, making these models valuable for PDX-guided treatment decisions, and offering the PDX model as a great tool for personalized treatment and translation research.

Data availability statement

The raw data supporting the conclusions of this article will be made available by the authors, without undue reservation.

Ethics statement

The studies involving human participants were reviewed and approved by the Ethics Committee of The First Affiliated Hospital, College of Medicine, Zhejiang University (No.2018-309 and IIT20221079A). The patients/participants provided their written informed consent to participate in this study. The animal study was reviewed and approved by the Animal Experimental Ethical Inspection of the First Affiliated Hospital, College of Medicine, Zhejiang University (No.2018-378). Written informed consent was obtained from the individual(s) for the publication of any potentially identifiable images or data included in this article.

Author contributions

XY and YRC are responsible for the study concept and design. YRC and JL are responsible for the acquisition of data and the development of methodology. KH, YYC, KJ, and HYW are responsible for the tumor sample collection and establishment of PDX. XY, YRC, and YD are responsible for the analysis and interpretation of data. YRC, XY, and JL are responsible for the writing of the manuscript. HZ, HHW, and LT are responsible for the review and/or revision of the manuscript. All authors contributed to the article and approved the submitted version.

Funding

This work was supported by grants from: Project of the regional diagnosis and treatment centre of the Health Planning Committee (No. JBZX-201903), Science and Technology Project of Zhejiang Province (2021C03119), Chinese Medicine Technology Project of Zhejiang Province (2020ZZ013) and Youth Project of Zhejiang Provincial Natural Science Foundation (LQ18H160012).

Conflict of interest

The authors declare that the research was conducted in the absence of any commercial or financial relationships that could be construed as a potential conflict of interest.

Publisher's note

Supplementary material

The Supplementary Material for this article can be found online at: https://www.frontiersin.org/articles/10.3389/fonc.2022.985154/full#supplementary-material

References

1. Cho SY, Kang W, Han JY, Min S, Kang J, Lee A, et al. An integrative approach to precision cancer medicine using patient-derived xenografts. *Mol Cells* (2016) 39 (2):77–86. doi: 10.14348/molcells.2016.2350

2. Byrne AT, Alferez DG, Amant F, Annibali D, Arribas J, Biankin AV, et al. Interrogating open issues in cancer precision medicine with patient-derived xenografts. *Nat Rev Cancer.* (2017) 17(4):254–68. doi: 10.1038/nrc.2016.140

3. Wang H, Lu J, Tang J, Chen S, He K, Jiang X, et al. Establishment of patient-derived gastric cancer xenografts: a useful tool for preclinical evaluation of targeted therapies involving alterations in HER-2, MET and FGFR2 signaling pathways. *BMC Cancer* (2017) 17(1):191. doi: 10.1186/s12885-017-3177-9

4. Gao H, Korn JM, Ferretti S, Monahan JE, Wang Y, Singh M, et al. High-throughput screening using patient-derived tumor xenografts to predict clinical trial drug response. *Nat Med* (2015) 21(11):1318–25. doi: 10.1038/nm.3954

5. Chen Z, Huang W, Tian T, Zang W, Wang J, Liu Z, et al. Characterization and validation of potential therapeutic targets based on the molecular signature of patient-derived xenografts in gastric cancer. *J Hematol Oncol* (2018) 11(1):20. doi: 10.1186/s13045-018-0563-y

6. Jin K, He K, Han N, Li G, Wang H, Xu Z, et al. Establishment of a PDTT xenograft model of gastric carcinoma and its application in personalized therapeutic regimen selection. *Hepatogastroenterology* (2011) 58(110-111):1814–22. doi: 10.5754/hge11136

7. Sung H, Ferlay J, Siegel RL, Laversanne M, Soerjomataram I, Jemal A, et al. Global cancer statistics 2020: GLOBOCAN estimates of incidence and mortality worldwide for 36 cancers in 185 countries. *CA Cancer J Clin* (2021) 71(3):209–49. doi: 10.3322/caac.21660

8. Liu Y, Sethi NS, Hinoue T, Schneider BG, Cherniack AD, Sanchez-Vega F, et al. Comparative molecular analysis of gastrointestinal adenocarcinomas. *Cancer Cell* (2018) 33(4):721–35.e8. doi: 10.1016/j.ccell.2018.03.010

9. Jin K, Teng L, Shen Y, He K, Xu Z, Li G. Patient-derived human tumour tissue xenografts in immunodeficient mice: a systematic review. *Clin Transl Oncol* (2010) 12(7):473–80. doi: 10.1007/s12094-010-0540-6

10. Chen X, Guan Z, Lu J, Wang H, Zuo Z, Ye F, et al. Synergistic antitumor effects of cMet inhibitor in combination with anti-VEGF in colorectal cancer patient-derived xenograft models. *J Cancer.* (2018) 9(7):1207–17. doi: 10.7150/jca.20964

11. Lu J, Li G, He K, Jiang W, Xu C, Li Z, et al. Luteolin exerts a marked antitumor effect in cMet-overexpressing patient-derived tumor xenograft models of gastric cancer. *J Transl Med* (2015) 13:42. doi: 10.1186/s12967-015-0398-z

12. Jin K, Li G, Cui B, Zhang J, Lan H, Han N, et al. Assessment of a novel VEGF targeted agent using patient-derived tumor tissue xenograft models of colon carcinoma with lymphatic and hepatic metastases. *PloS One* (2011) 6(12):e28384. doi: 10.1371/journal.pone.0028384

13. Jin K, Lan H, Cao F, Xu Z, Han N, Li G, et al. Antitumor effect of FP3 in a patient-derived tumor tissue xenograft model of gastric carcinoma through an antiangiogenic mechanism. *Oncol Lett* (2012) 3(5):1052–8. doi: 10.3892/ol.2012.603

14. Jin K, Lan H, Xie B, He K, Xu Z, Li G, et al. Antitumor effects of FP3 in combination with capecitabine on PDTT xenograft models of primary colon carcinoma and related lymphatic and hepatic metastases. *Cancer Biol Ther* (2012) 13(9):737–44. doi: 10.4161/cbt.20556

15. Bi T, Bi T, Lan H, Hu X, Zhu M, Xu Z, et al. Antitumor effect of FP3 on a patient-derived tumor tissue xenograft model of rectal carcinoma. *Hepatogastroenterology* (2013) 60(128):1950–4. doi: 10.5754/hge13157

16. Lu J, Ding Y, Chen Y, Jiang J, Chen Y, Huang Y, et al. Whole-exome sequencing of alpha-fetoprotein producing gastric carcinoma reveals genomic profile and therapeutic targets. *Nat Commun* (2021) 12(1):3946. doi: 10.1038/s41467-021-24170-0

17. Voskoglou-Nomikos T, Pater JL, Seymour L. Clinical predictive value of the *in vitro* cell line, human xenograft, and mouse allograft preclinical cancer models. *Clin Cancer Res* (2003) 9(11):4227–39.

18. Maris JM, Courtright J, Houghton PJ, Morton CL, Gorlick R, Kolb EA, et al. Initial testing of the VEGFR inhibitor AZD2171 by the pediatric preclinical testing program. *Pediatr Blood Cancer* (2008) 50(3):581–7. doi: 10.1002/pbc.21232

19. Zhu Y, Tian T, Li Z, Tang Z, Wang L, Wu J, et al. Establishment and characterization of patient-derived tumor xenograft using gastroscopic biopsies in gastric cancer. *Sci Rep* (2015) 5:8542. doi: 10.1038/srep08542

20. Wang J, Xing B, Liu W, Li J, Wang X, Li J, et al. Molecularly annotation of mouse avatar models derived from patients with colorectal cancer liver metastasis. *Theranostics* (2019) 9(12):3485–500. doi: 10.7150/thno.32033

21. Chen Y, Zhang R, Wang L, Correa AM, Pataer A, Xu Y, et al. Tumor characteristics associated with engraftment of patient-derived non-small cell lung cancer xenografts in immunocompromised mice. *Cancer* (2019) 125(21):3738–48. doi: 10.1002/cncr.32366

22. Tanaka T, Nishie R, Ueda S, Miyamoto S, Hashida S, Konishi H, et al. Patient-derived xenograft models in cervical cancer: A systematic review. *Int J Mol Sci* (2021) 22(17):9369. doi: 10.3390/ijms22179369

23. Zou J, Liu Y, Wang J, Liu Z, Lu Z, Chen Z, et al. Establishment and genomic characterizations of patient-derived esophageal squamous cell carcinoma xenograft models using biopsies for treatment optimization. *J Transl Med* (2018) 16(1):15. doi: 10.1186/s12967-018-1379-9

24. Kuwata T, Yanagihara K, Iino Y, Komatsu T, Ochiai A, Sekine S, et al. Establishment of novel gastric cancer patient-derived xenografts and cell lines: Pathological comparison between primary tumor, patient-derived, and cell-line derived xenografts. *Cells* (2019) 8(6):585. doi: 10.3390/cells8060585

25. Chon HJ, Hyung WJ, Kim C, Park S, Kim JH, Park CH, et al. Differential prognostic implications of gastric signet ring cell carcinoma: Stage adjusted analysis from a single high-volume center in Asia. *Ann Surg* (2017) 265(5):946–53. doi: 10.1097/SLA.0000000000001793

26. Taghavi S, Jayarajan SN, Davey A, Willis AI. Prognostic significance of signet ring gastric cancer. *J Clin Oncol* (2012) 30(28):3493–8. doi: 10.1200/JCO.2012.42.6635

27. Kao YC, Fang WL, Wang RF, Li AF, Yang MH, Wu CW, et al. Clinicopathological differences in signet ring cell adenocarcinoma between early and advanced gastric cancer. *Gastric Cancer* (2019) 22(2):255–63. doi: 10.1007/s10120-018-0860-8

28. Murakami H, Nakanishi H, Tanaka H, Ito S, Misawa K, Ito Y, et al. Establishment and characterization of novel gastric signet-ring cell and non signet-ring cell poorly differentiated adenocarcinoma cell lines with low and high malignant potential. *Gastric Cancer* (2013) 16(1):74–83. doi: 10.1007/s10120-012-0149-2

29. Hidalgo M, Amant F, Biankin AV, Budinska E, Byrne AT, Caldas C, et al. Patient-derived xenograft models: an emerging platform for translational cancer research. *Cancer Discov* (2014) 4(9):998–1013. doi: 10.1158/2159-8290.CD-14-0001

30. Jung J, Seol HS, Chang S. The generation and application of patient-derived xenograft model for cancer research. *Cancer Res Treat* (2018) 50(1):1–10. doi: 10.4143/crt.2017.307

31. Zhuo J, Lu D, Wang J, Lian Z, Zhang J, Li H, et al. Molecular phenotypes reveal heterogeneous engraftments of patient-derived hepatocellular carcinoma xenografts. *Chin J Cancer Res* (2021) 33(4):470–9. doi: 10.21147/j.issn.1000-9604.2021.04.04

32. Zeng W, Tang Z, Li Y, Yin G, Liu Z, Gao J, et al. Patient-derived xenografts of different grade gliomas retain the heterogeneous histological and genetic features of human gliomas. *Cancer Cell Int* (2020) 20:1. doi: 10.1186/s12935-019-1086-5

33. Lu D, Luo P, Zhang J, Ye Y, Wang Q, Li M, et al. Patient-derived tumor xenografts of lung squamous cell carcinoma alter long non-coding RNA profile but not responsiveness to cisplatin. *Oncol Lett* (2018) 15(6):8589–603. doi: 10.3892/ol.2018.8401

34. Na YS, Ryu MH, Park YS, Lee CW, Lee JK, Park Y, et al. Establishment of patient-derived xenografts from patients with gastrointestinal stromal tumors: Analysis of clinicopathological characteristics related to engraftment success. *Sci Rep* (2020) 10(1):7996. doi: 10.1038/s41598-020-64552-w

35. Forrester K, Almoguera C, Han K, Grizzle WE, Perucho M. Detection of high incidence of K-ras oncogenes during human colon tumorigenesis. *Nature* (1987) 327(6120):298–303. doi: 10.1038/327298a0

36. Pretlow TP, Brasitus TA, Fulton NC, Cheyer C, Kaplan EL. K-Ras mutations in putative preneoplastic lesions in human colon. *J Natl Cancer Inst* (1993) 85 (24):2004–7. doi: 10.1093/jnci/85.24.2004

37. Vaughn CP, Zobell SD, Furtado LV, Baker CL, Samowitz WS. Frequency of KRAS, BRAF, and NRAS mutations in colorectal cancer. *Genes Chromosomes Cancer.* (2011) 50(5):307–12. doi: 10.1002/gcc.20854

38. Yokota T, Ura T, Shibata N, Takahari D, Shitara K, Nomura M, et al. BRAF mutation is a powerful prognostic factor in advanced and recurrent colorectal cancer. *Br J Cancer.* (2011) 104(5):856–62. doi: 10.1038/bjc.2011.19

39. Lochhead P, Kuchiba A, Imamura Y, Liao X, Yamauchi M, Nishihara R, et al. Microsatellite instability and BRAF mutation testing in colorectal cancer prognostication. *J Natl Cancer Inst* (2013) 105(15):1151–6. doi: 10.1093/jnci/djt173

40. Van Cutsem E, Lenz HJ, Kohne CH, Heinemann V, Tejpar S, Melezinek I, et al. Fluorouracil, leucovorin, and irinotecan plus cetuximab treatment and RAS mutations in colorectal cancer. *J Clin Oncol* (2015) 33(7):692–700. doi: 10.1200/JCO.2014.59.4812

41. Douillard JY, Oliner KS, Siena S, Tabernero J, Burkes R, Barugel M, et al. Panitumumab-FOLFOX4 treatment and RAS mutations in colorectal cancer. *N Engl J Med* (2013) 369(11):1023–34. doi: 10.1056/NEJMoa1305275

42. Benson AB, Venook AP, Al-Hawary MM, Arain MA, Chen YJ, Ciombor KK, et al. Colon cancer, version 2.2021, NCCN clinical practice guidelines in oncology. *J Natl Compr Canc Netw* (2021) 19(3):329–59. doi: 10.6004/jnccn.2021.0012

43. Van Cutsem E, Kohne CH, Lang I, Folprecht G, Nowacki MP, Cascinu S, et al. Cetuximab plus irinotecan, fluorouracil, and leucovorin as first-line treatment for metastatic colorectal cancer: Updated analysis of overall survival according to tumor KRAS and BRAF mutation status. *J Clin Oncol* (2011) 29(15):2011–9. doi: 10.1200/JCO.2010.33.5091

44. Van Cutsem E, Kohne CH, Hitre E, Zaluski J, Chang Chien CR, Makhson A, et al. Cetuximab and chemotherapy as initial treatment for metastatic colorectal cancer. *N Engl J Med* (2009) 360(14):1408–17. doi: 10.1056/NEJMoa0805019

45. Bokemeyer C, Bondarenko I, Makhson A, Hartmann JT, Aparicio J, de Braud F, et al. Fluorouracil, leucovorin, and oxaliplatin with and without cetuximab in the first-line treatment of metastatic colorectal cancer. *J Clin Oncol* (2009) 27 (5):663–71. doi: 10.1200/JCO.2008.20.8397

46. Bokemeyer C, Bondarenko I, Hartmann JT, de Braud F, Schuch G, Zubel A, et al. Efficacy according to biomarker status of cetuximab plus FOLFOX-4 as first-line treatment for metastatic colorectal cancer: The OPUS study. *Ann Oncol* (2011) 22(7):1535–46. doi: 10.1093/annonc/mdq632

frontiers | Frontiers in Oncology

TYPE Original Research
PUBLISHED 01 December 2022
DOI 10.3389/fonc.2022.1057147

OPEN ACCESS

EDITED BY
Hatim E. Sabaawy,
University of Colorado, United States

REVIEWED BY
Luz Jubierre Zapater,
Memorial Sloan Kettering Cancer Center, United States
Yirizhati Aili,
First Affiliated Hospital of Xinjiang Medical University, China

*CORRESPONDENCE
Shuzhen Liu
shuzhen.liu@utsouthwestern.edu
Jiang I. Wu
jiang9.wu@utsouthwestern.edu
Xuanming Shi
xuanming.shi@ahmu.edu.cn

†These authors have contributed equally to this work

SPECIALTY SECTION
This article was submitted to Cancer Molecular Targets and Therapeutics, a section of the journal Frontiers in Oncology

RECEIVED 29 September 2022
ACCEPTED 21 November 2022
PUBLISHED 01 December 2022

CITATION
Deng H, Guo X, Feng N, Luo Y, Liu B, Liu S, Wu JI and Shi X (2022) Targeting H3K27me3 demethylase to inhibit Shh signaling and cholesterol metabolism in medulloblastoma growth. *Front. Oncol.* 12:1057147. doi: 10.3389/fonc.2022.1057147

Targeting H3K27me3 demethylase to inhibit Shh signaling and cholesterol metabolism in medulloblastoma growth

Hongshi Deng[1†], Xueli Guo[1†], Na Feng[2†], Yi Luo[2], Bei Liu[2], Shuzhen Liu[2*], Jiang I. Wu[2*] and Xuanming Shi[1,2*]

[1]School of Basic Medical Sciences, Anhui Medical University, Hefei, Anhui, China, [2]Department of Physiology, University of Texas Southwestern Medical Center, Dallas, TX, United States

Previously we uncovered the epigenetic regulation of medulloblastoma that low levels of H3K27me3 are required for Shh target gene expression and medulloblastoma growth. Since Jmjd3, an H3K27me3 demethylase, is responsible for maintaining low H3K27me3 at Shh target genes, targeting Jmjd3 could be an efficient way to inhibit Shh signaling and medulloblastoma growth. Here we show that the small molecule GSK-J4, an inhibitor of Jmjd3, significantly inhibited the expression of Shh target genes in Shh responsive cell models and primary cerebellar granule neuron precursors. GSK-J4 also significantly reduced the growth of primary Shh medulloblastoma cultures. Treating human medulloblastoma cell line DaoY by GSK-J4 led to cell cycle arrest at G0/G1 phase with decreased cells in S-phase. Tumor cell proliferation was significantly inhibited by GSK-J4 treatment. Gene expression analyses showed that GSK-J4 additionally constrained the expression of key genes in cholesterol biosynthesis. Our results highlight the possibility that targeting H3K27me3 demethylase Jmjd3 with GSK-J4 to inhibit Shh signaling and cholesterol metabolism is a potential application to treat Shh medulloblastoma.

Introduction

Shh ligand covalently modified with N-terminal palmitoylation and C-terminal cholesterol plays essential roles in mammalian embryonic development, cell homeostasis and tumor formation (1). When Shh ligand binds to its receptor Patched (Ptch), Smoothened (Smo) is released from Ptch to activate transcription activator Gli1/2-Act. The translocated Gli1/2-Act in the nucleus activates Shh signaling by increasing the expression of general Shh target genes such as *Gli1*, *Ptch1* and *Hhip* (2, 3). During cerebellar development, Shh molecules are produced from Purkinje neurons and activate mitogenic target genes such as *N-myc* and *Ccnd1* in cerebellar granule neural precursors (CGNPs). Hence, Shh drives the proliferation of CGNPs and contributes to cerebellar development (4–6). During normal cerebellar development, Shh levels are properly

modulated and reach a peak at an early postnatal stage. However, the overactive Shh signaling caused by mutations in Shh pathway genes such as *Smo* and *Ptch1* is the driving force for Shh-type medulloblastoma (7, 8). SmoM2 is a Smo mutant resulting in constitutively active Shh signaling (9). This mutant has been widely used to establish mouse Shh medulloblastoma tumor models (10, 11).

Medulloblastoma is the most common malignant pediatric brain tumor, and accounts for about 20% of all childhood brain tumors (12, 13). Genomic studies classified medulloblastoma into four subgroups: Wnt, Shh, Group 3 and Group 4 (8, 14–17). The Wnt and Shh groups were named according to the principally activated signaling pathways in the tumors. Wnt-type tumors arise from the embryonic brain stem and lower rhombic lip progenitor cells (18). In contrast, Shh-type tumors originate from CGNPs with active Shh signaling (19, 20). This type of tumor is often found in infants and adults and accounts for about 25% of all medulloblastoma (11). Group 3 tumor features large cell/anaplastic phenotype and is driven by oncogenes *c-myc* and *OTX2* (18, 21, 22). The cell origin of Group 4 medulloblastoma is thought to originate from unipolar brush cells (23–25). Current therapies for medulloblastoma consist of surgery, radiotherapy and chemotherapy. The standard radiotherapy includes craniospinal irradiation with a radiation boost to tumor bed. More often, radiotherapy medicated by Linac-based photons is being replaced by proton-beam based radiotherapy. Although prognosis is improved, patients still have severe long-term side effects (8, 26). Having a better understanding of both the active Shh signaling pathway and cell of origin provides possibilities of targeted therapies for medulloblastoma (27).

Epigenetic regulators play important roles in Shh signaling and medulloblastoma development (10, 11, 28–31). Previously we identified histone 3 lysine 27 trimethylation (H3K27me3) demethylase Jmjd3 as a key player in Shh target gene activation (10). We showed that Jmjd3 mediated H3K27me3 demethylation and epigenetic changes are required for the activation of Shh target genes in response to Shh stimulation (11, 31). Genetic knockout of Jmjd3 significantly inhibited Shh medulloblastoma growth in culture and in mouse models (10). Therefore, pharmacological inhibition of Jmjd3 could be a promising treatment option for medulloblastoma. Kruidenier et al. reported that an ethyl ester GSK-J4 inhibits H3K27me3 demethylase activities (32). By targeting Jmjd3, GSK-J4 has been successfully applied to inhibit the growth and proliferation of various tumors including pediatric brainstem glioma, chondrosarcomas, and lung adenocarcinoma in mouse xenograft models or *in vivo* studies (33–35).

In this report, we demonstrated that GSK-J4 efficiently inhibits Shh signaling and Shh-type medulloblastoma growth. We confirmed the notion in several Shh responsive cell models including immortalized fibroblasts NIH3T3, primary MEFs, normal CGNPs, primary mouse tumor cells, and human medulloblastoma cell line DaoY. In DaoY medulloblastoma cells, GSK-J4 additionally inhibits tumor cholesterol metabolism, which contributes to Shh signaling and cell proliferation. These results highlighted the potential translation to use the small molecule inhibitor GSK-J4 targeting H3K27me demethylase Jmjd3 for Shh-type medulloblastoma treatment.

Materials and methods

Mice

The *SmoM2* transgenic mice were purchased from Jackson Laboratory (Strain #:005130). *SmoM2 CAG-CreER* mice spontaneously develop Shh-type medulloblastoma (9).

Cell lines, primary MEF, CGNP and medulloblastoma cell cultures

NIH3T3 cells, DaoY cells, wild type MEF cells, *Gli3*$^{-/-}$ and *Jmjd3*$^{-/-}$ MEF cells were cultured in DMEM containing 10% FBS, sodium pyruvate, penicillin, streptomycin, minimal amino acid, L-glutamine and 2-mercaptoethanol. *Jmjd3*$^{-/-}$ MEF cells were provided by Dr. T. Akira (36). Primary CGNP cultures were derived from dissociated P4 wild type mouse cerebella and cultured in DMEM/F12 media containing 25 mM KCl, N2, penicillin, streptomycin, and 10% FBS as previously described (31). For Shh induction, Shh conditioned media produced from Shh-CM 293T cells (37) were added to MEF and CGNP cultures at 1:20 dilution. NIH3T3 cells or primary MEF cells were treated with Shh in 0.5% FBS media for 24 hours before harvesting. Primary tumor cells were derived from dissociated SmoM2 medulloblastoma and cultured in DMEM/F12 media containing B27, N2, EGF, and FGF2. For GSK-J4 (XcessBio, M60063-2) treatment, media were mixed with indicated concentrations of the compound, and DMSO was used as a solvent control. The ATP assay for cell viability analysis was carried out as described (10).

Western blot

Western blot was carried out as previously described (38). In detail, cultured cells were washed with ice-cold 1x PBS for three times, and lysed in RIPA buffer (50 mM Tris, pH 8.0, 150 mM NaCl, 0.05% SDS, 0.5% DOC, 1% NP-40). Cell lysates were separated on SDS-PAGE gels. Antibodies against Gli1 and Caspase3 were purchased from Cell Signaling and Protein Tech, respectively. HRP-conjugated secondary antibodies were from Jackson Immunology. GAPDH was detected as a loading control.

Reverse-transcription quantitative PCR

RT-qPCR was performed as described (38). RNAs from cells or tissues were extracted with TRIZOL (Invitrogen). The concentration of RNA samples was determined with NanoDrop One (Thermo Scientific). cDNAs were synthesized by reverse transcription using Iscript. iTaq reagents were used for quantitative PCR. Both Iscript and iTaq were purchased from Bio-Rad. A Bio-Rad real-time PCR system (C1000 Thermal Cycler) was used for quantitative PCR. Levels of GAPDH mRNA were used to normalize input RNAs. Relative gene expression was calculated by ΔΔCt as previously described (38). Graphics shown are representative of experiments performed in triplicate. Sequences of PCR-primers are listed in extended data.

Chromatin immunoprecipitation assay

ChIP experiments were performed as previously described (10). Dissociated cells were crosslinked with paraformaldehyde, and DNA was sonicated to fragments (200-1000 bp) in the nuclear lysis buffer using a Sonic Dismembrator 550 (Fisher Scientific) at level 3, output 10%, for 5 cycles of 7 sec on, 30 sec off, in ice water. An antibody against H3K27me3 (#39536, Active Motif) was used in the precipitation step. Precipitated DNA was captured using pre-blocked Protein G agarose beads (Pierce) in the presence of BSA and salmon sperm DNA, followed by purification and subjection to quantitative PCR. The primer sequences are CGCTCACTTCCCTCGTATATCCTTC, GGCAGTATAGGGTCCCTCAAGGG. 10% of input was used for positive control and normalizing results, which were presented as percentages of input.

RNA-seq and bioinformatics analyses

RNA-seq analyses were performed in the Sequencing and Bioinformatics Center in Anhui Medical University. Total RNAs were extracted using TRIzol Reagents (Invitrogen), and mRNAs were separated using magnetic beads (Vazyme, N401). Reverse transcription was performed to obtain cDNA using SuperScript™ II (Invitrogen, # 18064014). cDNA libraries were established using the Tn5 DNA Library Prep Kit from Illumina (TRANS, KP101-11) and sequenced for PE150. Fastq data were analysed with Fastqc and processed using the pipeline described in the Linux system (39). The expression levels of genes were quantified with featureCounts (40), and the differentially expressed genes were called by DESeq2 program with a fold-change > 2 and padj <0.05. Data were analysed and presented using R studio for GO, KEGG, GSEA and STRING analyses.

Immunofluorescence staining

DaoY cells were seeded on cover glasses at a density of 10^5 cells/well in 24-well plates. Cells were treated with 10 μM of BrdU for 2 hours before staining. For staining, cells on cover glasses were fixed using methanol, then washed with PBS for 3 times. The cells were then treated with 2 M of HCl for 20 min, and blocked with 5% goat serum for 30 min at room temperature. The cells were incubated with mouse anti-BrdU antibodies (ABclonal, A1482) o/n at 4°C and then with GFP-Conjugated goat anti-mouse IgG antibodies (ZGGB-BIO, ZF-0312) for 30 min at 20°C.

Cell cycle assay

The cells were cultured with GSK-J4 for 24 hours in 6 cm dishes at a density of 4 x 10^5 cells per dish. Cell cycle assay was performed according to the manufacturer's instructions (Beyotime, C1052). Stained cells were applied to a BD FACSVerse flow cytometer (BD Bioscience), and data were analysed using ModFit software.

Statistical analysis

Each experiment was repeated at least three times except for RNA-seq analyses, data shown were from representative assays with 3 technical repeats. Data are expressed as means plus standard deviation (s.d.). Statistical analyses were performed using a two-tailed, unpaired Student's *t*-test provided by Microsoft Office Excel. A p value of <0.05 will be considered significant.

Results

Shh signaling is impaired by GSK-J4 targeting H3K27me3 demethylase Jmjd3

Since Shh medulloblastoma is caused by over-active Shh signaling in cerebellum, modulating Shh signaling could be an effective way to constrain the tumor growth. Previously we reported that Jmjd3 plays an essential role in Shh signaling activation and Shh-medulloblastoma growth (10). Kruidenier et al. developed an H3K27me3 demethylase inhibitor, GSK-J4, to modulate Jmjd3 activity, making it possible to intervene the diseases that depend on Jmjd3 (32). To determine whether GSK-J4 can block Shh signaling by targeting Jmjd3, we chose the immortalized embryonic fibroblast NIH3T3 cells (41), which is responsive to Shh signaling and could activate Shh target genes such as *Gli1*, *Ptch1*, *Hhip*, and *Hck* (10, 11, 31, 38). Among them,

Gli1 encodes a transcription factor forming a positive feedback loop to further activate Shh/Gli1 target genes. The mRNA level of *Gli1* faithfully reflects the activities of Shh pathway (31), hence we use *Gli1* as a readout of the pathway. Previously 30 μM of GSK-J4 was applied to inhibit the proinflammatory macrophage response through targeting the jumonji domain of histone demethylase (32), we hence tested this concentration of GSK-J4 on NIH3T3 cells, and treated the cells with Shh conditioned media and various concentrations of GSK-J4 at 0.01, 0.05, 0.24, 1.2, 6, and 30 μM (Figures 1A, B). The Treatment of GSK-J4 (Figure 1A, lane 4-8) significantly reduced the Shh induced Gli1 protein levels (Figure 1A, lane 2) when the concentration of

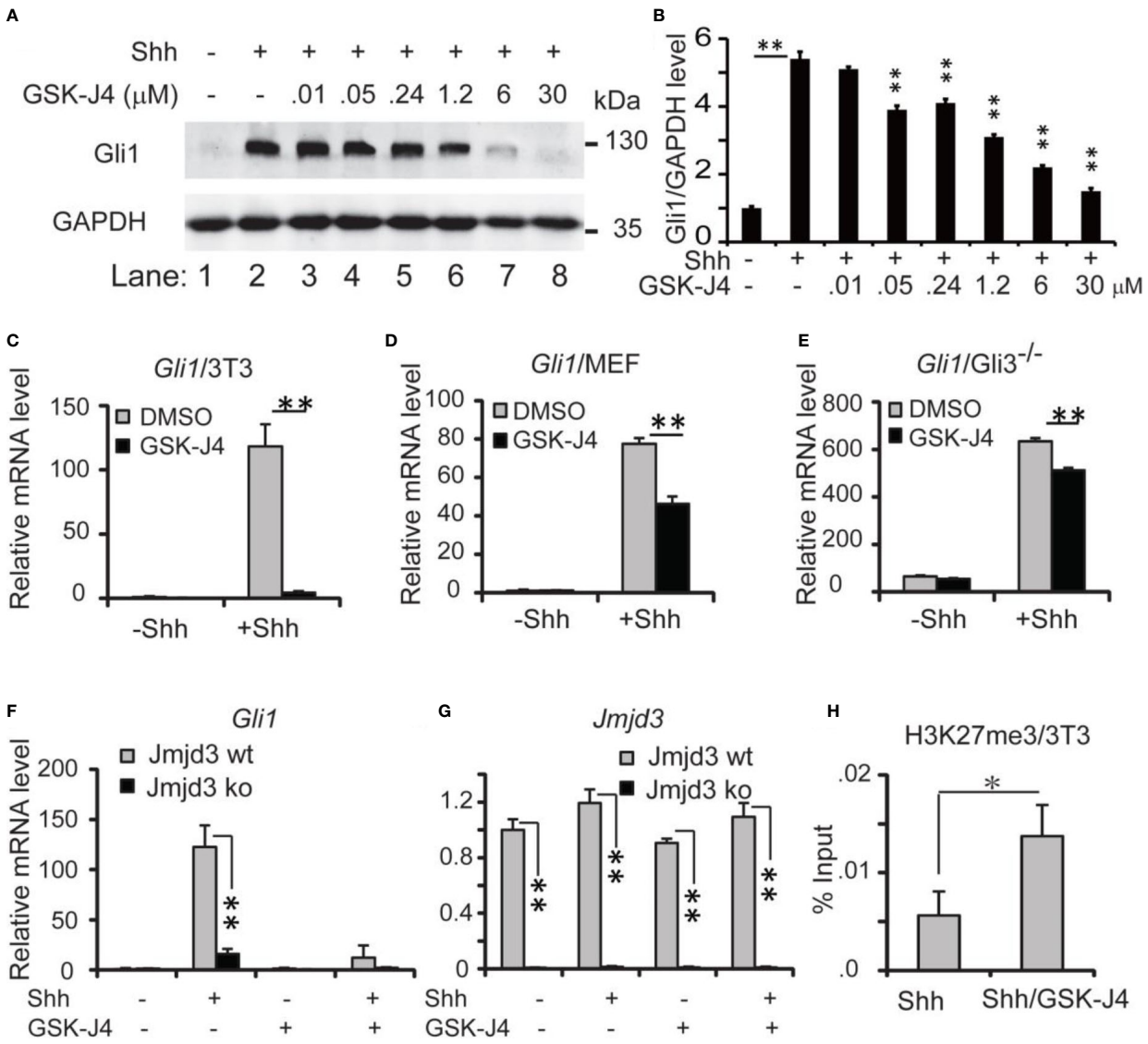

FIGURE 1
Shh signaling is impaired by GSK-J4 targeting H3K27me3 demethylase Jmjd3. **(A)** Effects of GSK-J4 at various concentrations on Gli1 protein levels. **(B)** Ratio of Gli1 protein levels against GAPDH in **(A)** calculated by Image J Significance is against Shh induced level (*rf* Figure 1A, lane 2) except for the one between Figure 1A lane 1 and Figure 1A lane 2. **(C)** GSK-J4 impairs Shh-induced *Gli1* mRNA expression in NIH3T3 cells by RT-qPCR analysis. **(D)** GSK-J4 inhibits Shh-induced *Gli1* mRNA expression in primary MEF cells. **(E)** GSK-J4 significantly inhibits Shh-induced *Gli1* mRNA expression in primary *Gli3*$^{-/-}$ MEF cells. **(F)** Shh-induced *Gli1* mRNA expression is impaired in primary *Jmjd3*$^{-/-}$ MEF cells, and GSK-J4 does not further decrease the *Gli1* mRNA level. **(G)** *Jmjd3* mRNA expression is reduced by *Jmjd3* knockout. **(H)** GSK-J4 raises the local H3K27me3 enrichment at mouse *Gli1* promoter region shown by ChIP q-PCR assay. The concentration of GSK-J4 is 30 μM if not indicated for all figures. Significance determined using Student's *t*-test. $^{**}p < 0.01$ and $^{*}p < 0.05$.

GSK-J4 is above 6 μM. The quantifications indicated that 30 μM of GSK-J4 is higher than the IC50 in NIH 3T3 cells for target gene Gli1 expression (Figure 1B).

Upon addition of Shh conditioned media to NIH3T3 cells, *Gli1* mRNA levels were significantly increased, indicating an activated Shh signaling pathway (Figure 1C). After cells were treated with 30 μM of GSK-J4 for 24 hours, *Gli1* expression was significantly decreased to ~10% (Figure 1C). Thus, GSK-J4 is a potential inhibitor of the Shh signaling pathway. Since the immortalized NIH3T3 cells were generated from mouse embryonic fibroblast (MEF), we carried out the GSK-J4 inhibition experiment using primary MEF cells. Similarly, the Shh-induced *Gli1* expression was significantly reduced by GSK-J4 treatment, albeit to a lesser extent than that in NIH3T3 cells (Figure 1D *vs* 1C). The GSK-J4 inhibition of Shh target genes was further confirmed in the primary *Gli3*$^{-/-}$ MEF cells (Figure 1E). The basal *Gli1* mRNA level in *Gli3*$^{-/-}$ MEFs is higher than that in wildtype MEF since Gli3 is a repressor in the Shh signaling pathway. GSK-J4 treatment also significantly reduced *Gli1* basal expression levels in *Gli3*$^{-/-}$ MEFs. Given our finding that Jmjd3 plays an important role in the Shh signaling pathway (10), we examined whether GSK-J4 inhibition of Shh gene expression is indeed through targeting Jmjd3. When primary *Jmjd3*$^{-/-}$ MEFs were treated with or without GSK-J4 in the presence or absence of Shh, we observed that Jmjd3 deficiency largely blocked both the Shh-induced target gene expression and GSK-J4 inhibition (Figures 1F, G). To understand the molecular mechanism in which GSK-J4 inhibits the Shh signaling pathway, we performed an H3K27me3 ChIP assay. In NIH3T3 cells treated with GSK-J4, the H3K27me3 levels at the *Gli1* gene regulatory region near its promoter were significantly increased (Figure 1H), suggesting impaired demethylation activities of Jmjd3. Taken together, GSK-J4 blocked Shh signaling by inhibiting Jmjd3 demethylase activities.

Growth of CGNP cells is sensitive to GSK-J4

Shh secreted from Purkinje neurons is essential for CGNP proliferation and cerebellar development (1). To determine whether GSK-J4 inhibits CGNP proliferation by inhibiting the Shh signaling pathway, we isolated primary CGNP cells from P4 mouse cerebella, and treated them with Shh conditioned media (37). Shh-induced target gene expression in CGNP cells was significantly impaired by 30 μM of GSK-J4 treatment for 24 hours (Figure 2A). To further investigate inhibition of GSK-J4 in detail, we treated CGNP cells with 30 μM of GSK-J4 for various durations. We observed that *Gli* mRNA levels were significantly decreased after 2 hours of treatment with GSK-J4, and the decrease reached 50% after 3 hours (Figure 2B). To quantitate the effects of GSK-J4 on CGNP cell growth, we treated the CGNP cells in the presence of Shh with various concentrations of GSK-J4 for 24 hours and measured ATP percentage to indicate cell survival. 6 μM of GSK-J4 treatment reduced 50% of cell growth in CGNP cells (Figure 2C). We further measured CGNP growth at various time points after 30 μM of GSK-J4 treatment. We observed no significant growth change until at 24 h time point (Figure 2D, E). Therefore, the decrease of *Gli1* expression after GSK-J4 treatment at earlier time points was not caused by GSK-J4 toxicity. These results confirmed that GSK-J4 inhibits the Shh signaling pathway in CGNP cells. Furthermore, at 24 h time point after GSK-J4 treatment, CGNP cell numbers were significantly reduced in Shh treated group, but not in the untreated one (Figures 2D, E), suggesting that the GSK-J4 inhibition of CGNP cell growth requires Shh signaling. Hence, consistent with our previous observation that Jmjd3 is required for Shh target gene expression and cerebellum development (10), pharmacological inhibition of Jmjd3 by GSK-J4 also efficiently inhibited Shh target gene expression during cerebellar development.

GSK-J4 shows antitumor activity in medulloblastoma

Next, we determined whether GSK-J4 inhibits Shh-type medulloblastoma. We bred *Rosa26-SmoM2*, *actin-creER* transgenic mice, in which SmoM2 mutation causes constitutive Shh signaling and Shh-type medulloblastoma (9). From mouse medulloblastoma tumors, we cultured primary tumor cells and treated them with 30 μM of GSK-J4. *Gli1* expression was significantly inhibited as shown by RT-qPCR and the tumor cell growth was completely blocked by GSK-J4 as measured by ATP assay (Figures 3A, C), suggesting that GSK-J4 is more effective in inhibiting the growth of medulloblastoma cells compared to CGNP cells. To find the minimal treatment time of GSK-J4, we treated the tumor cells with 30 μM of GSK-J4 in a time course (Figure 3B) and found that the *Gli1* mRNA level decreased 50% after 6-7 hours. Consistently, most of the tumor cells were killed before 8 hours (Figure 3B). We next determined minimal concentration of GSK-J4 to inhibit medulloblastoma growth by treating the tumor cells with various concentrations of GSK-J4 for 24 hours. Our results suggested that 6 μM of GSK-J4 significantly inhibited the tumor cell growth (Figures 3C–E). Since Shh signaling is constitutively elevated in Shh-type medulloblastoma, Shh ligand had no significant effect on *Gli1* expression, and GSK-J4 showed similar effects on tumor cell growth in the presence or absence of Shh (Figure 3F).

GSK-J4 inhibits the proliferation of medulloblastoma cells

To translate the finding that GSK-J4 is a candidate to treat medulloblastoma, we measured *Gli1* mRNA level changes

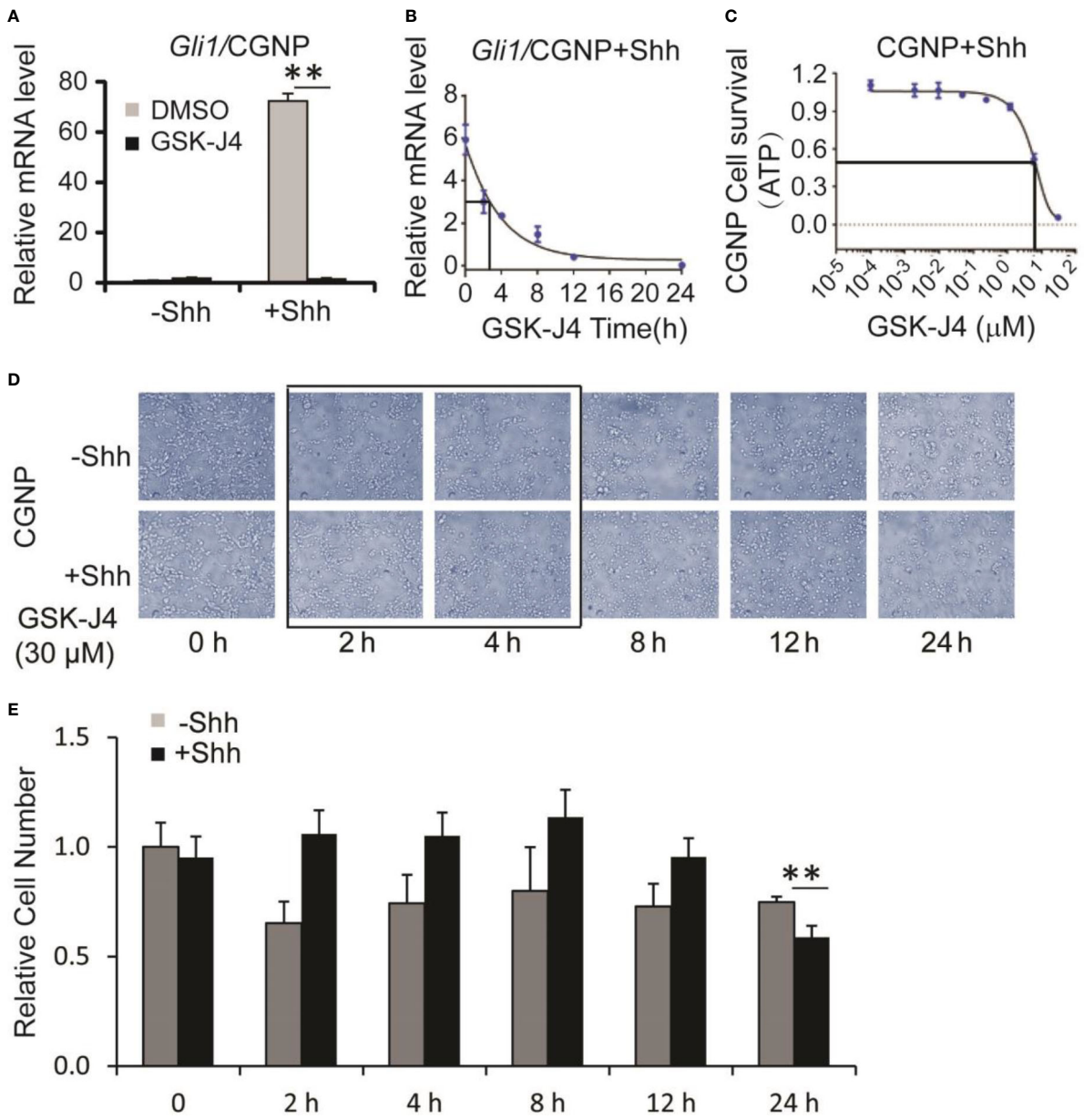

FIGURE 2
Shh signaling and growth of CGNP cells are inhibited by GSK-J4. **(A)** GSK-J4 decreases Shh-induced *Gli1* expression in P4 CGNP cells. **(B)** Time course of GSK-J4 effect on *Gli1* expression in P4 CGNP cells. **(C)** Dose dependent survival of CGNP cells after the treatment of GSK-J4 shown by ATP assay. **(D, E)** Cell performances after the treatment of GSK-J4 for indicated time courses and doses. The cells with frame have significant changes after treatment with GSK-J4. Significance determined using *t*-test. $^{**}p < 0.01$.

before and after GSK-J4 treatments in a human Shh-type medulloblastoma cell line DaoY. *Gli1* was expressed actively in DaoY cells regardless of Shh treatment, and GSK-J4 significantly inhibited *Gli1* expression (Figure 4A). To determine the sensitivity of DaoY cells to GSK-J4 treatment, we measured cell survival under 2 μM, 6 μM or 30μM of GSK-J4 treatment, and found that 30 μM GSK-J4 significantly hindered cell viability of DaoY medulloblastoma cells (Figure 4B). To determine whether the cell number reduction was caused by inhibition of proliferation or increase of apoptosis, we performed cell cycle analyses. We found that 30μM of GSK-J4 treatment significantly induced cell cycle arrest at G0/G1 phase, with an extension at G0/G1phase and a reduction of S-phase (Figure 4C). BrdU

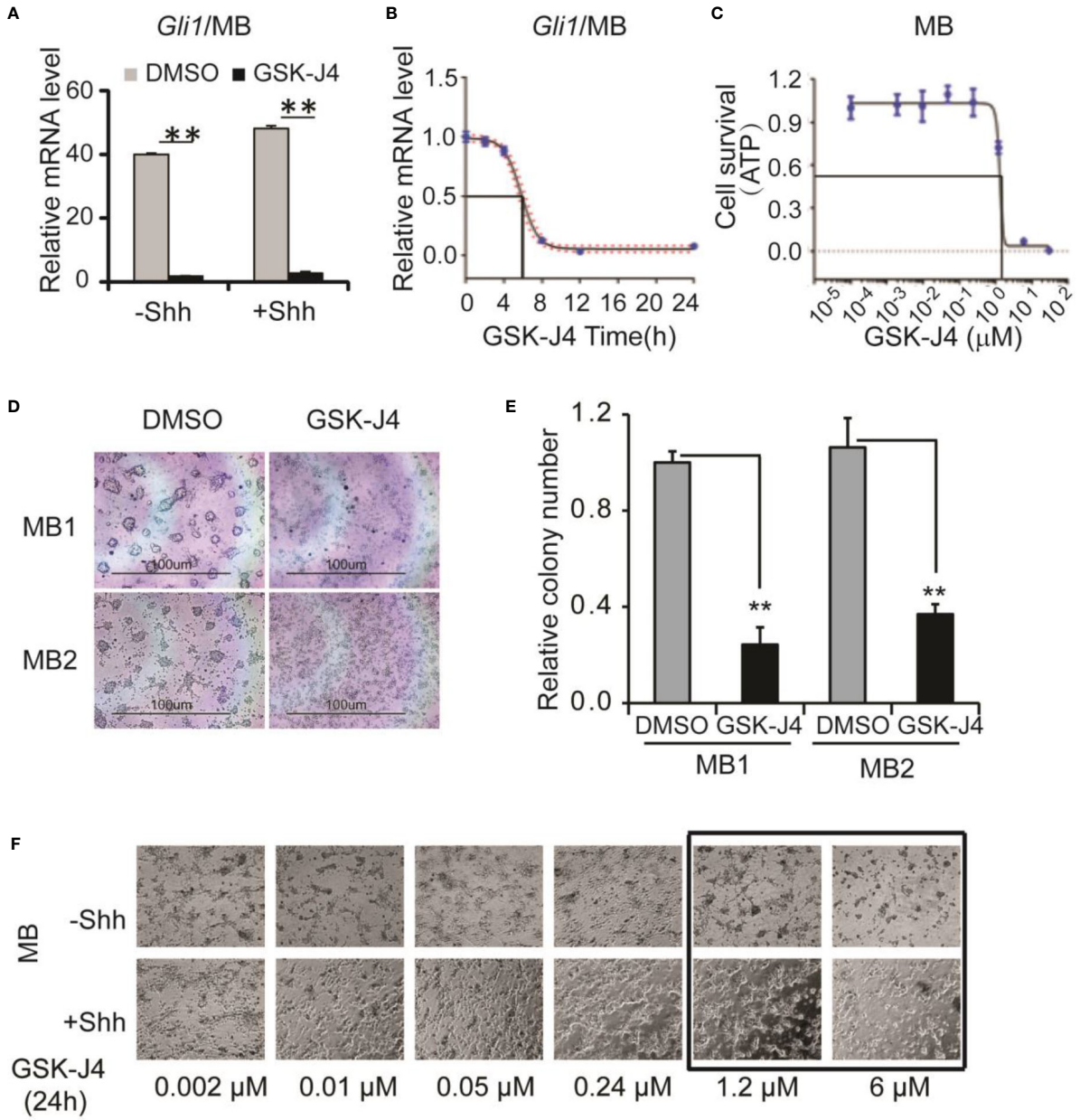

FIGURE 3
GSK-J4 shows antitumor activity in mouse primary medulloblastoma cells. **(A)** Shh target gene *Gli1* mRNA expression is inhibited by the treatment of GSK-J4 on mouse Shh-type primary medulloblastoma cells (MB). **(B)** Time course of GSK-J4 effects on *Gli1* expression in mouse primary medulloblastoma cells. **(C)** Dose dependent survival of primary medulloblastoma cells after the treatment of GSK-J4 shown by ATP assay. **(D)** Survival of primary medulloblastoma cells treated with GSK-J4. **(E)** Tumor colonies after treatment of GSK-J4. **(F)** Time course performances of primary medulloblastomas after the treatment of GSK-J4. The cells with frame have significant performance changes after treatment with GSK-J4. Significance determined using *t*-test. $^{**}p < 0.01$.

incorporation assay in DaoY cell cultures further verified our hypothesis that GSK-J4 could inhibit DaoY medulloblastoma cell cycle progression. BrdU positive cells were significantly decreased upon 6 μM of GSK-J4 treatment, and 30 μM of GSK-J4 treatment showed further reduction (Figures 4D, E). After treatment with GSK-J4, Caspase3 levels were slightly increased as shown by western blot (Figure 4F), suggesting minor cell apoptosis caused by GSK-J4 treatment. Taken together, GSK-J4 inhibits the proliferation of human DaoY medulloblastoma cells.

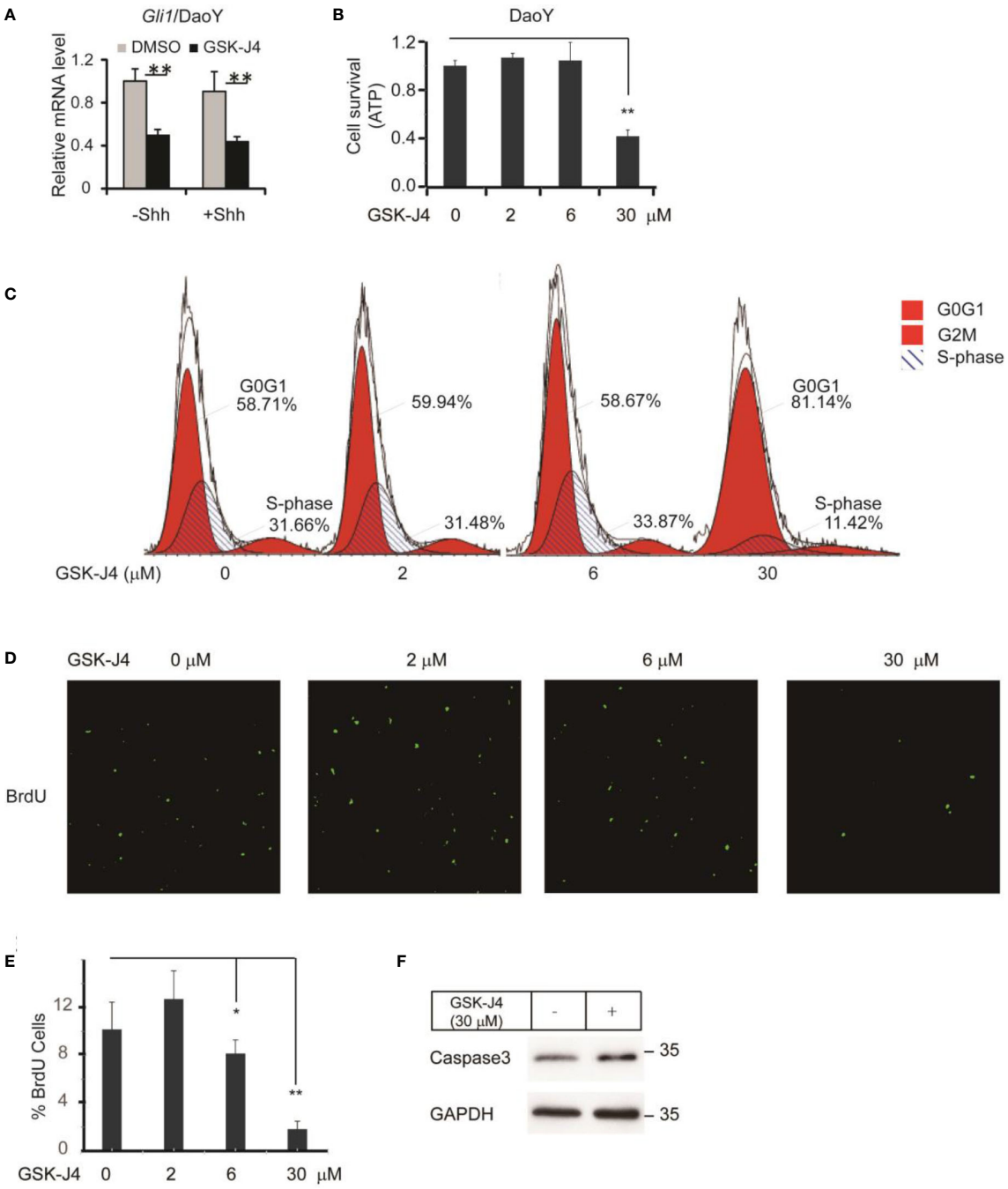

FIGURE 4
Growth of human DaoY medulloblastoma cells is inhibited and cells are arrested at G0/G1 by treatment of GSK-J4. **(A)** Shh target gene *Gli1* expression is impaired by GSK-J4 in human medulloblastoma cell line DaoY. **(B)** Growth of DaoY Cells is inhibited by GSK-J4. **(C)** Growth of DaoY Cells is arrested at G0/G1 phase with decrease of S-phase by GSK-J4. **(D, E)** The proliferation of DaoY cells is reduced by treatment of GSK-J4. **(F)** Apoptosis of DaoY tumor cells is not dramatically induced by GSK-J4. Significance determined using Student's t-test; *$p<0.05$, **$p<0.01$.

RNA-seq and bioinformatics analyses show biosynthesis of cholesterol as an additional target of GSK-J4

To understand the global effects of GSK-J4 on medulloblastoma cells, we carried out RNA-seq of DaoY cells treated with or without GSK-J4 (n=2). Heatmap of mRNA levels showed comparable samples used for this assay (Figure 5A). Totally, 1208 genes had higher expression after treatment with GSK-J4, and 1154 genes decreased their expression (Figure 5B). The down-regulation of these genes possibly resulted from the inhibition of H3K27me3 demethylase activities, while the upregulation could be caused by indirect effects. GO analysis showed sterol biosynthesis genes were enriched in the down-regulated gene population (Figure 5D). The heatmap further confirmed the significant down-regulation of cholesterol biosynthesis genes (Figure 5C). Consistently, KEGG assay also showed steroid biosynthesis genes decreased after treatment with GSK-J4 (Figure 5E). Using STRING package, we

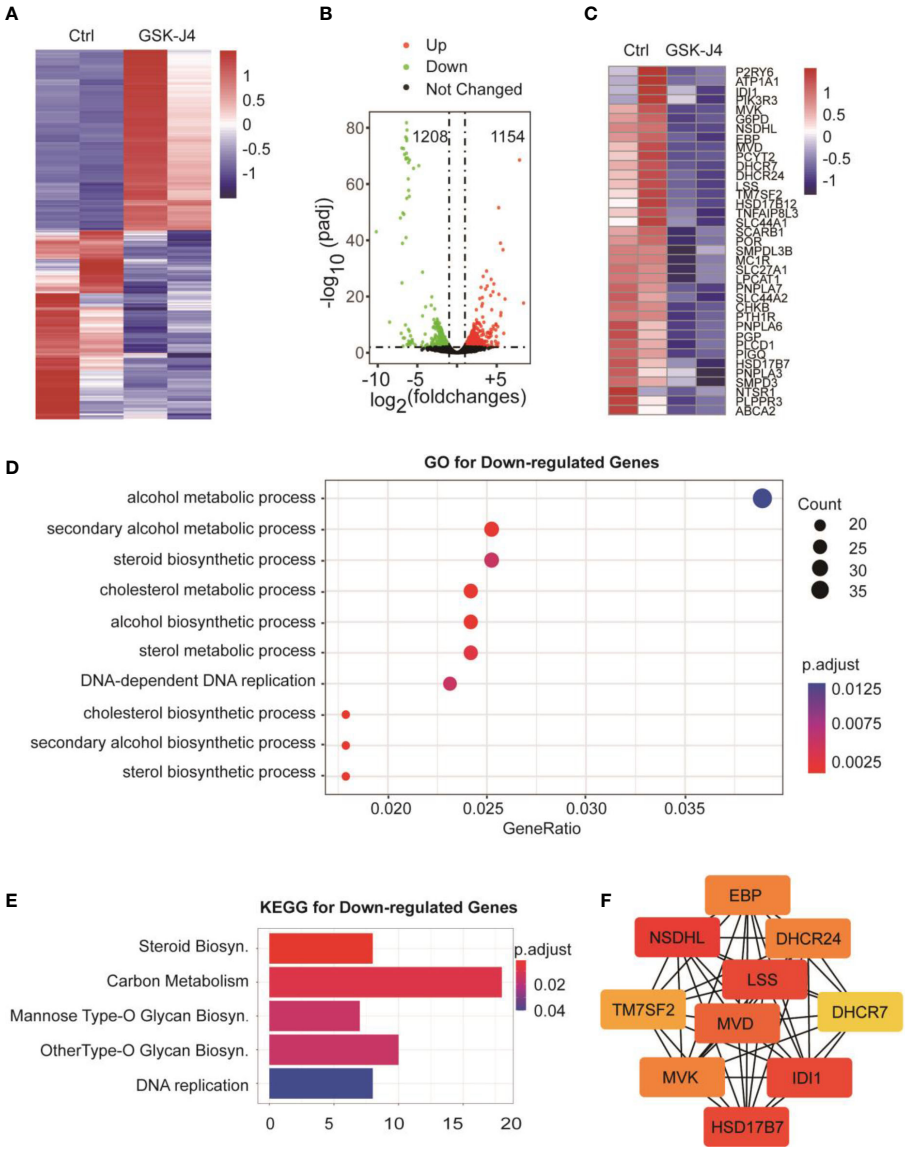

FIGURE 5
Biosynthesis of cholesterol and phospholipids are impaired by GSK-J4 in DaoY cells. **(A)** Heatmap of gene mRNA levels in DaoY cells after treatment with GSK-J4. **(B)** Volcano plot of the differentially expressed genes in DaoY cells after treatment with GSK-J4. **(C)** Heatmap of the mRNA level of cholesterol biosynthesis genes in DaoY cells after treatment with GSK-J4. **(D)** GO analysis of the down-regulated genes in DaoY cells treated with GSK-J4. **(E)** KEGG analysis of the down-regulated genes in DaoY cells treated with GSK-J4. **(F)** STRING analysis for key genes in cholesterol biosynthesis.

identified the top 10 genes of sterol biosynthesis pathway as presented in Figure 5F, highlighting *MVD*, *DHCR7*, *DHCR24*, *LSS* and *HSD17B7* in cholesterol biosynthesis. On the other hand, the up-regulated genes mostly were associated with protein degradation and unfolding pathways (Figure 6A), which may result in dys-regulated metabolism and disease (Figure 6B).

Discussion

We broadly tested an epigenetic inhibitor GSK-J4 in Shh-responsive tissue cultures, including Shh responsive cell models NIH3T3, primary MEF cells, primary CGNP cells and medulloblastoma cells. Importantly, we did pilot experiments in human DaoY Shh-medulloblastoma cell line. We provide strong evidences showing decreased mRNA levels of the key Shh target gene *Gli1* by GSK-J4 treatment in all settings. Since Gli1 is a positive feedback transcription factor in Shh signaling, it plays important roles to amplify Shh signals *in vivo*. One strategy for inhibiting Shh signaling in tumor growth is by inhibiting Gli1 levels (27).

Our results together showed that GSK-J4 is a potential inhibitor for Shh-type medulloblastoma growth (Figures 4B–D), and it can be developed for possible targeted therapy of pediatric Shh-type medulloblastoma. Hashizume et al. showed that GSK-J4 is a candidate for brainstem glioma therapy by inhibiting H3K27me3 demethylase (33). The group administered GSK-J4 by intraperitoneal injection, and observed active derivative GSK-J1 in brain tissues, suggesting the small molecule can reach cerebellum for medulloblastoma therapy. In our study, GSK-J4 treatment reduced active tumor cells and BrdU incorporation to genome. Cells were arrested at G0/G1 phase with significant decrease in S-phase after GSK-J4 treatment, together showing inhibited proliferation by GSK-J4.

Surprisingly, we found the expression of cholesterol biosynthesis genes was significantly reduced by GSK-J4 treatment. The key biosynthesis genes included *MVD*, *DHCR7*, *DHCR24*, *LSS*, *HSK17B7* and *TM7SF2* (Figure 7A), suggesting that the biosynthesis of cholesterol was impaired in cells treated with GSK-J4. These cholesterol biosynthesis genes were possibly directly regulated by Jmjd3. It was reported that the reduction of cholesterol biosynthesis resulted in S-phase decrease and G0/G1

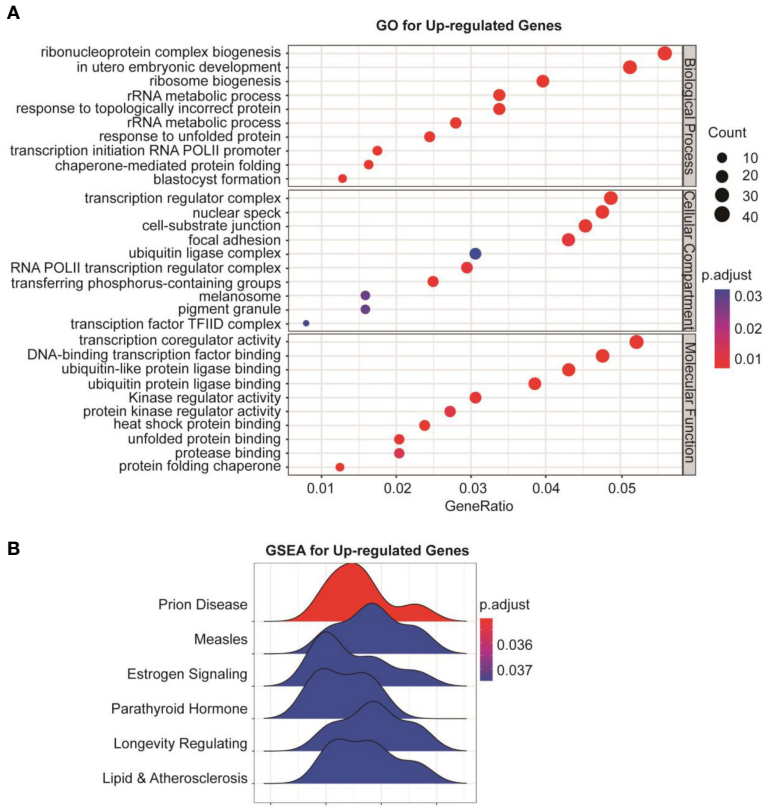

FIGURE 6
Protein degradation and unfolding are activated by GSK-J4 in DaoY cells. **(A)** GO analysis of the up-regulated genes in DaoY cells treated with GSK-J4. **(B)** GSEA analysis of the up-regulated genes in DaoY cells treated with GSK-J4.

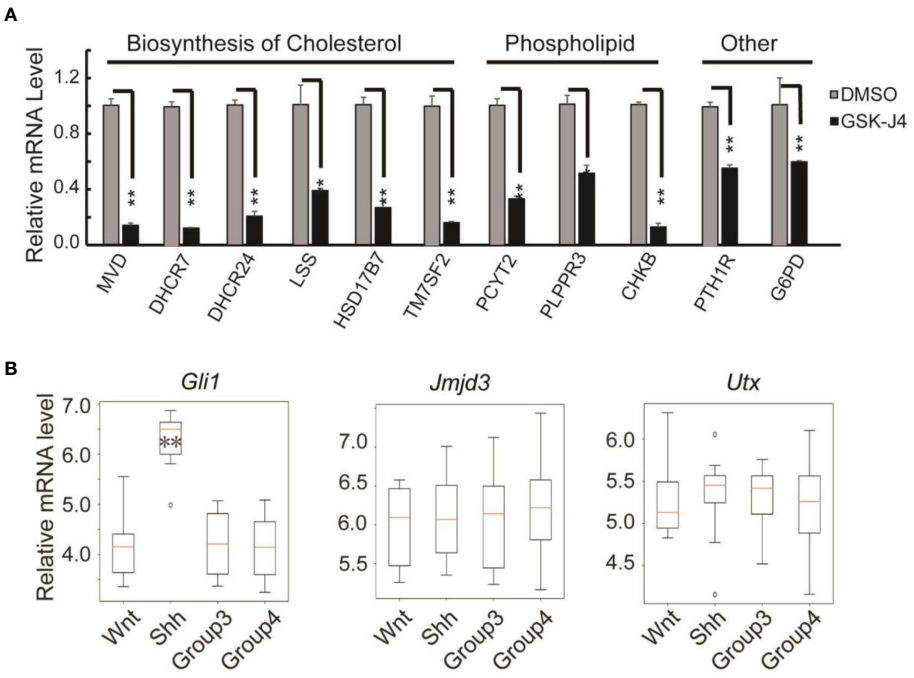

FIGURE 7
Verification of cholesterol and phospholipids biosynthesis gene expression decreases in DaoY cells treated with GSK-J4. **(A)** RT-qPCR verification of the expression of cholesterol and phospholipids biosynthesis genes in DaoY cells treated with GSK-J4. **(B)** Gene expression levels by microarray analysis in four subgroups of human medulloblastoma (GSE37418 (7)). Number of samples in each group, wnt: 8, Shh: 10, Group3: 17, Group4: 41. Significance determined using Student's t-test. $^{**}p < 0.01$, $^{*}p < 0.05$.

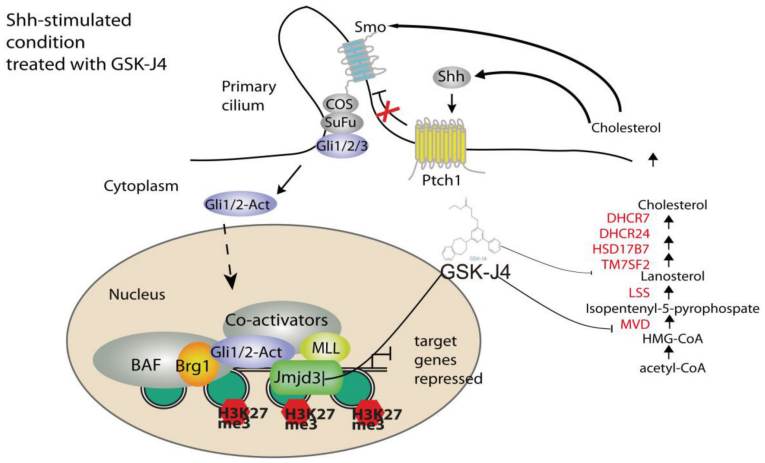

FIGURE 8
A model of Shh signaling regulated by small molecule compound GSK-J4 targeting the epigenetic switch. At basal condition, the processed transcriptional factor Gli3R represses Shh target gene and maintains high level of H3K27me3 on the regulatory region of target genes. In the presence of Shh, Gli3R is replaced with Gli1/2-Act, which recruits the coactivators Brg1 and Jmjd3. Decreases of H3K27me3 turn on the target gene expression. While acetyl-CoA is present, serial enzymes including MVD, DHCR7, and DHCR24, LSS convert acetyl-CoA to form cholesterol. With the treatment of GSK-J4, activity of Jmjd3 is inhibited and H3K27me3 increases, which leads to impaired Shh signaling and cholesterol biosynthesis.

extension (42), which is consistent with our current finding. Besides the essential role in cell physiological activities, cholesterol is a functional modification of the Shh signaling pathway proteins. Both Shh ligand and membrane protein Smoothed are covalently modified by cholesterol (43, 44). Hence, our study suggested GSK-J4 can also regulate Shh signaling by restraining cholesterol metabolism.

GSK-J4 could inhibit the H3K27me3 demethylase activities of both Jmjd3 and Utx. We think the GSK-J4 effects on Shh signaling and medulloblastoma were largely through targeting Jmjd3. The two H3K27me3 demethylases have diverse functions in Shh-type medulloblastoma formation, though they have similar expression levels among different types of medulloblastoma (Figure 7B). Jmjd3 functions as a co-activator for Shh target genes, whereas UTX could inhibit medulloblastoma initiation by promoting tumor differentiation (29). Our study together with others' showed that GSK-J4 is a promising agent for targeted therapy of human medulloblastoma, and other tumors dependent on Shh signaling and cholesterol metabolism (Figure 8). Hence, our study highlights the possibility of using GSK-J4 that targets H3K27me3 demethylase Jmjd3 to treat Shh medulloblastoma patients.

Data availability statement

The datasets presented in this study can be found in online repositories. The names of the repository/repositories and accession number(s) can be found in the article/supplementary material.

Ethics statement

The animal study was reviewed and approved by University of Texas Southwestern Medical Center.

Author contributions

JW and XS designed the experiments. HD, XG, XS, NF, YL and BL performed the experiments, collected the data and analysed the results. XS, SL, and JW wrote the paper. All authors contributed to the article and approved the submitted version.

Funding

This study was supported by Grants for Scientific Research of BSKY (XJ2020039) from Anhui Medical University, the Natural Science Foundation of China (82073124), and Scientific Research Platform and Base Upgrading Plan of Anhui Medical University (2021xkjT048).

Acknowledgments

We appreciate the *Jmjd3*$^{-/-}$ MEF cells from Dr. Akira from Japan.

Conflict of interest

The authors declare that the research was conducted in the absence of any commercial or financial relationships that could be construed as a potential conflict of interest.

Publisher's note

Supplementary material

The Supplementary Material for this article can be found online at: https://www.frontiersin.org/articles/10.3389/fonc.2022.1057147/full#supplementary-material

References

1. Jiang J, Hui CC. Hedgehog signaling in development and cancer. *Dev Cell* (2008) 15(6):801–12. doi: 10.1016/j.devcel.2008.11.010

2. Bai CB, Auerbach W, Lee JS, Stephen D, Joyner AL. Gli2, but not Gli1, is required for initial shh signaling and ectopic activation of the shh pathway. *Development* (2002) 129(20):4753–61. doi: 10.1242/dev.129.20.4753

3. Bai CB, Joyner AL. Gli1 can rescue the *in vivo* function of Gli2. *Development* (2001) 128(24):5161–72. doi: 10.1242/dev.128.24.5161

4. Dahmane N, Ruiz i Altaba A. Sonic hedgehog regulates the growth and patterning of the cerebellum. *Development* (1999) 126(14):3089–100. doi: 10.1242/dev.126.14.3089

5. Wechsler-Reya RJ, Scott MP. Control of neuronal precursor proliferation in the cerebellum by sonic hedgehog. *Neuron* (1999) 22(1):103–14. doi: 10.1016/S0896-6273(00)80682-0

6. Wallace VA. Purkinje-cell-derived sonic hedgehog regulates granule neuron precursor cell proliferation in the developing mouse cerebellum. *Curr Biol* (1999) 9(8):445–8. doi: 10.1016/S0960-9822(99)80195-X

7. Robinson G, Parker M, Kranenburg TA, Lu C, Chen X, Ding L, et al. Novel mutations target distinct subgroups of medulloblastoma. *Nature* (2012) 488(7409):43–8. doi: 10.1038/nature11213

8. Parsons DW, Li M, Zhang X, Jones S, Leary RJ, Lin JC, et al. The genetic landscape of the childhood cancer medulloblastoma. *Science* (2011) 331 (6016):435–9. doi: 10.1126/science.1198056

9. Mao J, Ligon KL, Rakhlin EY, Thayer SP, Bronson RT, Rowitch D, et al. A novel somatic mouse model to survey tumorigenic potential applied to the hedgehog pathway. *Cancer Res* (2006) 66(20):10171–8. doi: 10.1158/0008-5472.CAN-06-0657

10. Shi X, Zhang Z, Zhan X, Cao M, Satoh T, Akira S, et al. An epigenetic switch induced by shh signalling regulates gene activation during development and medulloblastoma growth. *Nat Commun* (2014) 5:5425. doi: 10.1038/ncomms6425

11. Shi X, Wang Q, Gu J, Xuan Z, Wu JI. SMARCA4/Brg1 coordinates genetic and epigenetic networks underlying shh-type medulloblastoma development. *Oncogene* (2016) 35(44):5746–58. doi: 10.1038/onc.2016.108

12. de Bont JM, Packer RJ, Michiels EM, den Boer ML, Pieters R. Biological background of pediatric medulloblastoma and ependymoma: a review from a translational research perspective. *Neuro Oncol* (2008) 10(6):1040–60. doi: 10.1215/15228517-2008-059

13. Pui CH, Gajjar AJ, Kane JR, Qaddoumi IA, Pappo AS. Challenging issues in pediatric oncology. *Nat Rev Clin Oncol* (2011) 8(9):540–9. doi: 10.1038/nrclinonc.2011.95

14. Taylor MD, Northcott PA, Korshunov A, Remke M, Cho YJ, Clifford SC, et al. Molecular subgroups of medulloblastoma: the current consensus. *Acta Neuropathol* (2012) 123(4):465–72. doi: 10.1007/s00401-011-0922-z

15. Northcott PA, Shih DJ, Peacock J, Garzia L, Morrissy AS, Zichner T, et al. Subgroup-specific structural variation across 1,000 medulloblastoma genomes. *Nature* (2012) 488(7409):49–56. doi: 10.1038/nature11327

16. Pugh TJ, Weeraratne SD, Archer TC, Pomeranz Krummel DA, Auclair D, Bochicchio J, et al. Medulloblastoma exome sequencing uncovers subtype-specific somatic mutations. *Nature* (2012) 488(7409):106–10. doi: 10.1038/nature11329

17. Roussel MF, Robinson G. Medulloblastoma: advances and challenges. *F1000 Biol Rep* (2011) 3:5. doi: 10.3410/B3-5

18. Gibson P, Tong Y, Robinson G, Thompson MC, Currle DS, Eden C, et al. Subtypes of medulloblastoma have distinct developmental origins. *Nature* (2010) 468(7327):1095–9. doi: 10.1038/nature09587

19. Schuller U, Heine VM, Mao J, Kho AT, Dillon AK, Han YG, et al. Acquisition of granule neuron precursor identity is a critical determinant of progenitor cell competence to form shh-induced medulloblastoma. *Cancer Cell* (2008) 14(2):123–34. doi: 10.1016/j.ccr.2008.07.005

20. Yang ZJ, Ellis T, Markant SL, Read TA, Kessler JD, Bourboulas M, et al. Medulloblastoma can be initiated by deletion of patched in lineage-restricted progenitors or stem cells. *Cancer Cell* (2008) 14(2):135–45. doi: 10.1016/j.ccr.2008.07.003

21. Kawauchi D, Robinson G, Uziel T, Gibson P, Rehg J, Gao C, et al. A mouse model of the most aggressive subgroup of human medulloblastoma. *Cancer Cell* (2012) 21(2):168–80. doi: 10.1016/j.ccr.2011.12.023

22. Zagozewski J, Shahriary GM, Morrison LC, Saulnier O, Stromecki M, Fresnoza A, et al. An OTX2-PAX3 signaling axis regulates group 3 medulloblastoma cell fate. *Nat Commun* (2020) 11(1). doi: 10.1038/s41467-020-17357-4

23. Vladoiu MC, El-Hamamy I, Donovan LK, Farooq H, Holgado BL, Sundaravadanam Y, et al. Childhood cerebellar tumours mirror conserved fetal transcriptional programs. *Nature* (2019) 572(7767):67–+. doi: 10.1038/s41586-019-1158-7

24. Hendrikse LD, Haldipur P, Saulnier O, Millman J, Sjoboen AH, Erickson AW, et al. Failure of human rhombic lip differentiation underlies medulloblastoma formation. *Nature* (2022) 609(7929):1021. doi: 10.1038/s41586-022-05215-w

25. Smith KS, Bihannic L, Gudenas BL, Haldipur P, Tao R, Gao QS, et al. Unified rhombic lip origins of group 3 and group 4 medulloblastoma. *Nature* (2022) 609(7929):1012–+. doi: 10.1038/s41586-022-05208-9

26. Crawford JR, MacDonald TJ, Packer RJ. Medulloblastoma in childhood: new biological advances. *Lancet Neurol* (2007) 6(12):1073–85. doi: 10.1016/S1474-4422(07)70289-2

27. Huang SY, Yang JY. Targeting the hedgehog pathway in pediatric medulloblastoma. *Cancers (Basel)* (2015) 7(4):2110–23. doi: 10.3390/cancers7040880

28. Yi JQ, Kim B, Shi XM, Zhan XM, Lu QR, Xuan ZY, et al. PRC2 heterogeneity drives tumor growth in medulloblastoma. *Cancer Res* (2022) 82 (16):2874–86. doi: 10.1158/0008-5472.CAN-21-4313

29. Yi JQ, Shi XM, Xuan ZY, Wu J. Histone demethylase UTX/KDM6A enhances tumor immune cell recruitment, promotes differentiation and suppresses medulloblastoma. *Cancer Lett* (2021) 499:188–200. doi: 10.1016/j.canlet.2020.11.031

30. Yi JQ, Wu J. Epigenetic regulation in medulloblastoma. *Mol Cell Neurosci* (2018) 87:65–76. doi: 10.1016/j.mcn.2017.09.003

31. Zhan X, Shi X, Zhang Z, Chen Y, Wu JI. Dual role of brg chromatin remodeling factor in sonic hedgehog signaling during neural development. *Proc Natl Acad Sci U.S.A.* (2011) 108(31):12758–63. doi: 10.1073/pnas.1018510108

32. Kruidenier L, Chung CW, Cheng Z, Liddle J, Che K, Joberty G, et al. A selective jumonji H3K27 demethylase inhibitor modulates the proinflammatory macrophage response. *Nature* (2012) 488(7411):404–8. doi: 10.1038/nature11262

33. Hashizume R, Andor N, Ihara Y, Lerner R, Gan H, Chen X, et al. Pharmacologic inhibition of histone demethylation as a therapy for pediatric brainstem glioma. *Nat Med* (2014) 20(12):1394–6. doi: 10.1038/nm.3716

34. Hong BJ, Park WY, Kim HR, Moon JW, Lee HY, Park JH, et al. Oncogenic KRAS sensitizes lung adenocarcinoma to GSK-J4-Induced metabolic and oxidative stress. *Cancer Res* (2019) 79(22):5849–59. doi: 10.1158/0008-5472.CAN-18-3511

35. Lhuissier E, Aury-Landas J, Allas L, Boittin M, Boumediene K, Bauge C. Antiproliferative effect of the histone demethylase inhibitor GSK-J4 in chondrosarcomas. *IUBMB Life* (2019) 71(11):1711–9. doi: 10.1002/iub.2110

36. Satoh T, Takeuchi O, Vandenbon A, Yasuda K, Tanaka Y, Kumagai Y, et al. The Jmjd3-Irf4 axis regulates M2 macrophage polarization and host responses against helminth infection. *Nat Immunol* (2010) 11(10):936–44. doi: 10.1038/ni.1920

37. Chen JK, Taipale J, Young KE, Maiti T, Beachy PA. Small molecule modulation of smoothened activity. *Proc Natl Acad Sci U.S.A.* (2002) 99 (22):14071–6. doi: 10.1073/pnas.182542899

38. Shi X, Zhan X, Wu J. A positive feedback loop between Gli1 and tyrosine kinase hck amplifies shh signaling activities in medulloblastoma. *Oncogenesis* (2015) 4:e176. doi: 10.1038/oncsis.2015.38

39. Pertea M, Kim D, Pertea GM, Leek JT, Salzberg SL. Transcript-level expression analysis of RNA-seq experiments with HISAT, StringTie and ballgown. *Nat Protoc* (2016) 11(9):1650–67. doi: 10.1038/nprot.2016.095

40. Liao Y, Smyth GK, Shi W. featureCounts: an efficient general purpose program for assigning sequence reads to genomic features. *Bioinformatics* (2014) 30(7):923–30. doi: 10.1093/bioinformatics/btt656

41. Todaro GJ, Green H. Quantitative studies of the growth of mouse embryo cells in culture and their development into established lines. *J Cell Biol* (1963) 17:299–313. doi: 10.1083/jcb.17.2.299

42. Singh P, Saxena R, Srinivas G, Pande G, Chattopadhyay A. Cholesterol biosynthesis and homeostasis in regulation of the cell cycle. *PloS One* (2013) 8(3): e58833. doi: 10.1371/journal.pone.0058833

43. Xiao X, Tang JJ, Peng C, Wang Y, Fu L, Qiu ZP, et al. Cholesterol modification of smoothened is required for hedgehog signaling. *Mol Cell* (2017) 66(1):154–162 e110. doi: 10.1016/j.molcel.2017.02.015

44. Porter JA, Young KE, Beachy PA. Cholesterol modification of hedgehog signaling proteins in animal development. *Science* (1996) 274(5285):255–9. doi: 10.1126/science.274.5285.255

frontiers | Frontiers in Oncology

TYPE Original Research
PUBLISHED 14 December 2022
DOI 10.3389/fonc.2022.1043479

OPEN ACCESS

EDITED BY
Massimo Broggini,
Mario Negri Institute for Pharmacological Research (IRCCS), Italy

REVIEWED BY
Yun Lu,
Huazhong University of Science and Technology, China
Jyotirmoi Aich,
Padmashree Dr. D.Y. Patil University, India

*CORRESPONDENCE
Changhong Shi
changhong@fmmu.edu.cn
Xu Ge
labaniz@fmmu.edu.cn

†The first author

SPECIALTY SECTION
This article was submitted to Cancer Molecular Targets and Therapeutics, a section of the journal Frontiers in Oncology

RECEIVED 13 September 2022
ACCEPTED 28 November 2022
PUBLISHED 14 December 2022

CITATION
Tan D, An J, Gong M, Wang H, Li H, Meng H, Zhang C, Zhao Y, Ge X and Shi C (2022) Screening of an individualized treatment strategy for an advanced gallbladder cancer using patient-derived tumor xenograft and organoid models.
Front. Oncol. 12:1043479.
doi: 10.3389/fonc.2022.1043479

Screening of an individualized treatment strategy for an advanced gallbladder cancer using patient-derived tumor xenograft and organoid models

Dengxu Tan[1,2†], Jiaze An[3†], Miaomiao Gong[4], Huihui Wang[2], Han Li[5], Han Meng[1], Caiqin Zhang[1], Yong Zhao[1], Xu Ge[1*] and Changhong Shi[1*]

[1]Division of Cancer Biology, Laboratory Animal Center, Fourth Military Medical University, Xi'an, Shaanxi, China, [2]Gansu Provincial Laboratory Animal Industry Technology Center, Gansu University of Chinese medicine, Lanzhou, Gansu, China, [3]Department of Hepatobiliary and Pancreaticosplenic Surgery, Xijing Hospital, The Fourth Military Medical University, Xi'an, China, [4]School of Basic Medical Sciences, Medical College of Yan'an University, Yan'an, China, [5]Group 4, School of Basic Medicine, Air Force Military Medical University, Xi'an, Shaanxi, China

Gallbladder cancer is a highly aggressive malignancy with poor sensitivity to postoperative radiotherapy or chemotherapy; therefore, the development of individualized treatment strategies is paramount to improve patient outcomes. Both patient-derived tumor xenograft (PDX) and patient-derived tumor organoid (PDO) models derived from surgical specimens can better preserve the biological characteristics and heterogeneity of individual original tumors, display a unique advantage for individualized therapy and predicting clinical outcomes. In this study, PDX and PDO models of advanced gallbladder cancer were established, and the consistency of biological characteristics between them and primary patient samples was confirmed using pathological analysis and RNA-sequencing. Additionally, we tested the efficacy of chemotherapeutic drugs, targeted drugs, and immune checkpoint inhibitors using these two models. The results demonstrated that gemcitabine combined with cisplatin induced significant therapeutic effects. Furthermore, treatment with immune checkpoint inhibitors elicited promising responses in both the humanized mice and PDO immune models. Based on these results, gemcitabine combined with cisplatin was used for basic treatment, and immune checkpoint inhibitors were applied as a complementary intervention for gallbladder cancer. The patient responded well to treatment and exhibited a clearance of tumor foci. Our findings indicate that the combined use of PDO and PDX models can guide the clinical treatment course for gallbladder cancer patients to achieve individualized and effective treatment.

KEYWORDS

gallbladder cancer, patient-derived tumor xenograft model, patient-derived tumor organoid model, individualized therapy, immune checkpoint inhibitors

Introduction

Gallbladder cancer is a highly aggressive biliary malignancy (1). The early symptoms of gallbladder cancer are not obvious, and thus, most patients have progressed to an advanced stage by the time of diagnosis (2, 3). Radical surgical resection of the gallbladder and regional lymph node dissection are currently the best treatments for gallbladder cancer (1); however, the recurrence rate after radical surgery remains high and is often accompanied by local or distant metastases (4). Furthermore, patients have a low response rate to postoperative chemotherapy (5). Thus, individualized therapeutic drug screening for patients with gallbladder cancer after surgery is particularly important.

Patient-derived tumor xenograft (PDX) and patient-derived tumor organoid (PDO) models serve as the best *in vivo* and *in vitro* models, respectively, for predicting clinical outcomes. Both models mimic the biological properties of the original patient tumor (PT) and maintain tumor heterogeneity (6). There is growing evidence that PDX (7–9) and PDO (10–13) models can accurately predict patient responses to anti-cancer treatment.

Currently, chemotherapy, targeted therapy, and immunotherapy are the most common drug treatments for cancer. Chemotherapeutic drugs, which suppress tumors by rapidly killing dividing cells, remain one of the main strategies for treating tumors, and our understanding of cancer pathogenesis, targeted drugs (14, 15), and immunotherapeutic drugs (16) are being developed by scientists. Targeted drugs inhibit molecular pathways that are critical for tumor growth and maintenance (17), while immunotherapy suppresses tumors by stimulating host immune responses (18). In this study, we established PDX and PDO models from a patient with advanced gallbladder cancer and conducted a multifaceted drug sensitivity trial that included chemotherapeutic agents, targeted drugs, and immune checkpoint inhibitors. The aim of this study was to guide the clinical treatment strategy for the patient by testing treatment options on the patient-derived models, with the goal of achieving individualized and effective treatment.

Materials and methods

Pre-operative diagnosis

Thickening, mild progressive magnetic resonance imaging (MRI) signal enhancement, and diffusion-weighted imaging hyperintensity were observed in the base and body wall of the gallbladder in one patient with gallbladder cancer. A patchy, slightly long T2 signal shadow was seen in the adjacent liver parenchyma, with mildly progressive enhancement on the enhancement scan. Slightly low signal was detected in the hepatobiliary specific phase, while high signal was detected *via* diffusion-weighted imaging, and a striped, slightly low-density shadow was observed in the adjacent right anterior lobe of the liver envelope. We observed several nodular soft tissue shadows in the upper abdomen and subperitoneum with a diameter of about 1.0 cm, high signal *via* diffusion-weighted imaging, and enlarged lymph nodes on the right side of the rectal mesentery. Pathological findings included a moderately differentiated adenocarcinoma of the gallbladder with focal findings of nerve invasion, infiltration of the entire wall of the gallbladder through to the adipose tissue with an infiltration depth of 11 mm, and tumor involvement of the liver. Cancer cells were observed in the fibrous adipose tissue of the greater omentum, and cancerous nodules were detected in the adipose tissue adjacent to the lymph nodes (pathological stage: AJCC pT3N0).

Clinical samples

Clinical tumor samples of advanced gallbladder cancer (F210708) and human peripheral blood mononuclear cells (PBMCs) were obtained from one patient admitted to the Xijing Hospital of the Fourth Military Medical University. Informed consent was obtained from the patient, and the study was approved by the Ethics Committee of Xijing Hospital (KY20203128-1). Tumor tissue samples were used to establish PDO and PDX models, as well as for histological analysis and transcriptome sequencing.

Laboratory animals

The animal experiments in this study were approved by the Laboratory Animals Welfare Ethics Committee of the Fourth Military Medical University (IACUC-20220259). Female NOD-*Prkdc*^{em26Cd52}*Il2rg*^{em26Cd22}/Gpt (NCG) mice (6–7 weeks old) were purchased from GemPharmatech LLC (China) and housed in the Specific Pathogen Free facility of the Laboratory Animal Center of the Air Force Medical University.

PDO model establishment and drug screening

Patient tumor samples were excluded from necrotic areas and washed twice with phosphate-buffered saline (PBS) and were minced using a human tumor dissociation kit (Miltenyi Biotec, Germany). Single cells were dissociated using a Gentle MACS Octo Dissociator (Miltenyi Biotec) according to the manufacturer's instructions. The dissociated tissues were washed with PBS, and the suspension was filtered through a 100 µm cell filter and centrifuged at 300 × *g* for 5 min. The supernatant was discarded and the precipitated cells were collected and resuspended in an appropriate amount of matrigel (356231, Corning, USA). Subsequently, 50 µl droplets were placed in 6-well plates, and organoid culture medium was

added to cover the droplets for incubation at 37°C under 5% CO_2. The organoid culture medium consisted of Advanced DMEM/F12 medium, 250 ng/ml Rspo-1, 100 ng/ml Wnt3a, 10 mM Y27632, 1:100 N2 supplement, 3 nM dexamethasone, 1.25 mM N-acetyl-l-cysteine, 100 ng/ml Noggin, 50 ng/ml EGF, 100 ng/ml FGF10, 10 nM gastrin, 1:50 B27 supplement, 10 mM nicotinamide, 5 µM A8301, 10 µM forskolin, 5 µg/ml prostaglandin E2, 1:500 Primocin, 1% penicillin/streptomycin, 1% Glutamax, and 1% HEPES.

The organoid cells were plated at 5×10^3 cells/well, and the culture medium was discarded 24 h after cell treatment. Each drug was diluted in organoid culture medium at different dilution ratios (Table S1) and applied to the PDO culture. The CellTiter-Glo 3D kit (Promega, USA) was used to detect cell viability. Maximal doses were capped at peak plasma concentrations reported earlier in patients (19).

Establishment of a PDO/immune cell co-culture model for drug screening

Human PBMCs were mixed with organoid cells in a 10:1 potent target ratio, resuspended in 40% matrigel, and mixed for 48 h in accordance with the density of organoid cells (5×10^3 cells/well) for plate culture. The original medium was discarded and replaced with fresh medium containing nivolumab (Table S1). After 72 h, the status of the PDOs was observed microscopically, and organoid activity was detected using the CellTiter-Glo 3D kit after removal of co-cultured PBMCs using the Human Lymphocyte Isolate kit (**TBD Science, China**).

PDX model establishment and drug screening

Patient-derived tumor samples were removed from necrotic sites and washed twice with PBS. The specimens were minced and transplanted subcutaneously on the backs of NCG mice. When the tumors (P0) grew to approximately 500 mm^3, tumor tissue was isolated under aseptic conditions and transplanted to the dorsal subcutis of new NCG mice (P1; n=30). When the P1 tumors reached 100–150 mm^3, the animals were randomly divided into six groups with five animals each. Animals were treated with single or combined drugs (see Table S2 for treatments and doses). Tumor volumes and animal body weight were measured every 3 days, and serum samples were collected at the end of the treatment period to measure CA19-9 levels by ELISA. When the P2 (n=10) generation tumors grew to approximately 500 mm^3, the most sensitive drug was administered to observe the inhibitory effect on larger tumors. After 3 weeks of treatment with the drug, treatment was discontinued for 100 days to observe the resulting changes in the tumor.

Establishment of a PDX model of the human immune system for drug screening

P0 generation tumors were transplanted subcutaneously into NCG mice, and 1×10^7 PBMCs were injected into the tail vein 20 days later. After 14 days, PBMCs were isolated from blood collected *via* the tail vein. Human $CD45^+$ cells were detected using flow cytometry; the mice (n=10) containing 5-10% human CD45+ cells were included in the study and randomly divided into two groups, and drugs were administered according to the schedule in Table S2. Tumor volume was measured three times a week. At the end of the experiment, tumors were collected for immunofluorescence staining of tumor-infiltrating human $CD45^+$ and $CD8^+$ cells. Additionally, PBMCs were isolated from the blood, and human $CD45^+$ and $CD8^+$ cells were detected using flow cytometry.

Flow cytometric examination

Whole blood was collected from PDX mice that received the human PBMC transplant. The cells were separated using a human lymphocyte isolation solution and processed for split red blood cells. The cells were incubated with $CD45^+$ (304006; BioLegend) and $CD8^+$ (12-0088-42; Invitrogen) antibodies according to the manufacturer's instructions, and flow cytometry (Attune NxT; Thermo Fisher) analysis was performed.

Staining and histopathology

Tumor tissues and organoids were fixed in 4% paraformaldehyde (Servicebio, China) at room temperature for 24 h. Paraffin-embedded samples were cut into 5-µm sections and used for hematoxylin & eosin, immunohistology, and immunofluorescence staining. The samples were stained using antibodies specific for HER2 (2165S, Cell signaling, 1:400), CA19-9 (ab398, Abcam, 1:100), CEA (ab133633, Abcam, 1:3000), EGFR (ab32198, Abcam, 1:100), Ki67 (27309-1-AP, Proteintech, 1:2000), and PD-L1 (ab205921, Abcam, 1:500) for immunohistology staining, and with antibodies against CD45 (13917S, Cell signaling, 1:200) and CD8 (66868-1-Ig, Proteintech, 1:200) for immunofluorescence staining.

Serum CA19-9 assay

Blood was collected from the mice at the end of the experiment, and serum was separated and sent to the Laboratory Department of Xijing Hospital for CA19-9 testing by ELISA.

RNA transcriptome sequencing

Total RNA was extracted using an RNA extraction kit (Tiangen, China). A strand-specific library was constructed by NovelBIo (Shanghai, China), enriched and purified, and reverse-transcribed into cDNA. The cDNA libraries were quantified and validated after end-repair, purification, and enrichment, and then sequenced and analyzed.

Statistical analysis

Statistical analysis was performed using SPSS version 18.0. Differences between two groups were analyzed using two-tailed unpaired t-tests. Differences between three or more conditions with one independent variable were analyzed using one-way analysis of variance (ANOVA); P values are reported as *<0.05, **<0.01, and ***<0.001. Image J software was used for immunofluorescence results, and the mean gray value was determined.

Results

Establishment of PDX and PDO models from patient gallbladder cancer tissue

Both the PDX and PDO models derived from a patient with gallbladder cancer were successfully established. The histological features of both the PDX-derived tumor tissues and the PDO were identical to those of the original PT (Figure 1A). Using RNA-sequencing, we detected a high correlation between the transcriptomes of tissue samples from the PDX or PDO models and primary PT samples (PDX vs. PT = 0.98; PDO vs. PT = 0.93), indicating that the models were transcriptionally representative of the original tumor (Figure 1B). To further confirm that tumor-associated hotspot genes from the PT were consistently expressed in the PDX and PDO models, the expression levels of genes representing several different signaling pathways were assessed. As shown in the heatmap in Figure 1C, the PDX, PDO, and PT samples all exhibited very similar expression patterns of genes in the p53 signaling pathway, mitogen-activated protein kinase (MAPK)-phosphatidylinositol-3-kinase (PI3K)-protein kinase B (AKT)-mammalian target of rapamycin (mTOR) signaling pathway, TNF signaling pathway, oxidative phosphorylation pathway, Notch signaling pathway, Ras pathway, and ErbB pathway. Next, we examined the expression levels of gallbladder cancer-related markers (ERBB2, CA19-9, CEA, EGFR, Ki67, PD-L1) using immunohistochemistry; all markers were detected in the PDX, PDO, and PT samples with the exception of PD-L1, which is a negative prognosticator for gallbladder cancer (Figure 1D). These data demonstrate that the PDX and PDO models maintained the histopathological, transcriptomic, and protein expression characteristics of the primary gallbladder tumor.

Drug screening using the PDO model

Next, we used our established PDO model to screen various drugs for the treatment of gallbladder cancer. Based on clinicians' recommendations, we selected four chemotherapeutic agents (gemcitabine [GEM], cisplatin [CIS], capecitabine [CAP], irinotecan [CPT-11]) and one targeted agent (trastuzumab [HER]) for single-agent treatment. We also performed multi-agent treatments using the following drug combinations: GEM +CIS, GEM+CAP, or CAP+HER. Importantly, because the organoids lacked the relevant enzymes to catalyze CAP to 5-fluorouracil (5-FU) *in vivo* (20), CAP was replaced with 5-FU in our PDO drug screen. After treatment with a high concentration of GEM, the PDO appeared necrotic and disintegrated; conversely, the PDO remained intact and exhibited good cellular activity after treatment with high concentrations of the other drugs (Figure 2A). Consistent with our microscopic results, quantification of organoid activity using the CellTiter-Glo 3D kit indicated that GEM treatment achieved stronger tumor suppression than the treatment using other test drugs (P<0.001, Figure 2B). Furthermore, both combination treatments involving GEM elicited stronger tumor-killing effects than GEM treatment alone, and combining higher doses of 5-FU with HER also resulted in better tumor suppression than each individual drug (Figure 2C); organoid activity levels were consistent with these results Furthermore, we assayed the organoid activity using the CellTiter-Glo 3D kit after treatment with the drug combinations, and the results were the same as those observed by microscopy (Figure 2D). There was no statistical difference between the GEM +CIS and GEM+5-FU groups (P>0.05), and both were significantly different compared to the 5-FU+HER group (P<0.05). Next, we quantified the area under the curve for all drug treatment outcomes, which can be used to assess drug responses in PDO models (12). Consistent with previous results, GEM+CIS or GEM+5-FU treatment resulted in the best tumor suppression (Figure 2E). We predict that these findings can be used to guide the clinical treatment strategy for patients.

Sensitivity of immune checkpoint inhibitors in PDO/PBMC co-cultures

To investigate the efficacy of immune checkpoint inhibitors in our PDO model, we co-cultured a PDO with PBMCs. We

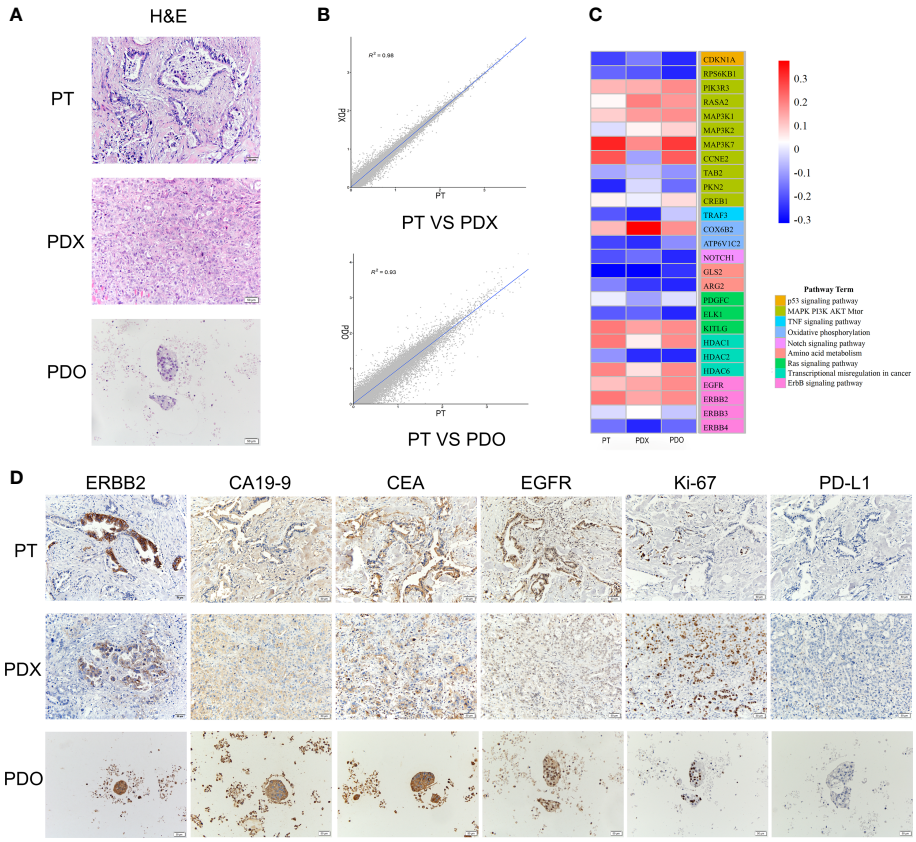

FIGURE 1
(A) H&E staining of the PT, PDO, and PDX samples. Scale bars, 50 μm. **(B)** Transcriptomic correlation analysis of the RNA transcriptome expression between the PDX and PT samples and between the PDO and PT samples. A total of 60,665 genes were analyzed. **(C)** A heatmap of representative genes in tumor-associated signaling pathways. RNA expression levels are indicated along a red and blue scale for high and low expression levels, respectively. **(D)** The expression of tumor markers detected using immunohistochemistry in PT, PDX, and PDO samples. Scale bar, 50 μm. H&E, hematoxylin & eosin staining; PDO, patient-derived tumor organoid; PDX, patient-derived tumor xenograft; PT, patient tumor.

observed that immune cells underwent fusion with the PDO, and a large number of PBMCs infiltrated the organoid (Figure 3A). We selected nivolumab for immunotherapy and diluted the drug according to the chart in Table S1. The addition of nivolumab to the co-culture resulted in PDO death (Figure 3B); notably, no significant tumor suppressive effect was observed after PDO treatment with nivolumab in the absence of PBMCs. Organoid activity was greatly reduced after treatment with high concentrations of nivolumab ($P<0.001$; Figure 3C). Quantification of the area under the curve indicated that nivolumab did not have a particularly prominent tumor suppressive effect on the PDO in co-culture (Figure 3D); however, our analysis of organoid tumor activity in co-culture indicated a highly significant reduction in PDO cell viability ($P<0.001$) after treatment with a high concentration of nivolumab compared to that in the control (Figure 3E). Thus, from these data we conclude that nivolumab had a strong tumor suppressive effect on organoids co-cultured with immune cells.

Drug screening using the PDX model

Tumor tissue from the PDX model was transplanted subcutaneously into the backs of 30 NCG mice (P1 generation tumors), and when the tumors had grown to approximately 100–150 mm^3, the animals were randomly divided into six treatment groups for drug screening: control, CPT-11, CAP, GEM+CIS, CAP+HER, and GEM+CAP (Table S2). Significant tumor suppression was observed in the GEM+CIS and GEM +CAP groups ($P<0.001$ for both groups compared to that in the control; Figure 4A). The CAP+HER group was significantly different compared to the control group ($P<0.05$). The two

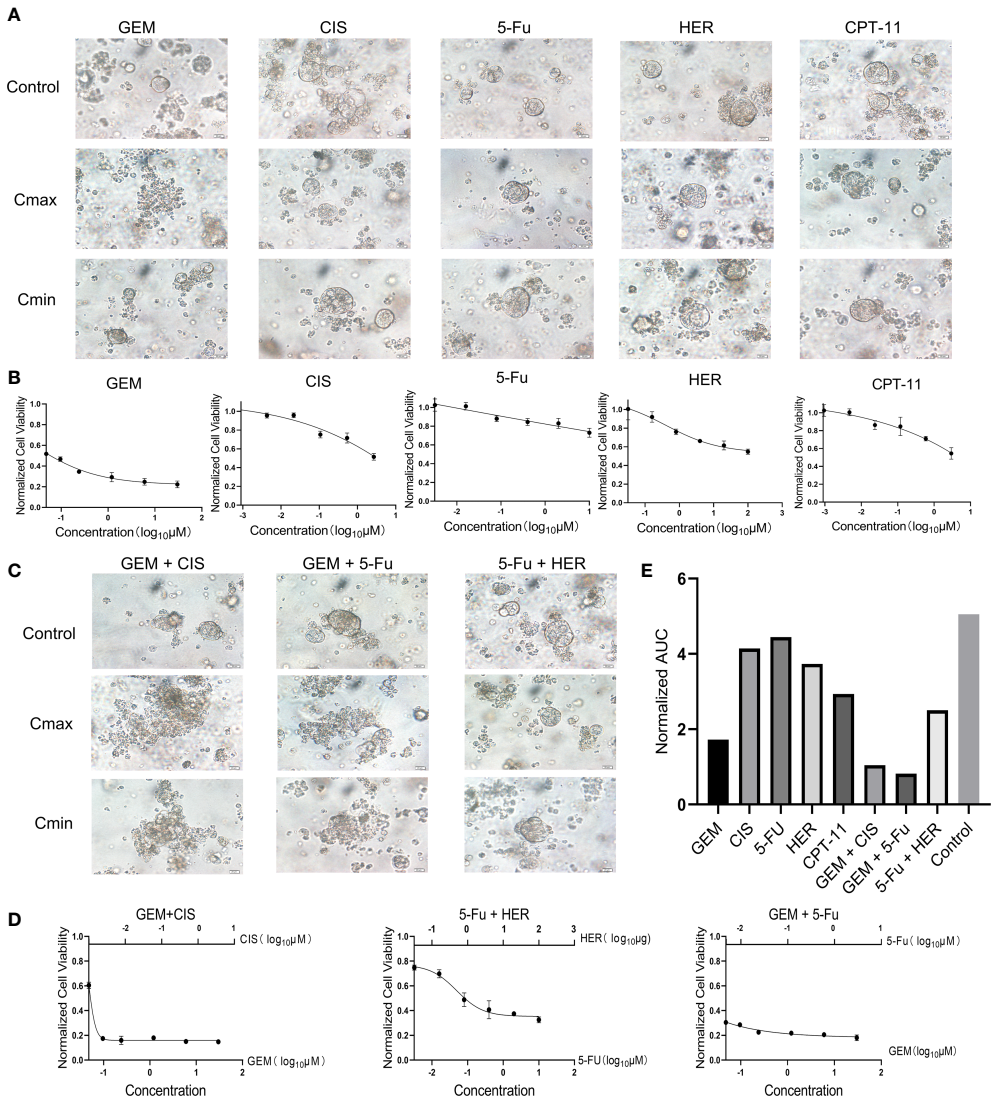

FIGURE 2
(A) Bright-field microscopy images of PDOs showing the results of treatment with five drugs (GEM, CIS, 5-Fu, HER, CPT-11), including controls and maximum (Cmax) and minimum concentration (Cmin). Scale bar, 20 μm. **(B)** Cell viability of PDOs after 24 h of treatment with different concentrations of each drug. **(C)** Bright-field microscopy images of PDOs showing the results of treatment with three combinations of drugs (GEM+CIS, GEM+5-Fu, 5-Fu+HER) including controls and maximum (Cmax) and minimum concentrations (Cmin). Scale bar, 20 μm. **(D)** Cell viability of PDOs after 24 h of treatment with different concentrations of combination drug treatments. **(E)** Area under the PDO cell viability curve for single and combination drug treatment. CAP, Capecitabine; CIS, Cisplatin; GEM, Gemcitabine; Cmax, maximum concentration; Cmin, minimum concentration; CPT-11, Irinotecan; HER, Trastuzumab; 5-Fu, Fluorouracil.

single-agent treatments, CAP and CPT-11, were not significantly different than the control (P>0.05). Overall, these results are consistent with the results of our PDO drug screening. For all treatments, the weight of the mice remained stable (Figure 4D), indicating that the administered doses were within safe limits and that tumor regression was not due to general drug toxicity. At the end of the experiment, we collected the tumors and found that the change in tumor weight was consistent with the change in tumor volume (Figures 4B, C). Given the high expression of CA19-9 in the serum of patients with gallbladder cancer (Figure S1B) and in tumors (Figure S1C), we assessed CA19-9 levels in the serum of the mice and found that CA19-9 expression levels reflected the degree of tumor suppression, suggesting that CA19-9 expression may be indicative of tumor treatment efficacy in the PDX model (Figure 4E). Histopathological analysis revealed that almost no tumor cells remained in the GEM+CIS group, indicating high efficacy of the combination of GEM and CIS in tumor treatment (Figure S1A). In order to explore the

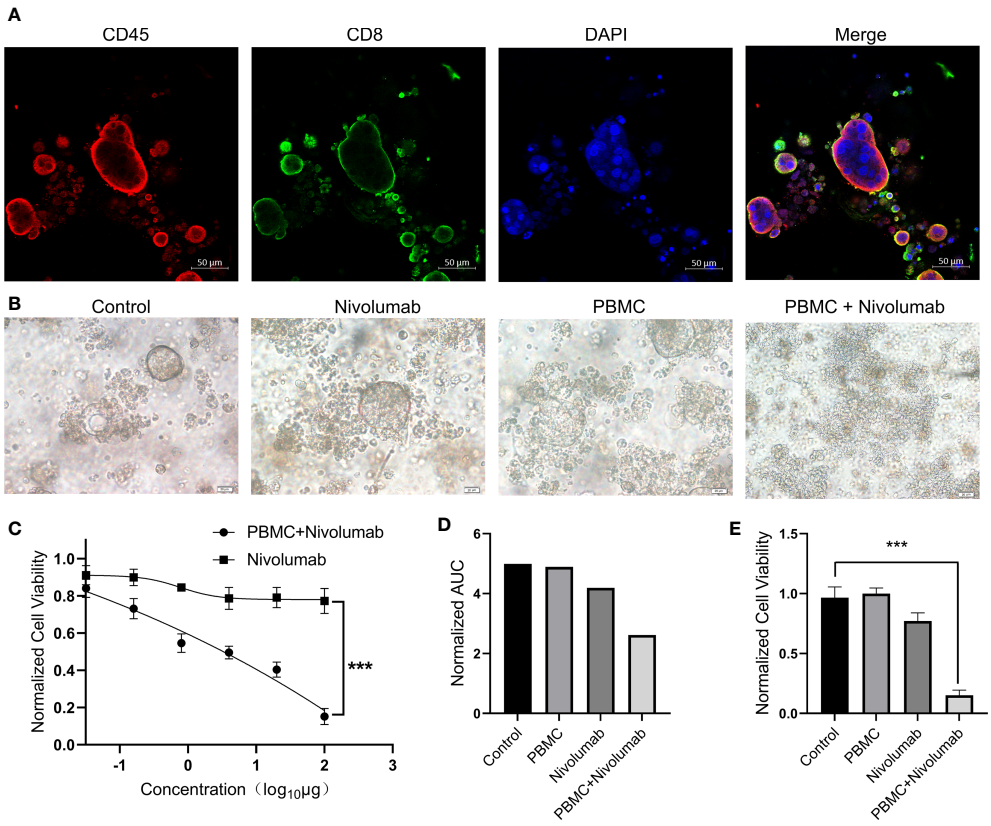

FIGURE 3
(A) PBMCs and PDOs were co-cultured for 48 **(h)** Immunofluorescence staining was performed for $CD45^+$ cells (red), $CD8^+$ cells (green), and DAPI (blue). Scale bars, 50 μm. **(B)** Bright-field microscopy images of PDOs showing the results of treatment with nivolumab. Results are shown for the control, nivolumab treatment alone, PBMC co-culture alone, and nivolumab treatment after co-culture groups. Scale bars, 20 μm. **(C)** PDO cell viability after 72 h of treatment with nivolumab. **(D)** Area under the PDO cell viability curve for each treatment group. **(E)** Cell viability in each group following nivolumab treatment at high concentrations. PDO, patient-derived tumor organoid; PMBC, peripheral blood mononuclear cell.

inhibitory effect of GEM+CIS treatment on large tumors and the growth of tumors after discontinuation of treatment, we transplanted P1 tumors subcutaneously on the backs of NCG mice (P2 generation). When the tumors grew to approximately 500 mm^3, we randomly divided the mice (n=12) into two groups. GEM+CIS treatment was discontinued after 3 weeks of treatment, and dynamic monitoring was performed for up to 100 days. The tumor volume decreased rapidly after treatment, and the tumor did not recur after discontinuation (Figure 4F). Overall, the trends observed in the PDX model were consistent with those in the PDO model. CA19-9 expression varied with tumor volume, indicating that CA19-9 expression may be indicative of the patient's treatment response. These results demonstrate that GEM+CIS treatment results in long-lasting suppression of large tumors and predict that patients may have a good prognosis after the discontinuation of GEM +CIS treatment.

Drug screening in humanized immuno-oncology models

To further validate the tumor suppressive effect of the immune checkpoint inhibitor nivolumab *in vivo*, we injected human PBMCs (1×10^7) into NCG mice with P1 tumors to establish a humanized immuno-oncology model (Figure 5A). Due to differences in the level of immune reconstitution, we included mice in which 5–10% of PBMCs comprised human $CD45^+$ T cells (n=10), as determined using flow cytometry, and randomly divided them into two groups for nivolumab

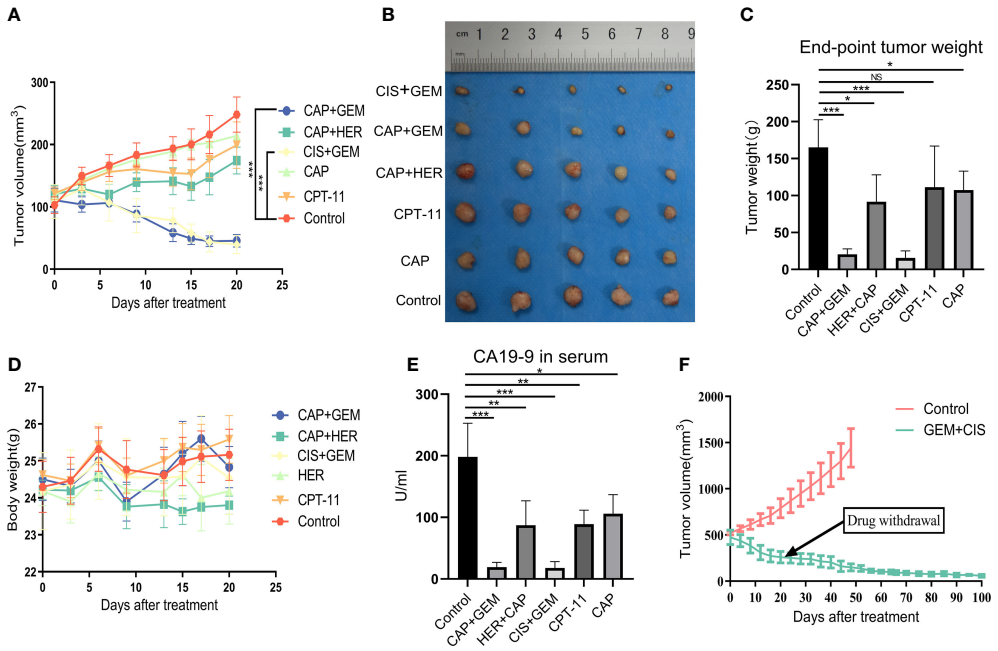

FIGURE 4
(A) Changes in tumor volume in each group. **(B)** Photographs of tumors in each group at the treatment endpoint. **(C)** Tumor weight in each group at the treatment endpoint. **(D)** Changes in mouse body weight in each group during treatment. **(E)** Serum CA19-9 levels in each group of mice at the treatment endpoint. **(F)** Long-term effects after the treatment of larger tumors and discontinuation of treatment. CAP, capecitabine; CIS, cisplatin; GEM, gemcitabine; CPT-11, irinotecan; HER, trastuzumab.

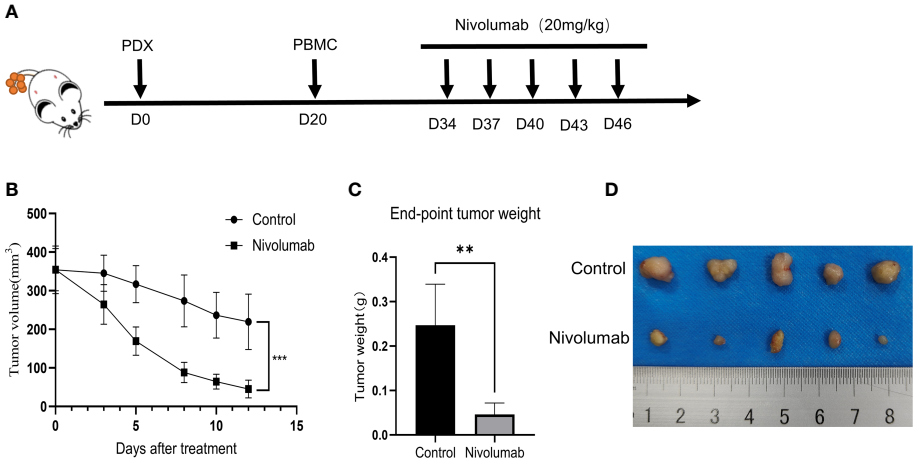

FIGURE 5
(A) Preparation of humanized tumor and immune system mice and drug delivery. **(B)** Change in tumor volume during treatment. **(C)** Tumor weight at the treatment endpoint. **(D)** Photographs of tumors at the end of the treatment.

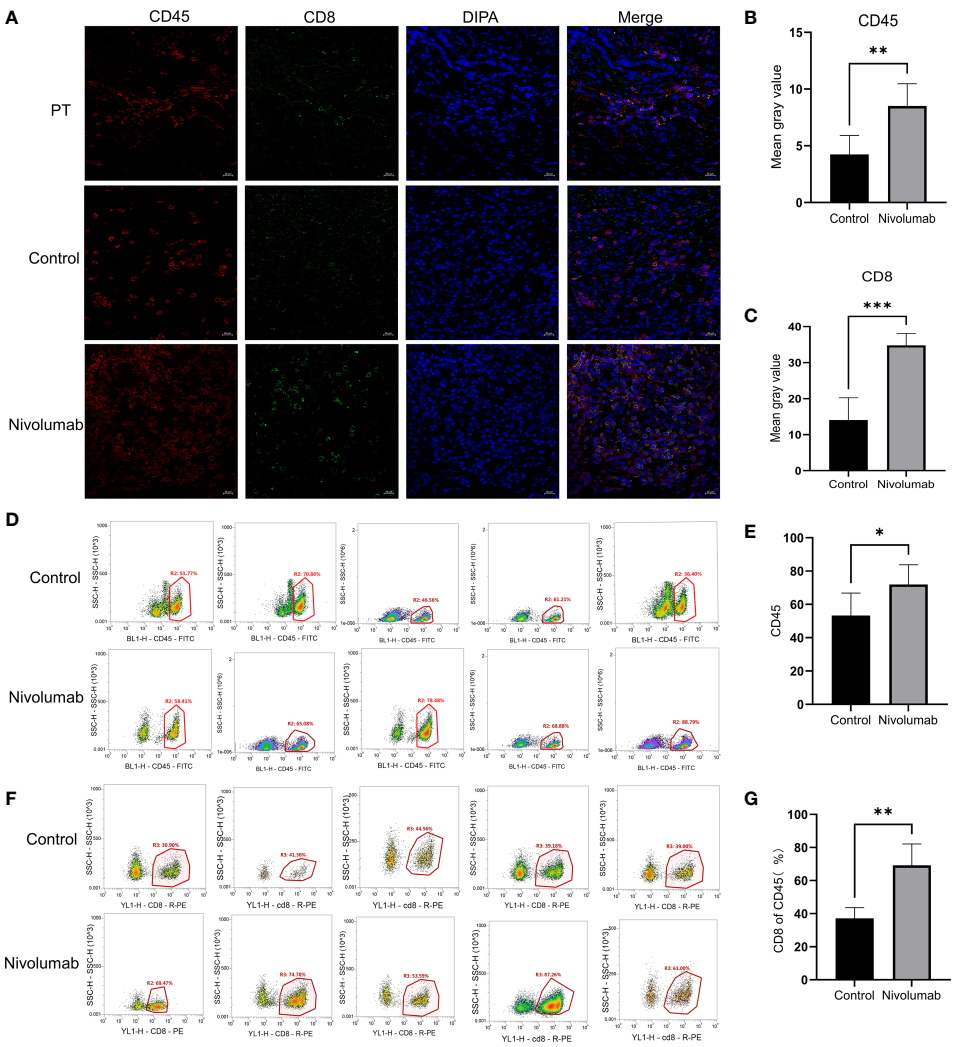

FIGURE 6
(A) Immunofluorescence staining of tumor sections from the PT, control, and nivolumab groups was performed for $CD45^+$ cells (red), $CD8^+$ cells (green), and DAPI (blue). Scale bars, 20 μm. **(B)** Quantification of $CD45^+$ immunofluorescence grayscale values in the control and nivolumab groups. **(C)** Quantification of $CD8^+$ immunofluorescence grayscale values in the control and nivolumab groups. **(D)** The proportion of $CD45^+$ cells in PBMCs from the blood of mice in the control and nivolumab groups detected using flow cytometry. **(E)** Statistical results of the proportion of $CD45^+$ cells. **(F)** Detection of the $CD8^+$ ratio in $CD45^+$ cells in the control and nivolumab groups using flow cytometry. **(G)** Statistics on $CD8^+$ ratio in $CD45^+$ cells. PT, patient tumor.

treatment (control and nivolumab groups). Two weeks after treatment was terminated, the tumor volume and weight in the nivolumab group were significantly less than those in the control group ($P< 0.001$ and $P<0.01$, respectively). Imaging analysis also revealed significant differences between the two groups (Figures 5B–D). Immunofluorescence analysis showed that the ratio of $CD45^+$ to PBMC and $CD8^+$ T cells to $CD45^+$ was significantly higher in the nivolumab-treated group than in the control group ($P<0.001$ and $P<0.01$, respectively; Figures 6A–C), which further demonstrates the efficacy of immunotherapy. Meanwhile, higher proportions of $CD45^+$ ($P<0.05$; Figures 6D, E) and $CD8^+$ ($P<0.01$; Figures 6F, G) cells were detected in the PBMCs of mice after nivolumab treatment. These results suggest that nivolumab treatment causes immune cell death in tumors after immune reconstitution by mimicking PD-1 expression and promoting effector T cell differentiation.

Guiding individualized clinical treatment strategies

Based on the PDO and PDX models, we found that GEM+CIS, GEM+CAP, and nivolumab treatments all achieved desired therapeutic outcomes, providing guidance for the treatment of

the patient. The patient was administered GEM combined with CIS as the base treatment and the immune checkpoint inhibitor nivolumab as a complementary intervention. One year after surgery, CA19-9 returned to healthy levels (Figure S1B). MRI results showed a reduction of fluid in the gallbladder area and a reduction in the size of the retroperitoneal and larger lymph nodes by approximately 0.5 cm. The patient's overall condition improved, and the prognosis was good.

Discussion

Gallbladder cancer is the most common biliary tract tumor (21), but is commonly diagnosed at advanced stages due to the lack of obvious disease symptoms and specific markers (22). Adjuvant therapy after cholecystectomy is not routine, as most regimens have a low response rate (23); therefore, individualized therapeutic drug screening for gallbladder cancer patients after surgery is especially important. Both the PDX and the PDO models preserve the biological characteristics and heterogeneity of the original tumor and display unique advantages for individualized therapy and predicting clinical outcomes (24, 25). Unfortunately, it often takes a long time to establish a PDX model (26), and patients with a rapidly progressive disease rarely benefit from this model. While establishing a PDO model requires less time, these models cannot be used to test all drugs because they lack functional vascular, metabolic, and nervous systems (27, 28). In this study, we adopted a strategy to use PDX and PDO models together, specifically the PDO model for initial rapid drug screening and the PDX model for *in vivo* drug efficacy validation, making these two models complementary.

Both the PDX and the PDO models were used to evaluate the treatment efficacy of chemotherapeutic agents, targeted agents, and immune checkpoint inhibitors. Ultimately, we found that GEM combined with CIS exhibited the best tumor suppressive effect, while immune checkpoint inhibitors also achieved good tumor suppression. Notably, chemotherapy can stimulate anti-cancer immunity and enhance the effect of immunotherapy by stimulating cancer cells to release immunostimulatory factors or by mediating off-target effects on immune cell populations (29). We continuously observed the growth and recurrence of tumors after 3 weeks of treatment with GEM+CIS. Even 79 days after the discontinuation of GEM+CIS treatment, we did not observe tumor recurrence; these data predicted that the patient may have a good prognosis after the discontinuation of GEM+CIS treatment. Therefore, we recommended the patient for GEM+CIS-based therapy with the immune checkpoint inhibitor nivolumab as a complementary intervention, which resulted in an improvement in the patient's condition. Because drug screening for the patients with tumor has time limit requirements, drug screening for too long will miss the best period of treatment, so we relied on clinicians' suggestions of the candidate drugs to test. These suggestions were made based on patient-specific pathology; for instance, the patient had an ERBB2 mutation, so the ERBB2-targeting drug HER was selected. It is possible that other targeted drugs may elicit tumor suppressive effects as well.

In the process of tumor drug screening, both chemotherapeutic drugs and targeted drugs act directly on PDO models (30); therefore, the choice of drug concentration is crucial. Blindly using the IC_{50} or higher drug concentrations will likely produce clinically irrelevant results. In designing our PDO drug test, we referred to the recommendations of the drug instructions and The peak concentration in the pharmacokinetics is set as the highest concentration for our drug test (19); in this way, we were able to align our drug test results with the actual needs of the patient.

CAP, a fluoropyrimidine carbamate, is widely absorbed. CAP is converted to 5-FU *via* a multiorgan, three-step enzymatic pathway, and malignant tissues have higher concentrations of thymidine phosphorylase, which is involved in drug conversion, so 5-FU increases enrichment at tumor sites, and CAP exhibits better tumor suppressive activity in multiple PDX models (20). However, because of the lack of an effective metabolic pathway in the PDO model, we switched from CAP to 5-FU for drug testing, which exemplifies a drawback in the PDO drug screening procedure.

Tumor immunotherapy is a novel therapeutic strategy that has shown good therapeutic efficacy in many individual patients. PD-L1 expression is an initial screening marker for tumor patients receiving immunotherapy. However, some reports have demonstrated that the expression of PD-L1 is not fully indicative of the effect of immunotherapy (31, 32). Indeed, some patients with low expression of PD-L1 still achieve good therapeutic results following PD-L1 antibody treatment. Therefore, although PD-L1 was absent in the gallbladder carcinoma tumor in this study, we included PD-L1 targeted drugs in our drug screen as an alternative treatment scheme, which achieved good therapeutic results.

Humanized immuno-oncology models recapitulate a partially functional humanized immune system and are the best preclinical immunotherapy models currently available, as they allow for the prediction of patient responses to immunotherapy (33–35). Mice with a partially functional humanized immune system constructed using PBMCs can rapidly produce human T cells and thus have been widely used in tumor immunotherapy research. A number of $CD45^+$ and $CD8^+$ T cells were detected in the tumor tissues of the patient, indicating immune cell infiltration into the tumor; this provided rationale for immunotherapy (36, 37). In our humanized immuno-oncology model, we observed a reduction in tumor size concurrent with increasing levels of immune reconstitution in the absence of drug intervention. This may be due to the strong antigenic properties of PDX grafts and the killing effect of mature T cells in the PDX model. However, after treatment with nivolumab, the tumor volume decreased rapidly, demonstrating the inhibitory activity of nivolumab on this tumor. Similarly, the results of immune cell analysis confirmed that levels of both $CD45^+$ and $CD8^+$ T cells were significantly higher after nivolumab intervention. Consistent with the data from previous studies

(31, 32), these results provide further evidence that PD-L1 expression is not a direct indicator of the tumor suppressive activity of immune checkpoint inhibitors, as nivolumab sharply suppressed tumor activity despite the absence of PD-L1 in the tumor.

In conclusion, both PDX and PDO models derived from one patient with advanced gallbladder cancer were successfully established. Treatment with GEM combined with CIS had significant therapeutic effects on both models, and immune checkpoint inhibitors responded well in the PDO/immune model and humanized mice. This strategy for drug selection ultimately displayed a good curative effect on the patient. Our findings indicate that the combination of PDO and PDX models can guide the clinical treatment strategy for cancer patients to achieve effective individualized treatments.

Data availability statement

The original contributions presented in the study are included in the article/Supplementary Material. Further inquiries can be directed to the corresponding authors.

Ethics statement

The study was approved by the Ethics Committee of Xijing Hospital (KY20203128-1). The patients/participants provided their written informed consent to participate in this study. The animal experiment in this study was approved by the Laboratory Animals Welfare Ethics Committee of the Fourth Military Medical University (IACUC-20220259).

Author contributions

DT, JA, and CS: conceptualization. MG, WH, HM, HL, and YZ: conducted experiments. XG and CS: wrote the manuscript. CZ and CS: revised the manuscript. All authors gave final approval and agreed to be accountable for all aspects of the study.

Funding

This study was funded by the National Natural Science Foundation Program of China (No. 32070532), Shaanxi Innovation Capacity Support Program (No. 2021PT-037, 2021PT-054), and Laboratory Animal Foundation Program (No. SYDW_KY 2021-14).

Conflict of interest

The authors declare that the research was conducted in the absence of any commercial or financial relationships that could be construed as a potential conflict of interest.

Publisher's note

Supplementary material

The Supplementary Material for this article can be found online at: https://www.frontiersin.org/articles/10.3389/fonc.2022.1043479/full#supplementary-material

References

1. Zhu AX, Hong TS, Hezel AF, Kooby DA. Current management of gallbladder carcinoma. *Oncol* (2010) 15(2):168–81. doi: 10.1634/theoncologist.2009-0302

2. Hundal R, Shaffer EA. Gallbladder cancer: Epidemiology and outcome. *Clin Epidemiol* (2014) 6:99–109. doi: 10.2147/clep.S37357

3. Kakaei F, Beheshtirouy S, Nejatollahi SM, Zarrintan S, Mafi MR. Surgical treatment of gallbladder carcinoma: A critical review. *Updates Surg* (2015) 67 (4):339–51. doi: 10.1007/s13304-015-0328-x

4. Shen H, He M, Lin R, Zhan M, Xu S, Huang X, et al. Plek2 promotes gallbladder cancer invasion and metastasis through Egfr/Ccl2 pathway. *J Exp Clin Cancer Res CR* (2019) 38(1):247. doi: 10.1186/s13046-019-1250-8

5. Shukla SK, Singh G, Shahi KS, Bhuvan, Pant P. Staging, treatment, and future approaches of gallbladder carcinoma. *J Gastrointest Cancer* (2018) 49(1):9–15. doi: 10.1007/s12029-017-0036-5

6. Yoshida GJ. Applications of patient-derived tumor xenograft models and tumor organoids. *J Hematol Oncol* (2020) 13(1):4. doi: 10.1186/s13045-019-0829-z

7. Izumchenko E, Paz K, Ciznadija D, Sloma I, Katz A, Vasquez-Dunddel D, et al. Patient-derived xenografts effectively capture responses to oncology therapy in a heterogeneous cohort of patients with solid tumors. *Ann Oncol* (2017) 28 (10):2595–605. doi: 10.1093/annonc/mdx416

8. Hidalgo M, Amant F, Biankin AV, Budinská E, Byrne AT, Caldas C, et al. Patient-derived xenograft models: An emerging platform for translational cancer research. *Cancer Discovery* (2014) 4(9):998–1013. doi: 10.1158/2159-8290.Cd-14-0001

9. Pompili L, Porru M, Caruso C, Biroccio A, Leonetti C. Patient-derived xenografts: A relevant preclinical model for drug development. *J Exp Clin Cancer Res CR* (2016) 35(1):189. doi: 10.1186/s13046-016-0462-4

10. Broutier L, Mastrogiovanni G, Verstegen MM, Francies HE, Gavarró LM, Bradshaw CR, et al. Human primary liver cancer-derived organoid cultures for disease modeling and drug screening. *Nat Med* (2017) 23(12):1424–35. doi: 10.1038/nm.4438

11. Ganesh K, Wu C, O'Rourke KP, Szeglin BC, Zheng Y, Sauvé CG, et al. A rectal cancer organoid platform to study individual responses to chemoradiation. *Nat Med* (2019) 25(10):1607–14. doi: 10.1038/s41591-019-0584-2

12. Seppälä TT, Zimmerman JW, Sereni E, Plenker D, Suri R, Rozich N, et al. Patient-derived organoid pharmacotyping is a clinically tractable strategy for precision medicine in pancreatic cancer. *Ann Surg* (2020) 272(3):427–35. doi: 10.1097/sla.0000000000004200

13. Vlachogiannis G, Hedayat S, Vatsiou A, Jamin Y, Fernández-Mateos J, Khan K, et al. Patient-derived organoids model treatment response of metastatic gastrointestinal cancers. *Sci (New York NY)* (2018) 359(6378):920–6. doi: 10.1126/science.aao2774

14. Kam AE, Masood A, Shroff RT. Current and emerging therapies for advanced biliary tract cancers. *Lancet Gastroenterol Hepatol* (2021) 6(11):956–69. doi: 10.1016/s2468-1253(21)00171-0

15. Parameswaran S, Kundapur D, Vizeacoumar FS, Freywald A, Uppalapati M, Vizeacoumar FJ. A road map to personalizing targeted cancer therapies using synthetic lethality. *Trends Cancer* (2019) 5(1):11–29. doi: 10.1016/j.trecan.2018.11.001

16. Galon J, Bruni D. Approaches to treat immune hot, altered and cold tumours with combination immunotherapies. *Nat Rev Drug Discovery* (2019) 18(3):197–218. doi: 10.1038/s41573-018-0007-y

17. Dugger SA, Platt A, Goldstein DB. Drug development in the era of precision medicine. *Nat Rev Drug Discovery* (2018) 17(3):183–96. doi: 10.1038/nrd.2017.226

18. Zhang Y, Zhang Z. The history and advances in cancer immunotherapy: Understanding the characteristics of tumor-infiltrating immune cells and their therapeutic implications. *Cell Mol Immunol* (2020) 17(8):807–21. doi: 10.1038/s41423-020-0488-6

19. Huang L, Bockorny B, Paul I, Akshinthala D, Frappart PO, Gandarilla O, et al. Pdx-derived organoids model in vivo drug response and secrete biomarkers. *JCI Insight* (2020) 5 (21):e135544. doi: 10.1172/jci.insight.135544

20. Venturini M. Rational development of capecitabine. *Eur J Cancer (Oxford Engl 1990)* (2002) 38 Suppl 2:3–9. doi: 10.1016/s0959-8049(01)00414-2

21. Kanthan R, Senger JL, Ahmed S, Kanthan SC. Gallbladder cancer in the 21st century. *J Oncol* (2015) 2015:967472. doi: 10.1155/2015/967472

22. Wang S, Zhang Y, Cai Q, Ma M, Jin LY, Weng M, et al. Circular rna Foxp1 promotes tumor progression and warburg effect in gallbladder cancer by regulating pklr expression. *Mol Cancer* (2019) 18(1):145. doi: 10.1186/s12943-019-1078-z

23. Caldow Pilgrim CH, Groeschl RT, Quebbeman EJ, Gamblin TC. Recent advances in systemic therapies and radiotherapy for gallbladder cancer. *Surg Oncol* (2013) 22(1):61–7. doi: 10.1016/j.suronc.2012.12.001

24. Guillen KP, Fujita M, Butterfield AJ, Scherer SD, Bailey MH, Chu Z, et al. A human breast cancer-derived xenograft and organoid platform for drug discovery and precision oncology. *Nat Cancer* (2022) 3(2):232–50. doi: 10.1038/s43018-022-00337-6

25. Pauli C, Hopkins BD, Prandi D, Shaw R, Fedrizzi T, Sboner A, et al. Personalized in vitro and in vivo cancer models to guide precision medicine. *Cancer Discovery* (2017) 7(5):462–77. doi: 10.1158/2159-8290.Cd-16-1154

26. Lai Y, Wei X, Lin S, Qin L, Cheng L, Li P. Current status and perspectives of patient-derived xenograft models in cancer research. *J Hematol Oncol* (2017) 10 (1):106. doi: 10.1186/s13045-017-0470-7

27. Qu J, Kalyani FS, Liu L, Cheng T, Chen L. Tumor organoids: Synergistic applications, current challenges, and future prospects in cancer therapy. *Cancer Commun (London England)* (2021) 41(12):1331–53. doi: 10.1002/cac2.12224

28. Wörsdörfer P IT, Asahina I, Sumita Y, Ergün S. Do not keep it simple: Recent advances in the generation of complex organoids. *J Neural Transm (Vienna Austria 1996)* (2020) 127(11):1569–77. doi: 10.1007/s00702-020-02198-8

29. Galluzzi L, Humeau J, Buqué A, Zitvogel L, Kroemer G. Immunostimulation with chemotherapy in the era of immune checkpoint inhibitors. *Nat Rev Clin Oncol* (2020) 17(12):725–41. doi: 10.1038/s41571-020-0413-z

30. Clevers H. Modeling development and disease with organoids. *Cell* (2016) 165(7):1586–97. doi: 10.1016/j.cell.2016.05.082

31. Shen X, Zhao B. Efficacy of pd-1 or pd-L1 inhibitors and pd-L1 expression status in cancer: Meta-analysis. *BMJ* (2018) 362:k3529. doi: 10.1136/bmj.k3529

32. Zhang F, Zhang J, Zhao L, Zhai M, Zhang T, Yu D. A pd-L1 negative advanced gastric cancer patient with a long response to pd-1 blockade after failure of systematic treatment: A case report. *Front Immunol* (2021) 12:759250. doi: 10.3389/fimmu.2021.759250

33. Pyo KH, Kim JH, Lee JM, Kim SE, Cho JS, Lim SM, et al. Promising preclinical platform for evaluation of immuno-oncology drugs using hu-Pbl-Nsg lung cancer models. *Lung Cancer (Amsterdam Netherlands)* (2019) 127:112–21. doi: 10.1016/j.lungcan.2018.11.035

34. Morillon YMI, Smalley Rumfield C, Pellom ST, Sabzevari A, Roller NT, Horn LA, et al. The use of a humanized nsg-B2m(-/-) model for investigation of immune and anti-tumor effects mediated by the bifunctional immunotherapeutic bintrafusp Alfa. *Front Oncol* (2020) 10:549. doi: 10.3389/fonc.2020.00549

35. De La Rochere P, Guil-Luna S, Decaudin D, Azar G, Sidhu SS, Piaggio E. Humanized mice for the study of immuno-oncology. *Trends Immunol* (2018) 39 (9):748–63. doi: 10.1016/j.it.2018.07.001

36. Valpione S, Mundra PA, Galvani E, Campana LG, Lorigan P, De Rosa F, et al. The T cell receptor repertoire of tumor infiltrating T cells is predictive and prognostic for cancer survival. *Nat Commun* (2021) 12(1):4098. doi: 10.1038/s41467-021-24343-x

37. Maibach F, Sadozai H, Seyed Jafari SM, Hunger RE, Schenk M. Tumor-infiltrating lymphocytes and their prognostic value in cutaneous melanoma. *Front Immunol* (2020) 11:2105. doi: 10.3389/fimmu.2020.02105

frontiers | Frontiers in Oncology

TYPE Mini Review
PUBLISHED 19 January 2023
DOI 10.3389/fonc.2022.1085270

OPEN ACCESS

EDITED BY
Shiv K. Gupta,
Mayo Clinic, United States

REVIEWED BY
John Morton,
University of Colorado Anschutz Medical Campus, United States
Lizzie Tucker,
Institute of Cancer Research (ICR), United Kingdom

*CORRESPONDENCE
Daniel Bexell
daniel.bexell@med.lu.se

SPECIALTY SECTION
This article was submitted to Cancer Molecular Targets and Therapeutics, a section of the journal Frontiers in Oncology

RECEIVED 31 October 2022
ACCEPTED 21 December 2022
PUBLISHED 19 January 2023

CITATION
Aaltonen K, Radke K, Adamska A, Seger A, Mañas A and Bexell D (2023) Patient-derived models: Advanced tools for precision medicine in neuroblastoma.
Front. Oncol. 12:1085270.
doi: 10.3389/fonc.2022.1085270

Patient-derived models: Advanced tools for precision medicine in neuroblastoma

Kristina Aaltonen, Katarzyna Radke, Aleksandra Adamska, Alexandra Seger, Adriana Mañas and Daniel Bexell*

Division of Translational Cancer Research, Department of Laboratory Medicine, Lund University, Lund, Sweden

Neuroblastoma is a childhood cancer derived from the sympathetic nervous system. High-risk neuroblastoma patients have a poor overall survival and account for ~15% of childhood cancer deaths. There is thus a need for clinically relevant and authentic models of neuroblastoma that closely resemble the human disease to further interrogate underlying mechanisms and to develop novel therapeutic strategies. Here we review recent developments in patient-derived neuroblastoma xenograft models and *in vitro* cultures. These models can be used to decipher mechanisms of metastasis and treatment resistance, for drug screening, and preclinical drug testing. Patient-derived neuroblastoma models may also provide useful information about clonal evolution, phenotypic plasticity, and cell states in relation to neuroblastoma progression. We summarize current opportunities for, but also barriers to, future model development and application. Integration of patient-derived models with patient data holds promise for the development of precision medicine treatment strategies for children with high-risk neuroblastoma.

KEYWORDS

drug screening, neuroblastoma, patient-derived models, patient-derived xenograft, pediatric cancer, precision medicine, tumor organoids

1 Introduction

Despite significant academic, industrial, and clinical efforts, successfully translating preclinical findings to clinical trials and practice remains challenging (1–4) and less than 10% of drugs entering oncology clinical trials are eventually approved for clinical use (1, 5). Furthermore, these efforts and failures come at high financial and ethical costs. Pediatric malignancies have special considerations, since clinical drug testing is even more restricted by the relatively small number of patients and the ethics related to long-term side-effects in children. Involvement of multiple stakeholders is important to address the lack of childhood-specific drug development in the pharmaceutical sector (6, 7). Thus, there is an urgent need for clinically relevant and biologically accurate

preclinical models to minimize these current bottlenecks to drug development and implementation (8).

Neuroblastoma (NB) is the most common solid extracranial pediatric tumor, accounting for ~15% of pediatric oncology deaths (9, 10). NB can be regarded as an aberration of neural crest development, and although it can arise anywhere along the sympathetic nervous system, most primary tumors are found in the adrenal gland (11). NB is biologically and clinically heterogenous, and patients are stratified into different risk groups based on tumor characteristics and disease presentation (12, 13). Clinical responses vary from spontaneous regression to metastatic and drug-resistant disease despite intensive treatment (13). Furthermore, patients often suffer from severe therapy-related long-term adverse effects (14).

NB is a copy number-driven disease with few targetable somatic mutations found at diagnosis, especially when compared with adult malignancies (15). The *MYCN* oncogene is amplified in ~20% of cases and is strongly correlated with aggressive phenotypes and unfavorable clinical outcomes (16). Other common chromosomal copy number changes, including 11q loss and 17q gain, are also poor prognostic features (17). Recurrent mutations are rare in NB but include *ALK* (9%), *ATRX* (7%), and *PTEN* (3%) mutations (15). In relapsed tumors, genome-wide sequencing has revealed a higher prevalence of recurrent mutations in targetable pathways, such as RAS-MAPK (18, 19), but at relatively low frequencies. Recent transcriptional and epigenetic analyses suggest that NB cells can adopt at least two phenotypic cell states, known as adrenergic (ADR)/differentiated and mesenchymal (MES)/immature (20–24). These findings highlight the heterogeneous and dynamic nature of NB.

Reliable, predictive, and authentic NB models are important because: (i) NB is uncommon, so sufficiently powered clinical trials are challenging and patient material is scarce for molecular studies (25), placing extra weight on the translatability of preclinical results; (ii) preclinical models that accurately recapitulate known clinical, genetic, and transcriptional intra- and inter-tumor heterogeneity are important for the identification of effective therapeutic targets; and (iii) patient-derived (PD) models resemble the clinical scenario better than conventional models and can therefore be used to screen for and test the most promising and safe novel therapies.

Here we discuss recent progress in patient-derived xenografts (PDXs) and PD *in vitro* cultures as preclinical NB models. We summarize the development of different PD models, their utility in studying biological mechanisms and treatment responses, and how they can be utilized for preclinical drug testing to improve treatment strategies against NB (Figure 1).

2 PD NB models

Conventional cell lines have been used as laboratory models for decades, and they have provided valuable knowledge about

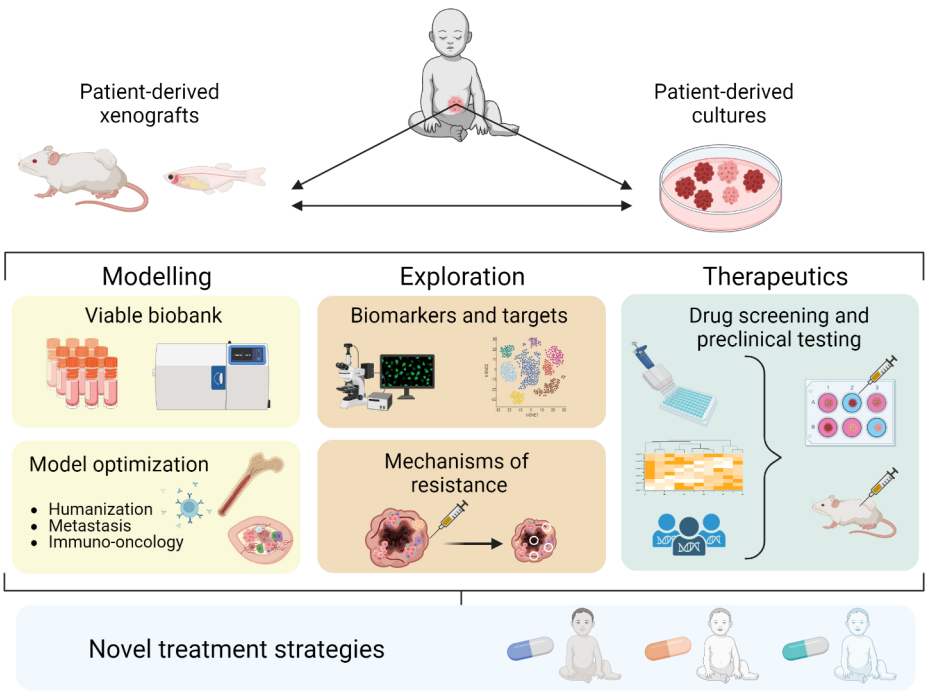

FIGURE 1
Establishment and application of PD models in NB contributing to novel treatment strategies.

tumor biology and drug efficacy in many cancer types. However, cancer cell lines are usually passaged under serum-containing conditions for years and thus their molecular profiles often differ from the original patient tumor (26, 27). This matters in terms of model fidelity, especially when considering clinical applicability; for example, clinically important features such as drug resistance might be lost after long-term *in vitro* passaging (27). PD NB models are established directly from tumor material obtained from children after parental informed consent. PD models have been shown to better reflect the features (e.g., treatment response) of their original tumors, compared with conventional models (28–31). PDXs have now been established from many diverse tumor types of adult and pediatric cancers including NB (32–35). Over the last few decades, the cancer research community has gradually turned towards PD model systems (8), and the US National Cancer Institute recently decided to replace its panel of human cancer cell lines (NCI-60) with well-characterized PDX models (36) for drug screening.

2.1 Establishment of NB PDXs *in vivo*

NB PDXs have been established in immunocompromised mice, mainly by implanting tumor samples or cells obtained from patients next to the adrenal gland (orthotopic implantation) or subcutaneously (ectopic/heterologous implantation). Established orthotopic PDX tumors can be monitored by clinical imaging techniques such as FDG-PET or MRI (37), and they have been shown to retain important patient tumor characteristics such as invasive growth patterns into surrounding tissues and spontaneous metastatic capacity to the bone marrow, lungs, and liver (37–39). PDX models retain NB-specific molecular features, including cellular differentiation status, protein marker expression (synaptophysin, chromogranin A, NCAM/CD56), chromosomal copy number changes (including 1p loss, *MYCN* amplification, 17q gain), mutational profiles, and DNA methylation status (32, 34, 37–41). Transcriptional analysis of orthotopic NB PDXs has shown that they also retain a certain degree of patient-specific gene expression, indicating transcriptional stability, from the corresponding NBs (32, 39, 40). Thus, although a PDX is established from only a fragment of the original patient tumor, data from multiple laboratories have shown that NB PDXs represent the main and clinically relevant features of NB patient tumors. There are now several sources of NB PDX tumors (detailed in (42)), including the US Pediatric Preclinical *In Vivo* Testing Consortium (PIVOT) and the European ITCC-P4 - Pediatric Preclinical Proof of Concept Platform.

The site of implantation affects the PDX model: orthotopic implantation has a higher engraftment rate and tumors grow faster than those implanted subcutaneously (32, 41). The human tumor microenvironment (TME) is gradually lost *in vivo*. Instead, orthotopic NB PDXs have been shown to contain a murine TME including for example vascularization, pericytes, macrophages, and extracellular matrix resembling the architecture in the parental NB (38). Potential functional differences between human and mouse TMEs are not fully elucidated and this uncertainty is important to consider (43). It has been debated whether the use of mice as hosts leads to murine-specific tumor evolution during PDX engraftment and propagation (44, 45). However, serial *in vivo* passaging of orthotopic NB PDXs for up to two years has shown that PDXs retain key genetic aberrations (e.g., 1p loss, *MYCN* amplification, and 17q gain) and acquire only minor genetic changes over time, as would be expected from their natural evolution (39). Clonal dynamics studies during tumor progression in PDXs have shown the presence of branched evolution, clonal sweeps, and convergent evolution of specific small deletions in potentially tumor-associated genes (46), a pattern similar to tumor evolution in NB patients (47).

There have been cases where human lymphomas have developed at the site of NB-cell injection (41, 48), or when murine-derived tumors have replaced the human PDX (49, 50), so thorough and frequent characterization of PDXs is necessary. Setting up robust biobanks for storage of well-characterized, early passage PDX-tumors will be of great benefit to the research community (8).

While most PDX models have been established in mice, zebrafish are increasingly used as hosts for implantation of PD tumor cells, including NB. Zebrafish allow for rapid and low-cost preclinical drug screening in an intact organism that may inform about precision medicine strategies in NB (51, 52). Furthermore, genetically-modified strains are available and tumors can be visualized from an early stage and followed dynamically. However, challenges in translating drug testing findings to patients include limited toxicity and pharmacodynamic data (51), temperature differences, and the non-mammalian TME.

PD cells and tumor biopsies have also been implanted into chick embryos with a high engraftment rate, forming metastases only from tumor cells from patients with metastatic NB and not from localized disease (53). NB cells migrated along the embryonic aorta and along peripheral nerves, demonstrating these as major routes for metastatic dissemination. This model allows for investigation of tumor progression and metastasis in an embryonic environment *in vivo* (53). However, the clinical relevance of the models remains uncertain.

2.2 PD cultures *in vitro*

PD tumor cultures are established *in vitro* directly from patients and can be grown as tumor organoids (PDOs), spheroids, or as semi-attached or attached cultures. PD cultures provide an opportunity to test potential therapeutics in a faster, high-throughput manner compared to PDXs.

PD NB cultures are isolated directly from primary or metastatic tumors from patients and are cultured in serum-

free medium with defined growth factors to avoid neurospecific differentiation. This is best achieved on low-attachment plastics, with or without Matrigel or other scaffolding materials. Several groups have shown that PD NB cultures retain the copy-number profiles, mutation patterns, and other genetic and phenotypic characteristics of the tumor of origin (54–57) in both Matrigel and as free-floating spheres, but PDOs in Matrigel have better self-organization (56). Establishing PD cultures from different stages and subgroups of NB has been challenging. In general, more aggressive, *MYCN*-amplified, and metastatic tumors are easier to propagate *in vitro*. Recent advances in 3D scaffolding with hydrogels and porous scaffolding (reviewed in (58)) together with further optimization of culture conditions might increase the probability of successful establishment. Characterization of culture conditions is also important to understand how different transcriptional cell states might be maintained *in vitro*. Notably, it is important to verify NB identity and lack of contamination with other cells, which can otherwise overtake PD NB cultures (59, 60).

Since the limited number of NB patients restricts the number of models, a complementary approach is to use PDX-derived *in vitro* cultures after expansion of patient material *in vivo* (37, 40, 57, 61–63). Similar to PD cultures, PDX-derived NB cells can be grown adherent or as free-floating 3D cultures, and they retain patient-specific genomic aberrations as well as tumorigenic and metastatic capacity *in vivo* (62). Drug responses between NB PD- and PDX-derived cultures are highly correlated, suggesting that these models can be used interchangeably for drug testing (41). Biobanking of PD- and PDX-derived NB cultures will be a very important tool for future drug screening and larger preclinical drug testing (8).

3 Applications of PD NB models

Conventional cell lines, cell-line derived xenografts, and genetically engineered mouse models have been the main preclinical tools used to study resistance mechanisms and for drug testing. By using PD models that retain the main characteristics and heterogeneity of the original tumors, patient tumors and their treatment response can be better represented in the laboratory, thereby bridging the gap between preclinical models and the clinic.

3.1 Identification of treatment resistance mechanisms and biomarkers

Treatment resistance, relapse after therapy, and metastasis are urgent clinical problems in NB. A few studies have used PD models to identify diverse mechanisms implicated in NB invasion, migration, metastasis (64, 65), and resistance to specific chemotherapies (66). Using a clinically relevant treatment protocol (COJEC-induction therapy), NB PDXs show similar chemotherapy responses to their corresponding patients, suggesting that NB PDXs are useful for modelling chemoresistance and relapse (46). The models showed that chemoresistant NBs have a lower ADR signature and enrichment for an immature MES-like phenotype, suggesting an association between the MES cell state and relapse (46). These results are consistent with recent findings in the clinical setting (24, 67). The ability to accurately model treatment responses and their association with phenotypic cell states make *in vivo* PDXs a very promising tool to explore NB phenotypes in a reproducible manner, as well as characterizing the role of phenotypic plasticity in acquired and intrinsic resistance.

Reliable biomarkers for monitoring tumor responses are important for longer-term studies of relapse and resistance, and in clinical diagnostics. NB PDXs reproduce the patient's relative levels of circulating metanephrines (68). Given that metanephrines are tumor progression biomarkers [plasma levels correlate with tumor volume (69)], this could pave the way for a minimally invasive method of monitoring tumor response/resistance in orthotopic PDX models. Another approach for monitoring responses is with gene signatures as recently optimized and used in a therapeutic study for high-risk relapsed NB in PD models (70).

3.2 Drug testing

3.2.1 Application in the preclinical setting

Preclinical PD model testing is now highly recommended for proof-of-concept studies of new drugs and drug combinations aiming for clinical trials in the pediatric population (8). Many NB targets identified in patients have been tested in PD models *in vitro* and *in vivo*, allowing the evaluation of specific responses in tumors harboring different underlying, molecular alterations. Some known genetic vulnerabilities in NB are still under investigation, while others, for example ALK, have been clinically tested (71, 72). Table 1 presents an overview of recent preclinical drug investigations of established and novel NB targets that were identified and tested in PD models.

High-throughput screens (HTS) *in vitro* can facilitate the discovery of specific targets and/or drugs using CRISPR/siRNA or phenotypic response. Most screening approaches still use conventional cell lines, but more recently PDX-derived cultures of high-risk NB have been used for the initial identification, for example for a KSP inhibitor (77). Compounds identified in drug screens can be further verified *in vivo* in PDXs.

In our experience, PD models show high intra-model variability in drug response (46, 75, 77) and are often less responsive to different treatments than conventional cell lines and xenografts [discussed also in (29)]. The lower sensitivity of PD models could indicate an even smaller effect in patients, thus

TABLE 1 Selected preclinical drug testing studies using NB patient-derived models.

Target	Description	PD *in vivo*	PD *in vitro*	References
Small molecules				
CNR2, MAPK8	TargetTranslator tool for drug discovery	✓	✓	Almstedt et al., 2020 (52)
SHP2	Targeting tumors with low expression of NF1	✓	✓	Cai et al., 2022 (73)
ROS (ferroptosis)	Antioxidant pathways inhibition	✓	✓	Floros et al., 2021 (74)
PIM/PI3K/mTOR	New triple inhibitor	✓	✓	Mohlin et al., 2019 (75)
RAS/antimitotic	Antimitotic effects of rigosertib	✓	✓	Radke et al., 2021 (76)
KSP (Eg5)	HTS identifying new inhibitors, complete response in PDXs	✓	✓	Hansson et al., 2020 (77)
KSP (Eg5)	New oral inhibitor, liver metastasis model	✓	–	Masanas et al., 2020 (78)
Antimitotic	New inhibitor in taxane- and chemoresistant models	✓	–	Grohman et al., 2021 (79)
PARP, ATM	Targeting DNA damage, ATRX mutant NB	✓	–	George et al., 2020 (80)
PP2A	New PP2A activators	✓	–	Bownes et al., 2022 (81)
TOP2B	HTS, redefining MoA of an inhibitor	✓	–	Pan et al., 2021 (82)
CHK1	Prexasertib with chemotherapy in NB	✓	–	Lowery et al., 2019 (83)
ALK, TRK, JAK2/STAT, Src/FAK	Multikinase targeting	✓	–	O´Donohue et al., 2021 (84)
PHGDH	LC-MS-based proteomics, MYCN-associated targets	✓	–	Arlt et al., 2021 (85)
PGDB5	DNA transposase inhibition impairs DNA repair	✓	–	Henssen et al., 2017 (86)
ALK	New molecule: lorlatinib	✓	–	Infarinato et al., 2016 (87)
CAIX/CAXII	New inhibitor, organotypic slice culture	–	✓	Huo et al., 2022 (88)
Drug combinations				
CHK1+RRM2	Synergistic effects on replication stress	✓	✓	Nunes et al., 2022 (89)
ALK+chemo	Crizotinib combination with chemotherapy	✓	✓	Krytska et al., 2016 (90)
ALK+CDK4/6	Combination screen identifying new synergistic targets	✓	✓	Wood et al., 2017 (91)
ALK+PIM1	CRISPR screen, targeting ALK resistance	✓	✓	Trigg et al., 2019 (92)
BCL2+MDM2; BCL2+ CYCLO/TOPO; BCL2 +MCL1	Venetoclax in combinations with clinically relevant agents	✓	✓	Dalton et al., 2021 (93)
BCL2+ferentidine	Synergistic effects of venetoclax and ferentidine	✓	✓	Nguyen et al., 2019 (94)
MGMT+TMZ+TOP2;	Combination of drugs targeting DNA damage	✓	✓	Hindle et al., 2021 (95)
HDAC+DOXO	Rapid zebra fish screen	✓	✓	Wrobel et al., 2020 (96)
PLK1/BRD4	Screen of dual inhibitors	✓	–	Timme et al., 2020 (97)
BCL-2+Aurora A	Screen of new venetoclax combinations	✓	–	Ham et al., 2016 (98)
TBX2	TF addiction is targeted by BETi + CDK7i	–	✓	Decaester et al., 2018 (99)
Immunotherapy & other				
ALK	Antibody-toxin conjugate directed towards ALK	✓	✓	Sano et al., 2019 (100)
Oncolytic therapeutics	oHSV expressing mIL-12	✓	✓	Quinn et al., 2022 (101)
aNK cells+anti-GD2	Residual disease targeting	✓	–	Barry et al., 2019 (102)

(Continued)

TABLE 1 Continued

Target	Description	PD *in vivo*	PD *in vitro*	References
IL-15+anti-GD2	Substitution of IL15 for IL2 to limit toxicities	✓	–	Nguyen et al., 2019 (103)
IL-15/21+anti-GD2	GD2-targeted IL delivery in orthotopic models	✓	–	Nguyen et al., 2022 (104)
TOP1+anti-GD2	GD2-targeted nanoparticle delivery of SN-38	✓	–	Monderrubio et al., 2017 (105)

ALK, anaplastic lymphoma kinase; ATM, ataxia-telangiectasia mutated serine/threonine kinase; BCL, B-cell lymphoma; BET, bromodomain and extra-terminal domain; BRD4, bromodomain containing 4; CA, carbonic anhydrase; CDK, cyclin-dependent kinase; CHK, checkpoint kinase; CNR, cannabinoid receptor; CYCLO, cyclophosphamide; DOXO, doxycycline; FAK, focal adhesion kinase; GD2, disialoganglioside; HDAC, histone deacetylase; IL, interleukin; JAK, Janus kinase; KSP, kinesin spindle protein; MAPK, mitogen-activated protein kinase; MCL, induced myeloid leukemia cell differentiation; MDM, E3 ubiquitin-protein ligase; MGMT, O-6-methylguanine-DNA methyltransferase; oHSV, oncolytic herpes simplex virus; mTOR, mammalian target of rapamycin; PARP, poly (ADP-ribose) polymerase; PGBD5, PiggyBac transposable element derived 5; PHGDH, phosphoglycerate dehydrogenase; PI3K, phosphoinositide 3-kinases; PIM, Pim-1 proto-oncogene, serine/threonine kinase; PLK, polo-like kinase; PP2A, protein phosphatase 2; ROS, reactive oxygen species; RRM2, ribonucleotide reductase regulatory subunit M2; SHP2, protein tyrosine phosphatase; STAT, signal transducer and activator of transcription; TBX, T-box transcription factor; TF, transcription factor; TOP2, topoisomerase II alpha; TOPO, topotecan; TRK, tropomyosin receptor kinase.

providing important information with respect to optimal clinical implementation.

3.2.2 Application for precision medicine in the clinic

The possibility of identifying actionable genetic alterations in pediatric cancers has contributed to optimism that the approach is useful for clinical trial design and target identification for high-risk and relapsed pediatric tumors, including high-risk NB (71, 72). Langenberg et al. thoroughly summarized current pediatric precision medicine programs around the world (106). Many of the programs/consortia [Pediatric MATCH (US) or INFORM (Europe)] have enabled patients to receive treatments tailored to the individual tumor's molecular profile (107–109). However, relatively few identified mutations (<30%) have led to targeted therapies (106, 107, 110). This highlights the need for molecular profiling of patients to be backed up by real-time functional testing of drug sensitivities in PD models.

Both the PIVOT (US, earlier PPTC) and ITCC-P4 (Europe) repositories hold PDXs. Considering that PDXs take time to establish, co-clinical avatar studies are generally very difficult. Nevertheless, the rarity of pediatric cancers and scarcity of models representing specific subtypes within pediatric tumors makes those repositories a valuable resource for the accelerated development and translation of novel therapeutics into early phase trials (34, 111, 112). Lau et al. developed a pediatric precision medicine platform (including a few high-risk NBs) of PDX models and HTS in PDOs, observing a correlation between PDX results, HTS-PDOs, and the clinical responses in patients (113). Importantly, the addition of functional drug testing to a genome-only analysis increased the number of patients with drug options by also identifying drug sensitivities not associated with molecular hallmarks (113).

Real-time drug testing for the immediate benefit of the patient is likely to be more feasible in PDO models where the time for establishment is much shorter and the readout can be performed with a higher throughput. The COMPASS consortium (Clinical implementation Of Multidimensional PhenotypicAl drug SenSitivities in paediatric precision oncology) is a large-scale effort to implement HTS in PD models. This European collaborative platform aims to implement PDO screening for individualized drug sensitivity assessment and therapy (114). Recently, the network also standardized drug scoring tools and developed machine learning approaches (115, 116).

4 Current and future model optimization

Although the successful establishment of PD NB models is encouraging, certain aspects can still be improved. For example, the distribution and function of the extracellular matrix (ECM) has been shown to influence NB progression in patient samples (117, 118). Consistently, modulation of ECM components induces specific cell behaviors of PD NB cultures (63). Optimization of ECM conditions could thus contribute to improved NB modelling.

The lack of a complete immune system is a limitation of most PDX models, since PD tumors are generally implanted in immunocompromised mouse strains (e.g., NSG) to permit tumor engraftment. Reconstitution of a humanized immune system, for example by injection of human hematopoietic stem cells into sub-lethally irradiated mice, could improve the immune status of the models (119). A technically advanced humanized mouse strain (MISTRG) supports the intrinsic development of human natural killer (NK) cells after bone marrow transplantation (120). When combined with orthotopic NB PDXs, these mice have allowed the identification of immune modulating functions in common between PDXs and patient tumors and suggest that the model is useful for immuno-oncology studies in general and in NB in particular (121). The use of PDO and stromal/immune cell co-cultures can be applied *in vitro*, where it has been very

challenging to optimize culture conditions for multiple cell types over longer periods (122, 123). Co-cultures of NB organoids and peripheral blood mononuclear cells (from a healthy donor) were recently used to test a novel immunotherapy (124).

Innovative technological advances have suggested that microfluidics (lab-on-a-chip) and bioprinting may provide future systems for studying tumor cell and stromal/immune cell interactions. Functional short-time cultures of both tumor cells and immune cells in a microfluidic system have been reported for adult cancers (125, 126) and might be applicable also to pediatric cancers. Very recently, the first bioprinted, vascularized NB microenvironment on a fluidic chip was reported (127). Implantation of cell line-derived NB spheroids led to NB cell survival for two weeks and successful micro-vessel infiltration of the spheroids (127). A different study managed to establish PD NB organotypic slice cultures that could potentially preserve an intact NB tumor microenvironment (88). This study used a perfusion-based bioreactor to force medium through the tissue, thereby providing continuous nutrient delivery to the whole tumor.

Orthotopic NB PDXs retain spontaneous metastatic capacity *in vivo* to the lungs, liver, and bone marrow, mimicking the entire process from primary tumor growth to invasion and metastasis (37, 39). However, the TME is generally murine (38) and there are uncertainties about cross reactivity between human NB cells and the mouse TME. The presence of human mesenchymal stem cells can increase growth and metastasis of NB cells *in vivo* (128), suggesting species preference. Recent advances in tissue engineering have produced *in vivo* models of humanized bone (so-called ossicles) in mice. Implanted PDX-derived NB cells form osteolytic tumor lesions in the ossicles and display higher and faster engraftment rates than in mouse bone (129). This model could thus be valuable for the investigation of human NB growth and treatment responses in a humanized metastatic niche.

Further optimization of PD models to account for more patient-like microenvironmental factors both *in vivo* and *in vitro* is ongoing and will likely contribute to improved translatability.

5 Conclusions

The use of clinically relevant preclinical models is of immense importance in childhood cancers, such as high-risk NB, where the access to patient material is limited. PD models reflect the characteristics of the tumor of origin better than conventional *in vivo* and *in vitro* models. Nevertheless, ongoing efforts may further optimize their translational relevance. Existing NB PDXs and PD cultures have been – and continue to be – used to decipher therapy resistance and for target identification and drug testing. Future studies will need to investigate how PD models can be used to exploit phenotypic plasticity and NB cell states in preclinical studies to better benefit NB patients.

Author contributions

KA, KR, AA, AS, AM and DB wrote and reviewed the manuscript. KA and DB supervised the project. All authors contributed to the article and approved the submitted version.

Funding

This work was supported by the following grants and fellowships: Swedish Cancer Society grant 20 0897 PjF (DB). Swedish Cancer Society postdoctoral fellowship 21 0346 PT (AM). The Swedish Childhood Cancer Foundation grant PR2020-0018 (DB). The Swedish Research Council grant 2021-02597 (DB).

Acknowledgments

Figure 1 was created using Biorender.com.

Conflict of interest

DB has received research funding from Healx, aPODD foundation, and Captor Therapeutics for unrelated work.

The remaining authors declare that the research was conducted in the absence of any commercial or financial relationships that could be constructed as a potential conflict of interest.

Publisher's note

References

1. Wong CH, Siah KW, Lo AW. Estimation of clinical trial success rates and related parameters. *Biostatistics* (2019) 20(2):273–86. doi: 10.1093/biostatistics/kxx069

2. Sharpless NE, Depinho RA. The mighty mouse: Genetically engineered mouse models in cancer drug development. *Nat Rev Drug discovery* (2006) 5 (9):741–54. doi: 10.1038/nrd2110

3. Johnson JI, Decker S, Zaharevitz D, Rubinstein LV, Venditti JM, Schepartz S, et al. Relationships between drug activity in NCI preclinical *in vitro* and *in vivo* models and early clinical trials. *Br J cancer* (2001) 84(10):1424–31. doi: 10.1054/bjoc.2001.1796

4. Lin A, Giuliano CJ, Palladino A, John KM, Abramowicz C, Yuan ML, et al. Off-target toxicity is a common mechanism of action of cancer drugs undergoing clinical trials. *Sci Transl Med* (2019) 11(509):eaaw8412. doi: 10.1126/scitranslmed.aaw8412

5. Hay M, Thomas DW, Craighead JL, Economides C, Rosenthal J. Clinical development success rates for investigational drugs. *Nat Biotechnol* (2014) 32 (1):40–51. doi: 10.1038/nbt.2786

6. Moreno L, Barone G, DuBois SG, Molenaar J, Fischer M, Schulte J, et al. Accelerating drug development for neuroblastoma: Summary of the second neuroblastoma drug development strategy forum from innovative therapies for children with cancer and international society of paediatric oncology Europe neuroblastoma. *Eur J Cancer* (2020) 136:52–68. doi: 10.1016/j.ejca.2020.05.010

7. Pearson AD, Heenen D, Kearns PR, Goeres A, Marshall LV, Blanc P, et al. 10-year report on the European paediatric regulation and its impact on new drugs for children's cancers. *Lancet Oncol* (2018) 19(3):285–7. doi: 10.1016/S1470-2045(18)30105-0

8. Vassal G, Houghton PJ, Pfister SM, Smith MA, Caron HN, Li XN, et al. International consensus on minimum preclinical testing requirements for the development of innovative therapies for children and adolescents with cancer. *Mol Cancer Ther* (2021) 20(8):1462–8. doi: 10.1158/1535-7163.MCT-20-0394

9. Gatta G, Botta L, Rossi S, Aareleid T, Bielska-Lasota M, Clavel J, et al. Childhood cancer survival in Europe 1999-2007: results of EUROCARE-5–a population-based study. *Lancet Oncol* (2014) 15(1):35–47. doi: 10.1016/S1470-2045(13)70548-5

10. Park JR, Eggert A, Caron H. Neuroblastoma: biology, prognosis, and treatment. *Hematol Oncol Clin North Am* (2010) 24(1):65–86. doi: 10.1016/j.hoc.2009.11.011

11. Matthay KK, Maris JM, Schleiermacher G, Nakagawara A, Mackall CL, Diller L, et al. Neuroblastoma. *Nat Rev Dis Primers* (2016) 2:16078. doi: 10.1038/nrdp.2016.78

12. Pinto NR, Applebaum MA, Volchenboum SL, Matthay KK, London WB, Ambros PF, et al. Advances in risk classification and treatment strategies for neuroblastoma. *J Clin Oncol Off J Am Soc Clin Oncol* (2015) 33(27):3008–17. doi: 10.1200/JCO.2014.59.4648

13. Tolbert VP, Matthay KK. Neuroblastoma: Clinical and biological approach to risk stratification and treatment. *Cell Tissue Res* (2018) 372(2):195–209. doi: 10.1007/s00441-018-2821-2

14. Cohen LE, Gordon JH, Popovsky EY, Gunawardene S, Duffey-Lind E, Lehmann LE, et al. Late effects in children treated with intensive multimodal therapy for high-risk neuroblastoma: High incidence of endocrine and growth problems. *Bone Marrow Transplant* (2014) 49(4):502–8. doi: 10.1038/bmt.2013.218

15. Pugh TJ, Morozova O, Attiyeh EF, Asgharzadeh S, Wei JS, Auclair D, et al. The genetic landscape of high-risk neuroblastoma. *Nat Genet* (2013) 45(3):279–84. doi: 10.1038/ng.2529

16. Brodeur GM, Seeger RC, Schwab M, Varmus HE, Bishop JM. Amplification of n-myc in untreated human neuroblastomas correlates with advanced disease stage. *Sci (New York NY)* (1984) 224(4653):1121–4. doi: 10.1126/science.6719137

17. Cohn SL, Pearson AD, London WB, Monclair T, Ambros PF, Brodeur GM, et al. The international neuroblastoma risk group (INRG) classification system: an INRG task force report. *J Clin Oncol Off J Am Soc Clin Oncol* (2009) 27(2):289–97. doi: 10.1200/JCO.2008.16.6785

18. Schramm A, Koster J, Assenov Y, Althoff K, Peifer M, Mahlow E, et al. Mutational dynamics between primary and relapse neuroblastomas. *Nat Genet* (2015) 47(8):872–7. doi: 10.1038/ng.3349

19. Eleveld TF, Oldridge DA, Bernard V, Koster J, Daage LC, Diskin SJ, et al. Relapsed neuroblastomas show frequent RAS-MAPK pathway mutations. *Nat Genet* (2015) 47(8):864–71. doi: 10.1038/ng.3333

20. van Groningen T, Koster J, Valentijn LJ, Zwijnenburg DA, Akogul N, Hasselt NE, et al. Neuroblastoma is composed of two super-enhancer-associated differentiation states. *Nat Genet* (2017) 49(8):1261–6. doi: 10.1038/ng.3899

21. Boeva V, Louis-Brennetot C, Peltier A, Durand S, Pierre-Eugène C, Raynal V, et al. Heterogeneity of neuroblastoma cell identity defined by transcriptional circuitries. *Nat Genet* (2017) 49(9):1408–13. doi: 10.1038/ng.3921

22. Jansky S, Sharma AK, Körber V, Quintero A, Toprak UH, Wecht EM, et al. Single-cell transcriptomic analyses provide insights into the developmental origins of neuroblastoma. *Nat Genet* (2021) 53(5):683–93. doi: 10.1038/s41588-021-00806-1

23. Bedoya-Reina OC, Li W, Arceo M, Plescher M, Bullova P, Pui H, et al. Single-nuclei transcriptomes from human adrenal gland reveal distinct cellular identities of low and high-risk neuroblastoma tumors. *Nat Commun* (2021) 12 (1):5309. doi: 10.1038/s41467-021-24870-7

24. Gartlgruber M, Sharma AK, Quintero A, Dreidax D, Jansky S, Park Y-G, et al. Super enhancers define regulatory subtypes and cell identity in neuroblastoma. *Nat Cancer* (2021) 2(1):114–28. doi: 10.1038/s43018-020-00145-w

25. Fletcher JI, Ziegler DS, Trahair TN, Marshall GM, Haber M, Norris MD. Too many targets, not enough patients: Rethinking neuroblastoma clinical trials. *Nat Rev Cancer* (2018) 18(6):389–400. doi: 10.1038/s41568-018-0003-x

26. Lee J, Kotliarova S, Kotliarov Y, Li A, Su Q, Donin NM, et al. Tumor stem cells derived from glioblastomas cultured in bFGF and EGF more closely mirror the phenotype and genotype of primary tumors than do serum-cultured cell lines. *Cancer Cell* (2006) 9(5):391–403. doi: 10.1016/j.ccr.2006.03.030

27. Gillet JP, Calcagno AM, Varma S, Marino M, Green LJ, Vora MI, et al. Redefining the relevance of established cancer cell lines to the study of mechanisms of clinical anti-cancer drug resistance. *Proc Natl Acad Sci United States America* (2011) 108(46):18708–13. doi: 10.1073/pnas.1111840108

28. Hidalgo M, Amant F, Biankin AV, Budinská E, Byrne AT, Caldas C, et al. Patient-derived xenograft models: An emerging platform for translational cancer research. *Cancer discovery* (2014) 4(9):998–1013. doi: 10.1158/2159-8290.CD-14-0001

29. Gao H, Korn JM, Ferretti S, Monahan JE, Wang Y, Singh M, et al. High-throughput screening using patient-derived tumor xenografts to predict clinical trial drug response. *Nat Med* (2015) 21(11):1318–25. doi: 10.1038/nm.3954

30. van de Wetering M, Francies HE, Francis JM, Bounova G, Iorio F, Pronk A, et al. Prospective derivation of a living organoid biobank of colorectal cancer patients. *Cell* (2015) 161(4):933–45. doi: 10.1016/j.cell.2015.03.053

31. Calandrini C, Schutgens F, Oka R, Margaritis T, Candelli T, Mathijsen L, et al. An organoid biobank for childhood kidney cancers that captures disease and tissue heterogeneity. *Nat Commun* (2020) 11(1):1310. doi: 10.1038/s41467-020-15155-6

32. Stewart E, Federico SM, Chen X, Shelat AA, Bradley C, Gordon B, et al. Orthotopic patient-derived xenografts of paediatric solid tumours. *Nature* (2017) 549(7670):96–100. doi: 10.1038/nature23647

33. Brabetz S, Leary SES, Gröbner SN, Nakamoto MW, Şeker-Cin H, Girard EJ, et al. A biobank of patient-derived pediatric brain tumor models. *Nat Med* (2018) 24(11):1752–61. doi: 10.1038/s41591-018-0207-3

34. Rokita JL, Rathi KS, Cardenas MF, Upton KA, Jayaseelan J, Cross KL, et al. Genomic profiling of childhood tumor patient-derived xenograft models to enable rational clinical trial design. *Cell Rep* (2019) 29(6):1675–89.e9. doi: 10.1016/j.celrep.2019.09.071

35. Tucker ER, George S, Angelini P, Bruna A, Chesler L. The promise of patient-derived preclinical models to accelerate the implementation of personalised medicine for children with neuroblastoma. *J Pers Med* (2021) 11(4):248. doi: 10.3390/jpm11040248

36. Ledford H. US Cancer institute to overhaul tumour cell lines. *Nature* (2016) 530(7591):391. doi: 10.1038/nature.2016.19364

37. Braekeveldt N, Wigerup C, Gisselsson D, Mohlin S, Merselius M, Beckman S, et al. Neuroblastoma patient-derived orthotopic xenografts retain metastatic patterns and geno- and phenotypes of patient tumours. *Int J cancer* (2015) 136(5): E252–61. doi: 10.1002/ijc.29217

38. Braekeveldt N, Wigerup C, Tadeo I, Beckman S, Sanden C, Jonsson J, et al. Neuroblastoma patient-derived orthotopic xenografts reflect the microenvironmental hallmarks of aggressive patient tumours. *Cancer letters* (2016) 375(2):384–9. doi: 10.1016/j.canlet.2016.02.046

39. Braekeveldt N, von Stedingk K, Fransson S, Martinez-Monleon A, Lindgren D, Axelson H, et al. Patient-derived xenograft models reveal intratumor heterogeneity and temporal stability in neuroblastoma. *Cancer Res* (2018) 78 (20):5958–69. doi: 10.1158/0008-5472.CAN-18-0527

40. Stewart E, Shelat A, Bradley C, Chen X, Federico S, Thiagarajan S, et al. Development and characterization of a human orthotopic neuroblastoma xenograft. *Dev Biol* (2015) 407(2):344–55. doi: 10.1016/j.ydbio.2015.02.002

41. Kamili A, Gifford AJ, Li N, Mayoh C, Chow SO, Failes TW, et al. Accelerating development of high-risk neuroblastoma patient-derived xenograft

models for preclinical testing and personalised therapy. *Br J cancer* (2020) 122 (5):680–91. doi: 10.1038/s41416-019-0682-4

42. Ornell KJ, Coburn JM. Developing preclinical models of neuroblastoma: Driving therapeutic testing. *BMC BioMed Eng* (2019) 1:33. doi: 10.1186/s42490-019-0034-8

43. Bleijs M, van de Wetering M, Clevers H, Drost J. Xenograft and organoid model systems in cancer research. *EMBO J* (2019) 38(15):e101654. doi: 10.15252/embj.2019101654

44. Ben-David U, Ha G, Tseng Y-Y, Greenwald NF, Oh C, Shih J, et al. Patient-derived xenografts undergo mouse-specific tumor evolution. *Nat Genet* (2017) 49:1567. doi: 10.1038/ng.3967

45. Woo XY, Giordano J, Srivastava A, Zhao Z-M, Lloyd MW, de Bruijn R, et al. Conservation of copy number profiles during engraftment and passaging of patient-derived cancer xenografts. *Nat Genet* (2021) 53(1):86–99. doi: 10.1038/s41588-020-00750-6

46. Mañas A, Aaltonen K, Andersson N, Hansson K, Adamska A, Seger A, et al. Clinically relevant treatment of PDX models reveals patterns of neuroblastoma chemoresistance. *Sci Adv* (2022) 8(43):eabq4617. doi: 10.1016/j.celrep.2019.09.071

47. Karlsson J, Valind A, Holmquist Mengelbier L, Bredin S, Cornmark L, Jansson C, et al. Four evolutionary trajectories underlie genetic intratumoral variation in childhood cancer. *Nat Genet* (2018) 50(7):944–50. doi: 10.1038/s41588-018-0131-y

48. Williams AP, Stewart JE, Stafman LL, Aye JM, Mroczek-Musulman E, Ren C, et al. Corruption of neuroblastoma patient derived xenografts with human T cell lymphoma. *J Pediatr Surg* (2019) 54(10):2117–9. doi: 10.1016/j.jpedsurg.2018.10.051

49. Moyer AM, Yu J, Sinnwell JP, Dockter TJ, Suman VJ, Weinshilboum RM, et al. Spontaneous murine tumors in the development of patient-derived xenografts: a potential pitfall. *Oncotarget* (2019) 10(39):3924–30. doi: 10.18632/oncotarget.27001

50. Tillman H, Janke LJ, Funk A, Vogel P, Rehg JE. Morphologic and immunohistochemical characterization of spontaneous Lymphoma/Leukemia in NSG mice. *Vet Pathol* (2020) 57(1):160–71. doi: 10.1177/0300985819882631

51. Gatzweiler C, Ridinger J, Herter S, Gerloff XF, ElHarouni D, Berker Y, et al. Functional therapeutic target validation using pediatric zebrafish xenograft models. *Cancers* (2022) 14(3):849. doi: 10.3390/cancers14030849

52. Almstedt E, Elgendy R, Hekmati N, Rosen E, Warn C, Olsen TK, et al. Integrative discovery of treatments for high-risk neuroblastoma. *Nat Commun* (2020) 11(1):71. doi: 10.1038/s41467-019-13817-8

53. Delloye-Bourgeois C, Bertin L, Thoinet K, Jarrosson L, Kindbeiter K, Buffet T, et al. Microenvironment-driven shift of Cohesion/Detachment balance within tumors induces a switch toward metastasis in neuroblastoma. *Cancer Cell* (2017) 32 (4):427–43.e8. doi: 10.1016/j.ccell.2017.09.006

54. Bate-Eya LT, Ebus ME, Koster J, den Hartog IJ, Zwijnenburg DA, Schild L, et al. Newly-derived neuroblastoma cell lines propagated in serum-free media recapitulate the genotype and phenotype of primary neuroblastoma tumours. *Eur J Cancer* (2014) 50(3):628–37. doi: 10.1016/j.ejca.2013.11.015

55. Barton J, Pacey K, Jain N, Kasia T, Edwards D, Thevanesan C, et al. Establishment and phenotyping of neurosphere cultures from primary neuroblastoma samples. *F1000Res* (2019) 8:823. doi: 10.12688/f1000research.18209.1

56. Fusco P, Parisatto B, Rampazzo E, Persano L, Frasson C, Di Meglio A, et al. Patient-derived organoids (PDOs) as a novel *in vitro* model for neuroblastoma tumours. *BMC cancer* (2019) 19(1):970. doi: 10.1186/s12885-019-6149-4

57. Thole TM, Toedling J, Sprüssel A, Pfeil S, Savelyeva L, Capper D, et al. Reflection of neuroblastoma intratumor heterogeneity in the new OHC-NB1 disease model. *Int J cancer* (2020) 146(4):1031–41. doi: 10.1002/ijc.32572

58. Nolan JC, Frawley T, Tighe J, Soh H, Curtin C, Piskareva O. Preclinical models for neuroblastoma: Advances and challenges. *Cancer letters* (2020) 474:53–62. doi: 10.1016/j.canlet.2020.01.015

59. Hansford LM, McKee AE, Zhang L, George RE, Gerstle JT, Thorner PS, et al. Neuroblastoma cells isolated from bone marrow metastases contain a naturally enriched tumor-initiating cell. *Cancer Res* (2007) 67(23):11234–43. doi: 10.1158/0008-5472.CAN-07-0718

60. Mohlin S, Pietras A, Wigerup C, Ora I, Andang M, Nilsson K, et al. Tumor-initiating cells in childhood neuroblastoma–letter. *Cancer Res* (2012) 72(3):821–2. author reply 3. doi: 10.1158/0008-5472.CAN-11-1761

61. Coulon A, Flahaut M, Mühlethaler-Mottet A, Meier R, Liberman J, Balmas-Bourloud K, et al. Functional sphere profiling reveals the complexity of neuroblastoma tumor-initiating cell model. *Neoplasia* (2011) 13(10):991–1004. doi: 10.1593/neo.11800

62. Persson CU, von Stedingk K, Bexell D, Merselius M, Braekeveldt N, Gisselsson D, et al. Neuroblastoma patient-derived xenograft cells cultured in stem-cell promoting medium retain tumorigenic and metastatic capacities but differentiate in serum. *Sci Rep* (2017) 7(1):10274. doi: 10.1038/s41598-017-09662-8

63. Gavin C, Geerts N, Cavanagh B, Haynes M, Reynolds CP, Loessner D, et al. Neuroblastoma invasion strategies are regulated by the extracellular matrix. *Cancers* (2021) 13(4):736. doi: 10.3390/cancers13040736

64. Ben Amar D, Thoinet K, Villalard B, Imbaud O, Costechareyre C, Jarrosson L, et al. Environmental cues from neural crest derivatives act as metastatic triggers in an embryonic neuroblastoma model. *Nat Commun* (2022) 13(1):2549. doi: 10.1038/s41467-022-30237-3

65. Bownes LV, Williams AP, Marayati R, Stafman LL, Markert H, Quinn CH, et al. EZH2 inhibition decreases neuroblastoma proliferation and *in vivo* tumor growth. *PloS One* (2021) 16(3):e0246244. doi: 10.1371/journal.pone.0246244

66. Koneru B, Farooqi A, Nguyen TH, Chen WH, Hindle A, Eslinger C, et al. ALT neuroblastoma chemoresistance due to telomere dysfunction-induced ATM activation is reversible with ATM inhibitor AZD0156. *Sci Transl Med* (2021) 13 (607):eabd5750. doi: 10.1126/scitranslmed.abd5750

67. Sengupta S, Das S, Crespo AC, Cornel AM, Patel AG, Mahadevan NR, et al. Mesenchymal and adrenergic cell lineage states in neuroblastoma possess distinct immunogenic phenotypes. *Nat Cancer* (2022) 3(10):1228–46. doi: 10.1038/s43018-022-00427-5

68. Abid K, Popovic MB, Bourloud KB, Schoumans J, Grand-Guillaume J, Grouzmann E, et al. The noradrenergic profile of plasma metanephrine in neuroblastoma patients is reproduced in xenograft mice models and arise from PNMT downregulation. *Oncotarget* (2021) 12(1):49–60. doi: 10.18632/oncotarget.27858

69. Eisenhofer G, Lenders JW, Goldstein DS, Mannelli M, Csako G, Walther MM, et al. Pheochromocytoma catecholamine phenotypes and prediction of tumor size and location by use of plasma free metanephrines. *Clin Chem* (2005) 51 (4):735–44. doi: 10.1373/clinchem.2004.045484

70. Müller M, Rösch L, Najafi S, Gatzweiler C, Ridinger J, Gerloff XF, et al. Combining APR-246 and HDAC-inhibitors: A novel targeted treatment option for neuroblastoma. *Cancers* (2021) 13(17):4476. doi: 10.3390/cancers13174476

71. Mosse YP, Fox E, Teachey DT, Reid JM, Safgren SL, Carol H, et al. A phase II study of alisertib in children with Recurrent/Refractory solid tumors or leukemia: Children's oncology group phase I and pilot consortium (ADVL0921). *Clin Cancer Res an Off J Am Assoc Cancer Res* (2019) 25(11):3229–38. doi: 10.1158/1078-0432.CCR-18-2675

72. Mossé YP, Lim MS, Voss SD, Wilner K, Ruffner K, Laliberte J, et al. Safety and activity of crizotinib for paediatric patients with refractory solid tumours or anaplastic large-cell lymphoma: A children's oncology group phase 1 consortium study. *Lancet Oncol* (2013) 14(6):472–80. doi: 10.1016/S1470-2045(13)70095-0

73. Cai J, Jacob S, Kurupi R, Dalton KM, Coon C, Greninger P, et al. High-risk neuroblastoma with NF1 loss of function is targetable using SHP2 inhibition. *Cell Rep* (2022) 40(4):111095. doi: 10.1016/j.celrep.2022.111095

74. Floros KV, Cai J, Jacob S, Kurupi R, Fairchild CK, Shende M, et al. MYCN-amplified neuroblastoma is addicted to iron and vulnerable to inhibition of the system xc-/Glutathione axis. *Cancer Res* (2021) 81(7):1896–908. doi: 10.1158/0008-5472.CAN-20-1641

75. Mohlin S, Hansson K, Radke K, Martinez S, Blanco-Apiricio C, Garcia-Ruiz C, et al. Anti-tumor effects of PIM/PI3K/mTOR triple kinase inhibitor IBL-302 in neuroblastoma. *EMBO Mol Med* (2019) 11(8):e10058. doi: 10.15252/emmm.201810058

76. Radke K, Hansson K, Sjölund J, Wolska M, Karlsson J, Esfandyari J, et al. Anti-tumor effects of rigosertib in high-risk neuroblastoma. *Transl Oncol* (2021) 14 (8):101149. doi: 10.1016/j.tranon.2021.101149

77. Hansson K, Radke K, Aaltonen K, Saarela J, Mañas A, Sjölund J, et al. Therapeutic targeting of KSP in preclinical models of high-risk neuroblastoma. *Sci Transl Med* (2020) 12(562):eaba4434. doi: 10.1126/scitranslmed.aba4434

78. Masanas M, Masiá N, Suárez-Cabrera L, Olivan M, Soriano A, Majem B, et al. The oral KIF11 inhibitor 4SC-205 exhibits antitumor activity and potentiates standard and targeted therapies in primary and metastatic neuroblastoma models. *Clin Transl Med* (2021) 11(10):e533. doi: 10.1002/ctm2.533

79. Grohmann C, Walker F, Devlin M, Luo MX, Chüeh AC, Doherty J, et al. Preclinical small molecule WEHI-7326 overcomes drug resistance and elicits response in patient-derived xenograft models of human treatment-refractory tumors. *Cell Death disease* (2021) 12(3):268. doi: 10.1038/s41419-020-03269-0

80. George SL, Lorenzi F, King D, Hartlieb S, Campbell J, Pemberton H, et al. Therapeutic vulnerabilities in the DNA damage response for the treatment of ATRX mutant neuroblastoma. *EBioMedicine* (2020) 59:102971. doi: 10.1016/j.ebiom.2020.102971

81. Bownes LV, Marayati R, Quinn CH, Beierle AM, Hutchins SC, Julson JR, et al. Pre-clinical study evaluating novel protein phosphatase 2A activators as therapeutics for neuroblastoma. *Cancers* (2022) 14(8):1952. doi: 10.3390/cancers14081952

82. Pan M, Wright WC, Chapple RH, Zubair A, Sandhu M, Batchelder JE, et al. The chemotherapeutic CX-5461 primarily targets TOP2B and exhibits selective

activity in high-risk neuroblastoma. *Nat Commun* (2021) 12(1):6468. doi: 10.1038/s41467-021-26640-x

83. Lowery CD, Dowless M, Renschler M, Blosser W, VanWye AB, Stephens JR, et al. Broad spectrum activity of the checkpoint kinase 1 inhibitor prexasertib as a single agent or chemopotentiator across a range of preclinical pediatric tumor models. *Clin Cancer Res an Off J Am Assoc Cancer Res* (2019) 25(7):2278–89. doi: 10.1158/1078-0432.CCR-18-2728

84. O'Donohue TJ, Ibáñez G, Coutinho DF, Mauguen A, Siddiquee A, Rosales N, et al. Translational strategies for repotrectinib in neuroblastoma. *Mol Cancer Ther* (2021) 20(11):2189–97. doi: 10.1158/1535-7163.MCT-21-0126

85. Arlt B, Zasada C, Baum K, Wuenschel J, Mastrobuoni G, Lodrini M, et al. Inhibiting phosphoglycerate dehydrogenase counteracts chemotherapeutic efficacy against MYCN-amplified neuroblastoma. *Int J cancer* (2021) 148(5):1219–32. doi: 10.1002/ijc.33423

86. Henssen AG, Reed C, Jiang E, Garcia HD, von Stebut J, MacArthur IC, et al. Therapeutic targeting of PGBD5-induced DNA repair dependency in pediatric solid tumors. *Sci Transl Med* (2017) 9(414):eaam9078. doi: 10.1126/scitranslmed.aam9078

87. Infarinato NR, Park JH, Krytska K, Ryles HT, Sano R, Szigety KM, et al. The ALK/ROS1 inhibitor PF-06463922 overcomes primary resistance to crizotinib in ALK-driven neuroblastoma. *Cancer discovery* (2016) 6(1):96–107. doi: 10.1158/2159-8290.CD-15-1056

88. Huo Z, Bilang R, Supuran CT, von der Weid N, Bruder E, Holland-Cunz S, et al. Perfusion-based bioreactor culture and isothermal microcalorimetry for preclinical drug testing with the carbonic anhydrase inhibitor SLC-0111 in patient-derived neuroblastoma. *Int J Mol Sci* (2022) 23(6):3128. doi: 10.3390/ijms23063128

89. Nunes C, Depestel L, Mus L, Keller KM, Delhaye L, Louwagie A, et al. RRM2 enhances MYCN-driven neuroblastoma formation and acts as a synergistic target with CHK1 inhibition. *Sci Adv* (2022) 8(28):eabn1382. doi: 10.1126/sciadv.abn1382

90. Krytska K, Ryles HT, Sano R, Raman P, Infarinato NR, Hansel TD, et al. Crizotinib synergizes with chemotherapy in preclinical models of neuroblastoma. *Clin Cancer Res an Off J Am Assoc Cancer Res* (2016) 22(4):948–60. doi: 10.1158/1078-0432.CCR-15-0379

91. Wood AC, Krytska K, Ryles HT, Infarinato NR, Sano R, Hansel TD, et al. Dual ALK and CDK4/6 inhibition demonstrates synergy against neuroblastoma. *Clin Cancer Res an Off J Am Assoc Cancer Res* (2017) 23(11):2856–68. doi: 10.1158/1078-0432.CCR-16-1114

92. Trigg RM, Lee LC, Prokoph N, Jahangiri L, Reynolds CP, Amos Burke GA, et al. The targetable kinase PIM1 drives ALK inhibitor resistance in high-risk neuroblastoma independent of MYCN status. *Nat Commun* (2019) 10(1):5428. doi: 10.1038/s41467-019-13315-x

93. Dalton KM, Krytska K, Lochmann TL, Sano R, Casey C, D'Aulerio A, et al. Venetoclax-based rational combinations are effective in models of MYCN-amplified neuroblastoma. *Mol Cancer Ther* (2021) 20(8):1400–11. doi: 10.1158/1535-7163.MCT-20-0710

94. Nguyen TH, Koneru B, Wei SJ, Chen WH, Makena MR, Urias E, et al. Fenretinide *via* NOXA induction, enhanced activity of the BCL-2 inhibitor venetoclax in high BCL-2-Expressing neuroblastoma preclinical models. *Mol Cancer Ther* (2019) 18(12):2270–82. doi: 10.1158/1535-7163.MCT-19-0385

95. Hindle A, Koneru B, Makena MR, Lopez-Barcons L, Chen WH, Nguyen TH, et al. The O6-methyguanine-DNA methyltransferase inhibitor O6-benzylguanine enhanced activity of temozolomide + irinotecan against models of high-risk neuroblastoma. *Anticancer Drugs* (2021) 32(3):233–47. doi: 10.1097/CAD.0000000000001020

96. Wrobel JK, Najafi S, Ayhan S, Gatzweiler C, Krunic D, Ridinger J, et al. Rapid *In vivo* validation of HDAC inhibitor-based treatments in neuroblastoma zebrafish xenografts. *Pharm (Basel)* (2020) 13(11):345. doi: 10.3390/ph13110345

97. Timme N, Han Y, Liu S, Yosief HO, García HD, Bei Y, et al. Small-molecule dual PLK1 and BRD4 inhibitors are active against preclinical models of pediatric solid tumors. *Transl Oncol* (2020) 13(2):221–32. doi: 10.1016/j.tranon.2019.09.013

98. Ham J, Costa C, Sano R, Lochmann TL, Sennott EM, Patel NU, et al. Exploitation of the apoptosis-primed state of MYCN-amplified neuroblastoma to develop a potent and specific targeted therapy combination. *Cancer Cell* (2016) 29(2):159–72. doi: 10.1016/j.ccell.2016.01.002

99. Decaesteker B, Denecker G, Van Neste C, Dolman EM, Van Loocke W, Gartlgruber M, et al. TBX2 is a neuroblastoma core regulatory circuitry component enhancing MYCN/FOXM1 reactivation of DREAM targets. *Nat Commun* (2018) 9(1):4866. doi: 10.1038/s41467-018-06699-9

100. Sano R, Krytska K, Larmour CE, Raman P, Martinez D, Ligon GF, et al. An antibody-drug conjugate directed to the ALK receptor demonstrates efficacy in preclinical models of neuroblastoma. *Sci Transl Med* (2019) 11(483):eaau9732. doi: 10.1126/scitranslmed.aau9732

101. Quinn CH, Beierle AM, Hutchins SC, Marayati R, Bownes LV, Stewart JE, et al. Targeting high-risk neuroblastoma patient-derived xenografts with oncolytic virotherapy. *Cancers* (2022) 14(3):762. doi: 10.3390/cancers14030762

102. Barry WE, Jackson JR, Asuelime GE, Wu HW, Sun J, Wan Z, et al. Activated natural killer cells in combination with anti-GD2 antibody dinutuximab improve survival of mice after surgical resection of primary neuroblastoma. *Clin Cancer Res an Off J Am Assoc Cancer Res* (2019) 25(1):325–33. doi: 10.1158/1078-0432.CCR-18-1317

103. Nguyen R, Moustaki A, Norrie JL, Brown S, Akers WJ, Shirinifard A, et al. Interleukin-15 enhances anti-GD2 antibody-mediated cytotoxicity in an orthotopic PDX model of neuroblastoma. *Clin Cancer Res an Off J Am Assoc Cancer Res* (2019) 25(24):7554–64. doi: 10.1158/1078-0432.CCR-19-1045

104. Nguyen R, Zhang X, Sun M, Abbas S, Seibert C, Kelly MC, et al. Anti-GD2 antibodies conjugated to IL15 and IL21 mediate potent antitumor cytotoxicity against neuroblastoma. *Clin Cancer Res an Off J Am Assoc Cancer Res* (2022) 28(17):3785–96. doi: 10.1158/1078-0432.CCR-22-0717

105. Monterrubio C, Paco S, Olaciregui NG, Pascual-Pasto G, Vila-Ubach M, Cuadrado-Vilanova M, et al. Targeted drug distribution in tumor extracellular fluid of GD2-expressing neuroblastoma patient-derived xenografts using SN-38-loaded nanoparticles conjugated to the monoclonal antibody 3F8. *J Control Release* (2017) 255:108–19. doi: 10.1016/j.jconrel.2017.04.016

106. Langenberg KPS, Looze EJ, Molenaar JJ. The landscape of pediatric precision oncology: Program design, actionable alterations, and clinical trial development. *Cancers* (2021) 13(17):4324. doi: 10.3390/cancers13174324

107. Parsons DW, Janeway KA, Patton DR, Winter CL, Coffey B, Williams PM, et al. Actionable tumor alterations and treatment protocol enrollment of pediatric and young adult patients with refractory cancers in the national cancer institute-children's oncology group pediatric MATCH trial. *J Clin Oncol Off J Am Soc Clin Oncol* (2022) 40(20):2224–34. doi: 10.1200/JCO.21.02838

108. van Tilburg CM, Pfaff E, Pajtler KW, Langenberg KPS, Fiesel P, Jones BC, et al. The pediatric precision oncology INFORM registry: Clinical outcome and benefit for patients with very high-evidence targets. *Cancer discovery* (2021) 11(11):2764–79. doi: 10.1158/2159-8290.CD-21-0094

109. Worst BC, van Tilburg CM, Balasubramanian GP, Fiesel P, Witt R, Freitag A, et al. Next-generation personalised medicine for high-risk paediatric cancer patients - the INFORM pilot study. *Eur J Cancer* (2016) 65:91–101. doi: 10.1016/j.ejca.2016.06.009

110. Newman S, Nakitandwe J, Kesserwan CA, Azzato EM, Wheeler DA, Rusch M, et al. Genomes for kids: The scope of pathogenic mutations in pediatric cancer revealed by comprehensive DNA and RNA sequencing. *Cancer discovery* (2021) 11(12):3008–27. doi: 10.1158/2159-8290.CD-20-1631

111. Houghton PJ, Morton CL, Tucker C, Payne D, Favours E, Cole C, et al. The pediatric preclinical testing program: Description of models and early testing results. *Pediatr Blood cancer* (2007) 49(7):928–40. doi: 10.1002/pbc.21078

112. Zwaan CM, Kearns P, Caron H, Verschuur A, Riccardi R, Boos J, et al. The role of the 'innovative therapies for children with cancer' (ITCC) European consortium. *Cancer Treat Rev* (2010) 36(4):328–34. doi: 10.1016/j.ctrv.2010.02.008

113. Lau LMS, Mayoh C, Xie J, Barahona P, MacKenzie KL, Wong M, et al. *In vitro* and in vivo drug screens of tumor cells identify novel therapies for high-risk child cancer. *EMBO Mol Med* (2022) 14(4):e14608. doi: 10.15252/emmm.202114608

114. Langenberg K, Dolman E, Molenaar J. Abstract A40: Integration of high-throughput drug screening on patient-derived organoids into pediatric precision medicine programs: The future is now! *Cancer Res* (2020) 80(s):A40. doi: 10.1158/1538-7445.PEDCA19-A40

115. ElHarouni D, Berker Y, Peterziel H, Gopisetty A, Turunen L, Kreth S, et al. iTReX: Interactive exploration of mono- and combination therapy dose response profiling data. *Pharmacol Res* (2022) 175:105996. doi: 10.1016/j.phrs.2021.105996

116. Berker Y, ElHarouni D, Peterziel H, Fiesel P, Witt O, Oehme I, et al. Patient-by-Patient deep transfer learning for drug-response profiling using confocal fluorescence microscopy of pediatric patient-derived tumor-cell spheroids. *IEEE Trans Med Imaging* (2022) 41(12):3981-99. doi: 10.1109/TMI.2022.3205554

117. Tadeo I, Berbegall AP, Castel V, García-Miguel P, Callaghan R, Påhlman S, et al. Extracellular matrix composition defines an ultra-high-risk group of neuroblastoma within the high-risk patient cohort. *Br J cancer* (2016) 115(4):480–9. doi: 10.1038/bjc.2016.210

118. Burgos-Panadero R, El Moukhtari SH, Noguera I, Rodríguez-Nogales C, Martín-Vañó S, Vicente-Munuera P, et al. Unraveling the extracellular matrix-tumor cell interactions to aid better targeted therapies for neuroblastoma. *Int J Pharm* (2021) 608:121058. doi: 10.1016/j.ijpharm.2021.121058

119. Martinov T, McKenna KM, Tan WH, Collins EJ, Kehret AR, Linton JD, et al. Building the next generation of humanized hemato-lymphoid system mice. *Front Immunol* (2021) 12:643852. doi: 10.3389/fimmu.2021.643852

120. Rongvaux A, Willinger T, Martinek J, Strowig T, Gearty SV, Teichmann LL, et al. Development and function of human innate immune cells in a humanized mouse model. *Nat Biotechnol* (2014) 32(4):364–72. doi: 10.1038/nbt.2858

121. Nguyen R, Patel AG, Griffiths LM, Dapper J, Stewart EA, Houston J, et al. Next-generation humanized patient-derived xenograft mouse model for pre-clinical antibody studies in neuroblastoma. *Cancer Immunol Immunother* (2021) 70(3):721–32. doi: 10.1007/s00262-020-02713-6

122. Drost J, Clevers H. Organoids in cancer research. *Nat Rev Cancer* (2018) 18 (7):407–18. doi: 10.1038/s41568-018-0007-6

123. Tuveson D, Clevers H. Cancer modeling meets human organoid technology. *Sci (New York NY)* (2019) 364(6444):952–5. doi: 10.1126/science.aaw6985

124. Kholosy WM, Derieppe M, van den Ham F, Ober K, Su Y, Custers L, et al. Neuroblastoma and DIPG organoid coculture system for personalized assessment of novel anticancer immunotherapies. *J Pers Med* (2021) 11(9):869. doi: 10.3390/jpm11090869

125. Jenkins RW, Aref AR, Lizotte PH, Ivanova E, Stinson S, Zhou CW, et al. Ex vivo profiling of PD-1 blockade using organotypic tumor spheroids. *Cancer discovery* (2018) 8(2):196–215. doi: 10.1158/2159-8290.CD-17-0833

126. Cui X, Ma C, Vasudevaraja V, Serrano J, Tong J, Peng Y, et al. Dissecting the immunosuppressive tumor microenvironments in glioblastoma-on-a-Chip for optimized PD-1 immunotherapy. *Elife* (2020) 9:e52253. doi: 10.7554/eLife.52253

127. Nothdurfter D, Ploner C, Coraça-Huber DC, Wilflingseder D, Müller T, Hermann M, et al. 3D bioprinted, vascularized neuroblastoma tumor environment in fluidic chip devices for precision medicine drug testing. *Biofabrication* (2022) 14 (3):035002. doi: 10.1088/1758-5090/ac5fb7

128. Yu JL, Chan S, Fung MK, Chan GC. Mesenchymal stem cells accelerated growth and metastasis of neuroblastoma and preferentially homed towards both primary and metastatic loci in orthotopic neuroblastoma model. *BMC cancer* (2021) 21(1):393. doi: 10.1186/s12885-021-08090-2

129. Grigoryan A, Zacharaki D, Balhuizen A, Côme CR, Garcia AG, Hidalgo Gil D, et al. Engineering human mini-bones for the standardized modeling of healthy hematopoiesis, leukemia, and solid tumor metastasis. *Sci Trans Med* (2022) 14 (666):eabm6391. doi: 10.1126/scitranslmed.abm6391

frontiers | Frontiers in Oncology

TYPE Original Research
PUBLISHED 20 January 2023
DOI 10.3389/fonc.2022.1082927

OPEN ACCESS

EDITED BY
Massimo Broggini,
Mario Negri Institute for Pharmacological Research (IRCCS), Italy

REVIEWED BY
Michael Volkmar,
Helmholtz Institute for Translational Oncology, German Cancer Research Center (DKFZ), Germany
Alfonso De Stefano,
G. Pascale National Cancer Institute Foundation (IRCCS), Italy

*CORRESPONDENCE
Michael Linnebacher
Michael.linnebacher@med.uni-rostock.de

†These authors have contributed equally to this work

SPECIALTY SECTION
This article was submitted to Cancer Molecular Targets and Therapeutics, a section of the journal Frontiers in Oncology

RECEIVED 28 October 2022
ACCEPTED 23 November 2022
PUBLISHED 20 January 2023

CITATION
von den Driesch J, Flöttmann J, Prall F, Mullins CS, Linnebacher M and Bürtin F (2023) HROP68: A rare case of medullary pancreatic cancer—characterization and chemosensitivity of the first patient-derived cell line. *Front. Oncol.* 12:1082927. doi: 10.3389/fonc.2022.1082927

HROP68: A rare case of medullary pancreatic cancer—characterization and chemosensitivity of the first patient-derived cell line

Jens von den Driesch[1†], Jana Flöttmann[1†], Friedrich Prall[2], Christina S. Mullins[1], Michael Linnebacher[1*] and Florian Bürtin[1]

[1]Clinic of General, Visceral, Vascular and Transplantation Surgery, University Medical Center Rostock, University of Rostock, Rostock, Germany, [2]Institute of Pathology, University Medical Center Rostock, University of Rostock, Rostock, Germany

Introduction: Medullary pancreatic carcinoma (MPC) is a rare subtype of pancreatic ductal adenocarcinoma. MPCs represent less than 1% of all pancreatic cancers, and, with only 26 cases in the literature, knowledge regarding drug response and treatment outcome is very limited.

Material and methods: We present the case of a 64-year-old male patient with MPC who was treated by left pancreatic resection and adjuvant chemotherapy. Due to local recurrence, the patient underwent intended curative reoperation. From both surgical specimens, patient-derived xenografts (PDXs) and, from the recurrence, a patient-derived cell line (PDCL) were established. We subsequently performed an in-depth characterization of this cell line including phenotypic characterization, surface protein expression, growth, and migratory performance as well as mutational analysis using whole-exome sequencing (WES). Additionally, *in vitro* drug sensitivity toward the standard-of-care chemotherapeutic regimen and selected targeted therapies was evaluated.

Results: The pathological and molecular properties of this rare MPC case observed in the patient's tumors are preserved in the corresponding PDX and the PDCL of HROP68Tu2. Despite displaying an "immunogenic phenotype" with marked T-cell infiltration and a high-level expression of HLA II and Programmed death-ligand 1 (PD-L1), molecular analysis revealed microsatellite stability but a multitude of mutations affecting KRAS, TP53, KAT6B, FOXG1, RUNX1, and GRIK2 among others. Furthermore, HROP68Tu2 cells were susceptible toward 5-FU, irinotecan, oxaliplatin, gemcitabine, paclitaxel, and erlotinib as single agents, but only a moderate synergistic response was seen to the drugs of the FOLFIRINOX regimen. Even worse, the drugs of the two combinations gemcitabine plus paclitaxel and gemcitabine plus erlotinib showed antagonistic effects. Moreover, lapatinib,

PRIMA-Met1, and olaparib selected as targeted therapeutics according to the mutational profiles and protein expression inhibited HROP68Tu2 cells' growth.

Conclusion: This study illustrates the establishment of the first preclinical MPC models as well as the first in-depth characterization of an MPC PDCL. Since the scientific and clinical knowledge of this rare pancreatic cancer type is very limited, the presented models contribute to a better understanding of MPC and might be a valuable tool for the development of future treatment options.

KEYWORDS

PDAC - pancreatic ductal adenocarcinoma, rare malignancy, medullary adenocarcinoma, precision medicine, patient-derived cell line

1 Introduction

Pancreatic ductal adenocarcinoma (PDAC) is the fourth leading cause of cancer-related death in the United States and the seventh worldwide (1, 2). Despite an increasing incidence, especially in countries with a high human development index, the prognosis remains dismal with reported 5-year survival rates ranging from 4.2% to 10% (1–3). Since most patients present with advanced cancer stages, only 10%–16% of the patients are eligible for resection, currently the only curative treatment option. Yet, those treated by surgery also show a poor prognosis with a median survival of 18 months and a 5-year survival rate of 15%–25% due to early local recurrence or metastasis (1, 4, 5).

Recent survival improvements are mainly attributed to intensified adjuvant and palliative chemotherapy regimens. In the adjuvant setting, modified FOLFIRINOX, a drug regimen comprised of folinic acid, fluorouracil (5-FU), irinotecan, and oxaliplatin, as well as the combination of gemcitabine with capecitabine has shown improved survival compared to gemcitabine monotherapy (6, 7). In locally advanced or metastatic stages, FOLFIRINOX and gemcitabine plus nanoparticle-bound paclitaxel are first-line treatment options (8). Nevertheless, most PDACs are characterized by a markedly low susceptibility to chemotherapy mediated by a specific tumor microenvironment with a dense desmoplastic reaction and the infiltrates of immune-suppressive cell populations as well as by a low tumor mutational burden (TMB) (9–11). In contrast, pancreatic medullary carcinoma (MPC), a rare subtype of PDAC, appears pathologically cell rich and low in stroma and is often characterized by a high TMB and microsatellite instability (12, 13). To the best of our knowledge, our group established the first patient-derived xenograft (PDX) and patient-derived cell line (PDCL) from a recurrent medullary pancreatic carcinoma, named HROP68Tu2, with distinct clinical, pathological, and molecular characteristics. In addition to the morphological and molecular characterization of the PDCL, the response to therapeutic agents was evaluated *in vitro*. 5-FU, irinotecan, oxaliplatin, gemcitabine, paclitaxel, and erlotinib were tested as single agents and in the clinically established combinations FOLFIRINOX, gemcitabine combined with paclitaxel (GemPac), and gemcitabine plus erlotinib (GemErlo). Since whole exome sequencing (WES) revealed a distinct mutational profile, and the tumor cells expressed high levels of HER2 and EGFR, the targeted drugs lapatinib, olaparib, and PRIMA-Met1 were additionally tested.

2 Materials and methods

2.1 Patient-derived xenograft and cell line establishment

The collection and processing of tumor tissue have been approved by the institutional review board of the University Medical Center Rostock (A 2018-0054). All animal experiments have been approved by the Landesamt für Landwirtschaft, Lebensmittelsicherheit und Fischerei Mecklenburg-Vorpommern under the registration numbers LALLF M-V/TSD/7221.3-1-007/19.

The tumor processing and establishment of PDX and PDCL were conducted as described previously (14, 15). In brief, after surgical en bloc resection of the tumor, a small tumor piece irrelevant for the evaluation of the resection margin was removed, cleaned, cut into cubes of 3 × 3 × 3 mm under sterile conditions, and cryopreserved immediately. Afterward, tumor specimens were thawed, incubated in Matrigel® (Corning, New York, USA), and subcutaneously implanted into the flanks of NSG mice. After reaching the required tumor size, mice were euthanized and PDX were explanted and cut accordingly for re-engraftment, histological examination, and snap freezing.

For cell line establishment, tumor tissue was mechanically dissected and passed through a 100 µm cell strainer. After centrifugation and resuspension in PBS, cells were seeded in a collagen-coated 6-well plate in a culture medium including antibiotics and antimycotics and incubated at 37°C in a humidified atmosphere of 5% CO_2. As stable growth was observed, cells were transferred into a 25 cm^2 culture flask with a standard culture medium (DMEM/F12 (1:1), 5% fetal calf serum (FCS), and 2 mM L-glutamine; all cell culture reagents were from PAN-Biotech, Aidenbach, Germany. Cells were regularly tested for mycoplasma contamination using the PlasmoTest™—Mycoplasma Detection Kit (*In vivo*Gen, San Diego, CA, USA) according to the manufacturer's protocol.

2.2 Short tandem repeat analysis

The concordance of HROP68Tu2 PDCL cells and healthy donor tissue was confirmed by short tandem repeat (STR) analysis as previously described (14). In short, DNA from donor tissue and tumor cells was isolated and the fragments of D5S818, D7S820, D16S539, D13S317, vWA, TPOX, THO1, CSF1PO, and Amelogenin were PCR-amplified with fluorescence-labeled primers. Subsequently, samples were size-separated and analyzed by automated capillary electrophoresis (Thermo Fisher Scientific, Waltham, MA, USA) (14).

2.3 Growth and migration

For doubling time determination, 4×10^4 HROP68Tu2 cells were seeded in a coated 24-well plate and allowed to attach for 72 h. To determine the mass of the vital cells, a crystal violet assay was conducted as described previously (16). Cells were stained with 0.2% crystal violet every 24 h in quadruplicates for six consecutive days and absorption was measured at 540 nm using the plate reader Tecan Infinite (Tecan, Männedorf, Switzerland). Migration speed was determined by the scratch assay. Cells grown to 100% confluency in a 6-well plate were switched to a serum-free medium and scratched with a 10 µl pipette tip. Three distances between edges were measured every 24 h for four consecutive days at 10× magnification using an inverted microscope (Carl Zeiss AG, Jena, Germany). The experiment was performed in independent triplicates.

2.4 Flow cytometry

The cell surface proteins of HROP68Tu2 cells were analyzed by flow cytometry using FACS Calibur (BD Bioscience, Franklin Lakes, NJ, USA) and open-source FCSalyser software. A panel of FITC-, PE-, and APC-conjugated antibodies was used for direct staining, targeting CD13, CD15, CD29, CD40, CD54, CD58, CD66adecb, CD71, CD86, CD95, HLA class I, HLA class II (Immunotools, Friesoythe, Germany); CD26, CD80, CD178 (eBioscience, Thermo Fisher Scientific, MA, USA); CD152, CD227 (Biolegend, San Diego, CA, USA); CD90 (Dianova, Eching, Germany); and CD326 (Miltenyi Biotech, Bergisch-Gladbach, Germany). Pembrolizumab (anti-PD-1), atezolizumab (anti-PD-L1), cetuximab (anti-EGFR), trastuzumab (anti-HER2), mesothelin (Biolegend, San Diego, CA, USA), and RP215 (Santa Cruz Biotechnologies, Dallas, TX, USA) were used as primary antibodies and labeled with FITC-conjugated polyclonal anti-human and anti-mouse IgG antibodies (Immunotools) for indirect staining.

2.5 Whole exome sequencing and microsatellite instability (MSI) score

The WES of the donor tumor tissue of HROP68 (primary and local recurrence as well as PDX models) was conducted by Centogene (Rostock, Germany) according to the protocol described by Trujillano and colleagues (17). In brief, DNA extraction was done using the QIAcube instrument with the QIAamp DNA Blood Mini QIAcube Kit (Qiagen, Hilden, Germany). In the exome, the target regions were amplified, and raw sequence data were analyzed. The HiSeq4000 platform (Illumina, San Diego, CA, USA) was used for sequencing. The used exome version was Centogene's "CentoXome," which covers approximately 33 Mb CCDS and is based on the Twist Bio Human Core Exome. Bioinformatic analysis was conducted as described by Matschos et al. (14). Pathogenetic classification was verified by an automated query to ClinVar (https://www.ncbi.nlm.nih.gov/clinvar/ accessed on 23.09.2022) followed by manual evaluation.

The MSI status of HROP68Tu2 was assessed using MSIsensor as described (18), a program that automatically detects somatic microsatellite changes, based on standard tumor-normal paired next- generation sequencing data. The number of somatic homopolymers and microsatellite sites is compared to the total number of sites. A percentage of 3.5%–20% somatic mutations is considered MSI-Low (MSI-L) and >20% MSI-High (MSI-H) (18).

2.6 *In vitro* drug response

The triplicates of HROP68Tu2 cells were seeded into a 96-well plate (1×10^4). After 24 h, chemotherapeutics were added with a serial dilution technique, sparing healthy controls. The medium and drugs, respectively, were changed after 96 h to avoid deterioration effects. After 168 h, the medium was discarded, and cells were rinsed with PBS and analyzed by the crystal violet assay as described above. All assays were performed in independent triplicates. Lapatinib, PRIMA-1Met and olaparib (Hölzel Diagnostika, Köln, Germany), 5-FU, irinotecan,

10.3389/fonc.2022.1082927

oxaliplatin, gemcitabine, paclitaxel, and erlotinib as single agents plus the combinations FOLFIRINOX, GemPac, and GemErlo in molar ratios analogous to the clinical regimen were tested (FOLFIRINOX: 1.07 folinic acid, 1.00 irinotecan, 80.95 5-FU, 0.80 oxaliplatin; GemPac: 1.00 gemcitabine, 0.04 paclitaxel (19). GemErlo: 1.00 gemcitabine, 0.21 erlotinib (20)). Individual interactions between 5-FU, irinotecan, and oxaliplatin were not assessed as monotherapy or other combinations are not recommended for clinical use. To evaluate the drug interactions, combination indices (CIs) (CI > 1.3 indicates antagonism, and CI = 0.6–0.8 indicates moderate synergism (19)) were calculated using the following equation (19):

$$CI = \frac{IC50\ of\ combination\ (Drug\ 1\ and\ 2)\ relative\ to\ Drug\ 1}{IC50\ of\ Drug\ 1\ alone} + \frac{IC50\ of\ combination\ (Drug\ 1\ and\ 2)\ relative\ to\ Drug\ 2}{IC50\ of\ Drug\ 2\ alone}$$

2.7 Statistics

IC_{50} and IC_{20} values were calculated and analyzed by an unpaired Student's t-test using Graph Pad Prism 5 (Graph Pad Software, San Diego, CA, USA). P-values ≤ 0.05 were considered statistically significant.

3 Results

3.1 Clinical case

A 64-year-old man presented with an excessive weight loss of 13 kg and fatigue during the last 5 months. Contrast-enhanced computed tomography (CEPT) revealed a large tumor of the pancreatic tail (Figure 1), and the patient was referred to our clinic for primary resection. He had no history of smoking, alcohol abuse, or prior cancer and neither did his first-degree relatives. Pancreatic left resection with splenectomy removed a soft and fragile, encapsulated tumor mass. Adjuvant treatment comprised of two cycles modified FOLFIRINOX, subsequently switched to five cycles of gemcitabine due to 5-FU-induced coronary vasospasm. Follow-up CEPT exhibited local recurrence in the left upper abdomen 11 months after resection. Since no distant metastasis was diagnosed, radical en bloc resection including the left

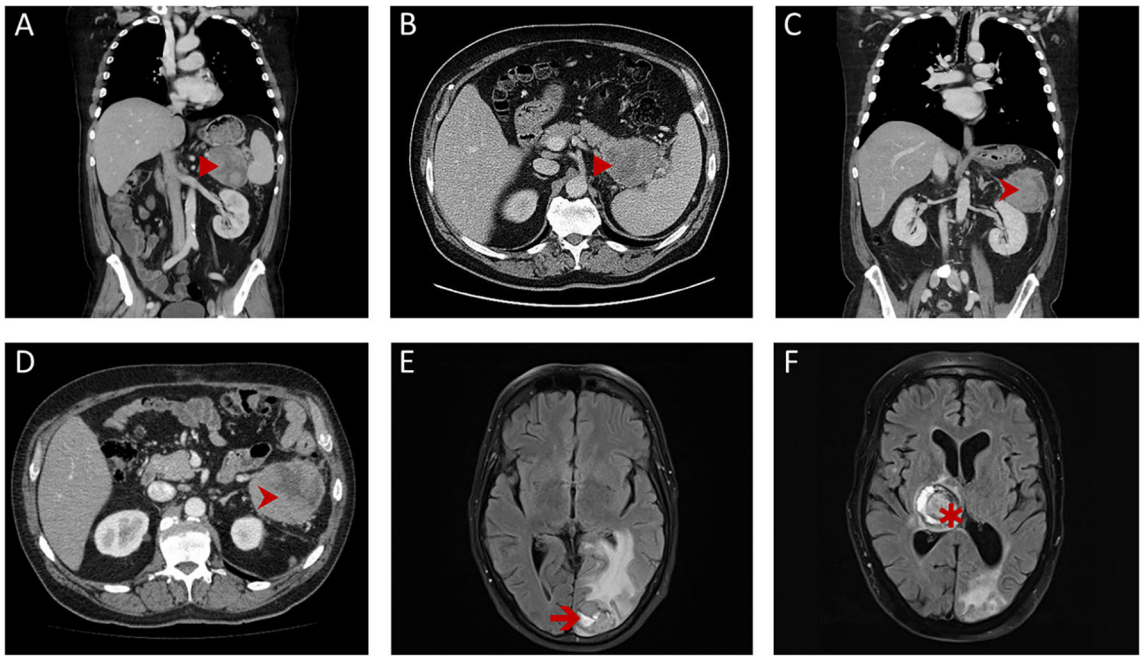

FIGURE 1
Radiological findings. First contrast-enhanced computed tomography (CEPT; **A**, **B**) of the thorax and abdomen revealed a large tumor (►) of the pancreatic tail, close to the splenic hilum with a pseudo-encapsulated appearance. Follow-up CEPT **(C, D)** showed isolated local recurrence (➢) with similar features in the left-upper abdomen and the retroperitoneum. Repeated magnetic resonance imaging scans of the brain showed a left occipital metastasis (➔) shortly after resection for local recurrence **(E)** and a rapidly progressing metastasis of the thalamus region (✻) over the course of palliative systemic treatment **(F)**.

colonic flexure and adrenal gland was performed. Pathological examination stated the completeness of resection and confirmed the origin of this second tumor from the previously resected MPC. The patient presented with severe disorientation and motor aphasia 2 weeks after discharge. Brain magnetic resonance imaging revealed occipital and parietal metastases, which were then treated by stereotactic radiotherapy. Subsequently, palliative systemic therapy was commenced, adding up to four cycles of gemcitabine plus nab-paclitaxel and one cycle of gemcitabine monotherapy in total. Although additional treatment with pembrolizumab was scheduled, the patient succumbed early to rapidly progressive cerebral metastases 23 months after the primary resection.

3.2 Pathology

The histologic examination of the primary tumor led to a diagnosis of MPC: the tumor was composed of solid sheets and nests of large polygonal neoplastic epithelial cells' paucity of stromal components with polymorphous vesicular nuclei (Figure 2) in a stroma-poor background. Tumor borders were pushing and sharply delineated, and a brisk lymphocytic and histiocytic infiltrate was seen. A high mitotic index of 80%–90% and fairly large areas of tumor necrosis attested to a rapidly growing neoplasm. The tumor cells were immunohistochemically positive using a pan-cytokeratin cocktail (AE1/3) as well as Ber-EP4 and CK7 positive, whereas CK20, CDX2, HMB45, Hepar-1, LCA, and AFP immunostains were negative. Mismatch repair protein MLH1 and MSH2 expression was retained, molecular MSI testing (Bethesda markers plus the mononucleotide marker CAT25 (21) additionally confirmed a microsatellite-stable tumor. PD-L1 (clone 22C3) immunostaining was positive in approximately 20% of the tumor cells, albeit membranous immunostaining was weak, mostly; the tumor-infiltrating lymphocytes and histiocytes were PD-L1 positive throughout. This allowed the conclusion that this MPC was immunogenic.

3.3 Patient-derived xenograft establishment

Successful engraftment, defined as tumor outgrowth to a target volume of 1,500 mm^3, was observed after the implantation of the primary resected tumor (HROP68Tu1) as well as the local recurrence (HROP68Tu2). In both cases, two out of two mice showed tumor outgrowth in at least one flank. HROP68Tu2 reached the target size 168 days after implantation. The growth kinetics of HROP86Tu2 compared well to those of other successfully engrafted pancreatic PDXs (n = 12) established from our group (Figure 3A). To confirm histopathological congruency with the original tumor and to exclude a potential murine lymphoma, a common pitfall in xenograft development, histologic sections (hematoxylin–eosin and PD-L1 immunostaining) were reviewed by an experienced pathologist (Figures 3B, C).

3.4 Morphology, growth kinetics, and migration of HROP68Tu2 cell line

A permanent 2-dimensional (2-D) cell line was established by immediate incubation of freshly resected tissue obtained from the secondary surgery (HROP68Tu2) as described before (22). After adaption to standard culture conditions, HROP68Tu2 cells were passaged more than 40 times as a permanent cell line. Cells were regularly tested negative for mycoplasma contamination. Cross-contamination or mix-up was excluded by STR analysis, confirming the donor–patient origin. HROP68Tu2 cells grew evenly as an adherent monolayer with heterogeneous cell size

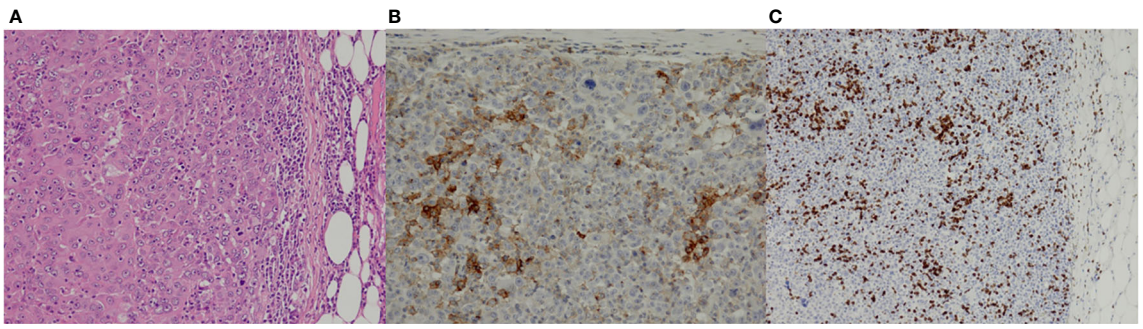

FIGURE 2
Pathological findings of the primary cancer. Hematoxylin–eosin stain (**A**; ×10) showed the solid sheets and nests of large polygonal neoplastic epithelial cells with a paucity of stromal components. Immunostaining for PD-L1 (**B**; ×20) and CD3 (**C**; ×10) reflected the immunogenic properties of the tumor.

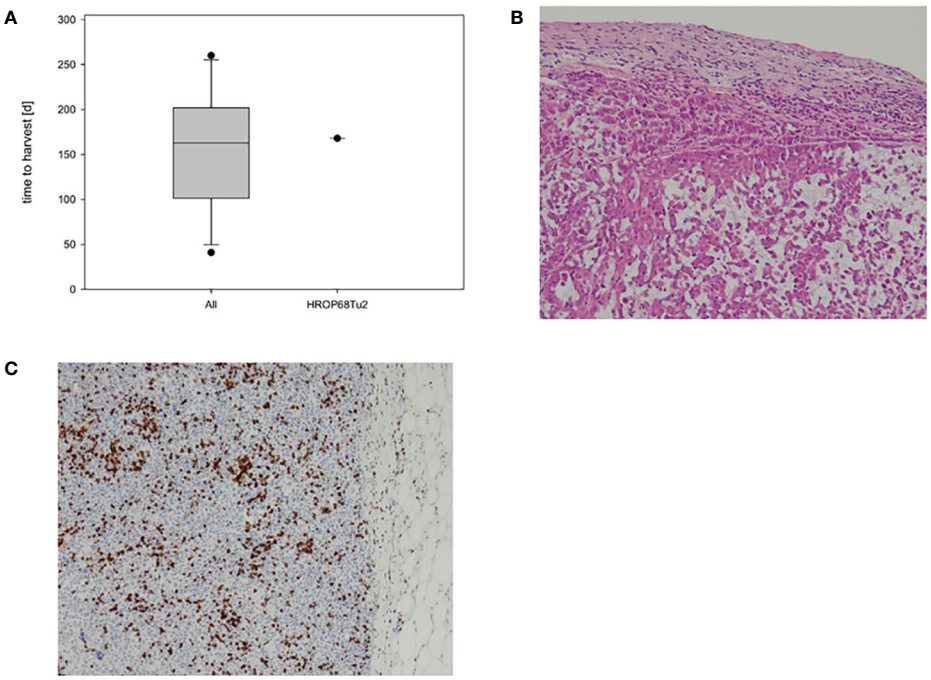

FIGURE 3
HROP68Tu2 PDX. Growth kinetics of HROP68Tu2 **(A)** compared to other pancreatic PDXs with successful outgrowth in passage fT0 (n = 12). The *in vivo* growth of HROP68Tu2 did not differ from the median growth rate of other pancreatic PDX. The hematoxylin–eosin stain of the PDX (B; 20x) revealed a close resemblance to the original donor tumor **(B)**. Tumor cells showed strong immunostaining for PD-L1 **(C)**.

and morphology (Figure 4). Doubling time in the exponential growth phase was 89.56 h (± 17.46). Morphology and growth did not change significantly during 40 consecutive passages.

Cells migrated with 1.78 µm/h (± 0.84) in a classical scratch assay. The migratory behavior appeared to be invasive as cells detached from the scratch's edges and migrated into the scratch as single cells (Figure 5).

3.5 Flow cytometric characterization

HROP68Tu2 cells´ expressions of surface proteins were evaluated by flow cytometry (Figure 6). Common epithelial and tumor markers were expressed to a variable extent: CD326 (EpCAM) (98.6% ± 1.7, MFI: 40.6 ± 3.1), CD227 (MUC-1) (58.4% ± 2.8, MFI: 7.8 ± 0.1), and CD66adecb (CEA) (38.2% ± 0.2, MFI: 5.0 ± 0.2). However, the epithelial markers CD15 (1.3% ± 0.6, MFI: 0.4 ± 0.3) and CD26 (7.3% ± 1.2, MFI: 0.4 ± 0.2) could not be detected. The adhesion marker CD29 (Integrin β - 1) was highly expressed (99.81% ± 0.01, MFI: 221.28 ± 19.23). A common pattern of the Fas receptor (CD95) (65.3% ± 11.6, MFI: 1.7 ± 0.3) and aberrant Fas ligand (CD178) (2.5% ± 0.9, MFI: 0.7 ± 0.3) expression was detected. HLA I expression was preserved homogeneously and with high intensity (99.7% ± 0.1, MFI: 165.6 ± 38.4). An average of 40.9% (± 12.0) of HROP68Tu2 cells expressed HLA II, albeit with low intensity (MFI: 1.8 ± 0.3). Furthermore, the cells expressed several proteins that are targets of antibody-based therapies. Matching the pathology report of the patient tumor, but even more so of the PDX, HROP68Tu2 cells showed homogeneous and high PD-L1 expression (95.9% ± 2.2, MFI:

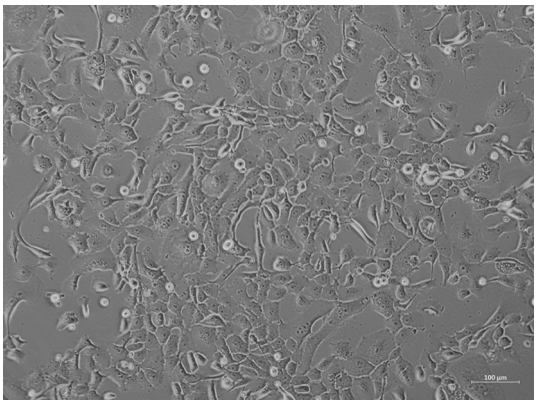

FIGURE 4
Cell morphology of the primary cell line HROP68Tu2 in passage 11. Picture was taken using an inverted microscope at ×40 magnification.

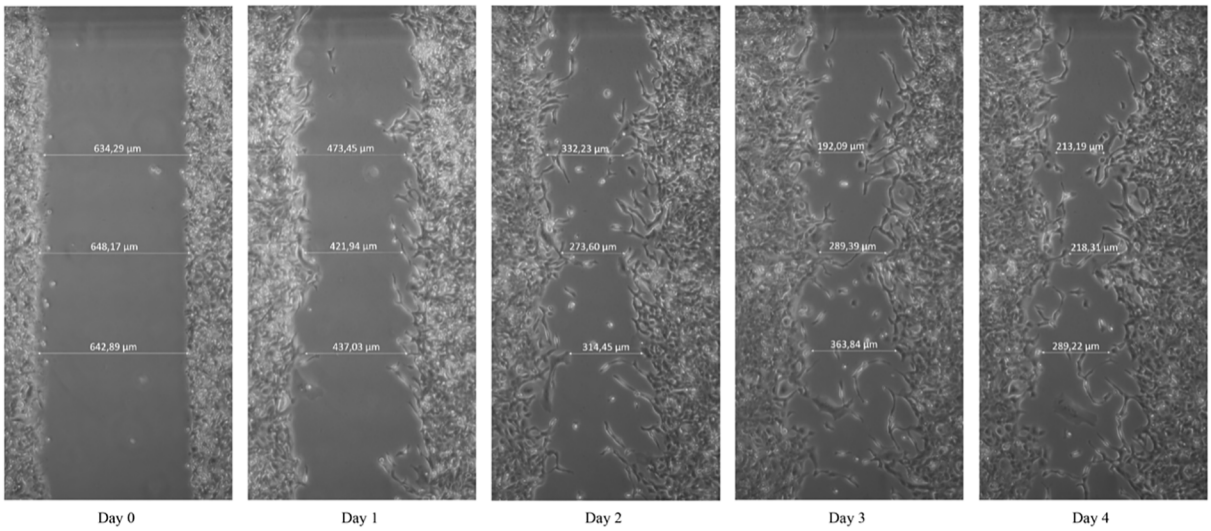

FIGURE 5
Scratch assay. Cells were scratched using a 10 µl pipet tip. Pictures were taken using an inverted microscope at ×10 magnification.

26.5 ± 0.8). Furthermore, CD90 (84.0% ± 3.2, MFI: 5.1 ± 0.6) and CD40 (TNFRS5) (41.3 ± 1.83, MFI: 4.6 ± 0.3) expression was observed.

3.6 Whole exome sequencing: Somatic mutations and MSI scoring

The overall number of somatic mutations was determined by the WES analysis of HROP68 tumor tissues (primary cancer and local recurrence), subtracting alterations from the reference genome observed in the normal DNA of the patient. In sum, there was a relatively high TMB with 486 somatic mutations for HROP68Tu1 and 729 for HROPTu2, as well as an even higher number of 1,498 for HROP68Tu1 T1 M2 and 1,964 for HROP68Tu2 T0 M2. The higher numbers on the PDX models likely reflect the high tumor cell purity and possibly the very short ischemic time between collection and snap freezing. No mutations were observed in the following MMR genes: *MLH1, MSH2, MSH6, PMS2*, and *EPCAM (CD326)*. In addition, we

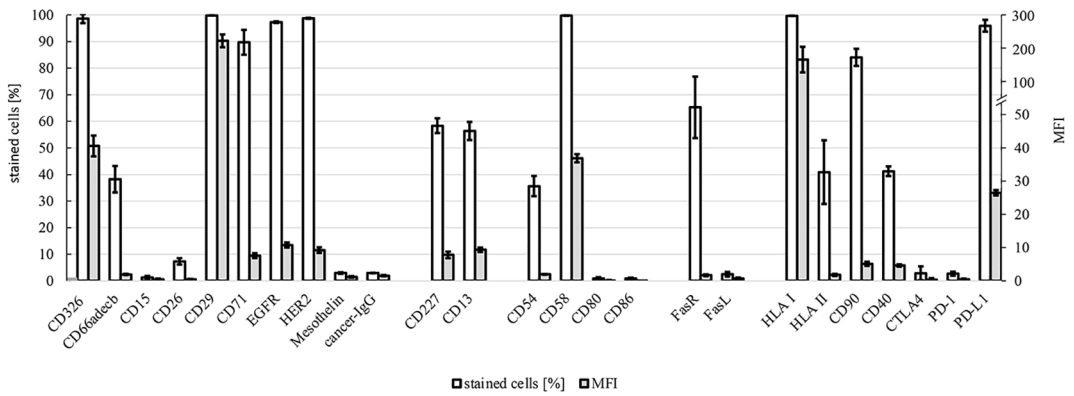

FIGURE 6
Flow cytometry. Expression of surface markers in HROP68Tu2 cells: tumor markers/signaling/proliferation (CD326, CD66adecb, CD15, CD26, CD29, CD71, EGFR, HER2, mesothelin, and cancer IgG), drug resistance (CD227 and CD13), adhesion/cell–cell interaction (CD54, CD58, CD80, and CD86), death ligand and receptor (CD95 and CD178), and immunogenicity/immunosuppression (HLA I, HLA II, CD90, CD40, CTLA4, PD-1, and PD-L1) were assessed by flow cytometry using FACS Calibur. Positively stained cells are given in % ± SEM and MFI (mean fluorescence intensity) ± SEM.

discovered a non-coding *POLD1* mutation in the PDX tissue of HROP68Tu2. Furthermore, the WES revealed a high amount of frameshift mutations, a total number of 92 in the primary tumor and 113 in the local recurrence, HROP68Tu1 T1 M2: 192 and HROP68Tu2 T0 M2: 154.

As can be depicted from Table 1, several mutations classified as pathogenic affecting tumor-relevant genes including *KRAS* and *TP53* could be identified. The mutations in *BRCA1* and *TP53* were subsequently included as targets in a precision oncology fashion sensitivity testing.

Moreover, WES data were also used to calculate an MSI score, which was determined by MSIsensor to be 16.28% for the primary tumor and 13.77% for HROP68Tu2. In comparison: 23 other pancreatic cancer cases in our biobank had a mean MSI score of 3.09 (range 0.52 to 6.38). Taking the limit of MSIsensor for MSI-H of at least 20% into account, this analysis confirmed the absence of MSI-H, thereby matching the pathological findings. Still, when considering the relatively high TMB, the overall number of mutations reflecting frameshifts in coding genomic regions as identified by MSIsensor analysis, we consider HROP68 as an MPC with a low level of MSI (MSI-L).

The WES data obtained from Centogene as. vcf files are available upon reasonable request.

3.7 *In vitro* drug response

The treatment response of HROP68Tu2 was tested toward selected clinically approved therapeutics and several novel targeted drugs selected according to the observed somatic mutations and membrane receptors expressed by HROP68Tu2 cells. These were lapatinib due to the EGFR and HER2 expression, PRIMA-1Met because of the TP53 mutation, and, similarly, olaparib due to the BRCA1 mutation. HROP68Tu2 cells were sensitive toward all tested drugs within the therapeutic range as defined by achievable human plasma levels (Table 2).

Next, the response to the clinically used combination therapy FOLFIRINOX was analyzed. Although a moderate synergistic effect of the drugs 5-FU, irinotecan, and oxaliplatin was observed, chemosensitivity to FOLFIRINOX compared to 5-FU alone was not significantly increased ($p = 0.118$). The interaction of the drugs involved can be judged by calculating a combination index (CI), which was in this case 0.71, thereby indicating a moderate synergistic effect for FOLFIRINOX (Table 3).

Contrary, combining gemcitabine with paclitaxel or erlotinib did not improve inhibitory effects compared to gemcitabine alone but rather showed antagonistic effects between gemcitabine and paclitaxel (GemPac; CI = 1.44, $p>0.05$) as well as gemcitabine and erlotinib (GemErlo; CI = 1.53, $p>0.05$) (Table 4).

4 Discussion

Patient-derived tumor models are the cornerstone of preclinical and translational research (14, 15, 22) and are valuable tools for the evaluation of novel drugs or treatment options for rare diseases (16, 31). The consequent biobanking of all resected pancreatic cancers at our department provided the opportunity to seize this rare case of primary and recurrent MPC, as well as to establish PDX from both the surgical specimen and a PDCL. The establishment of stable cell lines derived directly from the fresh surgical PDAC specimen is rarely successful, which can be mostly attributed to a low tumor–stroma ratio frequently causing fibroblastic overgrowth (32, 33). The positive model establishments of HROP68 might thus be mostly attributable to the high tumor–stroma ratio diagnosed in this case.

Generally, the evaluation of treatment efficacy for the individual PDAC patient is challenging since long-term survival remains an exception. This is explained by the intrinsic chemoresistance of PDAC, attributable to the large

TABLE 1 Mutational profiling of the HROP68 primary tumor (HROP68Tu1), HROP68 recurrent tumor (HROP68Tu2), and their PDX models (HROP68Tu1 T1 M2 and HROP68Tu2 T0 M2).

Gene	Ref	Alt	Type	Coding Pep	dbSNP ID	HROP68Tu1	HROP68Tu1 T1 M2	HROP68Tu2	HROP68Tu2 T0 M2
BRCA1	T	C	missense	Asn277Asp	rs2054040121				15
CDKN2A	G	A	missense	Pro75=	rs762397298				38
FOXG1	CG	C	in/del	Glu154fs	rs398124204	54	73	49	45
GRIK2	C	T	stop	Arg198*	rs749995448		17		
KAT6B	T	C	missense	Ile413Thr	rs1842099343		25		31
KRAS	C	T	missense	Gly12Asp	rs121913529	18	30	35	24
RUNX1	A	C	missense	Ser424Ala	rs2056451534		24		20
SMAD4	T	A	synonymous	Pro303	rs141149381		17		
TP53	C	A	missense	Cys277Phe	rs763098116	95	98	87	100

Given are somatic mutations affecting tumor-relevant genes as determined by WES. Also displayed are reference (Ref) and alternative (Alt) nucleobases, the type of mutation, effects on the protein sequence (Coding Pep), dbSNP IDs, and the variant allele frequencies in %. * marks a premature stop codon.

TABLE 2 Chemosensitivity of HROP68Tu2 toward single drugs: IC_{50} and IC_{20} values.

	5-FU	Irinotecan	Oxaliplatin	Gemcitabine	Paclitaxel	Erlotinib	Lapatinib	PRIMA-1Met	Olaparib
IC_{50}	6.83 (± 2.52)	0.32 (± 0.06)	1.55 (± 0.74)	0.00057 (± 0.00016)	0.0070 (± 0.00162)	6.52 (± 1.72)	6.27 (± 2.96)	23.98 (± 5.40)	6.69 (± 1.9)
IC_{20}	1.18 (± 33.33)	0.09 (± 0.01)	0.30 (± 0.15)	0.00024 (± 0.00024)	0.0024 (± 0.00142)	2.99 (± 0.86)	1.87 (± 2.36)	17.94 (± 4.88)	1.35 (± 0.09)
C_{max}	384.40 (23)	17.04 (24)	5.03 (25)	98.3 (26)	5.10 (27)	10.20 (28)	14 (29)	250,000 (30)	13.1 (26)

IC_{50} and IC_{20} values of HROP68Tu2 are given in µM for the single therapeutic drugs tested. To allow the integration of the data into a clinical context, the maximum plasma concentrations (C_{max} [µM]), reported in patients undergoing chemotherapy, were supplemented (references in brackets).

and dense tumor stroma, decreasing microvascularity and thereby drug delivery, to the epithelial cancer cell nests embedded into this stroma (34, 35). Due to the paucity of stromal components in HROP68, this relationship is unlikely in this case and might explain the observed drug responses of the present study. Compared to published data from many long-term established PDAC cell lines, HROP68Tu2 cells were highly responsive to gemcitabine but only moderately to 5-FU. Moreover, a moderate synergism was observed between the components of the FOLFIRINOX regimen. Contrary to that, an antagonistic interaction was observed for the combination of gemcitabine with both paclitaxel and erlotinib. However, due to the rareness of MPC, the comparison of these results with clinical data or even the retrospective translation of the presented case into the clinical context is hardly possible.

PDAC are bona fide non-immunogenic due to their low TMB; only 1%–2% of PDAC exhibit high levels of MSI, which is typically associated with a hypermutated phenotype (36). However, the associations of MSI to a medullary and mucinous histology have been described (37). Despite the high level of T-cell infiltration, the hallmark of ongoing immune recognition, observed in HROP68, the case was diagnosed as MSS both by immunostaining with a retained expression of the mismatch repair proteins MLH1 and MSH2, as well as by molecular microsatellite stability testing. Somehow challenging this diagnosis, WES analysis, however, identified a proportionally large number of somatic mutations, including a relevant fraction of insertions and deletions leading to frameshift mutations in coding regions. The latter translates to an elevated score in the MSIsensor analysis, albeit not reaching the 20% threshold to allow formally judging the case as MSI-H. Mutations of other candidate genes associated with a high TMB, like *POLE* (38), *POLD1* (39), and *MUTYH* (40), could not be detected in the clinical samples, although the PDX HROP68Tu2 T0 M2 harbored a *POLD1* mutation of uncertain significance. By applying a less rigorous tertiary data interpretation of the WES analysis, likely pathogenic mutations of DNA repair genes, known to be associated with an increased TMB and immunogenicity, like PALB2, ATR, and CHECK2 (41–43), were identified. However, when summing up all pieces of information, the uncommonly high TMB (44), combined with the MSI score, led us to the conclusion that HROP68 is an MSI-L MPC.

Although mutations of *BRCA1/2* in PDAC are associated with increased survival due to a higher susceptibility to platinum-based chemotherapy (45, 46), this observation could not be confirmed for HROP68, harboring a *BRCA1* mutation. While *BRCA*-mutated ovarian cancers respond well to the inhibitors of the poly-ADP ribose (PARPi), the PARPi olaparib improved progression-free survival in metastatic PDAC patients with a germline *BRCA* mutation but failed to improve overall survival (47, 48). In our study, olaparib had an inhibitory effect on HROP68Tu2 cells *in vitro*.

TABLE 3 Drug interaction of FOLFIRINOX.

FOLFIRINOX							
IC50 values in µM						Interaction	
5-FU	FOLFIRINOX (Relative to 5-FU)	Irinotecan	FOLFIRINOX (Relative to Irinotecan)	Oxaliplatin	FOLFIRINOX (Relative to oxaliplatin)	CI value	
6.83	3.70	0.32	0.05	1.55	0.04	0.71	moderate synergism

IC_{50} values of HROP68Tu2 are given for the single drugs and for the FOLFIRINOX combinations, respectively, in µM. The IC_{50} values of FOLFIRINOX are given as relative to the corresponding single drug, based on the molar ratios (2.6). The combination index (CI) and the resulting conclusion of moderate synergism between the components of the regimen are also given.

Similarly successful, HROP68Tu2 cells showed marked susceptibility to the tyrosine kinase inhibitors erlotinib and lapatinib, which were selected as targeted agents due to the homogeneous and high expression of EGFR and HER2. In the clinical setting, erlotinib led to small survival benefits, but lapatinib recently failed to improve the survival of patients with metastatic PDAC (49, 50).

The *TP53* mutation displayed by HROP68 is classified as uncertain significance in the ClinVar database. However, it might be pivotal regarding the proliferation of HROP68 cells since it replaces a cysteine on the protein level and this, together with the loss of the second allele, likely results in a loss of proper protein function. Our data of the PRIMA-Met1 treatment response support this hypothesis since this drugs' ability to restore wild-type p53 conformation has been shown for several mutant p53 proteins (51). The clear impact of PRIMA-Met1 on HROP68Tu2 cells would thus deliver evidence for the pathogenic character of the Cys277Phe p53 mutation with the dbSNP-ID rs763098116.

The immune landscape and interplay between various cell types contributing to immune evasion and a pro-inflammatory microenvironment are complex and not fully understood (52). On one hand, HROP68Tu2 showed a robust and homogeneous expression of HLA I as well as the expression of HLA II, CD58 (LFA3), and CD54 (ICAM1), allowing recognition by antigen-specific immune cells. On the other hand, the homogenous expression of PD-L1, CD90, and CD40 probably facilitated T-cell inactivation and likely immune evasion. PD-L1 expression is uncommon in PDACs and can only be found in 3% of cases (53). Although Le et al. (54) reported promising results for the efficiency of the PD-L1-inhibitor pembrolizumab for the treatment of different solid, MSI-positive tumors, the tumor response to pembrolizumab in MSI-positive PDCAs was rather modest with 18% in the KEYNOTE-158 Study (54, 55). Due to the uncommon combination of proteins expressed by HROP68 tumor cells, we consider it likely that an early application of checkpoint inhibitors in the clinical course of this patient might have improved the outcome, at least the overall survival time. It is one of the weak points of the current study that autologous immune analyses have not (yet) been performed *in vitro* using the HROP68Tu2 cell line and the peripheral as well as tumor-infiltrating T cells of the patient. Such analyses are planned, but, due to the restricted number of T cells available in our biobank, they shall be combined with an analysis of tumor-specific antigenic epitopes presented by HROP68Tu2 cells.

In summary and to the best of our knowledge, the PDX and PDCL of HROP68Tu2 are the first preclinical models established from an MPC. Although their preclinical implications are limited by the rarity of MPC, they are perfect tools for the establishment of novel drugs in the context of this rare subset of PDAC. Moreover, the observed good *in vitro* responses toward several drugs tested also emphasize the necessity to evaluate

TABLE 4 Drug interaction of GemPac and GemErlo.

GemPac					
IC50 values in nM				Interaction	
Gemcitabine	GemPac (Relative to Gemcitabine)	Paclitaxel	GemPac (Relative to Paclitaxel)	CI value	
0.57	0.82	7.04	0.01	1.44	Antagonism
GemErlo					
IC50 values in nM				Interaction	
Gemcitabine	GemErlo (Relative to Gemcitabine)	Erlotinib	GemErlo (Relative to Erlotinib)	CI value	
0.57	0.87	652	0.18	1.53	Antagonism

IC50 values are given for the single drugs and for the GemPac and GemErlo combinations, respectively in nM. The IC_{50} values of GemPac and GemErlo are given as relative to the corresponding single drug, based on the molar ratios (2.6). The combination index (CI) and the resulting conclusion of antagonism between the components of the regimen are also given.

therapeutic options on a patient–individual level, i.e., precision oncology, in order to optimize the clinical outcome, especially for rare cancer cases.

Data availability statement

The original contributions presented in the study are publicly available. The data has been uploaded to the NCBI BioProject repository and can be found using accession number PRJNA915478.

Ethics statement

The studies involving human participants were reviewed and approved by Institutional review board of the University Medical Center Rostock (A 2018-0054). The patients/participants provided their written informed consent to participate in this study. The animal study was reviewed and approved by Landesamt für Landwirtschaft, Lebensmittelsicherheit und Fischerei Mecklenburg-Vorpommern.

Author contributions

Design and conception of the study: ML. Patients' consent and clinical material acquisition: FB, ML, CM, and FP. Experiments: JvdD, JF, FB, and FP. Manuscript draft: JvdD, JF, FB, FP, CM, and ML. All authors contributed to the article and approved the submitted version.

Funding

This research was, in part, funded by grant number TBI-V-1-241-VBW-084 and TBI-V-240-VBW-084 from the state of Mecklenburg-Vorpommern.

Acknowledgments

The authors thank Mathias Krohn for his excellent help with cell culture and performing the STR analysis. Furthermore, we would like to thank Centogene (Rostock, Germany) for performing whole exome sequencing.

Conflict of interest

The authors declare that the research was conducted in the absence of any commercial or financial relationships that could be construed as a potential conflict of interest.

Publisher's note

References

1. Siegel RL, Miller KD, Fuchs HE, Jemal A. Cancer statistics, 2021. *CA Cancer J Clin* (2021) 71(1):7–33. doi: 10.3322/caac.21654

2. Arnold M, Abnet CC, Neale RE, Vignat J, Giovannucci EL, McGlynn KA, et al. Global burden of 5 major types of gastrointestinal cancer. *Gastroenterology* (2020) 159(2):335–349.e15. doi: 10.1053/j.gastro.2020.02.068

3. Bengtsson A, Andersson R, Ansari D. The actual 5-year survivors of pancreatic ductal adenocarcinoma based on real-world data. *Sci Rep* (2020) 10 (1):16425. doi: 10.1038/s41598-020-73525-y

4. Latenstein AEJ, van Roessel S, van der Geest LGM, Bonsing BA, Dejong CHC, Groot Koerkamp B, et al. Conditional survival after resection for pancreatic cancer: A population-based study and prediction model. *Ann Surg Oncol* (2020) 27 (7):2516–24. doi: 10.1245/s10434-020-08235-w

5. Huang L, Jansen L, Balavarca Y, Babaei M, van der Geest L, Lemmens V, et al. Stratified survival of resected and overall pancreatic cancer patients in Europe and the USA in the early twenty-first century: a large, international population-based study. *BMC Med* (2018) 16(1):125. doi: 10.1186/s12916-018-1120-9

6. Conroy T, Hammel P, Hebbar M, Ben Abdelghani M, Wei AC, Raoul J-L, et al. FOLFIRINOX or gemcitabine as adjuvant therapy for pancreatic cancer. *N Engl J Med* (2018) 379(25):2395–406. doi: 10.1056/NEJMoa1809775

7. Neoptolemos JP, Palmer DH, Ghaneh P, Psarelli EE, Valle JW, Halloran CM, et al. Comparison of adjuvant gemcitabine and capecitabine with gemcitabine monotherapy in patients with resected pancreatic cancer (ESPAC-4): a multicentre, open-label, randomised, phase 3 trial. *Lancet* (2017) 389(7):1011–24. doi: 10.1016/S0140-6736(16)32409-6

8. Tempero MA, Malafa MP, Al-Hawary M, Behrman SW, Benson AB, Cardin DB, et al. Pancreatic adenocarcinoma, version 2.2021, NCCN clinical practice guidelines in oncology. *J Natl Compr Canc Netw* (2021) 19(4):439–57. doi: 10.6004/jnccn.2021.0017

9. Martinez-Useros J, martin-galan m, Garcia-foncillas j. the match between molecular subtypes, histology and microenvironment of pancreatic cancer and its relevance for chemoresistance. *Cancers (Basel)* (2021) 13(2):322. doi: 10.3390/cancers13020322

10. Blando J, Sharma A, Higa MG, Zhao H, Vence L, Yadav SS, et al. Comparison of immune infiltrates in melanoma and pancreatic cancer highlights VISTA as a potential target in pancreatic cancer. *Proc Natl Acad Sci U.S.A.* (2019) 116(5):1692–7. doi: 10.1073/pnas.1811067116

11. Chalmers ZR, Connelly CF, Fabrizio D, Gay L, Ali SM, Ennis R, et al. Analysis of 100,000 human cancer genomes reveals the landscape of tumor mutational burden. *Genome Med* (2017) 9(11):34. doi: 10.1186/s13073-017-0424-2

12. Goggins M, Offerhaus GJ, Hilgers W, Griffin CA, Shekher M, Tang D, et al. Pancreatic adenocarcinomas with DNA replication errors (RER+) are associated with wild-type K-ras and characteristic histopathology. poor differentiation, a syncytial growth pattern, and pushing borders suggest RER+. *Am J Pathol* (1998) 152(6):1501–7.

13. Wilentz RE, Goggins M, Redston M, Marcus VA, Adsay NV, Sohn TA, et al. Genetic, immunohistochemical, and clinical features of medullary carcinoma of the pancreas. *Am J Pathol* (2000) 156(5):1641–51. doi: 10.1016/S0002-9440(10)65035-3

14. Matschos S, Bürtin F, Kdimati S, Radefeldt M, Krake S, Prall F, et al. The HROC-Xenobank-A high quality assured PDX biobank of 100 individual colorectal cancer models. *Cancers (Basel)* (2021) 13(23):5882. doi: 10.3390/cancers13235882

15. Bürtin F, Matschos S, Prall F, Mullins CS, Krohn M, Linnebacher M. Creation and maintenance of a living biobank - how we do it. *J Vis Exp* (2021) 170:170. doi: 10.3791/62065

16. Wagner S, Beger NT, Matschos S, Szymanski A, Przybylla R, Bürtin F, et al. Tumour-derived cell lines and their potential for therapy prediction in patients with metastatic colorectal cancer. *Cancers (Basel)* (2021) 13(18):4717. doi: 10.3390/cancers13184717

17. Trujillano D, Bertoli-Avella AM, Kumar Kandaswamy K, Weiss ME, Köster J, Marais A, et al. Clinical exome sequencing: results from 2819 samples reflecting 1000 families. *Eur J Hum Genet* (2017) 25(2):176–82. doi: 10.1038/ejhg.2016.146

18. Niu B, Ye K, Zhang Q, Lu C, Xie M, McLellan MD, et al. MSIsensor: microsatellite instability detection using paired tumor-normal sequence data. *Bioinformatics* (2014) 30(7):1015–6. doi: 10.1093/bioinformatics/btt755

19. Begg SKS, Birnbaum DJ, Clark JW, Mino-Kenudson M, Wellner UF, Schilling O, et al. FOLFIRINOX versus gemcitabine-based therapy for pancreatic ductal adenocarcinoma: Lessons from patient-derived cell lines. *Anticancer Res* (2020) 40(7):3659–67. doi: 10.21873/anticanres.14355

20. Moore MJ, Goldstein D, Hamm J, Figer A, Hecht JR, Gallinger S, et al. Erlotinib plus gemcitabine compared with gemcitabine alone in patients with advanced pancreatic cancer: a phase III trial of the national cancer institute of Canada clinical trials group. *J Clin Oncol* (2007) 25(15):1960–6. doi: 10.1200/JCO.2006.07.9525

21. Bianchi F, Galizia E, Catalani R, Belvederesi L, Ferretti C, Corradini F, et al. CAT25 is a mononucleotide marker to identify HNPCC patients. *J Mol Diagn* (2009) 11(3):248–52. doi: 10.2353/jmoldx.2009.080155

22. Mullins CS, Micheel B, Matschos S, Leuchter M, Bürtin F, Krohn M, et al. Integrated biobanking and tumor model establishment of human colorectal carcinoma provides excellent tools for preclinical research. *Cancers (Basel)* (2019) 11(10):1520. doi: 10.3390/cancers11101520

23. Bocci G, Danesi R, Di Paolo AD, Innocenti F, Allegrini G, Falcone A, et al. Comparative pharmacokinetic analysis of 5-fluorouracil and its major metabolite 5-fluoro-5,6-dihydrouracil after conventional and reduced test dose in cancer patients. *Clin Cancer Res* (2000) 6(8):3032–7.

24. Chabot GG. Clinical pharmacokinetics of irinotecan. *Clin Pharmacokinet* (1997) 33(4):245–59. doi: 10.2165/00003088-199733040-00001

25. Graham MA, Lockwood GF, Greenslade D, Brienza S, Bayssas M, Gamelin E. Clinical pharmacokinetics of oxaliplatin: a critical review. *Clin Cancer Res* (2000) 6(4):1205–18.

26. Liston DR, Davis M. Clinically relevant concentrations of anticancer drugs: A guide for nonclinical studies. *Clin Cancer Res* (2017) 23(14):3489–98. doi: 10.1158/1078-0432.CCR-16-3083

27. Stage TB, Bergmann TK, Kroetz DL. Clinical pharmacokinetics of paclitaxel monotherapy: An updated literature review. *Clin Pharmacokinet* (2018) 57(1):7–19. doi: 10.1007/s40262-017-0563-z

28. Faivre L, Gomo C, Mir O, Taieb F, Schoemann-Thomas A, Ropert S, et al. A simple HPLC-UV method for the simultaneous quantification of gefitinib and erlotinib in human plasma. *J Chromatogr B Analyt Technol BioMed Life Sci* (2011) 879(23):2345–50. doi: 10.1016/j.jchromb.2011.06.026

29. Spector NL, Robertson FC, Bacus S, Blackwell K, Smith DA, Glenn K, et al. Lapatinib plasma and tumor concentrations and effects on HER receptor phosphorylation in tumor. *PloS One* (2015) 10(11):e0142845. doi: 10.1371/journal.pone.0142845

30. Bykov VJN, Zhang Q, Zhang M, Ceder S, Abrahmsen L, Wiman KG. Targeting of mutant p53 and the cellular redox balance by APR-246 as a strategy for efficient cancer therapy. *Front Oncol* (2016) 6:21. doi: 10.3389/fonc.2016.00021

31. Rivera M, Fichtner I, Wulf-Goldenberg A, Sers C, Merk J, Patone G, et al. Patient-derived xenograft (PDX) models of colorectal carcinoma (CRC) as a platform for chemosensitivity and biomarker analysis in personalized medicine. *Neoplasia* (2021) 23(1):21–35. doi: 10.1016/j.neo.2020.11.005

32. Xie D, Xie K. Pancreatic cancer stromal biology and therapy. *Genes Dis* (2015) 2(2):133–43. doi: 10.1016/j.gendis.2015.01.002

33. Rückert F, Aust D, Böhme I, Werner K, Brandt A, Diamandis EP, et al. Five primary human pancreatic adenocarcinoma cell lines established by the outgrowth method. *J Surg Res* (2012) 172(1):29–39. doi: 10.1016/j.jss.2011.04.021

34. Jacobetz MA, Chan DS, Neesse A, Bapiro TE, Cook N, Frese KK, et al. Hyaluronan impairs vascular function and drug delivery in a mouse model of pancreatic cancer. *Gut* (2013) 62(1):112–20. doi: 10.1136/gutjnl-2012-302529

35. Olive KP, Jacobetz MA, Davidson CJ, Gopinathan A, McIntyre D, Honess D, et al. Inhibition of hedgehog signaling enhances delivery of chemotherapy in a mouse model of pancreatic cancer. *Science* (2009) 324(5933):1457–61. doi: 10.1126/science.1171362

36. De' Angelis GL, Bottarelli L, Azzoni C, De' Angelis N, Leandro G, Di Mario F, et al. Microsatellite instability in colorectal cancer. *Acta BioMed* (2018) 89(9-S)::97–101. doi: 10.1186/s13045-020-00958-3

37. Luchini C, Brosens LAA, Wood LD, Chatterjee D, Shin JI, Sciammarella C, et al. Comprehensive characterisation of pancreatic ductal adenocarcinoma with microsatellite instability: histology, molecular pathology and clinical implications. *Gut* (2021) 70(1):148–56. doi: 10.1136/gutjnl-2020-320726

38. Kryklyva V, Ter Linden E, Kroeze LI, de Voer RM, van der Kolk BM, Stommel MWJ, et al. Medullary pancreatic carcinoma due to somatic POLE mutation: A distinctive pancreatic carcinoma with marked long-term survival. *Pancreas* (2020) 49(7):999–1003. doi: 10.1097/MPA.0000000000001588

39. He J, Ouyang W, Zhao W, Shao L, Li B, Liu B, et al. Distinctive genomic characteristics in POLE/POLD1-mutant cancers can potentially predict beneficial clinical outcomes in patients who receive immune checkpoint inhibitor. *Ann Transl Med* (2021) 9(2):129. doi: 10.21037/atm-20-7553

40. Robinson PS, Thomas LE, Abascal F, Jung H, Harvey LMR, West HD, et al. Inherited MUTYH mutations cause elevated somatic mutation rates and distinctive mutational signatures in normal human cells. *Nat Commun* (2022) 13(1):3949. doi: 10.1038/s41467-022-31341-0

41. Waddell N, Pajic M, Patch A-M, Chang DK, Kassahn KS, Bailey P, et al. Whole genomes redefine the mutational landscape of pancreatic cancer. *Nature* (2015) 518(7540):495–501. doi: 10.1038/nature14169

42. Jiang M, Jia K, Wang L, Li W, Chen B, Liu Y, et al. Alterations of DNA damage response pathway: Biomarker and therapeutic strategy for cancer immunotherapy. *Acta Pharm Sin B* (2021) 11(10):2983–94. doi: 10.1016/j.apsb.2021.01.003

43. Parikh AR, He Y, Hong TS, Corcoran RB, Clark JW, Ryan DP, et al. Analysis of DNA damage response gene alterations and tumor mutational burden across 17,486 tubular gastrointestinal carcinomas: Implications for therapy. *Oncologist* (2019) 24(10):1340–7. doi: 10.1634/theoncologist.2019-0034

44. Qian Y, Gong Y, Fan Z, Luo G, Huang Q, Deng S, et al. Molecular alterations and targeted therapy in pancreatic ductal adenocarcinoma. *J Hematol Oncol* (2020) 13(1):130. doi: 10.1186/s13045-020-00958-3

45. Seeber A, Zimmer K, Kocher F, Puccini A, Xiu J, Nabhan C, et al. Molecular characteristics of BRCA1/2 and PALB2 mutations in pancreatic ductal adenocarcinoma. *ESMO Open* (2020) 5(6):e000942. doi: 10.1136/esmoopen-2020-000942

46. Pishvaian MJ, Blais EM, Brody JR, Lyons E, DeArbeloa P, Hendifar A, et al. Overall survival in patients with pancreatic cancer receiving matched therapies following molecular profiling: a retrospective analysis of the know your tumor registry trial. *Lancet Oncol* (2020) 21(4):508–18. doi: 10.1016/S1470-2045(20)30074-7

47. Miller RE, Leary A, Scott CL, Serra V, Lord CJ, Bowtell D, et al. ESMO recommendations on predictive biomarker testing for homologous recombination deficiency and PARP inhibitor benefit in ovarian cancer. *Ann Oncol* (2020) 31(12):1606–22. doi: 10.1016/j.annonc.2020.08.2102

48. Kindler HL, Hammel P, Reni M, van Cutsem E, Macarulla T, Hall MJ, et al. Overall survival results from the POLO trial: A phase III study of active maintenance olaparib versus placebo for germline BRCA-mutated metastatic pancreatic cancer. *J Clin Oncol* (2022) 6:JCO2101604. doi: 10.1200/JCO.21.01604

49. Safran H, Miner T, Bahary N, Whiting S, Lopez CD, Sun W, et al. Lapatinib and gemcitabine for metastatic pancreatic cancer. a phase II study. *Am J Clin Oncol* (2011) 34(1):50–2. doi: 10.1097/COC.0b013e3181d26b01

50. van Cutsem E, Vervenne WL, Bennouna J, Humblet Y, Gill S, van Laethem J-L, et al. Phase III trial of bevacizumab in combination with gemcitabine and erlotinib in patients with metastatic pancreatic cancer. *J Clin Oncol* (2009) 27(13):2231–7. doi: 10.1200/JCO.2008.20.0238

51. Bykov VJN, Issaeva N, Shilov A, Hultcrantz M, Pugacheva E, Chumakov P, et al. Restoration of the tumor suppressor function to mutant p53 by a low-molecular-weight compound. *Nat Med* (2002) 8(3):282–8. doi: 10.1038/nm0302-282

52. Goulart MR, Stasinos K, Fincham REA, Delvecchio FR, Kocher HM. T Cells in pancreatic cancer stroma. *World J Gastroenterol* (2021) 27(46):7956–68. doi: 10.3748/wjg.v27.i46.7956

53. Liang X, Sun J, Wu H, Luo Y, Wang L, Lu J, et al. PD-L1 in pancreatic ductal adenocarcinoma: a retrospective analysis of 373 Chinese patients using an *in vitro* diagnostic assay. *Diagn Pathol* (2018) 13(1):5. doi: 10.1186/s13000-017-0678-4

54. Le DT, Durham JN, Smith KN, Wang H, Bartlett BR, Aulakh LK, et al. Mismatch repair deficiency predicts response of solid tumors to PD-1 blockade. *Science* (2017) 357(6349):409–13. doi: 10.1126/science.aan6733

55. Marabelle A, Le DT, Ascierto PA, Di Giacomo AM, de Jesus-Acosta A, Delord J-P, et al. Efficacy of pembrolizumab in patients with noncolorectal high microsatellite Instability/Mismatch repair-deficient cancer: Results from the phase II KEYNOTE-158 study. *J Clin Oncol* (2020) 38(1):1–10. doi: 10.1200/JCO.19.02105

frontiers | Frontiers in Oncology

TYPE Original Research
PUBLISHED 28 February 2023
DOI 10.3389/fonc.2023.1070505

OPEN ACCESS

EDITED BY
Hatim E. Sabaawy,
University of Colorado, United States

REVIEWED BY
Francesca Bianchini,
University of Florence, Italy
Ernest Nadal,
Catalan Institute of Oncology, Spain

*CORRESPONDENCE
Stefano Indraccolo
stefano.indraccolo@unipd.it

SPECIALTY SECTION
This article was submitted to Cancer Molecular Targets and Therapeutics, a section of the journal Frontiers in Oncology

RECEIVED 14 October 2022
ACCEPTED 07 February 2023
PUBLISHED 28 February 2023

CITATION
Ferrarini F, Zulato E, Moro M, Del Bianco P, Borzi C, Esposito G, Zanin T, Sozzi G and Indraccolo S (2023) Metabolic classification of non-small cell lung cancer patient-derived xenografts by a digital pathology approach: A pilot study.
Front. Oncol. 13:1070505.
doi: 10.3389/fonc.2023.1070505

Metabolic classification of non-small cell lung cancer patient-derived xenografts by a digital pathology approach: A pilot study

Federica Ferrarini[1], Elisabetta Zulato[2], Massimo Moro[3], Paola Del Bianco[4], Cristina Borzi[3], Giovanni Esposito[1], Tiziana Zanin[2], Gabriella Sozzi[3] and Stefano Indraccolo[2,5]*

[1]Immunology and Molecular Oncology Diagnostics Unit, Istituto Oncologico Veneto IOV IRCCS, Padova, Italy, [2]Basic and Translational Oncology Unit, Istituto Oncologico Veneto IOV IRCCS, Padova, Italy, [3]Tumor Genomics Unit Department of Research, Fondazione IRCCS Istituto Nazionale dei Tumori, Milan, Italy, [4]Clinical Research Unit, Istituto Oncologico Veneto IOV IRCCS, Padova, Italy, [5]Department of Surgery, Oncology and Gastroenterology, Università degli Studi di Padova, Padova, Italy

Introduction: Genetically characterized patient-derived tumor xenografts (PDX) are a valuable resource to understand the biological complexity of cancer and to investigate new therapeutic approaches. Previous studies, however, lack information about metabolic features of PDXs, which may limit testing of metabolism targeting drugs.

Methods: In this pilot study, we investigated by immunohistochemistry (IHC) expression of five essential metabolism-associated markers in a set of lung adenocarcinoma PDX samples previously established and characterized. We exploited digital pathology to quantify expression of the markers and correlated results with tumor cell proliferation, angiogenesis and time of PDX growth in mice.

Results: Our results indicate that the majority of the analyzed PDX models rely on oxidative phosphorylation (OXPHOS) metabolism, either alone or in combination with glucose metabolism. Double IHC enabled us to describe spatial expression of the glycolysis-associated monocarboxylate transporter 4 (MCT4) marker and the OXPHOS-associated glutaminase (GLS) marker. GLS expression was associated with cell proliferation and with expression of liver-kinase B1 (LKB1), a tumor suppressor involved in the regulation of multiple metabolic pathways. Acetyl CoA carboxylase (ACC) was associated with the kinetics of PDX growth.

Conclusion: Albeit limited by the small number of samples and markers analyzed, metabolic classification of existing collections of PDX by this mini panel will be useful to inform pre-clinical testing of metabolism-targeting drugs.

KEYWORDS

NSCLC, metabolic classification, OXPHOS metabolism, IHC, digital pathology

1 Introduction

In the last decade, many studies uncovered the metabolic complexity and heterogeneity of cancer. By using advanced technologies such as transcriptomics or metabolomics, distinct metabolic entities have been identified in the main types of human tumors, enabling metabolic classification of human tumors (1–3). Some studies classified tumors based on high, intermediate and low metabolic activity, inferred from expression levels of metabolism-related gene sets (4, 5), whereas others stratified tumors into glycolytic or oxidative metabolism classes according to expression levels of genes/metabolites belonging to glycolysis or oxidative phosphorylation (OXPHOS) (6–8). Recently, a pathway-based classification was proposed in brain tumors based on single cell RNA sequencing, including both mitochondrial and glycolytic/plurimetabolic subtypes endowed with different clinical outcomes (9).

With regard to NSCLC, a landmark study using intraoperative (10)C-glucose infusions in patients compared metabolism between tumors and benign lung and reported marked heterogeneity in tumor metabolism *in vivo*, but also highlighted the strong influence of the microenvironment on this feature (11). Additional studies described lactate uptake and its utilization as a fuel by lung cancer cells (12) and uncovered the role of the microenvironment as determinant of the metabolic phenotype of lung cancer cells *in vivo* (13). Numerous studies have delineated how cell-intrinsic factors, such as oncogenic lesions or epigenetic events, alter cellular metabolism, causing phenotypes characterized by increased glycolysis (10, 14) or other metabolic alterations, as reviewed by B. Majem et al. (15).

When approaching the complexity of cancer metabolism, it can be useful to adopt a simplified classification of tumors into "glycolytic" and "OXPHOS" subsets (6–8). Glycolytic tumors uptake glucose and preferentially metabolize it *via* glycolysis to lactate, which is exported from cells *via* monocarboxylate transporters (MCTs), such as MCT4 (16). In contrast, OXPHOS tumors can utilize several substrates as mitochondrial fuels, the main being represented by glutamine and fatty acids (FA) (17).

In this study, we set-up a panel of immunohistochemistry (IHC) markers including some enzymes and/or transporters belonging to these key metabolic pathways, implementing a panel that we recently used to profile patient-derived xenograft (PDX) samples from ovarian cancer (18). For the purpose of this pilot study, we considered monocarboxylate transporter 4 (MCT4) as proxy of glycolysis (16, 19), acetyl CoA carboxylase (ACC), fatty acids synthase (FAS) and carnitine palmitoyl transferase 1A (CPT1A) as proxy of FA metabolism (20, 21) and glutaminase (GLS) as proxy of glutamine metabolism (22).

We exploited this panel to investigate by IHC expression of these essential metabolism-associated markers in a set of previously established lung adenocarcinoma PDX samples. We exploited digital pathology to quantify expression of the markers and correlated results with tumor cell proliferation and angiogenesis, time of PDX growth and with known driver mutations of the cancer cells. Metabolic classification of existing collections of PDX by this mini panel will be useful to inform pre-clinical testing of metabolism-targeting drugs.

2 Material and methods

2.1 Patient data

Tumor samples were collected as described by Moro et al. (23). Samples of primary non small-cell lung cancer (NSCLC) were obtained from patients undergoing surgical resection, who gave their informed consent after approval from the Internal Review and the Ethics Boards of the Fondazione IRCCS Istituto Nazionale Tumori and all methods were performed in accordance with institutional guidelines and regulation and with the declaration of Helsinki. Patient data relevant to this study are reported in Table 1.

2.2 Generation of lung cancer xenografts

PDXs were generated as previously described (24). Once mice developed tumor, they were sacrificed by cervical dislocation. The tumors were harvested by dissection and fixed in formalin and embedded in paraffin for histology and immunohistochemistry analyses. All procedures involving animals and their care conformed to institutional guidelines that comply with national and international laws and policies (EEC Council Directive 86/609, OJ L 358, 12 December 1987) and were authorized by the Italian Ministry of Health.

2.3 Histology and immunohistochemistry

Four-micron-thick formalin-fixed, paraffin-embedded (FFPE) tumor samples were stained either with hematoxylin and eosin or processed for IHC, which was performed by using the automatic stainer BOND III, (Leica Microsystems, Wetzlar, Germany). The following antibodies were used, according to the manufacturer's instructions: anti-ACC Rabbit mAb detecting all isoforms of human ACC (clone C83B10, Cell Signaling Technology, dilution 1:100), anti-CPT1A Goat pAb (Novus Biologicals, dilution 1:300), anti-FAS Rabbit mAb (clone C20G5, Cell Signaling Technology, dilution 1:100), anti-GLS Rabbit mAb (clone EP7212, Abcam, dilution 1:200), anti-Ki67 (clone MIB-1, Dako Omnis, dilution 1:50), anti-LKB1 Mouse mAb (clone Ley 37D/G6, Santa Cruz Biotechnology, dilution 1:100), anti-MCT4 Mouse pAb (clone D-1, Santa Cruz Biotechnology, dilution 1:200) and anti-CD31 Rat mAb (clone SZ31, DIANOVA, dilution 1:40). Liquid diaminobenzidine (DAB; Bond Polymer Refine Detection, Leica Biosystems, Newcastle, UK) was used as a chromogenic agent and sections were counter-stained with Mayer's hematoxylin. For the double staining with the anti-GLS Rabbit mAb and anti-MCT4 Rabbit pAb the DAB chromogenic agent and the Green chromogen (Bond Polymer Refine HRP-PLEX Detection, Leica Biosystems, Newcastle, UK) were used in a sequential assay (further details are listed in Table 1, Supplementary Materials).

TABLE 1 Clinical and biological features of the NSCLC patient-derived xenografts (PDXs) utilized in this study.

PDX ID	Clinical features			Biological features		
	Stage	Grade	Time of collection	Histo type	Mutated genes	TT(days)
LT 66	IIIA (T1aN2M0)	G3	Relapse	ADC	*CDKN2A, KRAS, LKB1, TP53*	34
LT 111	IIB (T2bN1M0)	G3	Relapse	ADC	*CDKN2A, CTNNB1, KRAS, MET, TP53*	37
LT 128	IIIA (T2bN2M0)	G3	Relapse	ADC	*CDKN2A, KRAS, LKB1, TP53*	55
LT 138	IA (T1aN0M0)	G3	Diagnosis	ADC	*ERBB4, FBXW7, LKB1*	73
LT 141	IIIA (T2aN2M0)	G3	Relapse	ADC	*CTNNB1, KRAS, TP53*	104
LT 215	IV (T2aN2M1)	G3	Relapse	ADC	*KRAS, TP53*	37
LT 220	IIIA (T3N1M0)	G3	Diagnosis	ADC	-	32
LT 255	IA (T1aN0M0)	G2	Diagnosis	ADC	*CDKN2A, CTNNB1, KRAS, TP53*	32
LT 265	IV (N/A)	N/A	Diagnosis	ADC	*FLT3, LKB1, TP53*	30
LT 267	IIIA (T1aN2M0)	G3	Diagnosis	ADC	*KRAS, PIK3CA*	37
LT 273	IIIB(N/A)	N/A	Diagnosis	ADC	*KRAS, LKB1, TP53*	34
LT 278	IIIA (TxN0M0)	y	Relapse	ADC	*LKB1*	69
LT 305	IIA (T2bN0M0)	G3	Diagnosis	ADC	*APC, KRAS*	38
LT 323	IIIA (T4N0M0)	G3	Diagnosis	ADC	*NRAS, TP53*	35
LT 431	IIIA (T4N0M0)	G3	Diagnosis	ADC	-	90
LT 458	IV (T3N3M1)	G3	Diagnosis	ADC	*KRAS, LKB1*	45
LT 497	IV (T3N3M1)	G3	Diagnosis	ADC	*KRAS, LKB1*	40

ADC, Adenocarcinoma; TT, time to transplantation (TT was defined by the tumor size. Tumors were explanted when their volume exceeded 600 mm^3), N/A, Not Available; Stage, stage refers to initial diagnosis and follow TNM edition 7^{th}; Genes: Adenomatous Polyposis Coli (APC), cyclin dependent kinase inhibitor 2A (CDKN2A), catenin beta 1 (CTNNB1), erb-b2 receptor tyrosine kinase 4 (ERBB4), F-box and WD repeat domain containing 7 (FBXW7), fms related receptor tyrosine kinase 3 (FLT3), serine/threonine kinase (LKB1), phosphatidylinositol-4,5-bisphosphate 3-kinase catalytic subunit alpha (PIK3CA).

2.4 Image acquisition and analysis

Tumor representation and quality of staining were initially evaluated by one experienced pathologist (GE). Slides were digitally acquired at 200x magnification by the Aperio CS2 (Leica Biosystems, Wetzlar, Germany) and the evaluation of IHC score was assessed through the ScanScope Image Analysis software (ImageScope v12.4.0.708). On the basis on their localization, the different markers were analyzed by using the Aperio membrane algorithm v9 (MCT4), the Aperio cytoplasmic algorithm v2 (GLS, CPT1A, FAS, ACC, LKB1), the Aperio nuclear algorithm (Ki67) and the microvessel analysis v1 (CD31), as previously described (18). Aperio Genie Classifier was trained to recognize tumor tissue, stroma and background (glass) and then combined with Aperio Membrane v9 and Aperio Cytoplasmic v9. Results provided the percentage of cells with different expression levels of proteins classified in 3+ (highly positive), 2+ (intermediate positive), 1+ (low positive) and 0 (negative) in the case of MCT4, ACC, LKB1 and Ki67 markers. The sum of percentage of marker positive cells for these 4 tiers equals 100%. Due to the lack of differences in intensity of expression, in the case of GLS, FAS and CPT1A markers results provide the percentage of marker positive cells (1+). Digital quantification performed by the software was verified by the pathologist (GE). Expression of the metabolism-associated markers was calculated according to the H-score system (reviewed in (25):), using as input digital pathology data, and values range between 0 and 300.

2.5 Statistical analysis

Data were analyzed with RStudio (RStudio: Integrated Development for R. RStudio Inc., Boston, MA, US). Quantitative variables were summarized as median and interquartile range. A descriptive analysis of the strength of relationship between the levels of all the considered markers was performed using the Spearman rank correlation coefficient. A two-tailed Mann-Whitney test was used to address the comparisons of each marker distribution between TP53, KRAS, LKB1 mutational status and between maximal growth inhibition levels (≤50% vs >50%). Survival times were estimated with the Kaplan Meier method and compared among groups of markers with the log-rank test. Each marker was dichotomized with cut-off corresponding to the most significant relation with the outcome, estimated from maximally selected log-rank statistics from the 'maxstat' R package and the association with the outcome was tested in univariate Cox

proportional hazards regression models. P-values were not adjusted for multiple comparisons.

3 Results

3.1 Selection of metabolism-associated markers and panel set-up

We analyzed by IHC expression of the following markers in PDX sections: MCT4, GLS, CPT1A, FAS, and ACC. These markers identify key transporters or enzymes involved in glycolysis (MCT4), glutamine (GLS), and fatty acid metabolism (CPT1A, FAS, ACC). For all markers analyzed, the algorithm first identifies tumor cells and then quantifies expression levels according to the tiering system described in the methods section.

We performed IHC and digital pathology analysis of the expression of the five metabolism-associated markers in all 17 PDX samples (Table 2; Supplementary materials). Representative pictures of one PDX sample stained for each marker and the related mark-up of the analyzed tissue are presented in Figure 1. Detailed digital pathology results are presented in Table 2, whereas some representative pictures showing expression of the five markers in PDX samples are shown in Figure 2.

With regard to the pattern of expression of these metabolism-associated markers in tumors, we found intra-tumor heterogeneity in three out of seventeen PDX samples stained with MCT4 (LT 111, LT 255, LT 431) and one PDX sample stained with GLS (LT265). In all other cases, heterogeneous expression of the metabolic markers was not observed. Representative pictures illustrating heterogeneous expression of MCT4 and GLS are shown in Supplementary Figures 1 and 2. Notably, in 2 out of 3 PDX samples, MCT4-positive cells were located near the necrotic areas, likely underscoring the well-known hypoxia-driven upregulation of MCT4 expression. We conclude that intra-tumor heterogeneity occurs at a limited degree for most of the markers analyzed.

Considering the possible heterogeneous expression of these markers in different tumor samples, to assess the consistency of our findings, we performed IHC staining of MCT4, GLS, ACC, FAS and CPT1A in 8 additional samples obtained by implantation of the same specimen (LT66, LT111, LT141, LT 220, LT255, LT267, LT278, LT458) in different mice. Quantification of the markers and statistical analysis by the Wilcoxon test did not show significant differences between replicates for each biomarker, except for FAS (p-value 0.01).

Based on median values of the H-score, the metabolism-associated marker most abundantly expressed in these PDX samples was GLS (228.41), followed by ACC (170.05), MCT4 (108.74), FAS (32.78) and CPT1A (19.87). For descriptive purposes, we stratified PDX samples into two groups (high and low), based on the expression of each marker above or below the median value. We defined as plurimetabolic those PDX which showed high expression of the glycolysis-associated marker MCT4 in combination with one or more of the OXPHOS-associated markers (GLS, FAS, ACC, CPT1A). Plurimetabolic PDX (n = 9, 53%) included LT66, LT128, LT215, LT220, LT265, LT267, LT273, LT431 and LT458.

To investigate the pattern of expression of some these markers in plurimetabolic tumors, we set-up double IHC for MCT4 and GLS. Interestingly, plurimetabolic PDX samples showed co-expression of the two markers by variable proportions of tumor cells, as shown in Figure 3. In some PDX (LT 267 and LT128) a substantial (>50%) of cells co-expressed MCT4 and GLS. In all other plurimetabolic PDX, however, MCT4 and GLS were expressed mainly by different tumor cells which were located in the same spatial region of the tumor (Figure 3).

Six out of 17 samples (35%) were classified OXPHOS, as they expressed OXPHOS markers but not MCT4 and included LT111, LT138, LT255, LT278, LT305 and LT323.

Altogether, these results suggest that OXPHOS is the main metabolic pathway sustaining energy and macromolecules production in the large majority (15/17, 88%) of these lung adenocarcinoma PDX samples, alone or in combination with glycolysis. Finally, two PDX (LT497 and LT141) expressed all markers at relatively low levels, suggesting utilization of other metabolic pathways not covered by the IHC panel.

3.2 Association between markers

As the markers selected identify key metabolic processes, it was interesting to investigate possible associations between the markers. This analysis disclosed that ACC was positively associated with CPT1A (r = 0.47) with borderline significance (Table 3), fitting the known biochemical role of these enzymes in FA metabolism (26). No other associations were found between the other metabolic markers analyzed (Table 3).

CPT1A levels were significantly higher in KRAS-wt NSCLC PDX samples (p=0.010). No further associations between the metabolism-associated markers and recurrent TP53 and LKB1 gene mutations were found.

Finally, since alterations of LKB1 are relatively common in lung adenocarcinoma (27), and in view of the established role of this serine/threonine kinase in the regulation of metabolism (28), we assessed LKB1 expression in these tumors by IHC (Supplementary Figure 3). Among PDX samples with low LKB1 expression, three (LT 128, LT273 and LT 458) were known to bear disruptive LKB1 mutations (Table 1), whereas two (LT 305 and LT323) had LKB1 WT sequence, suggesting epigenetic down-regulation of LKB1 protein expression. Interestingly, we found a significant positive association between LKB1 and GLS expression (r= 0.59, Table 3).

3.3 Association with proliferation and angiogenesis

Next, we investigated whether expression of any of these markers was associated with proliferation, in view of the well-established link between certain metabolic processes and proliferation (29). We found that the proliferation marker Ki67 in

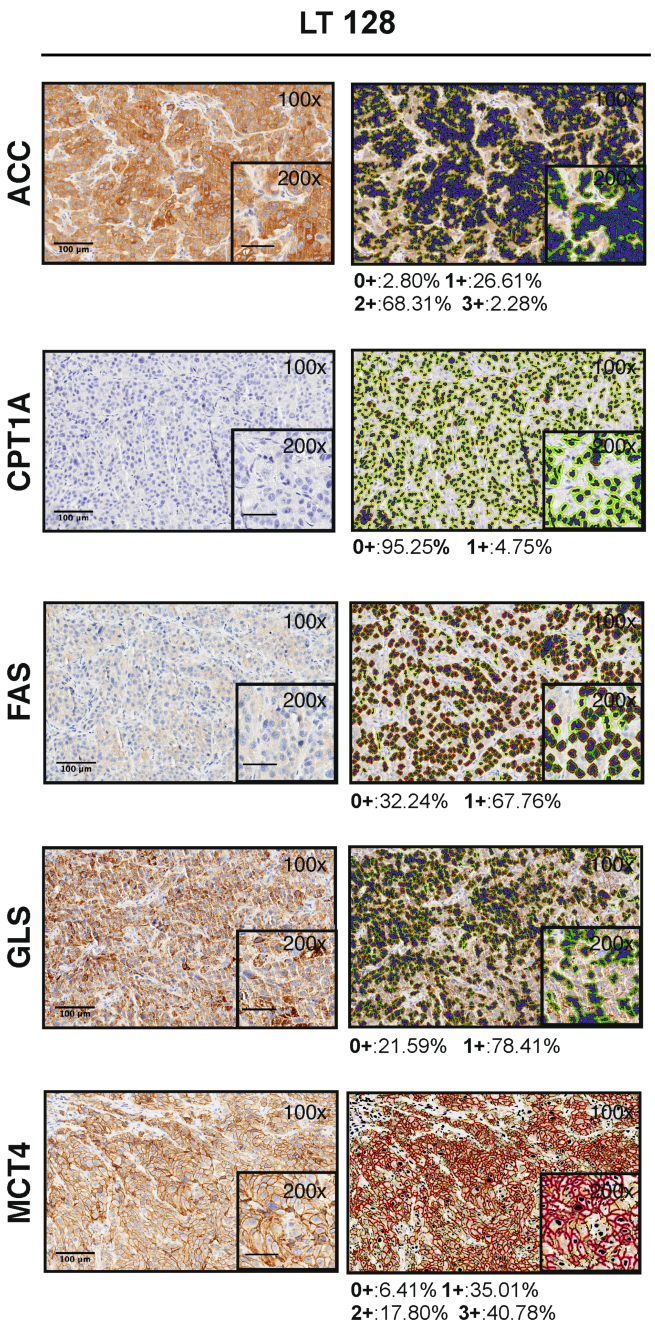

FIGURE 1
Visualization of the Aperio algorithms used to quantify metabolic markers expression in tissue (original magnification 100x and 200x, scale bar represents 100 µm or 50 µm, respectively). On the left, representative images of PDX LT 128 sections stained for ACC, FAS, GLS, MCT4 and CPT1A (hematoxylin counterstain). On the right, images showing the final mark-up of the sample. Quantification of the marker expression is shown below each panel: positive (1+/brown) or negative (0+/yellow) for CPT1A, FAS and GLS staining; strong (3+/brown or red), moderate (2+/orange), or weak (1+/yellow) for ACC and MCT4 staining. Negative/0+ cells show only hematoxylin counterstain.

tumor sections was positively associated with GLS (r=0.59) and FAS (r=0.52). In contrast, no association was found between Ki67 and any of the other metabolic markers; LKB1 was also positively associated with Ki67 in this dataset (r = 0.62) (Table 3).

Angiogenesis is a biological process which strongly contributes to tumor growth and is partially regulated by metabolic features of tumors, such as the production of lactate by highly glycolytic tumors (30). We analyzed possible associations between expression levels of the five metabolism-associated markers and microvessel density (MVD), calculated based on quantification of CD31 positive cells, as readout of angiogenesis (Supplementary Figure 3). Results, however, did not disclose any significant association (Table 3), perhaps due to the low number of samples analyzed.

10.3389/fonc.2023.1070505

TABLE 2 Quantification of marker expression in lung adenocarcinoma PDXs by digital pathology.

A. Expression levels of metabolism-associated markers MCT4, GLS, ACC, FAS and CPT1A					
PDX ID	MCT4	GLS	ACC	FAS	CPT1A
LT 431	127.07	259.22	75.18	88.98	35.83
LT 323	55.35	3.01	253.65	1.33	216.22
LT 215	163.10	289.14	212.41	150.69	2.89
LT 141	106.36	155.91	18.02	4.98	2.35
LT 497	63.05	NA	2.41	0.91	0.77
LT 305	80.75	0.26	180.92	60.39	NA
LT 278	20.44	25.72	23.73	15.91	99.21
LT 265	153.25	147.56	222.45	39.22	25.49
LT 138	75.83	282.47	176.96	299.15	240.00
LT 273	109.68	197.16	187.33	0.25	9.62
LT 255	61.00	245.48	110.97	138.61	2.67
LT 267	160.74	289.78	222.25	8.68	32.23
LT 458	181.75	2.37	104.88	32.78	1.50
LT 66	181.04	245.39	290.98	297.84	142.99
LT 128	192.95	235.22	170.05	203.29	14.25
LT 111	101.63	236.32	46.69	31.36	6.98
LT 220	108.74	221.59	99.07	11.49	93.10
Median	**108.74**	**228.41**	**170.05**	**32.78**	**19.87**
B. Expression levels of CD31, LKB1 and the proliferation marker Ki67					
PDX ID	CD31	LKB1	Ki67		
LT 431	53.2	259.99	164.04		
LT 323	45.0	126.88	53.99		
LT 215	64.8	197.71	193.55		
LT 141	77.3	148.07	98.91		
LT 497	105	NA	72.15		
LT 305	26.3	96.01	80.34		
LT 278	270	230.48	121.42		
LT 265	67.5	179.81	119.03		
LT 138	280	NA	130.22		
LT 273	120	130.94	92.20		
LT 255	220	192.79	84.34		
LT 267	54.1	186.90	109.04		
LT 458	NA	114.58	68.30		
LT 66	200	181.59	122.25		
LT 128	75.8	108.79	138.14		
LT 111	82.8	182.17	92.61		
LT 220	132	295.27	173.71		
Median	**80.05**	**181.59**	**109.04**		

NA, Not Available. Values are expressed according to the H-score system. Bold, median values.

10.3389/fonc.2023.1070505

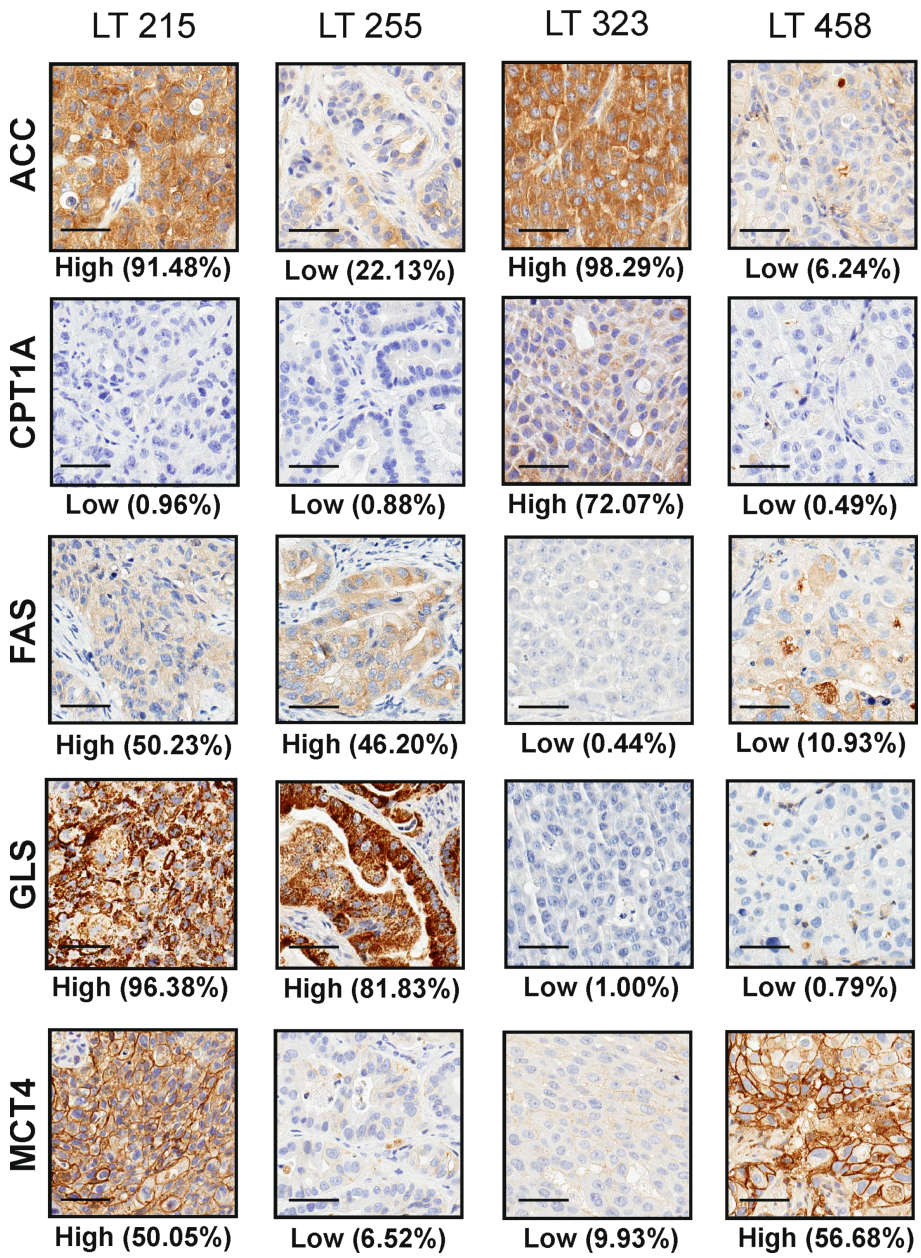

FIGURE 2
Representative pictures of four PDX (LT 215, LT 255, LT 323 and LT 458) stained for the selected metabolism-associated markers: ACC, CPT1A, FAS, GLS and MCT4 (original magnification 200x, scale bar represents 50 µm). The labels "High" and "Low" below each panel indicate the stratification of the sample according to the median value of expression of the marker according to digital pathology analysis, as detailed in the M&M section.

3.4 Association with the kinetics of tumor growth

Finally, we investigated the association between the metabolism-associated markers and the kinetics of tumor growth in mice, indicated by the parameter time to transplantation (TT – time from implant to explant) and the initial latency time (LT) (Table 4A, B, respectively). For this analysis, PDX samples were stratified into two groups based on the value of the marker obtained by maximizing its discriminative ability (best cut-off). The only marker positively associated with tumor growth in mice was ACC (Table 4 and Figure 4). Among other markers analyzed, LKB1 was not associated with TT.

Finally, we tested the correlation between marker expression and tumor volume at sacrifice calculating Spearman's rank correlation coefficient. We included in the analysis all samples available (n=24, including also the PDX specimens with two replicates). MCT4, ACC, FAS and CPT1A have a weak to moderate correlation (r MCT4 = 0.26, r GLS = 0.20, r ACC = 0.43, r FAS = 0.35, r CPT1A = 0.26) and ACC was the only marker statistically significant (p = 0.03), in line with the above results of correlations with LT and TT parameters. Moreover, plurimetabolic

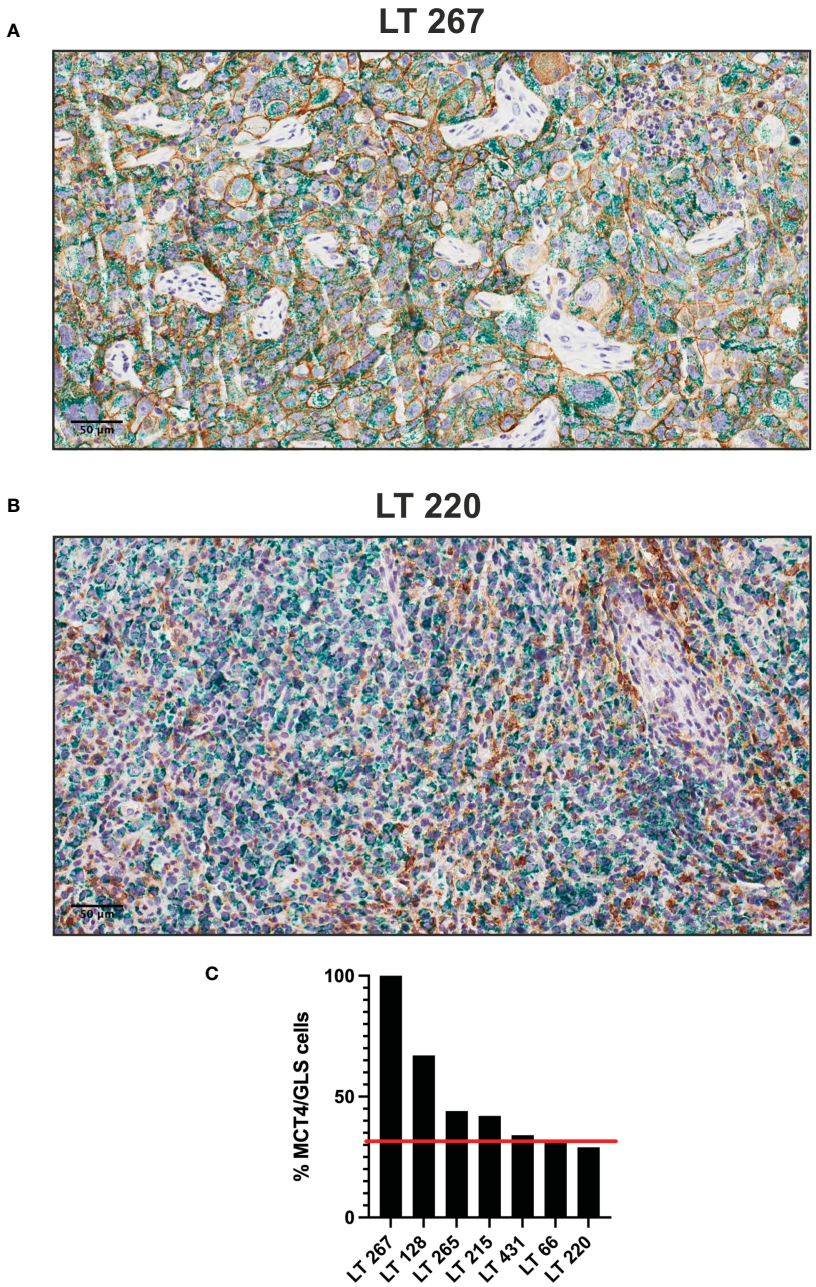

FIGURE 3
Plurimetabolic PDX showing expression of MCT4 (membrane, brown staining) and GLS (cytoplasm, green staining) by the tumor cells (two representative pictures in panel **(A, B)**, original magnification 200x, scale bar represents 50 µm). Relative percentage of PDX's double stained (MCT4/GLS) cells is reported as histogram **(C)**. Red line indicates the median value of MCT4/GLS co-expression (32%).

PDX positively correlated with tumor volume at sacrifice: the median tumor size for pluri-metabolic PDX was 700 mm^3 (n = 11), versus a median tumor size of 500 mm^3 (n= 13) for the OXPHOS group (p = 0.03, Mann-Whitney test).

4 Discussion

PDX are a valuable resource both to understand the biological complexity of cancer and to investigate new therapeutic approaches in pre-clinical models considered closer to the patients compared with other available *in vivo* models. PDXs have been reported for many types of solid tumors (31). In the case of lung cancer, several groups established PDX models (32–36) and reported their genetic fingerprint (23, 37). This associated genetic information was key to the discovery of new targets, such as the identification of HER2 as an effective therapeutic target in cetuximab-resistant colorectal cancer (38). In all previous studies, however, there is a lack of information about the metabolic features of PDXs. This gap may limit testing of metabolism targeting drugs, whose therapeutic activity is likely dependent on the metabolic set-up of tumor cells, as shown by several recent studies (39). Moreover, it appears that

TABLE 3 Association between the analyzed markers.

Parameter1	Parameter2	rho	95% CI	p
MCT4	GLS	0.24	[-0.31, 0.66]	*0.3804*
MCT4	ACC	0.34	[-0.18, 0.71]	*0.1809*
MCT4	LKB1	-0.18	[-0.64, 0.38]	*0.5243*
MCT4	Ki67	0.39	[-0.13, 0.74]	*0.1220*
MCT4	FAS	0.34	[-0.19, 0.71]	*0.1842*
MCT4	CPT1A	-0.16	[-0.61, 0.38]	*0.5643*
MCT4	CD31	-0.26	[-0.68, 0.28]	*0.3218*
GLS	ACC	0.12	[-0.41, 0.59]	*0.6643*
GLS	LKB1	0.59	[0.09, 0.85]	***0.0208***
GLS	Ki67	0.59	[0.11, 0.84]	***0.0165***
GLS	FAS	0.41	[-0.12, 0.76]	*0.1102*
GLS	CPT1A	0.11	[-0.44, 0.60]	*0.7039*
GLS	CD31	0.17	[-0.38, 0.64]	*0.5327*
ACC	LKB1	-0.29	[-0.71, 0.28]	*0.2957*
ACC	Ki67	0.04	[-0.46, 0.52]	*0.8738*
ACC	FAS	0.27	[-0.26, 0.67]	*0.2999*
ACC	CPT1A	0.47	[-0.05, 0.79]	*0.0639*
ACC	CD31	-0.29	[-0.70, 0.25]	*0.2739*
LKB1	Ki67	0.62	[0.15, 0.87]	***0.0127***
LKB1	FAS	0.05	[-0.49, 0.56]	*0.8595*
LKB1	CPT1A	0.26	[-0.33, 0.70]	*0.3664*
LKB1	CD31	0.38	[-0.20, 0.77]	*0.1745*
Ki67	FAS	0.52	[0.04, 0.81]	***0.0325***
Ki67	CPT1A	0.38	[-0.16, 0.74]	*0.1472*
Ki67	CD31	0.16	[-0.38, 0.62]	*0.5569*
FAS	CPT1A	0.27	[-0.28, 0.68]	*0.3163*
FAS	CD31	0.18	[-0.36, 0.63]	*0.5061*
CPT1A	CD31	0.11	[-0.44, 0.60]	*0.6945*

Association between the different analyzed markers using the Spearman correlation test. p-value adjustment method: none. Bold, statistically significant values ($p<0.05$).

specific metabolic activities of cancer cells also modulate response to conventional chemotherapies (8) and therapeutic resistance (39, 40), suggesting that metabolic features should be taken into consideration when new drugs are tested in PDX models.

Although comprehensive metabolic portraits of tumors are best obtained through mass-spectrometry-based analysis, we propose a simplified metabolic classification of tumors using quantitative measurement of the expression at protein level of well-established enzymes or transporters involved in key metabolic pathways. In this pilot study, we tested the feasibility of this approach in a small subset of NSCLC PDX, previously established and characterized by M. Moro et al. (23). These NSCLC PDX retained the key genetic alterations of the matched patients tumor samples and were also shown to reproduce their main metabolic features, as shown by [18F]FDG PET imaging studies (41).

Our results indicate that the majority of the analyzed models rely on OXPHOS metabolism, either alone or in combination with glucose metabolism. Notably, 9 out of 17 PDX showed a plurimetabolic phenotype, with co-expression of MCT4 and GLS at high (above the median value) levels. Double IHC disclosed that in some plurimetabolic PDX the two markers were co-expressed by the same tumor cells, whereas in others MCT4 and GLS were mostly expressed by different cells which, however, clustered in the same spatial area of the tissue. While plurimetabolic tumors have been identified also by using other techniques, such as single cell RNAseq (9), imaging of metabolism-associated markers by

TABLE 4 Association of the metabolic-associated markers with the kinetics of tumor growth.

A. Association with TT (time from implant to explant)							
	IHC-Expression Cut-off		N	Median TT (95%CI)	logrank	HR (95%CI)	p-value
MCT4	106.358	Above cut-off	9	37.3 (30.0;55)	*0.3237*	Ref	
		Below cut-off	8	38.9 (32.3;73)		0.62 [0.23;1.63]	*0.3265*
GLS	245.479	Above cut-off	4	55.2 (37.3;NA)	*0.3505*	Ref	
		Below cut-off	12	36.0 (32.0;55)		1.62 [0.56;5.55]	*0.3871*
ACC	75.176	Above cut-off	12	36.4 (32.0;45)	***0.0327***	Ref	
		Below cut-off	5	69.0 (36.7;NA)		0.29 [0.07;0.91]	***0.0330***
FAS	1.325	Above cut-off	14	37.5 (32.3;69)	*0.2968*	Ref	
		Below cut-off	3	35.4 (33.9;NA)		2.21 [0.54;7.30]	*0.2464*
CPT1A	2.354	Above cut-off	13	36.7 (32.3;55)	*0.1641*	Ref	
		Below cut-off	3	45.0 (40;NA)		0.43 [0.08;1.45]	*0.1878*
CD31	0.00022	Above cut-off	2	71 (69.0;NA)	*0.3590*	Ref	
		Below cut-off	14	37 (32.3;40)		1.70 (0.48;8.94)	*0.4365*
B. Association with LT (latency time)							
	IHC-Expression Cut-off	Below cut-off	N	Median TT (95%CI)	logrank	HR (95%CI)	p-value
MCT4	101.627	Above cut-off	10	20 (10.3; 26.0)	*0.2903*	Ref	
		Below cut-off	7	17 (8.3; 23.3)		1.73 [0.62; 4.72]	*0.2849*
GLS	245.479	Above cut-off	4	26.5 (11.7;NA)	*0.4658*	Ref	
		Below cut-off	12	18.2 (10.3;25)		1.43 [0.49;4.96]	*0.5209*
ACC	176.960	Above cut-off	7	15.0 (10.3;19.3)	***0.0009***	Ref	
		Below cut-off	10	24.2 (8.3;33.3)		0.21 [0.05;0.72]	***0.0135***
FAS	1.326	Above cut-off	14	20 (11.7;26)	*0.2276*	Ref	
		Below cut-off	3	17 (13.3;NA)		2.44 [0.58;8.66]	*0.2061*
CPT1A	2.354	Above cut-off	13	19.3 (11.7;23.3)	*0.1957*	Ref	
		Below cut-off	3	25.0 (17.0;NA)		0.46 [0.09;1.56]	*0.2350*
CD31	0.000077	Above cut-off	8	17.0 (8.33;23.3)	*0.3226*	Ref	
		Below cut-off	8	19.5 (10.33;40.0)		0.58 (0.20;1.70)	*0.3200*

The TT parameter (time from implant to explant) was used for association analysis. HR, Hazard Ratio; N, number of mice.
The LT parameter (latency time) was used for association analysis. HR, Hazard Ratio; N, number of mice. Bold, statistically significant p and logrank values.

quantitative IHC has the advantage to enable spatial localization of the two signals. This feature will likely be increasingly important in future studies to better understand metabolic heterogeneity of tumors. We highlighted a correlation between LKB1, GLS and Ki67 expression levels, although we did not explore the exact spatial localization of Ki67+ cells and that of the other associated markers, which represents a limitation of our pilot study. LKB1 is a tumor suppressor that acts by suppressing growth under energetic stress conditions, through its action on the AMPK/mTOR pathway (28). A positive correlation between LKB1 and Ki67 may seem counter-intuitive, especially for tumors that grow under the pressure of a non-orthotopic murine microenvironment. Nevertheless, our observation suggests that LKB1 wild type NSCLC rely on glutamine consumption to sustain the proliferation induced by hyperactivation of oncogenes such as KRAS (Table 1). Glutamine sustains cell growth as a nitrogen source for the synthesis of purine and pyrimidine bases, and it is also important for maintaining redox homeostasis within highly proliferating cells (42). Furthermore, a strong correlation of glutamine dependency with cell proliferation has been observed in a landmark study involving hundreds of cancer cell lines (43). A higher dependency on glutamine-related ROS detoxyfication activity has been reported for KRAS/LKB1/KEAP1 triple mutants compared to KRAS/LKB1- or KRAS-mutated NSCLC (44). However, in the same manuscript a reduction of ATP production upon glutaminase inhibition was reported also in LKB1 wild type

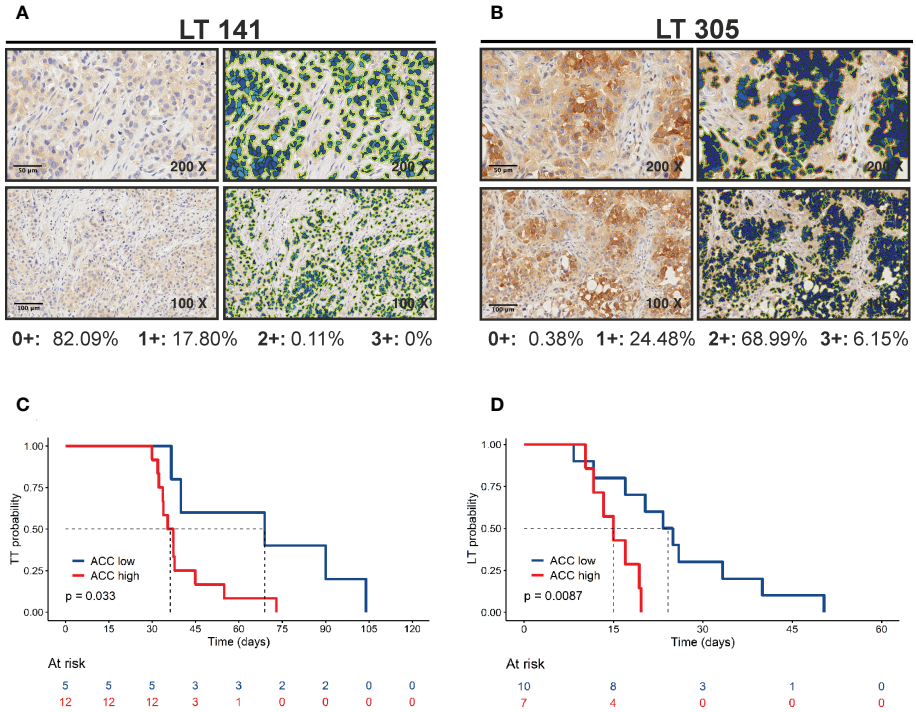

FIGURE 4
Positive correlation of ACC expression with tumor growth. **(A, B)** ACC expression was quantified by Aperio Cytoplasmic v9 algorithm. The panels show representative samples with low (LT 141) and high (LT 305) ACC expression levels (original magnification 200x for upper panels or 100x for lower panels, scale bar represents 50 or 100 µm, respectively). **(C)** Kaplan-Meier curves show faster growth of PDXs with high ACC expression levels. The best cut-off value used to generate this curve was 75.176. Statistical significance was calculated with the log-rank test **(D)** Kaplan-Meier curves show shorter latency time of PDXs with high ACC expression levels. The best cut-off value used to generate this curve was 176.96. Statistical significance was calculated with the log-rank test.

NSCLC cells. ATP reduction leads to cell growth arrest through activation of the LKB1/AMPK pathway. Since the energetic stress induced by biguanides in LKB1 mutated NSCLC models has been reported to cause apoptotic cell death (45), inhibiting at the same time GLS and AMPK activity may represent a new therapeutic option to investigate in NSCLC LKB1 wild type preclinical models.

Of note, we reported here a correlation between PDX *in vivo* growth rate, measured as time-to-transplantation (TT) and ACC expression. PDXs grow *in vivo* with a two-step kinetic; after an initial latency time (LT) tumors start growing "exponentially". LT may be considered as a measure of the time needed by tumor cells to productively interact with the murine microenvironment. Both LT and exponential growth contribute to TT. Interestingly, correlation between LT and ACC expression was also significant (Figure 4). Thus, ACC seems to be related to tumor growth when these interactions are being established. Speculatively, lipid metabolism within PDXs may be important for *in vivo* increase in tumor growth by inducing the recruitment of stromal cells, such as fibroblasts and innate immune cells. Alternatively, ACC could modulate cell autonomous features of cancer cells, although ACC expression did not correlate with cell proliferation markers (Ki67). Finally, lipid metabolism could regulate tumor cell apoptosis, which we did not evaluate in these samples. As note of cautiousness, given the small number of PDX analyzed, hypothesis about the prognostic role of ACC in NSCLC need to be confirmed by larger studies involving either PDX or patients' samples.

In conclusion, results of this pilot study support the feasibility of a metabolic classification of NSCLC PDXs based on quantification of IHC markers by digital pathology. There are, however, some intrinsic limitations of our study, including the small number of PDX samples and markers analyzed, the limited investigation of the spatial distribution of the different markers and the lack of orthogonal validation of findings by state-of-the-art techniques used to study tumor metabolism. Additional constraints are represented by the lack of comparison between the PDX and the original primary tumor and lack of validation between the metabolic characterization and response to metabolic therapies. Therefore, additional studies will be required to consolidate these preliminary results and identify additional markers for a refinement of the proposed panel. Finally, larger cohorts of samples need to be analyzed to establish the possible prognostic or predictive value of these metabolism-associated markers in NSCLC.

Data availability statement

The original contributions presented in the study are included in the article/Supplementary Material. Further inquiries can be directed to the corresponding author.

Ethics statement

Approval of the research protocol by an Institutional Reviewer Board: The study was conducted in accordance with the Declaration of Helsinki, and approved by the Institutional Review and the Ethics Boards of the Fondazione IRCCS Istituto Nazionale Tumori.

Author contributions

Conceptualization, EZ and SI. Methodology, FF, EZ, MM, TZ, and GE. Software, FF and PD. Validation, FF. Formal analysis, FF and PD. Resources, SI. Data curation, SI. Writing—original draft preparation, SI. Writing—review and editing, SI, MM, CB, GS, EZ, and FF. Visualization, SI. Supervision, SI. Project administration, SI. Funding acquisition, SI. All authors contributed to the article and approved the submitted version.

Funding

The research leading to these results has received funding from AIRC under IG 2020 - ID. 25179 project – P.I. Stefano Indraccolo and AIRC IG 2019 – ID. 23244 – P.I. Gabriella Sozzi and from IOV Intramural Grant 5x1000 (year 2018), PI Stefano Indraccolo.

Acknowledgments

We thank Dr. Antonio Scapinello for technical support eoth Ki67 IHC staining and Dr. Giovanni Centonze for technical support.

Conflict of interest

The authors declare that the research was conducted in the absence of any commercial or financial relationships that could be construed as a potential conflict of interest.

Publisher's note

All claims expressed in this article are solely those of the authors and do not necessarily represent those of their affiliated organizations, or those of the publisher, the editors and the reviewers. Any product that may be evaluated in this article, or claim that may be made by its manufacturer, is not guaranteed or endorsed by the publisher.

Supplementary material

The Supplementary Material for this article can be found online at: https://www.frontiersin.org/articles/10.3389/fonc.2023.1070505/full#supplementary-material

References

1. Hu J, Locasale JW, Bielas JH, O'Sullivan J, Sheahan K, Cantley LC, et al. Heterogeneity of tumor-induced gene expression changes in the human metabolic network. *Nat Biotechnol* (2013) 31:522–9. doi: 10.1038/nbt.2530

2. Monferrer E, Vieco-Martí I, López-Carrasco A, Fariñas F, Abanades S, de la Cruz-Merino L, et al. Metabolic classification and intervention opportunities for tumor energy dysfunction. *Metabolites* (2021) 11:264. doi: 10.3390/metabo11050264

3. Rosario SR, Long MD, Affronti HC, Rowsam AM, Eng KH, Smiraglia DJ. Pan-cancer analysis of transcriptional metabolic dysregulation using the cancer genome atlas. *Nat Commun* (2018) 9:5330. doi: 10.1038/s41467-018-07232-8

4. Yang C, Huang X, Liu Z, Qin W, Wang C. Metabolism-associated molecular classification of hepatocellular carcinoma. *Mol Oncol* (2020) 14:896–913. doi: 10.1002/1878-0261.12639

5. Zhang M, Wang H, Peng R, Xu F, Wang F, Zhao Q. Metabolism-associated molecular classification of colorectal cancer. *Front Oncol* (2020) 10:602498. doi: 10.3389/fonc.2020.602498

6. Caro P, Kishan AU, Norberg E, Stanley IA, Chapuy B, Ficarro SB, et al. Metabolic signatures uncover distinct targets in molecular subsets of diffuse Large b cell lymphoma. *Cancer Cell* (2012) 22:547–60. doi: 10.1016/j.ccr.2012.08.014

7. Farge T, Saland E, de Toni F, Aroua N, Hosseini M, Perry R, et al. Chemotherapy-resistant human acute myeloid leukemia cells are not enriched for leukemic stem cells but require oxidative metabolism. *Cancer Discovery* (2017) 7:716–35. doi: 10.1158/2159-8290.CD-16-0441

8. Gentric G, Kieffer Y, Mieulet V, Goundiam O, Bonneau C, Nemati F, et al. PML-regulated mitochondrial metabolism enhances chemosensitivity in human ovarian cancers. *Cell Metab* (2019) 29:156–173.e10. doi: 10.1016/j.cmet.2018.09.002

9. Garofano L, Migliozzi S, Oh YT, D'Angelo F, Najac RD, Ko A, et al. Pathway-based classification of glioblastoma uncovers a mitochondrial subtype with therapeutic vulnerabilities. *Nat Cancer* (2021) 2:141–56. doi: 10.1038/s43018-020-00159-4

10. Koh YW, Lee SJ, Park SY. Differential expression and prognostic significance of GLUT1 according to histologic type of non-small-cell lung cancer and its association with volume-dependent parameters. *Lung Cancer* (2017) 104:31–7. doi: 10.1016/j.lungcan.2016.12.003

11. Hensley CT, Faubert B, Yuan Q, Lev-Cohain N, Jin E, Kim J, et al. Metabolic heterogeneity in human lung tumors. *Cell* (2016) 164:681–94. doi: 10.1016/j.cell.2015.12.034

12. Faubert B, Li KY, Cai L, Hensley CT, Kim J, Zacharias LG, et al. Lactate metabolism in human lung tumors. *Cell* (2017) 171:358–371.e9. doi: 10.1016/j.cell.2017.09.019

13. Davidson SM, Papagiannakopoulos T, Olenchock BA, Heyman JE, Keibler MA, Luengo A, et al. Environment impacts the metabolic dependencies of ras-driven non-small cell lung cancer. *Cell Metab* (2016) 23:517–28. doi: 10.1016/j.cmet.2016.01.007

14. Schuurbiers OCJ, Meijer TWH, Kaanders JHAM, Looijen-Salamon MG, de Geus-Oei L-F, van der Drift MA, et al. Glucose metabolism in NSCLC is histology-specific and diverges the prognostic potential of 18FDG-PET for adenocarcinoma and squamous cell carcinoma. *J Thorac Oncol* (2014) 9:1485–93. doi: 10.1097/JTO.0000000000000286

15. Majem B, Nadal E, Muñoz-Pinedo C. Exploiting metabolic vulnerabilities of non small cell lung carcinoma. *Semin Cell Dev Biol* (2020) 98:54–62. doi: 10.1016/j.semcdb.2019.06.004

16. Payen VL, Mina E, Van Hée VF, Porporato PE, Sonveaux P. Monocarboxylate transporters in cancer. *Mol Metab* (2020) 33:48–66. doi: 10.1016/j.molmet.2019.07.006

17. Pavlova NN, Thompson CB. The emerging hallmarks of cancer metabolism. *Cell Metab* (2016) 23:27–47. doi: 10.1016/j.cmet.2015.12.006

18. Piga I, Verza M, Montenegro F, Nardo G, Zulato E, Zanin T, et al. *In situ* metabolic profiling of ovarian cancer tumor xenografts: A digital pathology approach. *Front Oncol* (2020) 10:1277. doi: 10.3389/fonc.2020.01277

19. Fabian C, Koetz L, Favaro E, Indraccolo S, Mueller-Klieser W, Sattler UGA. Protein profiles in human ovarian cancer cell lines correspond to their metabolic activity and to metabolic profiles of respective tumor xenografts. *FEBS J* (2012) 279:882–91. doi: 10.1111/j.1742-4658.2012.08479.x

20. Menendez JA, Lupu R. Fatty acid synthase and the lipogenic phenotype in cancer pathogenesis. *Nat Rev Cancer* (2007) 7:763–77. doi: 10.1038/nrc2222

21. Zaidi N, Lupien L, Kuemmerle NB, Kinlaw WB, Swinnen JV, Smans K. Lipogenesis and lipolysis: The pathways exploited by the cancer cells to acquire fatty acids. *Prog Lipid Res* (2013) 52:585–9. doi: 10.1016/j.plipres.2013.08.005

22. Matés JM, Campos-Sandoval JA, Márquez J. Glutaminase isoenzymes in the metabolic therapy of cancer. *Biochim Biophys Acta (BBA) - Rev Cancer* (2018) 1870:158–64. doi: 10.1016/j.bbcan.2018.07.007

23. Moro M, Bertolini G, Caserini R, Borzi C, Boeri M, Fabbri A, et al. Establishment of patient derived xenografts as functional testing of lung cancer aggressiveness. *Sci Rep* (2017) 7:6689. doi: 10.1038/s41598-017-06912-7

24. Moro M, Bertolini G, Tortoreto M, Pastorino U, Sozzi G, Roz L. Patient-derived xenografts of non small cell lung cancer: Resurgence of an old model for investigation of modern concepts of tailored therapy and cancer stem cells. *J Biomed Biotechnol* (2012) 2012:1–11. doi: 10.1155/2012/568567

25. Fedchenko N, Reifenrath J. Different approaches for interpretation and reporting of immunohistochemistry analysis results in the bone tissue – a review. *Diagn Pathol* (2014) 9:221. doi: 10.1186/s13000-014-0221-9

26. Cao Y. Adipocyte and lipid metabolism in cancer drug resistance. *J Clin Invest* (2019) 129:3006–17. doi: 10.1172/JCI127201

27. Sanchez-Cespedes M, Parrella P, Esteller M, Nomoto S, Trink B, Engles JM, et al. Inactivation of LKB1/STK11 is a common event in adenocarcinomas of the lung. *Cancer Res* (2002) 62:3659–62.

28. Shackelford DB, Shaw RJ. The LKB1–AMPK pathway: metabolism and growth control in tumour suppression. *Nat Rev Cancer* (2009) 9:563–75. doi: 10.1038/nrc2676

29. Vander Heiden MG, Cantley LC, Thompson CB. Understanding the warburg effect: The metabolic requirements of cell proliferation. *Science* (2009) 324:1029–33. doi: 10.1126/science.1160809

30. Ippolito L, Morandi A, Giannoni E, Chiarugi P. Lactate: A metabolic driver in the tumour landscape. *Trends Biochem Sci* (2019) 44:153–66. doi: 10.1016/j.tibs.2018.10.011

31. Hidalgo M, Amant F, Biankin AV, Budinská E, Byrne AT, Caldas C, et al. Patient-derived xenograft models: An emerging platform for translational cancer research. *Cancer Discovery* (2014) 4:998–1013. doi: 10.1158/2159-8290.CD-14-0001

32. Dong X, Guan J, English JC, Flint J, Yee J, Evans K, et al. Patient-derived first generation xenografts of non–small cell lung cancers: Promising tools for predicting drug responses for personalized chemotherapy. *Clin Cancer Res* (2010) 16:1442–51. doi: 10.1158/1078-0432.CCR-09-2878

33. Fichtner I, Rolff J, Soong R, Hoffmann J, Hammer S, Sommer A, et al. Establishment of patient-derived non–small cell lung cancer xenografts as models for the identification of predictive biomarkers. *Clin Cancer Res* (2008) 14:6456–68. doi: 10.1158/1078-0432.CCR-08-0138

34. Ilie M, Nunes M, Blot L, Hofman V, Long-Mira E, Butori C, et al. Setting up a wide panel of patient-derived tumor xenografts of non–small cell lung cancer by improving the preanalytical steps. *Cancer Med* (2015) 4:201–11. doi: 10.1002/cam4.357

35. Lee HW, Lee J, Lee SJ, Cho HJ, Song HJ, Jeong DE, et al. Patient-derived xenografts from non–small cell lung cancer brain metastases are valuable translational platforms for the development of personalized targeted therapy. *Clin Cancer Res* (2015) 21:1172–82. doi: 10.1158/1078-0432.CCR-14-1589

36. Russo MV, Faversani A, Gatti S, Ricca D, Del Gobbo A, Ferrero S, et al. A new mouse avatar model of non-small cell lung cancer. *Front Oncol* (2015) 5:52. doi: 10.3389/fonc.2015.00052

37. Hao C, Wang L, Peng S, Cao M, Li H, Hu J, et al. Gene mutations in primary tumors and corresponding patient-derived xenografts derived from non-small cell lung cancer. *Cancer Lett* (2015) 357:179–85. doi: 10.1016/j.canlet.2014.11.024

38. Bertotti A, Migliardi G, Galimi F, Sassi F, Torti D, Isella C, et al. A molecularly annotated platform of patient-derived xenografts ("Xenopatients") identifies HER2 as an effective therapeutic target in cetuximab-resistant colorectal cancer. *Cancer Discovery* (2011) 1:508–23. doi: 10.1158/2159-8290.CD-11-0109

39. Morandi A, Indraccolo S. Linking metabolic reprogramming to therapy resistance in cancer. *Biochim Biophys Acta (BBA) - Rev Cancer* (2017) 1868:1–6. doi: 10.1016/j.bbcan.2016.12.004

40. Bacci M, Lorito N, Smiriglia A, Morandi A. Fat and furious: Lipid metabolism in antitumoral therapy response and resistance. *Trends Cancer* (2021) 7:198–213. doi: 10.1016/j.trecan.2020.10.004

41. Valtorta S, Moro M, Prisinzano G, Bertolini G, Tortoreto M, Raccagni I, et al. Metabolic evaluation of non–small cell lung cancer patient–derived xenograft models using ^{18} f-FDG PET: A potential tool for early therapy response. *J Nucl Med* (2017) 58:42–7. doi: 10.2967/jnumed.116.176404

42. DeBerardinis RJ, Cheng T. Q's next: the diverse functions of glutamine in metabolism, cell biology and cancer. *Oncogene* (2010) 29:313–24. doi: 10.1038/onc.2009.358

43. Li H, Ning S, Ghandi M, Kryukov GV, Gopal S, Deik A, et al. The landscape of cancer cell line metabolism. *Nat Med* (2019) 25:850–60. doi: 10.1038/s41591-019-0404-8

44. Galan-Cobo A, Sitthideatphaiboon P, Qu X, Poteete A, Pisegna MA, Tong P, et al. LKB1 and KEAP1/NRF2 pathways cooperatively promote metabolic reprogramming with enhanced glutamine dependence in *KRAS* -mutant lung adenocarcinoma. *Cancer Res* (2019) 79:3251–67. doi: 10.1158/0008-5472.CAN-18-3527

45. Shackelford DB, Abt E, Gerken L, Vasquez DS, Seki A, Leblanc M, et al. LKB1 inactivation dictates therapeutic response of non-small cell lung cancer to the metabolism drug phenformin. *Cancer Cell* (2013) 23:143–58. doi: 10.1016/j.ccr.2012.12.008

frontiers | Frontiers in Oncology

TYPE Review
PUBLISHED 24 March 2023
DOI 10.3389/fonc.2023.1098581

OPEN ACCESS

EDITED BY
Shiv K. Gupta,
Mayo Clinic, United States

REVIEWED BY
Qingjia Chi,
Wuhan University of Technology, China
Song Xu,
Tianjin Medical University General Hospital, China
Depeng Jiang,
Second Affiliated Hospital of Chongqing Medical University, China

*CORRESPONDENCE
Guogui Sun
guogui_sun2021@sina.com

SPECIALTY SECTION
This article was submitted to Cancer Molecular Targets and Therapeutics, a section of the journal Frontiers in Oncology

RECEIVED 15 November 2022
ACCEPTED 13 March 2023
PUBLISHED 24 March 2023

CITATION
Liu W, Cui Y, Zheng X, Yu K and Sun G (2023) Application status and future prospects of the PDX model in lung cancer. *Front. Oncol.* 13:1098581. doi: 10.3389/fonc.2023.1098581

Application status and future prospects of the PDX model in lung cancer

Wei Liu, Yishuang Cui, Xuan Zheng, Kunpeng Yu and Guogui Sun*

Department of Hebei Key Laboratory of Medical-Industrial Integration Precision Medicine, School of Public Health, School of Clinical Medicine, Affiliated Hospital, North China University of Science and Technology, Tangshan, China

Lung cancer is one of the most prevalent, fatal, and highly heterogeneous diseases that, seriously threaten human health. Lung cancer is primarily caused by the aberrant expression of multiple genes in the cells. Lung cancer treatment options include surgery, radiation, chemotherapy, targeted therapy, and immunotherapy. In recent decades, significant progress has been made in developing therapeutic agents for lung cancer as well as a biomarker for its early diagnosis. Nonetheless, the alternative applications of traditional pre-clinical models (cell line models) for diagnosis and prognosis prediction are constrained by several factors, including the lack of microenvironment components necessary to affect cancer biology and drug response, and the differences between laboratory and clinical results. The leading reason is that substantial shifts accrued to cell biological behaviors, such as cell proliferative, metastatic, invasive, and gene expression capabilities of different cancer cells after decades of growing indefinitely *in vitro*. Moreover, the introduction of individualized treatment has prompted the development of appropriate experimental models. In recent years, preclinical research on lung cancer has primarily relied on the patient-derived tumor xenograft (PDX) model. The PDX provides stable models with recapitulate characteristics of the parental tumor such as the histopathology and genetic blueprint. Additionally, PDXs offer valuable models for efficacy screening of new cancer drugs, thus, advancing the understanding of tumor biology. Concurrently, with the heightened interest in the PDX models, potential shortcomings have gradually emerged. This review summarizes the significant advantages of PDXs over the previous models, their benefits, potential future uses and interrogating open issues.

KEYWORDS

lung cancer, PDX model, pre-clinical research, personalized medicine, co-clinical trials

1 Introduction

Lung cancer, also termed known as bronchogenic carcinoma, is a malignant lung tumor originating in the lung parenchyma or within the bronchi, accounting for approximately 22.7% of malignant tumors. Lung cancer development involves complex and multiple factors and genes. There are more than 50 subtypes of lung cancers broadly classified into small cell lung cancer (SCLC) and non-small cell lung cancer (NSCLC), which account for 15% and 85% of lung cancers, respectively. There are several types of NSCLC, including lung adenocarcinoma (LUAD) (40-50%) and lung squamous cell carcinoma (LUSC) (30%). Other pathological types (5%) include adenosquamous carcinoma (ASC), large cell lung carcinoma (LCLC), and carcinoid tumor (CT) (1–3). The onset of lung cancer is insidious and most clinical patients have distant metastases at the time of definite diagnosis. Regrettably, the overall five-year survival rate of patients with lung cancer is only 17.8% (4, 5). Lung cancer has emerged as the leading cause of cancer-related mortality worldwide. China has experienced an alarming increase in lung cancer incidences and mortality rates yearly (6). Research is needed to identify early markers for lung cancer development to improve treatment outcomes and reduce related mortality. Overall, there is an urgent need to reduce the poor prognosis of lung cancer through accurate early diagnosis and treatment.

There has been rapid and tremendous progress in the development of anti-tumor drugs. In the 1970s, scholars used two-dimensional monolayer cultured cell lines as cancer research models for drug screening. It was later discovered that the established cell lines are selected from specific tumor subsets. Therefore, they do not fully represent the complex clinical intra-tumoral heterogeneity (7). In addition, cell lines lose critical properties after long-term *in vitro* culture. Thus, given the low clinical predictive power of cell lines, most anti-tumor drugs fail in phase III clinical trials. Accordingly, fewer than 5% of candidate drugs are approved for the market (8). In response to the need for effective anti-cancer drugs, the National Cancer Institute (NCI, MD, USA) recommended the PDX models and discontinued the NCI-60 cancer cell line approach (9). The EurOPDX Consortium, containing more than 1500 samples in a PDX bank, also demonstrated that the PDX model is a more feasible tool for *in vitro* research (10, 11). PDX models are developed by implanting cancerous tissue from a patient's tumor into immunodeficient mice (12). Compared with the cell line models, a PDX model better reflects the structure and microenvironment of the original tumor, and shows less genetic divergence. Besides, PDX models largely retain the primary patient tumor histopathological characteristics and molecular features (13–15). Since PDX model allows several subclones to grow in parallel, it enables them to retain their heterogeneity (10). These advantages make the PDX model a superior platform to facilitate drug development within a shorter period, and identify new targets for cancer therapy. In contrast to cell line models, PDX models can reveal the patterns of tumor evolutionary dynamics under the strong environmental selection pressure and drug resistance mechanisms *in vivo*. Notably, a strong correlation between drug response in PDX models and clinical response (16). Experiments PDXs have revealed accurate therapeutic candidates, minimizing treatment-related toxicity. This review summarizes the salient advantages, recent advances, and gaps in lung cancer precision medicine based on PDX models. Generally, PDX models are key to tackling the precision medicine challenges.

2 The pre-clinical models for lung cancer research

To date, a substantial number of the preclinical models for lung cancer research, including traditional lung cancer cell lines (A549, SK-MES-1, HCC827) and genetically engineered mouse models (GEMM), which remain the primary tools for incipient drug development, have been developed (17). Cell line models are rapid and efficient in investigating the potential epigenetic and lung cancer drug treatment mechanisms, attributed to their operation, low cost, high success rate, and high reproducibility. However, the traditional models for lung cancer research face numerous challenges, including cell lines' loss of critical properties after prolonged *in vitro* culture and the technological inability to interplay with the tumor microenvironment (18). In addition, pre-clinical models may experience gene alterations that cause gain/loss of genetic information and alter the seeding ability and the invasiveness of tumor cells (19). On the other hand, GEMM establishment promotes tumor formation by interfering with specific small molecules, which might influence tumor progression through the alteration of multiple gene loci. For the GEMM model, human-specific immunotherapeutic cannot be tested because mouse biology is not exactly similar to that of humans (20). Therefore, the GEMM model limits preclinical drug research.

Current and ongoing studies based on the PDX models have opened a new avenue for cancer treatment by overcoming the inherent limitations of the traditional models (21–23). The PDX model is the most accurate platform for predicting drug response (24–30). One striking feature of PDX is its ability to overcome cell-line-related limitations. At the cellular level, PDXs retain patients' heterogeneity and histopathology. Moreover, whole-exome sequencing revealed the high genomic and transcriptional similarity between the PDX model and the primary tumor rearing (31, 32). The PDX model provides clinically relevant pre-clinical tools that simulate the clinical response of patients (33). Also, studies show that PDX models consistently predict response to therapy in patients regardless of passages, supporting the phenotypic stability of these models (34). The PDXs accurately predict cancer treatment response, promoting their use in cancer therapy research. Combined with the molecular omics analysis of PDX models, pathways related to patient tumor biogenesis and development may be discovered. Consequently, in the context of personalized medicine, a PDX model can identify biomarkers that predict cancer treatment response, underlining its usefulness for preclinical cancer research. Thus, PDX can facilitate the identification of lung cancer pathophysiologies and accurate

treatment targets. Furthermore, the tumor samples from PDXs provide sufficient materials for cancer-related studies. Research is needed to identify the dynamic changes and genetic characteristics of different tumors to promote the development of targeted therapy and precision medicine (35–37). A PDX model is invaluable for mechanistic research, new drug development, and personalized therapy (38, 39), and relevant for pre-clinical research. High-quality PDX models can have a prognostic value and predict tumor evolution and recurrence probability. They can also reveal potential diagnostic and therapeutic targets, promoting the development of precision medicine (40–42).

3 The establishment of the PDX model

3.1 Mouse strains used for the PDX model

The mice with an intact immune system will produce robust immune responses to abrogate the implanted tumor tissue. Thus, immunodeficient mice are required to develop the PDX models. Nude CB17-SCID mice, NOD-SCID mice, NOG (NOD/SCID/IL-2γpartial deficiency) mice, and NSG (NOD/SCID/IL-2Rγcomplete deficiency) mice are the common mainstay mouse strains for PDX model establishment. Among them, nude mice are the most commonly used. These mice lack body hair and thymus. Given the absence of the thymus, these mice are T-cell deficient and, thus, cannot induce an adaptive immune response. The nude mouse model was first reported in 1966 by Flanagan (43), which allowed the growth of human cancer cells in mice. Subsequently, the use of CB17-SCID mice and NOD-SCID mice emerged successively. However, due to the high incidence of spontaneous lymphoma, CB17-SCID mice mostly die prematurely (44). In addition, the incidence of immunological leakage in CB17-SCID mice is extremely high.

Similarly, spontaneous lymphoma, in most cases, occurs later in NOD-SCID mice aged around 8.5 months (45). Consequently, neither mouse is suitable for long-term experiments. By the early 2000s, the Central Institute for Experimental Animals (CIEA) developed a severely immunocompromised NOG mouse, significantly improving the survival rate of human cell and tissue transplantation in immunocompromised mice. In 2005, the US Jackson Laboratory cultured NOD/SCID/IL2R gamma (null) mouse, also known as NSG mouse, with a higher transplantation rate and lower tumor graft rejection (46). The NSG mice lack mature T, B, and NK cells for genetic mutations. Thus, the NSG mice are currently the most ideal tumor graft receptors and are less prone to lymphoma development, and have a longer lifespan than other mice (Nude, SCID mice, NOD-SCID mice). The tabular comparison of several immunodeficient mice is shown in Table 1. Therefore, the NSG recipient mice offer several advantages for transplantation with human hematopoietic stem cells (46, 47). The NSG mouse is also called "humanized mouse," or the human immune system (HIS) model because it supports the growth of human hematopoietic stem cells. Thus, it developed an immune system and produced human T cells similar to those of humans (48). The processes of developing the HIS model are sketched in Figure 1. The humanized PDX model with patient-matched immune components has several advantages over the alternative models for decoding tumor biology and anti-tumor drug development.

3.2 Implantation tissues and cells and methods

The implanted tissues or cells can be patient biopsies or tumor cells derived from ascites or pleural fluid (Figure 2). The implantation tissues comprise small 1-3 mm^3 clumps or single cell suspensions prepared by digesting small tissue fragments. Co-transplanting with the matrigel increases the engraftment success rates (Figure 2). In 1990, Fridman et al. reported that the transplant success rate was significantly higher when lung cancer tissue and matrigel were intertwined and implanted into nude mice (49). To this end, tumor-associated fibroblasts and mesenchymal stem cells provide functional support for tumor progression and development. Furthermore, diversities that may also interfere with the ability of the graft to grow successfully were assessed and compared for ligand-receptor interactions between humans and mice. It was found that some mouse ligands do not activate the corresponding human receptors (50–52).

In brief, proper expression of some human ligands in immunocompromised mice may stimulate graft growth. Ectopic or orthotopic transplantation is traditionally performed *via* subcutaneous and intravenous injection and other forms. The

TABLE 1 Comparison between immunized mice.

	Nude	SCID mouse	NOD-scid mouse	NOG/NSG mouse
Mature T cell	–	–	–	–
Mature B cell	++	–	–	–
NK cell	+++	++	+	–
Macrophage	++++	+++	++	+
Dendritic cell	++++	+++	++	+
Incidence of immune leakage	High	High	Lower	Lower
Tumor formation rate	Low	Higher	High	High

Immune function: Hardly (-); Low (+); Medium (++/+++); High (++++).

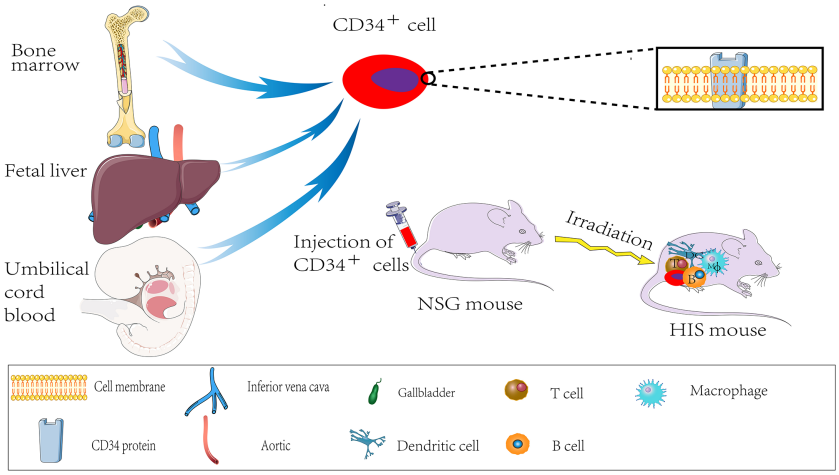

FIGURE 1
HIS mouse production process.

subcutaneous transplantation model is the most extensively used owing to its simple operation and convenient measurement of tumor size. The implantation site is often the back or underarm of mice, which is an excellent model for drug response assessment. Nonetheless, given the limited tumor space, the transplant does not grow in the correct anatomical location. Therefore, this could not be a suitable approach for tumor metastasis research since the tumor does not grow in the correct anatomical location and microenvironment. A differential display analysis is required to compare graft biology and drug response on the *in situ* model and the ectopic model.

Priority should be given to tail vein injection to build an orthotopic transplantation model for tumor metastasis study. The advantage of tail vein injection is that the external environment of *in situ* tumor is closer to the human tumor, providing an experimental basis for subsequent tumor metastasis research (Figure 2). Effective transplantation is the nascent basis of the experiment, and many factors can affect the implantation rate. The large vascular bed beneath the renal capsule facilitates the growth of the graft. Xin et al. implanted tumor tissue from NSCLC patients under the renal capsule to obtain an implantation rate of up to 90% (53) and successfully evaluated the sensitivity of patients' chemotherapy regimen using PDX models. The subcutaneous transplantation success rate is only about 23% (54).

Furthermore, Chen et al. (55) reported that PDX was higher in squamous cell carcinoma, stage II, stage III, and poorly differentiated tumor specimens by following clinically confirmed NSCLC patients for up to 1.5 to 6 years. Additionally, some studies have shown that the implantation rate of PDX tumors after passage increases with the number of passages, and the long-time of tissue *in vitro* is associated with low implantation rates. Moreover, the implantation rate of brain NSCLC metastases is higher than the primary tumor (56), suggesting that the source of the samples potentially affects the implantation rate. Notably, the PDX was not

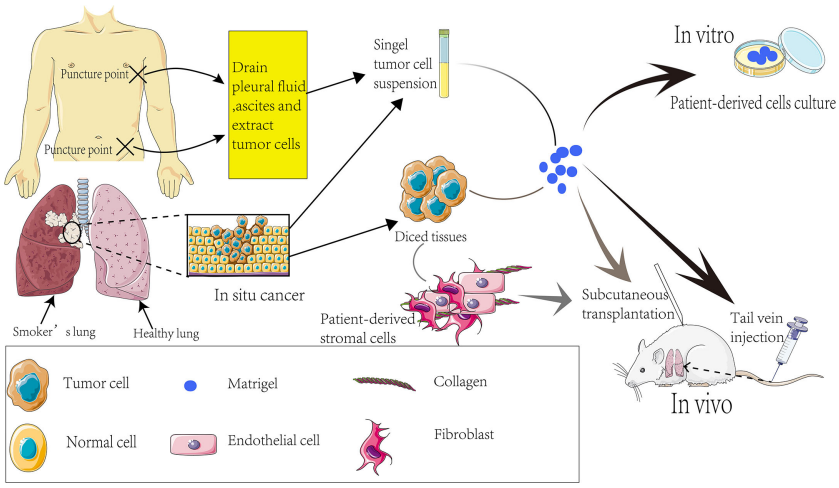

FIGURE 2
Establishment process of PDX models.

established in the mouse generating human $CD20^+$ immune cells. Therefore, adding rituximab during primary tumor implantation may decrease the frequency of lymphoma formation and promote PDX growth.

4 Applications of the PDX model for lung cancer research

4.1 Immunotherapy

The immune system is responsible for maintaining tumor regression (57). Programmed death ligand 1 (PD-L1) is present on the surface of tumor cells and inhibits the activation and proliferation of T cells, which results in immune escape of tumor cells by specifically binding the programmed death receptor-1 (PD-1) (58, 59). Moreover, T cell depletion is common in people with cancer or chronic infection (60, 61). The T cell depletion is characterized by loss of T cell effector function and continuously increased expression of immune-inhibitory receptors, one of the leading causes of immune disorders in cancer patients. Fortunately, numerous studies have demonstrated the vital role of PD-1 inhibitors in reversing T cell depletion (62–64). In other research, the use of cancer immunotherapy with antibodies, cancer vaccines, and immune checkpoint inhibitors (ICIs) as an emerging and efficient pathway has attracted widespread attention (65–67). Researchers have made unprecedented advances in immunotherapy by utilizing humanized mouse PDX models to accelerate acquired studies of clinically relevant tumors and evaluation of the clinical value of cancer immunotherapy. Humanized mice with human hematopoietic stem cells have been broadly reported as a potent tool in studying targeted PD-1 antibodies (68). Injecting PDX mice with fresh cord blood containing $CD34^+$ hematopoietic stem cells to rebuild the immune system significantly shortens the time and regenerates functional, active immune cells. This overrides the delayed tumor transplantation caused by prolonged immune system establishment and the limitation of the incomplete immune system. Immunotherapy provides a new strategy for lung cancer treatment (69, 70). The optimized PDX models are ideal for testing the significant inhibitory effect of the antagonistic PD-1 checkpoint drug-pembrolizumab on lung cancer PDX tumors. Research shows that pembrolizumab-activated human immune cells could effectively limit tumor growth. Targeting cytotoxic T lymphocyte-associated protein 4, PD-1, and PD-L1 using antibodies to block immunomodulatory checkpoints on tumor cells, immune cells, and endothelial cells is an effective NSCLC therapy. Numerous studies have shown that immune checkpoint inhibitors such as PD-L1 and CTLA4 significantly increase the survival rate of advanced NSCLC patients.

Moreover, long patient follow-up studies reveal that the five-year survival rate of NSCLC patients receiving such treatment is as high as 16% (71). The anti-PD-1 drug pembrolizumab is currently approved as an immunotherapy regimen for patients with advanced NSCLC expressing PD-L1 (72–75). Moreover, Nivolumab and Atezolizumab can be used despite PD-L1 expression in NSCLC (76, 77). The studies cited above show great promise in oncology research *via* the use of the PDX model to study and evaluate the necessity of immunotherapy (78).

4.2 Drug resistance models for lung cancer

The US Food and Drug Administration has approved more than 20 drugs for the NSCLC treatment, including 14 targeted and immunotherapy drugs. However, the rapid emergence of drug resistance and the diverse resistance mechanisms continue to threaten the ability to treat NSCLC patients. While significant advancements have been made for NSCLC treatment, acquired resistance remains a significant barrier to therapeutic response (79, 80). The genetic alteration uncertainties in patients after treatment is an obstacle to conducting prospective studies. There is an urgent need to identify biomarkers for predicting acquired resistance or poor response of lung cancer to ICIs. The PDX model is ideal for drug resistance studies, including identifying mutations that promote treatment resistance (81). Therefore, the PDX model is critical in the next phase of drug development and reduces the lag in clinical trials. The SCLC patient's response rate to first-line chemotherapy is about 70%. Nevertheless, most patients experience rapidly acquired resistance within months of treatment, rapid relapse, and poor efficacy of second-line treatment (82, 83). The development of PDX models has been invaluable for investigating acquired drug resistance of tumors.

Previous research reported that EZH2 promotes the development of acquired resistance of PDX by silencing SLFN11. However, after EZH2 knockdown, the PDX tumors' resistance was suppressed, and the drug efficacy was optimized (84). The exact resistance mechanism of the original tumor was observed in the PDX model of LUAD (85). These studies demonstrate that PDX models accurately predict the patient's drug response. The widespread uses of ICIs, including PD-1, PD-L1, and CTLA4 antagonistic antibodies, ushered in a new era of cancer immunotherapeutic. However, as PD-1 axis inhibitors become increasingly established in standard treatment options for lung cancer, more patients show resistance to these therapies. Research is needed to identify the mechanisms underlying the acquired resistance of ICIs in lung cancer to overcome the drug resistance of ICIs.

4.3 Identification and evaluation of drugs and treatment regimens for lung cancer

The emergence of the PDX model in drug research development and addressing cancer treatment challenges provides tools for better research. Using the PDX model carrying tumor as the embodiment to evaluate drug efficacy before treatment, it can not only screen for the best anti-cancer treatment but also avoid some adverse drug reactions, which will have a significant impact on patients' treatment decisions (Figure 3). As indicated earlier, the

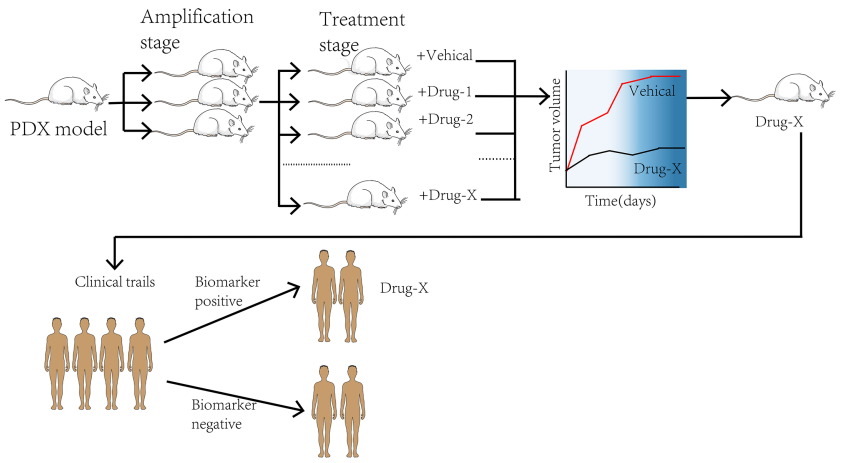

FIGURE 3
The process of co-clinical trial.

PDX model identifies fewer common microwaves, nanoparticles, gene therapies, and the potential of new anti-cancer drugs for future intervention in tumor development, thus providing a new therapeutic indicator (86). For instance, a PDX model has been used to evaluate three clinical standard protocols for NSCLC patients. The results showed that patients had different sensitivity to the three regimens. Moreover, the patients were not equally sensitive to the same regimen. These findings suggest that the PDX model determines the treatment response and predicts individualized treatment regimens for patients with NSCLC (61). Furthermore, the PDX model predictably addresses the effects of small molecule compounds, antibodies, and microorganisms on lung cancer (87). There are three molecular LUAD subtypes (88–90), with the highly proliferative PP being the most malignant. No validated targeted therapy and immunotherapy have been developed for clinical use against the PP subtype. Therefore, developing specific therapeutic agents will restore hope to patients with the PP subtype. Using nucleic aptamer, Sun et al. found that the leucine-rich PPR-motif containing (LRPPRC) is a specific nucleic aptamer binding protein significantly overexpressed in PP subtype and is strongly linked with the disease stage and patient prognosis. Gossypol acetic acid (GAA) was successfully screened using aptamer-assisted high-throughput methods to specifically bind LRPPRC and cause its degradation in a ubiquitin-proteasome-independent manner. After treatment with GAA, a robust anti-tumor function was shown in the LRPPRC-positive LUAD-PDX models but not in the LRPPRC-negative PDX models. These findings suggest that GAA specifically targeted LRPPRC knockout is a promising therapeutic strategy targeting the PP subtype (91). The above research has entered phase II clinical practice, extending the treatment strategy for lung cancer and highlighting the role of PDX models in developing efficient treatment regimens. Among the functions mentioned earlier, the increase in studies targeting PDXs suggests that PDX models can accurately predict drug response in clinical patients. Therefore, PDX tumor cells can be used for high-throughput screening of anti-cancer therapeutics (92). A study evaluating the use of zebrafish in PDX models reported that transparent zebrafish larvae could visualize individual tumor cells and their response to treatment, acting as a rapid drug screening platform (29). In other words, researchers can fetch the information from the models directly. An intensive drug screening was performed in more than 1,000 PDX models (93). Based on the obtained data, the PDX model has become an essential part of the preclinical screening for new anti-cancer drugs. However, there exist theoretical differences in drug absorption, distribution, and pharmacokinetics between mice and humans, and there may be no natural drug reaction in humans (94, 95). This may result in undesirable consequences after drugs enter clinical trials to determine the pharmacological discrepancies between the two for better future development and testing of anti-tumor drugs.

4.4 Co-clinical trials

With the development of individualized, targeted therapies for genotypes, the preclinical studies and clinical trials are conducted simultaneously to elucidate disease mechanisms. In this context, a PDX model can be used as a personalized “Avatar model” for precision medicine in cancer treatment (96). The pre-clinical and clinical trials are conducted simultaneously in tumor patients with specific genetic structures and the corresponding PDX models in co-clinical trials. The trials compare the response between patients and the models in determining the mechanism of action of drugs and finding new targets and biomarkers (97) (Figure 3). A group of PDX models directly derived from T2 or T3 stage NSCLC patients was established by Iduna et al. (54). The downregulation of EGFR was observed in the sensitive PDX models after the treatment with cetuximab but not in the resistance models. Iduna confirmed the association of KRAS mutations with the EGFR resistance phenotype, demonstrating that KRAS wild-type status is a clinical biomarker for targeted therapy of NSCLC (54). With such fidelity of

the PDX models, it is envisioned that if the pre-clinical studies are performed simultaneously or earlier, the discovery and validation of KRAS mutations as a biomarker for drug resistance will be facilitated. Consequently, such validation linking impactful biomarkers to treatment efficacy will lead to direct clinical effects. The fibroblast growth factor receptor (FGFR) gene is one of the molecular targets of LUSC. As is known to all, dovitinib is a tyrosine kinase inhibitor targeting FGFR. Previous studies have demonstrated that dovitinib has potential anti-tumor capability against tumor cell lines with FGFR1 amplification. Related reports indicated that FGFR1 amplification is associated with poor prognosis in LUSC patients (98). A co-clinical trial concurrent with phase II trials in LUSC patients demonstrated that PDX models accurately replicated patient response to dovitinib. These findings revealed that FGF3 and FGF19 genes were significantly enriched in dovitinib -sensitive tumor cells. In addition, the findings suggest that activation of genes involved in FGFR signaling may be a critical factor in sensitivity to dovitinib (99). The above evidence indicates that the PDX model has strong potential in identifying predictive biomarkers and advancing precision medicine and drug development (100).

5 Limitations of the PDX models

Beyond the aforementioned observations, several aspects of the authenticity of the PDX models in oncology research remain to be clarified. For instance, the engraftment of a PDX can cause lymphoma but not the expected tumors. Besides lymphoma, immune cells present in tumors may induce graft versus host disease (GVHD) (101). The tumor samples obtained by means of surgery are limited by the donor site and size, which subtracts from the value of the PDX models constructed that may not cover the overall tumor heterogeneity of patients. Patients with advanced SCLC release a large number of CTCs (102, 103), and because of the random process of CTCs generation in peripheral blood, establishing PDX models through CTCs may be an effective approach to at least partially resolve some problems. Other studies reported some traces of tumor evolution in PDX models, and continuous aged PDX models improved the tumor biology over time (104–106). Surprisingly, alterations in copy number aberrations (CNAs) were found in the models after serial passages, which were somewhat different from the original tumors. The level of CNAs is closely related to drug sensitivity (107) and cancer lethality. When the xenografts are grown to be able for drug screening, the human stromal cells originally present in the original tumor have been replaced by mouse stromal cells, however, some cytokines derived from mice do not exert human-derived cytokines (108), in accordance, some researchers have implanted the patient's stromal cells together with tumor tissue in mice (Figure 2). The cross-reactive between LUSC cells and tumor microenvironment was elucidated in the study by Chen et al. (109). Cancer-associated fibroblasts (CAFs) inhibit SOX2-induced dysplasia and abnormal proliferation of acinar phenotypes in the PDX model-derived TUM622 cell line, and the drug distribution interfered by new mouse stroma can also affect experimental results (109). Studies have shown that the matrigel promotes the survival of mice (48). However, matrigel, a basement membrane substrate derived from EHS mice (110), can cause murine virus infection, hence, its function remains to be clarified, with regard to this facet, using the production of matrigel by ourselves is able to avoid viral contamination to some extent. In addition to the above obvious limitations of the PDX model, the following issues remain to be addressed. Above all, the engraftment failure rate is still high as before (30), it is expensive with little benefit (16). In the next place, the disconnection between the time needed for PDX expansion and treatment (which usually takes 4 to 8 months to build a PDX model) and the rapidity of disease progression in patients. There may be ethical problems under certain conditions (111). Despite the application of "humanized mice" to screen immunomodulators such as vaccines, the challenges that are intrinsic to successfully reconstruct the immune system in mice and maintain a long-term effect. The limitations of the PDX model should be addressed to improve its application in the management of lung cancer.

6 Organoids

Given the aforementioned disadvantages of PDX models, stem cells and 3D culture techniques have been used to study organoids. Compared with PDX models, patient-derived organoids shorten the duration of PDX model establishment cycle, increase the transplantation rate, and reduces production costs (112), which contributes to the development of personalized medicine, and are more suitable for large-scale drug screening (Figure 4). Notably, organoids combined with other technologies, such as organ chips, 3D printing, and the recently developed approaches that rely upon CRISPR-HOT have improved research on the impact of the tumor microenvironment on tumor development. Organ chips combine organoid technology and microfluidics to provide better control of tumor-related experimental parameters as well as the simulation of the tumor microenvironment during drug screening. Thus, organoids have a greater advantage over the labor-intensive PDX model, and have fewer adverse effects because they gradually replace the human matrix with the mouse matrix at later stages. Furthermore, patient-derived organoid tissue could similarly be used as implant samples for the PDX model. The EVIDENT technology drives the use of microfluidic technology, which allows simultaneous testing of multiple experimental parameters on the same chip, shortens the time course before organoids can be used for drug screening and evaluating patient response to treatment, and reduces experimental errors (113).

7 Discussion

A growing body of studies has demonstrated that lung cancer is an evolving cellular ecosystem following Darwinian laws. In light of the intrinsic variability of cancer cells, an early tumor clone produces the offspring of a genetically heterogeneous subclone,

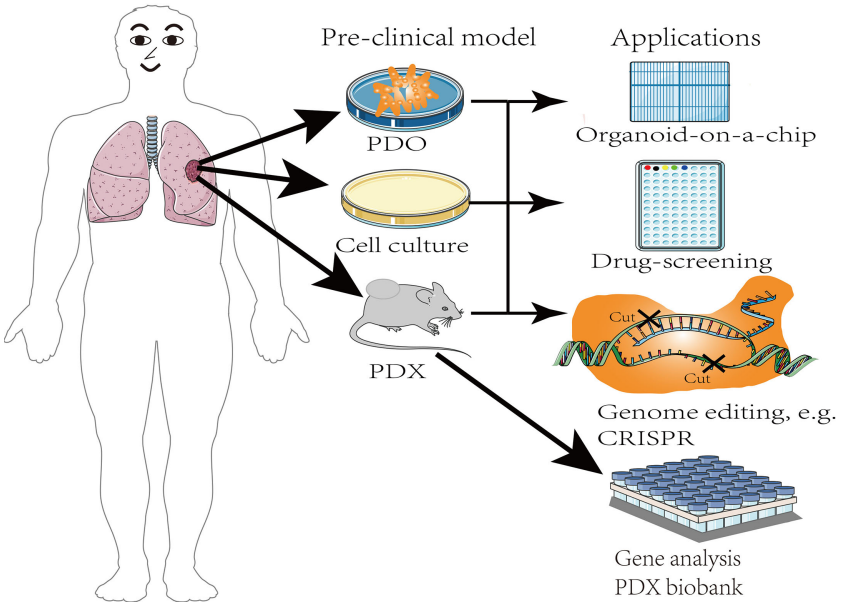

FIGURE 4
The applications of pre-clinical models.

which is more malignant. Tumor heterogeneity has a considerable impact on clinical treatment, but its effect on patient response to cancer drugs and how it changes at the genomic and phenotypic level during treatment have not been resolved. These problems highlight the need for pre-clinical research models, increasing interest in developing and applying PDX models in lung cancer research. The PDX model has enabled the production of samples that truly match the patient's tumor, accurate replication of tumor heterogeneity, progression, and metastatic potential. Considering the growing demand for personalized medicine, the PDX model provides opportunities for developing lung cancer treatment. Using these models for tumor research *in vivo* matches the developmental process of patients' tumors, which improves drug development for tumor treatment. Although the PDX models meet requirements above, there are several unresolved problems, including implantation methods and selection of mouse strains which influence the implantation rate for lung cancer subtypes with low implantation success rate. Currently, the United States, Europe, and several large pharmaceutical companies such as Novartis have developed systematic PDX resources, a biobank housing thousands of PDX models for lung cancer to solve the precision medical challenges. The PDX samples should be equipped with patients' clinical data, gene expression patterns, mutation status, drug reactivity, pathological analysis and other data to form a high-precision PDX library and create authoritative resources for personalized treatment of cancer. These PDX biobanks provide good platforms for studying lung cancer and develop new drugs for clinical application.

Author contributions

GS conceived and designed the, supervised the study, and edited the manuscript. All authors contributed to the article and approved the submitted version.

Funding

This work was supported by the National Natural Science Foundation of China (grant no. H82172658).

Conflict of interest

The authors declare that the research was conducted in the absence of any commercial or financial relationships that could be construed as a potential conflict of interest.

Publisher's note

References

1. Siegel RL, Miller KD, Jemal A. Cancer statistics, 2017. *Ca-Cancer J Clin* (2017) 67 (1):7–30. doi: 10.3322/caac.21387

2. Travis WD, Brambilla E, Burke AP, Marx A, Nicholson AG. Introduction to The 2015 World Health Organization classification of tumors of the lung, pleura, thymus, and heart. *J Thorac Oncol* (2015) 10(9):1240–2.

3. Travis WD, Brambilla E, Nicholson AGWHO Panel. The 2015 world health organization classification of lung tumors: Impact of genetic, clinical and radiologic advances since the 2004 classification. *J Thorac Oncol* (2015) 10(9):1243–60. doi: 10.1097/JTO.0000000000000630

4. Ettinger DS, Wood DE, Aisner DL, Akerley W, Bauman J, Chirieac LR, et al. Non-small cell lung cancer, version 5. 2017, NCCN clinical practice guidelines in oncology. *Natl Compr Cancer Netw Jnccn.* (2015) 2(2):94–123. doi: 10.6004/jnccn.2017.0050

5. Zappa C, Mousa SA. Non-small cell cancer: current treatment and future advances. *Transl Lung Cancer Res* (2016) 5(3):288–300. doi: 10.21037/tlcr.2016.06.07

6. Zhou C. Lung cancer molecular epidemiology in China: recent trends. *Transl Lung Cancer Res* (2014) 3:270–9. doi: 10.3978/j.issn.2218-6751.2014.09.01

7. Gao D, Chen Y. Organoid development in cancer genome discovery. *Curr Opin Genet Dev* (2015) 30:42–8. doi: 10.1016/j.gde.2015.02.007

8. DiMasi JA, Reichert JM, Feldman L, Malins A. Clinical approval success rates for investigational cancer drugs. *Clin Pharmacol Ther* (2013) 94:329–35. doi: 10.1038/clpt.2013.117

9. Ledford H. Us cancer institute to overhaul tumour cell lines. *Nature* (2016) 530 (7591):391. doi: 10.1038/nature.2016.19364

10. Hidalgo M, Amant F, Biankin AV, Budinská E, Byrne AT, Caldas C, et al. Patient-derived xenograft models: An emerging platform for translational cancer research. *Cancer Discovery* (2014) 4(9):998–1013. doi: 10.1158/2159-8290.CD-14-0001

11. Byrne AT, Alférez DG, Amant F, Annibali D, Arribas J, Biankin AV, et al. Interrogating open issues in cancer precision medicine with patient-derived xenografts. *Nat Rev Cancer.* (2017) 17(4):254–68. doi: 10.1038/nrc.2016.140

12. Vareslija D, Cocchiglia S, Byrne C, Young L. Patient-derived xenografts of breast cancer. *Methods Mol Biol* (2017) 1501:327–36. doi: 10.1007/978-1-4939-6475-8_17

13. Hidalgo M, Bruckheimer E, Rajeshkumar NV, Garrido-Laguna I, De Oliveira E, Rubio-Viqueira B, et al. A pilot clinical study of treatment guided by personalized tumorgrafts in patients with advanced cancer. *Mol Cancer Ther* (2011) 10(8):1311–6. doi: 10.1158/1535-7163.MCT-11-0233

14. Garralda E, Paz K, López-Casas PP, Jones S, Katz A, Kann LM, et al. Integrated next generation sequencing and avatar mouse models for personalized cancer treatment. *Clin Cancer Res* (2014) 20(9):2476–84. doi: 10.1158/1078-0432.CCR-13-3047

15. Stebbing J, Paz K, Schwartz GK, Wexler LH, Maki R, Pollock RE, et al. Patient-derived xenografts for individualized care in advanced sarcoma. *Cancer* (2014) 120 (13):2006–15. doi: 10.1002/cncr.28696

16. Aparicio S, Hidalgo M, Kung AL. Examining the utility of patient-derived xenograft mouse models. *Nat Rev Cancer.* (2015) 15(5):311–6. doi: 10.1038/nrc3944

17. Firestone B. The challenge of selecting the 'right' *in vivo* oncology pharmacology model. *Curr Opin Pharmacol* (2010) 10(4):391–6. doi: 10.1016/j.coph.2010.06.012

18. Johnson JI, Decker S, Zaharevitz D, Rubinstein LV, Venditti JM, Schepartz S, et al. Relationships between drug activity in NCI preclinical *in vitro* and *in vivo* models and early clinical trials. *Br J Canc.* (2001) 84(10):1424–31. doi: 10.1054/bjoc.2001.1796

19. Gillet JP, Calcagno AM, Varma S, Marino M, Green LJ, Vora MI, et al. Redefining the relevance of established cancer cell lines to the study of mechanisms of clinical anti-cancer drug resistance. *Proc Natl Acad Sci U S A.* (2011) 108(46):18708–13. doi: 10.1073/pnas.1111840108

20. Politi K, Pao W. How genetically engineered mouse tumor models provide insights into human cancers. *J Clin Oncol* (2011) 29(16):2273–81. doi: 10.1200/JCO.2010.30.8304

21. Pauli C, Hopkins BD, Prandi D, Shaw R, Fedrizzi T, Sboner A, et al. Personalized *in vitro* and *in vivo* cancer models to guide precision medicine. *Canc Discovery* (2017) 7 (5):462–77. doi: 10.1158/2159-8290.CD-16-1154

22. Kim M, Mun H, Sung CO, Cho EJ, Jeon HJ, Chun SM, et al. Patient-derived lung cancer organoids as *in vitro* cancer models for therapeutic screening. *Nat Commun* (2019) 10(1):3991. doi: 10.1038/s41467-019-11867-6

23. Ibarrola-Villava M, Cervantes A, Bardelli A. Preclinical models for precision oncology. *Biochim Biophys Acta Rev Canc.* (2018) 1870(2):239–46. doi: 10.1016/j.bbcan.2018.06.004

24. Okada S, Vaeteewoottacharn K, Kariya R. Establishment of a patient-derived tumor xenograft model and application for precision cancer medicine. *Chem Pharm Bull (Tokyo).* (2018) 66(3):225–30. doi: 10.1248/cpb.c17-00789

25. Tentler JJ, Tan AC, Weekes CD, Jimeno A, Leong S, Pitts TM, et al. Patient-derived tumour xenografts as models for oncology drug development. *Nat Rev Clin Oncol* (2012) 9(6):338–50. doi: 10.1038/nrclinonc.2012.61

26. Gargiulo G. Next-generation in vivo modeling of human cancers. *Front Oncol* (2018) 8:429. doi: 10.3389/fonc.2018.00429

27. Collins AT, Lang SH. A systematic review of the validity of patient derived xenograft (pdx) models: The implications for translational research and personalised medicine. *PeerJ* (2018) 6:e5981. doi: 10.7717/peerj.5981

28. Bleijs M, van de Wetering M, Clevers H, Drost J. Xenograft and organoid model systems in cancer research. *EMBO J* (2019) 38(15):e101654. doi: 10.15252/embj.2019101654

29. Gao H, Korn JM, Ferretti S, Monahan JE, Wang Y, Singh M, et al. High-throughput screening using patient-derived tumor xenografts to predict clinical trial drug response. *Nat Med* (2015) 21(11):1318–25. doi: 10.1038/nm.3954

30. Pompili L, Porru M, Caruso C, Biroccio A, Leonetti C. Patient-derived xenografts: A relevant preclinical model for drug development. *J Exp Clin Cancer Res* (2016) 35(1):189. doi: 10.1186/s13046-016-0462-4

31. Wilding JL, Bodmer WF. Cancer cell lines for drug discovery and development. *Cancer Res* (2014) 74(9):2377–84. doi: 10.1158/0008-5472.CAN-13-2971

32. Misale S, Bozic I, Tong J, Peraza-Penton A, Lallo A, Baldi F, et al. Vertical suppression of the EGFR pathway prevents onset of resistance in colorectal cancers. *Nat Commun* (2015) 6:8305. doi: 10.1038/ncomms9305

33. Zhao X, Liu Z, Yu L, Zhang Y, Baxter P, Voicu H, et al. Global gene expression profiling confirms the molecular fidelity of primary tumor-based orthotopic xenograft mouse models of medulloblastoma. *Neuro Oncol* (2012) 14(5):574–83. doi: 10.1093/neuonc/nos061

34. Keysar SB, Astling DP, Anderson RT, Vogler BW, Bowles DW, Morton JJ, et al. A patient tumor transplant model of squamous cell cancer identifies PI3K inhibitors as candidate therapeutics in defined molecular bins. *Mol Oncol* (2013) 7(4):776–90. doi: 10.1016/j.molonc.2013.03.004

35. Ilie M, Nunes M, Blot L, Hofman V, Long-Mira E, Butori C, et al. Setting up a wide panel of patient-derived tumor xenografts of non-small cell lung cancer by improving the preanalytical steps. *Cancer Med* (2015) 4(2):201–11. doi: 10.1002/cam4.357

36. Urman A, Dean Hosgood H. Lung cancer risk, genetic variation, and air pollution. *EBioMedicine* (2015) 2(6):491–2. doi: 10.1016/j.ebiom.2015.05.007

37. Wang Y, Sun Y. Clinical experiences with molecular targeted therapy in lung cancer in China. *Thorac Cancer.* (2015) 6(4):379–84. doi: 10.1111/1759-7714.12243

38. Zhang Y, Yao K, Shi C, Jiang Y, Liu K, Zhao S, et al. 244-MPT overcomes geftinib resistance in non-small cell lung cancer cells. *Oncotarget* (2015) 6(42):44274–88. doi: 10.18632/oncotarget.6236

39. Schild SE, Vokes EE. Pathways to improving combined modality therapy for stage III nonsmall-cell lung cancer. *Ann Oncol* (2016) 27(4):590–9. doi: 10.1093/annonc/mdv621

40. Ryan MB, Fece de la Cruz F, Phat S, Myers DT, Wong E, Shahzade HA, et al. Vertical pathway inhibition overcomes adaptive feedback resistance to KRASG12C inhibition. *Clin Canc Res* (2020) 26(7):1633–43. doi: 10.1158/1078-0432.CCR-19-3523

41. Clappier E, Gerby B, Sigaux F, Delord M, Touzri F, Hernandez L, et al. Clonal selection in xenografted human T cell acute lymphoblastic leukemia recapitulates gain of malignancy at relapse. *J Exp Med* (2011) 208(4):653–61. doi: 10.1084/jem.20110105

42. Meyer LH, Eckhoff SM, Queudeville M, Kraus JM, Giordan M, Stursberg J, et al. Early relapse in ALL is identifified by time to leukemia in NOD/SCID mice and is characterized by a gene signature involving survival pathways. *Canc Cell* (2011) 19 (2):206–17. doi: 10.1016/j.ccr.2010.11.014

43. Flanagan SP. 'Nude', a new hairless gene with pleiotropic effects in the mouse. *Genet Res* (1966) 8(3):295–309. doi: 10.1017/S0016672300010168

44. Custer RP, Bosma GC, Bosma MJ. Severe combined immunodeficiency (SCID) in the mouse. pathology, reconstitution, neoplasms. *Am J Pathol* (1985) 120(3):464–77.

45. Chateau-Joubert S, Hopfe M, Richon S, Decaudin D, Roman-Roman S, Reyes-Gomez E, et al. Spontaneous mouse lymphoma in patient-derived tumor xenografts: The importance of systematic analysis of xenografted human tumor tissues in preclinical efficacy trials. *Transl Oncol* (2021) 14:101133. doi: 10.1016/j.tranon.2021.101133

46. Shultz LD, Lyons BL, Burzenski LM, Gott B, Chen XH, Chaleff S, et al. Human lymphoid and myeloid cell development in NOD/LtSz-scid IL2R gamma null mice engrafted with mobilized human hemopoietic stem cells. *J Immunol* (2005) 174 (10):6477–89. doi: 10.4049/jimmunol.174.10.6477

47. McDermott SP, Eppert K, Lechman ER. Comparison of human cord blood engraftment between immunocompromised mouse strains. *Blood* (2010) 116(2):193–200. doi: 10.1182/blood-2010-02-271841

48. Shultz LD, Brehm MA, Garcia-Martinez JV, Greiner DL. Humanized mice for immune system investigation: Progress, promise and challenges. *Nat Rev Immunol* (2012) 12(11):786–98. doi: 10.1038/nri3311

49. Fridman R, Giaccone G, Kanemoto T, Martin GR, Gazdar AF, Mulshine JL. Reconstituted basement membrane (matrigel) and laminin can enhance the tumorigenicity and the drug resistance of small cell lung cancer cell lines. *Proc Natl Acad Sci USA* (1990) 87(17):6698–702. doi: 10.1073/pnas.87.17.6698

50. Rong S, Oskarsson M, Faletto D, Tsarfaty I, Resau JH, Nakamura T, et al. Tumorigenesis induced by coexpression of human hepatocyte growth factor and the

human met protooncogene leads to high levels of expression of the ligand and receptor. *Cell Growth Differ* (1993) 4(7):563–9.

51. Utama FE, LeBaron MJ, Neilson LM, Sultan AS, Parlow AF, Wagner KU, et al. Human prolactin receptors are insensitive to mouse prolactin: implications for xenotransplant modeling of human breast cancer in mice. *J Endocrinol* (2006) 188 (3):589–601. doi: 10.1677/joe.1.06560

52. Rong S, Bodescot M, Blair D, Dunn J, Nakamura T, Mizuno K, et al. Tumorigenicity of the met protooncogene and the gene for hepatocyte growth factor. *Mol Cell Biol* (1992) 12(11):5152–8. doi: 10.1128/mcb.12.11.5152-5158.1992

53. Dong X, Guan J, English JC, Flint J, Yee J, Evans K, et al. Patient-derived first generation xenografts of non–small cell lung cancers: promising tools for predicting drug responses for personalized chemotherapy. *Clin Cancer Res* (2010) 16(5):1442–51. doi: 10.1158/1078-0432.CCR-09-2878

54. Fichtner I, Rolff J, Soong R, Hoffmann J, Hammer S, Sommer A, et al. Establishment of patient-derived non–small cell lung cancer xenografts as models for the identification of predictive biomarkers. *Clin Cancer Res* (2008) 14(20):6456–68. doi: 10.1158/1078-0432.CCR-08-0138

55. Chen Y, Zhang R, Wang L, Correa AM, Pataer A, Xu Y, et al. Tumor characteristics associated with engraftment of patient-derived non–small cell lung cancer xenografts in immunocompromised mice. *Cancer* (2019) 125(21):3738–48. doi: 10.1002/cncr.32366

56. Lee HW, Lee JI, Lee SJ, Cho HJ, Song HJ, Jeong DE, et al. Patient-derived xenografts from non–small cell lung cancer brain metastases are valuable translational platforms for the development of personalized targeted therapy. *Clin Cancer Res* (2015) 21(5):1172–82. doi: 10.1158/1078-0432.CCR-14-1589

57. Rakhra K, Bachireddy P, Zabuawala T, Zeiser R, Xu L, Kopelman A, et al. CD4 (+) T cells contribute to the remodeling of the microenvironment required for sustained tumor regression upon oncogene inactivation. *Cancer Cell* (2010) 18 (5):485–98. doi: 10.1016/j.ccr.2010.10.002

58. Dyck L, Mills KHG. Immune checkpoints and their inhibition in cancer and infectious diseases. *Eur J Immunol* (2017) 47(5):765–79. doi: 10.1002/eji.201646875

59. Hsu J, Hodgins JJ, Marathe M, Nicolai CJ, Bourgeois-Daigneault MC, Trevino TN, et al. Contribution of NK cells to immunotherapy mediated by PD-1/PD-L1 blockade. *J Clin Invest.* (2018) 128(10):4654–68. doi: 10.1172/JCI99317

60. Wherry EJ, Kurachi M. Molecular and cellular insights into T cell exhaustion. *Nat Rev Immunol* (2015) 15(8):486–99. doi: 10.1038/nri3862

61. Baitsch L, Baumgaertner P, Devevre E, Raghav SK, Legat A, Barba L, et al. Exhaustion of tumor-specific CD8(+) T cells in metastases from melanoma patients. *J Clin Invest.* (2011) 121(6):2350–60. doi: 10.1172/JCI46102

62. Freeman GJ, Long AJ, Iwai Y, Bourque K, Chernova T, Nishimura H, et al. Engagement of the PD-1 immunoinhibitory receptor by a novel B7 family member leads to negative regulation of lymphocyte activation. *J Exp Med* (2000) 192(7):1027–34. doi: 10.1084/jem.192.7.1027

63. Dong H, Strome SE, Salomao DR, Tamura H, Hirano F, Flies DB, et al. Tumor associated B7-H1 promotes T-cell apoptosis: A potential mechanism of immune evasion. *Nat Med* (2002) 8(8):793. doi: 10.1038/nm730

64. Iwai Y, Ishida M, Tanaka Y, Okazaki T, Honjo T, Minato N. Involvement of PD-L1 on tumor cells in the escape from host immune system and tumor immunotherapy by PD-L1 blockade. *Proc Natl Acad Sci U S A.* (2002) 99(19):12293–7. doi: 10.1073/pnas.192461099

65. Waldmann TA. Immunotherapy: Past, present and future. *Nat Med* (2003) 9 (3):269–77. doi: 10.1038/nm0303-269

66. Pardoll DM. The blockade of immune checkpoints in cancer immunotherapy. *Nat Rev Cancer.* (2012) 12(4):252–64. doi: 10.1038/nrc3239

67. Zhang H, Chen J. Current status and future directions of cancer immunotherapy. *J Cancer.* (2018) 9(10):1773–81. doi: 10.7150/jca.24577

68. Wang M, Yao LC, Cheng M, Cai D, Martinek J, Pan CX, et al. Humanized mice in studying efficacy and mechanisms of PD-1-targeted cancer immunotherapy. *FASEB J* (2018) 32(3):1537–49. doi: 10.1096/fj.201700740R

69. Olaussen KA, Postel-Vinay S. Predictors of chemotherapy efcacy in non-small-cell lung cancer: a challenging landscape. *Ann Oncol* (2016) 27(11):2004–16. doi: 10.1093/annonc/mdw321

70. Tomasini P, Barlesi F, Mascaux C, Greillier L. Pemetrexed for advanced stage nonsquamous non-small cell lung cancer: latest evidence about its extended use and outcomes. *Ther Adv Med Oncol* (2016) 8(3):198–208. doi: 10.1177/1758834016644155

71. Zou W, Wolchok JD, Chen L. PD-L1 (B7-H1) and PD-1 pathway blockade for cancer therapy: mechanisms, response biomarkers, and combinations. *Sci Transl Med* (2016) 8(328):328rv4. doi: 10.1126/scitranslmed.aad7118

72. Sawant A, Schafer CC, Jin TH, Zmijewski J, Tse HM, Roth J, et al. Enhancement of antitumor immunity in lung cancer by targeting myeloid-derived suppressor cell pathways. *Cancer Res* (2013) 73(22):6609–20. doi: 10.1158/0008-5472.CAN-13-0987

73. Yamauchi Y, Safi S, Blattner C, Rathinasamy A, Umansky L, Juenger S, et al. Circulating and tumor myeloid-derived suppressor cells in resectable non-small-cell lung cancer. *Am J Respir Crit Care Med* (2018) 198(6):777–87. doi: 10.1164/rccm.201708-1707OC

74. Liu J, Cho S-N, Akkanti B, Jin N, Mao J, Long W, et al. ErbB2 pathway activation upon Smad4 loss promotes lung tumor growth and metastasis. *Cell Rep* (2015) 10 (9):1599–613. doi: 10.1016/j.celrep.2015.02.014

75. Wrangle JM, Velcheti V, Patel MR, Garrett-Mayer E, Hill EG, Ravenel JG, et al. ALT-803, an IL-15 superagonist, in combination with nivolumab in patients with metastatic non-small cell lung cancer: a non-randomised, open-label, phase 1b trial. *Lancet Oncol* (2018) 19(5):694–704. doi: 10.1016/S1470-2045(18)30148-7

76. Borghaei H, Paz-Ares L, Horn L, Spigel DR, Steins M, Ready NE, et al. Nivolumab versus docetaxel in advanced nonsquamous non-small cell lung cancer. *N Eng J Med* (2015) 373:1627–39. doi: 10.1056/NEJMoa1507643

77. Brahmer J, Reckamp KL, Baas P, Crino L, Crinò L, Eberhardt WE, et al. Nivolumab versus docetaxel in advanced squamous-cell non-small-cell lung cancer. *N Eng J Med* (2015) 373(2):123–35. doi: 10.1056/NEJMoa1504627

78. Zacarias-Fluck MF, Morancho B, Vicario R, Luque Garcia A, Escorihuela M, Villanueva J, et al. Effect of cellular senescence on the growth of HER2-positive breast cancers. *J Natl Cancer Inst* (2015) 107(5):djv020. doi: 10.1093/jnci/djv020

79. Camidge DR, Pao W, Sequist LV. Acquired resistance to TKIs in solid tumours: learning from lung cancer. *Nat Rev Clin Oncol* (2014) 11(8):473–81. doi: 10.1038/nrclinonc.2014.104

80. Restifo NP, Smyth MJ, Snyder A. Acquired resistance to immunotherapy and future challenges. *Nat Rev Cancer.* (2016) 16(2):121–6. doi: 10.1038/nrc.2016.2

81. Berger AH, Brooks AN, Wu X, Shrestha Y, Chouinard C, Piccioni F, et al. High-throughput phenotyping of lung cancer somatic mutations. *Cancer Cell* (2016) 30 (2):214–28. doi: 10.1016/j.ccell.2016.06.022

82. Farago AF, Keane FK. Current standards for clinical management of small cell lung cancer. *Transl Lung Cancer Res* (2018) 7(1):69–79. doi: 10.21037/tlcr.2018.01.16

83. Horn L, Mansfield AS, Szczesna A, Havel L, Krzakowski M, Hochmair MJ, et al. First-line atezolizumab plus chemotherapy in extensive stage small-cell lung cancer. *N Engl J Med* (2018) 379(23):2220–9. doi: 10.1056/NEJMoa1809064

84. Gardner EE, Lok BH, Schneeberger VE, Desmeules P, Miles LA, Arnold PK, et al. Chemosensitive relapse in small cell lung cancer proceeds through an EZH2-SLFN11 axis. *Cancer Cell* (2017) 31(2):286–99. doi: 10.1016/j.ccell.2017.01.006

85. Kim KT, Lee HW, Lee HO, Kim SC, Seo YJ, Chung W, et al. Single-cell mRNA sequencing identifies subclonal heterogeneity in anti-cancer drug responses of lung adenocarcinoma cells. *Genome Biol* (2015) 16(1):127. doi: 10.1186/s13059-015-0692-3

86. Zhang XC, Zhang J, Li M, Huang XS, Yang XN, Zhong WZ, et al. Establishment of patient-derived non-small cell lung cancer xenograft models with genetic aberrations within EGFR, KRAS and FGFR1: useful tools for preclinical studies of targeted therapies. *J Transl Med* (2013) 11:168. doi: 10.1186/1479-5876-11-168

87. Martin P, Stewart E, Pham NA, Mascaux C, Panchal D, Li M, et al. Cetuximab inhibits T790M-mediated resistance to epidermal growth factor receptor tyrosine kinase inhibitor in a lung adenocarcinoma patient-derived xenograft mouse model. *Clin Lung Cancer.* (2016) 17(5):375–383. e2. doi: 10.1016/j.cllc.2016.01.002

88. Cancer Genome Atlas Research, N. Comprehensive molecular profiling of lung adenocarcinoma. *Nature* (2014) 511(7511):543–50. doi: 10.1038/nature13385

89. Hayes DN, Monti S, Parmigiani G, Gilks CB, Naoki K, Bhattacharjee A, et al. Gene expression profiling reveals reproducible human lung adenocarcinoma subtypes in multiple independent patient cohorts. *J Clin Oncol* (2006) 24(31):5079–90. doi: 10.1200/JCO.2005.05.1748

90. Zhou W, Sun G, Zhang Z, Zhao L, Xu L, Yuan H, et al. Proteasome-independent protein knockdown by small-molecule inhibitor for the undruggable lung adenocarcinoma. *J Am Chem Soc* (2019) 141(46):18492–9. doi: 10.1021/jacs.9b08777

91. Sugimoto K, Hayakawa F, Shimada S, Morishita T, Shimada K, Katakai T, et al. Discovery of a drug targeting microenvironmental support for lymphoma cells by screening using patient-derived xenograft cells. *Sci Rep* (2015) 5:13054. doi: 10.1038/srep13054

92. Fior R, Povoa V, Mendes RV, Carvalho T, Gomes A, Figueiredo N, et al. Single-cell functional and chemosensitive profiling of combinatorial colorectal therapy in zebrafish xenografts. *J Proc Natl Acad Sci U S A.* (2017) 114(39):E8234–43. doi: 10.1073/pnas.1618389114

93. Peterson JK, Houghton PJ. Integrating pharmacology and *in vivo* cancer models in preclinical and clinical drug development. *Eur J Cancer.* (2004) 40(6):837–44. doi: 10.1016/j.ejca.2004.01.003

94. Thompson J, Stewart CF, Houghton PJ. Animal models for studying the action of topoisomerase I targeted drugs. *Biochim Biophys Acta* (1998) 1400(1-3):301–19. doi: 10.1016/S0167-4781(98)00143-2

95. Ben-David U, Ha G, Tseng YY, Greenwald NF, Oh C, Shih J, et al. Patient-derived xenografts undergo mouse-specific tumor evolution. *Nat Genet* (2017) 49 (11):1567–75. doi: 10.1038/ng.3967

96. Garber K. Personal mouse colonies give hope for pancreatic cancer patients. *J Natl Cancer Inst* (2007) 99(2):105–7. doi: 10.1093/jnci/djk046

97. Skowron KB, Pitroda SP, Namm JP, Balogun O, Beckett MA, Zenner ML, et al. Basal tumor cell isolation and patient-derived xenograft engraftment identify high-risk clinical bladder cancers. *Sci Rep* (2016) 6:35854. doi: 10.1038/srep35854

98. Kim HR, Kim DJ, Kang DR, Lee JG, Lim SM, Lee CY, et al. Fibroblast growth factor receptor 1 gene amplification is associated with poor survival and cigarette smoking dosage in patients with resected squamous cell lung cancer. *J Clin Oncol* (2013) 31(6):731–7. doi: 10.1200/JCO.2012.43.8622

99. Kim HR, Kang HN, Shim HS, Kim EY, Kim J, Kim DJ, et al. Co-Clinical trials demonstrate predictive biomarkers for dovitinib, an FGFR inhibitor, in lung squamous cell carcinoma. *Ann Oncol* (2017) 28(6):1250–9. doi: 10.1093/annonc/mdx098

100. Tellez-Gabriel M, Cochonneau D, Cadé M, Jubellin C, Heymann MF, Heymann D. Circulating tumor cell-derived pre-clinical models for personalized medicine. *Cancers* (2018) 11(1):19. doi: 10.3390/cancers11010019

101. Radaelli E, Hermans E, Omodho L, Francis A, Vander Borght S, Marine JC, et al. Spontaneous post-transplant disorders in NOD. cg-prkdcscid Il2rgtm1Sug/JicTac (NOG) mice engrafted with patient-derived metastatic melanomas. *PloS One* (2015) 10 (5):e0124974. doi: 10.1371/journal.pone.0124974

102. Klameth L, Rath B, Hochmaier M, Moser D, Redl M, Mungenast F, et al. Small cell lung cancer: model of circulating tumor cell tumorospheres in chemoresistance. *Sci Rep* (2017) 7(1):5337. doi: 10.1038/s41598-017-05562-z

103. Crystal AS, Shaw AT, Sequist LV, Friboulet L, Niederst MJ, Lockerman EL, et al. Patient-derived models of acquired resistance can identify effective drug combinations for cancer. *Science* (2014) 346(6216):1480–6. doi: 10.1126/science.1254721

104. Wegner CS, Hauge A, Andersen LMK, Huang R, Simonsen TG, Gaustad JV, et al. Increasing aggressiveness of patient-derived xenograft models of cervix carcinoma during serial transplantation. *Oncotarget* (2018) 9(30):21036–51. doi: 10.18632/oncotarget.24783

105. Chaudary N, Pintilie M, Schwock J, Dhani N, Clarke B, Milosevic M, et al. Characterization of the tumor-microenvironment in patient-derived cervix xenografts (OCICx). *Cancers (Basel).* (2012) 4(3):821–45. doi: 10.3390/cancers4030821

106. Pearson AT, Finkel KA, Warner KA, Nör F, Tice D, Martins MD, et al. Patient-derived xenograft (PDX) tumors increase growth rate with time. *Oncotarget* (2016) 7 (7):7993–8005. doi: 10.18632/oncotarget.6919

107. Ben-David U, Ha G, Tseng YY, Greenwald NF, Oh C, Shih J, et al. Patient derived xenografts undergo mouse-specifific tumor evolution. *Nat Genet* (2017) 49 (11):1567–75. doi: 10.1038/ng.3967

108. Pennacchietti S, Cazzanti M, Bertotti A, Rideout WM3rd, Han M, Gyuris J, et al. Microenvironment-derived HGF overcomes genetically determined sensitivity to anti-MET drugs. *Cancer Res* (2014) 74(22):6598–609. doi: 10.1158/0008-5472.CAN-14-0761

109. Chen S, Giannakou A, Wyman S, Gruzas J, Golas J, Zhong W, et al. Cancer-associated fibroblasts suppress SOX2-induced dysplasia in a lung squamous cancer coculture. *Proc Natl Acad Sci U S A.* (2018) 115(50):E11671–80. doi: 10.1073/pnas.1803718115

110. Chou JL, Shen ZX, Stolfi RL, Martin DS, Waxman S. Effects of extracellular matrix on the growth and casein gene expression of primary mouse mammary tumor cells in vitro. *Cancer Res* (1989) 49(19):5371–6.

111. Bernards R. A missing link in genotype-directed cancer therapy. *Cell* (2012) 151(3):465–8. doi: 10.1016/j.cell.2012.10.014

112. Sachs N, Clevers H. Organoid cultures for the analysis of cancer phenotypes. *Curr Opin Genet Dev* (2014) 24:68–73. doi: 10.1016/j.gde.2013.11.012

113. Moore N, Doty D, Zielstorff M, Kariv I, Moy LY, Gimbel A, et al. A multiplexed microflfluidic system for evaluation of dynamics of immunetumor interactions. *Lab Chip.* (2018) 18(13):1844–58. doi: 10.1039/C8LC00256H

frontiers | Frontiers in Oncology

TYPE Original Research
PUBLISHED 11 April 2023
DOI 10.3389/fonc.2023.1129627

OPEN ACCESS

EDITED BY
Vuong Trieu,
Oncotelic, Inc., Agoura Hills, United States

REVIEWED BY
David Bakhshinyan,
University of Toronto, Toronto Canada
Niyati Jhaveri,
Keck School of Medicine, University of Southern California, Los Angeles, United States

*CORRESPONDENCE
Joshua Alcaniz
joshua.alcaniz@epo-berlin.com

SPECIALTY SECTION
This article was submitted to Cancer Molecular Targets and Therapeutics, a section of the journal Frontiers in Oncology

RECEIVED 22 December 2022
ACCEPTED 14 March 2023
PUBLISHED 11 April 2023

CITATION
Alcaniz J, Winkler L, Dahlmann M, Becker M, Orthmann A, Haybaeck J, Krassnig S, Skofler C, Kratzsch T, Kuhn SA, Jödicke A, Linnebacher M, Fichtner I, Walther W and Hoffmann J (2023) Clinically relevant glioblastoma patient-derived xenograft models to guide drug development and identify molecular signatures.
Front. Oncol. 13:1129627.
doi: 10.3389/fonc.2023.1129627

Clinically relevant glioblastoma patient-derived xenograft models to guide drug development and identify molecular signatures

Joshua Alcaniz[1]*, Lars Winkler[1], Mathias Dahlmann[1], Michael Becker[1], Andrea Orthmann[1], Johannes Haybaeck[2,3,4], Stefanie Krassnig[2], Christina Skofler[3], Tobias Kratzsch[5], Susanne A. Kuhn[6], Andreas Jödicke[7], Michael Linnebacher[8], Iduna Fichtner[1], Wolfgang Walther[1,9,10] and Jens Hoffmann[1]

[1]Experimental Pharmacology and Oncology GmbH, Berlin, Germany, [2]Department of Neuropathology, Diagnostic & Research Center for Molecular BioMedicine, Institute of Pathology, Medical University of Graz, Graz, Austria, [3]Center for Biomarker Research in Medicine, Graz, Austria, [4]Institute of Pathology, Neuropathology, and Molecular Pathology, Medical University of Innsbruck, Innsbruck, Austria, [5]Department of Neurosurgery, Charité Universitätsmedizin, Berlin, Germany, [6]Department of Neurosurgery, Ernst von Bergmann Hospital, Potsdam, Germany, [7]Department of Neurosurgery, Vivantes Hospital Berlin Neukölln, Berlin, Germany, [8]Department of Surgery, Molecular Oncology and Immunotherapy, University Medical Center Rostock, Rostock, Germany, [9]Max Delbrück Center for Molecular Medicine, Berlin, Germany, [10]Experimental and Clinical Research Center, Charité Universitätsmedizin, Berlin, Germany

Glioblastoma (GBM) heterogeneity, aggressiveness and infiltrative growth drastically limit success of current standard of care drugs and efficacy of various new therapeutic approaches. There is a need for new therapies and models reflecting the complex biology of these tumors to analyze the molecular mechanisms of tumor formation and resistance, as well as to identify new therapeutic targets. We established and screened a panel of 26 patient-derived subcutaneous (s.c.) xenograft (PDX) GBM models on immunodeficient mice, of which 15 were also established as orthotopic models. Sensitivity toward a drug panel, selected for their different modes of action, was determined. Best treatment responses were observed for standard of care temozolomide, irinotecan and bevacizumab. Matching orthotopic models frequently show reduced sensitivity, as the blood-brain barrier limits crossing of the drugs to the GBM. Molecular characterization of 23 PDX identified all of them as IDH-wt (R132) with frequent mutations in EGFR, TP53, FAT1, and within the PI3K/Akt/mTOR pathway. Their expression profiles resemble proposed molecular GBM subtypes mesenchymal, proneural and classical, with pronounced clustering for gene sets related to angiogenesis and MAPK signaling. Subsequent gene set enrichment analysis identified hallmark gene sets of hypoxia and mTORC1 signaling as enriched in temozolomide resistant PDX. In models sensitive for mTOR inhibitor everolimus, hypoxia-related gene sets reactive oxygen species pathway and angiogenesis were enriched. Our results highlight how our platform of s.c. GBM PDX can reflect the complex, heterogeneous biology of GBM. Combined with transcriptome analyses, it is a valuable tool in identification of

molecular signatures correlating with monitored responses. Available matching orthotopic PDX models can be used to assess the impact of the tumor microenvironment and blood-brain barrier on efficacy. Our GBM PDX panel therefore represents a valuable platform for screening regarding molecular markers and pharmacologically active drugs, as well as optimizing delivery of active drugs to the tumor.

KEYWORDS

glioblastoma, glioma, patient-derived xenograft (PDX), preclinical oncology, drug efficacy, targeted therapy, blood-brain barrier, mTORC1

1 Introduction

Glioblastoma (GBM) is the most common brain intrinsic neoplasia of the central nervous system, characterized by diffuse and infiltrative growth. About 90% of GBMs are diagnosed *de novo* and test negative for isocitrate dehydrogenase (IDH) 1 mutation R132H. Based on the 2016 WHO classification, they are considered a separate entity of brain tumors, IDH-wildtype (wt) GBM (1, 2). Currently available standard of care is resection, followed by radio-chemotherapy with alkylating agent temozolomide (3, 4). Patients with a high methylation status (> 20%) of the promoter region of O6-methylguanine-DNA methyltransferase (MGMT) show significantly better treatment responses toward temozolomide and better overall survival (5, 6). Another FDA approved drug for recurring GBM is the humanized antibody bevacizumab binding the circulating vascular endothelial growth factor A (VEGF-A). However, despite its successful use for therapy of other cancers (7), it did not reach the same efficacy in GBM. Combination of bevacizumab with temozolomide in recurring GBM did improve patients' progression free survival and quality of life, but not overall survival (8, 9).

Molecularly, IDH-wt GBM are characterized by frequent mutations in TP53 and phosphatase and tension homologue (PTEN), as well as by epidermal growth factor receptor (EGFR) mutation and amplification (10). Deregulations in PTEN/PI3K/Akt/mTOR signaling, including increased receptor tyrosine kinase signaling, occur in about 80% of GBM (11). Analysis of transcriptional features furthermore revealed different molecular GBM subtypes, hinting towards different tumor evolution and biology within the group of IDH-wt GBM (12, 13). Still, their potential use as predictive markers or targets remains limited. The high heterogeneity of GBM and redundant activation of downstream signaling pathways suggest targeting one molecule alone might be insufficient to improve patients' outcome (14–17).

To better understand GBM biology and resistance formation, PDX models have been a valuable tool in preclinical and translational research. Subcutaneous (s.c.) GBM PDX have been shown to closely resemble the original tumor's morphology and molecular heterogeneity, and they thus allow for the testing of new treatment approaches on a patient individual basis (18–21). However, since these models are not able to recapitulate critical physiological structures like the blood-brain barrier (BBB) and its potential to limit availability of anti-cancer compounds within the brain, orthotopic PDX represent a crucial addition in assessment of treatment efficacy and optimization (22).

In this study we aimed to establish a well characterized panel of GBM PDX of matching s.c. and orthotopic models. Analysis of chemosensitivity, as well as the available molecular data on gene expression and mutation allows for identification of molecular signatures and markers, and for identification of advantageous treatment regimens and combinations. Orthotopic PDX allow validation in a model more closely resembling the GBM physiological tumor microenvironment within the central nervous system and the BBB's impact on drug efficacy (23).

2 Materials and methods

2.1 Patient tumors

Tumor tissue was collected directly during surgery. Patients included in the study gave written informed consent and specimen collection was approved by the local Institutional Review Board of Charité University Medicine, Germany (EA4/019/12), the Ethics Committee of the University of Rostock, Germany (A 2009/34) and the Institutional Ethics Committee of the Medical University of Graz, Austria (24-402 ex 11/12).

2.2 Generation of s.c. PDX GBM models

Animal studies were performed in accordance with the German Animal Welfare Act and approved by local authorities (Landesamt für Gesundheit und Soziales, LaGeSo Berlin, Germany) under the permission H0308/18 for the PDX generation and proliferation *in vivo* and A0010/19 for *in vivo* therapy experiments. For establishment of s.c. PDX models, patient tumor specimens were cut into 3-4 mm sized fragments and transplanted s.c. on anesthetized NOD.Cg-Prkdcscid Il2rgtm1Wjl/SzJ (NSG) mice (Charles River Laboratories, Sulzfeld, Germany). Health status of mice was checked daily, and body weight and tumor size were measured twice per week. When tumors successfully engrafted and

reached a size of about 1 cm^3, they were excised, cut into 3×3×3 mm sized fragments and transplanted s.c. on female NMRI Foxn1nu mice for the consecutive *in vivo* passage. Mice were housed under standard conditions in IVC caging systems with 22°C +/- 1°C, 12 h light-dark cycle, food, water and nesting material *ad libitum*.

2.3 Generation of orthotopic PDX GBM models

PDX tumor tissue obtained from s.c. *in vivo* passage (passage numbers between 4 and 9) was used to prepare a single cell suspension *via* mechanical break up (gentleMACS Dissociator, Miltenyi Biotec, Teterow, Germany). Anesthetized mice were fixed in a stereotactic frame, the skin on the scull was opened and 2 µl cell suspension of 1×10^5 tumor cells was injected intracerebral (i.cer.) into the cortex of the right hemisphere. After cell injection, the syringe was removed slowly, and the skin was closed using Histoacryl ® tissue adhesive (B.Braun, Melsungen, Germany). The following day mice received meloxicam subcutaneously.

Animal health condition was checked daily and body weight was measured at least twice weekly. Mice were terminated for ethical reasons when showing behavioral abnormalities and body weight loss > 10%; both signs for progressive intracranial tumor growth. Brains were dissected and frozen in isopentane at -80°C. Sequential 10 µm cryostat microtome sections in coronal plane were prepared, cresyl violet-stained and the tumor area measured as described previously (18, 24).

2.4 Chemosensitivity testing of GBM PDX

For sensitivity testing of s.c. PDX models, 3×3×3 mm tumor fragments (passage numbers between 2 and 6) were transplanted subcutaneously onto female Rj : NMRI-Foxn1nu/nu nude mice (Janvier Labs, Le Genest-Saint-Isle, France) as described (see above). Animals were randomized and treated at palpable tumor size (0.08 to 0.2 cm^3) with the respective drugs: bevacizumab (10 mg/kg intraperitoneally, 3× per week for 2 weeks; Roche, Basel, Switzerland), everolimus (5 mg/kg orally, (day 1-5)×2; Novartis, Basel, Switzerland), irinotecan (15 mg/kg intraperitoneally, (day 1-5)×2; Fresenius, Bad Homburg, Germany), salinomycin (10 mg/kg orally, day 1-14; Sigma-Aldrich, St. Louis, MI, USA), Sorafenib (80 mg/kg, orally, (day 1-5)×2; Bayer, Leverkusen, Germany) and temozolomide (90 mg/kg orally, day 1-5; MSD, Kenilworth, NJ, USA). Drug efficacy was determined by measurement of tumor volumes (TV). TV measurement was performed with a digital caliper and volumes were calculated using the formula:

$$TV\ [cm^3] = \frac{length\ \times\ width^2}{2}$$

Studies were terminated for ethical reasons when first animals reached a TV > 1.5 cm^3. To describe therapeutic responses, the ratio (T/C, in %) of mean volumes of tumors in treatment (T) versus control groups (C), as well as relative tumor volumes (RTV) in treatment groups were used:

$$RTVx\ [\%] = \frac{TVx}{TVo} \times 100$$

A T/C value > 50% was defined as no response, > 25% as minor response, > 10% as moderate response and T/C ≤ 10% a strong response. We furthermore considered a RTV value > 1.7 as progression, a RTV > 0.3% stable disease, and RTV ≤ 0.3% as partial remission.

For sensitivity testing of orthotopic GBM PDX models, tumor cells were inoculated, and animals randomly distributed into control and treatment groups. Treatment was started 6 to 7 days after tumor cell inoculation. Once first animals showed health impairments, the study was terminated and maximum tumor area in coronal plane measured microscopically and used to evaluate therapeutic responses.

2.5 Statistical analyses

For statistical analyses of tumor size differences between control and treatment groups at study end, one-way ANOVA followed by Dunnett's multiple comparison test were performed. Prism software v5.02 (GraphPad Software, San Diego, USA) was used for all analyses.

2.6 Histology and immunohistochemistry of PDX models

For histopathological analysis, 5 µm sections of formalin fixed paraffin embedded (FFPE) tumor samples were deparaffinized in ROTICLEAR® (Carl Roth GmbH, Karlsruhe, Germany) and rehydrated using ethanol and distilled water. Sections were then stained according to a standard hematoxylin-eosin protocol (24). For immunohistochemistry (IHC) antigen retrieval was done in hot citrate buffer for 15 min, followed by cooling for 40 min and washing with PBS.

For MGMT staining, slides were blocked with 5% goat serum in PBS for 1 h at room temperature (RT), and subsequently incubated with primary antibody (5 µg/ml rabbit anti-MGMT, PA5-79668, ThermoFisher Scientific, Germany), for 1 h at RT. Sections were then washed twice in TBST buffer (20 mM Tris/HCl pH 7.5, 150 mM NaCl, 0.1% Tween-20) and incubated with the SuperVison 2 Single Species HRP-polymer rabbit kit (DCS GmbH, Hamburg, Germany) according to the manufacturer's instructions. Sections were counterstained with hematoxylin solution.

For Ki-67 staining, slides were first blocked with 3% hydrogenperoxide for 30 min, washed twice with PBS and then with 5% normal goat serum in PBS for 30 min, both at RT. After blocking, sections were incubated with primary antibody (6.5 µg/ml rabbit anti-Ki-67 in PBS, ab15580, Abcam, Cambridge, UK) for 1 h at RT. Sections were then washed twice in TBST buffer and incubated with HRP-conjugated secondary antibody (#111035003, 1:200, Jackson ImmunoResearch Laboratory, West Grove, USA) for 30 min, RT. Sections were washed twice in TBST, followed by detection of secondary antibody using chromogen substrate buffer

DAB+ (#K3468, Dako North America, Inc., Carpinteria, CA, USA) and DAB-chromogen (#K3468, Dako North America, Inc., Carpinteria, CA, USA). Sections were washed with PBS, then with distilled water and counterstained with hematoxylin solution.

All Images were acquired using the Axioskop 40 and AxioVision V3.5 (Zeiss, Jena, Germany).

2.7 Molecular characterization of s.c. PDX models by RNA sequencing

RNA sequencing (RNASeq) of untreated s.c. tumor tissue samples was performed for 23 established GBM PDX models. Next-generation sequencing and processing of the raw data was performed by ATLAS Biolabs GmbH (Berlin, Germany).

About 50-100 mg snap frozen PDX tumor tissue was dissolved in 1.5 ml of TRIzol™ (ThermoFisher Scientific, Carlsbad, CA, USA) using a gentle MACS dissociator and M tubes (Miltenyi Biotec, Bergisch Gladbach, Germany). The integrity of the isolated total RNA was analyzed using an Agilent Bioanalyzer 2100 and the RNA 6000 Nano Kit (Agilent, Santa Clara, CA, USA). The Illumina TrueSeq Stranded mRNA Library Prep Kit was used for preparation of RNAseq libraries, followed by 100 bp PE-sequencing on an Illumina HiSeq 2500 device with a depth of 80–100 million reads (40–50 Mio cluster) (Illumina, Cambridge, UK).

2.8 Bioinformatic data processing

Read quality was validated with FastQC v0.11.8 (25). Human (reference: ensembl hg38) and mouse (reference: ensembl mm10) reads were split with Xenome v1.0.1 (26). STAR aligner v2.6.1a (27), QualiMap v2.2.1 (28) and eXpress v1.5.1 (29) were used to map the human-specific reads and quantify transcript expression.

GATK 4.0.2.1 (https://github.com/broadinstitute/gatk/releases) (30) and the Ensemble Variant Effect Predictor (VEP), release 94 (https://www.ensembl.org/info/docs/tools/vep/index.html) (31) were used for variant calling and annotation of mapped reads. Additionally, to verify annotations and to further interpret variants of interest the openCRAVAT pipeline v2.2.7 was used (32). The mutational analysis was performed for a set of GBM-relevant genes (33). Quality-tested variant calls were filtered based on allele frequencies from gnomAD 3.1. to identify somatic alterations. Variants not included in gnomAD 3.1 or with a gnomAD allele frequency below 0.001 were considered (Supplementary Table S1).

Copy Number Variations (CNV) were predicted from gene expression mutational data using RNAseqCNV (34) and CaSpER (35).

RNAseq raw count data were transformed to gene length corrected trimmed mean of M-values (GeTMM) (36) to perform single-sample gene set enrichment analyses (36) (https://github.com/broadinstitute/ssGSEA2.0) regarding gene sets of the molecular signature database (MsigDB v2022.1) (37). Subtype classification was performed based on published gene set expression profiles (12). Group-wise comparison of enriched gene sets between responding and resistant PDX models towards individual therapy was performed with gene set enrichment analyses v4.3.2 (37).

3 Results

3.1 Engraftment of PDX models

A total of 131 tumor tissues from patients diagnosed with GBM were used for PDX generation. Of these, 39 models (30%) engrafted and were consecutively passaged subcutaneously for a minimum of three times and were then considered stable, established s.c. PDX. Median age of patients at resection is 63, and 15 of the characterized GBM PDX were from male patients (58%) (Table 1), reflecting the clinical situation of GBM grade IV. Until now, 26 GBM PDX models have been subject to chemosensitivity testing, 23 of which subject to molecular characterization by RNA sequencing. These 26 models include 19 GBM, 4 recurrences of GBM and 3 GBMs with unknown treatment history. In addition, 15 GBM PDX were established as orthotopic, intracranial models, of which 4 have been subject to sensitivity testing.

3.2 Morphology and growth characteristics of PDX over several *in vivo* passages

Our established GBM PDX models closely resemble the respective patient's tumor histology, with similar morphology and expression patterns of MGMT and Ki-67 (Figure 1A). Expression of proliferation marker Ki-67 was comparable over several s.c. passages and after parallel orthotopic inoculation, as seen in immunohistological stainings of PDX tumor sample sections (Figure 1E). Individual orthotopic PDX models were able to retain the characteristic infiltrative growth of GBM (Figure 1D), compared to nodular growing s.c. tumors. Furthermore, each model displayed stable characteristic growth patterns over several s.c passages, with a slight increase in tumor growth rate in higher passage numbers (Figure 1B). Tumor doubling times varied highly between different s.c. models (Figure 1C), reflecting the heterogeneity of our GBM PDX panel.

3.3 Chemosensitivity of s.c. GBM PDX models

PDX tumor bearing mice received monotherapies of everolimus, sorafenib, bevacizumab, irinotecan, salinomycin or standard of care temozolomide for up to 2 weeks. Tumor growth was monitored during therapies until the study was terminated for ethical reasons (Figure 2A). Of the administered compounds, salinomycin and sorafenib showed no efficacy in our panel of GBM PDX. The anti-VEGF antibody bevacizumab and mTORC1 inhibitor everolimus showed only limited efficacy, leading to moderate (T/C < 25%) to strong responses (T/C < 10%) and stable tumor volumes (RTV 0.34-1.7) in 7 and 4 out of 26 models, respectively. A better response rate was seen for topoisomerase I

10.3389/fonc.2023.1129627

TABLE 1 Clinical characteristics of patients that provided tumor tissue of subcutaneously established and chemosensitivity-tested PDX models.

PDX	Patient		Tumor characteristics	
	sex	age	Diagnosis	Past treatments
Glio10193	male	n.a.	Glioblastoma Grade IV	no
Glio10315	male	n.a.	Glioblastoma Grade IV	no
Glio10485	female	n.a.	Glioblastoma	n.a.
Glio10535	male	n.a.	Glioblastoma Grade IV	no
Glio10618	female	66	Glioblastoma Grade IV	no
Glio10888	male	n.a.	Glioblastoma Grade IV	no
Glio10995	female	n.a.	Glioblastoma	n.a.
Glio11305	male	71	Glioblastoma Grade IV	no
Glio11368	male	49	Glioblastoma Grade IV	no
Glio11413	female	n.a.	Glioblastoma	n.a.
Glio11414	female	60	Glioblastoma Grade IV	recurrence, yes
Glio11415	male	55	Glioblastoma Grade IV	recurrence, n.a.
Glio11575	male	66	Glioblastoma Grade IV	recurrence, n.a.
Glio11874	male	63	Glioblastoma Grade IV	no
Glio12032	male	69	Glioblastoma Grade IV	no
Glio12421	male	61	Gliosarcoma Grade IV	no
Glio12464	female	62	Glioblastoma Grade IV	no
Glio12826	male	53	Glioblastoma Grade IV	no
Glio12827	male	60	Glioblastoma Grade IV	recurrence, n.a.
Glio12856	female	77	Glioblastoma Grade IV	no
Glio13066	male	68	Glioblastoma Grade IV	no
Glio14227B	male	61	Glioblastoma Grade IV	no
Glio15194	female	67	Glioblastoma Grade IV	no
Glio15380B	female	49	Glioblastoma Grade IV	no
Glio15782	female	79	Glioblastoma	no
Glio15807	male	42	Glioblastoma Grade IV	no

n.a., data not available.

inhibitor irinotecan, which led to stable tumor volumes in 20 and tumor regression (RTV > 0.34) in 2 models. When compared compared to untreated PDX tumors we only observed a moderate to strong response in 17 models. The standard of care drug temozolomide showed the best tumor growth inhibition among the tested compounds. We observed moderate to strong responses in 21 models, with treatment leading to stable tumor volumes in 15 models and tumor regression in 7 models (Figure 2B). Interestingly, Glio11414, a PDX established from a recurrent GBM previously treated with temozolomide, showed resistance toward temozolomide.

3.4 Chemosensitivity of orthotopic GBM PDX models

The BBB and the tumor microenvironment within the brain parenchyma significantly contribute to tumor biology and eventually treatment outcome in GBM. We therefore compared efficacy of bevacizumab, everolimus, irinotecan and temozolomide in 4 orthotopic GBM PDX (Figure 2C). To evaluate treatment responses between s.c. and orthotopic PDX we used T/C at study end [%].

The targeted drugs bevacizumab and everolimus performed less efficiently in orthotopic PDX tumors compared with matching subcutaneously growing PDX tumors (Figure S1). None of the orthotopic models were considered responders to everolimus (T/C > 50%), while it caused a reduction of tumor volumes (T/C < 50%) in two out of four matching s.c. models. For bevacizumab, differences in efficacy in s.c. versus orthotopic models were even more pronounced. All s.c. growing PDX models were considered minor to moderate responders (T/C 50 - 10%), but no response was seen in the four matching orthotopic GBM models. Regarding irinotecan, chemosensitivity of s.c. vs. orthotopic models was different. Irinotecan showed similar efficacy in orthotopic and matching s.c. Glio10618 and Glio12032 models. Compared to their respective vehicle treated control group, orthotopic tumors were significantly reduced in size (Figures S1B, C) and showed moderate responses (T/C 10% - 25%). However, in the orthotopic PDX Glio13066, irinotecan showed no efficacy (T/C 84%), whereas it caused pronounced tumor growth inhibition in the matching s.c. model (T/C 7%). Out of the four tested drugs, temozolomide showed best efficacy in the orthotopic PDX, where in all 4 tested models glioma growth was reduced (T/C 2% - 41%), with significant differences to control groups in 2 out of 4 tested models (Figures S1A–D). Temozolomide efficacy in s.c. models was slightly better in all models showing moderate to strong responses (T/C 1% - 13%). In conclusion, our diverging results point to the importance of orthotopic GBM PDX models to evaluate drug efficacy in a clinically relevant setting.

3.5 Mutation profile of s.c. GBM PDX models

The mutational status of 23 GBM PDX was analyzed using the available RNA sequencing data regarding genes frequently mutated in GBM (Table S2). In 23 of these genes, we could identify somatic mutations, with the most frequent mutations occurring in EGFR and PARP1 in 9 PDX models each. In addition, mutations in TP53 (7 PDX), FAT1 and PTEN (6 PDX each), as well as ATM, BRCA2 and MTOR (each in 5 PDX) were identified. Overall, in 12 PDX mutations within the PI3K/Akt/mTOR signaling pathway could be found (Figure 3A). We furthermore used available RNA sequencing data to visualize the expression of mutated genes, allowing for selection of PDX expressing specific targets for preclinical studies. Interestingly, 6 of the 9 PDX bearing mutations in EGFR showed a comparably high expression of the mutated receptor (Figure 3B).

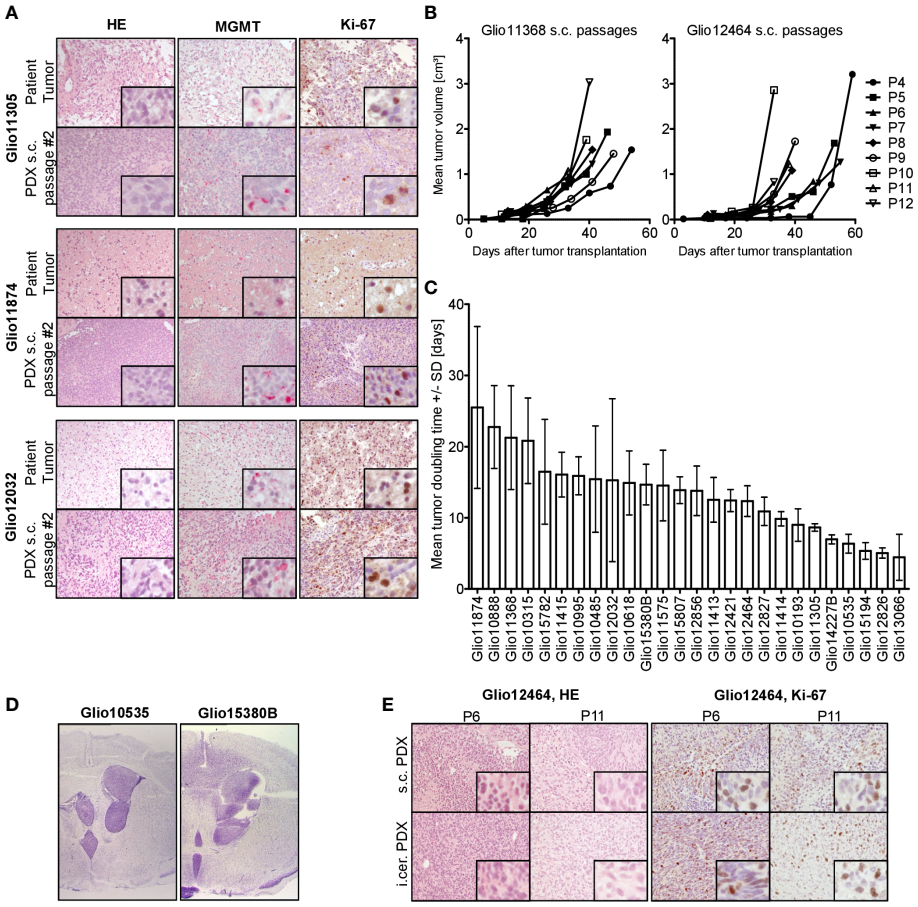

FIGURE 1
Histological and biological characteristics of GBM PDX. **(A)** Analysis of three representative patient tissue samples and respective s.c. PDX tissue from *in vivo* passage #2 revealed comparable histology (HE), MGMT expression (red staining) and expression of proliferation marker Ki-67 (brown staining), 200-fold magnification, inset 800-fold magnification. **(B)** Comparable growth over several consecutive s.c. passages of PDX models Glio11368 and Glio12464. **(C)** Heterogeneous tumor doubling times in our panel of established PDX models, n=3-6. Mean and standard deviation (SD). **(D)** Comparison of nodular and infiltrative growth in two different orthotopic (intracerebral, i.cer.) PDX models (cresyl violet staining, tumor tissue stained purple) (0.9-fold magnification). **(E)** Analysis of PDX Glio12464 revealed comparable histology and Ki-67 expression over several consecutive s.c. passages and parallel orthotopic inoculation. Examination of Ki-67 expression (proliferation marker) in PDX tumor tissue *via* IHC. Positive areas in the sections are stained brown. 20-fold magnification, inset 160-fold magnification.

3.6 Molecular GBM PDX subtypes

We performed copy number variation analysis and principal component analysis to determine transcriptomic similarities within the cohort and to identify potential molecular subgroups. While clustering in copy number variation remained inconclusive (Figure S2), the principal component analysis revealed two clusters of three and four models, and a third cluster of 16 models. Cluster I consists of Glio10995, Glio12421 and Glio11413, whereas cluster II contains Glio10535, Glio10888, Glio11368 and Glio13066 (Figure 4A). To clarify whether the observed clustering is in line with molecular GBM subtypes mesenchymal, classical and proneural, we analyzed a set of 150 genes described as characteristically expressed in these subtypes (Figure 4B) (12). Members of cluster I are enriched for mesenchymal signature genes, while members of cluster II are enriched for signature genes of the classical phenotype. The remaining 16 models formed a third cluster defined by comparably high enrichment of genes related to the proposed proneural subtype, but with enrichment in more than one molecular subtype in individual models.

3.7 Transcriptome and correlation analysis of s.c. GBM PDX models

To gain further insight into the tumor biology and cancer-related pathways of tumor progression in our PDX models, we compared their transcriptomes according to gene sets of cancer hallmarks (Figure 4C). Models of cluster I, the proposed mesenchymal subtype, also clustered in gene sets like epithelial mesenchymal transition, hypoxia, glycolysis and the P53 pathway, inflammation-related signatures like response to interferon alpha/gamma and TNF signaling, as well as angiogenesis. The two adjacent clusters of three models each showed comparably low enrichment scores in the mentioned hallmarks, but high scores in hallmarks G2M checkpoints, as well as E2F targets. The remaining

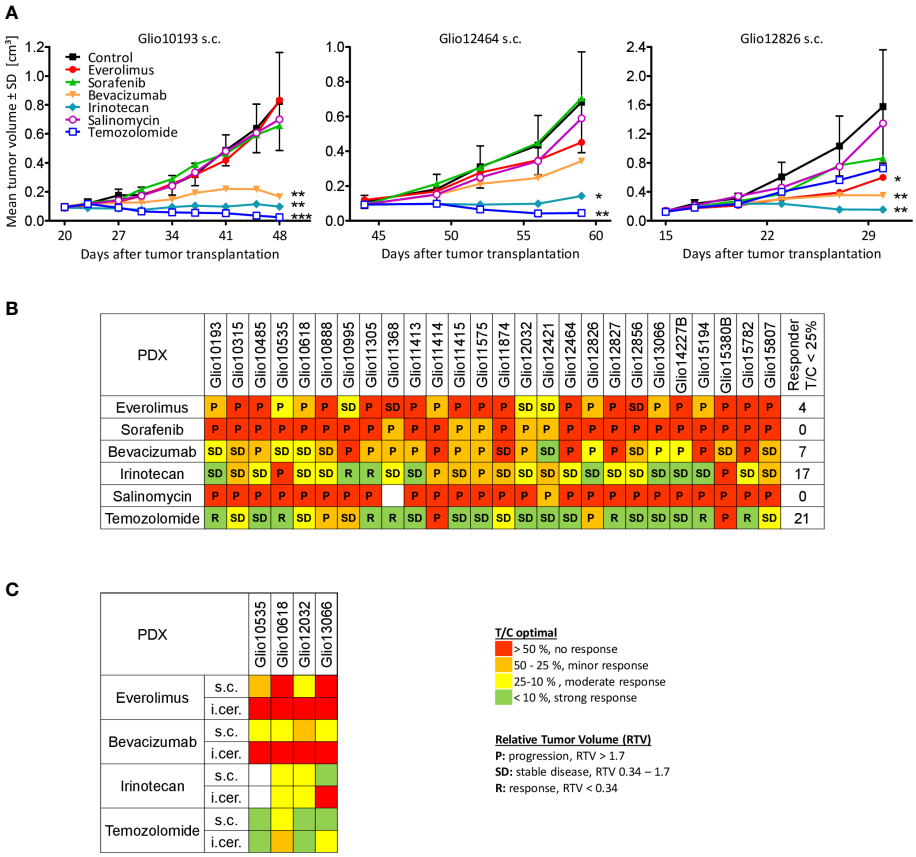

FIGURE 2
Chemosensitivity of established glioma PDX. **(A)** Examples of drug testings of three s.c. glioma PDX models, illustrating model-specific growth characteristics and treatment responses to different drugs, like temozolomide. N=3-5. Mean and standard deviation (SD). One-way ANOVA, Dunnett's multiple comparison test. Significant differences to control (PBS) at study end: * $p < 0.05$, ** $p < 0.01$, *** $p < 0.001$. **(B)** Treatment response evaluation as mean tumor volume of treated tumors divided by mean tumor volume of tumors in the corresponding control group (T/C optimal in %) revealed PDX individual sensitivity profiles. In addition, RTV as response criteria is indicated as progression, stable disease or regression in respective groups. N=2-6 per group. **(C)** T/C values at study end of orthotopic PDX models Glio10535, Glio10618, Glio12032 and Glio13066 revealed reduced sensitivities when compared to matching s.c. models. The maximum tumor area in coronal plane was used as measure for i.cer. tumor growth. RTV could not be calculated for orthotopic PDX, as tumor sizes were only measured once at study end.

PDX models showed individual expression profiles regarding the analyzed hallmarks, with three of the four PDX resembling the classical subtype grouping together.

Since we observed pronounced clustering in VEGF signaling and angiogenesis, the PI3K/Akt/mTOR pathway, and MAPK and JAK/STAT signaling (Figure 4D), all commonly deregulated in GBM, we analyzed expression of related gene sets in more detail. In VEGF and angiogenesis-related gene set analyses (Figure S3A), models resembling the mesenchymal subtype grouped together with two PDX mostly resembling the classical subtype, but with additional enrichment of the mesenchymal gene expression signature (Glio10535 and Glio13066). Another cluster of five models had comparably low enrichment of analyzed gene sets, while the remaining PDX showed different individual expression profiles. Clustering could also be observed in gene set enrichment analyses of PI3K/Akt/mTOR-related gene sets (Figure S3B), where four models were separated by comparably high enrichment scores, especially in PI3K/Akt dependent signaling. Another seven models showed comparable low enrichment scores for PI3K/Akt-dependent signaling, while the remaining 12 models showed different individual expression profiles regarding the analyzed gene sets. In analyses of MAPK/ERK and JAK/STAT signaling-related gene sets (Figure S3C), models of the mesenchymal subtype were again separate from the remaining models and characterized by overall high enrichment scores. The two PDX resembling the classical subtype the most pronounced (Glio10888 and Glio11368) were localized in a cluster of four models with comparably low enrichment scores, while remaining models showed individual expression profiles.

In a next step we analyzed potential correlations between gene expression profiles and treatment responses of PDX tumors *via* gene set enrichment analyses. Comparison of expression profiles of irinotecan responders and non-responders did not reveal significant differences between the two phenotypes. Despite the observed clustering of PDX models in single-sample gene set enrichment analyses regarding their expressions of different VEGF signaling and angiogenesis-related gene sets, there was no statistically significant difference in between bevacizumab non-responders and responders. For temozolomide, our analyses did reveal significant differences ($p < 0.1$ and FDR < 25%) in expression profiles between responding and non-responding PDX (Figure 5A).

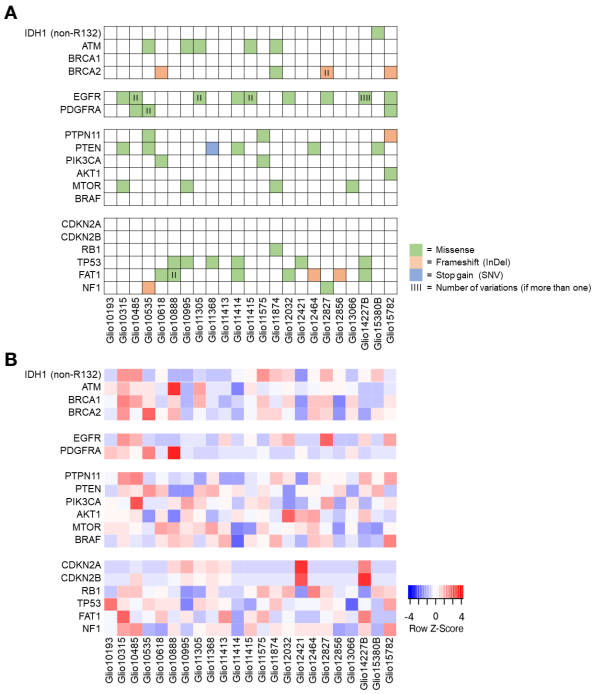

FIGURE 3
Mutation status of selected genes and their expression in GBM PDX models. **(A)** Using available RNA sequencing data, a selection of genes frequently mutated in GBM was analyzed for mutations in our panel of GBM PDX, revealing PDX individual profiles. **(B)** Expression of the genes listed, with comparably high EGFR expression in most PDX bearing EGFR mutations.

In temozolomide resistant models, expression of hallmark gene sets hypoxia and mTORC1 signaling were upregulated, while no correlation between the expression of MGMT, a known predictive marker for temozolomide resistance (5, 6), and monitored responses could be detected. However, only one of these models were sensitive towards the mTOR inhibitor everolimus. Comparing expression profiles of everolimus responders and non-responders, responders showed higher scores for hallmark gene sets epithelial mesenchymal transition and angiogenesis, as well as in inflammatory response, TNF alpha signaling *via* NF-kappaB, IL6/JAK/STAT3 signaling and the reactive oxygen species pathway (Figures 5B, S4).

4 Discussion

There is an urgent need in preclinical research to identify and validate therapeutic alternatives for treatment of GBM and their subsequent clinical translation. Panels of PDX models that retain intertumoral heterogeneity and can approximate a cohort of cancer patients with individual chemosensitivities are therefore considered a valuable tool in drug testing and biomarker identification (20, 21, 38–40). In this study, we established and characterized 26 high-grade GBM PDX from mostly untreated primary patients, and established 15 matching orthotopic models. Histologically, PDX tumors showed comparable morphology and expression of MGMT and proliferation marker Ki-67 in comparison to the patients' tumors and over a range of up to 11 *in vivo* passages. While s.c. PDX tumors exhibit nodular growth, orthotopic PDX models retain the typical infiltrative phenotype to varying degrees (19). Tumor doubling time of PDX models was heterogeneous but comparable over several subsequent s.c. passages, with their range reflecting intertumoral heterogeneity. At passage numbers > 10, we observed a drift towards increased tumor growth in individual models. This might be caused by stepwise adaption of the PDX tumor to the altered microenvironment in the immuno-compromised mice (41). Overall, our results confirm the stability of PDX models regarding their histology and growth characteristics, as seen in other panels of GBM PDX and of other tumor entities (19, 24, 39, 40, 42).

Extensive chemosensitivity testing of our PDX models revealed individual responses towards selected drugs. They included standard of care temozolomide, bevacizumab and irinotecan as drugs identified as beneficial in combination with temozolomide in subsets of patients, as well as compounds targeting different pathways identified as crucial in GBM biology, like mTOR inhibitor everolimus and multikinase inhibitor sorafenib. As expected, the standard of care temozolomide showed the best efficacy with 22 of 26 (85%) PDX models showing a response (T/C < 25%). This is higher than the up to 30% initial response seen in patients (43, 44), possibly in part due to the absence of the concentration limiting BBB (45). Irinotecan had an overall high, but compared to temozolomide, reduced efficacy with 3 out of 5 temozolomide-resistant PDX responding to irinotecan. Irinotecan as monotherapy and in combination with e.g. temozolomide and bevacizumab could not significantly improve outcome over temozolomide alone in various clinical trials (46–49), but still can be considered a treatment alternative for individual patients. However, the observed high initial sensitivity to temozolomide and irinotecan might be in part over-predictive due to different drug pharmacokinetics between humans and mice. Bevacizumab was clearly inferior regarding its anti-tumor efficacy in our panel. Tumor growth was inhibited in individual models, but no reduction of tumor size in any of our tested PDX was monitored. This is in line with various clinical trials showing that bevacizumab as first line monotherapy lacks sufficient efficacy but can improve progression-free survival in recurring GBM (50). As bevacizumab is specific for human VEGF, efficacy is also reduced in xenograft models where parts of the VEGF could be of murine origin. Our PDX panel furthermore confirmed the limited efficacy of the mTOR inhibitor everolimus currently used in clinical trials, despite the crucial role the PI3K/Akt/mTOR pathway in many GBM (13, 51). In 4 models however, we saw a moderate response. Sorafenib and salinomycin both showed anti-tumor activity in preclinical *in vitro* and *in vivo* studies (52–54), but not in clinical applications (55, 56). In our screenings we did not observe a tumor growth inhibition in any of the PDX. While this reflects the mentioned limited efficacy of these monotherapies, it remains unclear whether higher doses could achieve better results. Overall, our screening results reflect some of the response patterns seen in patients, and strongly indicate that intratumoral heterogeneity and clonal complexity is maintained, contributing to the monitored highly tumor individual sensitivity profiles. With subsequent gene set enrichment analyses, we tried to

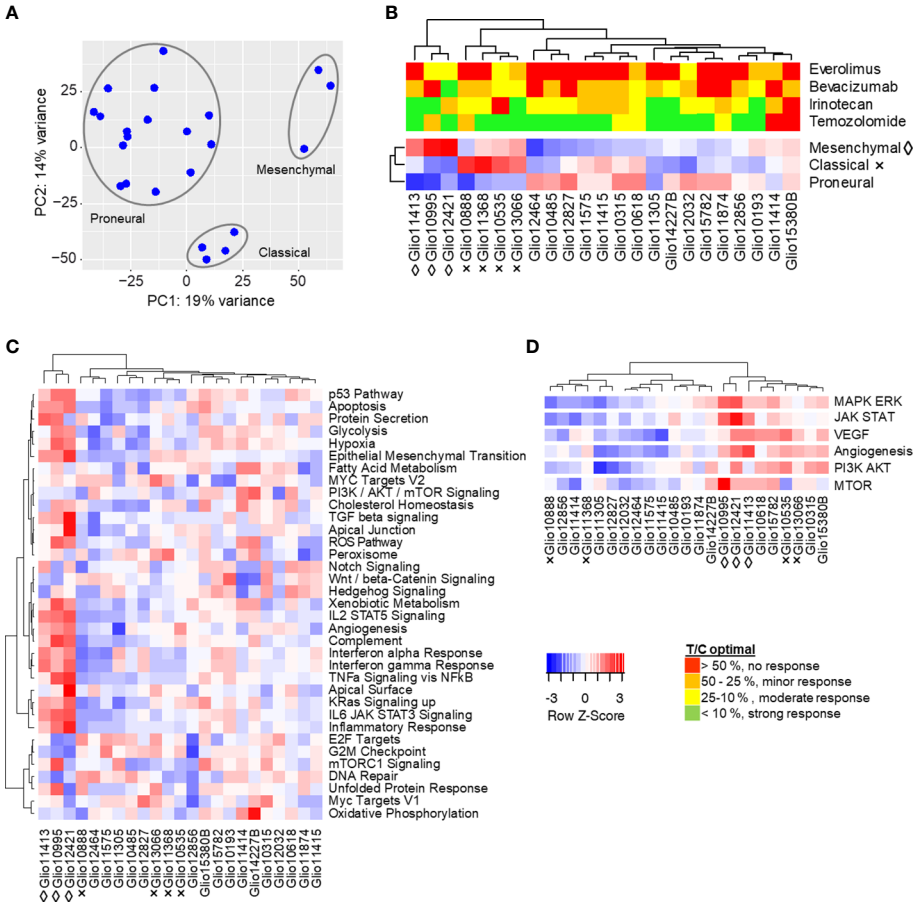

FIGURE 4
Molecular characteristics of s.c. glioma PDX models. **(A)** Global gene expression of 23 glioma PDX models by principal component analysis. Similarity of transcriptomes is represented by their spacial distribution in the plot, with three custers visible. **(B)** The observed clustering into three groups could be replicated in subsequent analyses of expressions of gene sets characteristic for proposed molecular subtypes mesenchymal (◊), classical (×) and proneural (no indication). **(C)** Single sample gene set enrichment analysis of glioma PDX models regarding 34 selected hallmarks and clustering of models resembling the mesenchymal subtype. **(D)** Combined enrichment scores of gene sets related to MAPK/Erk, JAK/STAT, VEGF, PI3K/Akt and mTOR signaling, as well as angiogenesis. Gene sets analyzed individually in Figure S3. Red (positive Z-score): higher expression of gene set than in the average of all models. Blue (negative Z-score): lower expression.

identify molecular marker profiles to identify patients that might benefit from personalized therapies.

As the tumor microenvironment has an important function in GBM development and proliferation, orthotopic models are the preferred setting for translational research. Comparing drug sensitivity between selected s.c. and matching orthotopic PDX models, we monitored a pronounced reduction of efficacy in the orthotopic setup. Irinotecan and temozolomide still caused inhibition of tumor growth, but to a lesser degree than in the respective s.c. PDX models. Both bevacizumab and everolimus performed notably worse, with no response in any of the tested orthotopic PDX. A possible reason for the reduced efficacy in orthotopic PDX is the BBB (57). It physically restricts diffusion of molecules into the brain and maintains a strict homeostasis *via* various efflux transporters. Both can drastically limit drug concentrations in the GBM (58), as observed in clinical studies with disappointing results in GBM patients, despite promising preclinical data (59, 60). Our results confirm that orthotopic PDX are a valuable tool to develop and test new therapy approaches that increase tissue selective drug delivery and efficacy while managing systemic side effects (61). However, as these orthotopic models are extremely time and cost sensitive, we suggest a two-step screening strategy for new therapies. In the first step, new compounds might be screened in s.c. transplanted models to identify potential active compounds. In a second step, one should test the selected compounds in orthotopic models to evaluate the potential effect of the BBB. Alternatively, one could transplant the GBM PDX in parallel s.c. and orthotopically to discriminate compounds affected by the BBB (62).

The available transcriptome sequencing data allowed us to analyze the PDX models mutation and gene expression status. We were able to confirm IDH-wt (R132) status in all models, with only one model bearing a mutation in IDH1, albeit not in codon R132. We furthermore found mutations frequently identified in patients' GBM like in the genes EGFR, TP53, FAT1, as well as PTEN and MTOR (33).

Principal component analyses revealed three molecular subgroups within our IDH-wt GBM. They resemble previously

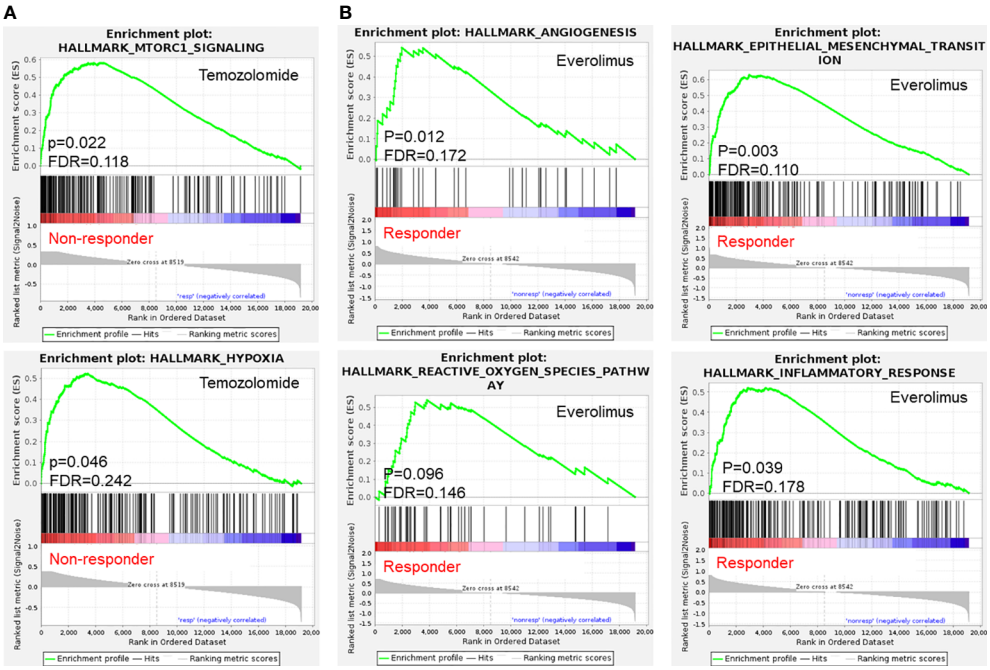

FIGURE 5
Selected gene set enrichment analysis plots of s.c. PDX tumor tissue based on results in chemosensitivity testing. **(A)** Enriched hallmark gene sets (p < 0.1 and FDR < 25%) in temozolomide resistant PDX and **(B)** PDX responding to mTOR inhibitor everolimus indicate possible implications of mTOR signaling and hypoxia for the monitored phenotypes.

described proposed molecular subtypes mesenchymal, classical and proneural regarding their expression profiles, reflecting the expression patterns and intratumoral heterogeneity seen in GBM patient cohorts (12). PDX models showed individual expression profiles of gene sets related to VEGF signaling and angiogenesis, and MAPK/Erk and STAT signaling, with comparably high expressions in the mesenchymal subtype. In PI3K/Akt/mTOR pathway-related gene sets, a majority of PDX showed enrichment in PI3K or mTOR signaling, or both. This well reflects the high prevalence of deregulation of this pathway seen in patients and its importance in GBM (63, 64).

Despite the observed clustering, for bevacizumab and irinotecan no relevant correlations between treatment response and gene expression profiles were detected. Gene set enrichment analyses of temozolomide response revealed high expression of hallmark gene sets for hypoxia and mTORC1 signaling in resistant models, while correlation between MGMT expression, a described predictive marker for response towards temozolomide, could not be identified (5, 6). It has been shown that a hypoxic microenvironment can induce the acquisition of temozolomide resistance *via* activation of HIF1-alpha signaling (65, 66), both mTOR dependent (67, 68) and independent (69, 70). Combination therapies of temozolomide and novel mTORC1/2 inhibitors for example have been successfully applied to overcome this temozolomide resistance *in vitro* (71–73). In a subgroup of patients in the EORTC trial 26082, activated mTOR signaling correlated with better treatment response towards monotherapy of mTOR inhibitor temsirolimus than to temozolomide (74). Our results strongly support these findings and could provide the basis for further analyses regarding the role of hypoxia and mTOR signaling in temozolomide resistance. Focus needs to be the evaluation of such combinations in orthotopic models since the altered microenvironment in the brain might impact the tumors response to hypoxia. In addtion, the BBB could limit the passage of different mTOR or PI3K inhibitors in the brain by varying degrees. Other *in vitro* studies however showed that mTOR inhibition under hypoxic conditions can promote survival of glioma cell lines *in vitro* by reducing oxygen and glucose consumption, and promotes temozolomide resistance by increasing MGMT protein levels (75, 76). These contrasting roles of mTOR signaling highlight the need for molecular markers to select GBM patients where hypoxia and mTOR signaling are true drivers of progression and temozolomide resistance. In our screening only 1 of 5 temozolomide resistant models was sensitive towards mTOR inhibition.

Enrichment of hypoxia-related hallmark gene sets, reactive oxygen species pathways and angiogenesis (67, 77) were also observed in everolimus responders and might be linked to the mesenchymal subtype, as indicated by enrichment of the hallmark gene set epithelial mesenchymal transition. Under hypoxic conditions, reactive oxygen species can accumulate and cause additional activation of HIF1-α, and thereby trigger various processes related to tumor progression, such as angiogenesis *via* expression of e.g., VEGFs and their receptors VEGFR1/2 (78–80). However, whether a combination therapy with e.g., bevacizumab would be beneficial in these GBM PDX needs further testing.

In conclusion, the enrichment of hypoxia and mTORC1 signaling in temozolomide resistant models, as well as enrichment of hypoxia-related gene sets in models susceptible for mTOR

inhibitor everolimus indicate a role of mTOR signaling in progression under hypoxic conditions in s.c. GBM PDX (70). Whether combination with mTOR inhibitors can overcome temozolomide resistance in s.c. and matching orthotopic PDX needs further investigation. This includes analyzing expression profiles of orthotopic models to help understand biology and resistance formation in comparison to s.c. PDX. Gained insight might reveal further, yet unknown vulnerabilities for novel therapies.

Our results highlight both the possible applications, as well as limitations of the two model types. Subcutaneous PDX panels, while not fully representing the GBM's tumor microenvironment, BBB, and their impact on treatment outcome, are suitable for larger screenings of new drugs or treatment regimens in a clinical study-like setup. Subcutaneous PDX panels can identify predictive markers, and mechanisms of intrinsic or treatment-induced drug resistance, and how to prevent or overcome it. Orthotopic GBM PDX - in a possible second step - enable analysis of the impact of the tumor microenvironment and the BBB on drug efficacy, their contribution to resistance formation, and whether drugs can reach therapeutically relevant concentrations within the tumor. This can be of particular interest in the development of new formulations or drug delivery systems that aim to increase BBB-crossing of available drugs in repurposing efforts and new drug candidates identified in previous screenings.

Data availability statement

All underlying RNA sequencing data have been deposited at the European Genome-phenome Archive (EGA), which is hosted by the EBI and the CRG, under accession number EGAS00001007119. Further information about EGA can be found on https://ega-archive.org.

Ethics statement

The animal studies were reviewed and approved by Landesamt für Gesundheit und Soziales, LaGeSo Berlin, Germany (H0308/18 and A0010/19).

Author contributions

JA, JeH and WW designed this work. JoH, ML, TK, AJ, SK, CS and SK were responsible for patient tumor tissue collection and inclusion for the project. JA and AO supervised the experimental studies. JA, AO, MD and MB analyzed the data. JA, LW, WW and JeH wrote the manuscript. All authors contributed to the article and approved the submitted version.

Acknowledgments

We would like to thank our EPO team (Britta Büttner, Elaine Burghardt, Diana Anders, Katharina Scholl and Laura Cristina Nicolae) for the excellent technical assistance.

Conflict of interest

JeH is CEO, WW is CSO, and JA, MB, MD and LW are employees of EPO Berlin-Buch GmbH, Berlin, Germany.

The remaining authors declare that the research was conducted in the absence of any commercial or financial relationships that could be construed as a potential conflict of interest.

Publisher's note

Supplementary material

The Supplementary Material for this article can be found online at: https://www.frontiersin.org/articles/10.3389/fonc.2023.1129627/full#supplementary-material

References

1. Louis DN, Ohgaki H, Wiestler OD, Cavenee WK, Burger PC, Jouvet A, et al. Erratum: The 2007 WHO classification of tumours of the central nervous system. *Acta Neuropathol* (2007) 114:97–109. doi: 10.1007/s00401-007-0278-6

2. Louis DN, Perry A, Reifenberger G, von Deimling A, Figarella-Branger D, Cavenee WK, et al. The 2016 world health organization classification of tumors of the central nervous system: A summary. *Acta Neuropathol* (2016) 131:803–20. doi: 10.1007/s00401-016-1545-1

3. Stupp R, Mason WP, van den Bent MJ, Weller M, Fisher B, Taphoorn MJB, et al. Radiotherapy plus concomitant and adjuvant temozolomide for glioblastoma. *New Engl J Med* (2005) 352:987–96. doi: 10.1056/nejmoa043330

4. Ostrom QT, Rubin JB, Lathia JD, Berens ME, Barnholtz-Sloan JS. Females have the survival advantage in glioblastoma. *Neuro Oncol* (2018) 20:576–7. doi: 10.1093/neuonc/noy002

5. Radke J, Koch A, Pritsch F, Schumann E, Misch M, Hempt C, et al. Predictive MGMT status in a homogeneous cohort of IDH wildtype glioblastoma patients. *Acta Neuropathol Commun* (2019) 7:89. doi: 10.1186/s40478-019-0745-z

6. Weller M, Tabatabai G, Kästner B, Felsberg J, Steinbach JP, Wick A, et al. MGMT promoter methylation is a strong prognostic biomarker for benefit from dose-intensified temozolomide rechallenge in progressive glioblastoma: The DIRECTOR trial. *Clin Cancer Res* (2015) 21:2057–64. doi: 10.1158/1078-0432.CCR-14-2737

7. Avastin | European Medicines AgencyAvailable at: https://www.ema.europa.eu/en/medicines/human/EPAR/avastin (Accessed July 29, 2022).

8. Gilbert MR, Dignam JJ, Armstrong TS, Wefel JS, Blumenthal DT, Vogelbaum MA, et al. A randomized trial of bevacizumab for newly diagnosed glioblastoma. *New Engl J Med* (2014) 370:699–708. doi: 10.1056/nejmoa1308573

9. Gramatzki D, Roth P, Rushing EJ, Weller J, Andratschke N, Hofer S, et al. Bevacizumab may improve quality of life, but not overall survival in glioblastoma: An epidemiological study. *Ann Oncol* (2018) 29:1431–6. doi: 10.1093/annonc/mdy106

10. Ohgaki H, Kleihues P. The definition of primary and secondary glioblastoma. *Clin Cancer Res* (2013) 19:764–72. doi: 10.1158/1078-0432.CCR-12-3002

11. McLendon R, Friedman A, Bigner D, van Meir EG, Brat DJ, Mastrogianakis GM, et al. Comprehensive genomic characterization defines human glioblastoma genes and core pathways. *Nature* (2008) 455:1061–8. doi: 10.1038/nature07385

12. Wang Q, Hu B, Hu X, Kim H, Squatrito M, Scarpace L, et al. Tumor evolution of glioma intrinsic gene expression subtype associates with immunological changes in the microenvironment. *Cancer Cell* (2017) 32:42. doi: 10.1016/J.CCELL.2017.06.003

13. Verhaak RGW, Hoadley KA, Purdom E, Wang V, Qi Y, Wilkerson MD, et al. Integrated genomic analysis identifies clinically relevant subtypes of glioblastoma characterized by abnormalities in PDGFRA, IDH1, EGFR, and NF1. *Cancer Cell* (2010) 17:98–110. doi: 10.1016/J.CCR.2009.12.020

14. Rajaratnam V, Islam MM, Yang M, Slaby R, Ramirez HM, Mirza SP. Glioblastoma: Pathogenesis and current status of chemotherapy and other novel treatments. *Cancers (Basel)* (2020) 12:937. doi: 10.3390/cancers12040937

15. White K, Connor K, Clerkin J, Murphy BM, Salvucci M, O'Farrell AC, et al. New hints towards a precision medicine strategy for IDH wild-type glioblastoma. *Ann Oncol* (2020) 31:1679–92. doi: 10.1016/j.annonc.2020.08.2336

16. Zhao H, Wang J, Shao W, Wu Cp, Chen Zp, To SsT, et al. Recent advances in the use of PI3K inhibitors for glioblastoma multiforme: Current preclinical and clinical development. *Mol Cancer* (2017) 16:1–16. doi: 10.1186/s12943-017-0670-3

17. Qin A, Musket A, Musich PR, Schweitzer JB, Xie Q. Receptor tyrosine kinases as druggable targets in glioblastoma: Do signaling pathways matter? *Neurooncol Adv* (2021) 3. doi: 10.1093/noajnl/vdab133

18. Kratzsch T, Kuhn SA, Joedicke A, Hanisch UK, Vajkoczy P, Hoffmann J, et al. Treatment with 5-azacitidine delay growth of glioblastoma xenografts: A potential new treatment approach for glioblastomas. *J Cancer Res Clin Oncol* (2018) 144:809–19. doi: 10.1007/S00432-018-2600-1

19. Vaubel RA, Tian S, Remonde D, Schroeder MA, Mladek AC, Kitange GJ, et al. Genomic and phenotypic characterization of a broad panel of patient-derived xenografts reflects the diversity of glioblastoma. *Clin Cancer Res* (2020) 26:1094–104. doi: 10.1158/1078-0432.CCR-19-0909/74378/AM/GENOMIC-AND-PHENOTYPIC-CHARACTERIZATION-OF-A-BROAD

20. Verreault M, Schmitt C, Goldwirt L, Pelton K, Haidar S, Levasseur C, et al. Preclinical efficacy of the MDM2 inhibitor RG7112 in MDM2-amplified and TP53 wild-type glioblastomas. *Clin Cancer Res* (2016) 22:1185–96. doi: 10.1158/1078-0432.CCR-15-1015

21. Gao H, Korn JM, Ferretti S, Monahan JE, Wang Y, Singh M, et al. High-throughput screening using patient-derived tumor xenografts to predict clinical trial drug response. *Nat Med* (2015) 21:1318–25. doi: 10.1038/NM.3954

22. Colclough N, Chen K, Johnstrom P, Strittmatter N, Yan Y, Wrigley GL, et al. Preclinical comparison of the blood-brain barrier permeability of osimertinib with other EGFR TKIs. *Clin Cancer Res* (2021) 27:189–201. doi: 10.1158/1078-0432.CCR-19-1871

23. Fichtner I, Klinghammer K, Behrens D, Flechsig S, Rolff J, Becker M, et al. Animal models for personalized treatment options. *Int J Clin Pharmacol Ther* (2017) 55:698–700. doi: 10.5414/CPXCES15EA09

24. William D, Mullins CS, Schneider B, Orthmann A, Lamp N, Krohn M, et al. Optimized creation of glioblastoma patient derived xenografts for use in preclinical studies. *J Transl Med* (2017) 15:27. doi: 10.1186/S12967-017-1128-5

25. Andrew S. *FastQC: A quality control tool for high throughput sequence data (2018)* (2018). Available at: https://www.bioinformatics.babraham.ac.uk/projects/fastqc.

26. Conway T, Wazny J, Bromage A, Tymms M, Sooraj D, Williams ED, et al. Xenome–a tool for classifying reads from xenograft samples. *Bioinformatics* (2012) 28: i172–8. doi: 10.1093/BIOINFORMATICS/BTS236

27. Dobin A, Davis CA, Schlesinger F, Drenkow J, Zaleski C, Jha S, et al. STAR: ultrafast universal RNA-seq aligner. *Bioinformatics* (2013) 29:15–21. doi: 10.1093/BIOINFORMATICS/BTS635

28. Okonechnikov K, Conesa A, García-Alcalde F. Qualimap 2: Advanced multi-sample quality control for high-throughput sequencing data. *Bioinformatics* (2016) 32:292–4. doi: 10.1093/BIOINFORMATICS/BTV566

29. Roberts A, Pachter L. Streaming fragment assignment for real-time analysis of sequencing experiments. *Nat Methods* (2013) 10:71. doi: 10.1038/NMETH.2251

30. *Genome analysis toolkit variant discovery in high-throughput sequencing data*. Available at: https://gatk.broadinstitute.org/hc/en-us.

31. McLaren W, Gil L, Hunt SE, Riat HS, Ritchie GRS, Thormann A, et al. The ensembl variant effect predictor. *Genome Biol* (2016) 17:1–14. doi: 10.1186/S13059-016-0974-4/TABLES/8

32. Pagel KA, Kim R, Moad K, Busby B, Zheng L, Tokheim C, et al. Integrated informatics analysis of cancer-related variants. *JCO Clin Cancer Inform* (2020) 4:310–7. doi: 10.1200/CCI.19.00132

33. Brennan CW, Verhaak RGW, McKenna A, Campos B, Noushmehr H, Salama SR, et al. The somatic genomic landscape of glioblastoma. *Cell* (2013) 155:462. doi: 10.1016/J.CELL.2013.09.034

34. Bařinka J, Hu Z, Wang L, Wheeler DA, Rahbarinia D, McLeod C, et al. RNAseqCNV: analysis of large-scale copy number variations from RNA-seq data. *Leukemia* (2022) 36:1492–8. doi: 10.1038/s41375-022-01547-8

35. Serin Harmanci A, Harmanci AO, Zhou X. CaSpER identifies and visualizes CNV events by integrative analysis of single-cell or bulk RNA-sequencing data. *Nat Commun* (2020) 11:89. doi: 10.1038/s41467-019-13779-x

36. Smid M, Coebergh van den Braak RRJ, van de Werken HJG, van Riet J, van Galen A, de Weerd V, et al. Gene length corrected trimmed mean of m-values (GeTMM) processing of RNA-seq data performs similarly in intersample analyses while improving intrasample comparisons. *BMC Bioinf* (2018) 19:1–13. doi: 10.1186/S12859-018-2246-7/TABLES/2

37. Subramanian A, Tamayo P, Mootha VK, Mukherjee S, Ebert BL, Gillette MA, et al. Gene set enrichment analysis: A knowledge-based approach for interpreting genome-wide expression profiles. *Proc Natl Acad Sci USA* (2005) 102:15545–50. doi: 10.1073/PNAS.0506580102

38. Gupta SK, Kizilbash SH, Carlson BL, Mladek AC, Boakye-Agyeman F, Bakken KK, et al. Delineation of MGMT hypermethylation as a biomarker for veliparib-mediated temozolomide-sensitizing therapy of glioblastoma. *J Natl Cancer Inst* (2015) 108(5):djv369. doi: 10.1093/JNCI/DJV369

39. Schütte M, Risch T, Abdavi-Azar N, Boehnke K, Schumacher D, Keil M, et al. Molecular dissection of colorectal cancer in pre-clinical models identifies biomarkers predicting sensitivity to EGFR inhibitors. *Nat Commun* (2017) 8:1–19. doi: 10.1038/ncomms14262

40. Gürgen D, Becker M, Dahlmann M, Flechsig S, Schaeffeler E, Büttner FA, et al. A molecularly characterized preclinical platform of subcutaneous renal cell carcinoma (RCC) patient-derived xenograft models to evaluate novel treatment strategies. *Front Oncol* (2022) 12:889789. doi: 10.3389/FONC.2022.889789

41. *Tumor-stromal cell turnover in PDX mice* . Available at: https://www.jax.org/news-and-insights/2014/november/tumor-stromal-cell-turnover-in-pdx-mice (Accessed August 10, 2022).

42. Joo KM, Kim J, Jin J, Kim M, Seol HJ, Muradov J, et al. Patient-specific orthotopic glioblastoma xenograft models recapitulate the histopathology and biology of human glioblastomas in situ. *Cell Rep* (2013) 3:260–73. doi: 10.1016/J.CELREP.2012.12.013

43. Newton HB. Clinical pharmacology of brain tumor chemotherapy. *Handb Brain Tumor Chemotherapy* (2006) 911–7. doi: 10.1016/B978-012088410-0/50040-8

44. Oshiro S, Tsugu H, Komatsu F, Ohmura T, Ohta M, Sakamoto S, et al. Efficacy of temozolomide treatment in patients with high-grade glioma. *Anticancer Res* (2009) 29.

45. Ostermann S, Csajkag C, Buclin T, Leyvraz S, Lejeune F, Decosterd LA, et al. Plasma and cerebrospinal fluid population pharmacokinetics of temozolomide in malignant glioma patients. *Clin Cancer Res* (2004) 10:3728–36. doi: 10.1158/1078-0432.CCR-03-0807

46. Quinn JA, Jiang SX, Reardon DA, Desjardins A, Vredenburgh JJ, Friedman AH, et al. Phase II trial of temozolomide (TMZ) plus irinotecan (CPT-11) in adults with newly diagnosed glioblastoma multiforme before radiotherapy. *J Neurooncol* (2009) 95:393. doi: 10.1007/S11060-009-9937-X

47. Friedman HS, Prados MD, Wen PY, Mikkelsen T, Schiff D, Abrey LE, et al. Paleologos n, Nicholas MK, Jensen r, et al. bevacizumab alone and in combination with irinotecan in recurrent glioblastoma. *J Clin Oncol* (2009) 27:4733–40. doi: 10.1200/JCO.2008.19.8721

48. Lu G, Rao M, Zhu P, Liang B, El-Nazer RT, Fonkem E, et al. Triple-drug therapy with bevacizumab, irinotecan, and temozolomide plus tumor treating fields for recurrent glioblastoma: A retrospective study. *Front Neurol* (2019) 10:42/BIBTEX. doi: 10.3389/FNEUR.2019.00042/BIBTEX

49. Herrlinger U, Schäfer N, Steinbach JP, Weyerbrock A, Hau P, Goldbrunner R, et al. Bevacizumab plus irinotecan versus temozolomide in newly diagnosed O6-methylguanine-DNA methyltransferase nonmethylated glioblastoma: The randomized GLARIUS trial. *J Clin Oncol* (2016) 34:1611–9. doi: 10.1200/JCO.2015.63.4691

50. Nagpal S, Harsh G, Recht L. Bevacizumab improves quality of life in patients with recurrent glioblastoma. *Chemother Res Pract* (2011) 2011:1–6. doi: 10.1155/2011/602812

51. Chinnaiyan P, Won M, Wen PY, Rojiani AM, Werner-Wasik M, Shih HA, et al. A randomized phase II study of everolimus in combination with chemoradiation in newly diagnosed glioblastoma: results of NRG oncology RTOG 0913. *Neuro Oncol* (2018) 20:666–73. doi: 10.1093/NEUONC/NOX209

52. Carra E, Barbieri F, Marubbi D, Pattarozzi A, Favoni RE, Florio T, et al. Sorafenib selectively depletes human glioblastoma tumor-initiating cells from primary cultures. *Cell Cycle* (2013) 12:491. doi: 10.4161/CC.23372

53. Magrath JW, Kim Y. Salinomycin's potential to eliminate glioblastoma stem cells and treat glioblastoma multiforme (Review). *Int J Oncol* (2017) 51:753–9. doi: 10.3892/IJO.2017.4082

54. Clavreul A, Roger E, Pourbaghi-Masouleh M, Lemaire L, Tétaud C, Menei P. Development and characterization of sorafenib-loaded lipid nanocapsules for the treatment of glioblastoma. *Drug Delivery* (2018) 25:1756–65. doi: 10.1080/10717544.2018.1507061/SUPPL_FILE/IDRD_A_1507061_SM1005.TIF

55. Nghiemphu PL, Ebiana VA, Wen P, Gilbert M, Abrey LE, Lieberman F, et al. Phase I study of sorafenib and tipifarnib for recurrent glioblastoma: NABTC 05-02. *J Neurooncol* (2018) 136:79. doi: 10.1007/S11060-017-2624-4

56. Chen H, Kuhn J, Lamborn KR, Abrey LE, Deangelis LM, Lieberman F, et al. Phase I/II study of sorafenib in combination with erlotinib for recurrent glioblastoma as part of a 3-arm sequential accrual clinical trial: NABTC 05-02. *Neurooncol Adv* (2020) 2:1–11. doi: 10.1093/NOAJNL/VDAA124

57. Pardridge WM. Drug transport across the blood–brain barrier. *J Cereb Blood Flow Metab* (2012) 32:1959. doi: 10.1038/JCBFM.2012.126

58. Sarkaria JN, Hu LS, Parney IF, Pafundi DH, Brinkmann DH, Laack NN, et al. Is the blood–brain barrier really disrupted in all glioblastomas? A critical assessment of existing clinical data. *Neuro Oncol* (2018) 20:184. doi: 10.1093/NEUONC/NOX175

59. de Vries NA, Buckle T, Zhao J, Beijnen JH, Schellens JHM, van Tellingen O. Restricted brain penetration of the tyrosine kinase inhibitor erlotinib due to the drug transporters p-gp and BCRP. *Invest New Drugs* (2012) 30:443–9. doi: 10.1007/S10637-010-9569-1

60. Agarwal S, Sane R, Gallardo JL, Ohlfest JR, Elmquist WF. Distribution of gefitinib to the brain is limited by p-glycoprotein (ABCB1) and breast cancer resistance protein (ABCG2)-mediated active efflux. *J Pharmacol Exp Ther* (2010) 334:147. doi: 10.1124/JPET.110.167601

61. Zhang Z, Fan Q, Luo X, Lou K, Weiss WA, Shokat KM. Brain-restricted mTOR inhibition with binary pharmacology. *Nature* (2022) 609:822–8. doi: 10.1038/s41586-022-05213-y

62. Hoffmann J, Fichtner I, Lemm M, Lienau P, Hess-Stumpp H, Rotgeri A, et al. Neuro-oNcology sagopilone crosses the blood-brain barrier *in vivo* to inhibit brain tumor growth and metastases. *Neuro Oncol* (2009) 11:158–66. doi: 10.1215/15228517-2008-072

63. Li X, Wu C, Chen N, Gu H, Yen A, Cao L, et al. PI3K/Akt/mTOR signaling pathway and targeted therapy for glioblastoma. *Oncotarget* (2016) 7:33440. doi: 10.18632/ONCOTARGET.7961

64. Sami A, Karsy M. Targeting the PI3K/AKT/mTOR signaling pathway in glioblastoma: novel therapeutic agents and advances in understanding. *Tumor Biol* (2013) 34:1991–2002. doi: 10.1007/S13277-013-0800-5

65. Ge X, Pan MH, Wang L, Li W, Jiang C, He J, et al. Hypoxia-mediated mitochondria apoptosis inhibition induces temozolomide treatment resistance through miR-26a/Bad/Bax axis. *Cell Death Dis* (2018) 9:1–16. doi: 10.1038/s41419-018-1176-7

66. Li DM, Chen QD, Wei GN, Wei J, Yin JX, He JH, et al. Hypoxia-induced miR-137 inhibition increased glioblastoma multiforme growth and chemoresistance through LRP6. *Front Oncol* (2021) 10:611699/FULL. doi: 10.3389/FONC.2020.611699/FULL

67. Karar J, Maity A. PI3K/AKT/mTOR pathway in angiogenesis. *Front Mol Neurosci* (2011) 4:51. doi: 10.3389/FNMOL.2011.00051

68. Huang W, Ding X, Ye H, Wang J, Shao J, Huang T. Hypoxia enhances the migration and invasion of human glioblastoma U87 cells through PI3K/Akt/mTOR/HIF-1α pathway. *Neuroreport* (2018) 29:1578–85. doi: 10.1097/WNR.0000000000001156

69. Pore N, Jiang Z, Shu HK, Bernhard E, Kao GD, Maity A. Akt1 activation can augment hypoxia-inducible factor-1α expression by increasing protein translation through a mammalian target of rapamycin–independent pathway. *Mol Cancer Res* (2006) 4:471–9. doi: 10.1158/1541-7786.MCR-05-0234

70. Wei W, Shi Q, Remacle F, Qin L, Shackelford DB, Shin YS, et al. Hypoxia induces a phase transition within a kinase signaling network in cancer cells. *Proc Natl Acad Sci USA* (2013) 110:E1352–60. doi: 10.1073/PNAS.1303060110/SUPPL_FILE/SAPP.PDF

71. Miyata H, Ashizawa T, Iizuka A, Kondou R, Nonomura C, Sugino T, et al. Combination of a STAT3 inhibitor and an mTOR inhibitor against a temozolomide-resistant glioblastoma cell line. *Cancer Genomics Proteomics* (2017) 14:83. doi: 10.21873/CGP.20021

72. Colella B, Colardo M, Iannone G, Contadini C, Saiz-Ladera C, Fuoco C, et al. mTOR inhibition leads to src-mediated EGFR internalisation and degradation in glioma cells. *Cancers (Basel)* (2020) 12:1–17. doi: 10.3390/CANCERS12082266

73. Colardo M, Segatto M, di Bartolomeo S. Targeting RTK-PI3K-mTOR axis in gliomas: An update. *Int J Mol Sci* (2021) 22:4899. doi: 10.3390/IJMS22094899

74. Wick W, Gorlia T, Bady P, Platten M, van den Bent MJ, Taphoorn MJB, et al. Phase II study of radiotherapy and temsirolimus versus radiochemotherapy with temozolomide in patients with newly diagnosed glioblastoma without MGMT promoter hypermethylation (EORTC 26082). *Clin Cancer Res* (2016) 22:4797–806. doi: 10.1158/1078-0432.CCR-15-3153/116090/AM/PHASE-II-STUDY-OF-RADIOTHERAPY-AND-TEMSIROLIMUS

75. Smalley S, Chalmers AJ, Morley SJ. MTOR inhibition and levels of the DNA repair protein MGMT in T98G glioblastoma cells. *Mol Cancer* (2014) 13:1–11. doi: 10.1186/1476-4598-13-144/FIGURES/5

76. Heinzen D, Divé I, Lorenz NI, Luger AL, Steinbach JP. Ronellenfitsch MW. second generation mTOR inhibitors as a double-edged sword in malignant glioma treatment. *Int J Mol Sci* (2019) 20:4474. doi: 10.3390/IJMS20184474

77. Tafani M, Sansone L, Limana F, Arcangeli T, de Santis E, Polese M, et al. The interplay of reactive oxygen species, hypoxia, inflammation, and sirtuins in cancer initiation and progression. *Oxid Med Cell Longev* (2016) 2016. doi: 10.1155/2016/3907147

78. Hanahan D, Weinberg RA. Hallmarks of cancer: The next generation. *Cell* (2011) 144:646–74. doi: 10.1016/J.CELL.2011.02.013

79. Drigotas M, Affolter A, Mann WJ, Brieger J. Reactive oxygen species activation of MAPK pathway results in VEGF upregulation as an undesired irradiation response. *J Oral Pathol Med* (2013) 42:612–9. doi: 10.1111/JOP.12056

80. Ahluwalia A, Jones MK, Szabo S, Tarnawski AS. Aberrant, ectopic expression of VEGF and VEGF receptors 1 and 2 in malignant colonic epithelial cells. implications for these cells growth *via* an autocrine mechanism. *Biochem Biophys Res Commun* (2013) 437:515–20. doi: 10.1016/J.BBRC.2013.06.096

frontiers | Frontiers in Oncology

TYPE Original Research
PUBLISHED 09 May 2023
DOI 10.3389/fonc.2023.1089681

OPEN ACCESS

EDITED BY
Massimo Broggini,
Mario Negri Institute for Pharmacological Research (IRCCS), Italy

REVIEWED BY
Massimo Moro,
National Cancer Institute Foundation (IRCCS), Italy
Satoshi Yoda,
Tango Therapeutics, United States

*CORRESPONDENCE
Michael Linnebacher
michael.linnebacher@med.uni-rostock.de

†Deceased

RECEIVED 04 November 2022
ACCEPTED 12 April 2023
PUBLISHED 09 May 2023

CITATION
Andus I, Prall F, Linnebacher M and Linnebacher CS (2023) Establishment, characterization, and drug screening of low-passage patient individual non-small cell lung cancer *in vitro* models including the rare pleomorphic subentity. *Front. Oncol.* 13:1089681. doi: 10.3389/fonc.2023.1089681

Establishment, characterization, and drug screening of low-passage patient individual non-small cell lung cancer *in vitro* models including the rare pleomorphic subentity

Ingo Andus[1], Friedrich Prall[2], Michael Linnebacher[3]* and Christina S. Linnebacher[1†]

[1]Patient Models for Precision Medicine, Department of General Surgery, University Medical Center Rostock, Rostock, Germany, [2]Institute of Pathology, University Medical Center Rostock, Rostock, Germany, [3]Molecular Oncology and Immunotherapy, Department of General Surgery, University Medical Center Rostock, Rostock, Germany

Introduction: For pre-clinical drug development and precision oncology research, robust cancer cell models are essential. Patient-derived models in low passages retain more genetic and phenotypic characteristics of their original tumors than conventional cancer cell lines. Subentity, individual genetics, and heterogeneity greatly influence drug sensitivity and clinical outcome.

Materials and methods: Here, we report on the establishment and characterization of three patient-derived cell lines (PDCs) of different subentities of non-small cell lung cancer (NSCLC): adeno-, squamous cell, and pleomorphic carcinoma. The in-depth characterization of our PDCs included phenotype, proliferation, surface protein expression, invasion, and migration behavior as well as whole-exome and RNA sequencing. Additionally, *in vitro* drug sensitivity towards standard-of-care chemotherapeutic regimens was evaluated.

Results: The pathological and molecular properties of the patients' tumors were preserved in the PDC models HROLu22, HROLu55, and HROBML01. All cell lines expressed HLA I, while none were positive for HLA II. The epithelial cell marker CD326 and the lung tumor markers CCDC59, LYPD3, and DSG3 were also detected. The most frequently mutated genes included TP53, MXRA5, MUC16, and MUC19. Among the most overexpressed genes in tumor cells compared to normal tissue were the transcription factors HOXB9, SIM2, ZIC5, SP8, TFAP2A, FOXE1, HOXB13, and SALL4; the cancer testis antigen CT83; and the cytokine IL23A. The most downregulated genes on the RNA level encode the long non-coding RNA LANCL1-AS1, LINC00670, BANCR, and LOC100652999; the regulator of angiogenesis ANGPT4; the signaling molecules PLA2G1B and RS1; and the immune modulator SFTPD. Furthermore, neither pre-existing therapy resistances nor drug antagonistic effects could be observed.

Conclusion: In summary, we successfully established three novel NSCLC PDC models from an adeno-, a squamous cell, and a pleomorphic carcinoma. Of note, NSCLC cell models of the pleomorphic subentity are very rare. The detailed characterization including molecular, morphological, and drug-sensitivity profiling makes these models valuable pre-clinical tools for drug development applications and research on precision cancer therapy. The pleomorphic model additionally enables research on a functional and cell-based level of this rare NCSLC subentity.

KEYWORDS

patient-derived cell lines (PDC), lung tumors, non-small cell lung cancer (NSCLC), *in vitro* therapy response, patient-individual tumor models

1 Introduction

According to the SEER database (https://seer.cancer.gov/csr/), lung and bronchus cancer ranks third within the category of common cancer types. The estimated number of new cases in 2022 in the US is 236,740, and the estimate for deaths is 130,180 accordingly. Thus, lung tumors account for 12% of all new cancer cases and 21% of all cancer deaths. The 5-year survival rate was 22.9% in the years 2012–2018. However, this large tumor entity is composed of a variety of subentities. In 2021, the updated "WHO Classification of Lung Tumors" was published (1). The principal components for classification remain morphology, supported by immunohistochemistry, followed by molecular techniques.

Many of the subentities are well studied, thanks to a large number and variety of available tumor models. These include small cell lung cancer and the most frequent non-small cell lung cancer (NSCLC) types: squamous cell carcinoma, adenocarcinoma, and large cell carcinoma. Pleomorphic carcinomas in contrast account for less than 1% of lung tumors (2). Published numbers go as low as 0.1% of all NSCLC (3), and to date, very few primary cell models are described in literature (4).

The goal of precision oncology is to offer highly effective treatment by an individualized therapy approach subsequent to comprehensive molecular, cellular, and functional analyses of the tumors. This approach is rapidly developing and has, especially for the molecular assessments, entered the mainstream of clinical practice. Functional analyses, however, require vital cells or better patient tumor models (5). Thus, in the era of precision oncology, patient tumor models are indispensable. Fittingly, the number and variety of patient-derived tumor models are ever growing. Currently, the most favored types for patient individual models are patient-derived cell lines (PDCs), patient-derived xenografts (PDXs), and patient-derived organoids (PDOs). The popularity of these models largely depends on level of complexity, required handling skillfulness, establishment success, and, especially in academia, costs.

Historically, the oldest models are cell lines. In 1951, the HeLa cell line was established from a patient with cervical cancer and thus became the first patient-derived tumor cell line (6). Since then, countless PDCs for most tumor entities have followed (5, 7–9). Only one decade later, in the 1960s, *in vivo* models followed suit. Engrafting tumor pieces to generate PDX models is a rather recent development (8, 10–12). The seminal description of the PDO culturing process by Clevers' lab in the early 2000s (13–15) has revolutionized the patient-derived tumor modeling techniques.

However, as advanced as the organoid modeling system is, this model type bares a series of pitfalls or disadvantages, especially for academic research: the level of required skillfulness is much greater than for adherent cell lines, high(er)-throughput screening without elaborate equipment is barely feasible, and, last but not least, time and cost efficiency of adherent cell lines surpass organoids by far. Also, adherent cell lines, especially PDCs, possess a high level of predictability and utility in pre-clinical tumor therapy assessments (7). Thus, we here report on the establishment and characterization of three novel NSCLC PDC models: one model derived from an adenocarcinoma, one established from the brain metastasis of a squamous cell carcinoma, and the third PDC is of the very rare pleomorphic subentity. Finally, all PDC models underwent extensive morphological, molecular, and drug response assessments.

2 Materials and methods

2.1 Cell line establishment

Cell lines were established as previously published (8). Briefly, small pieces of the resection specimen, not required for diagnostic analyses, were received fresh from surgery. Single-cell suspensions were prepared by mechanic dissection of the tissue. The suspension was passed through a 100-µm cell strainer and washed with PBS. The cell pellet was resuspended in culture medium as described (8) and seeded in collagen-coated six-well plates. Continually growing cells were passaged and stocked regularly. Cells were routinely checked for absence of mycoplasma contamination.

The names of the cell lines consist of the following information: pseudonymized patient ID containing information on place of material collection (HRO = Hanse City of Rostock) and tumor entity/organ of origin (Lu = lung tumor, BML = brain metastasis of

a primary lung tumor). Passage numbers are given for all experiments.

All processes involving patients and patient-derived material were approved by the ethics committee of the University Medical Center Rostock (UMR): A 2019-0187. General guidelines for working with patient material were followed; this included obtaining written consent for each patient in advance.

2.2 Cell culture

Cells were cultured in standard cell culture flasks using DMEM/F12 medium supplemented with 10% fetal calf serum (FCS) and 2 mM L-glutamine in a humidified CO_2 incubator at 37°C. All cell culture media and reagents were purchased from PAN (PAN-Biotech GmbH, Aidenbach, Germany), and all culture plates and flasks were from Sarstedt (Sarstedt AG & Co. KG, Nümbrecht, Germany).

2.3 PDC quality control

2.3.1 Mycoplasma

The absence of contaminating mycoplasma was checked on a routine basis using cell culture supernatant and the PlasmoTest™ - Mycoplasma Detection Kit (InvivoGen, San Diego, California, USA) according to the manufacturer's recommendation.

2.3.2 STR profiling

Concordance of PDCs and patient donor tissue was confirmed by short tandem repeat (STR) analysis as previously described (10). In short, DNA from PDCs and patient tissue was isolated and fragments of D5S818, D7S820, D16S539, D13S317, vWA, TPOX, THO1, CSF1PO, and Amelogenin were PCR-amplified with fluorescence-labeled primers. Subsequently, samples were size separated and analyzed by automated capillary electrophoresis (Thermo Fisher Scientific, Waltham, MA, USA).

2.4 Growth kinetics

Cells (2–5 × 10^4 cells per well) were seeded in a 24-well plate and incubated for 24 h to allow attachment. One column of the 24-well plate was washed with PBS and stained with crystal violet solution every 24 h for 7 consecutive days resulting in quadruplicates for each time point. On the last day, plates were washed three times with PBS and left to dry at room temperature. After complete drying, 100 µl/well 1% sodium dodecyl sulfate solution was added, and plates were placed on a shaker for 10 min to dissolve the crystal violet. Absorbance measurements at 590 nm were performed using a Tecan Infinite 200 Pro (Tecan Group AG, Männedorf, Switzerland) plate reader. Measurements were normalized to the first time point measurement, and doubling time was calculated with GraphPad Prism 9.4.1 using the exponential growth equation for nonlinear regression.

2.5 Flow cytometry

Cells were harvested, washed, and resuspended in PBS, resulting in a concentration of 2 × 10^5 cells/100 µl. The antibodies (1 µg per antibody and tube containing 100 µl of cell suspension) were added and incubated at 4°C for 30 min in the dark (for detailed information on antibodies, see Table 1). For measurement of stainings with anti-EGFR and -PD-L1 antibodies, cells were incubated with 1 µg cetuximab and durvalumab, respectively. For fluorescent detection, the primary antibodies were stained using an FITC-labeled anti-human IgG secondary antibody. Following antibody incubation, cells were washed three times with PBS and resuspended in 200 µl of PBS for measurement with a BD FACS Calibur (Becton, Dickinson & Co., Franklin Lakes, USA) device. Data analysis was done using FCSalyzer 0.9.22-alpha software.

2.6 Chemotherapy

Cells were seeded on a 96-well plate (1–2 × 10^4 cells per well) in 150 µl/well standard medium and incubated for 24 h to facilitate

TABLE 1 Antibodies used for flow cytometry.

Antigen	Conjugate	Manufacturer	Catalog no.
CD26	PE	eBioscience/Thermo Fisher Scientific Inc., Waltham, USA	12-0269-42
HLA I	APC	ImmunoTools GmbH, Friesoythe, Germany	21159036
HLA II	FITC	ImmunoTools GmbH	21279983
CD 326	APC	Miltenyi Biotec B.V. & Co. KG, Bergisch Gladbach, Germany	130091254
CD 90	FITC	Dianova GmbH, Hamburg, Germany	DIA120
LYPD3	APC	Sino Biological Europe GmbH, Düsseldorf, Germany	11836-H08H
DSG3	FITC	Cusabio, Houston, USA	CSB-PA007205YC01HU
CD27	FITC	ImmunoTools GmbH	21270273
Cetuximab (EGFR)	FITC	Merck KGaA, Darmstadt, Germany	Erbitux®
Durvalumab (PDL1)	FITC	AstraZeneca PLC, Cambridge, UK	Imfinzi®
human IgG	FITC	Bethyl Laboratories, Inc., Montgomery, USA	800-338-9579

attachment. The chemotherapeutics were added to the wells in 50 µl of standard medium yielding the desired final concentrations. For every single agent tested, detailed information can be found in Supplementary Data 1 (Supplementary Table 1). After a 72-h incubation period, a second treatment cycle was initiated by the removal of old medium and the addition of new medium and chemotherapeutics. Plates were incubated for an additional 72 h. After a total of 144 h of treatment, cells were washed with PBS and stained with 50 µl/well crystal violet solution for 20 min. The crystal violet solution was then removed, and plates were washed three times with PBS. After complete drying at room temperature, 100 µl/well 1% sodium dodecyl sulfate solution was added, and plates were placed on a shaker for at least 10 min to dissolve the crystal violet. Absorbance measurements at 590 nm were performed using a Tecan Infinite 200 Pro plate reader and normalized viability was calculated in relation to untreated control samples using the following formula:

$$\text{normalized viability} = \frac{\text{OD[sample]} - \text{OD[blank]}}{\text{OD[living control]} - \text{OD[blank]}}$$

2.6.1 Determination of single-agent IC_{50} value

Cells were seeded in triplicate on a 96-well plate and chemotherapy testing was performed as described above. IC_{50} values were calculated using the nonlinear regression function with a four-parameter variable slope and automatic outliner elimination with Q = 1% of GraphPad Prism 9.4.1. We repeated this for each substance at least three times independently, but with adapted concentrations at times.

2.7 Drug combinations and identification of additive, synergistic, or antagonistic effects

Same as for the single-agent testing, cells were seeded in a 96-well plate in standard medium. One row was used as blank control (cells incubated with PBS instead of standard medium, thus leading to cell death by starvation) and one row was used as living control (≙ untreated cells), leaving two 6 × 6 dose response matrices for drug sensitivity testing. We tested drug combinations that are typically used in clinical practice, by combining a platinum-based drug (cisplatin and carboplatin) with etoposide, vinorelbine, and paclitaxel, resulting in six paired combinations (for detailed information, please refer to Supplementary Data 2 (Supplementary Table 2). Each dose–response pair experiment was repeated at least three times. Chemotherapy was performed as described above. Data obtained from the spectrometer were annotated, and normalized viability was calculated using in-house software. Synergy was calculated using the bayesynergy R package (16) and RStudio. This uses a probabilistic approach based on the Bliss independence model. The bayesynergy R package essentially describes drug interaction by comparing the zero-interaction model to the observed data using differences in normalized volume under the surface [VUS(Δ)], resulting in measures that can be directly used as percentage points of efficacy gained or lost. Values are calculated separately for antagonism VUS(Δ+) and synergism VUS (Δ−). The final synergy score is calculated by dividing VUS(Δ−) by its standard deviation (see formula below).

$$\text{Synergy Score} = \frac{\text{mean}(\text{VUS}(\Delta -))}{\text{SD}(\text{VUS}(\Delta -))}$$

2.8 Colony formation

Single-cell suspension was seeded at 100 cells/well in quadruplicate in a 24-well plate in 2 ml of standard medium. Outgrowing colonies were photo documented using a Primo Vert microscope and Axiocam USB camera (Zeiss, Jena, Germany).

2.9 Spheroid formation

After preparing a single-cell suspension, cells were seeded at 1,000 cells/well in duplicate in a cell-repellant six-well plate (Greiner AG Kremsmünster, Austria) in 5 ml of spheroid medium (CLS, Eppelheim, Germany) coated with 0.4% base agar and 0.35% top agar. Formation of spheres was checked daily and the final outcome (outgrowth or no outgrowth) was scored as positive or negative at day 14.

2.10 Invasion and migration

Cells were incubated in FCS-free standard medium for at least 24 h and then cells were harvested and a cell suspension of 1×10^3 cells/µl was prepared in FCS-free standard medium. A 24-well plate with TC inserts (Greiner) was prepared and 500 µl of the cell suspension (≙ 5×10^5 cells) was added to each insert. For the invasion assay, inserts were coated with Matrigel® Basement Membrane Matrix (Corning Inc., Corning, New York, USA) prior to the addition of the cell suspension. Then, 750 µl of 10% FCS containing medium was added to the lower wells. After incubation for 72 h at 37°C and 5% CO_2, the medium was removed, and inserts were washed twice with PBS. Finally, 1 ml of 0.2% crystal violet solution was added to each insert for cell staining. After 15 min of incubation, removal of the staining solution, and three washing steps with PBS, the non-invasive cells on the upper side of the insert were scraped off with a cotton swab. The addition of 0.75 ml of 1% SDS solution and 15 min incubation on a shaker led to solvation of crystal violet. The inserts were removed, the plate was placed in the Tecan reader, and absorbance was measured (measurement: 570 nm; reference: 620 nm). Measurements were normalized to the HROC24 cell line (17). For data analysis, again, the GraphPad Prism software was used.

2.11 Wound healing assay

Cells were seeded on six-well plates and allowed to grow until full confluency was reached. After starving cells for 24 h with FCS-free standard medium, a scratch was performed using a standard

200-µl pipette tip. Photos were taken with the Primo Vert microscope and Axiocam USB camera at different time periods to account for the different wound closure rates. For each cell line, the assay was done at least three times and the mean wound closure rate and standard deviation was calculated. Photos were analyzed using ImageJ 1.53 and wound healing size tool (18). Wound closure rate in µm/h was calculated in Microsoft Excel by finding the beginning (t_0) and end point (t_1)of the linear migration phase, calculating the difference in wound width during linear migration and dividing the difference by time in hours.

$$\text{wound closure rate} = \frac{\text{wound width } t_0(\mu\text{m}) - \text{wound width } t_1\ (\mu\text{m})}{\text{time (h)}}$$

For each cell line, the assay was done at least three times and the mean wound closure rate and standard deviation were calculated.

2.12 DNA extraction and next-generation sequencing by whole exome sequencing

2.12.1 DNA isolation

DNA from cell pellets was extracted using the Promega Wizard® Genomic DNA Purification Kit and DNA from tissue was extracted using the Precellys Tissue DNA Kit (PeqLab by VWR, Darmstadt, Germany). Successful DNA isolation was confirmed by measuring DNA concentration with Nano-Drop (Thermo Scientific™, Waltham, Massachusetts, USA).

2.12.2 DNA NGS sequencing and bioinformatic analysis

Library preparation and sequencing was done by an external facility (IKMB, Kiel, Germany). Bioinformatics were partly done on the Galaxy Europe platform (19, 20). After initial quality control with FastQC, reads were trimmed by removing adapter sequences and low-quality reads using Trimmomatic (21). BWA-MEM (22) was used for read mapping to the reference genome GRCh38 (December 2013). Mapped reads were then filtered with BAMtools (23) in order to only keep reads where both reads have mapped to the reference genome, with a minimum mapping quality of 1. Duplicate reads were removed with the RmDup function from SAMtools (24) and indels were left aligned with the leftalign utility from FreeBayes (25). For samples with matched tumor–normal pair somatic variant, calling was done with VarScan Somatic (26) by setting the estimated tumor purity to 50% for tissue samples and 100% for cell culture and normal tissue samples. The *p*-value threshold for calling variants was set to 0.99 and the *p*-value threshold for calling somatic variants was set to 0.05. The resulting variants were then filtered using vcflib (27) and bcftools view (24) to retain only variants that have passed previous filters, are marked as somatic variants by VarScan, and have a somatic *p*-value of< 0.05. For samples without matched normal tissue samples, GATK 4.2.6.1 Mutec2 (28) was used in tumor-only mode with standard settings for somatic variant calling. In order to reduce false-positive somatic calls, we used the gnomAD (29) database as the common germline variant database for Mutec2 to identify possible germline variants better. The resulting VCF files were then converted with vcf2maf (30) and annotated by the included VEP (31) function.

For mutational signature analysis, we used the maftools (32) R package. The analysis was done with all somatic mutations including introns and synonymous mutations for each of the cell lines.

For the oncoplot visualization, in order to pick 30 mutations that could be relevant, we first included genes where multiple samples have somatic mutations. All remaining mutations from the matched tumor–normal paired samples were annotated with the Catalogue of Somatic Mutation In Cancer (COSMIC) gene (33) database using OpenCRAVAT (34) and sorted by frequency reported in the database. The most frequently mutated genes were included in the final oncoplot by using maftools (32) oncoplot function.

Tumor mutational burden (TMB) calculation was done using maftools by dividing the total number of non-synonymous coding somatic mutations by the size of the human exome [30 MB (35)].

2.13 RNA extraction and NGS RNA sequencing

2.13.1 RNA isolation

Total RNA from cell lines was isolated by using the EurX RNA Purification Kit. Total RNA from tissue was extracted using the Precellys Tissue RNA Kit (PeqLab by VWR).

2.13.2 RNA NGS sequencing and bioinformatic analysis

Sequencing was done by an external facility (IKMB). After quality control with FastQC, raw reads were trimmed using Cutadapt (36) removing low-quality reads (quality cutoff = 20) and adapter content. After alignment to the reference genome hg38 with HISAT2 (37), gene expression was measured with featureCounts (38). Differential expression analysis was then done with DESeq2. The heatmap was created by including differentially expressed genes from DESeq2 with an adjusted *p*-value< 0.01 and selecting the top 20 most significantly up- and downregulated genes.

2.14 Histology

Per cell line, 5×10^6 cells were harvested by scraping, resuspended in PBS, and embedded in paraffin, and 4-µm sections were stained by applying the same SOP for diagnostic immunohistochemistry assessments. The following reagents/antibodies were used for staining: hematoxylin and eosin for H&E, clone 22C3 for PD-L1, polyclonal AE1/3 for pan-cytokeratin, and clone Ber-EP4 for Ep-CAM.

3 Results

3.1 Clinical and patient information

Three patients operated on at the UMR in the years 2009–2020 and enrolled in the BioBank Rostock (BBR) presented with either primary lung tumors or brain metastases (see Table 2). Patient HROBML01 was a male patient who presented with a metastatic lung tumor in the brain at age 67 and had no smoking habit. Patient HROLu22 was a female patient who presented with a primary tumor of the lung at age 64 and also did not smoke. Patient HROLu55 was a male patient who presented with a primary lung tumor at age 48 and was, at least at times, a heavy smoker.

Routine diagnostic procedures included histological assessment of the tumor tissue, determination of the subentity, TNM classification, and grading. The primary lung tumors were further analyzed for TTF1 and PD-L1 protein expression and an NGS Illumina focus panel assessment was performed (see Table 3, and for detailed information on the Illumina focus panel, see Supplementary Data 3). The compiled data for the tumor of patient HROLu22 reveal a primary adenocarcinoma of the lung grade 3 with no nodal or distant metastases. Tumor cells stained positive for both TTF1 and PD-L1. The detailed molecular profiling revealed a complex mutation in the EGF receptor (EGFR). Assessments of patient HROLu55's tumor revealed a rare pleomorphic cell tumor of the lung. The tumor was graded as G3/4 and distant lymph nodes had already been infiltrated with tumor cells. While the majority of tumor cells stained positive for PD-L1, no TTF1 protein could be detected. Tumor HROBML01 was classified as a brain metastasis of a primary squamous cell carcinoma of the lung. The origin of derived PDC models from the NSCLC patients was ensured by confirming matching STR profiles of the patients with respective PDCs (Table 4).

3.2 Tumor model characteristics

The cells of HROBML01 and HROLu22 grow as tumor islands, and the cells possess a morphology frequently associated with epithelial tumor (i.e., cobblestone-like) cells. The cells of HROLu55 start of as large(r) cells, which reduce their size according to the space available and finally form a 100% confluent monolayer consisting of small cells in the end. Microphotographic images of all three cell lines can be found in Figure 1.

Cell doubling times were between 3 and 5 days. The highest doubling time with 69.31 h (ranging from 57.60 h to 87.00 h; 95% CI) was calculated for HROBML01, closely followed by HROLu55 with 72.06 h (61.85 h to 86.32 h; 95% CI). The lowest proliferation was observed for HROLu22 with a doubling time surpassing 100 h: 101.6 h (91.77 h to 113.7 h; 95% CI).

3.3 Histology

Paraffin-embedded immunohistochemical assessments performed by an expert pathologist (FP) of the three cell lines (see Figure 2) confirmed in H&E overview staining that the cell line HROBML01 is most likely derived from a squamous cell type, HROLu22 from an adenocarcinoma, and HROLu55 from a pleomorphic carcinoma. Additionally, the embedded cells of HROLu55 stained positive for pan-cytokeratin and Ep-CAM as well as PD-L1, which further supports the pleomorphic subentity of the cell line HROLu55 as well.

3.4 Flow cytometry

After confirmation that the cell lines represent the subentities of the tumors they were derived from, the expression of several surface

TABLE 2 Overview of patient information.

	HROLu22	HROLu55	HROBML01
Gender	Female	Male	Male
Age at diagnosis	64 years	48 years	67 years
Diagnosis	Primary lung tumor	Primary lung tumor	Brain metastasis
Smoking habit	No	Yes	No

TABLE 3 Routine diagnostic histological and molecular pathological tumor assessment.

	HROLu22	HROLu55	HROBML01
Subentity	Adenocarcinoma	Pleomorphic tumor	Squamous cell carcinoma
Tumor classification	G3 pT2a pN0 cM0	G3/4 pT4 pN2 cM0	Not analyzed
TTF1 protein expression	Positive	Negative	Not analyzed
PD-L1 protein expression	Positive	Positive	Not analyzed
Illumina focus panel	EGFR: E746 T751delinsV-Mutation (Exon19)	No mutations detected	Not analyzed

TABLE 4 STR profiles.

		D5S818		D13S317		D7S820		D16S539		vWA		TH01		TPOX		CSF1 P0		Amelogenin
HROBML01	Tumor	12	13	10		10	11	11	12	17		7		8		12		f
	PDC	12	13	10		10	11	11	12	17		7		8		12		f
HROLu22	Normal	10	12	11	12	8	10	12	14	17	18	7	9	8		10	11	f
	Tumor	10	12	11	12	8	10	12	14	17	18	7	9	8		10	11	f
	PDC	10	12	11		8	10	12	14	17	18	7	9	8		10	11	f
HROLu55	Normal	11	12	11	15	8	11	11	13	16	18	7	9	8	11	12		m
	Tumor	11	12	11	15	8	11	11	13	16	18	7	9	8	11	12		m
	PDC	11	12	11		8	11		13	16	18	7	9	8	11	12		m

Normal: STR profile of normal lung tissue, Tumor: STR profile of NSCLC tissue, PDC: STR profile of PDC model.

markers was assessed by flow cytometry (Figure 3). All three PDCs expressed HLA I and lacked HLA II expression (data not shown). Because high levels of CD326 (Ep-CAM) were considered as a marker for the epithelial origin of cells, the absence of CD90 as a marker for fibroblast cells, and expression of proteins as a marker for lung tumors, LYPD3, DSG3, and CCD59 (39) were analyzed. All cells expressed CD326, were negative for CD90, and had varying degrees of the lung tumor markers. Additionally, the presence of the immune checkpoint protein PD-L1 and the growth receptor EGFR was analyzed. The cell lines derived from the primary lung tumors were strongly positive for PD-L1 and EGFR. The brain metastasis cell line HROBML01 only showed weak staining for both markers.

3.5 DNA sequencing

In addition to the focus panel sequencing, which was performed during routine pathological assessment for the tumors of patients HROLu22 and HROLu55, we performed whole exome sequencing (WES) analyses, comparing the cell lines with the original patient tumors for all three models. For patients HROLu22 and HROLu55, tumor adjacent normal tissue was assessed in parallel. Due to the fact that HROBML01 was derived from a brain metastasis, no normal brain tissue was available.

The mutational signature analysis of HROLu55 shows high similarity to cosmic signature 4, which is consistent with the mutational pattern caused by exposure to tobacco smoke (Figure 4). No such clear association with a mutational pattern could be observed for either HROLu22 or HROBML01 (see Figure 4). However, HROLu22 shows similarities to signatures 1, 5, and 16. Signature 1 is believed to be related to an endogenous mutational process, signature 5 is not yet associated with an underlying mechanism but is often observed in lung adenocarcinomas (40), and signature 16 does not have any described underlying mechanism so far. HROBML01 shows again the highest similarity to signature 5.

In a second step, we identified the top 30 mutated genes by the WES approach across all three tumor tissues and cell lines (see

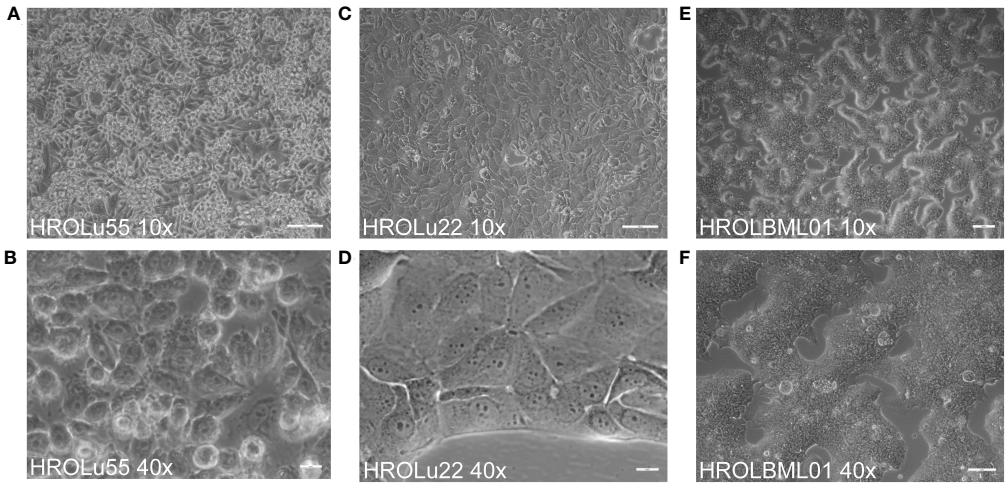

FIGURE 1
Cell morphology. Depicted are light microscopy images of the cell lines HROLu55 (left, **A**, **B**), HROLu22 (middle, **C**, **D**), and HROBML01 (right **E**, **F**) at 10-fold (top row) and 40-fold (bottom row) magnification.

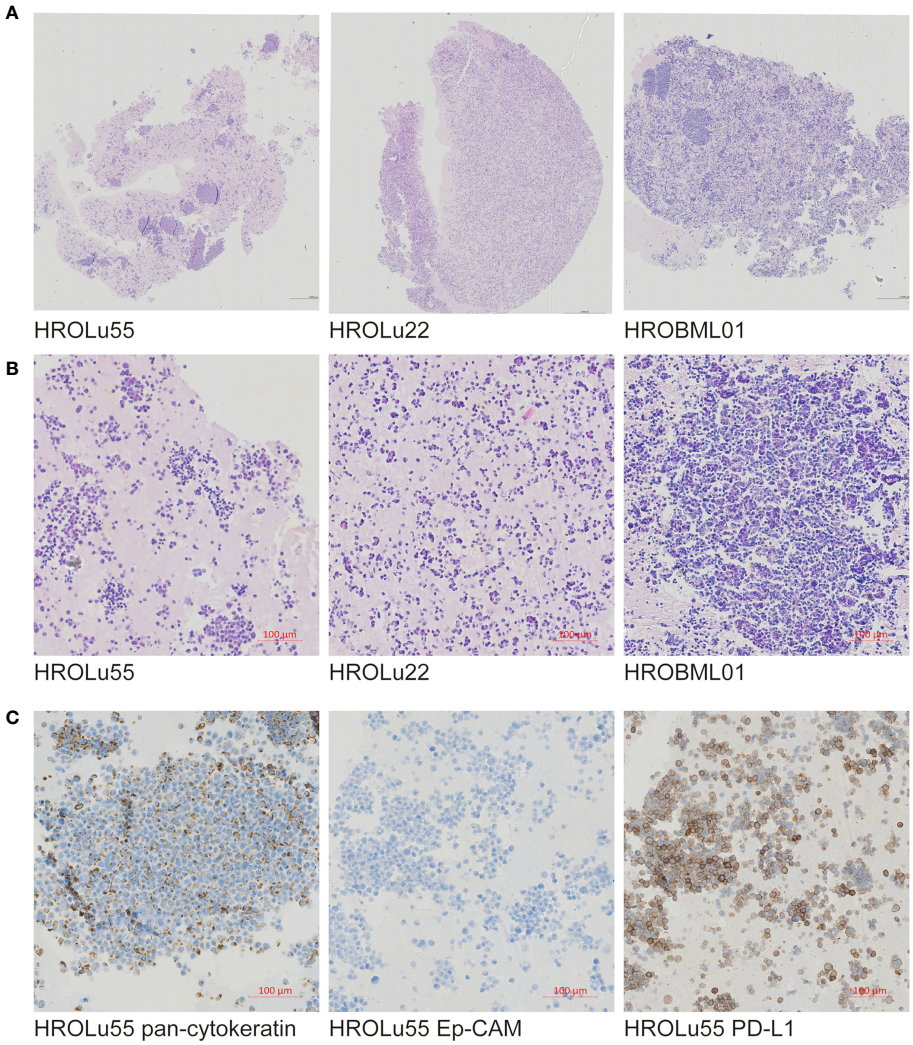

FIGURE 2
Immunohistochemistry. Presented are scans of slides from FFPE embedded cells of the cell lines HROLu22, HROLu55, and HROBML01. The top row **(A)** shows H&E overview staining for all three cell lines [HROLu55 (left), HROLu22 (middle), and HROBML01 (right)]. The middle row **(B)** shows part of the H&E staining for all three cell lines [HROLu55 (left), HROLu22 (middle), and HROBML01 (right)]. The bottom row **(C)** shows protein staining against pan-cytokeratin (left), Ep-CAM (middle), and PD-L1 (right).

Figure 5). Among these, common general cancer mutations in the genes TP53 and MUC16 (41) and lung cancer-associated mutations in the genes MXRA5 (42, 43) and MUC19 (44) could be observed. The genes MXRA5 and MUC16 were mutated in all three tumors. However, the mutation in MXRA5 could not be detected in the cell line HROBML01 and the MUC16 mutation was not detected in the cell line HROLu22. Mutations in the gene TP53 could be observed for both tumors of patients HROLu55 and HROBML01 as well as their cell line counterparts.

Finally, we calculated the TMB for all cancer samples (tissues and cell lines). The tumor tissue always had a higher TMB than the corresponding cell line (see Table 5). HROBML01 presented with the highest TMB for both tumor tissue and cell line. In total, all three tumors and cell lines have a comparably high TMB (see Figure 6).

3.6 RNA sequencing

In addition to the WES analyses, matched RNA expression levels were assessed by RNA sequencing of the same tissue piece or cell pellet, respectively. Principal component analysis (PCA) for quality control revealed clustering of the normal tissue, the tumor tissue of HROLu22 and HROLu55 with their cell line counterparts, and a third cluster of tumor tissue and cell line for HROBML01 (see Supplementary Data 4 consisting of Supplementary Figures 2, 3). Further "sample-to-sample distance" calculations revealed that the normal tissues of HROLu22 and HROLu55 are (very) close (see Supplementary Data 4). This confirms the QC assessment of the PCA.

Thus, the 20 most up- and downregulated genes on RNA expression level were identified (Figure 7). The difference in expression level of normal to tumor tissue and cell lines is at least

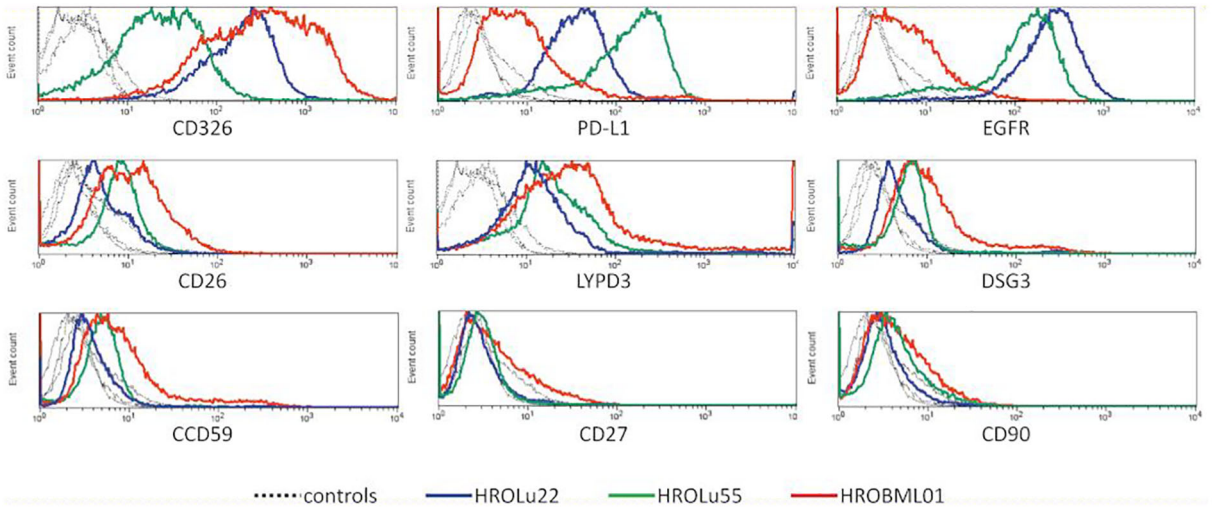

FIGURE 3
Flow cytometry. Histogram overlays of unstained controls (dotted lines for all three cell lines) and measurements for HROLu55 (green), HROLu22 (blue), and HROBML01 (red) for the epitopes CD326, PD-L1, EGFR, CD26, LYPD3, DSG3, CCD59, CD27, and CD90 are shown.

log2. Among the most overexpressed genes in tumor cells compared to normal tissue are genes coding for transcription factors (HOXB9, SIM2, ZIC5, SP8, TFAP2A, FOXE1, HOXB13, and SALL4), cancer testis antigens (CT83), and cytokines activating regulatory Th17 cells (IL23A). The most downregulated genes on the RNA level code for long non-coding RNA (lncRNA; LANCL1-AS1, LINC00670, BANCR, and LOC100652999) and proteins involved in the regulation of angiogenesis (ANGPT4), signaling cascades (PLA2G1B and RS1), and immune response (SFTPD).

3.7 Invasion, migration, and wound healing activity

A common feature of cancer cells that serves as a unit to measure the degree of aggressiveness is invasion and migration. Thus, the invasion and migration potential of the three cell lines was assessed in classical transwell assays. In comparison to the reference HROC24, the cells of cell line HROLu55 possessed a higher capacity for invasion and migration. The cells of HROLu22 and HROBML01 were comparable to the reference with regard to both invasion and migration (Table 6 and Figure 8).

These properties of higher invasion and migration capacity resulted in faster wound closure rates (Table 7 and Figure 9) for HROLu55. These cells are capable of a rapid wound closure (25.21 µm/h). Cells of HROLu22 were 8.99 µm/h slower than cells of HROLu55 but substantially faster than HROBML01. The cell line HROBML01 shows a very slow closure rate (1.23 µm/h). Unfortunately, the results for HROBML01 are inconclusive since cells tend to detach from the culture flask during or after wound infliction.

3.8 Colony and spheroid formation

Further properties associated with tumorigenicity are the capacity to form colonies starting with very few tumor cells (≈100

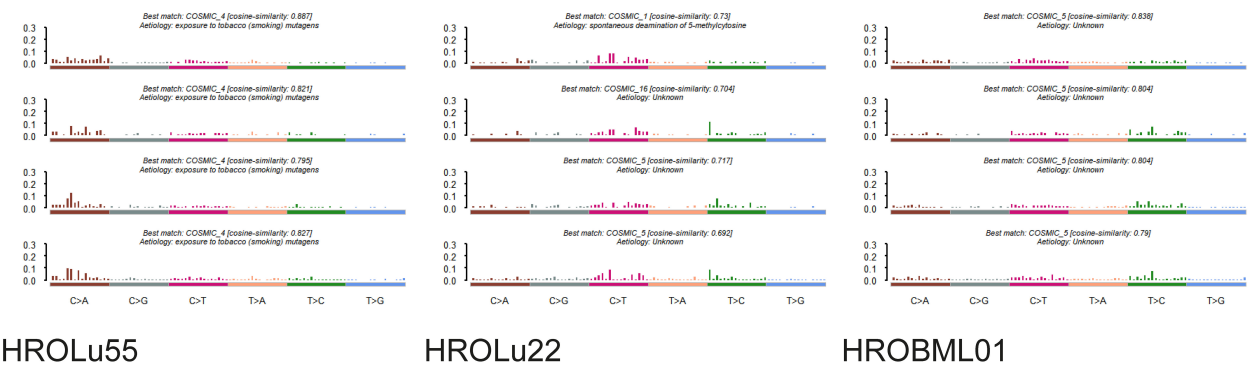

FIGURE 4
Mutational signatures. Represented are the base substitutional distributions and most probable associations according to COSMIC (https://cancer.sanger.ac.uk/signatures/) for the cell lines HROLu55 (left), HROLu22 (middle), and HROBML01 (right).

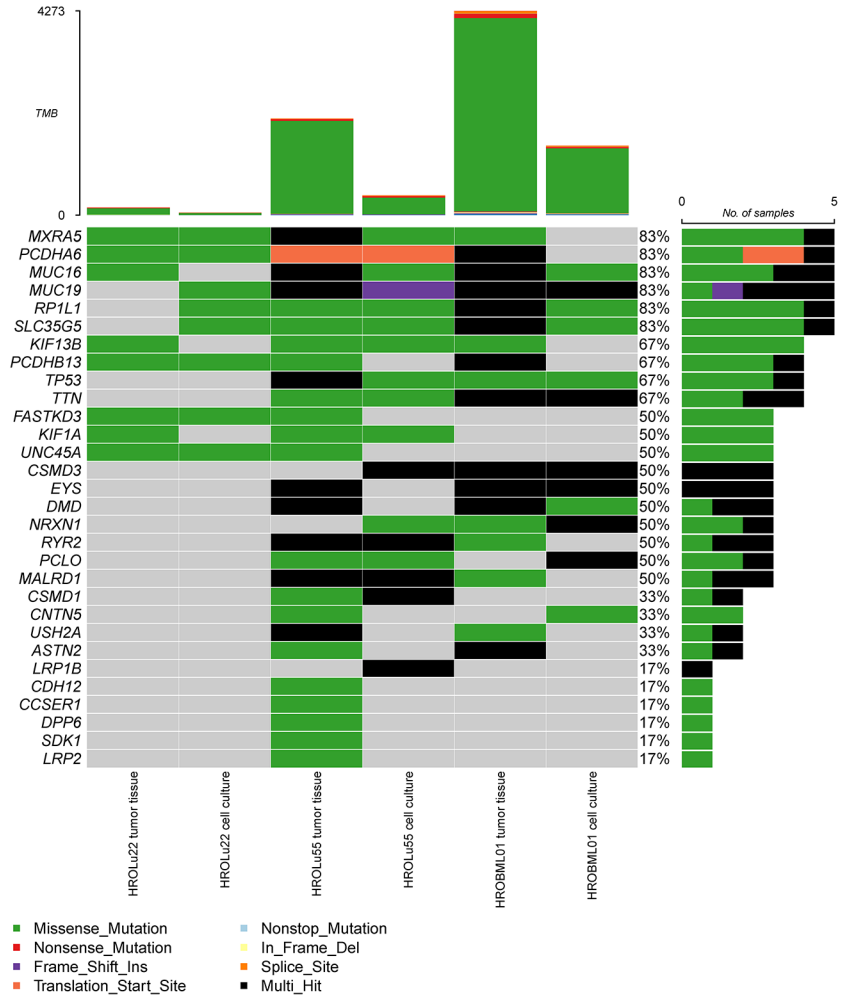

FIGURE 5
Most frequent mutations. The oncoplot shows the most frequent mutations and types across all samples for tumor tissues and cell cultures of commonly mutated genes present in the COSMIC gene database.

cells) and three-dimensional spheroids (Figure 10). Classical epithelial tumor cell colony formation was observed for HROBML01 and HROLu22. Cells of the cell line HROLu55 also grew in colony-like formations; however, these resemble more a loose accumulation of cells without direct cell-to-cell interaction.

Spheroid formation was observed after 7–10 days for all three cell lines. The earliest onset and most pronounced spheroid formation was observed for HROLu55 (data not shown).

3.9 *In vitro* drug response

Adherent 2D cell lines, especially in the NCI-60 panel, have a long-standing tradition as tools for *in vitro* response testing (45). In particular, patient-derived cell lines possess great potential for highly accurate predictability (7). Thus, response to a broad variety of therapeutics commonly administered for treatment of lung tumors was determined in dose-kinetic analyses (Figure 11).

TABLE 5 Number of somatic mutations and TMB.

Sample		Total somatic mutations	TMB (per MB)	log TMB (per MB)
HROLu22	Cell culture	52	1.73	0.23
HROLu22	Tumor tissue	160	5.33	0.72
HROLu55	Cell culture	413	13.76	1.13
HROLu55	Tumor tissue	1,454	48.46	1.68
HROBML01	Cell culture	2,025	67.50	1.82
HROBML01	Tumor tissue	4,273	142.43	2.15

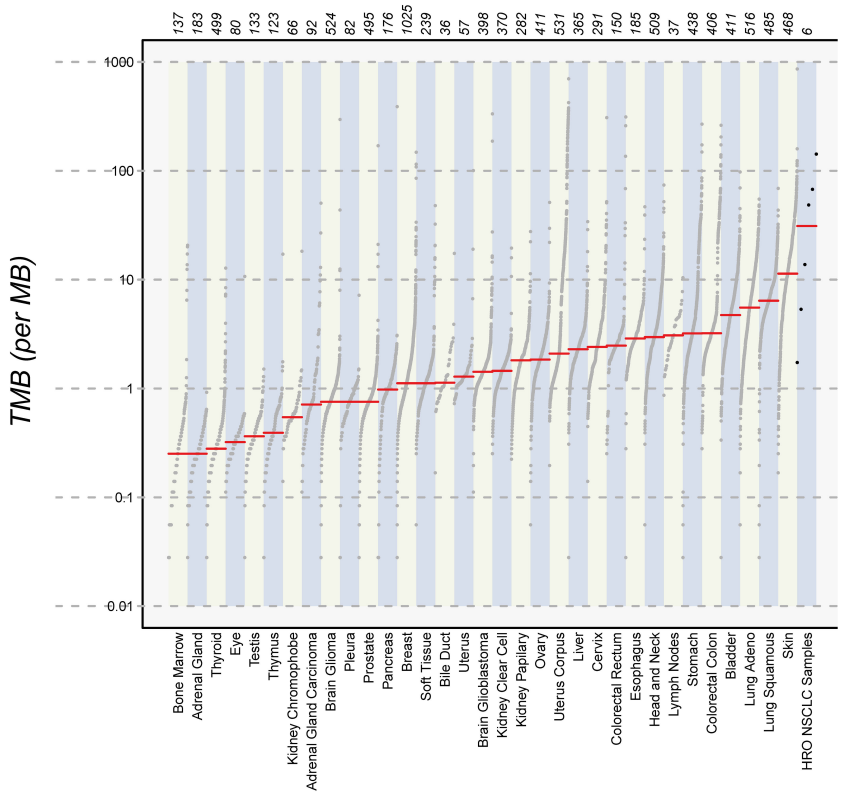

FIGURE 6
Number of mutations. The images show the extent of TMB for the HRO NSCLC samples, encompassing data from both tumor tissues and cell lines in comparison to TMB values of other cancer types recorded in the TCGA database.

All IC_{50} value calculations are in the range typically found in clinical settings (Table 8). Thus, pre-existing drug resistance for all three cell lines and tested reagents is unlikely. HROLu22 tended to be least sensitive towards treatment with cisplatin, carboplatin, and etoposide. Response to vinorelbine in HROLu22 cells plateaued over a (wide) range of concentrations until viability finally decreased to 0.

3.10 Drug combinations and additive, synergistic, or antagonistic effects

Treatment of patients with a single substance is rarely performed. Thus, clinically more relevant are drug combinations, which were tested in a so-called checkerboard assay (Figures 12, 13 and Supplementary Data 2 consisting of Supplementary Table 2 and Supplementary Figure 1). Observed interaction scores range from −9.63 (for HROBML01 and the combination of cisplatin with vinorelbine) to 10.95 (for HROLu22 and the combination carboplatin with vinorelbine). Most studies suggest a cutoff at about −10 and 10 (46–48) for calling synergy or antagonism, respectively. None of the tested combinations largely surpass these values; thus, observed effects were most likely additive. More importantly, no antagonistic effects occurred.

4 Discussion

Lung cancer is one of the most common tumor entities and accounts, especially in absolute numbers, for many cancer-related deaths, thus underlining the urgency of further research. Precision medicine is on the rise. The individualized therapy selection process and research in this context largely profit from relevant tumor models. We describe three novel PDCs with high similarity to their original tumors and good utility for research in either a basic or translational context. Of special interest is that cell line HROLu55 is derived from the rare subentity of pleomorphic lung tumors. PDC models of this rare subentity are very scarce, especially HROLu55, given the extensive characterization, including WES and RNA-seq analyses. Most importantly, all three cell lines maintained the histological and molecular characteristics of the original patient tumor counterparts.

The cell line HROLu22 represents the adenomatous type, HROBML01 represents the squamous cell type, and HROLu55 represents the pleomorphic lung cancer type. This was confirmed by an expert pathologist (FP). From the generally high level of data concordance, we conclude that these models represent the patients they are derived from very well. This is in line with what we previously already observed for models established from colorectal cancer (8) and glioblastoma (5). These models, in low passages

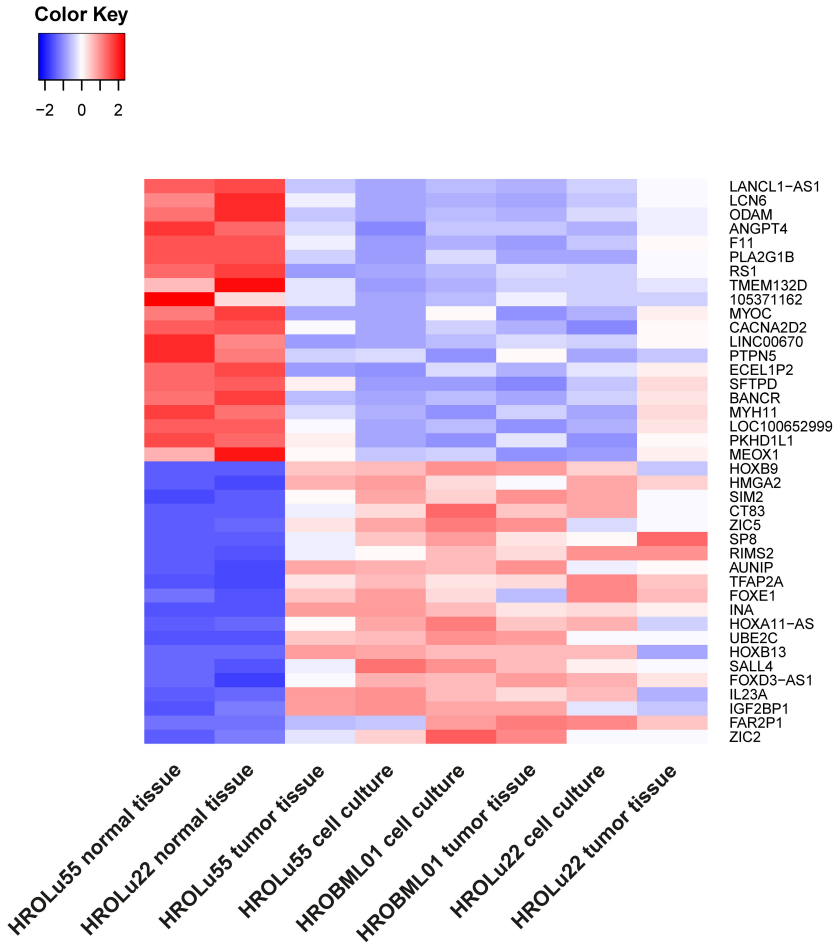

FIGURE 7
Differential RNA expression. In this graphic, the 20 most upregulated (red) and downregulated (blue) genes in tumor tissues and cell lines (on RNA level) in comparison to the corresponding normal lung tissue from the same patients with an adjusted *p*-value of< 0.01 are given.

(below passage 30), are thus very useful for general or basic research on the respective subentity, especially HROLu55 for the pleomorphic type. Of note, it was the most invasive (145.4% of control vs. 70.2% and 68.0%) and had the highest migration rate (209.2% of control vs. 90.6% and 70.0%), nearly doubling the values observed for HROBML01 and HROLu22. At the same time, it can be very useful in pre-clinical projects. HROLu55 enables scientists to study mechanisms, functional parameters, and responses of pleomorphic lung tumors. In our dose–response kinetics with drugs commonly used for treatment of lung tumors, no pre-existing resistances were identified and no antagonistic effects were observed for the drug combinations. Although not the focus of this study, we could show in previous investigations that experimentally observed responses (*in vitro* and *in vivo*) corresponded well to the actual clinical outcome of the patients (7). Furthermore, response intensity to classical platinum-based

TABLE 6 Invasion and migration.

		HROC24	HROLu55	HROLu22	HROBML01
Invasion (% cntrl)	Mean %	100.2	145.4	68.0	70.2
	Std. deviation	27.8	36.5	19.2	27.2
Migration (% cntrl)	Mean %	100.0	209.2	70.0	90.6
	Std. deviation	23.3	68.8	19.1	40.2

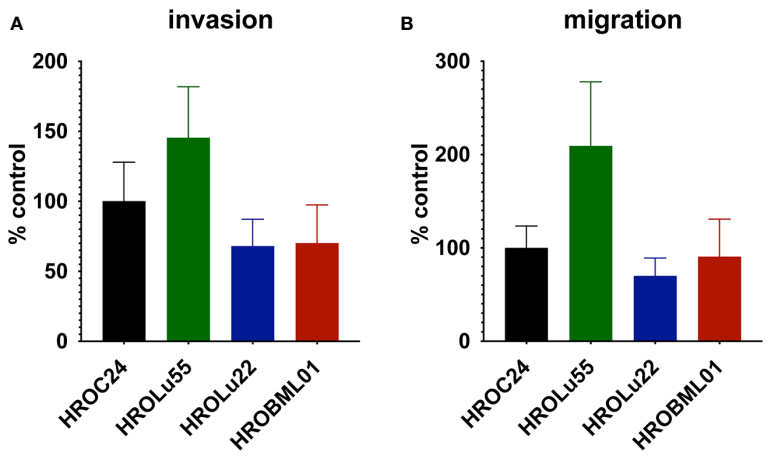

FIGURE 8
Invasion and migration. The bar graph shows the percentage of cell invasion **(A)** and cell migration **(B)** for the cell lines HROLu55 (green), HROLu22 (blue), and HROBML01 (red) in comparison to highly invasive and migration active cells HROC24 (17).

TABLE 7 Wound healing.

Closure rate (µm/h)	HROLu55	HROLu22	HROBML01
Mean	25.21	8.99	1.22
Std. deviation	10.18	2.36	0.73

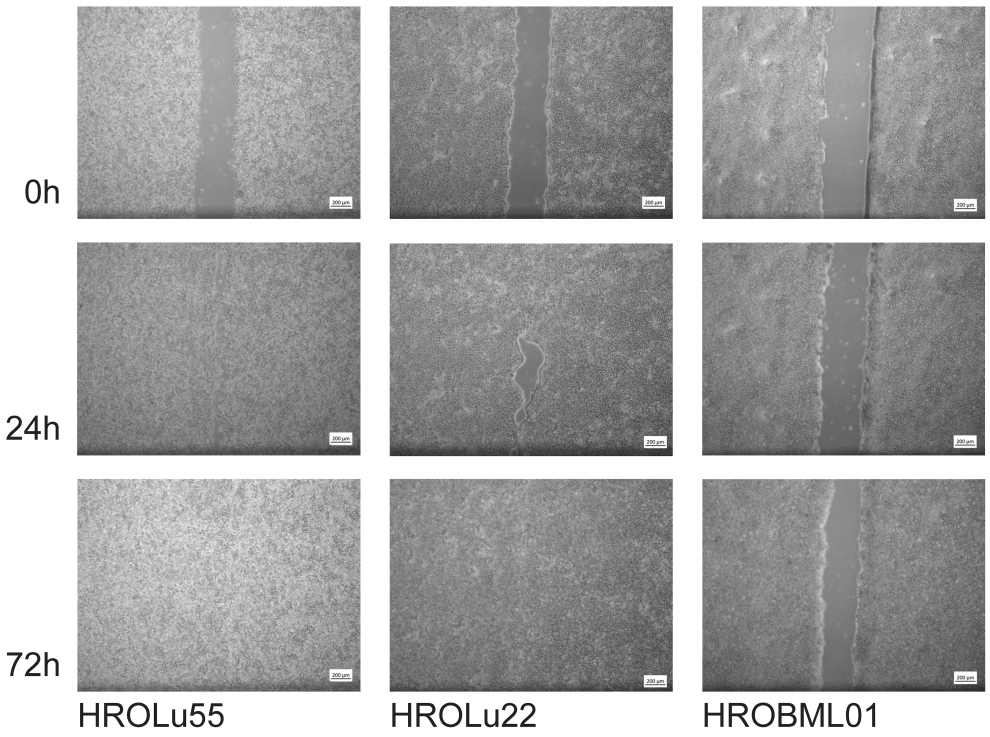

FIGURE 9
Scratch assay. Light microsopy images at 0 h, 24 h, and 72 h of scarring represent the time necessary for wound closure and thus thespeed of wound healing.

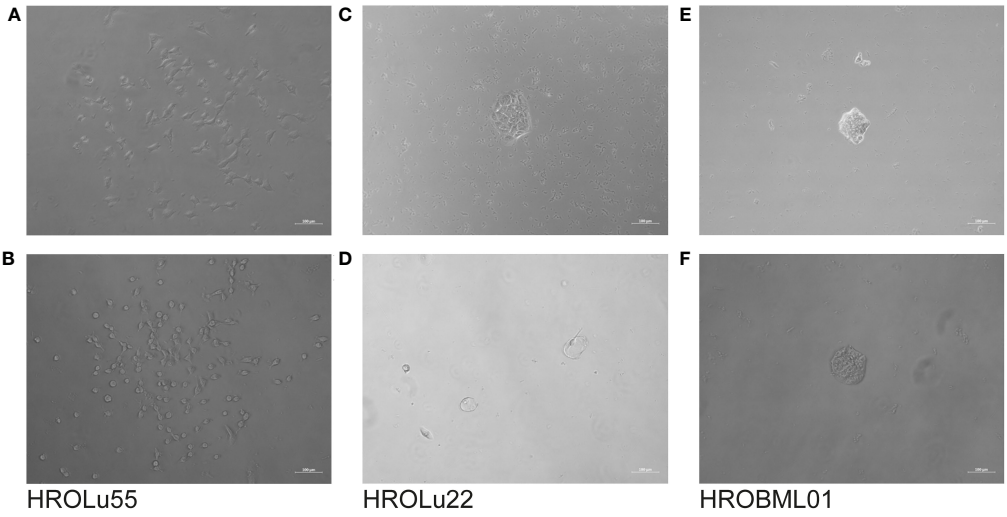

FIGURE 10
Colony formation. The light microscopy images show the progress of colony formation for the cell lines HROLu55 (left, **A, B**), HROLu22 (middle, **C, D**), and HROBML01 (right, **E, F**). The images are representative of four wells each.

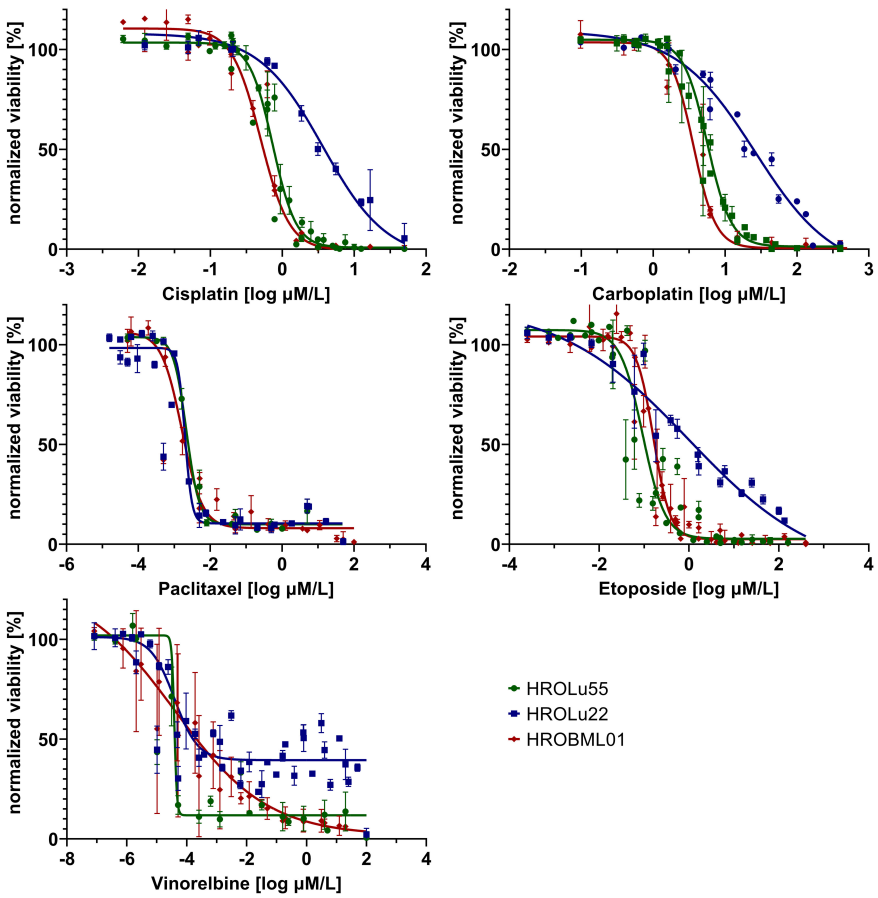

FIGURE 11
Dose response. Dose kinetic response of single-agent treatments of the cell lines HROLu55 (green), HROLu22 (blue), and HROBML01 (red) for 144 h for the agents: cisplatin, carboplatin, paclitaxel, etoposide, and vinorelbine are plotted as normalized viability with standard deviation over dose range in log µM.

TABLE 8 IC_{50} values.

IC_{50} (in µM)	HROLu55	HROLu22	HROBML01
Cisplatin	0.737	3.659	0.501
Carboplatin	5.657	26.160	3.623
Paclitaxel	2.169×10^{-3}	1.978×10^{-3}	1.632×10^{-3}
Etoposide	0.093	0.987	0.162
Vinorelbine	2.615×10^{-5}	3.596×10^{-5}	15.3×10^{-5}

chemotherapeutics of the cell lines and calculated doubling times was weakest for lowest cell proliferation. HROLu22 was least sensitive to cisplatin (IC_{50} of 3.66 vs. 0.73 and 0.50) and carboplatin (IC_{50} of 26.16 vs. 5.66 and 3.62), and at the same time, proliferation was lowest (doubling time of 101.60 h vs. 69.31 h and 72.06 h).

One corner stone of precision medicine is the integration of NGS techniques in the molecular pathological assessments (49). At the UMR, pathological examinations of NSCLC include an Illumina focus panel (for a detailed list of genes included, please see Supplementary Data 3). For our small sampling of the three NSCLC patients, we additionally performed WES analyses for the

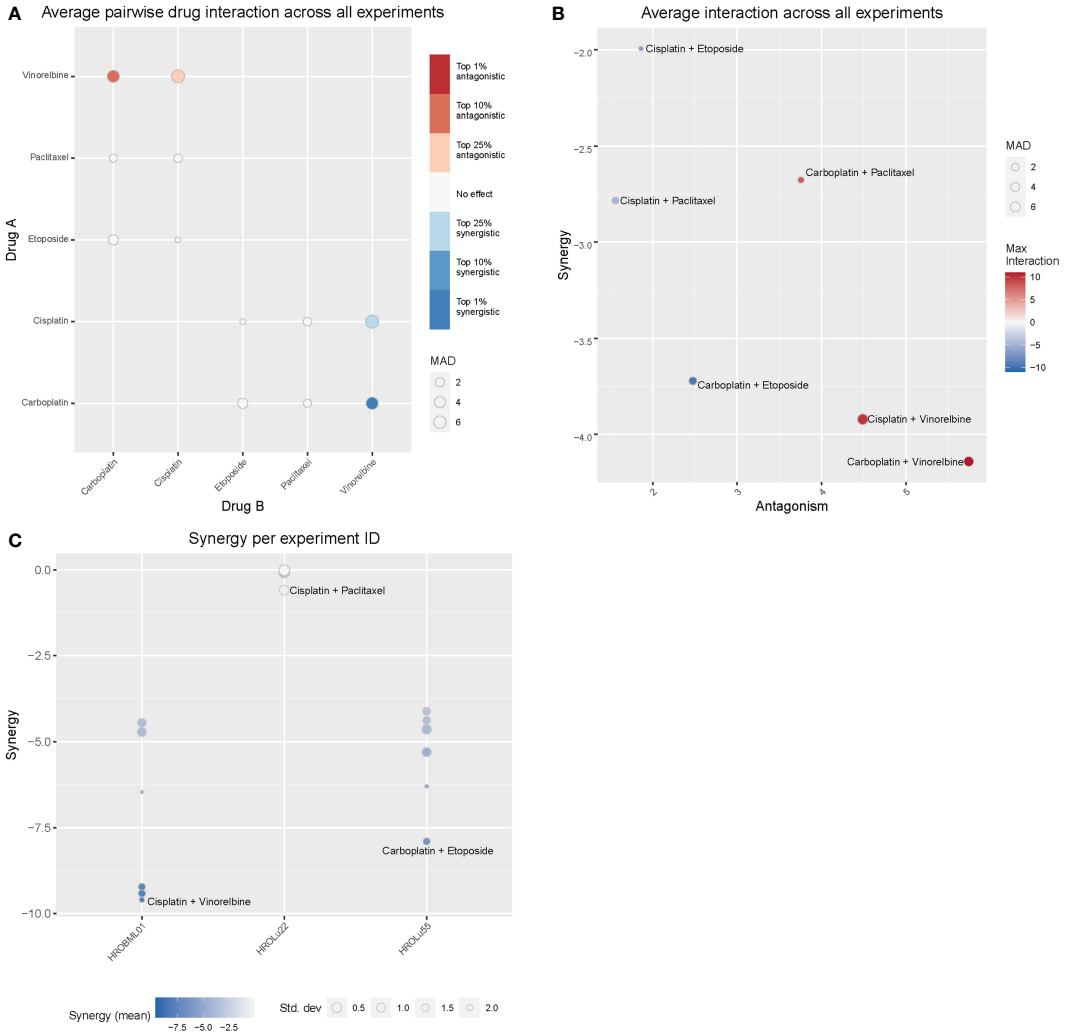

FIGURE 12
Drug combination treatments. Bliss independence-based synergy/antagonism scores are given for **(A)** the average pairwise drug interactions across all three cell lines, **(B)** the synergy/antagonism scores for each combination, and **(C)** the synergy scores observed for each cell line individually. MAD = median average deviation of scores across samples.

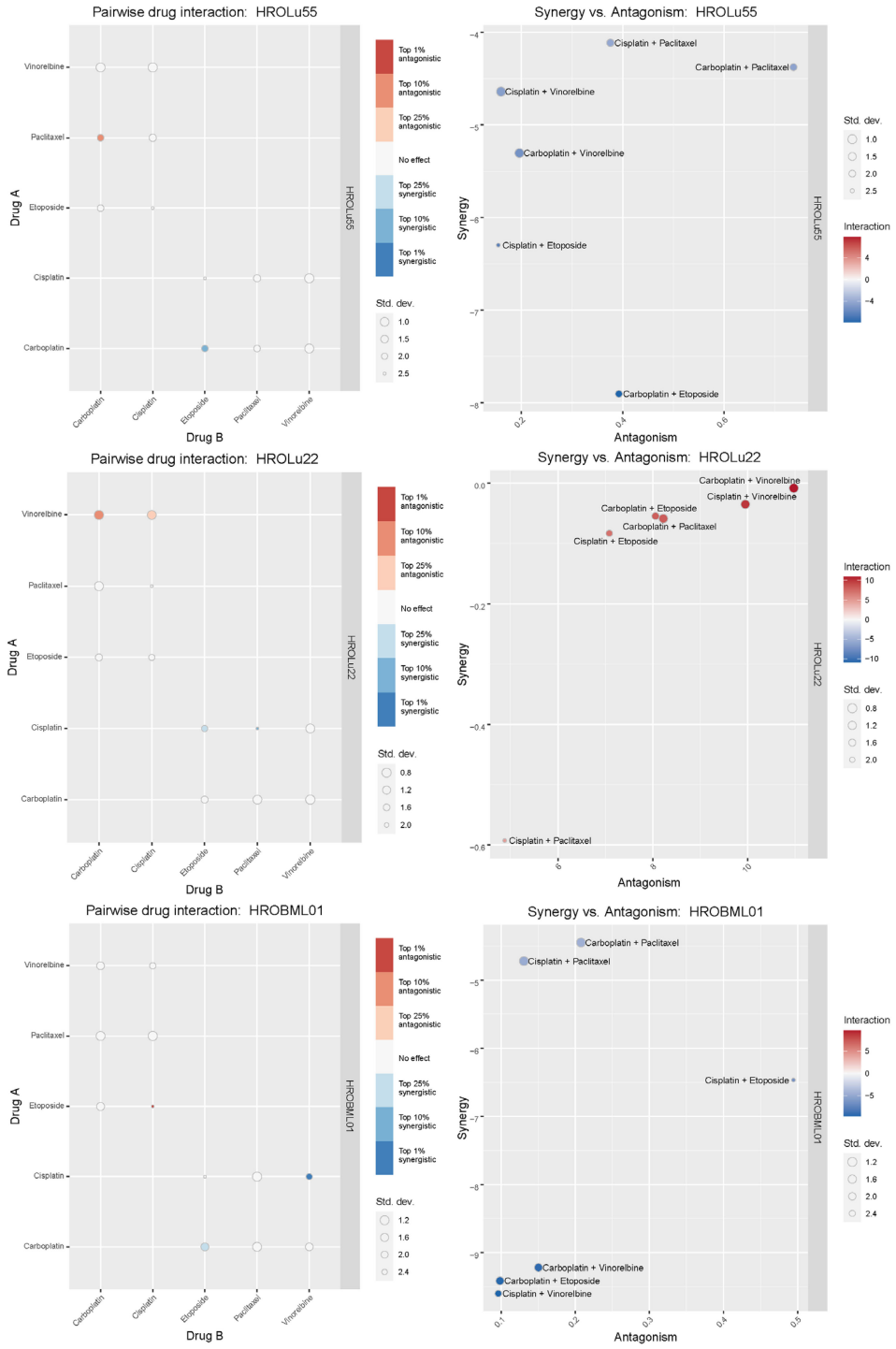

FIGURE 13
Synergistic effects of drug combinations. The Bliss independence-based synergy scores for HROLu55, HROLu22, and HROBML01 are presented in the graphic.

original tumors in comparison to the tumor tissue-derived cell lines. The surprisingly low frequency of mutations identified with the focus panel in routine diagnostics was not confirmed by the high TMB calculated for tumor tissues and PDCs of the WES results. In absolute numbers, the TMB was always higher in the tumor tissue than the corresponding PDC, which, in parts, may be explained by the PDCs consisting of a purer tumor cell population than the tumor tissue. This leads to the comparison of results obtained with 100% pure tumor cells in the PDCs with approximately 50% tumor cells in the tumor tissue. Generally, NSCLC has one of the highest overall TMB with lung adenocarcinoma and lung squamous carcinoma only surpassed by melanoma (40). The discrepancy of focus panel and WES results in our case most likely arises from the observation that most mutations detected in the tumors and PDCs

were unique to the tumor tissue and corresponding PDCs. Thus, most likely, many mutations were simply not covered by the focus panel. Also, the EGFR mutation, one of the most common mutations in NSCLC, found in pathological assessment of tumor HROLu22, is present in the WES (raw) data but was discarded in the final report for not passing the variant call quality control filter. The lack of a precisely defined standard for analyzing NGS data, at least on the research level, increases data "variance" enormously and further contributes to our observed discrepancies. Finally, tumor heterogeneity may add to the differences found for tumor tissue and corresponding PDCs since the sample used for DNA isolation and the one used for model establishment might consist of different dominant clones. Additionally, the PDCs undergo further clonal selection simply by *in vitro* culturing processes.

Among the 30 most mutated genes, we discovered familiar cancer candidates such as TP53 and MUC16 (41) and lung cancer associated mutations in the genes MXRA5 (42, 43) and MUC19 (44). The UNC45A mutation detected in the brain metastasis HROBML01 and its corresponding PDCs contributes to tumorigenesis and its expression in cancer cells correlates with proliferation and metastasis of solid tumors (50). In summary, samples of HROLu22 have the lowest numbers of total mutations, samples of HROLu55 have higher mutation rates, and samples from HROBML01 have the highest mutational burden. The TMB for HROLu22 in comparison to the other two samples is even substantially lower. The TBM ratio of approximately 1/10 (HROLu22 vs. HROLu55 and HROBML01) suggests differences in malignant development. Patient HROLu55 is fairly young (48 years) and has a history of (high) nicotine consumption. The tumor of patient HROBML01 metastasized to the brain; thus, accumulation of additional mutations in order to successfully complete the metastasizing process can be assumed. In contrast, the tumor of patient HROLu22 developed without a history of smoking from the fairly old female patient. The cause for mutagenic transformation in this case can only be guessed at. These results are thus not unexpected; they should, however, be interpreted with caution since the lack of normal tissue for HROBML01 may impede correct distinction between germline and somatic mutations.

When it comes to the discovery of new biomarkers and therapeutic targets for personalized medicine, large-scale studies that include multi-omics data are needed, which, in turn, can link genomic and transcriptomic data to phenotypical data. In our small sampling, we observed transcriptomic changes that are currently researched: HOXB9 (Homeobox protein Hox-B9) is the most overexpressed gene across all three of our cell lines. It is often overexpressed in lung cancer, and some studies suggest that overexpression could be linked to promoting invasive properties (51) and small studies in mice have shown a promotion of brain metastases (52). Across the three cell lines tested in this study, HROBML01 has the highest expression followed by HROLu55. A second example of overexpression in our samples is the high-mobility group AT-hook 2 (HMGA2) gene. Overexpression of this gene can be seen in multiple cancer entities and seems to be associated with poor prognosis in lung cancer (53–55). Kita-Kyushu Lung Cancer Antigen-1 (KK-LC-1/CT83) is also highly expressed in our sampling, and the overexpression of this gene was proposed as a target for new precision immunotherapy approaches (56, 57). The observed high expression of ZIC5 is in line with experiments by Sun et al. who could show that ZIC5 is highly upregulated in NSCLC tumor tissues (58), and they suggested that ZIC5 may act as an oncogene by influencing CCNB1 and CDK1 complex expression. Finally ZIC5 is recommended as a biomarker and potential therapeutic target for NSCLC patients (58). Scientists Yang and Liu described that overexpression of BANCR suppresses cell viability and invasion and promotes apoptosis in NSCLC cells *in vitro* and *in vivo* (59). Our observed downregulation thus is, most likely, one of the oncogenic mechanisms exerted by our cell lines. Potential therapeutic effects by BANCR inhibition could be assessed by taking advantage of our PDCs.

In conclusion, we report on three PDCs established from different subentities of NSCLC including the very rare pleomorphic cell type. All PDCs retained morphological, molecular, and genetic properties of their patient tumor tissue originals. Additionally, these PDCs are a 100% pure tumor cell population and, thus, allow, besides functional analyses and response testing *in vitro*, for an easier linking of NGS results to phenotypical tumor characteristics.

Data availability statement

The raw WES and RNA-Seq Datasets presented in this article are not readily available because they contain confidential information about individuals protected under the General Data Protection Regulation. Requests to access the datasets should be directed to the corresponding author.

Ethics statement

The studies involving human participants were reviewed and approved by the ethics committee of the University Medical Center Rostock. The patients/participants provided their written informed consent to participate in this study.

Author contributions

As principal investigator, CL designed the project and supervised experimental execution as well as data analysis. The experiments were performed and obtained data were analyzed by IA. Histological assessments were performed and analyzed by the expert pathologist FP. ML was involved in all project discussions and helped with problem solving. The manuscript was drafted by CL and IA, all authors read and approved the final version of the manuscript.

In Memoriam

This paper is dedicated to the memory of Christina S. Linnebacher, who passed away unexpectedly while this paper was

being peer-reviewed. CSL was an esteemed author whose contributions to the field of oncology research were invaluable. CSL was widely known for her expertise in patient-derived cancer models, which provided crucial insights into the development and treatment of cancer. Her pioneering research will continue to have a profound impact on the scientific community, and she will be deeply missed by her family, friends, and colleagues.

Conflict of interest

The authors declare that the research was conducted in the absence of any commercial or financial relationships that could be construed as a potential conflict of interest.

Publisher's note

Supplementary material

The Supplementary Material for this article can be found online at: https://www.frontiersin.org/articles/10.3389/fonc.2023.1089681/full#supplementary-material

References

1. Nicholson AG, Tsao MS, Beasley MB, Borczuk AC, Brambilla E, Cooper WA, et al. The 2021 WHO classification of lung tumors: impact of advances since 2015. *J Thorac Oncol* (2022) 17:362–87. doi: 10.1016/j.jtho.2021.11.003

2. Travis WD, Brambilla E, Nicholson AG, Yatabe Y, Austin JH, Beasley MB, et al. The 2015 world health organization classification of lung tumors: impact of genetic, clinical and radiologic advances since the 2004 classification. *J Thorac Oncol* (2015) 10:1243–60. doi: 10.1097/JTO.0000000000000630

3. Lui NS. Commentary: pleomorphic carcinoma: an aggressive type of non-small cell lung cancer that should be treated like the others. *J Thorac Cardiovasc Surg* (2019) 158:592–3. doi: 10.1016/j.jtcvs.2019.04.074

4. So T, Takenoyama M, Ichiki Y, Mizukami M, So T, Hanagiri T, et al. A different pattern of cytotoxic T lymphocyte recognition against primary and metastatic tumor cells in a patient with nonsmall cell lung carcinoma. *Cancer* (2005) 103:200–8. doi: 10.1002/cncr.20782

5. Mullins CS, Schneider B, Stockhammer F, Krohn M, Classen CF, Linnebacher M. Establishment and characterization of primary glioblastoma cell lines from fresh and frozen material: a detailed comparison. *PloS One* (2013) 8:e71070. doi: 10.1371/journal.pone.0071070

6. BJ C. HeLa (for Henrietta lacks). *Science* (1974) 184:1268. doi: 10.1126/science.184.4143.1268

7. Wagner S, Beger NT, Matschos S, Szymanski A, Przybylla R, Bürtin F, et al. Tumour-derived cell lines and their potential for therapy prediction in patients with metastatic colorectal cancer. *Cancers* (2021) 13:4717. doi: 10.3390/cancers13184717

8. Mullins CS, Micheel B, Matschos S, Leuchter M, Bürtin F, Krohn M, et al. Integrated biobanking and tumor model establishment of human colorectal carcinoma provides excellent tools for preclinical research. *Cancers* (2019) 11:1520. doi: 10.3390/cancers11101520

9. Palechor-Ceron N, Krawczyk E, Dakic A, Simic V, Yuan H, Blancato J, et al. Conditional reprogramming for patient-derived cancer models and next-generation living biobanks. *Cells* (2019) 8:1327. doi: 10.3390/cells8111327

10. Matschos S, Bürtin F, Kdimati S, Radefeldt M, Krake S, Prall F, et al. The HROC-Xenobank-A high quality assured PDX biobank of 100 individual colorectal cancer models. *Cancers* (2021) 13:5882. doi: 10.3390/cancers13235882

11. William D, Mullins CS, Schneider B, Orthmann A, Lamp N, Krohn M, et al. Optimized creation of glioblastoma patient derived xenografts for use in preclinical studies. *J Transl Med* (2017) 15:27. doi: 10.1186/s12967-017-1128-5

12. Pillai SPS, Uthamanthil RK. PDX models: history and development: chapter 1. In: *Patient derived tumor xenograft models*. Elsevier (2017). p. 1–12. doi: 10.1016/B978-0-12-804010-2.00001-1

13. van de Wetering M, Francies HE, Francis JM, Bounova G, Iorio F, Pronk A, et al. Prospective derivation of a living organoid biobank of colorectal cancer patients. *Cell* (2015) 161:933–45. doi: 10.1016/j.cell.2015.03.053

14. Sato T, Stange DE, Ferrante M, Vries RG, van Es JH, van den Brink S, et al. Long-term expansion of epithelial organoids from human colon, adenoma, adenocarcinoma, and barrett's epithelium. *Gastroenterology* (2011) 141:1762–72. doi: 10.1053/j.gastro.2011.07.050

15. Sato T, Vries RG, Snippert HJ, van de Wetering M, Barker N, Stange DE, et al. Single Lgr5 stem cells build crypt-villus structures *in vitro* without a mesenchymal niche. *Nature* (2009) 459:262–5. doi: 10.1038/nature07935

16. Rønneberg L, Cremaschi A, Hanes R, Enserink JM, Zucknick M. Bayesynergy: flexible Bayesian modelling of synergistic interaction effects in *in vitro* drug combination experiments. *Brief Bioinform* (2021) 22:1–12. doi: 10.1093/bib/bbab251

17. Maletzki C, Stier S, Gruenert U, Gock M, Ostwald C, Prall F, et al. Establishment, characterization and chemosensitivity of three mismatch repair deficient cell lines from sporadic and inherited colorectal carcinomas. *PloS One* (2012) 7:e52485. doi: 10.1371/journal.pone.0052485

18. Suarez-Arnedo A, Torres Figueroa F, Clavijo C, Arbeláez P, Cruz JC, Muñoz-Camargo C. An image J plugin for the high throughput image analysis of in vitro scratch wound healing assays. *PloS One* (2020) 15:e0232565. doi: 10.1371/journal.pone.0232565

19. The Galaxy Community. The galaxy platform for accessible, reproducible and collaborative biomedical analyses: 2022 update. *Nucleic Acids Res* (2022) 50(12):8999. doi: 10.1093/nar/gkac247

20. Maier W. *Identification of somatic and germline variants from tumor and normal sample pairs (Galaxy training materials)* (2021). Available at: https://training.galaxyproject.org/training-material/topics/variant-analysis/tutorials/somatic-variants/tutorial.html.

21. Bolger AM, Lohse M, Usadel B. Trimmomatic: a flexible trimmer for illumina sequence data. *Bioinformatics* (2014) 30:2114–20. doi: 10.1093/bioinformatics/btu170

22. Li H, Durbin R. Fast and accurate short read alignment with burrows-wheeler transform. *Bioinformatics* (2009) 25:1754–60. doi: 10.1093/bioinformatics/btp324

23. Barnett DW, Garrison EK, Quinlan AR, Strömberg MP, Marth GT. BamTools: a c++ API and toolkit for analyzing and managing BAM files. *Bioinformatics* (2011) 27:1691–2. doi: 10.1093/bioinformatics/btr174

24. Li H, Handsaker B, Wysoker A, Fennell T, Ruan J, Homer N, et al. The sequence Alignment/Map format and SAMtools. *Bioinformatics* (2009) 25:2078–9. doi: 10.1093/bioinformatics/btp352

25. Garrison E, Marth G. Haplotype-based variant detection from short-read sequencing. *arXiv* (2012), 1–9. doi: 10.48550/arXiv.1207.3907

26. Koboldt DC, Zhang Q, Larson DE, Shen D, McLellan MD, Lin L, et al. VarScan 2: somatic mutation and copy number alteration discovery in cancer by exome sequencing. *Genome Res* (2012) 22:568–76. doi: 10.1101/gr.129684.111

27. Garrison E, Kronenberg ZN, Dawson ET, Pedersen BS, Prins P. A spectrum of free software tools for processing the VCF variant call format: vcflib, bio-vcf, cyvcf2, hts-nim and slivar. *PloS Comput Biol* (2022) 18:e1009123. doi: 10.1371/journal.pcbi.1009123

28. McKenna A, Hanna M, Banks E, Sivachenko A, Cibulskis K, Kernytsky A, et al. The genome analysis toolkit: a MapReduce framework for analyzing next-generation DNA sequencing data. *Genome Res* (2010) 20:1297–303. doi: 10.1101/gr.107524.110

29. Karczewski KJ, Francioli LC, Tiao G, Cummings BB, Alföldi J, Wang Q, et al. The mutational constraint spectrum quantified from variation in 141,456 humans. *Nature* (2020) 581:434–43. doi: 10.1038/s41586-020-2308-7

30. Kandoth C. (2020). vcf2maf v1.6.21. Zenodo.

31. McLaren W, Gil L, Hunt SE, Riat HS, Ritchie GR, Thormann A, et al. The ensembl variant effect predictor. *Genome Biol* (2016) 17:122. doi: 10.1186/s13059-016-0974-4

32. Mayakonda A, Lin D-C, Assenov Y, Plass C, Koeffler HP. Maftools: efficient and comprehensive analysis of somatic variants in cancer. *Genome Res* (2018) 28:1747–56. doi: 10.1101/gr.239244.118

33. Forbes SA, Beare D, Boutselakis H, Bamford S, Bindal N, Tate J, et al. COSMIC: somatic cancer genetics at high-resolution. *Nucleic Acids Res* (2017) 45:D777–83. doi: 10.1093/nar/gkw1121

34. Pagel KA, Kim R, Moad K, Busby B, Zheng L, Tokheim C, et al. Integrated informatics analysis of cancer-related variants. *JCO Clin Cancer Inform* (2020) 4:310–7. doi: 10.1200/CCI.19.00132

35. Ng SB, Turner EH, Robertson PD, Flygare SD, Bigham AW, Lee C, et al. Targeted capture and massively parallel sequencing of 12 human exomes. *Nature* (2009) 461:272–6. doi: 10.1038/nature08250

36. Martin M. Cutadapt removes adapter sequences from high-throughput sequencing reads. *EMBnet J* (2011) 17:10. doi: 10.14806/ej.17.1.200

37. Kim D, Langmead B, Salzberg SL. HISAT: a fast spliced aligner with low memory requirements. *Nat Methods* (2015) 12:357–60. doi: 10.1038/nmeth.3317

38. Liao Y, Smyth GK, Shi W. featureCounts: an efficient general purpose program for assigning sequence reads to genomic features. *Bioinformatics* (2014) 30:923–30. doi: 10.1093/bioinformatics/btt656

39. Cohen AS, Khalil FK, Welsh EA, Schabath MB, Enkemann SA, Davis A, et al. Cell-surface marker discovery for lung cancer. *Oncotarget* (2017) 8:113373–402. doi: 10.18632/oncotarget.23009

40. Alexandrov LB, Nik-Zainal S, Wedge DC, Aparicio SA, Behjati S, Biankin AV, et al. Signatures of mutational processes in human cancer. *Nature* (2013) 500:415–21. doi: 10.1038/nature12477

41. Zhang L, Han X, Shi Y. Association of MUC16 mutation with response to immune checkpoint inhibitors in solid tumors. *JAMA Netw Open* (2020) 3:e2013201. doi: 10.1001/jamanetworkopen.2020.13201

42. Xiong D, Li G, Li K, Xu Q, Pan Z, Ding F, et al. Exome sequencing identifies MXRA5 as a novel cancer gene frequently mutated in non–small cell lung carcinoma from Chinese patients. *Carcinogenesis* (2012) 33:1797–805. doi: 10.1093/carcin/bgs210

43. Sun J-Z, Zhang J-H, Li J-B, Yuan F, Tong L-Q, Wang X-Y, et al. MXRA5 is a novel immune-related biomarker that predicts poor prognosis in glioma. *Dis Markers* (2021) 2021:6680883. doi: 10.1155/2021/6680883

44. Zhou L, Huang L, Xu Q, Lv Y, Wang Z, Zhan P, et al. Association of MUC19 mutation with clinical benefits of anti-PD-1 inhibitors in non-small cell lung cancer. *Front Oncol* (2021) 11:596542. doi: 10.3389/fonc.2021.596542

45. Roschke AV, Tonon G, Gehlhaus KS, McTyre N, Bussey KJ, Lababidi S, et al. Karyotypic complexity of the NCI-60 drug-screening panel. *Cancer Res* (2003) 63:8634–47.

46. Pogacar Z, Groot K, Jochems F, Dos Santos Dias M, Mulero-Sánchez A, Morris B, et al. Genetic and compound screens uncover factors modulating cancer cell response to indisulam. *Life Sci Alliance* (2022) 5(9):e20210348-1. doi: 10.26508/lsa.202101348

47. Ianevski A, Giri AK, Aittokallio T. *SynergyFinder - user documentation* . Available at: https://synergyfinder.fimm.fi/synergy/synfin_docs/.

48. Ianevski A, Giri AK, Aittokallio T. SynergyFinder 2.0: visual analytics of multi-drug combination synergies. *Nucleic Acids Res* (2020) 48:W488–93. doi: 10.1093/nar/gkaa216

49. Dotolo S, Esposito Abate R, Roma C, Guido D, Preziosi A, Tropea B, et al. Bioinformatics: from NGS data to biological complexity in variant detection and oncological clinical practice. *Biomedicines* (2022) 10:2074. doi: 10.3390/biomedicines10092074

50. Eisa NH, Jilani Y, Kainth K, Redd P, Lu S, Bougrine O, et al. The co-chaperone UNC45A is essential for the expression of mitotic kinase NEK7 and tumorigenesis. *J Biol Chem* (2019) 294:5246–60. doi: 10.1074/jbc.RA118.006597

51. Hayashida T, Takahashi F, Chiba N, Brachtel E, Takahashi M, Godin-Heymann N, et al. HOXB9, a gene overexpressed in breast cancer, promotes tumorigenicity and lung metastasis. *Proc Natl Acad Sci U.S.A.* (2010) 107:1100–5. doi: 10.1073/pnas.0912710107

52. Zheng H, Li C, Li Z, Zhu K, Bao H, Xiong J, et al. HOXB9 enhances the ability of lung cancer cells to penetrate the blood-brain barrier. *Aging (Albany NY)* (2020) 13:4999–5019. doi: 10.18632/aging.202324

53. Gao X, Dai M, Li Q, Wang Z, Lu Y, Song Z. HMGA2 regulates lung cancer proliferation and metastasis. *Thorac Cancer* (2017) 8:501–10. doi: 10.1111/1759-7714.12476

54. Mansoori B, Mohammadi A, Ditzel HJ, Duijf PH, Khaze V, Gjerstorff MF, et al. HMGA2 as a critical regulator in cancer development. *Genes (Basel)* (2021) 12:269. doi: 10.3390/genes12020269

55. Meyer B, Loeschke S, Schultze A, Weigel T, Sandkamp M, Goldmann T, et al. HMGA2 overexpression in non-small cell lung cancer. *Mol Carcinog* (2007) 46:503–11. doi: 10.1002/mc.20235

56. Bai R, Yuan C. Kita-Kyushu lung cancer antigen-1 (KK-LC-1): a promising cancer testis antigen. *Aging Dis* (2022) 13:1267–77. doi: 10.14336/AD.2021.1207

57. Marcinkowski B, Stevanović S, Helman SR, Norberg SM, Serna C, Jin B, et al. Cancer targeting by TCR gene-engineered T cells directed against kita-Kyushu lung cancer antigen-1. *J Immunother Cancer* (2019) 7:229. doi: 10.1186/s40425-019-0678-x

58. Sun Q, Shi R, Wang X, Li D, Wu H, Ren B. Overexpression of ZIC5 promotes proliferation in non-small cell lung cancer. *Biochem Biophys Res Commun* (2016) 479:502–9. doi: 10.1016/j.bbrc.2016.09.098

59. Yang L, Liu G. lncRNA BANCR suppresses cell viability and invasion and promotes apoptosis in non-small-cell lung cancer cells *in vitro* and in vivo. *Cancer Manag Res* (2019) 11:3565–74. doi: 10.2147/CMAR.S194848

frontiers | Frontiers in Oncology

TYPE Original Research
PUBLISHED 26 May 2023
DOI 10.3389/fonc.2023.1130048

OPEN ACCESS

EDITED BY
W. Nathaniel Brennen,
Johns Hopkins University, United States

REVIEWED BY
Mitchell Lawrence,
Monash University, Australia
Giorgia Zadra,
National Research Council (CNR), Italy

*CORRESPONDENCE
Claire Béraud
claire.beraud@urosphere.com

†These authors have contributed equally to the work

RECEIVED 22 December 2022
ACCEPTED 25 April 2023
PUBLISHED 26 May 2023

CITATION
Béraud C, Bidan N, Lassalle M, Lang H, Lindner V, Krucker C, Masliah-Planchon J, Potiron E, Lluel P, Massfelder T, Allory Y and Misseri Y (2023) A new tumorgraft panel to accelerate precision medicine in prostate cancer. *Front. Oncol.* 13:1130048. doi: 10.3389/fonc.2023.1130048

A new tumorgraft panel to accelerate precision medicine in prostate cancer

Claire Béraud[1*†], Nadege Bidan[1†], Myriam Lassalle[1], Hervé Lang[2], Véronique Lindner[3], Clémentine Krucker[4,5], Julien Masliah-Planchon[6], Eric Potiron[7], Philippe Lluel[1], Thierry Massfelder[8], Yves Allory[4,5] and Yolande Misseri[1]

[1]Urosphere, Toulouse, France, [2]Department of Urology, Nouvel Hopital Civil, Strasbourg, France, [3]Department of Pathology, Hôpital de Hautepierre, Strasbourg, France, [4]Department of Pathology, Institut Curie, Paris, France, [5]Institut Curie, PSL Research University, CNRS, Equipe Labellisée Ligue Contre le Cancer, Paris, France, [6]Department of Genetics, Institut Curie, Paris, France, [7]Department of Urology, Clinique Urologique, Nantes, France, [8]UMR 1260 INSERM/Université de Strasbourg, Regenerative Nanomedicine (RNM), FMTS, Centre de Recherche en Biomédecine de Strasbourg, Strasbourg, France

Background: Despite the significant advances in the management of advanced prostate cancer (PCa), metastatic PCa is currently considered incurable. For further investigations in precision treatment, the development of preclinical models representing the complex prostate tumor heterogeneity are mandatory. Accordingly, we aimed to establish a resource of patient-derived xenograft (PDX) models that exemplify each phase of this multistage disease for accurate and rapid evaluation of candidate therapies.

Methods: Fresh tumor samples along with normal corresponding tissues were obtained directly from patients at surgery. To ensure that the established models reproduce the main features of patient's tumor, both PDX tumors at multiple passages and patient's primary tumors, were processed for histological characteristics. STR profile analyses were also performed to confirm patient identity. Finally, the responses of the PDX models to androgen deprivation, PARP inhibitors and chemotherapy were also evaluated.

Results: In this study, we described the development and characterization of 5 new PDX models of PCa. Within this collection, hormone-naïve, androgen-sensitive and castration-resistant (CRPC) primary tumors as well as prostate carcinoma with neuroendocrine differentiation (CRPC-NE) were represented. Interestingly, the comprehensive genomic characterization of the models identified recurrent cancer driver alterations in androgen signaling, DNA repair and PI3K, among others. Results were supported by expression patterns highlighting new potential targets among gene drivers and the metabolic pathway. In addition, *in vivo* results showed heterogeneity of response to androgen deprivation and chemotherapy, like the responses of patients to these treatments. Importantly, the neuroendocrine model has been shown to be responsive to PARP inhibitor.

Conclusion: We have developed a biobank of 5 PDX models from hormone-naïve, androgen-sensitive to CRPC primary tumors and CRPC-NE. Increased copy-number alterations and accumulation of mutations within cancer driver genes as well as the metabolism shift are consistent with the increased resistance mechanisms to treatment. The pharmacological characterization suggested that the CRPC-NE could benefit from the PARP inhibitor treatment. Given the difficulties in developing such models, this relevant panel of PDX models of PCa will provide the scientific community with an additional resource for the further development of PDAC research.

KEYWORDS

PDX, prostate cancer, neuroendocine tumors, genomic characteristics, PARP inhibitor, metabolism, tumor heterogeneity, castrate-resistant prostate cancer (CRPC)

Introduction

Prostate Cancer (PCa) is the second most frequent cancer in men and the fifth leading cause of cancer death, with an incidence rate of 14.3% (1). Different molecular subtypes of PCa have been determined according to their genomic alterations. They have been classified from localized early stage to advanced/metastatic tumors. Localized/primary PCa generally demonstrate few genomic alterations and are sensitive to androgen deprivation therapies (ADT). Castrate-Resistant Prostate Cancers (CRPC) and metastatic prostate cancers mPCa demonstrate an increase in number and severity of genomic alterations and become insensitive to ADT (2). Locally confined PCa can be treated effectively, as first line therapy either, by surgical resection or radiation therapy (3). For non-organ-confined tumors, the standard treatment is medical or surgical castration. Androgen Receptor (AR) overexpression is a main driver of progression to CRPC for most patients (4). Androgen deprivation is an effective therapeutic strategy, widely used in clinical practice. These treatments include potent new generation hormonotherapy such as abiraterone acetate and enzalutamide, that has improved patient outcomes. However, most patients relapse within 2-3 years after initial response and the disease progresses to CRPC (5–7). Metastatic CRPC (mCRPC) is a heterogeneous disease with poor outcomes. In up to 30% of patients, tumors harbour deleterious aberrations in the genes involved in repairing DNA damage. Pembrolizumab, an immune checkpoint inhibitor, demonstrates a high response rate in tumors with mismatch repair deficiency regardless of primary site (8), leading to tissue-agnostic FDA approval, including for PCa (9). Pharmacological inhibitors of poly (ADP-ribose) polymerase (PARP) have been recently approved for use in patients with advanced PCa harbouring homologous recombination defects, including *BRCA1* and *BRCA2* alterations (10). These mutations are not present in all PCa, and despite these new clinical developments, PCa remains incurable when these therapies fail. Further new preclinical models and studies should thus explore mechanisms of resistance based on clinical data and available experimental models.

Patient-Derived-Xenografts (PDXs) are based on the direct implantation of fresh cancer tissue specimens from individual patients into immunodeficient mice or rats (11). Their development has been optimized over time concomitantly with the discovery of and advancements in immunocompromised animal models. PDXs have the advantage of retaining the cellular heterogeneity, architecture, and molecular characteristics of the parental tumor (12, 13). Numerous studies have cited them as the best predictors of response compared to cell line-derived xenografts which, with time, lose heterogeneity and tend to be clonally selected (14). Efforts to develop xenografts from PCa have been made since the 1970's with varying degrees of success due to the particular difficulty of developing these models. Reported take rate in established PDX from PCa range between 0 to 33%, while longest spanning latencies vary from 60 to 1,147 days (15). Despite these drawbacks and due to the heterogeneity of the disease and complexity, PCa PDX models remain the most accurate preclinical models for biological studies, drug development and personalized medicine strategies (16–20).

As a result of a 10-year research project in urological PDX models, the present work describes a prostate PDX biobank of 5 established PDXs models (out of 240 PCa originally implanted). The developed panel of PDXs recapitulate the progression of the disease from androgen sensitive to CRPC, including CRPC with neuroendocrine (NE) features. In addition, from the same patient that became AR-resistant after treatment, an AR-sensitive adenocarcinoma and an AR-resistant neuroendocrine PDXs have been derived and characterized.

Materials and methods

Acquisition of PCa patient tissues

Between 2010 and 2019, thanks to a close collaboration with the Pathology and Urology departments of Strasbourg Hospital and the urological Clinic of Nantes, we collected 240 PCa samples from 237 patients. Human prostate cancer tissues were retrieved directly after

surgery (radical prostatectomy, palliative TURP, surgical resection of node metastasis, pelvectomy) or biopsy (Supplementary Table 1). The use of patients' tissues complied with a protocol approved by both the "Comité de Protection des Personnes Est IV" and the "Comité de Protection des Personnes Sud-Ouest et Outre-mer" (Approval numbers: *DC-2010-1193 and DC-2019-3565, respectively*). Patients enrolled in the study provided written informed consent allowing the use of discarded surgical samples for research purposes. In addition, relevant clinical information was recorded from the patients' data including age, PSA levels, treatments, and treatment responses when available. Tumor regions within surgical specimens were identified by uro-pathologists. Once collected, prostate tissues were transported in an appropriate solution (Custodiol). Prostate tissues were implanted within 24 hr from collection.

Animals

Four to five-week-old immuno-deficient mice including athymic Swiss-Nude (Crl : NU(Ico)-*Foxn1nu*), NMRI-Nude (Rj : NMRI-Foxn1$^{nu/nu}$) or Shrn (NOD.Cg-Prkdc^{scid}Hr^{hr}/NCrHsd) male mice were purchased from Charles River Laboratories (L'Abresle, France), Envigo (Gannat, France) or Janvier Labs (Saint-Berthevin, France). Animals were handled under specific pathogen-free conditions. Their care and housing complied with guidelines set out in French animal welfare regulations referred as the European Community Council Directive 2010/63/UE. All tumorgraft studies were reviewed by CEE-35 and CEE-122 (ethical committees for the protection of animals used for scientific purposes) and approved by the French Ministry for National Education, Higher Education and Research under the numbers *APAFIS#2949-2015113017594629v5* and *APAFIS#14811-2018042316405732v6*. The animal facility was maintained under standardized conditions: artificial 12h light-dark cycles between 7:00 a.m. and 7 p.m., ambient temperature of 22 ± 2°C and relative humidity maintained at 55 ± 10%.

Development of PDX models

The establishment of PDX models was carried out as previously described (21, 22). Briefly, different adult male immunodeficient mice strains were used for tissue implantation: Swiss-nude mice (G266, C901 and C1022) and Shrn mice (PCU-012 and PCU-018) for primo-implantations. At the time of grafting, mice were intact (G266, C901 and C1022) or had androgen supplementation (PCU-012 and PCU-018) (Supplementary Table 2). Grafts were implanted into the interscapular fat pad and monitored weekly for tumor growth for up to 9 months post-implantation for initial growth. When xenografted tumors reached ~1500 mm^3, they were sequentially passaged into new mice under the same conditions and using the same protocol as the original implants. A PDX model was defined as established when stable growth over at least three passages and regrowth after a freeze-thaw cycle could be observed. At each mouse-to-mouse passage, representative samples were cryopreserved, snap-frozen in liquid nitrogen and/or FFPE processed.

Immunohistochemistry

FFPE patient tumors and PDX blocks were sectioned and slides immunostained with the following antibodies: cytokeratin cocktail AE1AE3 (M3515, Agilent), androgen receptor (M3562, Agilent), hCD45 (IR751, Agilent), PSA (M0750, Agilent), ERG (AC-0105, Clinisciences), NKX3.1 (AC-0314, Clinisciences), PTEN (ab228466, Abcam), Ki67 (M7240, Agilent), P53 (GA616, Agilent), synaptophysin (IR660, Agilent) and chromogranin A (M0869, Agilent). After heat antigen retrieval as specified by provider, experiments were performed using Dako Omnis Instrument, EnVision FLEX, High pH kit for revelation (GV800, Agilent) for hCD45, cytokeratin cocktail AE1AE3, PSA, P53, synaptophysin, ERG and chromogranin A, or Leica Bond III Instrument for androgen receptor, Ki67 and NKX3.1 and on Autostainer 480S instrument for PTEN. The conditions are described in the Supplementary Table 3.

Tissue processing for transcriptomic and genomic studies

Frozen samples were processed on ice. For DNA and RNA isolation, patient and PDX tumor fragments were processed using Qiagen Allprep DNA/RNA mini kit according to manufacturer's instructions. Briefly, DNA and RNA were simultaneously extracted and purified. Nucleic acid yield and quality was assessed by NanoDrop spectophotometer ND8000 and RNA quality was further evaluated using Agilent 2100 Bioanalyzer.

Short tandem repeat signature

The identity of each PDX was periodically authenticated by profiling STRs. Patient tumors and corresponding PDX DNA samples were subjected to STR using PowerPlex® 16 HS System (Promega, ref DC2101) that amplifies 16 STR loci and the amelogenin gender-determining marker, according to manufacturer's instructions. PDXs passed authenticity when >80% match in alleles was obtained. PCR products were separated by capillary electrophoresis on ABI prism 3500 and results were analyzed using GeneMapper software (v5).

Whole exome sequencing

DNA extracted from tumorgraft tissues with adequate quality was subjected to WES by IntegraGen (France, Evry).

Sequence alignment and variant calling

Base calling was conducted using the Real-Time Analysis software sequence pipeline (2.7.7) from Illumina with default parameters. In order to remove contaminating mouse reads, raw reads were classified depending on their species of origin (graft or host) using the Xenome tool (23). Raw human reads were aligned on

human hg38 genome using the Burrows-Wheeler Aligner (BWA) tool (24). Duplicated reads were removed using Sambamba (25). Variant calling of somatic single nucleotide variants (SNVs) and small insertions/deletions (indels) was performed using the Broad Institute's GATK MuTect2 tool (2.0, –max_alt_alleles_in_normal_count=2; –max_alt_allele_in_normal_fraction=0.04) against a Panel of Normals (PON) comprising 107 normal samples sequenced by IntegraGen following the same protocol (26). Ensembl' Variant Effect Predictor (27) (VEP, release 95) was used to annotate variants with respect to functional consequences (type of mutation and prediction of the functional impact on the protein by SIFT 5.2.2 and PolyPhen 2.2.2) and frequencies in public (dbSNP151, 1000 Genomes phase 3, gnomAD 17-02-28, COSMIC v86) and in-house databases.

Somatic variant analysis

To keep/detect only reliable somatic variants, the following post-filtering steps were applied:

-QSS score ≥ 20 (the average base quality of variant bases)

-coverage ≥10 in the tumor

-variant allele fraction in the tumor (VAF_T)≥0.05 with ≥5 mutated reads

-gnomAD_Global_AF < 1e-5

-IntegraGen proprietary database AF < 0.01

-coding

We highlighted genes belonging to the list of 120 prostate cancer drivers defined by Armenia et al. (28).

Copy-number analysis using genotype data

Two complementary approaches were used to reconstruct the copy-number profiles of the tumors.

* Copy-number analysis using genotype data

We identified germline Single-Nucleotide Polymorphisms (SNPs) in each sample, and we calculated the coverage log-ratio (LRR) and B allele frequency (BAF) at each SNP site. Genomic profiles were divided into homogeneous segments by applying the circular binary segmentation algorithm, as implemented in the Bioconductor package *DNAcopy*, to both LRR and BAF values. We then used the Genome Alteration Print (GAP) method to determine the ploidy of each sample, the level of contamination with normal cells and the allele-specific copy number of each segment (29). Ploidy was estimated as the median copy-number across the genome. Chromosome aberrations were then defined using empirically determined thresholds as follows: gain, copy number > ploidy + 0.5; loss, copy number < ploidy – 0.5. We considered a segment to have undergone Loss of Heterozygosity (LOH) when the copy number of the minor allele was equal to 0.

* Copy-number analysis based on coverage

We calculated the coverage log ratio in each bait of the exon capture kit between the tumor and a panel of normal. Log-ratio profiles were then smoothed using the circular binary segmentation algorithm as implemented in the Bioconductor package *DNAcopy*. The most frequent smoothed value was the zero level of each sample. Segments with a smoothed log ratio above zero + 0.3 or below zero – 0.3 were considered to have gains and deletions, respectively. High-level amplification and homozygous deletion thresholds were defined as the mean +/- 5 s.d. of smoothed log ratios in normal regions, respectively. This approach does not provide absolute copy-number estimates but has a higher definition than the previous one as there are more exon capture baits than germline polymorphisms. It was used to characterize focal aberrations such as high-level amplifications and homozygous deletions.

Genomic analyses were performed with MERCURY™, an online biological interpretation tool for oncology. https://integragen.com/fr/bioinformatique/mercury

RNA-Seq sequencing and analysis

Libraries were prepared with NEBNext® Ultra™ II Directional RNA Library Prep Kit for Illumina protocol according to supplier recommendations.

Briefly, the key stages of this protocol are successively: the purification of PolyA containing mRNA molecules using poly-T oligo-attached magnetic beads from 100ng total RNA (with the Magnetic mRNA Isolation Kit from NEB); a fragmentation using divalent cations under elevated temperature to obtain approximately 300bp pieces; double strand cDNA synthesis, and finally Illumina adapter ligation and cDNA library amplification by PCR for sequencing. Sequencing was then carried out on Paired-end 100b reads of Illumina NovaSeq. Image analysis and base calling is performed using Illumina Real Time Analysis with default parameters.

First analysis

Quality of reads was assessed for each sample using FastQC (V.0.11.4; http://www.bioinformatics.babraham.ac.uk/projects/fastqc/).

RNA-SeQC provided key measures of data quality. These metrics were shown within Reporting and included yield, alignment, and duplication rates, rRNA content, regions of alignment (exon, intron and intragenic). Alignment was performed by STAR (https://github.com/alexdobin/STAR).

The duplicate reads (*e.g.*, paired-end reads in which the insert DNA molecules have identical start and end locations in the Human genome) were removed using Sambamba tools (https://github.com/biod/sambamba).

Second analysis

Variant calling for the identification of SNVs (Single Nucleotide Variations) and small insertions/deletions (up to 20bp) was performed *via* the Broad Institute's GATK Haplotype Caller GVCF tool.

Ensembl' VEP (Variant Effect Predictor, Release) program was used to process variants for further annotation. This tool annotates variants, determines the effect on relevant transcripts and proteins, and predicts the functional consequences of variants. This included

considering data available in gnomAD, the 1000 Genomes Project and the Kaviar databases. Moreover, an in-house database enabled to filter out sequencing artefacts.

Third analysis

Five bioinformatics algorithms for pathogenicity were used to predict the functional, molecular, and phenotypic consequences of coding and non-coding SNPs. This included DANN, FATHMM, MutationTaster, SIFT and Polyphen. The clinical and pathological significance was also added from the ClinVar database. Other information reported included quality score, homozygote/heterozygote status, count of variant allele reads, and presence of the variant in the COSMIC and OncoKB databases.

RegulomeDB was used to annotate SNPs in known and predicted regulatory elements in the intergenic regions.

Fusion transcript analysis

To detect fusion-genes candidates in RNA-seq data, FusionCatcher (start with fastq files) and STAR-Fusion (start with alignment files) were used to achieve higher detection efficiency (30, 31). These were run using default configurations. In silico validation of a list of fusion transcript predictions was then performed using FusionInspector, a component of the Trinity Cancer Transcriptome Analysis Toolkit (CTAT) (32). FusionInspector assisted in fusion transcript discovery by performing a supervised analysis of fusion predictions, attempting to recover and re-score evidence for such predictions. Fusion-gene candidates were annotated according to several databases of known fusion genes found in healthy samples (known false positives) including the 1000 Genome Project, ChimerDB2, GTEx and cancer databases such as COSMIC, 18Cancers.

Expression

Counting of reads per gene was performed using STAR with –quantMode GeneCounts option. Next, raw count was normalized using the Transcripts Per Kilobase Million (TPM) method.

Analyses were performed with Galiléo™, a cloud-based app for dynamic exploration of RNA-Seq expression data. https://integragen.com/fr/bioinformatique/galileo

In vivo efficacy studies

For preclinical *in vivo* drug testing, tumor fragments were implanted into the interscapular fat pad of NMRI nude immunodeficient mice strain as described above. When tumors reached a volume comprised between 65 and 270 mm^3, mice were randomly assigned to the vehicle or treatment groups (n=6-8 per group). Mice were then treated with 20 mg/kg docetaxel (1 dose every 3 weeks by intraperitoneal route, MedChemExpress, HY-B0011), 12 mg/kg leuprorelin (1 dose/week by subcutaneous injection, MedChemExpress HY-13665), 60 mg/kg enzalutamide (5 doses/week by oral gavage, MedChemExpress HY-70002), 200 mg/kg abiraterone (daily by oral gavage, MedChemExpress HY-70013) and 75 mg/kg olaparib (daily by oral gavage, MedChemExpress HY-10162). Olaparib was also administered in combination with abiraterone and enzalutamide at the same doses and schedule. Drugs were prepared in different solution; in 20% of a mix (50% Tween80 + 50% Ethanol), 80% NaCl 0.9% for docetaxel, in NaCl 0.9% for leuprorelin, in 10% DMSO + 40% PEG300 + 50% (0,5% Tween80) in NaCl 0.9% for enzalutamide, and in 10% DMSO + 90% (10% HP-β-CD) in PBS 1x for abiraterone and olaparib. Mice were treated until one animal reached the maximum ethical limit tumor volume of 1500 mm^3 and/or a body weight loss > 20% for 3 consecutive measurements compared to the first day of treatment, in this case the entire group was removed from the study. Tumor volume was measured twice a week with a caliper and calculated as: TV (mm^3) = [length (mm) x width (mm) ^{2}]*π/6, where the length and width are the longest and shortest diameters of the tumor, respectively. For evaluation of therapeutic response, tumor growth was calculated as ΔT/ΔC in percentage where ΔT and ΔC are tumor volume changes relative to initial mean tumor volume for treated group (T) and control group (C), respectively, at a specific day. Response to treatment was also classified using the modified Response Evaluation Criteria in Solid Tumors (mRECIST) using the percentage of tumor volume change at the last day of treatment compared with the tumor volume at day 0 and classified as follows: complete response, BestResponse < −95% and BestAvgResponse < −40%; partial response, BestResponse < −50% and BestAvgResponse < −20%; stable disease, BestResponse < 35% and BestAvgResponse < 30%; progressive disease, not otherwise categorized (33). Health status and body weight for all mice were recorded twice weekly to control any adverse effects.

Statistical analysis

Comparisons between PDX treatment responses were presented as mean ± SEM. ^{ns}, P>0.05; *, P<0.05; **, P<0.01; ***, P<0.001; ****, P<0.0001 comparing treated to control groups using a two-way ANOVA followed by a Dunnet's multiple comparisons post-test.

Results

Establishment of prostate PDXs

The aim of the present work was to generate PCa PDX models for preclinical applications. To this end, we worked in close collaboration with the Urology department of Strasbourg Hospital and the urological Clinic of Nantes to collect specimens from patients who had undergone surgery or, in a few cases, biopsy. Between 2010 and 2019, we processed 240 PCa samples from 237 patients. Collected samples were obtained from therapeutic or diagnostic procedures: 205 prostatectomies (85%), 31 transurethral resections of the prostate (TURP) (13%), 1 pelvectomy and 1 directly after biopsy (Supplementary Table 1). All men with a presumed diagnosis of PCa were eligible. The median patient age was 64 years (range 43 - 89 years). All the implanted tumors were obtained from localized or regionally advanced diseases, namely 238 primary tumors and 2 samples that were derived from regional lymph node metastasis

(Supplementary Table 1). PDX models were developed from patients across the disease progression, *i.e.*, treatment-naïve to castrate resistant disease.

Viable tumor tissues were xenografted subcutaneously into various strains of immune-deficient mice (for details see materials and methods). For each graft, 2 to 5 mice were used depending on material availability. Eighteen primary implants gave rise to a first tumor growth in mouse: 67% originated from prostatectomies (11 RP and 1 pelvectomy out of 18), 28% from specimens harvested following TURP (5 out of 18) and 5% from lymph node metastasis (1 out of 18). We obtained a low take rate probably due to the variability of the amount of viable tissue submitted for PDX development, mouse strain used and engraftment site. It took between 2.5 and 7.5 months to observe the first growth in mouse irrespectively of tumor stage. Nine tumors that grew did not survive after passage 1. The other half (9 tumors) were successfully propagated beyond three passages. Unfortunately, 3 models did not grow after freezing/thawing despite attempts in several strains of mice and 1 model was contaminated by lymphoma.

In total, we established 5 sequentially transplantable PDXs as working models. PCU-012 and PCU-018 PDX models were derived from primary local tumor samples from treatment-naïve patients. C901 PDX model was obtained from TURP. At the time of surgery, the corresponding patient was responsive to androgen-deprivation therapy (ADT). Cancer progressed and the patient underwent an additional palliative TURP eight months later. TURP chips were obtained and successfully implanted to generate the C1022 PDX model, which displays a neuroendocrine phenotype. PCa samples for the establishment of G266 were obtained at pelvectomy and correlated with a recurrence. Supplementary Table 4 summarizes the whole clinical annotated data from patients from whom PDXs were derived.

Histological and genomic characterizations of PDXs

H&E

A histopathological comparative analysis of the H&E-stained slides of patient tumors and PDXs was performed. In 4/5 cases, the morphological features of the PDX replicated closely the human primary tumors. PCU-012 primary tumor and PDX model were Gleason 5 + 4 with solid pattern and scattered glandular lumens. PCU-018 PDX model had the same pattern of pleomorphic giant cell adenocarcinoma as observed for the primary tumor (Gleason 5 + 5). C901 PDX displayed the same cribriform and complex papillary pattern (equivalent Gleason 4 + 4) as for the primary tumor classified as ductal adenocarcinoma (Gleason 5 + 4). C1022 human tumor showed two distinct components, an adenocarcinoma with the same cribriform/papillary features described for C901, and a neuroendocrine small cell carcinoma with sheets of basophilic cells and extensive necrosis; the C1022 PDX mimicked only the neuroendocrine carcinoma component. G266 patient tumor and PDX were both graded Gleason 5 + 5 (Figure 1A).

STR

Using Short Tandem Repeat (STR) profiling, we confirmed the concordant genetic identity between patient tumors and derived PDXs (Supplementary Figure 1), with 100% of conserved STR for 4 models, an example of C901 STR profile is shown in Figure 1B. PDX G266 appeared to have minor alleles differences between the patient sample and the derived PDX with a homology rate superior to 80%. Discrepancies were due to the ploidy of the primary tumor since the Copy Number Alterations (CNA) revealed a tetraploid genome (Supplementary Figure 2A).

Genomic alterations

We investigated genomic alterations for cancer-related genes in all 5 PDXs using a whole exome sequencing (WES) assay, which enabled the detection of mutations (Supplementary Table 5), CNA (Supplementary Tables 6, 7), tumor mutational burden (TMB), and MSI status (Figure 1 and Supplementary Figure 2).

We initially considered 97 cancer driver genes and added 23 genes with unknown but recurrent significance (28, 34, 35). The frequency of alterations for each gene was compared to data obtained by Armenia et al. (28). As expected, the main altered pathways were the AR, the cell cycle and DNA repair, *AKT/mTOR*, epigenetic regulators, Wnt and the ubiquitin pathways.

PDX G266 harbored the highest mutational burden (30,99 variant/Mb) (Figure 1C and Supplementary Figure 2B) followed by PDXs C901 (8,46 variant/Mb), C1022 (7,64 variant/Mb), PCU-012 (5,99 variant/Mb), and PCU-018 (3,6 variant/Mb), respectively. G266 displayed a microsatellite instability profile with a homozygous deletion of *MSH2* and a loss of *MSH6*. PDXs G266, C901 and C1022 shared a mutation profile representative of those observed in prostate metastatic tumors such as *TMPRSS2-ERG* fusion, *TMPRSS2*, *RB1*, *BRCA2*, and *KMT2D* mutations. For C1022, TMPRSS2-ERG fusion was not detected first and analyzed by Mercury™, probably because it was present in an inferior percentage of cells in C1022 compared to C901 and filtered as not supported by a sufficient number of reads. Based on WES data, this TMPRSS2-ERG fusion was deduced due to the presence of a small deletion on chromosome 21, where the terminals coincided specifically with those genes (Supplementary Figure 3). The deletion appeared more clearly within the genome of PDX C901 but the same breakpoints were found on the logR ratio profile of PDX C1022. G266 and C1022 profiles were consistent with the patients' tumor history since they were relapses from a primary tumor and were more aggressive than the other patients' tumors. C901 and C1022 had a homologous deletion of both *BRCA2* and *RB1*, and G266 harbored a deletion leading to a frameshift. Together with other mutations implicated in DNA homologous recombination repair genes, these three PDX models had an eligible profile for pharmacology studies with PARP inhibitors. G266 was the only one to demonstrate *AR* missense activating mutations (p.(Thr878Ala)) and (p.(Trp742Cys)) present in castration-resistant disease but also a *PIK3R2* missense (p.(Gly373Arg)) and *PTEN* nonsense mutations (p.(Arg233Ter)) stop gained).

PCU-012 had a profile compatible with a genomic instability associated with a CDK12 inactivation, copy number amplifications

10.3389/fonc.2023.1130048

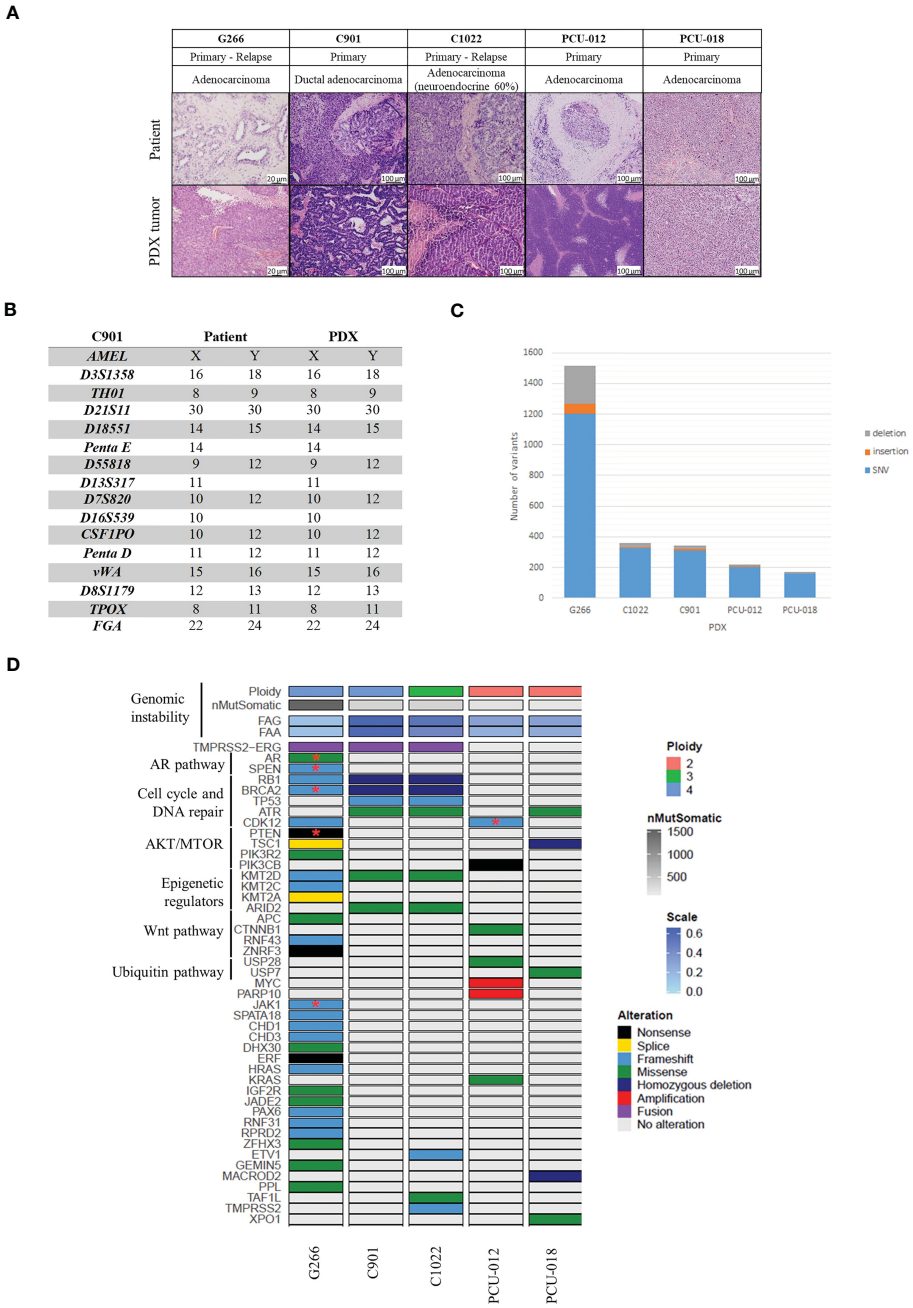

FIGURE 1
Histological and genomic characteristics of patient's tumors and paired derived patient-derived xenografts (PDXs). **(A)** Comparative analysis between patient tumor and corresponding PDX model assessed by hematoxylin and eosin (H&E) staining and demonstrating feature preservation. Scale bar corresponds to 100 µm except for G266 (20 µm). H&E slides were reviewed by a board-certified pathologists and representative pictures are shown. **(B)** Short tandem repeat signature of a patient specimen and PDX tumor, an example of the C901 case. **(C)** Number of variants identified. **(D)** Somatic genomic landscape of 5 prostate PDXs analyzed using a whole exome sequencing approach. FAA (Fraction of Aberrant chromosome Arms); FAG (Fraction of Aberrant Genome); SNV: single nucleotide variation; Stars indicate two mutations in the same gene.

dispersed across the genome, a copy number aberration on chromosome 8q with focal amplification of *MYC* and *PARP10* and a high number of gene fusions compared to other PDXs. Two alterations were found in the *CDK12* gene, a frameshift in exon 6 and a pathogenic missense mutation in exon 10 (p.(Cys952Arg)) in the kinase domain of the protein (Supplementary Table 5). The associated copy number was 2.52 with a high expression level of *CDK12* transcript. This model also presented a deletion in *BRCA2* (p.(Cys1200Ter)) leading to a frameshift and mutations in two hot spot genes, *CTNNB1* (p.(Asp32Tyr)) and *KDR* (p.(Cys482Arg)). No *ETS* fusion, nor *PTEN*, *ATM* or *SPOP* mutations were detected which was consistent with the CDK12 phenotype.

PCU-018 had a diploid profile with an important number of deletions (383 deleted cancer genes) spread widely all over the

genome with homozygous deletions of the tumor suppressor *TSC1* and *MACROD2*, a hydrolase, which removes mono-ADP-ribosylation and which is implicated in chromosome instability in colorectal cancer (36). Few gains (2 amplifications and 77 gains) and 9 fusions of interest were also found. Three portions of copy neutral loss of heterozygosity (CN-LOH) in chromosomes 1 (77 mb), 11 (11 mb) and 17 (56 mb) were found, respectively. Missense mutations were identified in 3 cancer gene drivers: *ATR* (p.(His4Tyr)) and Rad3-related protein, implicated in replication stress response (37); *USP7* (p.(Arg634Asp)) for ubiquitin specific protease 7, member of the deubiquitinating enzyme family (38); and *XPO1* (p.(Ser1031Thr)) a nuclear export protein implicated in cellular homeostasis (Supplementary Table 5) (39).

Taken together, these data highlighted the genetic heterogeneity between our PDX models with common mutations in those from advanced PCa compared to localized ones. They were consistent with genomic aberrations previously described in literature regarding their phenotype and grade.

CRPC-NE and HSPC tumors appear clonal in origin with clonal ancestry

C901 and C1022 PDX models were derived from tumor samples from the same patient at two different time points. The patient was diagnosed with an adenocarcinoma and treated with adjuvant ADT before surgery. He had a transurethral resection of the prostate TURP for a clinical localized Gleason 8 (4 + 4) prostate adenocarcinoma and was treated with ADT. The cancer relapsed eight months later and an adenocarcinoma with 60% of neuroendocrine component was removed (Supplementary Table 4). C901 was tetraploid and C1022 triploid. The mutations of the two PDXs derived from these surgeries were analyzed and compared. They shared 245 mutations. 112 and 129 were specific to C901 and C1022, respectively (Supplementary Figure 2C). Six non-synonymous mutations were identified in cancer driver genes. Mutations of *TP53* (p.(Arg335ValfsTer10) frameshift), *ARID2* (p.(Glu44Asp)) and *KMT2D* (p.(Lys5091Arg)) were present in both PDXs as well as the TMPRSS2-ERG fusion, although less were detected in C1022. Two homozygous deletions on chromosome 13 implicating tumor suppressor genes *BRCA2* and *RB1* were also observed (Figure 1D and Supplementary Table 5). *TMPRSS2* (p.(Ser234GlufsTer16)) frameshift, *ETV1* (CN-LOH) and *TAF1L* (*p*.(Val495Glu)) mutations were only present in C1022. The *TMPRSS2* mutation was a translocation between exon 7 and intron 2 of the enzyme β-carotene oxygenase 1, *BCO1*, a survival prognostic gene (40).

Taken together, these results suggested that these two PDXs models had a common precursor with common mutations but had then evolved separately, under ADT (Supplementary Figure 4) (41).

PDXs recapitulate the molecular subtypes of prostate cancer

Immunohistochemical phenotypes

A nuclear ERG expression was observed for the C901 primary tumor and PDX, as well as in the adenocarcinoma component of human tumor C1022, consistent with the *TMPRSS2-ERG* fusion detected in C901 and C1022 PDX. Of note, ERG was not expressed in the C1022 human tumor and PDX neuroendocrine carcinoma, however a strong expression of synaptophysin and chromogranin was measured confirming the NE phenotype (Supplementary Figure 5). A loss of PTEN expression was observed for the G266 primary tumor and corresponding PDX in agreement with the non-sense *PTEN* mutation detected in the PDX. The other primary tumor/PDX pairs showed a conserved expression of PTEN. Among the two PDX derived from hormonal treatment naïve tumors, the androgen receptor expression ranged between low (PCU-018) to high (PCU-12). The expression was also high for the G266 and C901 PDX derived from a tumor collected in a hormone treated patient. It was absent within the C1022 neuroendocrine carcinoma (Figure 2). NKX3.1 expression was detected in all tested PDX, to a lower extend for PDX C1022 consistent with its neuroendocrine profile (Supplementary Figure 5). PDXs were stained for hCD45, a nonspecific lymphocyte marker, to evaluate human lymphoma presence (Supplementary Figure 5). No expression was seen for 4/5 models, a low expression associated with background noise was seen for the C901 PDX model. The stained areas are free of cells or contain red blood cells.

Hierarchical clustering

We then sought to determine whether our PDX models could be segregated by hormone-sensitive or castrate-resistant tumor phenotype using an unsupervised clustering analysis based on the topmost 1 000 variant genes after RNASeq (Figure 3A). No segregation regarding treatment sensitivity was found but rather a stratification separating PDXs derived from primary tumors from PDX tumors derived from recurrent or metastatic tumors. Derived from a primary localized tumor, PCU-018 was clustered alone. PDXs G266, C1022, C901 and PCU-012 belonged to the same cluster but C1022 appeared in a different subcluster as it was from a CRPC-neuroendocrine tumor. Interestingly, although derived from a primary localized tumor, PCU-012 was also clustered with PDXs derived from recurrent and metastatic tumors. This was consistent with the patient's outcome since metastases developed shortly after surgery. This supports the accuracy of a gene signature in localized prostate cancer that can predict whether the cancer is likely to spread, or metastasize, early in the course of the disease.

GSEA (Gene Set Enrichment Analysis)

Among all 3 011 differential mRNAs, 1 980 genes were over-expressed, and 1 031 genes were under-expressed in cluster 2 (C1022, C901, G266 and PCU-012) compared to cluster 1 (PCU-018) (Figure 3B, Supplementary Table 8). To explore this result further, we performed a GSEA of the MSigDB collections between cluster 1 and cluster 2. GSEA revealed the enrichment of several expected pathways for cluster 2 such as for the gene associated to a metastatic phenotype (NES, 2.81; $p=1.14 \times 10^{-26}$). Notably, cluster 2 samples showed overexpression of genes implicated in fatty acid/glycolysis metabolism, whereas cluster 1 samples overexpressed genes involved in oxidative phosphorylation (NES, 1.45; p=0.009) consistent with the metabolic reprogramming occurring across PCa progression (Figures 3C, D). Additionally, a pathway analysis

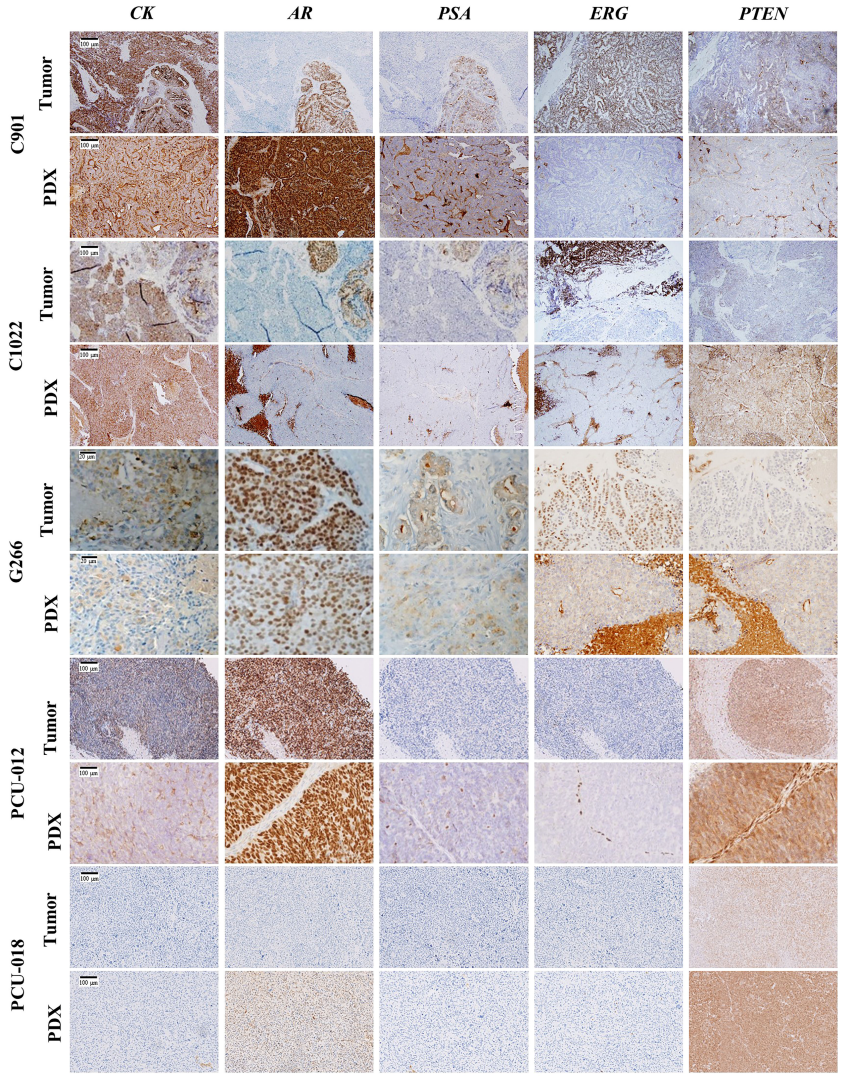

FIGURE 2
Immunohistochemical characterization of the 5 PCa PDX models. Representative immunochemical staining for CK (cytokeratin), AR (androgen receptor), PSA (prostate specific antigen), ERG, and PTEN in patient tumor and corresponding PDX model. Scale bar corresponds to 100 µm unless specified.

between the two clusters highlighted the top up and down pathways. Cluster 2, associated with a metastatic phenotype, showed upregulation of androgen/estrogen pathways whereas cluster 1 (localized tumor) highlighted upregulation of inflammation response and IL6-JAK-STAT3, IL2-STAT5 pathways.

Metabolic reprogramming in prostate cancer

We subsequently focused our analysis on metabolism since recent studies have revealed new insights into specific PCa metabolic reprogramming vulnerabilities that can be targeted (42–45). The metabolism gene signature of the 5 PDX models recapitulating some genes involved in oxidative phosphorylation/mitochondrial DNA, in glycolysis and lipid metabolism showed the same clustering as for the topmost 1 000 variant genes (Figures 3A–E). PCU-018 highly expressed oxidative phosphorylation (OXPHOS) and mitochondrial genes such as *ACO2*, *FH* and *OGDH* involved in tricarboxylic acid (TCA) cycle and *MT-CO1*, *MT-CO2*, *MT-CO3* coding for mitochondrial cytochrome c oxidase and *MT-ATP6*, *MT-ATP8* coding for ATP synthase (Figure 3E). On the other hand, late stage PDX tumors overexpressed a clear subset of genes implicated in glycolysis, fatty acid (FA) oxidation and lactate production such as *FBP*, *FASN* or *LDH* genes. Several studies have shown that TCA cycle dysregulation through OXPHOS inhibition leads to an increased expression of *ACACA* and *FASN* genes, suggesting an enhanced FA synthesis and PCa progression (46, 47). Interestingly, the *MAOA* gene which is shown as responsible for mitochondrial dysfunction and glycolysis promotion in gastric cancer was over expressed in PCU-012, G266 and C901 (48). Overall, these data reflected the metabolic changes that occur in PCa, first from aerobic/anaerobic glycolysis in normal prostate cells to oxidative phosphorylation of cancer cells, and then in metastasis, glycolytic activities and increased oxidation of fatty acids (49). This opened up the possibility to target OXPHOS and mitochondrial activities in PCa to prevent the metabolic switch required for PCa progression (50, 51) and to defuel advanced PCa with metabolic inhibitors (44, 52).

10.3389/fonc.2023.1130048

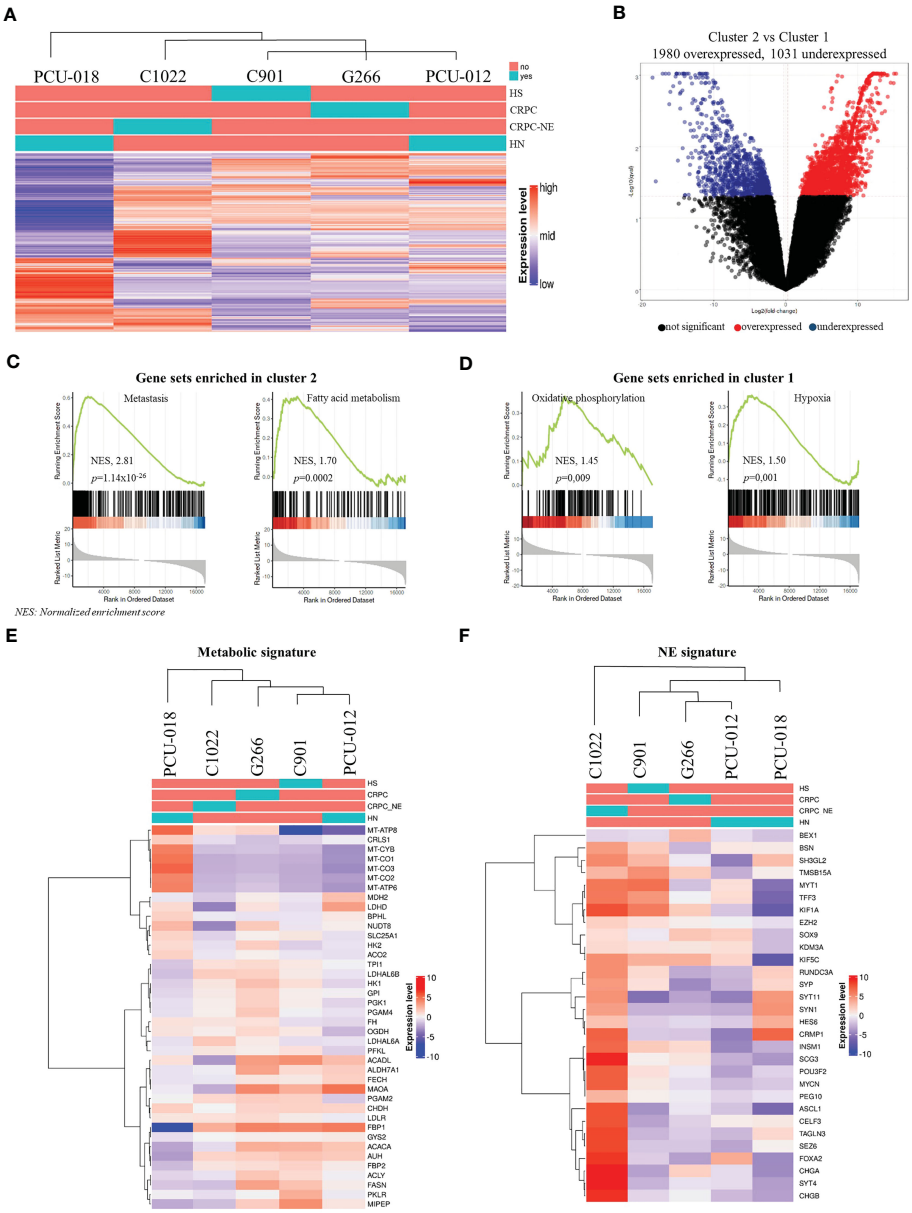

FIGURE 3
Analysis of gene expression by RNA sequencing of prostate cancer PDXs. **(A)** Unbiased hierarchical clustering with a color code panel depicting treatment status (naïve or treated), castrate resistant and neuroendocrine status (CRPC and CRPC-NE) based on genes with the most variant expression (n=1000). **(B)** Volcano plot representation showing top up and down-regulated genes in tumor with metastatic molecular features (Cluster 2) vs. localized tumors (Cluster 1). **(C, D)** Gene set enrichment analysis (GSEA) analysis of RMA normalized gene expression. Biological processes are significantly different between Cluster 2 and Cluster 1. **(E, F)** Heatmap of gene expression signature for the selected gene signature: metabolic gene signature and neuroendocrine gene signature. (HS, hormone-sensitive; CRPC, castrate resistant prostate cancer; CRPC-NE, castrate resistant prostate cancer neuroendocrine; HN, hormone-naïve; NES, normalized enrichment score).

It could be noted that C1022 CRPC-NE PDX also appeared in a different subcluster with an intermediate metabolic state. Neuroendocrine PCa AR-null phenotype presents an unmet clinical challenge and requires further investigation of its metabolic regulation which is still not fully understood. Choi et al., reported enhanced glycolysis associated with lactic acid production in NEPC and proposed to target MCT4 (53); while other groups reported the significance of fatty acid (FA) metabolism, glycolysis or the importance of the carnitine palmitoyl transferase I (CPT1) (54–57). Interestingly, our neuroendocrine PDX model did not express *MCT4*; no over expression of *CPT1* or specific metabolic pathway was noticed, suggesting heterogeneity of neuroendocrine prostate tumors already described (58–60).

NE signature

To validate the neuroendocrine profile of C1022, we evaluated PDX patterns using previously defined NE signatures (61, 62). As

expected, the NE subtype PDX was markedly different from non-NE PDX (Figure 3F) and had a pattern of expression in accordance with its neuroendocrine profile, with an absence of *AR* expression, *RB1* loss, low *TP53* expression, *MYCN* overexpression as well as upregulation of *POUF2R3*, *SOX2* and *PEG10* and *ERG* rearrangement (Supplementary Figure 6B). Additionally, the neuroendocrine chromogranin A and synaptophysin markers were diffusely expressed in C1022 primary tumor and PDX, supporting the diagnosis of poorly differentiated neuroendocrine carcinoma (Supplementary Figure 5).

C1022 PDX also overexpressed epigenetic factors such as *SRRM4* and *EZH2* and showed a downregulation of *REST*, all implicated in tissue plasticity (Supplementary Figure 6B) (63). Interestingly, PDX C901 revealed expression of some NE genes, which could have predicted the fate of this tumor.

Predictive evolution of the tumor

AR is known to be a key regulator that orchestrates metabolic reprogramming depending on the stage of disease progression (64). Indeed, PDX's metabolism profiles can be linked to AR status with a drop of oxidative/fatty acid metabolism associated to loss of AR expression for C1022 (Supplementary Figure 6C). These results highlighted the link between metabolic pathways, AR signaling and the stage of the tumor, as well as the importance of identifying the metabolic weaknesses of PCa.

Overall, these molecular signatures highlighted the importance of this analysis as a particularly informative resource for predicting tumor progression and tailoring patient treatment accordingly, as it could have been done for tumor C901 which already expressed NE signature, or for PCU-012, which showed a metastasis signature even though it was a local tumor.

Sensitivity of patient-derived xenografts to standard of care treatment

As described above, the PDX panel presented tumors with diverse clinical and genomic characteristics across the course of PCa disease, allowing to evaluate drug efficacy on either treatment-naïve tumors, hormone-sensitive tumors, or castrate-resistant tumors. We investigated the sensitivity to docetaxel, a standard of care chemotherapy, and enzalutamide, a new generation androgen pathway inhibitor in our established PDX cohort (Figure 4A, Supplementary Figure 7). The response to each treatment reflected the heterogeneous clinical and genomic characteristics of the tumors. As expected, both G266 and C1022 CRPC PDX models were resistant to enzalutamide while the hormone-sensitive C901 PDX model was sensitive and exhibited a partial response. C901 and C1022 PDX models, derived from the same patient, were sensitive to docetaxel with a clear response for C901 and a partial response for C1022, while G266 was resistant (Figure 4A). Treatment responses of these two models reflected the hormone-resistance acquisition of the patient over time. Interestingly, PCU-018 from a localized and treatment-naïve tumor, was resistant to docetaxel and enzalutamide (Figure 4A).

In a clinical situation, the Response Evaluation Criteria in Solid Tumor (RECIST) are prevalently used to assess treatment responsiveness. Correspondingly, modified RECIST (mRECIST) was suggested to evaluate the treatment response in PDX model (33, 65). The mRECIST is estimated using the percentage of tumor volume change at the last day of treatment compared with tumor volume at day 0. We considered "responders" PDXs that showed a complete response (CR), partial response (PR) or stable disease (SD) and "non-responders" those with a progressive disease (PD) status. C901 was responsive to docetaxel treatment with a negative tumor volume change indicating shrinkage of the tumor after treatment, even though a tiny ball remained palpable; whereas using the modified RECIST classification, C901 was classed as a stable disease (SD) and not a responsive tumor (Figure 4B). The tumor response associated with C1022 was classed as a progressive disease (PD).

We then focused on C901 and C1022 PDX models which are interesting as they can provide a relevant preclinical tool to identify resistance mechanisms and to develop new therapeutic strategies. Both models were treated with androgen deprivation therapies (ADT), leuprorelin and enzalutamide, and with the chemotherapeutic docetaxel for at least 21 days. The hormone-sensitive model, C901, displayed relatively slow growth compared to the neuroendocrine castrate-resistant model C1022 as it took 60 days to reach tumor ethical size in the C901 vehicle group compared to 21 days for C1022 (Figure 4C). C901 tumor growth was significantly delayed when treated with enzalutamide while C1022 was a non-responder, correlating with their respective characteristics. Both models were responsive to docetaxel treatment, but an acquired resistance appeared for C1022. None of these two PDX responded to leuprorelin treatment which was used to treat the patient before and after the first surgery, the tumor of whom became resistant at the time of the second surgery, eight months later. Collectively, these analyses shed light on the occurrence of resistance in the same patient and the possibility of studying this through corresponding PDXs. Furthermore, the characteristics of PDX C1022 were consistent with the differentiation of neuroendocrine tumors, which were characterized by a highly proliferative profile, lack of responsiveness to hormonal therapies, and poor prognosis (66, 67).

Inhibition of PARP significantly improves antitumoral response of CRPC-NE PDX compared to ADT

PARP inhibitors have recently been approved for patients presenting defects in homologous recombination repair (68, 69). Since the neuroendocrine castrate resistant C1022 model was unresponsive to all tested drugs and had a homologous deletion of *BRCA2*, we assessed the antitumor activity of the PARP inhibitor, olaparib, on this model. Given that previous works have demonstrated the improved efficacy of olaparib compared to androgenic pathway inhibitors (70) and given that clinical trials are now focusing on combining PARP inhibitors with other

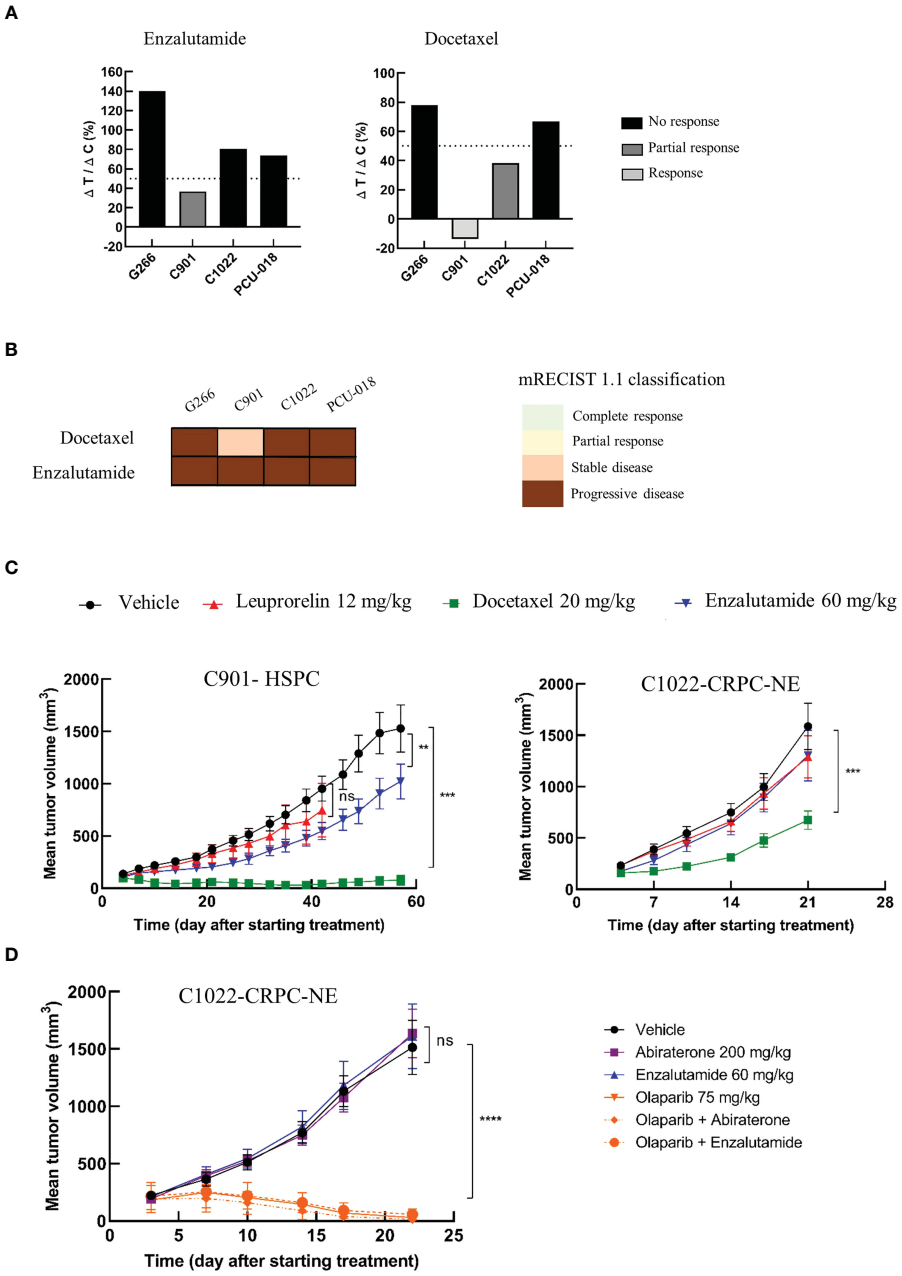

FIGURE 4
Preclinical testing of a panel of therapies from chemotherapy to targeted therapy. Mice (n=6-8 per group) with established PDXs (65 mm^3 - 270 mm^3) were treated with various drugs or control vehicle. Tumors were measured at the indicated time points. **(A)** PDX response to docetaxel and enzalutamide according to tumor growth inhibition (TGI) presented as the ΔT/ΔC ratio and calculated as the ratio of the mean tumor volume for the treated vs. control group, with a response when ΔT/ΔC < 0%, a partial response when ΔT/ΔC 0-50% and no response when ΔT/ΔC >50%. **(B)** PDX response to docetaxel and enzalutamide treatment according to modified mRECIST 1.1 classification. **(C)** Growth response curves of C901 (androgen-dependent) and C1022 (castrate-resistant) PDX models generated from the same patient to docetaxel, leuprorelin and enzalutamide administrations. **(D)** Sensitivity of the castrate resistant neuroendocrine PDX (C1022) to androgen receptor inhibitors, to olaparib, a PARP inhibitor, given alone or in combination. Data are presented as mean ± SEM. ^{ns}P>0.05; **P<0.01; ***P<0.001; ****P<0.0001 comparing treated to control groups using a two-way ANOVA followed by a Dunnet's multiple comparisons post-test.

treatments such as androgenic pathway inhibitors (71), we decided to evaluate the efficacy of olaparib also in combination with either enzalutamide or abiraterone. As previously observed (Figure 4C), this rapidly growing PDX reached maximum ethical tumor volume between days 21 and 22. The response to androgenic pathway inhibitors was also consistent with our previous results; C1022 PDX was unresponsive to enzalutamide and presented no response to the other inhibitor abiraterone (Figure 4D). Tumor growth was drastically reduced upon treatment with olaparib. In some mice, no tumors were even detectable at the end of the study. Of note, no adverse effects were noticed in any of the treated groups (data not shown).

Taken together, these data were consistent with the patient's tumor responses and paved the way to new therapeutic strategies for patients with CRPC-NE.

Discussion

Preclinical relevant models for drug development are still very much needed. Genetic and molecular characterizations of PDX models have confirmed their utility as avatars for testing new therapies and combinations as they maintain a high degree of molecular fidelity to the original patient's tumor (33, 72–74). PCa PDX models have been shown to capture the biological and molecular heterogeneity of the patient's tumor, preserved histopathology features as well as genome architecture and global gene expression (75). However, their development remains challenging as their take rate is amongst the lowest, they proliferate very slowly and only high grade PCa with Gleason scores above 8 culminate in research ready to use preclinical models (15, 76).

We report here, like others, that our collection of 5 PDXs derived from PCa preserved the histological and molecular properties of patients' tumors (15, 77).

From weakly to highly rearranged genomes, these PDX models reflect the heterogeneity of genomic variations in PCa encompassing different patterns of alterations. We described potential actionable genetic drivers such as *MYCN* and *PARP10* (78) that are amplified in the PCU-012 model. These mutations were sufficient to induce a CDK12 phenotype as described by Wu et al. (79).

We also described a drug response effect using new therapies such as the PARP inhibitor olaparib with our CRPC-NE PDX model that, used as a monotherapy, could reduce tumor growth significantly. Combination therapy did not improve efficacy, probably due to the high dose of olaparib, which, already greatly reduced tumor volume alone and because of the neuroendocrine nature of the C1022 tumor given that abiraterone and enzalutamide are efficient on AR+ tumors. In order to optimize treatment and evaluate a potential additive or synergistic effect for combination treatments, it would be interesting to explore the effect of olaparib at graded doses on *BRCA2* and AR+ mutated PDX models. Overall, these data confirmed the efficacy of PARP inhibition on *BRCA2*-mutated tumors. This opens the field for targeting other Homology Directed Repairs (HDRs) in PCa, including the aggressive neuroendocrine subset that presents very few treatment options. Beyond PDXs with *BRCA2* mutations, those PDXs with deficiencies in other DNA-damage repair-associated genes (*e.g.*, *PALB2*) should be eligible to treatments with PARP inhibitors since they may benefit from PARP inhibition, as suggested by Abida et al. (80). With its MSI-H profile, G266 should be a good model for testing immune checkpoint inhibitors (81). Our models could thus be useful for evaluating such new potential therapies alone or in combination.

We identified two clusters according to their hierarchical expression pattern characterization: a cluster with PDXs derived from primary localized tumors and a cluster derived from advanced tumors. It was interesting to observe that these two clusters could be further characterized by their metastatic potential, as highlighted by the expression levels of both the genes involved in metastasis processes and EMT and FA genes known to be key instruments of tumor dissemination. This information is crucial in the choice of the patient's further treatment, as demonstrated by our PDXs PCU-012 and C901: both of which were derived from local primary tumors, but which already harboured the molecular signatures of epithelial to mesenchymal transition and FA metabolism. It has been previously published that repeated exposure to anticancer therapies may select carcinoma cells with partial mesenchymal phenotype coincident with the emergence of drug resistance (82, 83). The C901 PDX model, although hormone-sensitive, already mirrored drug resistance with its intrinsic tumor heterogeneity. This was supported by the stable disease (SD) state measured with mRECIST classification, where a residual tumor was still measurable after treatment with enzalutamide. It would be of interest to test different therapies based on the expression pattern analysed combining anti-MYC and PARP inhibitors with metabolic inhibitors for the PDX PCU-012 with a CDK12 phenotype.

As described previously, the remarkable plasticity in lineage identity of PCa cells might explain the development of ADT resistance and the emergence of CRPC and CRPC-NE phenotypes (63). This could be observed thanks to a further analysis of epigenetic drivers responsible for cellular plasticity and/or neuroendocrine differentiation (41, 84–86). High expression levels of those biomarkers of plasticity were measured in PDX C1022, probably promoting lineage, resistance to androgen-targeting therapies and confirming its NE phenotype. PDXs C901 and C1022 illustrate the selective pressure under ADT from the primary tumor that was hormone sensitive until the CRPC-NE phenotype.

Finally, we analysed the expression of biomarkers of the metabolism. The dysregulation of metabolism in cancer cells was first described a hundred years ago and is now being reconsidered taking into consideration non-cancer cells from the tumor microenvironment (87). The TCA cycle is truncated in normal epithelial cells from the prostate and low rate of oxidative phosphorylation is observed (OXPHOS) (88). In PCa with genetic alterations such as PTEN loss, P53 loss and MYC overexpression, the TCA cycle is reactivated for energy production and *de novo* lipid synthesis. The Warburg effect or aerobic glycolysis is observed in the metastatic stages of the disease. In accordance with the literature, our clustering highlights the metabolic shift in PCa cells with metabolic vulnerabilities that could be novel targets in PCa. As an example, the PCU-018 PDX model is an interesting tool to test small-molecule metabolic inhibitors of the mitochondrial oxidative phosphorylation (89) alone or in combination with other therapies. G266, C901 and PCU-012, according to their profile, could be used to test ACLY and FASN inhibitors (90, 91). With its neuroendocrine phenotype, C1022 appeared to have a different

metabolic profile which did not correspond to those already described, opening up other possibilities for new targets (92).

The different molecular signatures identified pave the way to therapeutic solutions and highlight the high heterogeneity of PCa with only these 5 PDX models, illustrated by our various pharmacological results. Different therapies can be tested based on identified genetic drivers, expression patterns and metabolic reprogramming. This information is critical for taking adapted treatment decision for patients, saving time and limiting side effects linked to inappropriate medication.

Overall, this collection spans the clinical heterogeneity of PCa including adenocarcinoma and neuroendocrine phenotypes. This is a dynamic repository, and, to date, we are constantly collecting samples to implement our PDX bank, allowing us to capture the evolving molecular landscape of PCa to support precision medicine.

Limitations of our analyses

In accordance with the patient's consent, no sequencing of the patient's tumor or fragment of normal tissue were performed. This introduced a background noise in the calculation of the tumor mutational burden estimated between 100 to 200 somatic variants as it was performed based on a panel of normal and not patient's tissue.

Data availability statement

The datasets presented in this study can be found in online repositories. The names of the repository/repositories and accession number(s) can be found in the article/Supplementary Material.

Ethics statement

The studies involving human participants were reviewed and approved by both Comité de Protection des Personnes Est IV and Comité de Protection des Personnes Sud-Ouest et Outre-mer, under approval numbers DC-2010-1193 and DC 2019-3565, respectively. Written informed consent was obtained from all participants for their participation in this study. The patients/participants provided their written informed consent to participate in this study. The animal study was reviewed and approved by Animal care and housing were conducted in accordance with the European Comity Council Directive 2010/63/UE and the French Ministry for Agriculture, Food and Forestry decree-2013. The study protocol was reviewed and approved by CEE-35 and CEEA-122 Ethical committee and approved by French Ministry for National Education, Higher Education and Research under approval numbers APAFIS#2949-2015113017594629v5 and APAFIS#14811-2018042316405732v6. Written informed consent was obtained from the individual(s) for the publication of any potentially identifiable images or data included in this article.

Author contributions

YM had full access to all the data in the study and takes responsibility for the integrity of the data and the accuracy of the data analysis. CB, NB and ML designed, performed experiments or bioinformatics analyses, analyzed and interpreted the data. HL, CB and ML developed the PDXs models. HL and EP provided samples and helped with clinical data analysis. CB, NB and ML performed the pharmacological characterization of the PDXs. CB performed STR analysis. CK performed histo- and immunohistopathological analysis under YA supervision. YM and NB performed most of the bioinformatics analyses together with help JM-P for PDXs' genomic and transcriptomic analysis. YM supervised CB, ML and NB. VL performed and supervised histopathological analysis of tumors and PDXs. YM and PL designed the study and supervised establishment of part of the PDXs and pharmacological characterization of PDXs. YM supervised the genomic analyses. TM and HL designed and supervised the establishment of part of the PDXs. YM designed and supervised the research, analyzed and interpreted the data. CB, NB and YM wrote the paper. All authors contributed to the article and approved the submitted version.

Funding

This work was supported by the Region Alsace (France) (FEDER - URTHER program), the Region Occitanie (France) (FEDER - Ugginnov program), and BPI France (OSEO ISI – Magenta program).

Conflict of interest

The authors declare that the research was conducted in the absence of any commercial or financial relationships that could be construed as a potential conflict of interest.

Publisher's note

Supplementary material

The Supplementary Material for this article can be found online at: https://www.frontiersin.org/articles/10.3389/fonc.2023.1130048/full#supplementary-material

SUPPLEMENTARY FIGURE 1
Short Tandem repeat (STR) profiling of patient tumors and matched PDXs.

SUPPLEMENTARY FIGURE 2
Next-generation sequencing results. **(A)** Copy Number alterations (CNA) and B-Allele frequency of each PDX model are presented. First panel (CNA): Amplifications are depicted in green, gains in blue, losses in orange and deletions in purple. Copy-neutral loss of heterozygosity is represented in red compared to the reference in black. Second panel B-allele frequency is in red, and reference is in black. **(B)** The mutational burden for each PDX is represented by a green bar compared to the mutational load of reference tumors. The tumor mutational burden per megabase (TMB) is indicated in the log2 scale for each sample, and microsatellite instability–high (MSI-H) versus a microsatellite-stable (MSS) status. **(C)** Variant allele frequency comparison between C901 and C1022 PDX models.

SUPPLEMENTARY FIGURE 3
TMPRSS2 ERG fusion. Chromosome 21 representation for C901 and C1022 PDX models.

SUPPLEMENTARY FIGURE 4
Deciphering of CRPC-NE emergence through genomic analysis. Model of evolution occurring during prostate cancer progression for the patient from whom C901 and C1022 were generated, suggesting a common precursor and a divergent clonal evolution.

SUPPLEMENTARY FIGURE 5
Immunohistochemical staining for PDX model characterization. Representative immunochemical staining for NKX3.1, CD45 in PDX models. SYN (synaptophysin), and CgA (chromogranin) immunochemical staining in patient tumor and corresponding PDX model. Scale bar corresponds to 100 µm.

SUPPLEMENTARY FIGURE 6
Transcriptomic analysis. **(A)** Normalized enrichment score (NES) of GSEA for hallmark gene sets showing top up and down-regulated genes in metastatic tumors vs. localized tumors. **(B)** Expression of neuroendocrine markers in all PDX models. **(C)** Upregulated and downregulated metabolic hallmark pathways according to the AR level expression in PDX models.

SUPPLEMENTARY FIGURE 7
PDX response to docetaxel and enzalutamide. PDX response to docetaxel and enzalutamide treatment (n= 6-8 mice per group). Data represent the average tumor volume (mm^3) of each group ± SEM. ns, P>0.05; *, P<0.05; **, P<0.01; ***, P<0.001; ****, P<0.0001 comparing treated to control groups using a two-way ANOVA followed by a Dunnet's multiple comparisons post-test.

SUPPLEMENTARY TABLE 1
Xenografted prostatic tissues.

SUPPLEMENTARY TABLE 2
Characteristics of the PCa PDX panel.

SUPPLEMENTARY TABLE 3
Immunohistochemical staining information.

SUPPLEMENTARY TABLE 4
Summary of clinical and pathological data of PCa patients whose tumor material was used to generate PDX models.

SUPPLEMENTARY TABLE 5
All somatic mutations.

SUPPLEMENTARY TABLE 6
All chromosome aberrations.

SUPPLEMENTARY TABLE 7
Amplifications and deletion.

SUPPLEMENTARY TABLE 8
List of differentially expressed genes.

References

1. Sung H, Ferlay J, Siegel RL, Laversanne M, Soerjomataram I, Jemal A, et al. Global cancer statistics 2020: GLOBOCAN estimates of incidence and mortality worldwide for 36 cancers in 185 countries. *CA Cancer J Clin* (2021) 71(3):209–49. doi: 10.3322/caac.21660

2. Arora K, Barbieri CE. Molecular subtypes of prostate cancer. *Curr Oncol Rep* (2018) 20(8):58. doi: 10.1007/s11912-018-0707-9

3. Klein EA, Ciezki J, Kupelian PA, Mahadevan A. Outcomes for intermediate risk prostate cancer: are there advantages for surgery, external radiation, or brachytherapy? *Urol Oncol* (2009) 27(1):67–71. doi: 10.1016/j.urolonc.2008.04.001

4. Knudsen KE. Penning TM. partners in crime: deregulation of AR activity and androgen synthesis in prostate cancer. *Trends Endocrinol Metab TEM.* (2010) 21 (5):315–24. doi: 10.1016/j.tem.2010.01.002

5. Boutros PC, Fraser M, Harding NJ, de Borja R, Trudel D, Lalonde E, et al. Spatial genomic heterogeneity within localized, multifocal prostate cancer. *Nat Genet* (2015) 47(7):736–45. doi: 10.1038/ng.3315

6. Shah RB, Mehra R, Chinnaiyan AM, Shen R, Ghosh D, Zhou M, et al. Androgen-independent prostate cancer is a heterogeneous group of diseases: lessons from a rapid autopsy program. *Cancer Res* (2004) 64(24):9209–16. doi: 10.1158/0008-5472.CAN-04-2442

7. Mateo J, Fizazi K, Gillessen S, Heidenreich A, Perez-Lopez R, Oyen WJG, et al. Managing nonmetastatic castration-resistant prostate cancer. *Eur Urol.* (2019) 75 (2):285–93. doi: 10.1016/j.eururo.2018.07.035

8. Le DT, Durham JN, Smith KN, Wang H, Bartlett BR, Aulakh LK, et al. Mismatch repair deficiency predicts response of solid tumors to PD-1 blockade. *Science* (2017) 357(6349):409–13. doi: 10.1126/science.aan6733

9. *Research c for DE and. FDA grants accelerated approval to pembrolizumab for first tissue/site agnostic indication*. FDA (2019). Available at: https://www.fda.gov/drugs/resources-information-approved-drugs/fda-grants-accelerated-approval-pembrolizumab-first-tissuesite-agnostic-indication.

10. *Research c for DE and. FDA approves olaparib for HRR gene-mutated metastatic castration-resistant prostate cancer*. FDA (2021). Available at: https://www.fda.gov/drugs/resources-information-approved-drugs/fda-approves-olaparib-hrr-gene-mutated-metastatic-castration-resistant-prostate-cancer.

11. Hidalgo M, Amant F, Biankin AV, Budinská E, Byrne AT, Caldas C, et al. Patient-derived xenograft models: an emerging platform for translational cancer research. *Cancer Discovery* (2014) 4(9):998–1013. doi: 10.1158/2159-8290.CD-14-0001

12. Namekawa T, Ikeda K, Horie-Inoue K, Inoue S. Application of prostate cancer models for preclinical study: advantages and limitations of cell lines, patient-derived xenografts, and three-dimensional culture of patient-derived cells. *Cells* (2019) 8(1): E74. doi: 10.3390/cells8010074

13. Tentler JJ, Tan AC, Weekes CD, Jimeno A, Leong S, Pitts TM, et al. Patient-derived tumour xenografts as models for oncology drug development. *Nat Rev Clin Oncol* (2012) 9(6):338–50. doi: 10.1038/nrclinonc.2012.61

14. Garber K. From human to mouse and back: "Tumorgraft" models surge in popularity. *JNCI J Natl Cancer Inst* (2009) 101(1):6–8. doi: 10.1093/jnci/djn481

15. Collins AT, Lang SH. A systematic review of the validity of patient derived xenograft (PDX) models: the implications for translational research and personalised medicine. *PeerJ* (2018) 6:e5981. doi: 10.7717/peerj.5981

16. Davies AH, Wang Y, Zoubeidi A. Patient-derived xenografts: a platform for accelerating translational research in prostate cancer. *Mol Cell Endocrinol* (2018) 462:17–24. doi: 10.1016/j.mce.2017.03.013

17. Nguyen HM, Vessella RL, Morrissey C, Brown LG, Coleman IM, Higano CS, et al. LuCaP prostate cancer patient-derived xenografts reflect the molecular heterogeneity of advanced disease and serve as models for evaluating cancer therapeutics. *Prostate* (2017) 77(6):654–71. doi: 10.1002/pros.23313

18. Risbridger GP, Clark AK, Porter LH, Toivanen R, Bakshi A, Lister NL, et al. The MURAL collection of prostate cancer patient-derived xenografts enables discovery through preclinical models of uro-oncology. *Nat Commun* (2021) 12(1):5049. doi: 10.1038/s41467-021-25175-5

19. Karkampouna S, La Manna F, Benjak A, Kiener M, De Menna M, Zoni E, et al. Patient-derived xenografts and organoids model therapy response in prostate cancer. *Nat Commun* (2021) 12(1):1117. doi: 10.1038/s41467-021-21300-6

20. Van Hemelryk A, Tomljanovic I, de Ridder CMA, Stuurman DC, Teubel WJ, Erkens-Schulze S, et al. Patient-derived xenografts and organoids recapitulate castration-resistant prostate cancer with sustained androgen receptor signaling. *Cells* (2022) 11(22):3632. doi: 10.3390/cells11223632

21. Lang H, Béraud C, Bethry A, Danilin S, Lindner V, Coquard C, et al. Establishment of a large panel of patient-derived preclinical models of human renal cell carcinoma. *Oncotarget* (2016) 7(37):59336–59. doi: 10.18632/oncotarget.10659

22. Lang H, Béraud C, Cabel L, Fontugne J, Lassalle M, Krucker C, et al. Integrated molecular and pharmacological characterization of patient-derived xenografts from bladder and ureteral cancers identifies new potential therapies. *Front Oncol* (2022) 12:930731. doi: 10.3389/fonc.2022.930731

23. Conway T, Wazny J, Bromage A, Tymms M, Sooraj D, Williams ED, et al. Xenome–a tool for classifying reads from xenograft samples. *Bioinforma Oxf Engl* (2012) 28(12):i172–178. doi: 10.1093/bioinformatics/bts236

24. Li H, Durbin R. Fast and accurate short read alignment with burrows-wheeler transform. *Bioinforma Oxf Engl* (2009) 25(14):1754–60. doi: 10.1093/bioinformatics/btp324

25. Tarasov A, Vilella AJ, Cuppen E, Nijman IJ, Prins P. Sambamba: fast processing of NGS alignment formats. *Bioinforma Oxf Engl* (2015) 31(12):2032–4. doi: 10.1093/bioinformatics/btv098

26. McKenna A, Hanna M, Banks E, Sivachenko A, Cibulskis K, Kernytsky A, et al. The genome analysis toolkit: a MapReduce framework for analyzing next-generation DNA sequencing data. *Genome Res* (2010) 20(9):1297–303. doi: 10.1101/gr.107524.110

27. McLaren W, Gil L, Hunt SE, Riat HS, Ritchie GRS, Thormann A, et al. The ensembl variant effect predictor. *Genome Biol* (2016) 17(1):122. doi: 10.1186/s13059-016-0974-4

28. Armenia J, Wankowicz SAM, Liu D, Gao J, Kundra R, Reznik E, et al. The long tail of oncogenic drivers in prostate cancer. *Nat Genet* (2018) 50(5):645–51. doi: 10.1038/s41588-018-0078-z

29. Popova T, Manié E, Stoppa-Lyonnet D, Rigaill G, Barillot E, Stern MH. Genome alteration print (GAP): a tool to visualize and mine complex cancer genomic profiles obtained by SNP arrays. *Genome Biol* (2009) 10(11):R128. doi: 10.1186/gb-2009-10-11-r128

30. Nicorici D, Şatalan M, Edgren H, Kangaspeska S, Murumägi A, Kallioniemi O, et al. FusionCatcher – a tool for finding somatic fusion genes in paired-end RNA-sequencing data. *bioRxiv* (2014), 011650. doi: 10.1101/011650v1

31. Haas BJ, Dobin A, Stransky N, Li B, Yang X, Tickle T, et al. STAR-fusion: fast and accurate fusion transcript detection from RNA-seq. *bioRxiv* (2017), 120295. doi: 10.1101/120295v1

32. Haas BJ, Dobin A, Ghandi M, Arsdale AV, Tickle T, Robinson JT, et al. Targeted in silico characterization of fusion transcripts in tumor and normal tissues *via* FusionInspector. *bioRxiv* (2021), 2021.08.02.454639. doi: 10.1101/2021.08.02.454639v1

33. Gao H, Korn JM, Ferretti S, Monahan JE, Wang Y, Singh M, et al. High-throughput screening using patient-derived tumor xenografts to predict clinical trial drug response. *Nat Med* (2015) 11):1318–25. doi: 10.1038/nm.3954

34. Zack TI, Schumacher SE, Carter SL, Cherniack AD, Saksena G, Tabak B, et al. Pan-cancer patterns of somatic copy number alteration. *Nat Genet* (2013) 45(10):1134–40. doi: 10.1038/ng.2760

35. Beroukhim R, Mermel CH, Porter D, Wei G, Raychaudhuri S, Donovan J, et al. The landscape of somatic copy-number alteration across human cancers. *Nature* (2010) 463(7283):899–905. doi: 10.1038/nature08822

36. Sakthianandeswaren A, Parsons MJ, Mouradov D, MacKinnon RN, Catimel B, Liu S, et al. MACROD2 haploinsufficiency impairs catalytic activity of PARP1 and promotes chromosome instability and growth of intestinal tumors. *Cancer Discov* (2018) 8(8):988–1005. doi: 10.1158/2159-8290.CD-17-0909

37. Lecona E, Fernandez-Capetillo O. Targeting ATR in cancer. *Nat Rev Cancer*. (2018) 18(9):586–95. doi: 10.1038/s41568-018-0034-3

38. Valles GJ, Bezsonova I, Woodgate R, Ashton NW. USP7 is a master regulator of genome stability. *Front Cell Dev Biol* (2020) 8:717. doi: 10.3389/fcell.2020.00717

39. Azmi AS, Uddin MH, Mohammad RM. The nuclear export protein XPO1 {{/amp]]mdash; from biology to targeted therapy. *Nat Rev Clin Oncol* (2021) 18 (3):152–69. doi: 10.1038/s41571-020-00442-4

40. Liu S, Wang W, Zhao Y, Liang K, Huang Y. Identification of potential key genes for pathogenesis and prognosis in prostate cancer by integrated analysis of gene expression profiles and the cancer genome atlas. *Front Oncol* (2020) 10:809. doi: 10.3389/fonc.2020.00809

41. Beltran H, Prandi D, Mosquera JM, Benelli M, Puca L, Cyrta J, et al. Divergent clonal evolution of castration-resistant neuroendocrine prostate cancer. *Nat Med* (2016) 22(3):298–305. doi: 10.1038/nm.4045

42. Xu H, Chen Y, Gu M, Liu C, Chen Q, Zhan M, et al. Fatty acid metabolism reprogramming in advanced prostate cancer. *Metabolites* (2021) 11(11):765. doi: 10.3390/metabo11110765

43. Chetta P, Zadra G. Metabolic reprogramming as an emerging mechanism of resistance to endocrine therapies in prostate cancer. *Cancer Drug Resist* (2021) 4 (1):143–62. doi: 10.20517/cdr.2020.54

44. Xu L, Zhao B, Butler W, Xu H, Song N, Chen X, et al. Targeting glutamine metabolism network for the treatment of therapy-resistant prostate cancer. *Oncogene* (2022) 41(8):1140–54. doi: 10.1038/s41388-021-02155-z

45. Fidelito G, Watt MJ, Taylor RA. Personalized medicine for prostate cancer: is targeting metabolism a reality? *Front Oncol* (2022) 11:778761. doi: 10.3389/fonc.2021.778761

46. Tessem MB, Bertilsson H, Angelsen A, Bathen TF, Drabløs F, Rye MB. A balanced tissue composition reveals new metabolic and gene expression markers in prostate cancer. *PloS One* (2016) 11(4):e0153727. doi: 10.1371/journal.pone.0153727

47. Latonen L, Afyounian E, Jylhä A, Nättinen J, Aapola U, Annala M, et al. Integrative proteomics in prostate cancer uncovers robustness against genomic and transcriptomic aberrations during disease progression. *Nat Commun* (2018) 9(1):1176. doi: 10.1038/s41467-018-03573-6

48. Chen L, Guo L, Sun Z, Yang G, Guo J, Chen K, et al. Monoamine oxidase a is a major mediator of mitochondrial homeostasis and glycolysis in gastric cancer progression. *Cancer Manag Res* (2020) 12:8023–35. doi: 10.2147/CMAR.S257848

49. Ahmad F, Cherukuri MK, Choyke PL. Metabolic reprogramming in prostate cancer. *Br J Cancer*. (2021) 125(9):1185–96. doi: 10.1038/s41416-021-01435-5

50. Ohishi T, Abe H, Sakashita C, Saqib U, Baig MS, Ohba Si, et al. Inhibition of mitochondria ATP synthase suppresses prostate cancer growth through reduced insulin-like growth factor-1 secretion by prostate stromal cells. *Int J Cancer*. (2020) 146(12):3474–84. doi: 10.1002/ijc.32959

51. Chen CL, Lin CY, Kung HJ. Targeting mitochondrial OXPHOS and their regulatory signals in prostate cancers. *Int J Mol Sci* (2021) 22(24):13435. doi: 10.3390/ijms222413435

52. Kushwaha PP, Gupta S. New insights for drug resistance in metastatic castration-resistant prostate cancer. *Cancer Drug Resist* (2022) 5(3):846–9. doi: 10.20517/cdr.2022.83

53. Choi SYC, Ettinger SL, Lin D, Xue H, Ci X, Nabavi N, et al. Targeting MCT4 to reduce lactic acid secretion and glycolysis for treatment of neuroendocrine prostate cancer. *Cancer Med* (2018) 7(7):3385–92. doi: 10.1002/cam4.1587

54. Gao B, Lue HW, Podolak J, Fan S, Zhang Y, Serawat A, et al. Multi-omics analyses detail metabolic reprogramming in lipids, carnitines, and use of glycolytic intermediates between prostate small cell neuroendocrine carcinoma and prostate adenocarcinoma. *Metabolites* (2019) 9(5):E82. doi: 10.3390/metabo9050082

55. Xu H, Li S, Sun Y, Xu L, Hong X, Wang Z, et al. ELOVL5-mediated long chain fatty acid elongation contributes to enzalutamide resistance of prostate cancer. *Cancers* (2021) 13(16):3957. doi: 10.3390/cancers13163957

56. Xu L, Yin Y, Li Y, Chen X, Chang Y, Zhang H, et al. A glutaminase isoform switch drives therapeutic resistance and disease progression of prostate cancer. *Proc Natl Acad Sci U S A*. (2021) 118(13):e2012748118. doi: 10.1073/pnas.2012748118

57. Joshi M, Kim J, D'Alessandro A, Monk E, Bruce K, Elajaili H, et al. CPT1A over-expression increases reactive oxygen species in the mitochondria and promotes antioxidant defenses in prostate cancer. *Cancers* (2020) 12(11):3431. doi: 10.3390/cancers12113431

58. Labrecque MP, Alumkal JJ, Coleman IM, Nelson PS, Morrissey C. The heterogeneity of prostate cancers lacking AR activity will require diverse treatment approaches. *Endocr Relat Cancer* (2021) 28(8):T51–66. doi: 10.1530/ERC-21-0002

59. Cejas P, Xie Y, Font-Tello A, Lim K, Syamala S, Qiu X, et al. Subtype heterogeneity and epigenetic convergence in neuroendocrine prostate cancer. *Nat Commun* (2021) 12(1):5775. doi: 10.1038/s41467-021-26042-z

60. Brady L, Nelson PS. Heterogeneity and the tumor microenvironment in neuroendocrine prostate cancer. *J Endocrinol* (2022) 256(2):e220211. doi: 10.1530/JOE-22-0211

61. Zhang W, Girard L, Zhang YA, Haruki T, Papari-Zareei M, Stastny V, et al. Small cell lung cancer tumors and preclinical models display heterogeneity of neuroendocrine phenotypes. *Transl Lung Cancer Res* (2018) 7(1):32–49. doi: 10.21037/tlcr.2018.02.02

62. Puca L, Vlachostergios PJ, Beltran H. Neuroendocrine differentiation in prostate cancer: emerging biology, models, and therapies. *Cold Spring Harb Perspect Med* (2019) 9(2):a030593. doi: 10.1101/cshperspect.a030593

63. Davies AH, Beltran H, Zoubeidi A. Cellular plasticity and the neuroendocrine phenotype in prostate cancer. *Nat Rev Urol*. (2018) 15(5):271–86. doi: 10.1038/nrurol.2018.22

64. Uo T, Sprenger CC, Plymate SR. Androgen receptor signaling and metabolic and cellular plasticity during progression to castration resistant prostate cancer. *Front Oncol* (2020) 10:580617. doi: 10.3389/fonc.2020.580617

65. Woo XY, Srivastava A, Mack PC, Graber JH, Sanderson BJ, Lloyd MW, et al. A genomically and clinically annotated patient derived xenograft (PDX) resource for preclinical research in non-small cell lung cancer. *Cancer Res* (2022) 82(22):4126–38. doi: 10.1158/0008-5472.CAN-22-0948

66. Aggarwal R, Zhang T, Small EJ, Armstrong AJ. Neuroendocrine prostate cancer: subtypes, biology, and clinical outcomes. *J Natl Compr Cancer Netw JNCCN*. (2014) 12 (5):719–26. doi: 10.6004/jnccn.2014.0073

67. Spetsieris N, Boukovala M, Patsakis G, Alafis I, Efstathiou E. Neuroendocrine and aggressive-variant prostate cancer. *Cancers* (2020) 12(12):3792. doi: 10.3390/cancers12123792

68. Abida W, Bryce AH, Balar AV, Chatta GS, Dawson NA, Guancial EA, et al. TRITON2: an international, multicenter, open-label, phase II study of the PARP inhibitor rucaparib in patients with metastatic castration-resistant prostate cancer (mCRPC) associated with homologous recombination deficiency (HRD). *J Clin Oncol* (2018) 36(6_suppl):TPS388–8. doi: 10.1200/JCO.2018.36.6_suppl.TPS388

69. Mateo J, Porta N, Bianchini D, McGovern U, Elliott T, Jones R, et al. Olaparib in patients with metastatic castration-resistant prostate cancer with DNA repair gene

aberrations (TOPARP-b): a multicentre, open-label, randomised, phase 2 trial. *Lancet Oncol* (2020) 21(1):162–74. doi: 10.1016/S1470-2045(19)30684-9

70. de Bono J, Mateo J, Fizazi K, Saad F, Shore N, Sandhu S, et al. Olaparib for metastatic castration-resistant prostate cancer. *N Engl J Med* (2020) 382(22):2091–102. doi: 10.1056/NEJMoa1911440

71. Clarke N, Wiechno P, Alekseev B, Sala N, Jones R, Kocak I, et al. Olaparib combined with abiraterone in patients with metastatic castration-resistant prostate cancer: a randomised, double-blind, placebo-controlled, phase 2 trial. *Lancet Oncol* (2018) 19(7):975–86. doi: 10.1016/S1470-2045(18)30365-6

72. PDXNET Consortium and EurOPDX Consortium, Woo XY, Giordano J, Srivastava A, Zhao ZM, et al. Conservation of copy number profiles during engraftment and passaging of patient-derived cancer xenografts. *Nat Genet* (2021) 53 (1):86–99. doi: 10.1038/s41588-020-00750-6

73. Bhimani J, Ball K, Stebbing J. Patient-derived xenograft models–the future of personalised cancer treatment. *Br J Cancer*. (2020) 122(5):601–2. doi: 10.1038/s41416-019-0678-0

74. Yoshida GJ. Applications of patient-derived tumor xenograft models and tumor organoids. *J Hematol OncolJ Hematol Oncol* (2020) 13(1):4. doi: 10.1186/s13045-019-0829-z

75. Lin D, Wyatt AW, Xue H, Wang Y, Dong X, Haegert A, et al. High fidelity patient-derived xenografts for accelerating prostate cancer discovery and drug development. *Cancer Res* (2014) 74(4):1272–83. doi: 10.1158/0008-5472.CAN-13-2921-T

76. Risbridger GP, Taylor RA. Patient-derived prostate cancer: from basic science to the clinic. *Horm Cancer*. (2016) 7(4):236–40. doi: 10.1007/s12672-016-0266-1

77. Navone NM, van Weerden WM, Vessella RL, Williams ED, Wang Y, Isaacs JT, et al. Movember GAP1 PDX project: an international collection of serially transplantable prostate cancer patient-derived xenograft (PDX) models. *Prostate*. (2018) 78(16):1262–82. doi: 10.1002/pros.23701

78. Schleicher EM, Galvan AM, Imamura-Kawasawa Y, Moldovan GL, Nicolae CM. PARP10 promotes cellular proliferation and tumorigenesis by alleviating replication stress. *Nucleic Acids Res* (2018) 46(17):8908–16. doi: 10.1093/nar/gky658

79. Wu YM, Cieślik M, Lonigro RJ, Vats P, Reimers MA, Cao X, et al. Inactivation of CDK12 delineates a distinct immunogenic class of advanced prostate cancer. *Cell* (2018) 173(7):1770–1782.e14. doi: 10.1016/j.cell.2018.04.034

80. Abida W, Campbell D, Patnaik A, Shapiro JD, Sautois B, Vogelzang NJ, et al. Non-BRCA DNA damage repair gene alterations and response to the PARP inhibitor rucaparib in metastatic castration-resistant prostate cancer: analysis from the phase II TRITON2 study. *Clin Cancer Res Off J Am Assoc Cancer Res* (2020) 11):2487–96. doi: 10.1158/1078-0432.CCR-20-0394

81. Salem ME, Bodor JN, Puccini A, Xiu J, Goldberg RM, Grothey A, et al. Relationship between MLH1, PMS2, MSH2 and MSH6 gene-specific alterations and tumor mutational burden in 1057 microsatellite instability-high solid tumors. *Int J Cancer*. (2020) 147(10):2948–56. doi: 10.1002/ijc.33115

82. Navas T, Kinders RJ, Lawrence SM, Ferry-Galow KV, Borgel S, Hollingshead MG, et al. Clinical evolution of epithelial-mesenchymal transition in human carcinomas. *Cancer Res* (2020) 80(2):304–18. doi: 10.1158/0008-5472.CAN-18-3539

83. Puisieux A, Brabletz T, Caramel J. Oncogenic roles of EMT-inducing transcription factors. *Nat Cell Biol* (2014) 16(6):488–94. doi: 10.1038/ncb2976

84. Beltran H, Rickman DS, Park K, Chae SS, Sboner A, MacDonald TY, et al. Molecular characterization of neuroendocrine prostate cancer and identification of new drug targets. *Cancer Discovery* (2011) 1(6):487–95. doi: 10.1158/2159-8290.CD-11-0130

85. Bishop JL, Thaper D, Vahid S, Davies A, Ketola K, Kuruma H, et al. The master neural transcription factor BRN2 is an androgen receptor-suppressed driver of neuroendocrine differentiation in prostate cancer. *Cancer Discov* (2017) 7(1):54–71. doi: 10.1158/2159-8290.CD-15-1263

86. Kim KH, Roberts CWM. Targeting EZH2 in cancer. *Nat Med* (2016) 22(2):128–34. doi: 10.1038/nm.4036

87. Stine ZE, Schug ZT, Salvino JM, Dang CV. Targeting cancer metabolism in the era of precision oncology. *Nat Rev Drug Discovery* (2022) 21(2):141–62. doi: 10.1038/s41573-021-00339-6

88. Frégeau-Proulx L, Lacouture A, Berthiaume L, Weidmann C, Harvey M, Gonthier K, et al. Multiple metabolic pathways fuel the truncated tricarboxylic acid cycle of the prostate to sustain constant citrate production and secretion. *Mol Metab* (2022) 62:101516. doi: 10.1016/j.molmet.2022.101516

89. Molina JR, Sun Y, Protopopova M, Gera S, Bandi M, Bristow C, et al. An inhibitor of oxidative phosphorylation exploits cancer vulnerability. *Nat Med* (2018) 24 (7):1036–46. doi: 10.1038/s41591-018-0052-4

90. Gu Y, Xue M, Wang Q, Hong X, Wang X, Zhou F, et al. Novel strategy of proxalutamide for the treatment of prostate cancer through coordinated blockade of lipogenesis and androgen receptor axis. *Int J Mol Sci* (2021) 22(24):13222. doi: 10.3390/ijms222413222

91. Shah S, Carriveau WJ, Li J, Campbell SL, Kopinski PK, Lim HW, et al. Targeting ACLY sensitizes castration-resistant prostate cancer cells to AR antagonism by impinging on an ACLY-AMPK-AR feedback mechanism. *Oncotarget* (2016) 7 (28):43713–30. doi: 10.18632/oncotarget.9666

92. Choi SYC, Ribeiro CF, Wang Y, Loda M, Plymate SR, Uo T. Druggable metabolic vulnerabilities are exposed and masked during progression to castration resistant prostate cancer. *Biomolecules* (2022) 12(11):1590. doi: 10.3390/biom12111590

Frontiers in Oncology

Advances knowledge of carcinogenesis and tumor progression for better treatment and management

The third most-cited oncology journal, which highlights research in carcinogenesis and tumor progression, bridging the gap between basic research and applications to imrpove diagnosis, therapeutics and management strategies.

Discover the latest Research Topics

See more →

Frontiers

Avenue du Tribunal-Fédéral 34
1005 Lausanne, Switzerland
frontiersin.org

Contact us

+41 (0)21 510 17 00
frontiersin.org/about/contact